Human induced pluripotent stem cells (iPSCs) in inherited cardiomyopathies: Generation and characterization of an iPSC-derived cardiomyocyte model system of dilated cardiomyopathy with ataxia (DCMA)

Humane induzierte pluripotente Stammzellen in vererbbaren Kardiomyopathien: Generierung und Charakterisierung eines auf Stammzellen basierenden Herzmuskelmodellsystems der Dilatativen Kardiomyopathie mit Ataxie (DCMA)

Thesis

for the conferral of the degree

"*Doctor rerum naturalis*" (Dr.rer.nat.)

at the Graduate School of Life Sciences, Section Biomedicine

Julius-Maximilians-Universität Würzburg

submitted by

Anna Janz

born in Talas, Kirgisistan

Würzburg, 2021

Submitted on: ……

Office stamp

Members of the Promotion Committee (“*Promotionskomitee”)*:

Chairperson:	Prof. Dr. Carmen Villmann
Primary Supervisor:	Prof. Dr. Brenda Gerull
Second Supervisor:	Prof. Dr. Eva Klopocki
Third Supervisor:	Prof. Dr. Süleyman Ergün
Fourth Supervisor:	Prof. Dr. Frank Edenhofer
Date of Public Defense:	……...
Date of Receipt of Certificates:	……

dedicated to my family

List of Contents

Summary

The emergence of human induced pluripotent stem cells (iPSCs) and the rise of the clustered regularly interspaced short palindromic repeats/CRISPR-associated protein 9 (CRISPR/Cas9) gene editing technology innovated the research platform for scientists based on living human pluripotent cells. The revolutionary combination of both Nobel Prize-honored techniques enables direct disease modeling especially for research focused on genetic diseases. To allow the study on mutation-associated pathomechanisms, we established robust human *in vitro* systems of three inherited cardiomyopathies: arrhythmogenic cardiomyopathy (ACM), dilated cardiomyopathy with juvenile cataract (DCMJC) and dilated cardiomyopathy with ataxia (DCMA).

Sendai virus vectors encoding OCT3/4, SOX2, KLF4, and c-MYC were used to reprogram human healthy control or mutation-bearing dermal fibroblasts from patients to an embryonic state thereby allowing the robust and efficient generation of in total five transgene-free iPSC lines. The nucleofection-mediated CRISPR/Cas9 plasmid delivery in healthy control iPSCs enabled precise and efficient genome editing by mutating the respective disease genes to create isogenic mutant control iPSCs. Here, a PKP2 knock-out and a DSG2 knock-out iPSC line were established to serve as a model of ACM. Moreover, a DNAJC19 C-terminal truncated variant (DNAJC19tv) was established to mimic a splice acceptor site mutation in DNAJC19 of two patients with the potential of recapitulating DCMA-associated phenotypes. In total eight self-generated iPSC lines were assessed matching internationally defined quality control criteria. The cells retained their ability to differentiate into cells of all three germ layers *in vitro* and maintained a stable karyotype. All iPSC lines exhibited a typical stem cell-like morphology as well as expression of characteristic pluripotency markers with high population purities, thus validating the further usage of all iPSC lines in *in vitro* systems of ACM, DCMA and DCMJC.

Furthermore, cardiac-specific disease mechanisms underlying DCMA were investigated using *in vitro* generated iPSC-derived cardiomyocytes (iPSC-CMs). DCMA is an autosomal recessive disorder characterized by life threatening early onset cardiomyopathy associated with a metabolic syndrome. Causal mutations were identified in the *DNAJC19* gene encoding an inner mitochondrial membrane (IMM) protein with a presumed function in mitochondrial biogenesis and cardiolipin (CL) remodeling. In total, two DCMA patient-derived iPSC lines (DCMAP1, DCMAP2) of siblings with discordant cardiac phenotypes, a third isogenic mutant control iPSC line (DNAJC19tv) as well as two control lines (NC6M and NC47F) were directed towards the cardiovascular lineage upon response to extracellular specification cues. The monolayer cardiac differentiation approach was successfully adapted for all five iPSC lines and optimized towards ventricular subtype identity, higher population purities and enhanced maturity states to fulfill all DCMA-specific requirements prior to phenotypic investigations. To provide a solid basis for the study of DCMA, the combination of lactate-based metabolic enrichment, magnetic-activated cell sorting, mattress-based cultivation and prolonged cultivation time was performed in an approach-dependent manner. The application of the designated strategies was sufficient to ensure adult-like characteristics, which included at least 60-day-old iPSC-CMs. Therefore, the novel human DCMA platform was established to enable the study of the pathogenesis underlying DCMA with respect to structural, morphological and functional changes.

The disease-associated protein, DNAJC19, is constituent of the TIM23 import machinery and can directly interact with PHB2, a component of the membrane bound hetero-oligomeric prohibitin ring complexes that are crucial for phospholipid and protein clustering in the IMM. *DNAJC19* mutations were predicted to cause a loss of the DnaJ interaction domain, which was confirmed by loss of full-length DNAJC19 protein in all mutant cell lines. The subcellular investigation of DNAJC19 demonstrated a nuclear restriction in mutant iPSC-CMs. The loss of DNAJC19 co-localization with mitochondrial structures was accompanied by enhanced fragmentation, an overall reduction of mitochondrial mass and smaller cardiomyocytes. Ultrastructural analysis yielded decreased mitochondria sizes and abnormal cristae providing a link to defects in mitochondrial biogenesis and CL remodeling. Preliminary data on CL profiles revealed longer acyl chains and a more unsaturated acyl chain composition highlighting abnormities in the phospholipid maturation in DCMA.

However, the assessment of mitochondrial function in iPSCs and dermal fibroblasts revealed an overall higher oxygen consumption that was even more enhanced in iPSC-CMs when comparing all three mutants to healthy controls. Excess oxygen consumption rates indicated a higher electron transport chain (ETC) activity to meet cellular ATP demands that probably result from proton leakage or the decoupling of the ETC complexes provoked by abnormal CL embedding in the IMM.

Moreover, in particular iPSC-CMs presented increased extracellular acidification rates that indicated a shift towards the utilization of other substrates than fatty acids, such as glucose, pyruvate or glutamine. The examination of metabolic features via double radioactive tracer uptakes (^{18}F-FDG, ^{125}I-BMIPP) displayed significantly decreased fatty acid uptake in all mutants that was accompanied by increased glucose uptake in one patient cell line only, underlining a highly dynamic preference of substrates between mutant iPSC-CMs.

To connect molecular changes directly to physiological processes, insights on calcium kinetics, contractility and arrhythmic potential were assessed and unraveled significantly increased beating frequencies, elevated diastolic calcium concentrations and a shared trend towards reduced cell shortenings in all mutant cell lines basally and upon isoproterenol stimulation. Extended speed of recovery was seen in all mutant iPSC-CMs but most striking in one patient-derived iPSC-CM model, that additionally showed significantly prolonged relaxation times. The investigations of calcium transient shapes pointed towards enhanced arrhythmic features in mutant cells comprised by both the occurrence of DADs/EADs and fibrillation-like events with discordant preferences.

Taken together, new insights into a novel *in vitro* model system of DCMA were gained to study a genetically determined cardiomyopathy in a patient-specific manner upon incorporation of an isogenic mutant control. Based on our results, we suggest that loss of full-length DNAJC19 impedes PHB2-complex stabilization within the IMM, thus hindering PHB-rings from building IMM-specific phospholipid clusters. These clusters are essential to enable normal CL remodeling during cristae morphogenesis. Disturbed cristae and mitochondrial fragmentation were observed and refer to an essential role of DNAJC19 in mitochondrial morphogenesis and biogenesis. Alterations in mitochondrial morphology are generally linked to reduced ATP yields and aberrant reactive oxygen species production thereby having fundamental downstream effects on the cardiomyocytes` functionality. DCMA-associated cellular dysfunctions were in particular manifested in excess oxygen consumption, altered substrate utilization and abnormal calcium kinetics. The summarized data highlight the usage of human iPSC-derived CMs as a powerful tool to recapitulate DCMA-associated phenotypes that offers an unique potential to identify therapeutic strategies in order to reverse the pathological process and to pave the way towards clinical applications for a personalized therapy of DCMA in the future.

Zusammenfassung

Die Entwicklung von induzierten pluripotenten Stammzellen (iPS-Zellen) und die biotechnologische Anwendung des „clustered regularly interspaced short palindromic repeats/CRISPR-associated protein 9“ (CRISPR/Cas9) Gen-Editierungssystems bilden eine innovative Forschungsplattform für Wissenschaftler basierend auf lebenden menschlichen pluripotenten Stammzellen. Die bahnbrechende Kombination beider nobelpreisprämierter Techniken erlaubt eine direkte Krankheitsmodellierung insbesondere für die Erforschung von genetisch bedingten Erkrankungen. Um die Untersuchung von mutationsassoziierten Pathomechanismen zu ermöglichen, etablierten wir robuste humane *in vitro* Systeme von drei vererbbaren Kardiomyopathien: die arrhythmogene Kardiomyopathie (AKM), die dilatative Kardiomyopathie mit juveniler Katarakt (DKMJK) und die dilatative Kardiomyopathie mit Ataxie (DKMA).

Zur Generierung von transgenfreien iPS-Zellen wurden für OCT3/4, SOX2, KLF4 und c-MYC kodierende Sendai-Virus-Vektoren verwendet um humane gesunde Kontroll- oder mutationstragende dermale Fibroblasten von Patienten in einen embryonalen Zustand zu reprogrammieren. Die Verwendung der SeV-vermittelten Reprogrammierung ermöglichte uns eine effiziente und robuste Herstellung von insgesamt fünf transgen-freien iPS-Zelllinien. Zudem befähigt die Nukleofektion der CRISPR/Cas9-Plasmide in gesunden Kontroll-iPS-Zellen eine präzise und effiziente Genom-Editierung krankheitsrelevanter Gene und damit die Generierung von isogenen mutierten iPS-Zelllinien. Mit diesem Verfahren wurden eine PKP2-Knock-out- und eine DSG2-Knock-out iPSZ-Linie hergestellt, die jeweils als Modell für AKM dienen. Darüber hinaus wurde eine mit DKMA-assoziierte Spleißakzeptormutation auf genetischer Basis imitiert, um die mit dem Phänotyp zweier Patienten in Verbindung gebrachte C-terminal verkürzte DNAJC19-Variante (DNAJC19tv) auf translationaler Ebene rekapitulieren zu können. Alle acht eigens generierten iPS-Zelllinien entsprachen international definierten Qualitätskontrollkriterien. Die hergestellten iPS-Zellen behielten die Fähigkeit *in vitro* in Zellen der drei Keimblätter zu differenzieren und zeigten darüber hinaus einen normalen Karyotyp. Alle iPS-Zelllinien wiesen eine typische stammzellähnliche Morphologie sowie die Expression charakteristischer Pluripotenzmarker bei gleichzeitig hoher Populationsreinheit auf. Die experimentelle Qualtitätskontrolle hat somit die weitere Verwendung aller iPS-Zelllinien in *in vitro* Systemen von AKM, DKMA und DKMJK validiert.

Die der DKMA zugrundeliegenden herzspezifischen Krankheitsmechanismen wurden zudem mithilfe von *in vitro* produzierten iPSZ-abgeleiteten Kardiomyozyten (iPSZ-KMs) untersucht. DKMA ist eine autosomal rezessiv vererbte Erkrankung, die durch Mutationen im DNAJC19 Gen hervorgerufen wird. Das wichtigste klinische Merkmal der Patienten ist eine früh einsetzende und lebensbedrohliche dilatative Kardiomyopathie, die oftmals mit einem metabolischen Syndrom einhergeht. DNAJC19 kodiert für ein Protein der inneren mitochondrialen Membran (IMM), dessen postulierte Funktion in der mitochondrialen Biogenese und der Remodellierung von Cardiolipin liegt. Zur Modellierung der DKMA wurden zwei von DKMA-Patienten abgeleitete iPS-Zelllinien (DCMAP1, DCMAP2) eines Geschwisterpaares mit unterschiedlich ausgeprägten kardialen Phänotypen, eine dritte isogene mutierte iPS-Zelllinie (DNAJC19tv) sowie zwei gesunden Kontroll-iPS-Zelllinien (NC6M und NC47F) mithilfe extrazellulärer Spezifikationsfaktoren zur kardiovaskulären Differenzierung angeregt.

Das Monolayer-Protokoll zur kardialen Differenzierung wurde erfolgreich für alle fünf iPSZ-Linien adaptiert und in Bezug auf die Anreicherung des ventrikulären Herzmuskelzellsubtyps, höhere Zellpopulationsreinheiten und adulte Reifegrade optimiert. Die Kombination der Laktat-basierten metabolischen Aufreinigung, der magnetisch-aktivierten Zellsortierung, der Anwendung einer Mattress-basierten Kultivierungsstrategie und verlängerte Kultivierungszeiten ermöglichte die Erfüllung aller DKMA-spezifischen Anforderungen. Zusammengefasst konnten insbesondere adulte Charakteristika durch die Kombination der benannten experimentellen Strategien unter Verwendung von mindestens 60 Tage kultivierten iPSZ-KMs nachgewiesen werden, um eine zuverlässige phänotypische Untersuchung der DKMA gewährleisten zu können. Die innovative humane Untersuchungsplattform

wurde etabliert, um die Pathogenese der DKMA im Hinblick auf strukturelle, morphologische und funktionelle Veränderungen entschlüsseln zu können.

Das mit DKMA assoziierte Protein DNAJC19 ist Bestandteil der TIM23-Importmaschinerie und besitzt zudem die Fähigkeit einer direkten Interaktion mit PHB2. PHB2 trägt zur Bildung der membrangebundenen hetero-oligomeren Prohibitin-Ringkomplexe bei, deren Hauptfunktion in der Anreicherung von Phospholipiden und Proteinen innerhalb von Clustern in der IMM liegt. Der durch DNAJC19 Mutationen vermutete hervorgerufenen Verlust der DnaJ-Interaktionsdomäne wurde durch die fehlende Expression des DNAJC19 Proteins in voller Länge in allen mutationstragenden Zellen bestätigt. Die subzelluläre Untersuchung von DNAJC19 zeigte ein auf den Kern beschränktes Expressionsmuster in mutierten iPSZ-KMs. Der Verlust der DNAJC19 Ko-Lokalisation mit mitochondrialen Strukturen ging mit einer abnormen mitochondrialen Fragmentierung, einer signifikanten Abnahme der mitochondrialen Masse und einer signifikant reduzierten Kardiomyozytengröße einher. Ultrastrukturelle Analysen ergaben zudem kleinere Mitochondrien und abnorme Cristae, die eine krankheitsrelevante Verbindung zu Defekten in der mitochondrialen Biogenese und der CL-Reifung darlegen. Vorläufige Daten zu CL-Profilen zeigten längere Acylketten und eine ungesättigtere Acylkettenzusammensetzung, was auf Anomalien in der Phospholipidmaturierung bei DKMA hinweist.

Der Vergleich aller Mutanten mit gesunden Kontrollen hinsichtlich der mitochondrialen Funktion in iPS-Zellen und Hautzellen (dermale Fibroblasten), zeigte eine insgesamt höhere Sauerstoffverbrauchsrate, die in iPSZ-KMs noch stärker ausgeprägt war. Der erhöhte Sauerstoffverbrauch deutet auf eine höhere Aktivität der Elektronentransportkette hin um den zellulären Energiebedarf decken zu können. Wir vermuten einen erhöhten Sauerstoffverbrauch als Konsequenz des Protonendurchsickerns oder der Entkopplung der ETC-Komplexe, das durch eine abnorme CL-Einbettung in der IMM bedingt sein könnte.

Darüber hinaus wiesen insbesondere iPSZ-KMs erhöhte extrazelluläre Säuerungsraten auf, die auf eine Verstoffwechselung anderer Substrate wie Glukose, Pyruvat oder Glutamin hinweisen, im Gegensatz zu der ansonsten bevorzugten Verstoffwechslung von Fettsäuren. Die Untersuchung der metabolischen Eigenschaften mittels der radioaktiven Tracer ^{18}F-FDG und ^{125}I-BMIPP zeigte eine signifikant verringerte Fettsäureaufnahme in allen Mutanten, die nur in einer Patientenzelllinie von einer erhöhten Glukoseaufnahme begleitet wurde. Diese Ergebnisse weisen auf eine DKMA-spezifische hochdynamische Präferenz der Substrate zwischen den unterschiedlichen Mutanten hin.

Um den Einfluss der molekularen Veränderungen direkt mit physiologischen Prozessen in Verbindung bringen zu können, wurden Untersuchungen der Kalziumkinetik, der Kontraktilität und des arrhythmischen Potentials durchgeführt. Einzelzellmessungen ergaben eine signifikant erhöhte Kontraktionsfrequenz, erhöhte diastolische Kalziumkonzentrationen und eine Tendenz zu reduzierten Zellverkürzungen in allen mutierten Zelllinien basal und verstärkt nach Isoproterenol-Stimulation. Zudem wurden verlangsamte Erholungsgeschwindigkeiten in allen mutierten iPSZ-KMs festgestellt, das in den iPSZ-KMs des einen Patienten besonders auffällig war und mit verlängerten Relaxationszeiten einherging. Die Evaluation der Kalziumtransientenformen deutet auf verstärkte arrhythmische Merkmale in den mutierten Zellen hin, die sowohl das Auftreten von DADs/EADs als auch Fibrillations-ähnlichen Ereignissen mit gegensätzlichen Präferenzen umfasste.

Insgesamt wurden unter der Verwendung patientenspezifischer iPS-Zellen und einer isogenen Mutantenkontrolle neue Einblicke in ein innovatives *in vitro* Modellsystem der DKMA gewonnen. Basierend auf unseren Ergebnissen vermuten wir, dass der Verlust des DNAJC19 Proteins in voller Länge die Stabilisierung von PHB-Komplexen innerhalb der IMM beeinträchtigt und damit PHB-Ringe an der Bildung von IMM-spezifischen Phospholipid-Clustern hindert. Diese Cluster sind essentiell um eine normale Cardiolipin-Reifung und dessen Funktion in der Cristae-Morphogenese gewährleisten zu können. Abnorme Cristae und fragmentierte mitochondriale Strukturen wurden beobachtet und deuten so auf eine essentielle Rolle von DNAJC19 in der mitochondrialen Morphogenese und Biogenese hin. Abnorme Veränderungen in der mitochondrialen Morphologie werden in der Regel mit einer

verminderten ATP-Verfügbarkeit und einer erhöhten Produktion an freien Sauerstoffradikalen assoziiert, das nachfolgend die gesamte Funktionalität der Kardiomyozyten negativ beeinflussen kann. Diese Veränderungen konnten anhand einer erhöhten Sauerstoffverbrauchsrate, unterschiedliche metabolische Eigenschaften und einer abnormalen Kalziumkinetik gemessen werden.

Die zusammengefassten Daten unterstreichen die Verwendbarkeit von humanen iPSZ-KMs als ein eindrucksvolles System zur Rekapitulation von herzspezifischen Phänotypen und haben damit neue Einblicke in die Pathogenese der DKMA ermöglicht. Das Modellsystem bietet ein einzigartiges Potenzial zur Identifizierung therapeutischer Strategien, um pathologische Prozesse umkehren zu können und so den Weg für zukünftige klinische Anwendungen im Rahmen der personalisierten Therapie zu ebnen.

List of Abbreviations

$(18:2)_4$	tetralinoleoyl cardiolipin
$[Ca^{2+}]_i$	intracellular calcium concentration
ΔμH	proton motive force
Δex4	transcript variant lacking exon 4
ΔpH	chemical potential (potential of hydrogen)
$\Delta\Psi_m$	mitochondrial membrane potential
°C	degree celsius
µl	microliter
µm	micrometer
µM	micromolar
^{125}I-BMIPP	^{125}I-β-methyl-iodophenyl-pentadecanoic acid
$^{13}C_{16}$	palmitate
^{18}F-FDG	^{18}F-2-fluoro-2-deoxy-d-glucose
2D	two-dimensional
3D	three-dimensional
3-MAG	3-methylglutaconic aciduria
4-HNE	4-hydroxy-trans-2-nonenal
Å	Ångström
aa	amino acid
AAV	adeno-associated viruses
acetyl-CoA	acetyl coenzyme A
ACM	arrhythmogenic cardiomyopathy
ADP	adenosine diphosphate
AFG3L2	ATPase family gene 3-like 2
AFP	α-1-fetoprotein
AGPAT2	1-acylglycerol-3-phosphate O-acyltransferase 2
ALCAT1	acyl-CoA:lysocardiolipin acyltransferase
AMD	age-related macular degeneration
ANK1	ankyrin 1
AP	action potential
ATP	adenosine triphosphate
ATP synthase, complex V	F_1F_O-ATP synthase
BAF	barrier-to-autointegration factor
BF	bright field
bFGF	basic fibroblast growth factor
BMP4	bone morphogenic protein 4
BN-PAGE	Blue Native Polyacrylamide Gel Electrophoresis
bp	base pairs
BSA	bovine serum albumin
BTHS	Barth syndrome

C	colony
Ca^{2+}	calcium ions
CAPZB	capping actin protein of muscle Z-line subunit beta
$Ca_v1.2$ / LTCC	L-(low threshold type) calcium channels (*CACNA1C*)
CCDC178	coiled-coil domain containing 178
cDNA	complementary DNA
CEM	cardiac enrichment medium
CETN1	centrin 1
cGMP	current Good Manufacturing Practice
CHIR	CHIR99021(6-[[2-[[4-(2,4-dichlorophenyl)-5-(5-methyl-1*H*-imidazol-2-yl)-2-pyrimidinyl]amino]ethyl]amino]-3-pyridinecarbonitrile)
chr.	chromosome
CICR	calcium-induced calcium release
CL	cardiolipin
CM	cardiomyocytes
c-MYC	c-myelocytomatosis oncogene product (tumorigenic transcription factor)
CO_2	carbon dioxide
complex I	NADH-ubiquinone oxidoreductase
complex II	succinate dehydrogenase
complex III	cytochrome bc_1 complex
complex IV	cytochrome c oxidase
Cr	creatine
CRISPR/Cas9	clustered regularly interspaced short palindromic repeats/ CRISPR-associated protein 9
cTnC	cardiac troponin C (calcium binding)
cTnI	cardiac troponin I (inhibitory)
cTnT	cardiac troponin T (tropomyosin binding)
Cx43	connexin 43
DAD	delayed after depolarization
DAPI	4′,6-diamidino-2-phenylindole
DCM	dilated cardiomyopathy
DCMA	dilated cardiomyopathy with ataxia
DCMAP1	dilated cardiomyopathy with ataxia patient 1, 8-year old boy carrying the homozygous *DNAJC19* (NM_145261.4):c.130-1G>C
DCMAP2	dilated cardiomyopathy with ataxia patient 2,10-year old girl carrying the homozygous *DNAJC19* (NM_145261.4):c.130-1G>C
DCMJC	dilated cardiomyopathy with juvenile cataract
DMSO	dimethyl sulfoxide
DNA	deoxyribonucleic acid
DNAJC19	DnaJ heat shock protein family (Hsp40) member C19
DNAJC19tv	DNAJC19 truncation variant
Drp1	dynamin-related protein 1
DSB	double strand break

dsDNA	double stranded DNA
DSG2	desmoglein-2
DSG2-KO	desmoglein-2 knock-out
E	embryonic day
e^-	free electrons
EAD	early after depolarization
E-C coupling	excitation-contraction coupling
ECAR	extracellular acidification rate
ECG	electrocardiogram
EE	extra-embryonic tissue
eGFP	enhanced green fluorescent protein
ER	endoplasmatic reticulum
et al.	et alii (and others)
ETC	electron transport chain
FA	fatty acid
FABPm	membrane-associated fatty acid-binding protein
FACS	fluorescence-activated cell sorting
$FADH_2$	flavin adenine nucleotide
fa-ls	fascia adherens-like structures
FAT	fatty acid translocase (CD36)
FATP	fatty acid transporter proteins
FCCP	carbonyl cyanide-4(trifluoromethoxy) phenylhydrazone
Fig.	figure
g	gram
GAPDH	housekeeping gene (glyceraldehyde 3-phosphate dehydrogenase)
GLIPR2	GLI pathogenesis related 2
GLUT	glucose transporters
GRCh38.p13	Genome Reference Consortium Human Build 38 patch release 13
gRNA	guide RNA
GSK3	glycogen synthase kinase-3
h	hour
H_2CO_3	carbonic acid
H_2O_2	hydrogen peroxide, non-free oxigen radicals
HCM	hypertrophic cardiomyopathy
HDR	homology-directed repair
HEK293T	human embryonic kidney 293 cells containing SV40 T-antigen
hESCs	human embryonic stem cells
HIF1α	hypoxia-inducible factor 1-alpha
hPSCs	human pluripotent stem cells, superordinate term for human iPSCs and human ESCs
Hsp40	heat shock protein 40 kD
Hz	Hertz (1/sec)
ICD	internal cardioverter defibrillator
ICM	inner cell mass

IMM	inner mitochondrial membrane
iPLA2	calcium-independent phospholipase A2
iPSC-CMs	iPSC-derived cardiomyocytes
iPSCs	induced pluripotent stem cells
Iso	isoproterenol
IWR-1	tankyrase inhibitor (4-(1,3,3a,4,7,7a-hexahydro-1,3-dioxo-4,7-methano-2H-isoindol-2-yl)-N-8-quinolinyl-Benzamide)
JAKMIP1	janus kinase and microtubule interacting protein 1
JP2	junctophilin-2
kDa	kilodalton
KLF4	Kruppel-like factor 4
KMOS	Yamanaka factors: KLF4, C-MYC, OCT3/4 and SOX2
l	liter
LA, 18:2	linoleic acid
LC3	microtubule-associated protein 1A/1B-light chain 3
LCFA	long-chain fatty acid
LDHA	lactate dehydrogenase A
LEMD2	LEM-domain containing protein 2
LEMD2 p.L13R	male 38-year olf patient suffering from DCMJC carrying the homozygous *LEMD2* (NM_181336.4) c.38T>G (p.L13R) mutation
LeV	lentivirus
LIN28	Lin-28 homolog A
LMNA	lamin A/C
LQT1	long QT syndrome type 1
LQT2	long QT syndrome type 2
m-AAA proease	matrix-oriented AAA protease
mA	milliampere
MACS	magnetic-activated cell sorting
Mbq	megabecquerel
M-CK	cytosolic/myofilament creatine kinase
MCTs	monocarboxylic acid transporters
MCU	mitochondrial Ca^{2+} uniporter
MDa	megadalton
MEF	mouse embryonic fibroblasts (MEF feeder cells)
MEM NEAA	minimum essential medium non-essential amino acids
mESCs	mouse embryonic stem cells
MFN2	mitofusin-2
mg	miligrams
Mge	mitochondrial homolog of the prokaryotic heat shock protein GrpE
min	minutes
MINOS	mitochondrial inner membrane organizing system
mitoCK	mitochondrial creatine kinase
ml	milliliter
MLCL	monolyso-cardiolipin

MLCLAT1	monolyso-cardiolipin acyltransferase 1
mM	millimolar
MMS	mismatches
MOI	multiplicity of infection
mPTP	mitochondrial permeability transition pore
mRNA	messenger RNA
ms	millisecond
mtHsp70	mitochondrial heat shock protein 70
MTS	matrix targeting signal
MYH7	myosin heavy chain 7
nM	nanomolar
NADH	nicotinamide adenine dinucleotide
$Na_V1.5$	voltage-gated sodium channels (*SCN5A*)
n_{BR}	number of biological replicates
NC47F	normal control 47-year-old female
NC6M	normal control 6-year-old male
NCBI	National Biocenter for Biotechnology Information
NCX	Na^+/Ca^{2+} exchanger
NHEJ	non-homologous end-joining
nm	nanometer
NM_	accession number mRNA NCBI database
NP_	accession number protein NCBI database
nt	nucleotide
NT	normal tyrode
NTN3	netrin 3
n_{TR}	number of technical replicates (wells or cell numbers)
O_2^-	superoxide, free oxigen radicals
OCR	oxygen consumption rate
OCT3/4	octamer-binding transcription factor 3/4
OLIGO	oligomycin
OMA1	metalloendopeptidase OMA1
OMM	outer mitochondrial membrane
OPA1	optic atrophy protein-1 (mitochondrial dynamin like GTPase)
OXPHOS	mitochondrial oxidative phosphorylation
p.	passage number
PA	phosphatidic acid
PAM	protospacer adjacent motif
PAM18	presequence translocase-associated motor 18
PBS	phosphate buffer saline
PC	phosphatidylcholine
PCr	phosphocreatine
PE	phosphatidyl ehanolamine
PFA	paraformaldehyd

PHB2	prohibitin-2
PI	phosphatidylinositol
pK	pharmacokinetic value
PKP2	plakophilin-2
PKP2-KO	plakophilin-2 knock-out
PMCA	sarcolemmal Ca^{2+}-ATPases
pmol	picomole
pre-crRNA	long precursor CRISPR RNA
PS	phosphatidylserine
PTPN11	tyrosine-protein phosphatase non-receptor type 11
RI	ROCK inhibitor Y27632 (Rho associated kinase inhibitor)
RNA	ribonucleic acid
RNP complex	ribonucleoprotein complex
ROCK	rho kinase
ROS	reactive oxygen species
ROT&AA	rotenone and antimycin A
rpm	rounds per minute
RT	room temperature
RT-PCR	reverse transcription polymerase chain reaction
RYR2	ryanodine receptor
s	seconds
S. pyogenes	*Streptococcus pyogenes*
sc	subcolony
SEM	standard error of the mean
SERCA2a	sarco/endoplasmic reticulum Ca^{2+}-ATPase 2a
SeV	Sendai virus
sgRNA	single guide RNA
siRNA	small interfering RNA
SLC35B4	solute carrier family 35 member B4
SNPs	single nucleotide polymorphisms
SOX2	sex determining region Y-box 2
SpCas9	*Streptococcus pyogenes* Cas9
SR	sarcoplasmic reticulum
SSEA-4	stage-specific embryonic antigen 3&4
SSNs	single-strand-specific nucleases
ssODNs	single stranded donor oligonucleotide
STR	short tandem repeat
Tab.	table
TALEN	transcription activator like effector nucleases
TAZ	tafazzin
TCA cycle	tricarboxylic acid cycle
TEM	transmission electron microscopy
TF	transcription factor

TGF1	transforming growth factor-1
TGFβ	transforming growth factor β
TIM14	translocase of the inner membrane 14
TIM23	translocase of the inner membrane 23
TOM	translocase of the outer membrane
TRA-1-60	surface tumor recognition antigens (stem cell glycoprotein)-1-60
TRA-1-81	surface tumor recognition antigens (stem cell glycoprotein)-1-81
tracrRNA	*trans*-activating crRNA
T-tubules	transverse tubules
TUBB3	tubulin-β-III
UTR	untranslated region
v/v	volume/volume
vol	volume
vs.	versus
WB	western blot
Wnt	wingless-related integration site
ZFNs	zinc-finger-nucleases
α-SMA	α-smooth muscle actin
β-oxidation, FAO	mitochondrial fatty acid oxidation

Amino acid code

3-letter code	single letter code	amino acid
Ala	A	Alanine
Arg	R	Arginine
Asn	N	Asparagine
Asp	D	Aspartic acid
Cys	C	Cysteine
Gln	Q	Glutamine
Glu	E	Glutamic acid
Gly	G	Glycine
His	H	Histidine
Ile	I	Isoleucine
Leu	L	Leucine
Lys	K	Lysine
Met	M	Methionine, start codon (ATG)
Phre	F	Phenylalanine
Pro	P	Proline
Ser	S	Serine
Stop	*	termination codons (TGA, TAA, TAG)
Thr	T	Threonine
Trp	W	Tryptophan
Tyr	Y	Tyrosine
Val	V	Valine

Nucleotide code code

Letter	Nucleotide
A	Adenine
C	Cytosine
G	Guanine
N	Any nucleotide
T	Thymine
U	Uracil

1. Introduction

1.1 Reprogramming human somatic cells into induced pluripotent stem cells (iPSCs)

1.1.1 The emerging field of stem cells

In 1868 the term `stem cell` was mentioned for the first time when the German scientist Ernst Haeckel described that all multicellular organisms originate from an common ancestor unicellular organism (Haeckel, 1868). The biologist Theodor Boveri took Haeckel`s definition and committed the fertilized egg derived germ cells to be called stem cells. At that time `stem cell` was used of what we now refer to as primordial germ line cells (Boveri, 1887, Boveri, 1892). The term was further adapted until 1980, when James Till and Ernest McCulloch demonstrated the existence of self-renewing cells within the hematopoietic system that are able to differentiate into a variety of cell types (Till and McCulloch, 1980, Till and Mc, 1961, Becker et al., 1963, Siminovitch et al., 1963, Metcalf, 1971). These findings redefined the term `stem cell` as undifferentiated cell with the properties of self-renewal and differentiation capacity that is valid until today (Till and McCulloch, 1980, Weissman, 2000). Several studies on stem cell phenotypes unraveled the dependency of the present state on the surrounding micro environmental cell niches (Morrison and Scadden, 2014, Mendelson and Frenette, 2014). The potential of stem cells relies on extracellular micro environmental factors which can be converted into intrinsic cellular signals that define a roadmap of stem cell function (Ogawa, 1993, Yamashita et al., 2005, Hackney et al., 2002).

Among humans three stem cell classes arose: totipotent, pluripotent and multipotent stem cells (Eckfeldt et al., 2005). Totipotent stem cells exist in the fertilized egg and can give rise to embryonic as well as extra-embryonic (EE) tissues such as the placenta (Lovell-Badge, 2001). Pluripotent stem cells form the inner cell mass of the blastocyst and evolve into germ line cells during embryonic development which give rise to the high variety of different cell types that exist in the human adult individual (Bradley et al., 1984, Eckfeldt et al., 2005, Bianconi et al., 2013). The mesodermal, ectodermal or endodermal fate specifically determines the rise of progenitors that turn into progeny with even more restricted differentiation potential that finally result in functional tissue-specific mature cells. Within adult humans some organs or tissues still contain cells with restricted differentiation potential known as multipotent stem cells with retained differentiation capacity. These multipotent stem cells exist in specific tissues like the bone marrow which contains hematopoietic stem cells that are able to differentiate into all hematopoietic cell types of the blood (Eckfeldt et al., 2005). The emerging field of stem cells allowed insights into embryonic development, regeneration and unraveled its promising future in therapeutic applications. Researchers assume numerous applications that raise the need of decoding the molecular regulation of stem cells to further exploit their enormous therapeutic potential.

1.1.2 The power and challenge of pluripotent stem cells (PSCs)

In 1981 mouse embryonic stem cells (mESCs) were isolated from the inner cell mass of a blastocyst for the first time (Evans and Kaufman, 1981, Martin, 1981). This achievement led to the establishment of multiple ESC lines from different species like sheep (Handyside et al., 1987), bovine (Cherny et al., 1994), rabbit (Giles et al., 1993) and marmoset monkey (Debowski et al., 2016). This was followed by the first *in vitro* culture system of human ESCs (hESCs) in the 1990s (Thomson et al., 1998, Loser et al., 2010). The main challenge for scientists was the identification of the appropriate cultivation method for ESCs to be able to further maintain pluripotent properties. At that time ESCs were cultured on mouse embryonic fibroblast (MEFs) feeder cells disregarding the risk of increased xeno-contamination and immune rejection thus hindering further applications like autologous transplantation (Thomson et al., 1998, Xu et al., 2001, Martin et al., 2005). Moreover, lot-to-lot inconsistencies and intense workload were aggravating the use of ESCs in many laboratories (Aguilar-Gallardo et al., 2010, Rajala et al., 2010). An appropriate solution was the establishment of a xeno-free and feeder-free culture system via combination of extracellular matrix proteins and growth factor supplementation such as the basic fibroblast growth factor (bFGF) (Xi et al., 2010). The extracellular matrix is isolated from mouse

Engelbreth-Holm-Swarm teratocarcinoma cells and contains a mixture of collagen IV, laminin and other growth factors (Xu et al., 2001, Thomson et al., 1998, Kleinman, 2001). The combination of the described coating reagent hESC-Matrigel™ with serum- and xeno-free medium like mTesr™1 was a milestone in ESC cultivation and is the most frequently used cultivation method up to now (Ludwig and J, 2007, Ludwig et al., 2006, Brimble et al., 2004, Hakala et al., 2009). The novel sustainable *in vitro* system offered scientists extensive research on pluripotent properties such as clonogenicity, self-renewal and multi-lineage differentiation (Harrison et al., 2007). Researchers were able to identify typical pluripotent key markers like the transcription factors octamer-binding transcription factor 3/4 (OCT3/4), sex determining region Y-box2 (SOX2), NANOG or the surface tumor recognition antigens (TRA) TRA-1-60 and TRA-1-81 (Thomson et al., 1998). Moreover, somatic differentiation of ESCs allowed scientists to get insights into early embryonic developmental processes accompanied by novel therapeutic implications (Smith et al., 1998, Reubinoff et al., 2000). For example, ESCs were differentiated into insulin-producing cells (Baharvand et al., 2006), neural precursor cells (Sundberg et al., 2011) and cardiomyocytes (CMs) (Pal et al., 2013) that enable the identification of novel therapeutic targets for type I diabetes, Parkinson`s disease or cardiovascular diseases. Early-stage clinical trials on macular degeneration have shown the applicability of ESCs to treat patients without substantial side effects (Schwartz et al., 2012).

Even though ESCs offer great potential for scientists profound ethic concerns arose. The fact that ESC line generation requires the sacrifice of post-fertilized embryos provokes ethical restrictions in a variety of countries. In Germany, the German Embryo Protection Act and Stem Cell Act prohibit the generation but allow the import of officially approved ESCs lines (Heinemann and Honnefelder, 2002). Therefore, scientists were in need of an alternative pluripotent stem cell source. The new scientific mission was to examine the differences between undifferentiated pluripotent stem cells and differentiated somatic cells to identify a conserved and an ideally conferrable stem cell unique molecular signature.

1.1.3 The advance of iPSCs

The first breakthrough was Sir John B. Gurdon’s nuclear transfer. He demonstrated that the transplantation of a single somatic nucleus into an enucleated and unfertilized egg is sufficient to fully develop an adult individual within the species *Xenopus laevis* (Gurdon et al., 1958). These findings emphasized the achievement of pluripotency in an appropriate environment. The transfer of somatic nuclei into oocytes or cellular hybrid systems underlined that pluripotency can be conferred to somatic cells (Wilmut et al., 1997, Cowan et al., 2005, Tada et al., 2001). Gene expression analysis of mESCs unraveled the importance of the pluripotency-associated transcription factor OCT3/4 in maintaining self-renewal and its downregulation upon differentiation (Rosner et al., 1990, Scholer et al., 1990, Okamoto et al., 1990, Niwa, 2001, Niwa et al., 2000, Ivanova et al., 2002, Reubinoff et al., 2000). Expressed sequence tag analysis revealed 75 genes to be specifically expressed in mESCs (Sharov et al., 2003). Several studies uncovered the molecular signature of `stemness` by comparing gene expression profiles of hESCs with mESCs and human somatic cell types (Sato et al., 2003, Sperger et al., 2003, Richards et al., 2004, Bhattacharya et al., 2004, Fortunel et al., 2003). The enormous discordance among those gene-expression studies impeded the identification of the detailed molecular signature (Fortunel et al., 2003). The main genes among hundreds that have been implicated in self-renewal and pluripotency were *OCT3/4*, *SOX2*, *NANOG* and transforming growth factor-1 (*TGF1)* that were ubiquitously expressed in hESCs (Abeyta et al., 2004, Chambers, 2004, Ivanova et al., 2002, Ramalho-Santos et al., 2002). Furthermore, mESC studies identified tumor-related genes like c-myelocytomatosis oncogene product (*c-Myc*) (Cartwright et al., 2005) and the zinc-finger transcription factor Kruppel-like factor 4 (*Klf4*) (Li et al., 2005) that are contributing to the long-term maintenance of pluripotency. The computational classification of all identified factors and the systematic assessment of 24 candidate genes led to the breakthrough of Takahashi and Yamanaka. In 2006, Yamanaka and colleagues identified four key genes that are capable of inducing pluripotency. They demonstrated that overexpression of the Yamanaka factors `KMOS` KLF4, C-MYC, OCT3/4 and SOX2 was able to reprogram murine dermal fibroblasts into induced pluripotent stem cells (iPSCs) (Takahashi and Yamanaka, 2006). Only one year later the group of Yamanaka accomplished to reprogram human

dermal fibroblasts by using the same subset of pluripotency key genes (Takahashi et al., 2007). The pioneer work of Gurdon and Yamanaka was honored with the Nobel Prize emphasizing the start of a new era for scientists (The Nobel Prize, 2012).

The unique properties of ESCs like self-renewal and differentiation potential were confirmed in iPSCs (Hu et al., 2010). Moreover, iPSCs were able to produce viable mice after tetraploid complementation comparable to ESCs (Zhao et al., 2009). Consistent to ESCs the same expression profiles and surface molecules were examined (Nakagawa et al., 2008, Yu et al., 2007). With regard to the cultivation method, the same ESC-dependent cultivation strategy proved to be suitable for iPSC culture but can be optimized by improving cultivation techniques using xeno-free medium such as mTesr™1 and Rho kinase (ROCK) inhibitor Y27632 (RI) supplementation (Hu et al., 2010, Liu et al., 2020, Watanabe et al., 2007). In contrast to ESCs it remains under debate to which extent iPSCs keep their genetic `memory` of their original cell type. For example, iPSCs derived from dermal fibroblasts were shown to be epigenetically unique which can explain the lineage-specific bias during differentiation to some extent (Sullivan et al., 2010, Hu et al., 2010, Bhutani et al., 2010). After confirming a tremendous equality of iPSCs with ESCs, constant optimization of reprogramming strategies towards efficiency, quality and genetic identity allowed the emergence of iPSC lines in disease modeling (Spitalieri et al., 2018).

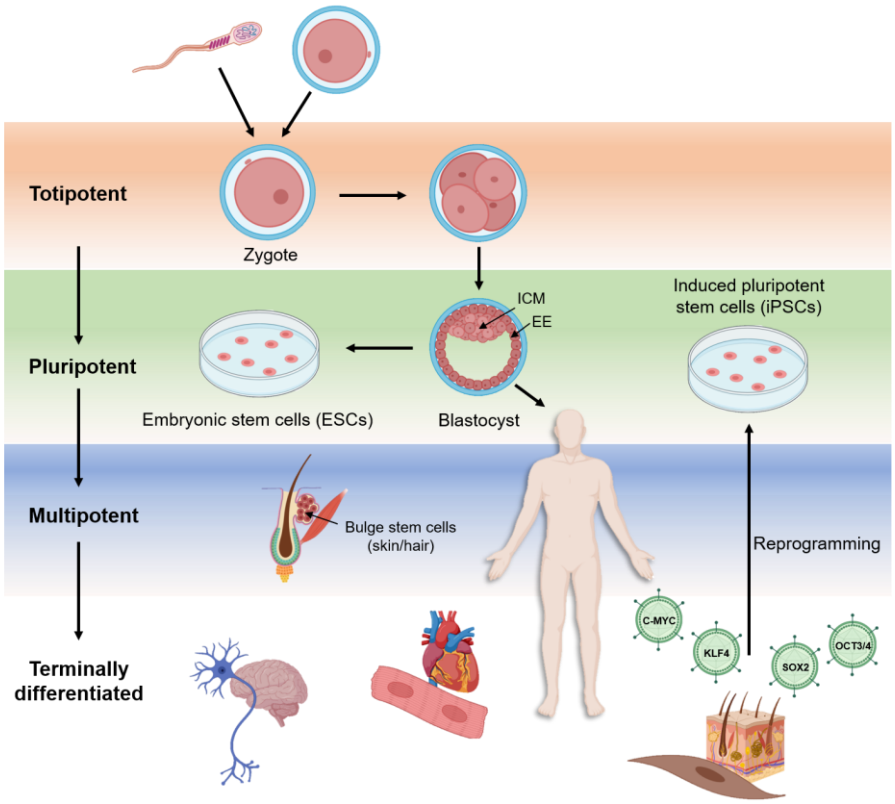

Figure 1.1 The stem cell hierarchy during human development and reverse states by molecular reprogramming using the Yamanaka factors `KMOS`.
After fusion of egg and sperm the totipotent zygote evolves into the blastocyst comprising two compartments, the inner cell mass (ICM) and the EE tissue. The isolation of ICM cells allow the further cultivation of embryonic stem cells (ESCs). During human development, the pluripotent stem cells become restricted in their capacity to differentiate by passing the three germ layer lineages to fully differentiate into adult cells, such as dermal fibroblasts of the skin or CMs of the heart, by losing pluripotent properties. Some organs still maintain tissue-specific multipotent stem cells such as bulge stem cells in the skin that can give rise to progenitors of a specific lineage only. Fully developed cells, such as dermal fibroblasts can be reprogrammed to regain the pluripotent fate by the induction of the Yamanaka factors `KMOS` that give rise to iPSCs. iPSCs share similar differentiation capacities with ESCs and therefore emerged as a promising tool for *in vitro* modeling of human diseases or for therapeutic approaches. The scheme was adapted after Eckfeldt et al., 2005, by BioRender.com (2021) (BioRender, 2017).

1.1.4 The molecular basis of reprogramming

The major hurdle of reprogramming was the considerably low efficiency. Extensive research on the molecular mechanisms of reprogramming revealed that the achievement and the maintenance of the pluripotent state in iPSCs requires the establishment of a complex endogenous pluripotency-network. During embryonic development stem cells differentiate into more specialized cell types leading to epigenetic silencing of this network. The overexpression of `KMOS` is able to force the somatic epigenome to undergo a remodeling process including conformational changes of chromatin by de-/methylation and de-/acetylation of histones. The new accessibility of pluripotency-associated genes in turn results in inaccessibility of somatic cell specific genes (Sims et al., 2003, Stadtfeld et al., 2008). Up to now, it is not entirely clear how the highly complex conformational changes of chromatin occur. Scientists suppose an early stochastic phase of reprogramming after performing single cell analysis. `KMOS` activate transcriptional changes in somatic cells that result in increased proliferation, modification of histones at somatic genes, induction of mesenchymal to epithelial transition, deoxyribonucleic acid (DNA) repair and RNA processing (Buganim et al., 2012). At that stage heterogeneous gene expression profiles were identified driving somatic cells into different cell fates such as transdifferentiation, transformation, senescence, apoptosis and reprogramming. Cells that gain the reprogramming fate undergo an unknown rate-limiting step that disembogues in the deterministic phase in which the pluripotency-network is fully established and stabilized (Buganim et al., 2012, Buganim et al., 2013). Within the late deterministic phase of reprogramming the epigenetic remodeling process is completed (Polo et al., 2012, Tiemann et al., 2011). At that stage, the process of X-chromosomal inactivation is fully inverted leading to a genome-wide resetting of posttranslational histone modifications and the maintenance of pluripotency. Therefore, no additional exogenous delivery of the `KMOS` is required (Buganim et al., 2013). Furthermore, the complex pluripotency-network can also be established through combinations of related pluripotency-associated factors like OCT3/4, SOX2, NANOG and LIN28 (Nakagawa et al., 2008).

Up to now, different reprogramming strategies arose that range from integrating to inducible up to non-integrating methods. The first reprogramming strategies contained the use of integrating viruses such as retroviruses (Takahashi et al., 2007, Takahashi and Yamanaka, 2006) or lentiviruses (LeV) (Sommer et al., 2009, Okita et al., 2011), followed by drug-inducible systems such as doxycycline-inducible reprogramming factors (Hamilton et al., 2009, Hockemeyer et al., 2008) and episomal-based reprogramming strategies (Chou et al., 2011, Yu et al., 2011). Currently, the most prominent non-integrating systems are adeno-associated virus (AAV) (Zhou and Freed, 2009), messenger ribonucleic acid (mRNA) (Warren et al., 2010), or Sendai virus (SeV) approaches (Ban et al., 2011, Fusaki et al., 2009). The establishment of multiple reprogramming strategies led to the enhancement of reprogramming efficiency thus facilitating the way towards commercially available reprogramming systems. To date scientists are able to generate current Good Manufacturing Practice (cGMP) compliant iPSC lines that underline the progress in the translational usage of iPSCs towards therapeutic approaches (Baghbaderani et al., 2015). Reprogramming into iPSCs offers unlimited accessibility to pluripotent cells together with the investigation of patient-specific diseases without ethical concerns. Especially the unique donor-derived origin of iPSCs will overcome the need of immunosuppressive therapy in transplantation (Coelho et al., 2017, Xian and Huang, 2015). In particular the link to genome editing systems like the clustered regularly interspaced short palindromic repeats (CRISPR)/CRISPR-associated protein 9 (CRISPR/Cas9) and *in vitro* differentiation approaches facilitates the generation of new model systems to study disease mechanisms, potential biomarkers, tissue repair and gene therapy applications (Stadtfeld and Hochedlinger, 2010, Sterneckert et al., 2014).

1.2 CRISPR/Cas9: A new era of genome editing in PSCs

Pioneering experiments demonstrated the optimized usage of single-strand-specific nucleases (SSNs) such as zinc-finger-nucleases (ZFNs) (Kim et al., 1996, Miller et al., 2007, Porteus and Baltimore, 2003, Sander et al., 2011) and transcription activator like effector nucleases (TALEN) (Christian et al., 2010, Zhang et al., 2011, Sanjana et al., 2012) to engineer human pluripotent stem cells (hPSCs). Their use in genetic knock-out models, cell-specific reporter lines, overexpression, insertion, deletion or

introduction of base pair (bp) changes unraveled the importance of gene editing approaches (DeKelver et al., 2010, Hockemeyer and Jaenisch, 2010, Hockemeyer et al., 2009, Hockemeyer et al., 2011, Lombardo et al., 2007, Sexton et al., 2014, Soldner et al., 2011, Zou et al., 2011). Gene editing systems like ZFNs (Kim et al., 1996) and TALENs (Christian et al., 2010) already represented the power of genome editing. The disadvantages of those systems include high costs and time-consuming implementations thus impeding their usage as gene editing tools in multiple laboratories. Extensive research on SSNs demonstrated another gene editing technology, the CRISPR/Cas9 gene editing system, with the advantages of higher preciseness, low costs, easier customization and the possibility of multiplex genome editing (Ran et al., 2013b, Cong et al., 2013, Mali et al., 2013, Cho et al., 2013, Jinek et al., 2012).

1.2.1 Principles of the CRISPR/Cas adaptive immune system

The CRISPR/Cas adaptive immune system revolutionized the scientific field of genome editing (Ran et al., 2013b, Cong et al., 2013, Mali et al., 2013, Cho et al., 2013, Jinek et al., 2012). This system enables target-specific DNA cleavage and is currently the most prominent method to implement genetic modifications in multiple species (Jang et al., 2020). CRISPR was originally discovered as RNA-guided adaptive immune system in bacteria and archaea. The self-defense system is used to identify and cleave DNA of invading viruses, bacteriophages or transferred plasmids to small genetic fragments thus enabling protection by silencing the foreign DNA (Jiang and Doudna, 2017). Each CRISPR/Cas system contains a cluster of CRISPR-associated (Cas) genes organized in operon(s) and CRISPR arrays that contain genome-targeting sequences (protospacers) and identical repetitive elements (Wiedenheft et al., 2012, Bhaya et al., 2011, Terns and Terns, 2011).

The self-defense mechanism is divided into three steps: the adaptive phase, the expression phase and the target recognition phase (Jinek et al., 2012). The adaptive phase of the immune response starts after first invasion of viruses, bacteriophages or plasmid transfer. The foreign DNA is recognized and directly integrated as short non-repetitive sequence elements (protospacers) into the host genome proximal to the CRISPR array. In the second phase, the new CRISPR array contains a subset of non-repetitive sequences (protospacers) and repetitive sequences. This combination is transcribed into the long precursor CRISPR RNA (pre-crRNA) (Wiedenheft et al., 2012, Bhaya et al., 2011, Terns and Terns, 2011). In most systems, like in *Streptococcus pyogenes* (*S. pyogenes*), the additionally transcribed *trans*-activating crRNA (tracrRNA) binds to the pre-crRNA. The fixed unit tracrRNA is used as scaffold and enables enzymatic RNA III processing and crRNA 5` trimming into mature crRNA fragments, that contain 20-nt short guide RNA (gRNA) sequences (Deltcheva et al., 2011). The mature crRNA:tracrRNA heteroduplex builds a ribonucleoprotein (RNP) complex with the Cas nucleases that initiates the third phase: the target recognition. The RNP complex(es) identifies the complementary protospacer sequences through the 20-nt guide sequence of the crRNA and the protospacer adjacent motif (PAM) interposed in front of it. This interaction mediates the cleavage of the complementary protospacer sequences that result in silencing of foreign DNAs (Jinek et al., 2012). The CRISPR/Cas system functions as long-term adaptive immune system by preventing re-infections of the same pathogens (Mei et al., 2016, Jiang and Doudna, 2017). In many prokaryotes this system is divided into class 1 (type I, III, IV), that involves more than one Cas protein and class 2 (type II, IV, VI) that contains a multidomain Cas protein (Song, 2017).

1.2.2 The adaptation of CRISPR/Cas9 for genome editing

Extensive research on CRISPR/Cas systems allowed their modification as programmable tools to mediate target-specific DNA cleavage. The best characterized system is the self-defense mechanism of the type II CRISPR/Cas9 system that originates from *S. pyogenes* (Garneau et al., 2010, Deltcheva et al., 2011, Jinek et al., 2012, Gasiunas et al., 2012). The CRISPR/Cas9 system contains the nuclease Cas9 that is composed of two domains: the HNH nuclease domain that cleaves the complementary strand and the Cas9 RuvC-like domain that cleaves the non-complementary strand of the gRNA containing crRNA (Jinek et al., 2012). The Cas9 nuclease lobe comprises a PAM-interacting domain next to both nuclease domains that is able to uniquely identify the *S. pyogenes* Cas9 (SpCas9) specific

5`-NGG-PAM (Nishimasu et al., 2014, Hsu et al., 2014). The optimized gene editing tool CRISPR/Cas9 contains the SpCas9 protein that is able to recognize an engineered dual RNA chimera of crRNA:tracrRNA. The direct connection of the crRNA to the tracrRNA by a linker loop is further defined as single guide RNA (sgRNA) that simplified the usage of this system (Jinek et al., 2012, Cong et al., 2013, Wu et al., 2014). Among the sgRNA the crRNA is the only modifiable component because it contains the programmable 20-nt gRNA. The *in silico* design of the gRNA sequence that is able to specifically target DNA sequences requires a unique genomic region that is preceded by a SpCas9 specific 5`-NGG PAM. Successful design would lead to the formation of a gRNA:DNA hetero-duplex by Watson-Crick base pairing that initiates the formation of Cas9-sgRNA-target ternary complex which in turn results in strand-specific blunt cleavage of the complementary sequence by SpCas9 three base pairs (bp) upstream of the PAM sequence (Jinek et al., 2012, Nishimasu et al., 2014, Mei et al., 2016, Kim et al., 2017). Depending on the Cas9 orthologues different PAMs are required, like *Streptococcus thermophiles* (5`-NNAGAA for CRISPR1 (Garneau et al., 2010, Cong et al., 2013)) or *Neisseria meningiditis* (5`-NNNNGATT (Hou et al., 2013)). The SpCas9 system is the most common used gene editing tool in human cells due to the high average of 5`-NGG PAMs every 8-12 bp (Cong et al., 2013, Hsu et al., 2013). The CRISPR/Cas9 technology was improved over time to increase the site-specific cleavage efficiencies, the preciseness of target-recognition and its easier customization. Novel adaptions, like the Cas9 double nicking system, were especially developed for the use in hard-to-transfect cell lines such as iPSCs (Ran et al., 2013b).

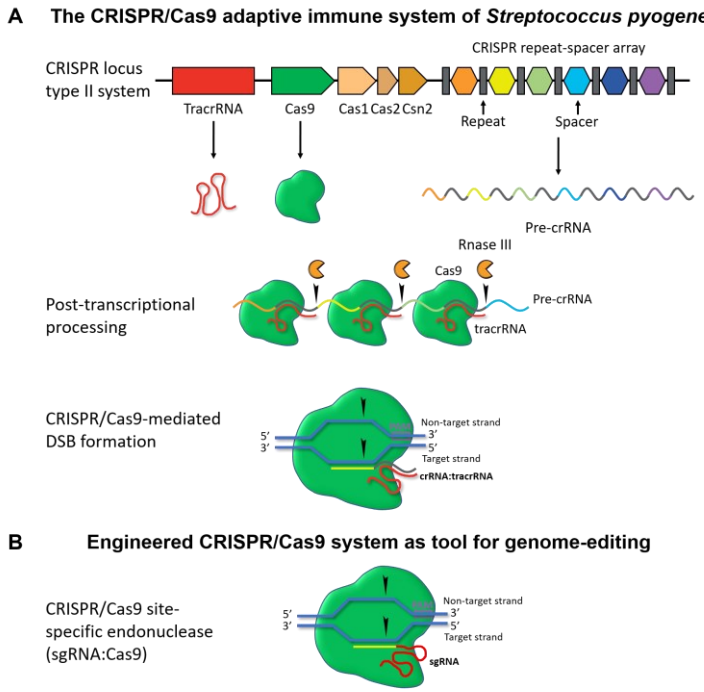

Figure 1.2: Schematic comparison of the original adaptive immune system of *S. pyogenes* and its adaptation as gene editing tool.
(A) The illustration of the CRISPR/Cas adaptive immune system type II based on the molecular mechanism of the bacterium *S. pyogenes*. **(B)** The engineering of the dual RNA chimera of crRNA:tracrRNA and the individually modifiable sequence of the sgRNA allows the usage of CRISPR/Cas9 as a precise gene editing tool. The scheme was adapted after the publication of Lino et al., 2018, by BioRender.com (2021) (BioRender, 2017).

1.2.3 The molecular mechanisms of genetic changes mediated by CRISPR/Cas9

The molecular groundwork of editing genomic sequences using the CRISPR/Cas9 system is based on the cleavage of the specifically targeted dsDNA. The induced double strand break (DSB) leads to the activation of the endogenous repair machinery that can undergo two different pathways: homology-directed repair (HDR) or more likely non-homologous end-joining (NHEJ) (Chapman et al., 2012, Hefferin and Tomkinson, 2005).

The HDR pathway is recruited during S and G_2 phase of the cell cycle only. This system requires a template DNA such as the sister chromatid, a single stranded donor oligonucleotide (ssODNs) or a double stranded DNA (dsDNA) fragment (or plasmid). The template contains homology arms that are complementary to the genomic region next to the computationally determined DSB. These homology arms are used to incorporate the provided sequence into the host genome. The HDR pathway is favored for knock-in approaches to mediate gene corrections, insertions or replacements. It allows precise modifications such as point mutations or gain-of-function variations to create accurate genomic sequence modifications or reporter lines or to insert selection cassettes (Yeh et al., 2019).

The NHEJ system is favored in loss-of-function approaches due to the high likelihood of creating error-prone genetic changes to achieve a knock-out of the gene of interest (Jiang and Doudna, 2017). The NHEJ pathway is active throughout the whole cell cycle and mediates the re-ligation of the previously cleaved dsDNA ends. In detail, double strand cleavage can lead to either blunt dsDNA ends or overhang single stranded DNA ends (sticky ends). In the case of blunt ends or 100 % compatible single strand overhang DNA ends re-ligation occurs accurately. Mismatches within single stranded overhangs lead to imprecise repair and are of high risk to create base pair changes close to the cleavage site. These abnormities are either nucleotide insertions, deletions (indels) or substitutions with a likelihood of 20-60 % (Mei et al., 2016). NHEJ-mediated DNA sequence variations can lead to silent, missense or nonsense mutations. Silent mutations have no pathophysiological impact. Missense mutations change the amino acid (aa) sequence without creating a premature termination codon. Missense mutations still result in the translation of the full-length protein but contain alterations in the aa sequence. For example, aa changes result in misfolding of the secondary and tertiary protein structure. Moreover, aa substitutions within interaction domains or catalytic centers may give rise to proteins with decreased enzymatic activities or reduced interaction capacities leading to low- or non-functional proteins. Nonsense mutations can cause a premature termination codon within coding regions that either result in a truncated most probably non-functional protein or lead to the activation of the nonsense-mediated mRNA decay mechanism in which premature termination codons are detected, translation is impeded and the mRNA is degraded. The error-prone NHEJ system is therefore the favored system in the generation of knock-out models *in vivo* and *in vitro* (Maruyama et al., 2015). CRISPR/Cas9-mediated editing of genomic sequences is applicable in multiple species including human cells (Cho et al., 2013, Cong et al., 2013, Mali et al., 2013, Jinek et al., 2013, Jinek et al., 2012). The unique features of the CRISPR/Cas9 system led to its raise as an incomparable gene editing tool in many research areas like agriculture, synthetic biology, therapeutics, gene therapy and disease remodeling (Kim et al., 2017). On the 7th October 2020, the great discovery of the RNA-guided CRISPR/Cas9 gene editing technology was honored with the Nobel Prize in Chemistry for Emmanuelle Charpentier and Jennifer A. Doudna underlining a new epoch in life sciences (The Nobel Prize, 2020).

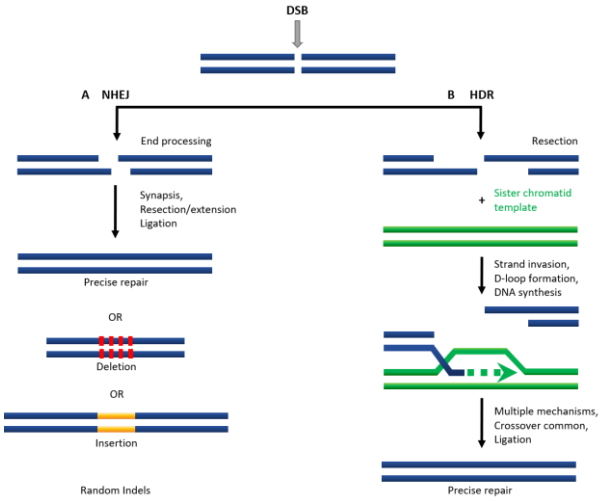

Figure 1.3 The CRISPR/Cas9-mediated DSB as basis of genetic knock-out models.
After complex formation of the Cas9-sgRNA-target ternary complex a DSB of the dsDNA occurs in close proximity of the 5`NGG-PAM. The endogenous repair mechanism **(A)** NHEJ or the **(B)** HDR mechanism. **(A)** NHEJ repair might result in mono- or biallelic precise repair or deletion or insertion of nucleotides. **(B)** The HDR repair mechanism uses the sister chromatid or an exogenously delivered template to allow the hybridization of the HDR arms to incorporate the provided sequence. The illustration was adapted after the publication of Lino et al., 2018.

1.2.4 CRISPR/Cas9 meets iPSCs

In particular, the combination of both Nobel Prize honored technologies CRISPR/Cas9 and iPSCs provides a novel tremendously powerful system for disease modeling. The high specificity of CRISPR/Cas9 allows its usage to generate genetic knock-out or knock-in iPSC lines that can be used to achieve isogenic mutant or isogenic healthy control systems. The generation of nucleotide changes in a gene of interest in a healthy control background enables an unique potential for the identification of the gene's functional relevance in forcing the outcome of the phenotype. The comparison of isogenic systems with an additional patient-derived iPSC line allows more precise insights into the effect of the underlying specific genetic background on the phenotype. The combination of both systems underlines a new era of `disease in a dish` that allows the evaluation of genetic variations in detail and the direct correlation of the pathological mechanism to the mutation itself (Soldner et al., 2011, Soldner and Jaenisch, 2012, Li et al., 2015, Stillitano et al., 2016, Lee et al., 2017). The efficiency of editing genomic sequences within iPSCs is highly dependent on the chosen delivery system and method. Similar to hESCs, human iPSCs are known as `hard-to-transfect´ cell lines with reduced genome editing frequencies (Kim et al., 2014). Delivery methods of the CRISPR/Cas9 system into iPSCs vary from physical delivery (microinjection, electroporation) to viral (AAV, LeV) and non-viral approaches (lipid, gold nanoparticles) (Lino et al., 2018). Electroporation strategies are one of the most difficult methods but can efficiently transfer the CRISPR/Cas9 system into cells that are basically more difficult to manipulate (Lino et al., 2018). Several protocols for electroporation of mammalian cells exist, demonstrating the need of precise voltages and fine-tuning of settings of the used electroporation system depending on the *in vitro* or *in vivo* approach. Nucleofection is one specialized electroporation procedure in particular for usage in hard-to-transfect cell lines like ESCs which is able to directly ingress the nucleus with 10-fold higher transfection efficiencies than conventional electroporation or lipofection (Lino et al., 2018, Lakshmipathy et al., 2004, Siemen et al., 2005). At present, no gold standard nucleofection protocol exists for iPSCs. Therefore, it is recommended to determine highly effective transfection protocols based on the parameters used in ESCs depending on the individual settings. Furthermore, the efficiency and off-target specificity in iPSCs is particularly depending on its delivery system. Those can be divided into three different strategies: DNA-based, mRNA-based or protein-RNA based approaches. First, DNA-based delivery contains vectors that encode the whole or parts of the

CRISPR/Cas9 system. One representative all-in-one plasmid was generated in the lab of F. Zhang and its efficient usage in iPSCs was demonstrated by nucleofection (Ran et al., 2013b). The Cas9 expressing vector contains the target-specific-designed gRNA that was previously cloned into a multiple cloning site to automatically be transcribed into a crRNA:tracrRNA scaffold under a strong promotor (e.g. U6). After transcription of the whole construct and translation of the Cas9 protein, the individual components are connected in the cytoplasm and re-localized to the nucleus to generate target-specific DSBs. Second, to avoid the need of cellular transcription, the system can be delivered as whole or in parts on RNA basis. Third, the usage of the protein-RNA-based approach overcomes the need of transcription and translation followed by linkage of the active recombinant Cas9-protein to the sgRNA *in vitro* prior to delivery. This system is able to directly target the DNA inside the nucleus after transfection and demonstrates a faster but simultaneously more labor-intensive procedure of gene editing (Lino et al., 2018).

The additional advantage of all-in-one CRISPR/Cas9 plasmids is the presence of selection cassettes like sequences encoding for fluorophores (enhanced green fluorescent protein, eGFP) or antibiotic resistances (puromycin) that enable easier screening of colonies (Ran et al., 2013b). The cellular expression of the pSpCas9(BB)-2A-Puro plasmid allows the screening of iPSCs on the basis of antibiotic resistance after medium supplementation with puromycin. This preselection step is essential to reduce the amount of iPSC colonies in the ongoing cultivation process to save time and costs during iPSC line production. Single colonies need to be further expanded to allow the investigation towards genomic changes. The crucial step after the generation of gene-edited iPSCs is the confirmation of nucleotide changes via Sanger sequencing within the gene of interest and no sequence alterations in off-target genes. Successful modification of genomic sequences within iPSCs enables the identification of potential treatments in a patient- and mutation-specific manner to evaluate suitable drug or gene therapeutic approaches which enlightens the path to personalized medicine (summarized (Eschenhagen et al., 2015, Robinton and Daley, 2012)). Unfortunately, the applicability of CRISPR/Cas9 on human cells can be violated on editing of human embryos. Despite of the restricted usage, the Chinese scientist Jiankui He reported the first CRISPR/Cas9-edited human embryos in November 2018 (MIT Technology Review, 2019). The abuse of CRISPR/Cas9 in human embryos especially in a non-life-saving context by mimicking a needless mutation in *CCR5* to enhance the HIV resistance not only is a criminal offense, but also casts a dark shadow on the powerful gene editing system and leads to the rise of ethical concerns.

1.3 The power of modeling inherited cardiomyopathies with iPSCs

The combination of gene-edited and patient-derived iPSC-based *in vitro* model systems offers a great potential in recapitulating disease specific phenotypes to get insights into molecular pathomechanisms of disorders like inherited cardiomyopathies. Up to now, modeling of genetically determined cardiomyopathies primarily relies on model organisms or tumor cell lines due to the inaccessibility of human heart tissue. The disadvantage of human derived tumor cell lines is their immortalized character that is present as a cause of genetic aberrations, thus making it difficult to fully recapitulate physiological disease-associated phenotypes. The use of other model organisms, like mice, allows the simultaneous investigation of complex tissue and organ systems given the evolutionary conservation of mammalian genomes, which also renders their application undeniable for studying molecular mechanisms of diseases and their treatments. However, 20 % of human genes have no orthologues in mice and paralogs are often linked to altered cellular functions, thus making it impossible to study some human specific phenotypes in animal models (Gabaldon and Koonin, 2013, Davis et al., 2011, Mouse Genome Sequencing et al., 2002). The emergence of gene-edited and patient-derived iPSC technology enables to fully recapitulate mutation-associated phenotypes in a human disease model that is identical to the patient`s genetic background. The self-renewal capacities of iPSCs allow scientists a novel unlimited source for research without ethical concerns. Together with the potential to be differentiated into any somatic cell type of interest, such as cells of the human heart, iPSCs are currently irreplaceable in disease remodeling of inherited cardiomyopathies (Laflamme et al., 2007, Zhang et al., 2009).

1.3.1 iPSC-derived cardiomyocyte (iPSC-CMs) model systems of congenital heart diseases mimic cardiac specific phenotypes

iPSC-CMs became a powerful tool especially in the field of inherited cardiac diseases. Congenital cardiomyopathies are classified into primary arrhythmias (long QT syndrome type 1 and type 2 (LQT1, LQT2)), cardiomyopathies (dilated cardiomyopathy (DCM), hypertrophic cardiomyopathy (HCM), arrhythmogenic cardiomyopathy (ACM)) and cardiometabolic diseases (Barth syndrome (BTHS)) (Brandao et al., 2017). The identification of linked gene mutations revealed a high variety in the subcellular localization of the affected proteins for each individual disease ranging from ion channels, sarcomeres, desmosomes and nuclei to mitochondria.

A study on LQT1 and LQT2 demonstrated a channelopathy connected phenotype in *in vitro*-derived CMs that can be linked to the patients' clinical data (Moretti et al., 2010, Giudicessi and Ackerman, 2012). They recognized prolonged action potentials (APs), development of early after depolarization (EAD) and increased risk of arrhythmias upon β-adrenergic agonist stimulation with isoproterenol (Iso) (Moretti et al., 2010). Additional studies on electrophysiological and calcium ion (Ca^{2+}) handling properties of iPSC-derived CMs illustrated their suitability in recapitulating disease-associated phenotypes (Moretti et al., 2010, Itzhaki et al., 2011, Sinnecker et al., 2013a, Sinnecker et al., 2013b).

Mutations in the tyrosine-protein phosphatase non-receptor type 11 (*PTPN11*) gene are involved in RAS-mitogen-activated protein kinase signaling and contribute to a hypertrophic phenotype of the inherited cardiomyopathy LEOPARD syndrome. The main findings in mutated iPSC-CMs were morphological differences including an enhanced degree of sarcomere organization in combination with increased median surface area (Carvajal-Vergara et al., 2010).

The first study of a sarcomere-related missense mutation within the myosin heavy chain 7 (*MYH7*) gene (MYH7 p.Arg663His) in iPSC-CMs is known to cause HCM. The affected patients demonstrated an HCM-associated phenotype such as arrhythmias, delayed after depolarization (DAD), hyper contractile cell function and cellular hypertrophy when using iPSC-derived CMs (Lan et al., 2013). Another sarcomere-related mutation in cardiac troponin T (*cTnT*) (cTnT p.Arg173Trp) is known to cause the disorganization of sarcomeres, an impaired sarcoplasmic reticulum (SR)-mediated reuptake of Ca^{2+}, aberrant contractility and abnormal Ca^{2+} transients in iPSC-CMs (Sun et al., 2012).

Impaired cell-cell adhesion by heterozygous or homozygous frameshift mutations in plakophilin-2 *(PKP2*) presented disease-associated phenotypes of ACM even though discrepancies of an immature state of iPSC-CMs and an adult-onset of the disease were noticeable (ACM median age is 26 years) (Caspi et al., 2013, Kim et al., 2013, Calkins and Marcus, 2008). The main findings include a loss of cell-cell adhesion, accumulation of lipids, increased cell size and first associations with pathological metabolic derangements (Caspi et al., 2013, Kim et al., 2013).

DCM-related phenotypes and treatment responses were analyzed in iPSC-derived CMs carrying various lamin A/C (*LMNA*) mutations. These studies demonstrated altered nuclear structures, Ca^{2+} abnormalities, instable electrophysiology and increased hypertrophic markers that were reversible upon gene correction by TALENs (Karakikes et al., 2015a, Karakikes et al., 2015b, Ho et al., 2011).

Mimicking mitochondrial cardiomyopathies like BTHS in a patient-derived and CRISPR/Cas9-mediated *in vitro* setting revealed the importance of the inner mitochondrial protein tafazzin (TAZ) for mitochondrial biogenesis and function. *TAZ* frameshift (c.517delG) and missense (c.328T>C) mutations in iPSC-CMs caused irregular sarcomeres, weakened contractility, abnormal cardiolipin (CL) profiles, increased reactive oxygen species (ROS) and metabolic abnormalities that were reversible upon gene replacement and small-molecule treatment, thus unraveling new potential therapies (Wang et al., 2014).

These insights into a variety of *in vitro* models of inherited cardiomyopathies conclude the usage of iPSC-derived CMs to study genetically determined forms of heart muscle diseases on the cellular level of human cells. Implicating the use of iPSC-derived CMs to examine morphology, contractility, Ca^{2+} flux, electrophysiology and metabolism allows to quantitatively assess cardiac specific phenotypes.

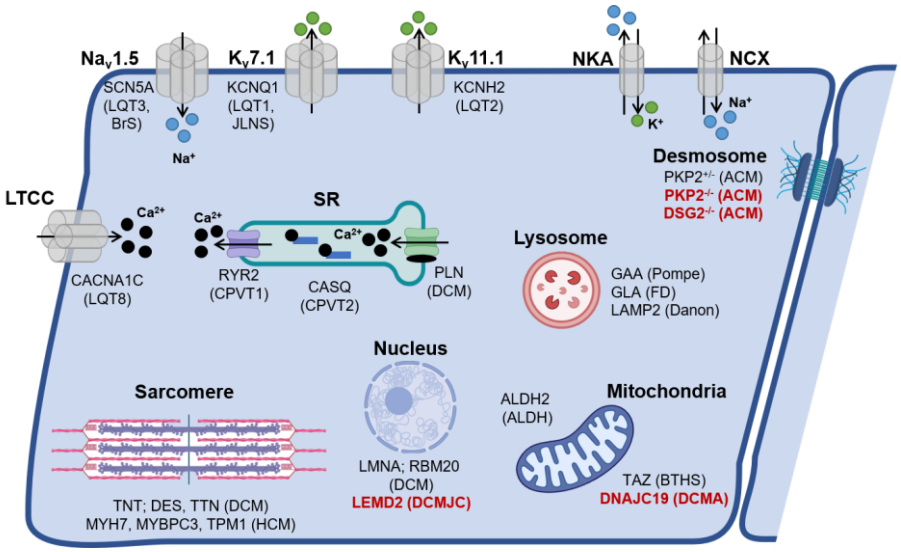

Figure 1.4 Human pluripotent stem cell-based *in vitro* model systems of congenital cardiomyopathies.
The figure was adapted based on the report of Brandao et al., 2017 and adjusted according to the aimed *in vitro* models of dilated cardiomyopathy with ataxia (DCMA), ACM and dilated cardiomyopathy with juvenile cataract (DCMJC), by BioRender.com (2021) (BioRender, 2017). iPSC-derived CMs are a promising tool in a high variety of congenital cardiomyopathies. The individual diseases are caused by defective proteins in multiple subcellular compartments, such as the nucleus, the desmosomes or the mitochondrion.

1.3.2 The usage of iPSC-CMs in transplantation and drug discovery

Moreover, short treatment of iPSC-CMs with antitumor drugs (anthracyclines and etoposide) induced cardio toxic biological processes, common signaling pathways and similar genomic biomarkers as observed during heart failure. These insights implement iPSC-CMs in cardiotoxicity studies with regard to the identification of novel antitumor drugs and their safer therapeutic applications (Sachinidis, 2020). Additionally, the usage of iPSC-CMs for allogeneic transplantation after myocardial infarction in non-primate *Macaca fascicularis* by direct intra-myocardial injection resulted in improved cardiac function without evidence of immune rejection (Shiba et al., 2016). The demonstration of a beneficial usage of iPSC-CMs in cardiac repair opens the way in therapeutic application which is under tremendous progress. iPSC master cell banks are currently established to produce iPSCs under cGMP compliant conditions by keeping the costs of generation, testing and storage reasonable (Baghbaderani et al., 2016, Baghbaderani et al., 2015). The first stem cell trial arose in which the usage of cGMP compliant iPSC-derived retinal pigment epithelium cells was described to treat one patient with Age-Related Macular Degeneration (AMD). The patient showed improvement of visual acuity without safety-related concerns. The study was halted to be resumed in 2016, when scientists identified new mutations that were not present in the original reprogrammed fibroblasts (Mandai et al., 2017). Another study on AMD, reported severe bilateral visual loss after intravitreal injections of autologous adipose-tissue derived “stem cells” (Kuriyan et al., 2017). The direct comparison of the opposite outcomes provides a valuable lesson for the premature usage of iPSCs in clinical trials. Future stem cell-based therapies will require solid preclinical evidence, accurate monitoring, government oversight and the spirit of “*primum non nocere*” (Li et al., 2017). Stringent quality control is necessary in the generation, maintenance and expansion of iPSCs and their somatic derivatives to ensure conditions of high quality. Internationally defined guidelines exist for detailed iPSC characterization only, including well-established criteria and the set of approaches to monitor their features (Baghbaderani et al., 2016, Baghbaderani et al., 2015, Elsevier B.V. Copyright © 2021, 2017). Up to now, no current consensus subsists that defines the state of mature adult CMs (Feric and Radisic, 2016).

Nevertheless, the iPSC-CMs based *in vitro* system provides the allocation of a human platform for remodeling cardiomyopathies, insights into cell replacement approaches and potential in drug testing of future therapeutics. The basis of all this predicates on the establishment of solid directed differentiation protocols to enable efficient generation of iPSC-derived somatic cells such as CMs.

1.3.3 Induction of the cardiovascular fate in iPSCs

Up to now a high variety of protocols were developed to direct iPSCs towards the cardiac specific lineage. Out of a biotechnological perspective the differentiation protocols are different when comparing two-dimensional (2D) to three-dimensional (3D) systems. The formation of iPSC aggregates in the appearance of 3D structures have shown to spontaneously differentiate into all cell types of the three germ layers. This process heavily relies on the removal of factors that are critical in the maintenance of pluripotency. With this knowledge different directed differentiation protocols were established to generate mesodermal, endodermal or ectodermal cell lineages (Desbaillets et al., 2000, Itskovitz-Eldor et al., 2000). To conduct iPSCs towards the cardiovascular lineage, the signaling pathways that are active during heart development (Activin/Nodal, transforming growth factor β (TGFβ), glycogen synthase kinase-3 (GSK3), wingless-related integration site (Wnt), bone morphogenic protein (BMP)) have to be replicated *in vitro* (Burridge et al., 2012, Yang et al., 2008, Mummery et al., 2012). Following that concept, scientists were able to generate contracting CMs out of mESCs (Wobus et al., 1991) and hESCs (Laflamme et al., 2007). The precise modulation of human embryonic heart development was afterwards transferred to monolayer cultures of iPSCs (Zhang et al., 2009, Burridge et al., 2012, Lian et al., 2013).

1.3.4 *In vitro* generation of cardiomyocytes: required signaling pathways and arising limitations

The *in vitro* generation of CMs mainly relies on precise regulation of the canonical Wnt signaling pathway in a dose and temporal dependent manner (Ueno et al., 2007). To drive PSCs towards the cardiovascular lineage the activation and inactivation of Wnt signaling is mediated by sequential addition of defined molecules to the cultivation medium to precise time points (Lian et al., 2012, Laflamme et al., 2007). First, the mesodermal fate is induced by the activation of Wnt signaling via activators like CHIR99021 (CHIR,6-[[2-[[4-(2,4-dichlorophenyl)-5-(5-methyl-1H-imidazol-2-yl)-2-pyrimidinyl]amino] ethyl]amino]-3-pyridinecarbonitrile) and/or TGFβ nodal signaling via BMP4 and activin A (Laflamme et al., 2007, Lian et al., 2012, Lian et al., 2013). The most prominent Wnt activator is CHIR, a known GSK3β inhibitor. GSK3β signaling inhibits the Wnt pathway, CHIR is therefore able to abrogate the GSK3β-mediated inhibition that in turn results in activation of Wnt signaling (Cao et al., 2008, Lian et al., 2012). This step initiates the formation of mesendodermal cells. Afterwards cardiac lineage is further specialized by inhibition of the Wnt signaling pathway that is mediated by small molecules such as the tankyrase inhibitor IWR-1 (4-(1,3,3a,4,7,7a-Hexahydro-1,3-dioxo-4,7-methano-2H-isoindol-2-yl)-N-8-quinolinyl-Benzamide) (Willems et al., 2011, Ueno et al., 2007). iPSCs that were successfully directed towards the cardiac fate can be visually recognized by the onset of contraction that starts between 7 to 16 days after cardiac induction. Varying differentiation efficiencies result in manifold CM yields and affect the proportion and the identity of non-CMs. iPSCs that do not acquire the cardiomyocyte fate result in cardiac fibroblasts, endothelial cells or smooth muscle cells (Yang et al., 2008, Huebsch et al., 2016, Humeres and Frangogiannis, 2019). Improvement of several monolayer protocols showed increased efficiencies after removal of insulin during cardiac specification (Lian et al., 2013, Lian et al., 2012) and the continuously supplementation of ascorbic acid (Cao et al., 2012). Differing CM yields in numerous studies unraveled great line-to-line variabilities that were partly solved after including a metabolic enrichment phase via glucose depletion and lactate supplementation one week after the onset of contraction (Tohyama et al., 2013). These insights demonstrated the requirement of optimized conditions for each individual cell line (Burridge et al., 2012). Additionally, the usage of chemical modulators during differentiation is able to contribute to different CM subtypes ranging from nodal and atrial to ventricular CMs (Zhang et al., 2009, Protze et al., 2017, Devalla et al., 2015, Cyganek et al., 2018, Josowitz et al., 2014). Optimal differentiation protocols are still required to achieve high efficiency and consistency in CM generation to allow broader applicability to multiple iPSC lines, especially with regard to its potential translational use in therapeutic interventions. Other studies on new differentiated iPSC-derived CMs discovered a typical fetal-like morphology and expression profiles that refer to immature CMs which represent the first-trimester gestational stage (van den Berg et al., 2015, Xu et al., 2009, Synnergren et al., 2012). To overcome the limitation of use caused by low maturity levels, novel

protocols were developed that are able to accelerate the maturation process including prolonged cultivation (Lundy et al., 2013), chemical induction (Birket et al., 2015), substrate stiffness (Feaster et al., 2015, Herron et al., 2016), mechanical (Akhyari et al., 2002) and electrical stimulation (Radisic et al., 2004, Marsano et al., 2016, Boudou et al., 2012). In conclusion, the disease specific onset of the cardiac phenotype defines the time point of investigation that depends on the maturation states of *in vitro* iPSC-derived CMs to be able to fully recapitulate disease-associated phenotypes. Furthermore, impurities and the individual cardiac subtype have to be taken into account for the distinct approach, before answering the scientific question, rushing to conclusions and defining their vague linkage to the specific cardiac disease.

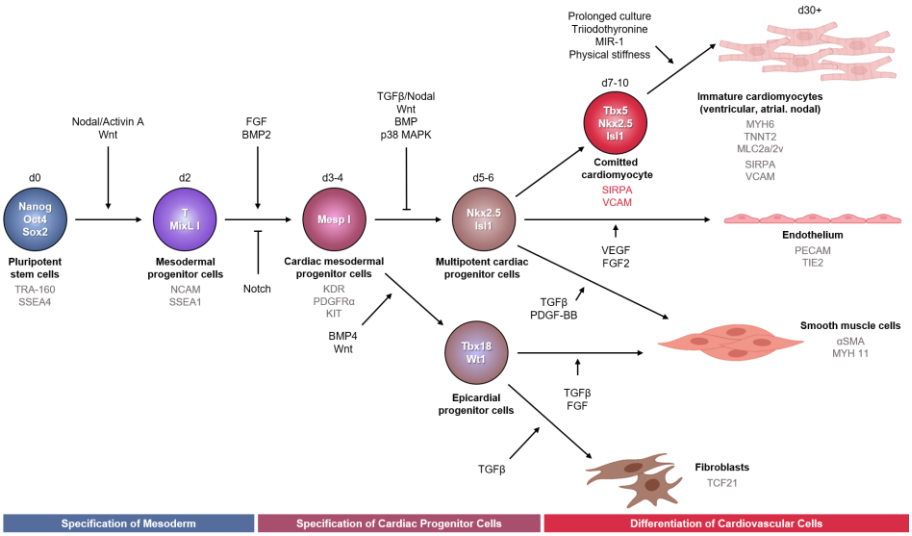

Figure 1.5 Cardiac lineage differentiation of human iPSCs to generate CMs *in vitro*.
The scheme was adapted after (Doyle et al., 2015). Three main stages are depicted: The specification of mesoderm, cardiac progenitors and the final differentiation into cells of the cardiovascular fate by using the individual signaling molecules. For the individual stages, important transcription factors (within cells), as well as cell expression markers (below the cells) are depicted. Finally differentiated cardiovascular cells are illustrated with typical gene expression profiles of CMs, endothelial cells, smooth muscle cells and fibroblasts (indicated below). The figure was created with BioRender.com.

1.3.5 Establishing novel *in vitro* models of inherited cardiomyopathies

In the present thesis, iPSC *in vitro* model systems of three different inherited cardiomyopathies were aimed to be generated: ACM, dilated cardiomyopathy with juvenile cataract (DCMJC) and dilated cardiomyopathy with ataxia (DCMA). As DCMA is the only disease that was investigated in more detail regarding the cardiac specific phenotype, disease-associated cellular mechanisms are separately described in the individual sections 1.4 and 1.5.

1.3.5.1 Genome editing of iPSCs to establish a novel isogenic model system of arrhythmogenic cardiomyopathy (ACM)

The clinical manifestation of ACM consists of enlargement of the left ventricle, fibro-fatty infiltration of the myocardium and life-threatening ventricular arrhythmias (Frank et al., 1978, Cerrone and Delmar, 2014, Cerrone et al., 2017, Pilichou et al., 2016, Awad et al., 2008). Causal mutations for ACM were already identified in genes encoding proteins of the desmosomes, predominantly in PKP2 (Gerull et al., 2004) and desmoglein-2 (DSG2) (Pilichou et al., 2006, Awad et al., 2008). ACM patients primarily present with heterozygous missense, nonsense and frameshift mutations revealing its autosomal dominant pattern of inheritance (Awad et al., 2008, Austin et al., 2019). The highest amount of known mutations lead to a functional knock-out of the corresponding desmosomal protein which negatively affects cell-to-cell adhesion of two neighboring CMs (Awad et al., 2008, Austin et al., 2019). Up to now, the detailed pathomechanisms of how desmosomal dysfunctions lead to fibro-fatty replacement of CMs remain elusive. It is hypothesized that a transcriptional switch from myogenesis to adipogenesis and

fibrogenesis is causative for the phenotype (Garcia-Gras et al., 2006). Moreover, to discover possible therapeutic targets, further investigations are required to understand the connection between disturbed cardiac tissue integrity and human heart function. First studies ablated *Pkp2* in mice and observed embryonic lethality on mid-gestation (embryonic day (E)10.5-E11) due to rupture of cardiac walls and an essential function of PKP2 in the assembly of junctional proteins (Grossmann et al., 2004). Additionally, examinations of *Dsg2* mutant mice displayed features of ACM such as fibro-fatty replacement of CMs and dilation (Krusche et al., 2011). The limiting factor in unraveling molecular pathomechanisms of the disease in mice was the embryonic lethality upon PKP2 (Grossmann et al., 2004) or DSG2 depletion (Eshkind et al., 2002). New conditional knock-out models of DSG2 (Kant et al., 2015) and PKP2 (Cerrone et al., 2017) arose with pronounced ACM-related phenotypes such as dilation, fibrosis and conduction defects. At the same time more and more limitations emerged when using murine models of human ACM due to the discrepancies in life span, immune response and epicardial fat proportion (Kant et al., 2015). Therefore, patient-derived cell lines were reprogrammed carrying homozygous *PKP2* c.2484C>T (Kim et al., 2013) or heterozygous *PKP2* c.972InsT/N (Caspi et al., 2013) frameshift mutations in *PKP2* to establish human models of ACM. Exaggerated lipogenesis upon reduced PKP2 levels was accompanied by prolonged field potential duration (FPD) and increased cell sizes (Kim et al., 2013, Caspi et al., 2013). Even though homozygous knock-out mice models, heterozygous and homozygous patient-derived iPSC lines exist, the molecular mechanisms leading to ACM are not entirely clear. It has been reported that genetic modifiers and environmental factors impede the identification of potential pathways in ACM (Awad et al., 2008, Austin et al., 2019). The observed cardiac phenotypes differ among and within the described species and cannot be connected given the lack of a powerful link, which we aim to provide by the generation of human PKP2 knock-out (PKP2-KO) and DSG2 knock-out (DSG2-KO) iPSC lines within the same genetic background of healthy iPSCs.

1.3.5.2 Generation of patient-derived LEMD2 p.L13R iPSCs to mimic dilated cardiomyopathy with juvenile cataract (DCMJC)

Patients suffering from DCMJC exhibit a clinical manifestation of left ventricular or biventricular dilatation, systolic dysfunction, inferolateral pattern of fibrosis that is accompanied by ventricular arrhythmias and sudden cardiac death. The unique phenotype with a heterogeneous incidence of juvenile cataract was identified in the genetically isolated Hutterite population in Canada (Dellefave and McNally, 2010, Boone et al., 2016, Abdelfatah et al., 2019b). Affected patients carry a homozygous, recessive missense mutation in *LEMD2* (NM_181336.4):c.38T>G encoding the inner nuclear envelope protein LEM-domain containing protein 2 (LEMD2)(Boone et al., 2016). The investigation of a LEMD2 knock-out mouse model demonstrated embryonic lethality by embryonic day 11.5 upon LEMD2 depletion underlining the importance of LEMD2 in developmental processes (Tapia et al., 2015). Examinations of the DCMJC patient`s (family 600) tissue revealed clumped heterochromatin, decreased proliferation and abnormally shaped nuclei together with hypertrophic CMs (Abdelfatah et al., 2019b). The homozygous *LEMD2* (NM_181336.4):c.38T>G mutation causes an aa substitution of leucine (L) to arginine (R) at position 13 (LEMD2 p.L13R) within the essential highly conserved N-terminal LEM-domain. The detailed pathomechanism remains unclear but it is hypothesized that p.L13R is impairing LEMD2 interaction capacities to other nuclear envelope proteins like barrier-to-autointegration factor (BAF), which may be crucial in maintaining nuclear integrity, chromatin remodeling, cellular proliferation and senescence (Abdelfatah et al., 2019b). Therefore, the link of the patients` missense mutation *LEMD2* (NM_181336.4):c.38T>G in provoking the cardiac phenotype needs further investigations. To overcome this issue a patient-derived LEMD2 p.L13R iPSC line was aimed to be generated by using dermal fibroblasts of a male 38-year-old mutation carrier from the same family cohort used in Abdelfatah et al., 2019 to provide a human *in vitro* system to study DCMJC-related pathomechanisms.

1.4 Insights into molecular mechanisms underlying dilated cardiomyopathy with ataxia (DCMA)

The autosomal recessive disease inherited DCMA was primarily reported in the consanguineous Canadian Hutterite population. The main clinical features are DCM, cerebellar ataxia, 3-methylglutaconic aciduria (3-MGA), prolonged QT interval and the association to a metabolic syndrome

(Davey et al., 2006). These pathological manifestations are accompanied by versatile phenotypes such as failure to thrive, developmental delay and male genital anomalies. Genetic familial screening of 18 patients revealed a causative homozygous *DNAJC19* (NM_145261.4):c.130-1G>C mutation encoding the inner mitochondrial protein DnaJ heat shock protein family (Hsp40) member C19 (DNAJC19) (Entrez Gene ID 131118) (Davey et al., 2006, Richter-Dennerlein et al., 2014). The guanine (G) to cytosine (C) transversion at the conserved splice acceptor site of intron 3 contributes to exon 4 skipping resulting in the loss of full-length *DNAJC19* (Davey et al., 2006). Given the mitochondrial localization of DNAJC19, DCMA is proposed to be a disease of defective mitochondria that is associated with abnormal mitochondrial homeostasis and altered mitochondrial energy metabolism (Lu and Claypool, 2015, Richter-Dennerlein et al., 2014). How *DNAJC19* mutations cause alterations in mitochondrial function and the impact on downstream processes causing DCMA and heart rhythm disturbances is unknown.

A study of two brothers of Finnish origin unraveled a novel *DNAJC19* mutation with a homozygous nucleotide deletion in exon 6 of *DNAJC19* (NM_145261.3):c.300delA (p.Ala100fsX11) resulting in a premature termination codon (Ojala et al., 2012). The main phenotypes were early onset-DCM, ataxia and male genital anomalies that overlap with previous findings, but these patients have extended features such as noncompaction cardiomyopathy (Ojala et al., 2012). The third case report of a 4-year-old female individual with a homozygous *DNAJC19* (NM_145261.3):c.280+1_280+5delGTAAG splice site deletion presented left ventricular DCM with non-compaction and additional neuronal features of progressive cerebellar atrophy (Al Teneiji et al., 2016). The DCMA-association of DNAJC19 was further confirmed in a study of a Turkish boy, who demonstrated dilatation of the whole heart, growth failure, facial dysmorphism, bilateral cryptorchidism, sensorineural hearing loss, mental and motor delay at the age of two months caused by a homozygous stop mutation c.63delC (p.Tyr21*) in *DNAJC19*. The cardiac phenotype evolved in the second year of his life but worsened until he died of aspiration at the age of three years (Ucar et al., 2017). These so far only reported studies underline that DCMA is not as rare as first suspected. In general, the average onset of DCMA was twelve months (range 1-36 months) quantified in a cohort of 30 patients (Sparkes et al., 2007). Additional 60 % of these patients demonstrated congestive heart failure and/or arrhythmias as cause of early death at the mean age of 22 months (range 4–48 months) (Sparkes et al., 2007, Davey et al., 2006). Affected patients consistently presented five- to tenfold increases in both plasma and urine 3-MGA, that demonstrate the suitability of 3-MGA as biomarker for the classification of DCMA into the group of 3-MGA type V (Wortmann et al., 2012, Davey et al., 2006). Treatments of those patients with available congestive heart failure therapy resulted in partial improvement of cardiac function, but there is to date no specific treatment available. To date no animal model exists for the investigation of DCMA, highlighting the necessity of novel model systems for studying the DNAJC19-associated pathological mechanism and potential treatments.

1.4.1 The generation of a novel human platform to study DCMA with patient-derived and genetically modified iPSCs

In the present thesis, we aimed to establish a novel *in vitro* system of DCMA in order to uncover the cellular and molecular mechanisms of DCMA in patient-derived and genetically modified iPSCs in a DNAJC19-specific manner. Our model system is based on dermal fibroblasts of two affected siblings of the Canadian Dariusleut Hutterite population who carry the same homozygous *DNAJC19* (NM_145261.4):c.130-1G>C mutation as reported in Davey et al., 2006. The homozygous mutation is predicted to provoke skipping of exon 4, resulting in a C-terminal truncated DNAJC19 protein that lacks the DnaJ domain only. The sib-pair of an 8-year-old boy (DCMAP1, DCMA patient 1) and his 10-year-old sister (DCMAP2, DCMA patient 2) presented early manifestations of DCMA with phenotypic variability. In detail, the male individual underwent a heart transplantation due to DCM with severe reduced cardiac functions at the age of two years. A less severe phenotype was observed in the sister´s heart as she presented only mild cardiac dysfunctions after conventional heart failure therapy. However, the presence of a prolonged QT interval of >510 milliseconds (ms) in her electrocardiogram (ECG) and ventricular arrhythmias led to the transplantation of an internal cardioverter defibrillator (ICD). The discordant features described in our patients are consistent with the heterogeneous clinical presentations of DCMA in previous studies, thus enabling a more detailed investigation of DCMA in a

patient-specific manner (Davey et al., 2006). Additionally, a third DNAJC19tv (DNAJC19 truncation variant) iPSC line was generated in the healthy genetic background of control iPSCs using CRISPR/Cas9 technology to generate an isogenic mutant control line that allows to draw more precise conclusions to the heterogenous phenotype of DCMA.

1.4.2 DNAJC19 structure and proposed functions

The DCMA-associated gene *DNAJC19* is located on chromosome (chr.) 3q26.33 and a study of *DNAJC19* expression in multiple human tissues revealed the presence of two main transcript variants (525 bp and 445 bp) that are expressed in both the fetal and adult heart. The 525 bp band that was detected in the report of Davey et al., 2006 corresponds to the full-length coding sequence containing the 5`and 3` untranslated region (UTR) boundaries and all six exons that results in the full-length protein isoform 1 comprising 116 aa with a mass of 12.5 kilodalton (kDa). The predicted domain structure of the full-length DNAJC19 protein contains a C-terminal DnaJ domain spanning 66-116 aa preceded by a N-terminal transmembrane domain ranging from residues 4-23 aa. Additionally, a mitochondrial targeting region was hypothesized given the presence of aa residues that may form an amphipathic α-helical structure. The second identified band of 445 bp lacks a part of the coding sequence corresponding to the region of exon 4 (Δex4) when compared to the full-length transcript variant 1. If translated, a C-terminal DNAJC19 truncated protein is expressed that would contain the predicted transmembrane domain only and lack the DnaJ domain (Davey et al., 2006).

DNAJC19 demonstrates a different domain structure in comparison with other DnaJ proteins and orthologs. Classical DnaJ proteins, such as the *E. coli* DnaJ/HSP40 proteins possess a N-terminal DnaJ domain and additional domains like a glycine/phenylalanine-rich linker domain, a cysteine-rich domain comprising four zinc-finger-like motifs (CXXCXGXG), as well as an unknown C-terminal domain (Davey et al., 2006). All DnaJ proteins share the DnaJ domain as a common characteristic unraveling 41 different family members in humans. Similar to 99 % of all mitochondrial proteins, DNAJC19 is encoded by the nuclear genome and transported into the mitochondria (Davey et al., 2006, Rehling et al., 2003). Sequence and topological homologies link human DNAJC19 to the yeast translocase of the inner membrane 14 (TIM14), that is part of the presequence translocase-associated motor 18 (PAM18)/TIM14 complex and is involved in the mitochondrial pre-sequence protein import. The high evolutionary conservation of *DNAJC19* in particular concerning the DnaJ domain among multiple species, raising from yeast to humans, highlights its undeniable function in mitochondria (Qiu et al., 2006, Davey et al., 2006). It was suggested that DNAJC19 is able to interact with the translocase of the inner membrane 23 (TIM23) via its matrix facing DnaJ domain and therefore aids pre-sequence protein trafficking into the mitochondrion (Davey et al., 2006). Another study using tetracycline-inducible human embryonic kidney 293 containing SV-40 T-antigen (HEK293T) cells that expressed C-terminally FLAG-tagged DNAJC19 confirmed the localization of DNAJC19 in the inner mitochondrial membrane (IMM) in human cells (Richter-Dennerlein et al., 2014). Furthermore, Richter-Dennerlein et al., 2014 demonstrated prohibitin-2 (PHB2) to be a novel direct interaction partner of DNAJC19. They proposed an essential interaction of DNAJC19 with PHB complexes (PHB1 and PHB2) in establishing scaffolds within the IMM that contribute to the regulation of CL remodeling (Richter-Dennerlein et al., 2014).

Taken together, two main mechanisms have been proposed for the function of DNAJC19: mitochondrial pre-sequence protein import and consequently mitochondrial biogenesis (fusion and fission) as well as mitochondrial lipid remodeling.

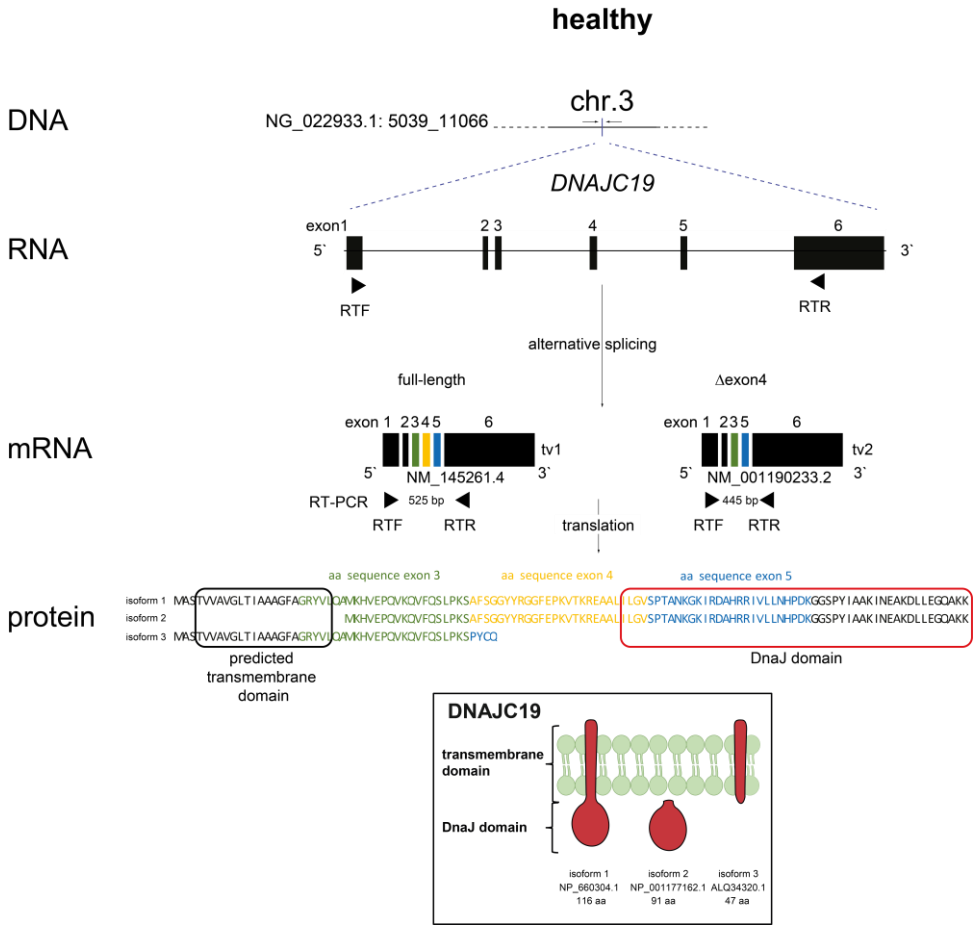

Figure 1.6 The expression hierarchies of DNAJC19 in humans.
DNAJC19 is located on chr. 3 and includes a maximum of six exons. Alternative spicing leads to the formation of two different transcript variants, one full-length containing all 6 exons and one lacking exon 4 (Δexon4). Reverse transcription polymerase chain reaction (RT-PCR) primer were adapted based on the report of Davey et al., 2005 to target the 5`and 3`boundaries to include the full coding sequence of both transcript variants, that would result in a PCR product size of 525 bp (full-length) and 445 bp (Δexon4). After translation the full-length transcript results into two different isoforms, 1 and 2, due to an alternative start codon. The Δexon4 transcript results in isoform 3, consisting of a transmembrane domain only. The distinct DNAJC19 domain structures comprise a N-terminal transmembrane domain (4-23 aa) and/or a C-terminal DnaJ interaction domain (66-116 aa). The schematic shows a representation of the topology of the human DNAJC19 isoforms anchored in the IMM, facing the DnaJ interaction domain into the matrix. All known three DNAJC19 isoforms were illustrated according to the information of the National Biocenter for Biotechnology Information (NCBI) database and previous reports (Davey et al., 2006, Richter-Dennerlein et al., 2014).

1.4.2.1 DNAJC19 in mitochondrial presequence protein import

DNAJC19 possesses a mitochondrial transit peptide within the first 18 N-terminal aa that directs the protein inside the mitochondria, where it is supposed to be anchored into the IMM via its transmembrane domain exposing the DnaJ domain to the mitochondrial matrix. In yeast, the DNAJC19 orthologue TIM14 itself is part of the mitochondrial import translocase machinery TIM23. In general, most of the mitochondrial preproteins are imported by a N-terminal matrix targeting signal (MTS) via the translocase of the outer membrane (TOM) complex together with TIM23. In eukaryotes ten components of TIM23 were identified that are all essential in maintaining cell viability. TIM23 can be subdivided into a membrane-integrated channel unit and an import motor unit. The channel unit recognizes new preproteins and mediates their insertion that depends on the inner mitochondrial membrane potential (Δψ). Further translocation into the matrix is performed by the import motor unit mainly formed by its central component: the mitochondrial heat shock protein 70 (mtHsp70). Hsp70 chaperones drive the transport of preproteins through conformational changes mediated by adenosine triphosphate (ATP)-hydrolysis to bind substrates and to fully accomplish the import into the mitochondrial matrix and to additionally prevent backsliding through the TIM23 pore (Rehling et al., 2003, Bukau and Horwich, 1998,

Matouschek et al., 2000, Neupert and Brunner, 2002). The mtHsp70 activity is mainly supported by two types of co-chaperones, nucleotide exchange factors like the mitochondrial homolog of the prokaryotic heat shock protein GrpE (Mge) and DnaJ proteins such as TIM14 (DNAJC19). Therefore, it is proposed that the yeast ortholog TIM14 (DNAJC19) stabilizes mtHsp70 through its DnaJ domain thus supporting its ATPase activity. The detailed import mechanisms and the precise function of DNAJC19 (TIM14) as mitochondrial co-chaperone is still under debate (Matouschek et al., 2000, Neupert and Brunner, 2002). However, the hypothesized link of DNAJC19 to a function in the mitochondrial import machinery directly contributes to a function in proper mitochondrial biogenesis including fusion and fission. Therefore, the hypothesis that DCMA syndrome phenotypes might be a result of impaired protein import and assembly of pre-sequence proteins in mitochondria was suggested (Davey et al., 2006).

1.4.2.2 DNAJC19 in cardiolipin (CL) remodeling

Another study of Richter-Dennerlein et al., 2014 linked DNAJC19 to a novel function in mitochondria by proposing a critical role in CL remodeling. It is hypothesized that the redistribution of lipids such as CLs in the IMM is maintained by the interaction of DNAJC19 with PHB complexes. The study used HEK293T cells to demonstrate that DNAJC19 predominantly associates with PHB complexes rather than with TIM23 and implicated DNAJC19 as a direct interaction partner of PHB2 (Richter-Dennerlein et al., 2014). PHBs form membrane bound hetero-oligomeric ring-like structures with alternating PHB1 (31 kDa) and PHB2 (35 kDa) subunits. Both subunits are highly conserved especially in the C-terminal coiled-coil regions that mediate the formation of large lipid and protein assemblies in the IMM (Tatsuta et al., 2005, Christie et al., 2011, Osman et al., 2009b). Most rings consist of 16 to 20 subunits that are assembled to high molecular weight complexes of around 1.2 megadalton (MDa) and can reach sizes to outer dimensions of ~270 x 200 Ångström (Å) (Steglich et al., 1999, Nijtmans et al., 2000, Artal-Sanz et al., 2003). Different sizes and shapes of PHB complexes reflect their dynamic nature and their link to many important cellular processes such as apoptosis (Vander Heiden et al., 2002, Fusaro et al., 2003), cellular senescence (Coates et al., 2001) or mitochondrial biogenesis (Berger and Yaffe, 1998, Steglich et al., 1999, Nijtmans et al., 2000, Artal-Sanz et al., 2003). PHB complexes regulate the turnover of membrane proteins through interactions with the matrix-oriented AAA (m-AAA) protease in quality control of mitochondria (Steglich et al., 1999). Additionally, the function of PHB rings was proposed to provoke cluster formation of phospholipids such as mitochondrial CL and phosphatidyl ethanolamine (PE) at distinct sites with a defined spatial organization within the IMM (Osman et al., 2009a, Osman et al., 2009b). These PHB-built membrane domains are essential in the life span and the integrity of mitochondria (Artal-Sanz and Tavernarakis, 2009). The mitochondrial morphology is highly dependent on the individual lipid composition of the outer mitochondrial membrane (OMM) and the IMM which sets the borders of the intermediate compartment termed intermembrane space. The outer membrane is smooth whereas the IMM gives rise to invaginations into the mitochondrial matrix that are referred to as cristae. The IMM has a special phospholipid class signature: phosphatidylcholine (PC), PE and CL, in a 2:1:1 molecular ratio, respectively (Horvath and Daum, 2013, Maniti et al., 2009). Typical phospholipids, like PE, possess two fatty acid (FA) chains linked to a phosphate head group which form straight lipid bilayers. CL is a phospholipid that is unique to mitochondrial membranes and almost entirely found in the IMM. CL is build up like a dimer of typical phospholipids that are connected by a glycerol bridge (Pangborn, 1946, Hostetler et al., 1971, Hoch, 1992). The four FA chains with only one polar double phosphate head group contribute to the conical shape of CL which is irreplaceable in establishing the highly folded curvatures of the IMM cristae (Signorile et al., 2019). Together with the more cone-shaped PE the negative curved monolayer leaflet is build up facing the polar groups to the cristae lumen. The CL pool is asymmetrically distributed in the IMM, having a higher concentration on the matrix side (Krebs et al., 1979). Along the lines, the matrix facing positively curved monolayer contains mostly PC (~80 %) and minor amounts of phosphatidylserine (PS) and phosphatidylinositol (PI) (Horvath and Daum, 2013). The unique phospholipid composition especially regarding CL species influences mitochondrial homeostasis by providing stability to individual enzymes and protein complexes involved in oxidative phosphorylation (i.e., energy metabolism) and mitochondrial fusion and fission (ie., mitochondrion morphology) (Lu and Claypool, 2015). CL is synthesized among an enzymatic cascade starting from phosphatidic acid (PA) derived from the endoplasmic reticulum (ER) ending in the formation of immature

CL in the mitochondrial matrix. Immature CL is afterwards remodeled into mature CL by the calcium-independent phospholipases (iPLA2 family) (Chang et al., 1998, Chen et al., 2006, Lu et al., 2006) and the mitochondrial enzymes TAZ, monolyso-cardiolipin acyltransferase 1 (MLCLAT1) (Taylor and Hatch, 2009, Taylor et al., 2012), acyl-CoA:lysocardiolipin acyltransferase (ALCAT1) (Li et al., 2012, Li et al., 2010). The iPLA2 family mediates the exchange of saturated acyl chains of immature CL into the intermediate form monolyso-cardiolipin (MLCL) (Mancuso et al., 2007). The IMM-located acyltransferase TAZ (Brandner et al., 2005, Claypool et al., 2006) catalyzes the transfer of an unsaturated acyl chain to remodel mature CL (Chang et al., 1998, Chen et al., 2006, Lu et al., 2006). Mature CL is characterized by symmetric acyl chain lengths and equal degree of saturation in all four acyl chains (Schlame et al., 2003, Schlame et al., 2005, Claypool and Koehler, 2012). CLs participate in different signaling pathways as the double bonds of the unsaturated acyl chains are oxidized by molecular oxygen (Saric et al., 2015, Tyurina et al., 2014). For example, the oxidation of CL result in lipid degradation products called 4-hydroxy-trans-2-nonenal (4-HNE) that are generated through cross-chain peroxyl radical addition, which is a typical signature in heart failure (Liu et al., 2011).

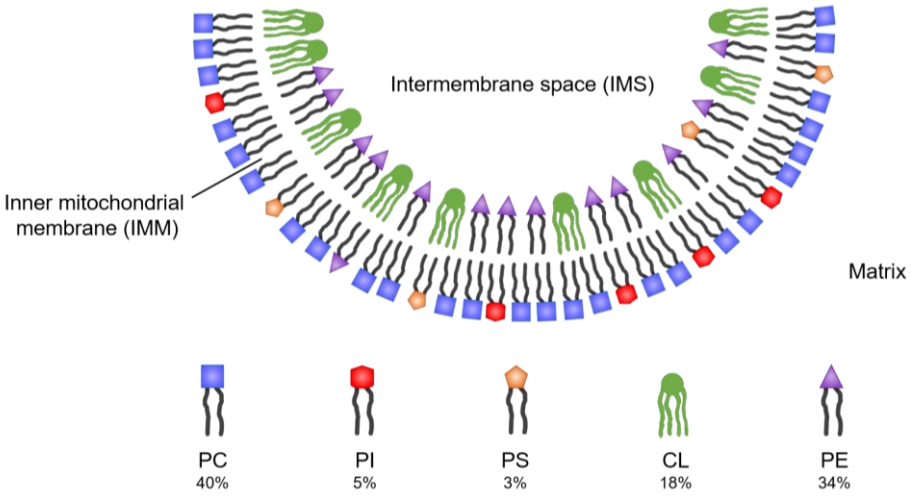

Figure 1.7 Asymmetrical phospholipid composition of the inner mitochondrial membrane
Mitochondrial phospholipids are asymmetrically distributed. The matrix facing leaflet (positively curved) is composed of PC, PI and PS. The intermembrane space facing leaflet (negatively curved) mainly includes PE and CL. The phospholipid composition of the rat liver mitohcondria is depicted (Horvath and Daum, 2013). The schematic illustration was modified after Ikon and Ryan, 2017. The illustrated segregation of phospholipids presents how the torsional strain is reduced that would otherwise result in a highly curved bilayer. CL with its unique conical shape allows the creation of IMM curvatures without impairing the phospholipid bilayer integrity. The figure was created with BioRender.com.

1.4.2.3 Relations between DCMA and Barth Syndrome (BTHS)

BTHS patients display a similar clinical presentation as DCMA patients including DCM, growth failure and raised levels of 3-MGA. The main phenotypic differences are neutropenia, skeletal myopathy and its X-linked heritage of mutations in the *TAZ* gene (Barth et al., 1983, Kelley et al., 1991). In addition, both proteins TAZ and DNAJC19, show the common feature of localization in the IMM and are both implicated in CL metabolism. In contrast to the proposed function of DNAJC19, TAZ mediates the remodeling process of CLs directly. The acyl chain composition is continuously reconstructed by the previous removal of one FA chain resulting in the immature MLCL and the subsequent re-acylation by TAZ (Osman et al., 2011). The CL remodeling of acyl chains is a highly dynamic process which gives rise to cell type specific CL profiles with certain FA compositions depending on multiple environmental keys (Ikon and Ryan, 2017, Cole et al., 2016, Dudek et al., 2016, Peyta et al., 2016). In the human heart the CL acyl chain composition primarily consists of double unsaturated linoleic acid (LA, (18:2)) at all four positions termed tetralinoleoyl cardiolipin $(18:2)_4$ (Schlame and Otten, 1991, Hoch, 1992). Therefore, the impairment of TAZ inevitably causes an accumulation of MLCL as well as a reduced amount of CL with altered acyl chain compositions that was observed in multiple species (Gu et al., 2004, Schlame et al., 2003, Houtkooper et al., 2009, Vaz et al., 2003). The increased MLCL to CL ratio

provides a useful marker for disturbed CL metabolism – i.e., BTHS (Barth et al., 1983, Bione et al., 1996, Vreken et al., 2000). As the same observations were made in yeast (Gu et al., 2004) and in several human tissues including left and right ventricle, skeletal muscle (Schlame et al., 2003) and dermal fibroblasts in TAZ-deficient conditions (Houtkooper et al., 2009, Vaz et al., 2003), the pathological mechanism underlying BTHS seems to be highly conserved. Dysfunctions in CL metabolism were linked to abnormal mitochondrial biogenesis including severe structural and functional impairments of mitochondria (Bissler et al., 2002, Xu et al., 2005, Acehan et al., 2007). Increasing evidence suggests an enormous influence of the mitochondrial phospholipid metabolism on mitochondrial structure and function in both diseases and underlines the idea of a similar molecular pathogenesis impacting the human heart function in DCMA and BTHS.

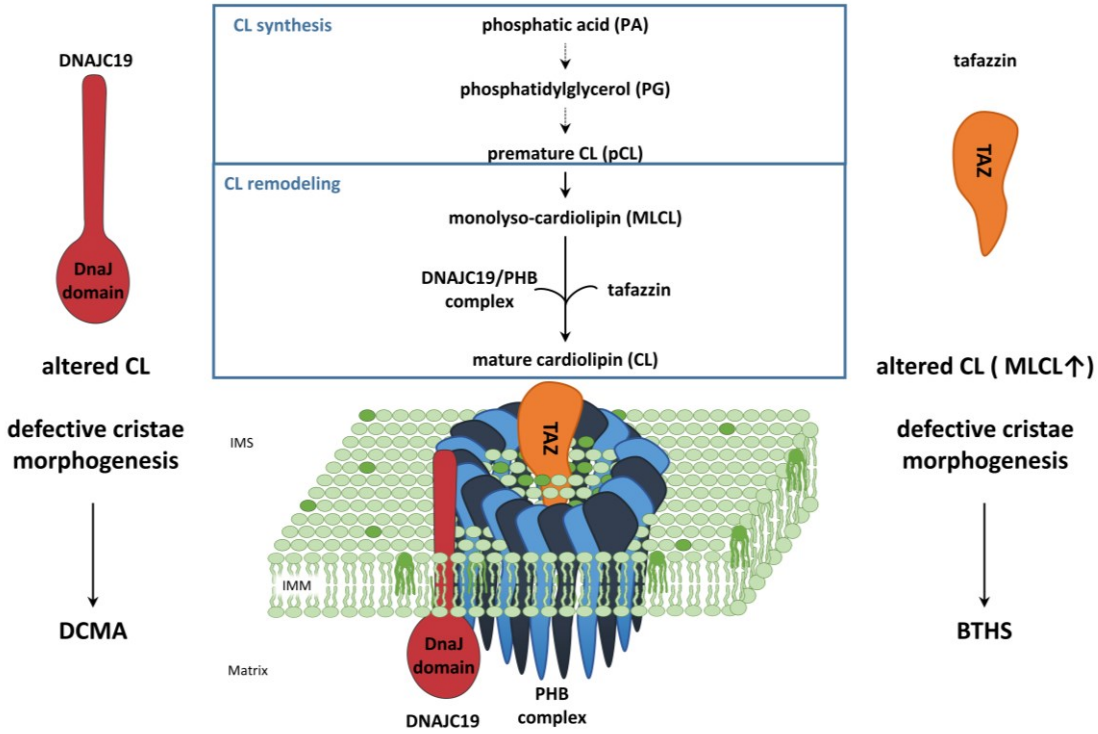

Figure 1.8 Potential overlapping pathomechanisms in DCMA and BTHS implicate defects in CL remodeling
The unique phospholipid of the IMM, CL, is synthesized by an enzymatic cascade starting with PA. After premature CL is generated, CL is remodeled by exchange of acyl chains that is mediated by acyltransferases such as TAZ. The functional knock-out of *TAZ* is known to cause BTHS, a disease provoked by impaired re-acylation of MLCL resulting in increased levels of MLCL and altered CL compositions. In DCMA a similar pathomechanism is hypothesized, in which the interaction of DNAJC19 with PHB complexes is predicted to serve as IMM-specific scaffold for TAZ to enable proper CL remodeling. The study of Richter-Dennerlein et al., 2014 unraveled altered CL profiles and changes in cristae morphogenesis, similar to in BTHS conditions. Shared alterations in CL compositions and defects in cristae morphogenesis support the hypothesis of a similar pathomechanism.

1.5 Mitochondria meet energy demands of CMs

Mitochondria are the most essential organelles in maintaining human heart function. Therefore, it is likely that dysfunctions are closely associated with the pathogenesis and the development of heart failure (Stoll, 2017). Within humans, the heart is the most metabolically active organ that consumes ATP through hydrolysis to maintain its contraction capacity continuously from fetus to death. The generation of energy to ensure heart function is mainly depending on mitochondrial metabolism thus it is not surprising that CMs have the highest concentration of mitochondria in the human body with an unique subsarcolemmal, perinuclear, and intrafibrillar distribution within the cell (Brown et al., 2017). Under normal conditions, 70-80 % cellular ATP is regenerated from mitochondrial fatty acid oxidation (β-oxidation, FAO), while the remaining 20-30 % derive from oxidation of glucose and lactate, with even minor contribution from ketones and amino acids. (Marin-Garcia and Goldenthal, 2002, Stanley et al.,

2005, Lopaschuk et al., 2010). Cardiac mitochondria are therefore the main regenerator of ATP. Other functions of this organelle are the generation and regulation of ROS, the buffering cytosolic Ca^{2+} and the regulation of cellular apoptosis through the mitochondrial permeability transition pore (mPTP) (Stoll, 2017). To understand the link between mitochondrial dysfunctions and inadequate cardiac function, essential molecular mechanisms of cardiomyocyte metabolism need to be considered.

1.5.1 Insights into the dynamics of cardiac metabolism

In 1939 the energy-starvation hypothesis was proposed by Herrmann and Decherd who described altered energetics levels due to reduced creatinine content in the failing myocardium for the first time (Herrmann, 1939). Since then, impaired cardiac energy metabolism became of great importance in understanding the progress of heart failure (summarized (Neubauer, 2007)). Cardiac energy metabolism relies on ATP regeneration from adenosine diphosphate (ADP) via mitochondrial oxidative phosphorylation (OXPHOS) to 95 % due to insufficient supply from the glycolytic mechanism (Dayer and Cowie, 2004, Stanley et al., 2005). Moreover, the heart needs to adapt the generation of energy to the varying demand continuously by controlling a highly complex mechanism of signaling and enzymatic pathways that mediate the metabolic flux towards their mitochondrial oxidation. This dynamic process to convert chemical energy into mechanical energy can be divided into three essential steps: substrate utilization, OXPHOS, phosphocreatine (PCr) and creatine (Cr) shuttle from mitochondria to the cytosol back and forth and utilization by excitation-contraction (E-C) coupling (Neubauer, 2007).

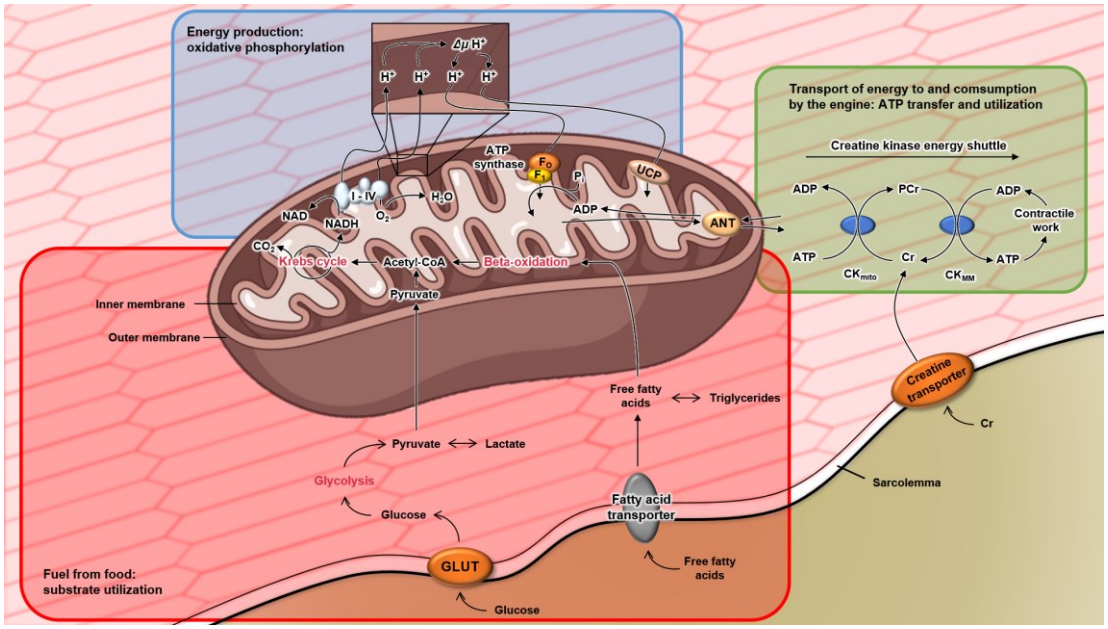

Figure 1.9 Complexity of cardiac energy metabolism.
The schematic illustration of the three main metabolic pathways to generate and transport energy throughout CMs: Substrate utilization (red), OXPHOS (blue), energy transfer and utilization (green). Original image of the report of Neubauer et al. 2007 was modified and created using BioRender.com (BioRender, 2017).

1.5.1.1 Substrate utilization in the human heart

The basis of substrate utilization is the processing of food into energy substrates followed by the cellular uptake of primarily FA and carbohydrates such as glucose (and to minor extent lactate). Medium- (10 to 12 carbons) and short-chain FA (2 to 8 carbons) comprise both favorable hydrophilic and lipophilic properties and therefore do not require a transport carrier and can be easily taken up by cells. In contrast, long-chain FAs (>14 carbons long, LCFA) require a protein-mediated mechanism driven by membrane-associated fatty acid-binding proteins (FABPm), the integral fatty acid transporter proteins 1-6 (FATP 1-6) and the fatty acid translocase (FAT, also known as CD36))(Glatz et al., 1997, Kazantzis and Stahl, 2012). Moreover, the utilization of glucose requires glucose transporters (GLUT) such as GLUT4 and GLUT1 (Mueckler and Thorens, 2013, Bertero and Maack, 2018). Minor source of energy is provided

by alternative substrates like ketones and amino acids (Stanley et al., 2005). The human heart has a limited capacity for long-term substrate storage of phosphor metabolites like phosphocreatine (PCr) which is derived from phosphorylation of creatine (Cr) via the mitochondrial creatine kinase (mitoCK) during OXPHOS using ATP regeneration mediated by the mitochondrial F_1F_O-ATP synthase (ATP synthase, complex V) (Dayer and Cowie, 2004, Neubauer, 2007). Typically the heart uses ~70-80 % β-oxidation of FA whereas the remaining ATP is provided through pyruvate oxidation (~20-30 %) that is preceded by equal amounts of oxidation of lactate and glycolysis of glucose that allows the generation of the intermediary metabolite acetyl coenzyme A (acetyl-CoA) that is transferred into the tricarboxylic acid (TCA) cycle (Stanley et al., 2005). Next, the TCA cycle mediates the oxidation of acetyl-CoA by a series of chemical reactions to the reduced pyridine nucleotides nicotinamide adenine dinucleotide (NADH) and flavin adenine nucleotide ($FADH_2$) that are transported to the mitochondrial electron transport chain (ETC) to serve as basis for OXPHOS.

1.5.1.2 Oxidative phosphorylation (OXPHOS), the mitochondrial electron transport chain (ETC) and the generation of reactive oxygen species (ROS)

OXPHOS comprises the mitochondrial ETC to mediate extracellular hydrogen transport upon oxygen consumption to re-phosphorylate ADP into ATP by the ATP synthase that is critical in all-energy consuming processes of the heart. The mitochondrial ETC includes a series of electron transfer steps with the help of protein complexes that either span the IMM ((NADH-ubiquinone oxidoreductase (complex I), cytochrome bc_1 (complex III), and cytochrome c oxidase (complex IV)) or reside inside the mitochondrial matrix (succinate dehydrogenase (complex II)). Additional accessory systems include the mobile carriers ubiquinone and cytochrome c in the intermembrane space as electron transporters. The components are specifically assembled in a closely configured supercomplex (Bogdanov et al., 2008, Szeto, 2014) that is directly alocated nearby the ATP synthase. This spatial arrangement is essential for ATP generation by OXPHOS that starts with the electron carriers NADH and $FADH_2$ as energy source. Two different electron transport pathways can be proceeded: NADH substrate based via complex I/III/IV or $FADH_2$ as substrate via complex II/III/IV. The utilization of NADH ($+H^+$) by complex I mediates its oxidation ($NAD^+ + e^-$) and the pass over of the released electron (e^-) to ubiquinone. $FADH_2$ follows a comparable mechanism as it is first reduced and then oxidized by complex II to transfer the electron to ubiquinone to give rise to the formation of ubiquinol ($Q+H_2$). The electron transfer of either complex I or complex II set the starting point of the electron flow, followed by ubiquinol-mediated electron delivery to complex III that itself passes them over to cytochrome c. Cytochrome c can freely move to complex IV and thereby transport electrons further. Complex IV then transfers electrons from reduced cytochrome c to oxygen, resulting in the production of H_2O. The electron flow through complex I, III and IV is accompanied by the pumping of protons (hydrogen ions) from the matrix into the intermembrane space. This proton flow creates both an electrical potential (mitochondrial membrane potential ($\Delta\psi_m$)) and a concentration gradient (chemical potential (ΔpH)). Accumulated protons from the inter membrane space are forced to equilibrate the proton gradient through the ATP synthase - the proton motive force ($\Delta\mu H$) - regenerating ATP molecules from ADP and a free phosphate (inorganic phosphate). This system is not 100 % efficient as electrons leak into the matrix and subsequently react with oxygen to generate ROS in the form of superoxide (free oxygen radicals (O_2^-)) or non-free radical hydrogen peroxide (H_2O_2) that are known to cause cellular damage to DNA, proteins and lipids (Jastroch et al., 2010, Szeto, 2014). In order to evaluate mitochondrial functionality the cellular oxygen consumption rate (OCR) and the extracellular acidification rate (ECAR) can serve as valuable parameters and can be determined with the help of the Seahorse XF96 extracellular flux analyzer (Ferrick et al., 2008). Individual characterization of OXPHOS intervenient is performed with inhibitory reagents including oligomycin (OLIGO) that inhibits the ATP synthase, carbonyl cyanide-4(trifluoromethoxy) phenylhydrazone (FCCP) as uncoupling agent that forces collapse of the $\Delta\psi_m$ and the proton gradient as well as rotenone and antimycin A (ROT&AA) that inhibit complex I and III respectively that enable access to critical information about respirative performance (Ferrick et al., 2008, Szeto, 2014).

1.5.1.3 Energy supply, calcium (Ca^{2+}) handling and excitation-contraction (E-C) coupling

In the mitochondrial intermembrane space, the mitochondrial isoform of the mitoCK transfers the phosphoryl group of newly regenerated ATP molecules to Cr, thus forming PCr. PCr is the necessary requirement to overcome the relatively slow cellular diffusion capacity of ATP (Greenhaff, 2001). At the myofilaments, myosin-hydrolyzed ATP is regenerated in the reverse reaction by the cytosolic/myofilament creatine kinase (M-CK). M-CK phosphorylates ATP from ADP at the expense of the PCr gradient. It is the PCr/Cr shuttle that maintains a high [ATP/ADP] ratio at the myofilament side and hence provides a stable spatial-temporal energetic network in the mitochondria to the myofilaments (Neubauer, 2007, Bertero and Maack, 2018, Bessman and Geiger, 1981, Wallimann et al., 1992, Greenhaff, 2001, Sequeira et al., 2015). The coordination of muscle contraction to supply the body with blood is the main function of the heart. It is accomplished by the E-C coupling mechanism within CMs and is initiated after AP-mediated excitation due to depolarization induced by the sinus node (Eisner et al., 2017a). Given their membrane invaginations the transverse tubules (T-tubules) are conducting the excitation signal throughout the whole cell. The depolarization process is mediated by the voltage-gated sodium channels ($Na_v1.5$) and enables the opening of the L-type calcium channels (LTCCs, in ventricular CMs $Ca_{V1.2}$) on the sarcolemma that in turn lead to the influx of Ca^{2+} towards the concentration gradient into the cell (Zimmer et al., 2014, Bodi et al., 2005). The change of the cellular charge state initiates the process of calcium-induced calcium release (CICR). This process includes the activation of the Ca^{2+} sensitive ryanodine receptors (RYR2) and the subsequent Ca^{2+} release out of the SR into the cytoplasm. The SR is known to be the main storage of Ca^{2+} and Ca^{2+} release is contributing to an increase in cytosolic (intracellular) Ca^{2+} levels about tenfold (~1 micromolar (µM) $[Ca^{2+}]_i$). This increase leads to the binding of Ca^{2+} to cardiac troponin C (cTnC) that is together with cardiac troponin I (cTnI) and cTnT part of the troponin-tropomyosin complex within the sarcomeric actin filaments. Ca^{2+} binding results in a series of conformational changes of myosin on actin, effecting the sliding and moving of CMs, visible by cellular shortening that sums up to the contraction of the entire heart (Bers, 2002b, Bers, 2006). This process is highly ATP dependent and consumes 90 % of the energy turnover of the in total 6 kg ATP amount daily (Ingwall, 2002). Contraction is followed by relaxation that is initiated by cellular repolarization based on the voltage dependent inactivation of the inwards directed Ca^{2+} current. Ca^{2+} is transferred back into the SR by sarco/endoplasmic reticulum Ca^{2+}-ATPase 2a (SERCA2a) to restore the SR Ca^{2+} pool and exported out of the cell by the Na^+/Ca^{2+} exchanger (NCX) that extrudes Ca^{2+} into the extracellular space (Bers, 2006). The tenfold reduction of cytoplasmatic Ca^{2+} levels leads to the dissociation of Ca^{2+} from TnC and thus results in the relaxation of myofilaments (Bers and Perez-Reyes, 1999, Bers, 2002b, Bers and Weber, 2002, Marks, 2013, Luo and Anderson, 2013).

1.5.1.4 Ca^{2+} buffering in mitochondria and ROS

The particularly exercise-mediated increased ATP consumption provokes the stimulation of the ATP synthase activity to increase the electron (e^-) flow and the turnover of NADH and $FADH_2$. Simultaneously, increasing contraction rates and an elevated amplitude of Ca^{2+} in response to chemical agents such as Iso promotes mitochondrial Ca^{2+} uptake via the mitochondrial Ca^{2+} uniporter (MCU) to regenerate NAD^+ and FAD to their reduced forms by the pyruvate dehydrogenase and the TCA cycle dehydrogenase respectively. Within this process the main mitochondrial H_2O_2 detoxifying systems (peroxiedoxin, glutathione, peroxidase, glutaredoxin) are reactivated. Therefore, mitochondrial ADP and Ca^{2+} are both controlling respiration, underlining the important role in mitochondrial Ca^{2+} buffering to match cellular energy requirements and to regenerate the antioxidative capacity to prevent mitochondrial ROS emission (Balaban, 2002, Bertero and Maack, 2018).

1.6 Aim of the thesis

The first aim of the present thesis was to assess the robustness of the SeV-based reprogramming method on multiple dermal fibroblast cell lines to allow the generation of mutant and healthy control human iPSCs. The efficiency will be explored with regard to age, gender and genetic background with focus on quality, time-consumption and retainment of mutations.

The precise CRISPR/Cas9 gene editing system was aimed to be established in healthy control iPSCs to generate known disease-gene specific knock-outs or truncation variants as isogenic mutant controls to remodel congenital heart diseases in an *in vitro* setting. The preciseness and efficiency of the gene editing tool should be evaluated to determine its robustness in specified genetic alterations.

After successful generation of human somatic cell-derived and gene-edited iPSC lines, all self-generated iPSC lines will be fully characterized according to international standards to ensure high qualities and typical pluripotent hallmarks to allow the further usage as personalized model systems of inherited cardiomyopathies such as ACM, DCMJC and DCMA. The novel human *in vitro* platform to study DCMA will be fully established by incorporation of patient-derived, gene-edited, age and gender-matched healthy control iPSC lines to allow detailed examination of a disease-associated mutation directly and to get insights into the permissive and protective genetic backgrounds in forcing the outcome of phenotypes.

To allow the study of disease-associated pathomechanisms of congenital heart diseases, *in vitro* settings, which are able to fully recapitulate heart-associated molecular mechanisms are required to ensure the translation of changes to the patients directly. Therefore, a monolayer differentiation protocol will be adapted to generate iPSC-derived CMs. With respect to DCMA, cultivation strategies will be optimized regarding cell purities, subtype identities and maturation states upon incorporation of different protocol strategies to accelerate maturation processes in particular to allow the investigation of E-C coupling mechanisms as a direct link to the heart rhythm disturbances.

After validation of purities, subtype identities and typical maturation hallmarks, the iPSC-derived CM-based *in vitro* system will be used to examine potential pathogenic mechanisms of DCMA as the main objective. We propose that the lack of the DnaJ domain in mutated *DNAJC19* leads predominantly to disturbed interaction with the PHB complex and thus may result in dysfunctional CL remodeling. We propose alterations in CL profiles that are known to affect the formation of cristae structures in the IMM that in turn are essential to maintain the assembly, the organization and function of the respiratory chain complexes to ensure OXPHOS. Therefore, mature-like iPSC-CMs will be investigated towards structural and morphological changes of mitochondria first.

We propose a mismatch between ATP demand and supply as well as aberrant ROS production in dysfunctional mitochondria that might also have downstream effects on sarcomere organization and cardiomyoycyte functionality and might finally lead to DCM and arrhythmias. Potential consequences of dysfunctional mitochondria will be examined by the assessment of mitochondrial function of the respiratory chain during OXPHOS. As we expect abnormal mitochondrial homeostasis in DCMA the connection to alterations of mitochondrial energy metabolism will be analyzed to get insights on DCMA-associated metabolic changes. To what extent potential mitochondrial dysfunctions limit the cell function will be evaluated by contraction capacities, intracellular Ca^{2+} homeostasis and arrhythmic potential.

Taken together, the personalized model system may contribute to the identification of molecular and metabolic mechanisms leading to DCMA. Further insights may enhance the understanding of more general questions of how abnormal mitochondrial homeostasis, energetic deficits and oxidative stress play a role in the pathophysiology of heart failure. This model system will offer an unique potential to identify therapeutic strategies in order to reverse the pathological process and to pave the way towards clinical applications for a personalized therapy in the future.

2. Material and Methods

2.1 Material

2.1.1 Laboratory equipment

Autoclaves		
	Systec VE-75 autoclave	Systec, Germany
Balance		
	Kern EW 200-2NM	Kern & Sohn GmbH, Germany
	Kern T3037	Kern & Sohn GmbH, Germany
Cell counter		
	TC20™ Automated Cell Counter	Bio-Rad Laboratories GmbH, USA
Centrifuges		
	Biofuge pico	Heraeus GmbH, USA (Kendro Laboratory Products GmbH, USA)
	Cenrifuge 2K15	Sigma Laborzentrifugen GmbH, Germany
	Mikro 220R	Andreas Hettich GmbH & Co.KG, Germany
	Mikro 200R	Andreas Hettich GmbH & Co.KG, Germany
	Rotina 380R	Andreas Hettich GmbH & Co.KG, Germany
	Rotina 420R	Andreas Hettich GmbH & Co.KG, Germany
	C1301-B Mini Centrifuge	Labnet International, Inc., USA
	Universal 32	Andreas Hettich GmbH & Co.KG, Germany
Cryo storage		
	Freezing container, Nalgene® Mr. Frosty	Merck KGaA, Germany
	BIOSAFE®	Cryotherm GmbH & Co. KG, Germany
Electrophoresis systems		
	Mini-PROTEAN® Tetra Vertical Electrophoresis Cell	Bio-Rad Laboratories GmbH, USA
	Sub-Cell GT Cell basic	Bio-Rad Laboratories GmbH, USA
	QIAxcell Advanced system	Qiagen GmbH, Germany
Flow Cytometer		
	BD FACSCanto II	BD Biosciences, USA
γ-counter		
	γ-counter wizard 2480 (#SGWC36160397)	PerkinElmer, Germany
Heaters		
	Thermomixer comfort	Eppendorf AG, Germany
	Thermostat™ C	Eppendorf AG, Germany
	Thermo Shaker TS-100C	Biosan, Kleinfeld Labortechnik GmbH, Germany
	Microwave MS23F301EAS	Samsung, South Korea
Homogenizer		
	Sonopuls™ homogenizer Mini20	Bandelin Electronic GmbH & Co.KG, Germany
	Branson Ultrasonics™ Sonifier Modell 250 CE	Thermo Fisher Scientific Inc., USA
Ice machine		
	Ice machine S-NO 162887	Zegra Eismaschinen GmbH, Germany
Incubators		
	Heracell™ 240i CO_2 Incubator	Thermo Fisher Scientific Inc., USA
	Heratherm™ Compact Microbiological Incubators	Thermo Fisher Scientific Inc., USA
	Multitron Standard	Infors HT AG, Switzerland
IonOptix		
	Acquisition Computer Optiplex 755	Dell Technologies, USA
	CFA300 Cell framing adapter (Image section adjustment)	IonOptix, USA
	Film sealing unit	Severin Elektrogeräte GmbH, Germany
	FSI700 Fluorescence system interface (D)	IonOptix, Dublin, Ireland
	µStep Light Source System (µStep filter wheel and controller (F), Xenon short arc lamp-75XE (75W), High Intensity Xenon Arc Lamp Power Supply (I)	F= IonOptix, USA, Xenon lamp=Ushio Inc. Japan, I= Cairn Research, United Kingdom

	Microscope Nikon Eclipse Ti-S & lamp power supply (E)	Nikon GmbH, Germany
	MSC100 MyoCam-S (High-Speed Contractility Camera) (G)	IonOptix, USA
	Photon to Voltage Converter (PTV) (H)	IonOptix, USA
	PMT400 Photomultiplier sub-system (IONOPTIX)	IonOptix, USA
	Pump SP302SA-V 230V/50Hz	Schwarzer Precision GmbH & Co.KG, Germany
	Stimulus Isolation Unit (SIU-102) (A)	Warner Instruments, USA
	Train/Delay Generator: Model DG2A (Stimulus pacer, J)	Digitimer Ltd., United Kingdom
	TC-324B automatic temperature controller (B) and Temperature Control (C)	Warner Instruments, USA
Laminar flow hoods		
	Safe 2020 biosafety cabinet	Thermo Fisher Scientific Inc., USA
Microscopes		
	Laser scanning confocal microscope LSM 780	Carl Zeiss Microscopy GmbH, Germany
	Olympus CKX53	Olympus Corporation, Japan
	Microscope color camera DFC 7000 T	Leica Microsystems CMS GmbH, Germany
	Microscope DMi8	Leica Microsystems CMS GmbH, Germany
	ZEISS LEO912AB	Zeiss NTS, Germany
Nucleofector		
	NEON™ Transfection System	Thermo Fisher Scientific Inc., USA
pH meter		
	FiveEasy™ F20	Mettler Toledo, USA
Pipettes		
	Pipetting aid accu-jet® pro	Brand, Germany
	Multipipette® stream	Eppendorf AG, Germany
	Pipette Eppendorf Research plus (diverse sizes)	Eppendorf AG, Germany
	Pipette Eppendorf Research (diverse sizes)	Eppendorf AG, Germany
	Research pro (diverse sizes)	Eppendorf AG, Germany
Plate Reader		
	Tecan Reader Spark™ 10M	Tecan Group Ltd., Switzerland
Power supply		
	PowerPac™ HC High-Current Power Supply	Bio-Rad Laboratories GmbH, USA
	Standard Power Pac P25	Biometra, Analytik Jena GmbH, Germany
Rocker		
	Multitron incubator shaker	Infors AG, Switzerland
	Rocking Shaker DRS-12	neoLabline GmbH, Germany
	MiniRocker MR-1	Biosan, Kleinfeld Labortechnik GmbH, Germany
	Oribital shaker L-40	Labinco B.V., Netherlands
Seahorse system		
	Seahorse XF96 extracellular flux analyzer	Agilent Technologies, Inc., USA
Stirrer		
	Magnetic stirrer L-71	Labinco B.V., Netherlands
	Kamag RCT	IKA®-Werke GmbH & Co. KG
	Magnetic stirrer Su1350	Sunlab GmbH, Germany
Spectrophotometer		
	NanoDrop™ One^{C}	Thermo Fisher Scientific Inc., USA
Transfer systems		
	Trans-Blot® Turbo™ Transfer System	Bio-Rad Laboratories GmbH, USA
Thermocycler		
	C1000 Touch™ Thermal Cycler	Bio-Rad Laboratories GmbH, USA
UV transilluminator		
	ChemiDoc™ Touch Imaging System	Bio-Rad Laboratories GmbH, USA
	N-90-M-UV benchtop	Benda Konrad GmbH, Germany
Vortex		
	Vortex Master Sun1901	Sunlab GmbH, Germany
	Vortex-Genie 2	Scientific Industries, Inc., USA
	Vortex Shaker VTX L-3000	LMS Inc., USA
Water baths		
	Water bath WNE-14	Memmert GmbH & Co. KG, Germany
Water System		
	Purelab® Flex pure water system PF2	ELGA LabWater Ltd., United Kingdom
	Milli-Q® IQ 7000	Merck KGaA, Germany

IonOptix mirror and filter sets (Chroma Technology GmbH)

Mirror/ filter sets	Mirrored wavelength [nm]	Transmitted wavelength [nm]	Dye	Location
D340/12x	-	340 ±6	Indo	filter wheel of excitation light source system (F0)
365/535pc (C120299)	340 / 540	405 / 485 / > 600	Indo/TMRM	filter wheel of the microscope (M1)
T660LPXR	< 660	> 660	transmitted light	Microscope (M2)
650DCXR	< 650	> 650	transmitted light	mirror in front of the camera (S1)
440DCLP	< 440	> 440	Indo/TMRM	mirror in front of PMT1 (S2)
D405/30x	-	405±15	Indo	filter in front of PMT1 (F1)
515DCXR	< 515	> 515	Indo/TMRM	mirror in front of PMT2 (S3)
D485/25x	-	485±15	Indo	filter in front of PMT2 (F2)

2.1.2 Disposables

2.1.3 Human cells and bacterial strains

Healthy control dermal fibroblasts can be traced back to the commercial provider (Promocell). One fibroblast cell line was obtained from a male 6-year-old donor (#C-12300) and the other one from a female 47-year-old donor (#C-12302). Three patient-derived dermal fibroblast cell lines derived from the Hutterite population and were obtained back in 2012 at the University of Calgary and approved by their ethical committee (ID-E20729) and are particularly intended for stem cell research. The investigation conforms to ethical guidelines for medical research involving human subjects and all principles outlined in the declaration of Helsinki. Fibroblasts have been transferred to the University Hospital Würzburg via Material Transfer Agreement (MTA; CAL01:426645;v1).

Normal control 6-year-old male (NC6M) iPSCs were generated by LeV reprogramming of Dr. K. Günther, Institute of Anatomy Würzburg (Günther, 2016).

The LEMD2 p.L13R patient was at the age of 38 years on the skin biopsy, carrying the recessive *LEMD2* c.T38G (p.L13R) mutation, He presented with Hutterite-type juvenile cataract and arrhythmic DCM (Abdelfatah et al., 2019a).

The male DCMAP1 and female DCMAP2-derived dermal fibroblasts were obtained at the ages of 8 and 10 years respectively, as the skin biopsy was performed in the year 2012. Both patients carry a recessive *DNAJC19* (NM_145261.4):c.130-1G>C mutation and suffer from DCMA.

Chemical competent *Escherichia coli* cells of the DH5α strain were used for all plasmid transformations.
MEF feeder cells

2.1.4 Chemicals, small molecules and growth factors

Product	Catalog number	Manufacturer
14:0 Cardiolipin (ammonium salt) 1',3'-bis[1,2-dimyristoyl-sn-glycero-3-phospho]-glycerol	710332-25G	Avanti Polar Lipids, USA
2-Propanol	20839.297	VWR International S.A.S., USA
4x Laemmli sample buffer	161-0747	Bio-Rad Laboratories GmbH, USA
6x DNA Loading Dye	R0611	Thermo Fisher Scientific Inc., USA
Accutase™	A1110501	Gibco™, Thermo Fisher Scientific Inc., USA
Agarose LE	M3044.0500	GENAXXON bioscience GmbH
Amersham™ ECL™ Rainbow™ Marker full range	RPN800E	GE Healthcare Inc., USA
Ammonium acetate for mass spectrometry	73594-25G-F	Merck KGaA, Germany
Ampicillin	K029.2	Carl Roth GmbH & Co.KG, Germany
Antimycin A	A8674-25 MG	Sigma-Aldrich GmbH, USA
Argon	8434469602	Riessner Gase GmbH, Germany
B-27™ supplement	17504044	Gibco™, Thermo Fisher Scientific Inc., USA
B-27™ supplement without insulin	A1895601	Gibco™, Thermo Fisher Scientific Inc., USA

Basic Fibroblast Growth Factor (bFGF) human, recombinant	13256-029	Gibco™, Thermo Fisher Scientific Inc., USA
BMP-4	PHC9534	Thermo Fisher Scientific Inc., USA
Bovine serum albumin	A2153-50G	Sigma-Aldrich GmbH, USA
Cacodylic acid	205541-100GM	Merck KGaA, Germany
Calcium chloride solution	21114	Honeywell Fluka, USA
Carbonyl cyanide 4-(trifluoromethoxy)-phenylhydrazone (FCCP)	C2920-10MG	Sigma-Aldrich GmbH, USA
CHIR99021 ((6-[[2-[[4-(2,4-dichlorophenyl)-5-(5-methyl-1H-imidazol-2-yl)-2-pyrimidinyl]amino]ethyl]amino]-3-pyridinecarbonitrile)	1386	Axon Medchem LLC., USA
cOmplete™, EDTA-free Protease Inhibitor Cocktail	11873580001	Merck KGaA, Germany
Crystal violet	C6158-100G	Merck KGaA, Germany
D-(+)-Glucose	G8270	Sigma-Aldrich GmbH, USA
DAPI	6335.1	Carl Roth GmbH & Co. KG, Germany
DMEM	41966-029	Gibco™, Thermo Fisher Scientific Inc., USA
DMEM/F-12	11320-074	Gibco™, Thermo Fisher Scientific Inc., USA
DMEM/F-12, Glutamax™ supplement	10565-018	Gibco™, Thermo Fisher Scientific Inc., USA
DMSO (Dimethyl sulfoxide)	D2650-100ML	Sigma-Aldrich GmbH, USA
dNTPs	U120A – U123A, or MPK10025	Promega Corporation or Thermo Fisher Scientific Inc.
Donkey serum	D9663-10ML	Sigma-Aldrich GmbH, USA
DPBS	D8537	Sigma-Aldrich GmbH, USA
EDTA	1.08418.1000	Merck KGaA, Germany
EDTA-free protease inhibitor cocktail	11873580001	Roche Diagnostics GmbH
Ethanol	32205-1L-M	Sigma-Aldrich GmbH, USA
Fetal calf serum (FCS)	S0615	Biochrom, United Kingdom
Gel Loading Dye, Purple (6x)	B7024S	New England Biolabs Inc., USA
Gelatin	G1890	Sigma-Aldrich GmbH, USA
GeneRuler™ 100 bp Plus DNA ladder	SM0321	Thermo Fisher Scientific Inc., USA
GlutaMAX™ Supplement	35050061	Gibco™, Thermo Fisher Scientific Inc., USA
Glutamine	G8540-25G	Sigma-Aldrich GmbH, USA
Glutaraldehyde 25 %	3778.1	Carl Roth, Germany
Glycerol	G5516-1L	Sigma-Aldrich GmbH, USA
Glycidyl ether 100	21045.01	SERVA Electrophoresis GmbH, Germany
Glycine	131340.1211	AppliChem GmbH
Hepes sodium salt	H7006	Sigma-Aldrich GmbH, USA
Hydrochloric acid solution, 1 M HCl (1N)	35328	Honeywell Fluka
Incidin® plus	3011510	Ecolab Inc., USA
Indo-1-AM	I1223	Invitrogen™, Thermo Fisher Scientific Inc., USA
Isopropanol	BDH1131-1LP	VWR International, LLC., USA
Isoproterenol, Isoprenaline hydrochloride	I5627	Sigma-Aldrich GmbH, USA
IWR-1	I0161-5MG	Sigma-Aldrich GmbH, USA
KaryoMAX® ColcemidTM Solution	15212012	Thermo Fisher Scientific Inc., USA
KCl	1.04936.1000	Merck KGaA, Germany
KH_2PO_4	1.04873.0250	Merck KGaA, Germany
KnockOut™ serum	10828-028	Gibco™, Thermo Fisher Scientific Inc., USA
L-ascorbic acid	A4544-500G	Sigma-Aldrich GmbH, USA
LB agar	L-2897	Sigma-Aldrich GmbH, USA
Magnesium chloride	1.05833	Merck KGaA, Germany
Matrigel® Growth Factor Reduced (GFR) Basement Membrane Matrix (mattress)	356230	Corning Inc., USA
Matrigel™ hESC-qualified matrix	354277	Corning Inc., USA
MEMNEAA	11140-050	Gibco™, Thermo Fisher Scientific Inc., USA
Methanol	8388.1	Carl Roth, Germany
MgCl x 6 H_2O	1.05833.0250	Merck KGaA, Germany
MitoTracker™ Deep Red FM	M22426	Thermo Fisher Scientific Inc., USA
Mowiol 4-88	81381	Sigma-Aldrich GmbH, USA
mTesr™1 basal medium + 5x supplement	85870	STEMCELL Technologies Inc., Canada
Na_2HPO_4	RES20908-A702X	Sigma-Aldrich GmbH, USA
Na_2HPO_4 x 2 H_2O	1.06580.1000	Merck KGaA, Germany
$Na_4P_2O_7$	1.06591.1000	Merck KGaA, Germany
NaCl	1367.1000	Th. Geyer GmbH & Co.KG, Germany
NaFl	S1504-100G	Sigma-Aldrich GmbH, USA
NaH_2PO_4 x H_2O	1.06346.1000	Merck KGaA, Germany
NaOH	S5881-1KG	Sigma-Aldrich GmbH, USA
NCS	N4762	Sigma-Aldrich GmbH, USA

Non-fat dried milk powder	A0830.0500	Applichem Inc., USA
Nonidet-P40	N3500	United States Biological Inc., USA
Oligomycin A	75351-5MG	Sigma-Aldrich GmbH, USA
Peptone	P7750-500G	Sigma-Aldrich GmbH, USA
PFA (paraformaldehyde)	P6148	Sigma-Aldrich GmbH, USA
Pfu DNA Polymerase	M7741	Promega Corporation or Thermo Fisher Scientific Inc., USA
Pluronic® F-127 20 % Solution in DMSO	59004	Biotium Inc., USA
Potassium chloride	1.04936	Merck KGaA, Germany
Puromycin	A1113803	Gibco™, Thermo Fisher Scientific Inc., USA
Pyruvate	P5280-25G	Sigma-Aldrich GmbH, USA
Q5® 5x High GC Enhancer	M0491S	New England Biolabs Inc., USA
Q5® 5x Reaction Buffer	B9027S	New England Biolabs Inc., USA
Q5® High-Fidelity DNA Polymerase	M0491S	New England Biolabs Inc., USA
RNAlater	1018087	Qiagen GmbH, Germany
ROCK Inhibitor Y27632	130-104-169	Miltenyi Biotec GmbH, Germany
Rotenone	557368-1GM	Sigma-Aldrich GmbH, USA
RPMI 1640 medium	21875034	Gibco™, Thermo Fisher Scientific Inc., USA
RPMI 1640 medium (-glucose)	11879020	Gibco™, Thermo Fisher Scientific Inc., USA
SDS	L4509-500G	Sigma-Aldrich GmbH, USA
Seahorse XF RPMI medium, pH7,4	103576-100	Agilent Technologies, Inc., USA
SOC outgrowth medium	B9020S	New England Biolabs Inc., USA
Sodium chloride	S7653	Sigma-Aldrich GmbH, USA
Sodium hydroxide	S5881	Sigma-Aldrich GmbH, USA
Sodium L-lactate	71718-10G	Sigma-Aldrich GmbH, USA
Sodium orthovanadate	S-6508	Sigma-Aldrich GmbH, USA
Sodium pyruvate	P2256	Sigma-Aldrich GmbH, USA
SPECTRA™ Multicolor Broad Range Protein Ladder	26623	Thermo Fisher Scientific Inc., USA
ß-mercaptoethanol (50 mM)	31350-010	Gibco™, Thermo Fisher Scientific Inc., USA
Terralin liquid	102001	Schülke & Mayr GmbH
TRIS base	T6066-500G	Sigma-Aldrich GmbH, USA
Triton X-100	28313	Thermo Fisher Scientific Inc., USA
Trypan blue dye 0.4 % solution	1450021	Bio-Rad Laboratories GmbH, USA
TrypLE	12604-021	Gibco™, Thermo Fisher Scientific Inc., USA
Trypsin-EDTA Solution 1x	59417C	Sigma-Aldrich GmbH, USA
Tween® 20	9127.1	Carl Roth GmbH + Co. KG
Yeast extract	70161-500G	Sigma-Aldrich GmbH, USA

2.1.5 Consumable supplies

Product	Manufacturer
Biosphere® filter tips (20, 100, 200, 1000 µl)	SARSTEDT AG & Co. KG, Germany
Biosphere® SafeSeal Tube (1.5, 2.0 ml)	SARSTEDT AG & Co. KG, Germany
Cell culture dishes (Ø 10 cm)	Greiner Bio-One GmbH, Austria
Cell Strainer Falcon™ 352360	Thermo Fisher Scientific Inc., USA
CELLSTAR® Polypropylen Tubes (15, 50 ml Falcon tubes)	Greiner Bio-One GmbH, Austria
CELLSTAR® Serological Pipettes (5, 10, 25, 50 ml)	Greiner Bio-One GmbH, Austria
Counting slides	Bio-Rad Laboratories GmbH, USA
Cryovials	Thermo Fisher Scientific Inc., USA
FACS tubes	SARSTEDT AG & Co. KG, Germany
Glass coverslips (Ø 10 mm, Ø 12 mm, 24 x 50 mm, 24 x 60 mm)	Paul Marienfeld GmbH & Co.KG, Germany
Kimtech wipes	Kimberley-Clark, USA
Menzel™ Microscope Coverslips 24 x 60 mm	Thermo Fisher Scientific Inc., USA
Microscope slides	Thermo Fisher Scientific Inc., USA
Microtupe strips	Brand, Germany
Mini-PROTEAN® TGX™ Precast Protein Gels (12-well, 15-well; 12,15 %, Any kD™)	Bio-Rad Laboratories GmbH, USA
Needles	B. Braun, Germany
Nickel grids	Plano, Germany
Nitril gloves	Hartmann, Austria
PARAFILM®	Bemis Company, Inc., USA
Pasteur pipets	A. Hartenstein GmbH, Germany
Petri dishes (Ø 10 cm)	SARSTEDT AG & Co. KG, Germany
Pipette tips (10, 100, 1000 µl)	SARSTEDT AG & Co. KG, Germany
RNAse, DNAse-free tubes (1.5 ml)	SARSTEDT AG & Co. KG, Germany
Secureline Lab Marker	Merck KGaA, Germany
Serological pipettes (5, 10, 25, 50 ml)	Greiner Bio-One GmbH, Austria

Syringe filters (0.2 µm)	Pall GmbH, Germany
Syringes	BD, USA
Tissue culture flasks (T25, T75, T175)	Greiner Bio-One GmbH, Austria
Tissue pads	MaiMed®, Germany
Tissues (Laboratory and hygenic wipes)	ZVG Zellstoff-Vertriebs-GmbH & Co.KG, Germany
Trans-Blot Turbo Mini 0.2 µm Nitrocellulose Transfer Packs	Bio-Rad Laboratories GmbH, USA
Weighing dishes	A. Hartenstein GmbH

2.1.6 Buffers

Buffer	Recipe
0.2 % Nonidet	Prepare a 1:500 dilution in 1xPBS
1x PBS	137 mM NaCl, 2.7 mM KCl, 8 mM Na_2HPO_4 x 2 H_2O, 1.3 mM KH_2PO_4 x H_2O in ddH_2O, pH 7.4
4 % PFA solution	4 % (w/v) paraformaldehyde in 1x PBS, pH 7.4
4′,6-diamidino-2-phenylindole (DAPI)	Prepare a 1:5000 dilution in 1xPBS
50xTAE buffer	2M (242 g) Tris base, 1M (57.1 ml) acedic acid, 0.5 M (100 ml) EDTA (pH 8.0) in 1 liter
5x buffer E	124 mM Tris base, 0.96 M glycine, 17 mM SDS in ddH_2O, pH 8.3
LB agar	1.5 % (w/v) LB agar in LB medium
LB medium	1 % (w/v) peptone, 0.5 % (w/v) yeast extract, 171 mM NaCl in ddH_2O, pH 7.0 - 7.5
MHC buffer	300 mM NaCl, 100 mM NaH_2PO_4 x H_2O, 50 mM Na_2HPO_4, 1 mM MgCl x 6 H_2O, 10 mM $Na_4P_2O_7$, 12.7 mM EDTA, 2.7 mM NaFl, 1 mM sodium orthovanadate in ddH_2O
Mild stripping buffer	200 mM glycine, 3.5 mM SDS, 1 % (w/v) Tween® 20 in ddH_2O, pH 2.2
Mowiol	6.5 mM Mowiol® 4-88, 5.4 M glycerol, in ddH_2O overnight; add same volume 0.2 M TRIS solution (pH 8.5), heat to 60 °C for 10 - 30 min, centrifuge 15 min 5000 g, use supernatant
TEM Cacodylate buffer (CB), 0.2 M stock solution	4.28 g Cacodylic acid sodium salt trihydrate in 100 ml ddH_2O and adjust to pH 7.5 using 1 N HCl
TEM Epon embedding mixture	26 g Glycidyl ether 100, 10 g Dodecenylsuccinic anhydrate, 15 g Methylnadic anhydride, 0.25 g 2,4,6-Tris(dimethylaminomethyl)phenol. The components were mixed until fully dissolved and degassed to avoid removing air bubbles.
TEM fixing buffer	2.5 % Glutaraldehyde (25 %), 0.8 % Tannic acid in 0.1 M CB, pH 7.5

2.1.7 Cell culture media and solutions

Buffer	Recipe
CBM	500 ml RPMI 1640 medium, 10 ml B-27™ supplement, 1 ml L-ascorbic acid, 1 ml ß-mercaptoethanol
CEM	500 ml RPMI 1640 medium without glucose, 0.5 ml sodium L-lactate
CSM	500 ml RPMI 1640 medium, 10 ml B-27™ supplement without insulin, 1 ml L-ascorbic acid, 1 ml ß-mercaptoethanol
Freeze medium (fibroblasts)	10 % (w/v) DMSO in fetal calf serum (FCS)
Freeze medium (iPSCs + iPSC-CMs)	10 % (w/v) DMSO in KnockOut™ serum
iPSC cultivation medium	400 ml mTesr™1 basal medium, 100 ml mTesr™1 5x supplement
MEF-medium	500 ml DMEM(1x), 50 ml FCS, 5 ml MEMNEAA, 1 ml ß-mercaptoethanol
Reprogramming medium	78 ml DMEM/F-12, GlutamaxTM supplement, 20 ml KnockOut™ serum, 1 ml MEMNEAA (10 mM), 100 µl ß-mercaptoethanol (55 mM), 40 µl bFGF (10 µg/ml)

Table 2.1 Normal Tyrode solution (NT) for IonOptix measurements

Compound	Molecular weight [g/mol]	Final Concentration [mM]	Amount for 1l of the 1x solution
NaCl	58,44	130	7,597 g
KCl	74,55	5	0,373 g
$MgCl_2$	203,30	1	0,203 g
Sodium Hepes	260,29	10	2,603 g
Sodium pyruvate	110,04	2	0,220 g
Ascorbic acid	176,12	0,3	0,053 g
Glucose	180,16	10	1,802 g
Calcium	110,98	2	2 ml

For storage, tenfold mass of sodium chloride, potassium chloride, magnesium chloride and sodium Hepes were added to 1l double distilled water. The NT-prebuffer was sterile filtered, aliquoted to 100 ml each and stored at 4°C. On the day of the IonOptix measurements 1 l of the 1x N-Tyrode was prepared by mixing 100 ml of the tenfold NT-prebuffer with 900 ml double distilled water. Afterwards the needed amounts of ascorbic acid, glucose and sodium pyruvate were added. After the buffer reached room temperature, the pH value was adjusted to 7.4 by adding hydrochloric acid or sodium hydroxide solution. Immediately before using the 1x N-Tyrode, 2ml of 1M calcium were added (2 millimolar (mM) calcium) to 1 l N-Tyrode.

Table 2.2 Reagents for the stress protocol and Ca^{2+} assessment using the IonOptix system

Compound	Diluted or solved in	Stock concentration	Dilution	Final concentration
Isoproterenol	ddH2O	100 µM	1:1000 (2 µl in 20 ml NT) 1:3333 (6 µl in 20 ml NT) 1:10000 (20 µl in 20 ml NT)	100 nM 30 nM 10 nM
Indo-1-AM	Pluronic-F-127	990.2 µM	1:1000 (0.5 µl in 0.5 ml CBM)	990.2 nM

Table 2.3 Reagents for the Mito Stress Test Assay using the Seahorse XF96 extracellular flux analyzer

Compound	Diluted or solved in	Stock concentration	Dilution	Final concentration
FCCP	95% ethanol	1 mM	1:1000 (in XF Assay medium)	1 µM
Oligomycin	DMSO	1 mM	1:1000 (in XF Assay medium)	1 µM
Rotenone	DMSO	500 µM	1:1000 (in XF Assay medium)	0.5 µM
Antimycin A	DMSO	500 µM	1:1000 (in XF Assay medium)	0.5 µM

Table 2.4 Reagents for the differentiation of iPSCs towards the cardiovascular lineage after Kadari et al., 2015

Compound	Diluted or solved in	Stock concentration	Dilution	Final concentration
BMP4	4mM HCl/01%BSA	50 µg/ml	1:2000 (10 µg BMP4 in 200 µl 4mM HCl/01%BSA)	25 ng/µl
CHIR99021	DMSO	10 mM	1:2000	5 µM
IWR1	DMSO	20 mM	1:2000	10 µM

Table 2.5: Small molecules for iPSC generation and cultivation and viability stains

Compound	Diluted or solved in	Stock concentration	Dilution	Final concentration
bFGF	10 mM Tris/0.1% BSA pH7.6	0.1 mg/ml	1:2500	4 ng/ml
ROCK Inhibitor Y27632	DMSO	10 mM	1:1000 (dissolve 2 mg into 624,4 µl DMSO), protect from light!	10 µM
MitoTracker™ Deep Red FM	DMSO	1 mM	1:2000	500 nM
DAPI	ddH_2O	50 mg/ml	1:50000	0.1µg/ml

2.1.8 Antibodies

Table 2.6 Antibodies

Antigen	Species	Working dilution			Catalog number #	Manufacturer
		IF	WB	FACS		
AFP	Rabbit, polyclonal	1:50	x	x	A0008	Agilent Technologies, Inc., USA
Anti-mouse Alexa Fluor A488	Donkey, IgG	1:1000	x	x	A21202	Invitrogen™, Thermo Fisher Scientific Inc., USA
Anti-mouse Alexa Fluor A594	Donkey, IgG	1:1000	x	x	A32744	Invitrogen™, Thermo Fisher Scientific Inc., USA
Anti-mouse IgG HRP linked F(ab')2	x	x	1:2000	x	NA9310V	GE Healthcare Inc., USA
Anti-rabbit Alexa Fluor A488	Donkey, IgG	1:1000	x	x	A21206	Invitrogen™, Thermo Fisher Scientific Inc., USA
Anti-rabbit Alexa Fluor A594	Donkey, IgG	1:1000	x	x	A21207	Invitrogen™, Thermo Fisher Scientific Inc., USA
Anti-rabbit IgG HRP linked F(ab')2	x	x	1:2000	x	NA9340V	GE Healthcare Inc., USA
αSMA	Rabbit, polyclonal	1:100	x	x	Ab5694	Abcam plc., United Kingdom
cTnI-C	Rabbit, monoclonal	1:100	x	x	sc-8118	Santa Cruz Biotechnology Inc, USA
cTnT	Mouse, monoclonal	1:500	x	x	MS-295-P0	Thermo Fisher Scientific Inc., USA
Cx43	Rabbit, polyclonal	1:50	x	x	ab11370	Abcam plc., United Kingdom
DNAJC19	Rabbit, polyclonal	1:500	1:500	x	12096-1-AP	Proteintech Group, Inc., USA
DSG1/2	Mouse, monoclonal	1:10	1:50	x	61002	Progen Biotechnik GmbH, Germany
GAPDH (14C10)-HRP Conjugate	Rabbit, monoclonal	x	1:2000	x	3683S	Cell Signaling Technology, USA
JP2	Rabbit, polyclonal	1:100	x	x	ab79071	Abcam plc., United Kingdom
MLC2v	Rabbit, polyclonal	1:200	x	x	10906-1-AP	Proteintech Group, Inc., USA
OCT3/4	Mouse, monoclonal	1:500	x	x	sc-5279	Santa Cruz Biotechnology Inc, USA
PKP2	Mouse, monoclonal	1:2.5	1:2.5	x	651101	Progen Biotechnik GmbH, Germany
SOX2	Mouse, monoclonal	1:100	x	x	MAB2018	R&D systems, USA
SSEA-4-APC	x	x	x	1:11	130-098-347	Miltenyi Biotec GmbH, Germany
TRA-1-60-PE	x	x	x	1:11	130-100-347	Miltenyi Biotec GmbH, Germany
TRA-1-81	Mouse, monoclonal	1:500	x	x	60065	STEMCELL Technologies Inc., Canada
TUBB3	Mouse, monoclonal	1:1000	x	x	MMS-435P	Biolegend, USA
Vimentin	Rabbit, monoclonal	1:1000	x	x	ab92547	Abcam plc., United Kingdom

2.1.9 Oligonucleotides

Oligonucleotides were synthesized by the Manufacturer Eurofins Genomics (Ebersberg, Germany) and dissolved in an appropriate volume of ddH_2O as indicated yielding a stock concentration of 10 µM. * indicated primers detect SeV genome sequences to identify the SeV vector derived transgenes. *MMS* mismatches

Table 2.7 Oligonucleotides

Name	Forward/Reverse primer (5`→3`)
DNAJC19 (RTF1 and RTR1 transcript variant length identification (Davey et al., 2006))	GGTAAAGGCGTGCAGGT/ AAAATTGTAGCTCTGAGGCATT
DNAJC19 genotyping and mutation sequencing	CTAAAATACCTCGGGAATTG/ AAGGAGAGAAGGTCTTTCTT
DNAJC19tv: Off-target sequencing 1, NM_020476, 3MMS (3:13:18)	GCTGTTGCCTCCTCCATTCA/ ATCTCACAGGGAAATGCCAGG
DNAJC19tv: Off-target sequencing 2, NM_198995, 3MMS (11:15:16)	GTGCACTTTCCTCTCCGCTA/ GTCCTCACTGCCAGGCATAAT
DNAJC19tv: Off-target sequencing 3, NM_022343, 3MMS (6:10:11)	CCCAGGCACTACTGAACTGA/ GGAGGAACAACTTTACCTCTCT
DSG2 mutation sequencing, DSG2 exon1	CCCGGCTCCATTTTCTCGC/ CTAGACCTCGCCTACCGACG
DSG2-KO: Off-target sequencing 1, CAPZB (NM_004930), 3MMS (4:9:10:13)	CAGTTAGCGCTGGCCTTCTG/ CACGTGGCACTAGGAACTCA
DSG2-KO: Off-target sequencing 1, JAKMIP1 (NM_144720), 3MMS (12:19:20)	AGCACTGTGAGATGTGGTCG/ GACCTTGCTATGGGTTCCCC
DSG2-KO: Off-target sequencing 1, SLC35B4 (NM_032826), 4MMS (1:2:11:12)	GCGAACTACAGCTTCTTGGC/ CTGCCCAGACAGGACGGATT
GAPDH houskeeping gene	TGCACCACCAACTGCTGCTTAGC/ GGCATGGACTGTTGGTCATGAG
PKP2 mutation sequencing, PKP2 exon1	CCAGCTGAGTACGGCTACAT/ TTTAGGAACAGGGGAACGGC
PKP2-KO: Off-target sequencing 1, CETN1 (NM_004066), 4MMS (3:6:8:9)	GACAGCGGATTCTCGCCTAA/ CCGATCAGCTTCGTCGATCA
PKP2-KO: Off-target sequencing 2, NTN3 (NM_006181), 4MMS (2:3:4:12)	CTTCTACTGCGACAGGCCAT/ GTGGTCTGGTTGCAGGTCTT
PKP2-KO: Off-target sequencing 3, AGPAT2 (NM_001012727), 4MMS (4:5:8:12)	CCGAGTTCTACGCCAAGGT/ AGGGAAGCCCAGAAGAAAGTT
SeV inactivation_ *c-MYC*	TAACTGACTAGCAGGCTTGTCG*/ TCCACATACAGTCCTGGATGATGATG
SeV inactivation_ *KLF4*	TTCCTGCATGCCAGAGGAGCCC/ AATGTATCGAAGGTGCTCAA*
SeV inactivation_ *KOS*	ATGCACCGCTACGACGTGAGCGC/ ACCTTGACAATCCTGATGTGG
SeV inactivation_ *SEV*	GGATCACTAGGTGATATCGAGC/ ACCAGACAAGAGTTTAAGAGATATGTATC

Name	Forward/Reverse oligonucleotides (5`→3`)	Manufacturer
DNAJC19_intron3_exon4_sgRNA	TTCTTTCAGGCCTTCAGTGG/ CCACTGAAGGCCTGAAAGAA	Eurofins Genomics
DSG2_exon1_sgRNA	AGCAGGGCGTACGCGCGTCC/ GGACGCGCGTACGCCCTGCT	Eurofins Genomics
PKP2_exon1_sgRNA	GTCTTGACTGTCTGGCCGCCG/ CGGCGGCCAGACAGTCAAGA	Eurofins Genomics

2.1.10 Plasmids

Name	Product	Manufacturer (Plasmid backbone)
DNAJC19i3_e4-PX459	Cas9, Puromycin resistance, sgRNA DNAJC19	Self-made
DSG2 e1-PX459	Cas9, Puromycin resistance, sgRNA DSG2	Self-made
PKP2_e1-PX459	Cas9, Puromycin resistance, sgRNA PKP2	Self-made
pSpCas9(BB)-2A-GFP (PX458)	Cas9, GFP	Addgene (#48138) (Ran et al., 2013b)
pSpCas9(BB)-2A-Puro (PX459) V2.0	Cas9, Puromycin resistance	Addgene (#62988) (Ran et al., 2013b)
pSpCas9n(BB)-2A-GFP (PX461)	Cas9n, GFP	Addgene (#48140) (Ran et al., 2013b)
pSpCas9n(BB)-2A-Puro (PX462) V2.0	Cas9n, Puromycin resistance	Addgene (#62987) (Ran et al., 2013b)

2.1.11 Kits

Product	Manufacturer
CytoTuneTM-iPS 2.0 Sendai Reprogramming Kit	#A16517, Invitrogen™, Thermo Fisher Scientific Inc., USA

DNeasy® Blood & Tissue Kit	#69504, Qiagen GmbH, Germany
E.Z.N.A® Cycle Pure Kit	#D6492-02, Omega Bio-tek
ECL™ Detection Reagents	#GERPN2109, GE Healthcare Inc., USA
High Capacity RNA-to-cDNA Kit	#4387406, Applied biosystems, Thermo Fisher Scientific Inc., USA
Mentype®Nonaplex I PCR Amplification Kit	#41-09113-0025, Biotype GmbH, Germany
NEB® PCR Cloning Kit	#E1202S, New England Biolabs Inc., USA
Neon™ Transfection System 100 µl Kit	#MPK10096, Invitrogen™, Thermo Fisher Scientific Inc., USA
Pierce™ BCA Protein Assay Kit	#23225, Thermo Fisher Scientific Inc., USA
PSC-Derived Cardiomyocyte Isolation Kit, human (MACS)	#130-110-188, Miltenyi Biotec GmbH, Germany
PureLink™ HiPure Plasmid Filter DNA Purification Kit	#K210015, Invitrogen™, Thermo Fisher Scientific Inc., USA
RNeasy Mini Kit	#74104, Qiagen GmbH, Germany

2.2 Methods

2.2.1 Cell culture

General Cell Culture

All cell types, including fibroblasts, iPSCs and iPSC-CMs were cultured in a humidified incubator at 37°C with 5 % CO_2. All cells were treated under a laminar sterile hood in a clean environment. Cells were maintained without penicillin, streptomycin or other antibiotics to ensure experimental settings of high quality. Additionally, mycoplasma contamination analysis was performed on a regular base.

Mycoplasma testing

To detect mycoplasma contamination the cellular supernatant was collected in a 1.5 ml Eppendorf tube. The tube was heated on 95°C for 10 minutes (min) and centrifuged at 13000 rpm at room temperature for 3 min. Afterwards 1 ml of the supernatant was pipetted into a new 1.5 ml Eppendorf tube and marked with the barcode label of the company Eurofins GATC. The samples were tested by the company and the results were received via E-Mail.

Coating of cell culture well plates and dishes

Gelatin coating

1 g gelatin was solved in 1 l PBS and autoclaved to obtain a sterile 0.1 % gelatin buffer. The appropriate amount was pipetted into the flask or well plate and prewarmed for 20-30 min at 37°C in the incubator. Afterwards the solution was replaced with the required cell culture medium for the maintenance of fibroblasts with the listed individual volumes per tissue culture format:

Table 2.8 Overview of used gelatin coating volumes.

Amount of coating [ml]	Tissue culture plate format
1	1well/6-well plate
0.5	1well/12-well plate
0.25	1well/24-well plate
0.2	1well/48-well plate
0.1	1well/96-well plate
5	Ø10 cm culture dish
0.1	1well/8-well chamber

hESC-Matrigel™ coating

Matrigel™-hESC-qualified Matrix was used for coating of cell culture well plates, flasks, dishes or sterile glass coverslips in tissue culture well plates. hESC-Matrigel™ was diluted according to the lot specific indications and 250 – 300 µl were pipetted into ice cold 25 ml DMEM/F12 (~1:100) using cold pipet tips. The mixture was vortexed and dispensed very fastly according to the following table in order to prevent gelation:

Table 2.9 Overview of Matrigel™-hESC-qualified Matrix coating volumes.

Amount of coating [ml]	Tissue culture plate format
1	1well/6-well plate
0.5	1well/12-well plate
0.25	1well/24-well plate
0.2	1well/48-well plate
0.1	1well/96-well plate
5	10 cm dish
0.1	1well/8-well chamber

Horizontal T-shaking was performed to equally distribute coating reagent over the whole area. Cell culture plates were either sealed with parafilm and stored at 4°C for up to six weeks or were used immediately. For direct usage the coated cell culture well plates were prewarmed at 37°C for 30 min. The hESC-Matrigel™ coating was recycled once in a new cell culture plate with twice of the volume used in the primary coating procedure.

MEF-feeder-layer

Irradiated MEF-feeders were seeded on 0.1 % gelatin coated plates using MEF-medium. During Reprogramming MEF-feeders were thawed with a density of 2 x 10^6 cells one day prior to cell plating.

Mattress cultivation

Matrigel® Growth Factor Reduced (GFR) Basement Membrane Matrix was used for matrigel-mattress cultivation of iPSC-CMs. Glass coverslips (Ø10 mm) were placed into each well of a 48-well plate. To draw a line, 2 µl of hESC-Matrigel™ coating agent were applied on a glass coverslip using an ice-cold pipet tip. The mattresses were incubated for 8 – 10 minutes at room temperature until polymerization could be visually observed by a switch from transparent to white color. Afterwards, 40,000 iPSC-CMs were seeded on the line in a drop of 50 -100 µl with cultivation medium. The dimensions of the mattresses were approximately ~0.5 mm wide and ~2 mm long.

Thawing of cells

Cells were regularly cryopreserved in liquid nitrogen or in a -80 °C freezer for short time spans. Cells were thawed in a 37°C water bath until small ice cubes were still visible. Cells were replaced into a falcon tube using a serological pipette containing 4 ml DMEM/F12. Cells were centrifuged at the appropriate speed:

Table 2.10 Centrifugation parameters for fibroblasts, iPSCs and iPSC-CMs

Cell type	Centrifugation speed	Centrifugation time
Fibroblasts	2000 rpm	5 min
iPSCs	1300 rpm	3 min
iPSC-CMs	1500 rpm	5 min

After centrifugation the supernatant was discarded and the cell pellet was resuspended in the cell type specific cultivation medium and the cells were seeded on cell culture dishes.

2.2.2 Generation of fibroblasts out of a skin biopsy

Isolation of human dermal fibroblasts from a skin punch biopsy

Healthy control lines were ordered from a commercial provider (NHDF, Promocell). One healthy control fibroblast cell line was obtained from a male 6-year-old donor (NC6M, Promocell, #C-12300) and the other one from a female 47-year-old donor (NC47F, Promocell, #C-12302). Patient-derived dermal fibroblasts were gained from a skin biopsy in the size of 3.0 x 5.0 mm of the donors forearm according to standard procedures (Park et al., 2008). Dermal fibroblasts of all three patients were gathered by Prof. Dr. Henry Duff and Prof. Dr. B. Gerull at the University of Calgary and approved by their ethical committee (ID-E20729) and were particularly intended for stem cell research. The fibroblasts of the

patients were obtained back in year 2012 and were transferred to Würzburg via MTA for the usage in this thesis. In brief, skin biopsies were dissected into small pieces using scissors and transferred into one well of 6-well plate that contains MEF medium [DMEM (1x), 10 % FCS, 1 % MEM-NEAA, 100 µM β-mercaptoethanol] (Park et al., 2008).

2.2.3 Cultivation of cells

Human dermal fibroblasts

Primary adult patient-derived dermal fibroblasts (DCMAP1, DCMAP2, LEMD p.L13R) and commercially purchased foreskin-derived fibroblasts (NC6M, NC47F) were cultivated in MEF medium [DMEM (Gibco), 10 % FCS (Sigma-Aldrich), 1 % MEMNEAA (Gibco), 100 µM β-mercaptoethanol (Thermo)] on 0.1 % gelatin coated cell culture dishes. Dermal fibroblasts were passaged after one rinse in dPBS using Trypsin/EDTA solution and were subjected to incubation at 37 °C for 5 min. The detachment of the cells was visually observed and terminated upon addition of MEF-medium. Cells were collected in a 15 ml falcon tube and pelleted at 2000 rpm for 5 min at room temperature. The supernatant was discarded, the cell pellet was resuspended in MEF medium and reseeded in 0.1 % gelatin coated cell culture dishes.

Human induced pluripotent stem cells

iPSCs were cultured in feeder-free conditions using hESC-Matrigel™-coated culture dishes and daily change of mTesr™1 medium. Passaging of cells was performed at 70-80 % confluency. iPSCs were washed with dPBS and enzymatically detached using Accutase® for 3 min at 37°C. The reaction was stopped using DMEM/F12 and the cells were collected in a 15 ml falcon tube. iPSCs were centrifuged at 1300 rpm for 3 min at room temperature. The supernatant was discarded and the cells were resuspended in mTesr™1 medium supplemented with RI Y27632 (10µM). RI Y27632 supplementation was used at the day of passaging and thawing only.

Cryopreservation of cells

For permanent storage of cells, dermal fibroblasts, iPSCs and iPSC-CMs were cryopreserved. Cells were harvested and pelleted by centrifugation according to the parameters described above. Thereafter, counted cell pellets with a maximum of 5 x 10^6 cells were resuspended in the appropriate freezing medium and dispensed into labeled cryovials. To ensure higher survival rates, a cryo container filled with isopropanol was used for controlled freezing of 1°C per min to -80°C.

Table 2.11 Freezing medium compositions for fibroblasts, iPSCs and iPSC-CMs.

Cell type	Freezing medium
Fibroblasts	Fetal calf serum + 10 % DMSO
iPSCs	KnockOut™ Serum Replacement + 10 % DMSO
iPSC-CMs	KnockOut™ Serum Replacement + 10 % DMSO

Cell Counting

Cell Numbers were determined using a Neubauer-hemocytometer and the TC20™ Automated Cell Counter. Cells were harvested in at least 1ml or more, depending on the cell density to achieve a single cell suspension. Using the Neubauer-hemocytometer 10 µl cell suspension were counted using an inverted microscope and a manual cell counter. Four squares were counted individually and the average was determined and multiplied with 10^5 cells/ml as well as the suspension volume to achieve the total number of cells (cells/ml x volume in ml = total cells). Using the BioRad TC20™ counter, a similar procedure was performed. If viability was required, 10 µl cell suspension were mixed with 10 µl trypan blue (1:1), and transferred into a BioRad counting slide. The same calculation was performed as with the Neubauer-hemocytometer.

2.2.4 Reprogramming of human fibroblasts and isolation of candidate iPSC colonies

NC6M was reprogrammed prior to this thesis using the hSTEMCCA-lentiviral construct by K. Günther as described by Somers and colleagues (Somers et al., 2010, Günther, 2016, Gonzalez et al., 2011). NC6M-SeV, NC47F, DCMAP1, DCMAP2 and LEMD2 p.L13R dermal fibroblasts were reprogrammed using the SeV to generate transgene-free hiPSCs (Fusaki et al., 2009). The SeV reprogramming technique was performed using the commercially available CytoTune Kit 2.0. In detail, 50,000 dermal fibroblasts were seeded on one well of a 24-well plate one day prior to reprogramming. Dermal fibroblasts were transduced at passage 5 using the integration-free SeV for 24 hours according to the lot specific multiplicity of infection (MOI) titers [KOS MOI=5, c-MYC MOI=5, KLF4 MOI=3]. As the concentration and activity of viral particles fluctuates from lot to lot, the concentration for every kit needed to be recalculated based on the lot-specific information found on the homepage. Medium was changed into fresh MEF medium daily. On day 8 post infection, cells were replaced onto MEF-feeder cells containing MEF medium supplemented with 10 µM RI Y27632. One day after, medium was changed into reprogramming medium [KnockOut™ DMEM/F-12, KnockOut™ Serum Replacement, 1 % MEM-NEAA, 100 µM β-mercaptoethanol, 2mM GlutaMAX™, 4ng/ml bFGF, 1 % Penicillin-Streptomycin, 200 µM Vitamin C] until colonies appeared. After 3 weeks large stem-cell like colonies were manually dissected by using an insulin syringe. For picking, an inverted microscope was placed into a laminar hood and decontaminated with Terralin and UV-light. iPSC colonies were selected according to typical stem cell-like morphology and circled using a syringe needle. Floating colonies were collected via aspiration with a pipette and transferred to a precoated well of a 96-well plate. Previously, coating was recycled and wells were filled with mTesr™1 medium supplemented with RI Y27632 (10µM). Each isolated colony was replaced into a separate hESC-Matrigel™-coated well of a 96-well plate. Afterwards, iPSCs were maintained in mTesr™1 without Pen/Strep with daily medium change. For passaging of iPSCs, Accutase® was used to detach cells according to standard cultivation. iPSCs were collected and centrifuged at 1300 rpm at room temperature for 3 min and resuspended in mTesr™1 supplemented with 10 µM RI Y27632.

2.2.5 Clonogenicity assay

Monoclonal iPSC lines were established from polyclonal iPSC lines *in vitro*. A highly diluted single cell suspension was plated on hESC-Matrigel™-precoated petri dishes (Ø 10 cm) using mTesr™1 supplemented with 10 µM RI Y27632. The next day, single cell attachment was visually checked and afterwards controlled to give rise to colonies until the required size was reached to allow manual picking.

2.2.6 Electroporation of iPSCs

At least two hours prior to electroporation, mTesr™1 cultivation medium of the iPS cells was changed and the required amount of petri dishes (Ø 10 cm) was prepared with hESC-Matrigel™ coating and prewarmed for 30 min at 37°C. Coating was recycled and dishes were filled with mTesr™1 supplemented with 10 µM RI Y27632 and continuously prewarmed at 37°C in the incubator. iPSCs were collected according to standard procedure and counted using the TC20™ Automated Cell Counter. For each condition 250,000 healthy NC6M iPSCs were resuspended in buffer R and electroporated with the NEON™ Transfection System by using 35 µg plasmid and the 100 µl tip according to the optimized parameters [Voltage: 1200 V, Pulse length: 35 ms, Number of pulses: 2].

Table 2.12 Experimental conditions prior to nucleofection.

Plasmid	Puromycin selection	Purpose
35 µg pSpCas9(BB)-2A-GFP	+	Control dish (puromycin induced cell death)
35 µg pSpCas9(BB)-2A-GFP	-	Control dish (use for screening of positive fluorescence signal to adjust puromycin selection times)
35 µg pSpCas9(BB)-2A-Puro with individually cloned sgRNAs	+	Control dish (puromycin induced cell death)

Nucleofected iPSCs were directly transferred into hESC-MatrigelTM-coated 10 cm dishes containing mTesr™1 supplemented with 10 µM RI Y27632. Puromycin selection was applied one day after at a concentration of 1 µg/ml dissolved in mTesr™1 supplemented with 10 µM RI Y27632 for 24h or as long as active transfection was identified visually by fluorescence of control cells containing the GFP-tagged plasmid. The treatment was stopped by medium change with mTesr™1 supplemented with 10 µM RI Y27632 after nearly all of the GFP$^+$ cells died in the puromycin treated control dish due to the missing puromycin resistance gene, which was on average after ~48 h. Afterwards the cells were maintained daily with mTesr™1 to allow growth of single cell clones. Surviving colonies were manually picked and individually transferred into hESC-Matrigel™-pre-coated wells of a 96-well plate as described above in the section `Reprogramming of human fibroblasts and isolation of candidate iPSC colonies`.

2.2.7 Default differentiation of iPSCs to generate progenies of the three germ layers

Spontaneous differentiation capacities of iPSCs were addressed in an *in vitro* approach resulting in the formation of cell types of the three germ layers. First, iPSCs were collected according to standard procedures and the cell pellet was resuspended in mTesr™1 supplemented with 10 µM RI Y27632. Afterwards, the single cell suspension of in total 10 x 10^6 cells in 13 ml medium was plated into a 10 cm non-TC-treated petri dish (bacterial dish). Medium was changed with mTesr™1 every day for 4 days until aggregates were formed. After reaching the size of ~400-500 µm diameter medium was replaced by serum-containing MEF-medium which induced spontaneous differentiation. MEF-medium was changed every other day for 7 to 8 days. The aggregates were afterwards transferred on 0.1 % gelatin coated glass coverslips placed into 1 well of a 48-well plate containing MEF-medium. Agitation was minimized to as little as possible to allow aggregates to firmly attach to the glass coverslips. Medium was then changed every 2 to 3 days of in total 3 months. Afterwards, cells were washed with dPBS and fixed in 4 % PFA for 1 hour. Germ layer differentiation potential was addressed by immunofluorescence staining by assessing TUBB3, AFP and α-SMA for ectoderm, endoderm and mesoderm respectively.

2.2.8 Differentiation into CMs

iPSCs were differentiated into CMs as previously described by Kadari with cell line specific modifications (Kadari et al., 2015). Briefly, iPSCs were seeded to different densities on hESC-Matrigel™-coated wells of 12-well plates two days prior to cardiac induction using mTesr™1 supplemented with 10 µM RI Y27632.

Table 2.13 iPSC line-dependent seeding densities for cardiac differentiation.

Cell line name	Cell density (1 well/ 12-well plate)
NC6M	6 x 10^5 -8 x 10^5
NC47F	6 x 10^5 -8 x 10^5
DNAJC19tv	8 x 10^5 -1 x 10^6
DCMAP1	8 x 10^5 -1 x 10^6
DCMAP2	8 x 10^5 -1 x 10^6

After approximately 24 hours (day -1), iPSC confluency should have reached around 50-60 % and medium was changed into mTesr™1. One day later, after iPSCs obtained 80-90 % confluency, cardiac induction was started using CBM (cardiac basal medium) supplemented with 5 µM CHIR and 25 ng/ml BMP4 using 1ml/well (day 0). On the next day, CBM containing 5 µM CHIR was used for medium change with 1ml/well (day 1). On day 2, medium was changed into 1ml/well CSM (cardiac specification medium) which was deficient for insulin. From day 3 to day 8 (or maximal day 12), CSM was supplemented with 10 µM IWR1 and changed daily until contracting CMs were visually recognized. After beating CMs were observed, the medium was changed one more day with CSM and 10 µM IWR1 and going from the day after the cells received CBM every other day for a time span of 5-7 days to allow proliferation of CMs. Afterwards, iPSC-CMs were enriched using glucose-depleted and lactate-enriched medium, termed CEM (cardiac enrichment medium) for 3-7 days with daily medium change. Thereafter, iPSC-CMs were

changed with CBM every other day until at least day 60. If high impurities with non-contracting non-CMs were still observed, iPSC-CMs were enriched using CEM a second time as previously described.

iPSC-CMs splitting

iPSC-CMs were cultured in feeder-free conditions using hESC-Matrigel™-coated culture dishes as previously described in subsection 2.3.1 hESC-Matrigel™ coating and medium was with CBM medium changed every other day (at least twice a week). Passaging of cells was performed by washing with dPBS and enzymatical detach using TrypLE for 5-30 min at 37°C. The detachment of cells was stopped using DMEM/F12 containing 10 % KnockOut™ Serum Replacement and the cells were collected in a 15 ml falcon tube. A 10 ml serological pipette was used to generate a single cell suspension by pipetting up and down and afterwards the iPSC-CMs were optionally counted. If cardiomyocyte networks were still not dissolved, a moistened cell strainer (~100 µm) was used to detach iPSC-CMs. Next, iPSC-CMs were centrifuged at 1500 rpm for 5 min at room temperature. The supernatant was discarded and iPSC-CMs were resuspended in CBM medium and were replated on hESC-Matrigel™-coated culture dishes or on matrigel-mattresses on the corresponding time points required for the individual experiments.

2.2.9 Magnetic-activated cell sorting (MACS)

Single cell suspensions of iPSC-CMs were stained with magnetically labeled antibodies in a two-step procedure using the human PSC-Derived Cardiomyocyte Isolation Kit (Miltenyi Biotec GmbH). First, iPSC-CMs were resuspended in 80 µl blocking buffer (dPBS, 0.5 % KnockOut™ Serum Replacement) per 5 x 10^6 cells. Afterwards, 20 µl of Non-Cardiomyocyte Depletion Cocktail per 5×10⁶ total cells were added and the mixture was incubated for 5 minutes in the refrigerator (4°C). Next, cells were washed by adding 1 ml blocking buffer per 5×10⁶ cells and centrifuged at 1500 rpm for 5 min at room temperature. The supernatant was aspirated completely and the cell pellet was resuspended in 80 µl blocking buffer. 20 µl Anti-Biotin MicroBeads were added, cells were mixed well and incubated for additional 10 minutes in the refrigerator (4 °C). Next, the volume was increased to 500 µl using blocking buffer to prepare for magnetic separation. In the next step, labelled cells were transferred into a MACS® Column, which was previously placed into the magnetic field of a MACS Separator and moistened with 3 ml blocking buffer. After 3 washes with 3 ml blocking buffer each, the flow-through was collected containing the unlabeled CM-enriched cell population. The non-CMs fraction persisted in the magnetic field. Optionally, if non-CMs were required, the column was removed from the separator and placed into a 15 ml falcon. Next, non-CMs were collected by adding 5 ml blocking buffer and pushing a plunger into the column to flush the cells out. Viability of the iPSC-CMs was controlled and if it was above 40 % the second sorting step was initiated. iPSC-CMs were centrifuged and labelling was performed upon resuspension in 80 µl blocking buffer and 20 µl Cardiomyocyte Enrichment Cocktail. The cells were afterwards again incubated in the refrigerator (4°C) for 10 min. In the next step, labelled cells were separated using a new MACS® Column as previously described. Thereafter, the plunger was pushed into the column to flush out positively labelled CMs.

2.2.10 Immunofluorescence and viability stains

One well of a 48-well plate containing 40 000 iPSC-CMs were seeded on a 10 mm coverslip at least 14 days prior to immunofluorescence or viability stains. iPSC-CMs used for staining were optionally incubated in MitoTracker Deep Red™ solved at 500 nM in CBM (dilution 1:2000 using 1 mM stock) by incubation in an total volume of 250 µl for 20 min at 37°C. Cells were washed with dPBS and fixed using 4 % PFA at room temperature with cell type-dependent incubation times:

Table 2.14 Cell type-dependent fixation times for immunofluorescence.

Cell type	Fixation time
Dermal fibroblasts	15 min
iPSCs	15 min
iPSC-CMs	30 min

Cells were washed with dPBS three times for in total 30 min at room temperature. Afterwards, cells were permeabilized with 0.2 % Nonidet in dPBS: 10 minutes for iPSCs and 30 minutes for iPSC-CMs at room temperature. Three additional washing steps were performed with dPBS for in total 30 min at room temperature. In the next step, dermal fibroblasts, iPSCs and iPSC-CMs were blocked for 3 to 5 hours with an individual blocking solution using a 1:10 dilution of the serum corresponding to the secondary antibody. Next, cells were incubated with the respective primary antibody (Table x) diluted in blocking solution overnight at 4°C. On the next day, cells were washed three times using dPBS for in total 30 minutes at room temperature. Cells were incubated with species-specific fluorochrome-conjugated secondary antibodies (Table x) diluted in blocking solution in a dark chamber to protect cells from light. After additional rinsing with dPBS three times for in total 30 min at room temperature, cells were incubated with DAPI (4`,6-diamidino-2-phenylindole) solution (1:5000 in dPBS) for 15 min room temperature to counterstain nuclei. Afterwards, cells were washed with dPBS three times for in total 30 min at room temperature. Glass coverslips were mounted with Mowiol 4-88 on glass slides and dried overnight at 4°C in a dark chamber. To validate specific binding, the immunofluorescence staining was performed without the application of a primary antibody on separated cells termed as negative control. Pictures were acquired using the LSM confocal microscope (LSM 780, Carl Zeiss).

2.2.11 Flow cytometry

For each cell line 5 x 10^6 cells were harvested using Accutase® as described for iPSC-specific standard cultivation procedures. Cells were pelleted at 1300 rpm for 5 min at room temperature. Next, cells were resuspended in 3 ml serum-free dPBS and separated into two falcons: one isotope unstained control and one for marker staining. Falcons were centrifuged and resuspended in staining buffer (5 % KnockOut™ Serum Replacement in dPBS). After one additional centrifugation step, cell pellets were resuspended in either 180 µl staining buffer and 10 µl fluorophore-conjugated APC isotope control together with 10 µl fluorophore-conjugated PE isotope control or in 100 µl staining buffer and 10 µl 1° antibody for surface markers (1:11) and were incubated for 15 min at 4°C. Next, two washing steps were performed with 1 ml dPBS for each falcon and the falcons were subjected to centrifugation with 1300 rpm for 5 min at room temperature. The supernatant was aspired and cells were resuspended in 100 µl 4 % PFA and were incubated for 15 min at room temperature. Two additional washes were performed and the unstained control was stored at 4°C in the dark for analysis at a later time point. Thereafter, cells were permeabilized with 1 ml 0.1 % Triton-X-100 in dPBS and incubated in the dark for 15 min at room temperature. Two additional washes were performed and the cell pellet was resuspended in 100 µl staining buffer and 10 µl 1° antibody for intracellular markers (1:11) and stained for 15 min at 4°C in the dark. Additional two washing steps were carried out and the supernatant was aspired. Cells were resuspended in 500 µl dPBS and transferred into flow cytometry tubes for data acquisition on the flow cytometer (BD FACSCanto II, Biosciences). Data analysis was addressed using the FlowJo7.6.1 or BD FACSDiva v6.1.3 software. The gates of positively labeled iPSCs were set on the basis of the signals with the negative control by using BD FACSCalibur with the appropriate laser and filter sets with the help of Dr. Ruping Chen in the Comprehensive Heart Failure Center (CHFC) and Department of Internal Medicine I, University Hospital Würzburg, Würzburg, Germany.

2.2.12 Western blot (WB)

Cells were pelleted, washed one time with dPBS and after centrifugation and supernatant aspiration, cells were resuspended in MHC buffer containing proteinase inhibitor. The cell pellet was sonicated on ice using the Sonopuls™ homogenizer Mini20 three times for 3 seconds each. The concentration of protein lysates was determined using the NanoDrop™ One system. Next, 50 µg protein of iPSC samples and 30 µg protein of iPSC-CMs samples were combined with 4x laemmli sample buffer and heated to 95 °C for exact 5 min. The mixtures were loaded on SDS gels with a range of 12 % to 15 % together with a full range or a broad range protein marker. The proteins were separated in 1x buffer E for 30 min at 80 V followed by 1 hour at 110 V. The protein bands were blotted onto a nitrocellulose membrane using the standard molecular weights setup (15 min) with the help ofthe Trans-Blot® Turbo™ system. Next, membranes were cut using a scalpel according to the desired protein masses. Membranes were incubated for at least one hour in blocking solution consisting of 5 % skim milk in PBST. In the next step,

membranes were incubated using primary antibodies dissolved in 5% blocking solution and sealed in a plastic cover over night at 4 °C. The day after, membranes were washed at least three times with PBST for a minimum of 1 hour. Thereafter, membranes were incubated with secondary HRP-labeled antibodies diluted in 5 % blocking solution for 2 hours at room temperature. After three PBST washes at room temperature for 15 min each, membranes were incubated with ECL™ detection solutions mixed 1:1 for 2 min at room temperature. Chemiluminescence was visualized using the ChemiDoc™ Touch Imaging system. In order to detach previously performed antibody-binding, membranes were washed in stripping buffer for 15 min at room temperature, followed by briefly washing with ddH_2O and three times PBST for 15 min each. Afterwards the procedure was repeated starting with the blocking solution step for 1 hour.

2.2.13 Dotblot

CRISPR/Cas9-edited iPSC colonies were separately cultured in 96-well plates. iPSC colonies were washed with dPBS and 5 µl MHC buffer containing proteinase inhibitor were added. The well plates were sealed and cells were lysed for 30 min at 4°C. Lysed iPSCs were blotted onto two different nitrocellulose membranes using 1 µl of each clone at the similar position. The membranes were afterwards blocked with 5 % milk blocking solution as previously described. The membranes were incubated using primary antibodies solved in 5 % blocking solution, one membrane with the antibody of interest and one membrane with the internal control antibody GAPDH over night at 4°C. The second day was proceeded as previously described in the WB set up. Individual dots were evaluated according to a positive expression of GAPDH and the corresponding loss or reduced expression of either PKP2 or DNAJC19.

2.2.14 Molecular cloning

2.2.14.1 Transformation in DH5α E. coli

The CRISPR/Cas9 plasmids (pSpCas9(BB)-2A-Puro, pSpCas9(BB)-2A-GFP) were transformed into a bacterial strain for plasmid amplification. For that purpose, 1 µl of plasmid (~500 ng/µl) was mixed with 50 µl thawed DH5α chemical competent E. coli cells on ice followed by 30 min incubation on ice. Plasmids were transformed by a heat shock for 90 seconds at 42°C. Bacteria were incubated for 5 min on ice, carefully resuspended in 400 µl outgrowth medium and shaken for 1 hour at 37 °C with 1000 rpm. In the following step, 50 µl of the mixture were plated on LB agar dishes containing 100 µg/ml ampicillin and incubated at 37 °C overnight. The day after, surviving bacterial colonies were manually picked as described in 2.2.15.2 plasmid DNA amplification and preparation (mini and midi-scale) section.

2.2.15 CRISPR/Cas9 plasmid cloning

CRISPR/Cas9 plasmids were cloned after the protocol of F. Zhang (Ran et al., 2013b). The ordered individual oligonucleotides were annealed and phosphorylated. The sgRNA comprised of top (100 µM) and bottom (100 µM) oligonucleotides was mixed with T4 Ligation buffer, T4 PNK and RNase-free ddH_2O into separate PCR reaction tubes. Phosphorylation was performed using the C1000 Touch™ Thermal Cycler with the following program:

Table 2.15 Thermocycler conditions to anneal and phosphorylate sgRNA oligonucleotides.

Thermocycler conditions		
Annealing + Phosphorylation	37 °C	30 min
	95 °C	5 min
Rampdown	to 25 °C	at 0.1 %/sec
Total time	~2 h	

1 µl of the annealed sgRNAs was diluted 1:200 in ddH_2O. The individual sgRNAs were cloned into the pSpCas9(BB)-2A-Puro (PX459) V2.0 plasmid backbone using BbsI restriction cloning and T4 Ligation.

Table 2.16 gRNA duplex – CRISPR/Cas9 plasmid ligation reaction mix.

	Per reaction
Plasmid (100 ng)	1 µl
gRNA duplex (diluted)	1 µl
Tango buffer (10x)	2 µl
DTT 10 mM	1 µl
ATP 10 mM	1 µl
BbsI	1.5 µl
T4 Ligase	0.5 µl
ddH20 (Rnase-free)	12 µl
Total volume	20 µl

The mixture was processed using the following C1000 Touch™ Thermal Cycler program:

Table 2.17 Thermocycler conditions for gRNA duplex ligation into CRISPR/Cas9 plasmids.

Thermocycler conditions		
Ligation reaction	37 °C	5 min
	21 °C	5 min
Cycles	X6	
Total time	~1 h	

The Ligation reaction was treated with the PlasmidSafe exonuclease to digest any residual linearized DNA. 11 µl of the ligation reaction were mixed with 10x Plasmid safe buffer (1.5 µl), 10 mM ATP (1.5 µl) and PlasmidSafe exonuclease (1 µl) and were incubated at 37 °C for 30 min followed by 30 min incubation at 70 °C. The self-cloned CRISPR/Cas9 plasmids were aliquoted, optionally stored at – 20°C or directly used for transformation in DH5α E. coli.

2.2.15.1 PCR-cloning for allele identification

RT-PCR products were cloned according to the manufacturers instructions (New England Biolabs, 2020). In brief, the PCR amplicon was mixed together with 1 µl the supplied linearized vector to a volume of 5 µl H_2O, followed by addition of 4 µl cloning mix 1 and 1 µl cloning mix 2. The mixture was incubated at room temperature for 15 min and transferred on ice for 2 min. Afterwards, 2 µl of the ligation reaction was added on 50 µl competent cells and incubated on ice for 20 min. The mixture was heat shocked for 42 °C for 30 seconds. The transformation reaction was incubated on ice for 5 min and afterwards 950 µl NEB 10-β Stable Outgrowth Medium were added for outgrowth. After 1 h at 37 °C 50 µl of the transformation reaction (or dilutions in NEB 10-β Stable Outgrowth Medium) were plated on 100 µg/ml ampicillin containing LB agar dishes.

2.2.15.2 Plasmid DNA amplification and preparation (mini and midi-scale)

Colonies were manually picked off the LB agar dishes with a 100 µl pipet tip and transferred into bacterial tubes containing 200 - 300 ml LB medium with 100 µg/ml ampicillin. The cultures were shaken at 37 °C with 300 rpm overnight. The plasmid DNA was isolated and purified using the PureLink™ HiPure Plasmid Filter DNA Purification Kit according to the manufacturer's instructions. Plasmid DNA was solved in 100 µl ddH_2O and the concentration was quantified using the NanoDrop™ One system. Dissolved plasmids were optionally aliquoted and stored at -20 °C.

2.2.16 DNA isolation from cell pellets

Cell pellets were collected according to standard cultivation procedures. After one additional dPBS washing step, DNA was isolated from cell pellets using the DNeasy Blood & Tissue Kit according to the manufacturer's instructions. DNA was solved in 10-20 µl ddH_2O and the concentration was examined with the help of the NanoDrop™ One system (Thermo Fisher).

2.2.17 RNA isolation and reverse transcription to complementary DNA (cDNA)

The RNA extractions were performed using the manufacturer´s instructions using the High Capacity RNA-to-cDNA™ Kit (Qiagen). In brief, cells were pelleted according to standard methods and dissolved in RLT plus buffer that was previously mixed with 10 µl mercaptoethanol (per 1 ml RLT). The pellet was dissolved by vortexing for 30 sec. Next, genomic DNA was eliminated by transferring the mixture into the gDNA elimination column and centrifuging for 30 sec at 8000 g. The flow through was collected, 350 µl of 70 % EtOH were added and the mixture was transferred into a new RNeasy spin column. After centrifugation at 8 000 g for 15 sec the flow through was discarded and 700 µl RW1 were added to wash the sample by an additional centrifugation step with equal settings. The procedure was repeated with 500 µl RPE buffer and a centrifugation step at 8000 g for 2 min. RNA was eluted by adding 30 µl RNase-free water, followed by a 2 min incubation before the column was transferred in a new RNase-free 1.5 ml tube and centrifuged for 1 min at 8000 g. The RNA concentration was measured using the NanoDrop™ One^C spectrophotometer and directly used for reverse transcription or aliquoted for storage at -20 °C.

2.2.18 Reverse transcription of RNA into complementary DNA (cDNA)

Each reverse transcription mix contained 200 ng - 1000 ng RNA, Oligo(dT) primers and sterile ddH_2O according to the manufacturer's instructions to generate a total volume of 5 µl.

Table 2.18: Reverse transcription mix.

7.5 µl	Sterile ddH_2O
4 µl	GoScript reaction buffer
2 µl	25 mM $MgCl_2$
1 µl	10 mM dNTPs
5 µl	RNA-dT Oligo Primer mix
1 µl	Reverse transcriptase

Following thermal cycler conditions were applied:

Table 2.19 Thermocycler conditions for reverse transcription.

25°C	5 min
42°C	60 min
70°C	15 min
4°C	∞

The reverse transcriptase mix was incubated at 70°C for 4 min and was afterwards incubated on ice for 5 min. Control samples were also processed by using ddH_2O only. The generated cDNA was either used directly for RT-PCR or aliquoted and stored at -20°C.

2.2.19 RT-PCR

RT-PCRs were performed to amplify the gene regions of interest based on isolated clonal DNA. DNA was transferred in a PCR reaction tube together with gene-specific forward and reverse primers, polymerase and the appropriate reaction buffers. The reaction setup was pipetted as indicated in the individual tables. After the polymerase chain reaction in a thermocycler, PCR products of different sizes were achieved. 5 µl of the PCR products supplemented with 1 µl 6x loading dye were analyzed on a 1-2 % agarose gel (GENAXXON). The remaining PCR reactions were purified using the E.Z.N.A.® Cycle Pure Kit (Omega Bio-tek). The purified DNA was solved in 15 µl ddH_2O, optionally aliquoted for further applications or stored at -20°C. As the amplified gene sequence contained GC-rich regions, the Q5® DNA polymerase (NEB) was chosen in combination with a Q5® High GC Enhancer (NEB). Otherwise *Pfu* DNA Polymerase was selected together with the corresponding 10 x Pfu reaction buffer. For Each RT-PCR ~100 ng DNA were transferred into separate PCR reaction tubes with the corresponding listed components of the master mix and were individually combined by using 10 µM gene specific forward and reverse primers.

2.2.19.1 Using DNA as template

2.2.19.1.1 **PKP2**

Table 2.20 Master mix of PKP2 RT-PCR to identify genomic alterations within *PKP2*.

Master mix (n=volume to calculate)	50 µl PCR reaction
10 x Pfu reaction buffer	5 µl
dNTP mix (25 µM)	1 µl
PKP2 Primer 1 fwd (10 µM)	1 µl
PKP2 Primer 1 rev (10 µM)	1 µl
Pfu DNA Polymerase	1 µl
DNA (100 ng)	n µl
ddH_2O	41 µl-DNA n µl

Thermocycler conditions		
Initial denaturation	95 °C	2 min
Denaturation	95 °C	1 min
Annealing	57 °C	30 sec
Elongation	72 °C	40 sec
Final extension	72 °C	5 min
Hold	4 °C	∞
Cycles	35x	

2.2.19.1.2 **DSG2**

Table 2.21 Master mix of DSG2 RT-PCR to identify genomic alterations within DSG*2*.

Master mix (n=volume to calculate)	50 µl PCR reaction
5 x Q5 reaction buffer	10 µl
5 x Q5 High GC Enhancer	10 µl
dNTP mix (25 µM)	2.5 µl
DSG2-Primer3-f fwd (10 µM)	1 µl
DSG2-Primer3-f rev (10 µM)	1 µl
5 x Q5 DNA Polymerase	1 µl
DNA (100 ng)	n µl
ddH_2O	41 µl-DNA n µl

Thermocycler conditions		
Initial denaturation	98 °C	3 min
Denaturation	98 °C	30 sec
Annealing	67 °C	30 sec
Elongation	72 °C	30 sec
Final extension	72 °C	3 min
Hold	4 °C	∞
Cycles	35x	

2.2.19.1.3 **LEMD2**

Table 2.22 Master mix of LEMD2 RT-PCR to identify genomic alterations within *LEMD2*.

Master mix (n=volume to calculate)	50 µl PCR reaction
5 x Q5 reaction buffer	10 µl
5 x Q5 High GC Enhancer	10 µl
dNTP mix (25 µM)	5 µl
LEMD2 Calgary Primer fwd (10 µM)	5 µl
LEMD2 Calgary Primer rev (10 µM)	5 µl
5 x Q5 DNA Polymerase	1 µl
DNA (100 ng)	n µl
ddH_2O	41 µl-DNA n µl

Thermocycler conditions		
Initial denaturation	98 °C	5 min
Denaturation	98 °C	40 sec
Annealing	66 °C	30 sec
Elongation	72 °C	40 sec

Final extension	72 °C	3 min
Hold	4 °C	∞
Cycles	35x	

2.2.19.1.4 **DNAJC19**

Table 2.23 Master mix of DNAJC19 RT-PCR to identify genomic alterations within *DNAJC19.*

Master mix (n=volume to calculate)	50 µl PCR reaction
10 x Pfu reaction buffer	5 µl
dNTP mix (25 µM)	1 µl
DNAJC19_exon4_Primer E (10 µM)	1 µl
DNAJC19_exon4_Primer f (10 µM)	1 µl
Pfu DNA Polymerase	1 µl
DNA (100 ng)	n µl
ddH_2O	41 µl-DNA n µl

Thermocycler conditions		
Initial denaturation	95 °C	2 min
Denaturation	95 °C	1 min
Annealing	51 °C	30 sec
Elongation	72 °C	90 sec
Final extension	72 °C	3 min
Hold	4 °C	∞
Cycles	35x	

2.2.19.1.5 **CRISPR/Cas9 off-target analysis**

Table 2.24 Master mix of off-targets RT-PCR to identify genomic alterations within *DNAJC19*, *PKP2-KO* and *DSG2-KO*

Master mix (n=volume to calculate) Used for NM_032826; NM_020476; NM_004930; NM_144720; NM_144720 (DSG2-KO, PKP2-KO and DNAJC19tv off-targets)	50 µl PCR reaction
10 x Pfu reaction buffer	5 µl
dNTP mix (25 µM)	1 µl
Primer fwd (10 µM)	1 µl
Primer rev (10 µM)	1 µl
Pfu DNA Polymerase	1 µl
DNA (100 ng)	n µl
ddH_2O	41 µl-DNA n µl

Table 2.25 Master mix of off-targets RT-PCR to identify genomic alterations within *DNAJC19*, *PKP2-KO* and *DSG2-KO*

Master mix (n=volume to calculate) Used for NM_004066; NM_001012727; NM_006181; NM_022343	50 µl PCR reaction
5 x Q5 reaction buffer	4 x n µl
5 x Q5 High GC Enhancer	4 x n µl
dNTP mix (25 µM)	2 x n µl
Primer fwd (10 µM)	2 x n µl
Primer rev (10 µM)	2 x n µl
5 x Q5 DNA Polymerase	0.4 x n µl
DNA (100 ng)	n µl
ddH_2O	41 µl-DNA n µl

Thermocycler conditions to amplify DSG2-KO off-targets

	NM_032826		NM_004930		NM_144720	
Initial denaturation	95 °C	2 min	95 °C	2 min	95 °C	2 min
Denaturation	95 °C	1 min	95 °C	1 min	95 °C	1 min
Annealing	51 °C	30 sec	63 °C	30 sec	51 °C	30 sec
Elongation	72 °C	90 sec	72 °C	2 min	72 °C	2 min
Final extension	72 °C	3 min	72 °C	5 min	72 °C	5 min
Hold	4 °C	∞	4 °C	∞	4 °C	∞
Cycles	35x		5 x		5 x	
Product length	433 bp		867 bp		421 bp	

Thermocycler conditions to amplify PKP2-KO off-targets

	NM_004066		NM_001012727		NM_006181	
Initial denaturation	98 °C	5 min	98 °C	5 min	98 °C	5 min
Denaturation	98 °C	40 sec	98 °C	40 sec	98 °C	40 sec
Annealing	68 °C	30 sec	69 °C	30 sec	68 °C	30 sec
Elongation	72 °C	30 sec	72 °C	30 sec	72 °C	30 sec
Final extension	72 °C	3 min	72 °C	3 min	72 °C	3 min
Hold	4 °C	∞	4 °C	∞	4 °C	∞
Cycles	35x		35x		35 x	
Product length	647 bp		191 bp		300 bp	

Thermocycler conditions to amplify DNAJC19tv off-targets

	NM_022343		NM_020476		NM_198995	
Initial denaturation	98 °C	5 min	95 °C	2 min	95 °C	2 min
Denaturation	98 °C	40 sec	95 °C	1 min	95 °C	1 min
Annealing	68 °C	30 sec	52 °C	30 sec	54 °C	30 sec
Elongation	72 °C	40 sec	72 °C	2 min	72 °C	90 sec
Final extension	72 °C	5 min	72 °C	5 min	72 °C	5 min
Hold	4 °C	∞	4 °C	∞	4 °C	∞
Cycles	45x		45 x			
Product length	899 bp		589 bp		464 bp	

2.2.19.2 Using cDNA as template

2.2.19.2.1 **SeV inactivation**

Corresponsing primers and RT-PCR temperatures and times were performed according to the manufacturers` instructions (Invitrogen, 2020).

Table 2.26 Master mix of SeV-vector-derived RNA RT-PCR to assess viral activity after reprogramming

Master mix (n=volume to calculate)	50 µl PCR reaction
10 x Pfu reaction buffer	5 µl
dNTP mix (25 µM)	1 µl
DNAJC19_ Primer RTF1 (10 µM)	1 µl
DNAJC19_Primer RTF2 (10 µM)	1 µl
Pfu DNA Polymerase	1 µl
cDNA (10 µl)	x µl
ddH_2O	41 µl-DNA n µl

	SEV		**KOS**		**c-MYC**		**KLF4**	
Initial denaturation	95 °C	3 min	95 °C	3 min	95 °C	3 min	95 °C	3 min
Denaturation	95 °C	30 sec	95 °C	30 sec	95 °C	30 sec	95 °C	30 sec
Annealing	55 °C	30 sec	55 °C	30 sec	55 °C	30 sec	55 °C	30 sec
Elongation	72 °C	30 sec	72 °C	30 sec	72 °C	30 sec	72 °C	30 sec
Final extension	72 °C	10 min	72 °C	10 min	72 °C	10 min	72 °C	10 min
Hold	4 °C	∞	4 °C	∞	4 °C	∞	4 °C	∞
Cycles	35x		35x		35x		35x	
Product length	181 bp		528 bp		410 bp		532 bp	

2.2.19.2.2 ***DNAJC19*** **transcript variants**

Table 2.27 Master mix of DNAJC19 RT-PCR to identify transcript variant lengthsof *DNAJC19.*

Master mix (n=volume to calculate)	50 µl PCR reaction
10 x Pfu reaction buffer	5 µl
dNTP mix (25 µM)	1 µl
DNAJC19_ Primer RTF1 (10 µM)	1 µl
DNAJC19_Primer RTR1 (10 µM)	1 µl
Pfu DNA Polymerase	1 µl
cDNA (1 µl)	n µl
ddH_2O	41 µl-DNA n µl

		RTF1 + RTR1
Initial denaturation	94 °C	3 min
Denaturation	94 °C	1 min
Annealing	55 °C	30 sec
Elongation	72 °C	70 sec
Final extension	72 °C	10 min
Hold	4 °C	∞
Cycles	35x	
Product length	899 bp	

2.2.19.2.3 *GAPDH* transcript as internal control

Table 2.28 Master mix of GAPDH RT-PCR as positive control used for internal validation of *DNAJC19* transcript variants or *SeV* inactivation

Master mix (n=volume to calculate)	50 µl PCR reaction
10 x Pfu reaction buffer	5 µl
dNTP mix (25 µM)	1 µl
hGAPDH-for (10 µM)	1 µl
hGAPDH-rev (10 µM)	1 µl
Pfu DNA Polymerase	1 µl
DNA (100 ng)	n µl
ddH_2O	41 µl-DNA n µl

		hGAPDH
Initial denaturation	94 °C	3 min
Denaturation	94 °C	30 sec
Annealing	56 °C	30 sec
Elongation	72 °C	30 sec
Final extension	72 °C	10 min
Hold	4 °C	∞
Cycles	35x	
Product length	89 bp	

2.2.20 Quantification of transcript variants using the QIAxcell Advanced system

RT-PCR products were used for quantitative analysis of *DNAJC19* (section 2.2.19.2.2) and *GAPDH* (section 2.2.19.2.3) to assess the expression of full-length and ∆ex4 DNAJC19 transcripts in dermal fibroblasts, iPSCs and iPSC-CMs. 1 µl cDNA was used for both RT-PCRs to allow normalization towards GAPDH. RT-PCR concentrations were automatically quantified by referencing to at least one sample containing PCR products of a known concentration and a known size (GAPDH: 87 bp; 50 ng/µl, 100 ng/µl, 250 ng/µl, 500 ng/µl) that was simultaneously measured. Details can be found in the manufacturers` instructions (Qiagen, 2017).

2.2.21 Agarose gel electrophoresis

1-3 % w/v agarose was diluted in TAE-buffer and heated in a microwave until fully dissolved. After cooling on a magnet stirrer for approximately 10-30 min at room temperature, 7 µl of the DNA-intercalating reagent Midori Green Advance were added per 100 ml agarose solution. Next, a comb of an appropriate size and well number was inserted prior to polymerization to generate a gel. Samples were then loaded and the electrophoresis was started in TAE buffer at 90 V for 45 min depending on the individual gel percentages. The gels were analyzed using the UV benchtop and/or images were acquired using the ChemiDoc™ Touch Imaging System. Intensities were quantified using the program Quantity One v.4.6.2.

2.2.22 Sequencing

Purified PCR samples of candidate clones or individual cell lines were sent to the company Microsynth Seqlab GmbH (Göttingen, Germany) for sequencing analysis. Sequencing samples consisted of 1 µl purified PCR product, 2 µl forward (or reverse) primers (10 µM) and 7 µl ddH_2O. Sequencing results were received via E-Mail and analyzed using the SnapGene® 3.3.3 software.

2.2.23 STR Analysis

The individual STR profiles of eight independent genomic loci AMEL, D3S1358, SE33, TH01, D18S51, FGA, vWA, D21S11, D8S1179 were investigated with the Mentype®Nonaplex I PCR Amplification Kit (Biotype) using 2 ng isolated DNA. The STR analysis was performed in the group of PD Dr. Simone Rost by Birgit Halliger-Keller in the Institute of Human Genetics, Biocentre, University of Würzburg, Würzburg, Germany.

2.2.24 Transmission electron microscopy (TEM)

iPSC-CMs were seeded on glass coverslips and cultured for 60 or 120 days and fixed with TEM fixing solution for 5 min at 37°C. Fresh fixing solution was added and cells were incubated for at least 90 min at room temperature. After 5 washing steps with CB for 5 min at room temperature each iPSC-CMs were covered with 1 % osmium tetroxide in CB for 60 min. The dehydration of cells was mediated by increasing concentrations of EtOH while including the en-bloc contrasting through 0.5 % uranyl acetate. In detail following steps were performed: 30 % EtOH for 5 min, 50 % EtOH for 5 min, 0.5 % uranyl acetate in 70 % EtOH for 30 min, 90 % EtOH for 5 min, 96 % EtOH for 5 min and finally twice 100 % EtOH for 10 min each. Next, iPSC-CMs were embedded in a mixture of one part of Epon embedding mixture and one part EtOH for 30 min at room temperature, followed by addition of pure Epon mixture that was changed after 2 h to a thin layer of fresh Epon mixture to allow polymerization for 48h at 60°C using an empty Epon block. For TEM imaging, ultrathin sections of ~80 nm were cut from resin blocks and transferred on Formvar-coated nickel grids. Afterwards, sections were stained with 2 % uranyl acetate and 0.2 % lead citrate to allow image acquisition with the Zeiss LEO912AB transmission electron microscope. TEM images were self-obtained with the help of Dr. Nicole Wagner in the Institute of Anatomy and Cell Biology II, University of Würzburg, Würzburg, Germany and the help of Prof. Dr. Christian Stiegloher in the Imaging Core Facility, Biocentre, University of Würzburg, Würzburg, Germany. iPSC-CMs were embedded with the help of the technical assistant Karin Reinfurt-Gehm in the Institute of Anatomy and Cell Biology II, University of Würzburg, Würzburg, Germany and the technical assistant Daniela Bunsen in the Imaging Core Facility, Biocentre, University of Würzburg, Würzburg, Germany.

2.2.25 Karyotype analysis

iPSCs were passaged one day before karyotype analysis in a ratio of 1:2 into six wells of a 6-well plate. Colcemid™ treatment [10 µg/ml] was addressed to inhibit mitosis and cells were thereafter processed according to standard methods. Conventional chromosome analysis of ten GTG-banded metaphases was made with a resolution of 300–500 bands per haploid-karyotype using an Axioskop (Zeiss) microscope. The karyotype analysis was performed in the group of Prof. Dr. Eva Klopocki by the technical assistant Noemi Knötgen in the Institute of Human Genetics, Biocentre, University of Würzburg, Würzburg, Germany.

2.2.26 Mass spectrometry

3 million iPSC-CMs were pelleted and washed twice with dPBS. Cells were centrifuged at 1500 rpm for 5 min at room temperature and the supernatant was discarded. Cells were covered with argon gas and directly frozen on dry ice and stored on -80°C. Further sample processing and mass spec analysis was performed by A. Cirnu and Dr. Werner Schmitz at the Chair of Biochemistry and Molecular Biology, Biocentre, University of Würzburg, Würzburg, Germany. Lipids were extracted by adding methanol to each cell pellet, followed by a sonification step. Internal standard CL(14:0)4 (Avanti Polar Lipids) and 0.2 M hydrochloric acid were added. Chloroform-based Bligh-Dyer extraction was performed (Bligh and Dyer, 1959) and the resulting lower phase was evaporated by a gentle stream of nitrogen at 45°C. The remaining protein-pellet was dried and stored at -20 °C until protein quantification. The lipid-containing lower phase was evaporated at 45 °C with the help of nitrogen gas. The remaining lipids were resuspended in methanol and separated by thin layer chromatography with a mixture consisting of chloroform/methanol/ammonium hydroxide (74/25/1, v/v/v) as mobile phase. The TLC plate was dried and a second TLC run was performed with chloroform/hexane/methanol/acetic acid (50/30/10/5,

v/v/v/v). After the plate was dried, it was reversibly stained with iodine vapor to visualize different lipid families. The silica gel layer with bound lipids was scratched off at the height of the CL standard for all samples, which were then committed to butanol/methanol extraction after (Lofgren et al., 2012). The lipid containing upper phases were evaporated by a gentle stream of nitrogen at 45°C, resuspended in 5 mM ammonium acetate in actetonitrile/water (75/25, v/v) and three dilutions (1:10; 1:100; 1:1000) were prepared. General HPLC–MS Solvents and standard compounds were purchased from Merck. The equipment used for LC/MS analysis was a Thermo Scientific Dionex Ultimate 3000 UHPLC system hyphenated with a Q Exactive™ mass spectrometer (QE-MS) equipped with a HESI probe (ThermoFisher Scientific) via direct injection with following parameters: Scan range= 1000-1700 $m/_z$, Resolution= 70000, AGC Target= $3x10^6$ ions, maximum injection time= 100 ms, acquisition time= 0.7 min. CL and MLCL were detected in negative ion mode by scanning for all combinations of the most common cellular acyl chains (16:0, 16:1, 18:0, 18:1, 18:2, 20:0, 20:1, 20:2, 20:3, 20:4, 22:4, 22:5, 22:6) as singly charged ions. Mass spectra and peak intensities correspond to the calculated monoisotopic metabolite masses (MIM +/- H^+ ± 3 mMU) and were integrated using TraceFinder software V. 3.3. The CL profile dataset could not be completed due to technical problems that could not be solved for an indefinite period of time due to COVID-19.

2.2.27 Radioactive tracer uptakes

500,000 MACS-sorted iPSC-CMs per well of a 24-well plate were seeded 14 to 7 days prior to the day of the experiment to ensure at least 60 days aged iPSC-CMs during the procedure. In brief, cells were washed once with dPBS and afterwards incubated in dPBS containing the individual tracers for 30 min at 37 °C (5 % CO_2). In detail, dPBS containing 5.0 x 10^{-1} MBq/ml ^{18}F-FDG (^{18}F-2-fluoro-2-deoxy-d-glucose) and 4.0 x 10^{-2} MBq/ml ^{125}I-BMIPP (^{125}I-β-methyl-iodo-phenyl-pentadecanoic acid) was calculated to add a total volume of 500 µl to each well of a 24-well plate. The ^{18}F-FDG tracer was produced from the in-house University Hospital of Würzburg cyclotron unit and ^{125}I-BMIPP/ml was received from Nihon Medi-Physics Co., Ltd., Japan with a previously verified purity of >95 % for both radioactively labelled tracers. The experiments were performed under the supervision of the technical assistants, Naoko Nose, Lars Mayer and the PhD student Saskia Mühlig. After the incubation, tracer suspensions were removed and radioactive tracer uptake was immediately stopped by the application of 0.5 ml ice-cold dPBS per well. The cells were washed in total three times with ice-cold dPBS and afterwards dissolved in 500 µl 0.1 M NaOH for 1 h at 37 °C. Each individual well was resuspended properly by pipetting up and down and transferred into a new 1.5 ml Eppendorf tube. The radioactivity of each sample together with a radioactivity standard of the dPBS tracer mixture (0.1 ml, 0.2 ml, 0.3 ml, 0.4 ml, 0.5 ml) was measured by the γ-counter wizard 2480 (#SGWC36160397, PerkinElmer, Germany) and subsequently stored at -20 °C until no radioactivity was recognized any more. The protein concentration of the protein lysates and blanks were quantified using Pierce™ BCA Protein Assay Kit in triplicates using the Tecan Reader Spark™ 10M according to the manufacturer's instructions for normalization of the uptake values. The uptake values were automatically corrected towards the half lifetime, blank values were subtracted and only technical replicates were included in which 0.15 mg/ml was detected to ensure the inclusion of viable cell lysates only. All replicates were normalized based on the individual tracer uptakes of ^{18}F-FDG and ^{125}I-BMIPP of the NC6M control further referred to as uptake index.

2.2.28 Seahorse XF96 extracellular flux analyzer measurements- XF Cell Mito Stress Test Assay

The Seahorse XF96 extracellular flux analyzer usage has been taught by Sudha Rani Janaki Raman and controlled by Dr. D. Gebhard (Product Specialist Cell Analysis Agilent). The 96-well microplates were coated with 0.1 % gelatin for fibroblasts and hESC-Matrigel™ for iPSCs and iPSC-CMs with 80 µl per well. Fibroblasts and iPSCs were seeded two days prior to the assay with a density of 40000 cells per well. iPSC-CMs were seeded 7 to 14 days prior to age day 60 directly after MACS with a density of 100 000 cells per well. For all cell types, the corresponding cultivation medium was changed one day before the measurements. The day prior to the measurements the cell morphologies were checked, the sensor cartridges were hydrated at 37 °C overnight in a non-CO_2 incubator with 200 µl XF Calibrant per

well and the Seahorse XF96 extracellular flux analyzer was activated to prewarm to a temperature of 37 °C. On the day of the Mito Stress Test Assay, XF Assay Medium was prepared in a cell type-specific manner according to the compositions mentioned in the table below. All reagents were prewarmed in the 37 °C water bath. The individual port buffers were prepared with 8 µM oligomycin (8x), 9 µM FCCP (9x) and 5 µM rotenone/antimycin A (10x) in XF Assay medium. For example, for port A 24 µl 1mM oligomycin stock were pipetted into 2976 µl XF Assay medium, for port B 27 µl 1mM FCCP stock were pipetted into 2973 µl XF Assay medium and for port C 30 µl were pipetted into 2970 µl XF Assay medium. The ports were loaded with 25 µl per port-well and the sensor cartridge was loaded into the instrument to initiate calibration. The cells were washed once with the corresponding XF Assay medium using 100 µl per well and were then freshly transferred to the microplate with 175 µl per well and placed for 1 hour at 37°C in a non-CO_2 incubator. After the calibration and the cell incubation the microplate with the cells was loaded into the Seahorse XF96 extracellular flux analyzer and the measurements were started. The measurements were performed according to established protocols corresponding to the individaually assessed cell type, including the manufacturers` manuals or other publications (Agilent Technologies, 2019, Agilent Technologies, 2018, Technologies, 2016, Wang et al., 2014). After the measurements were completed, the XF Assay medium was removed and 4 % PFA was added to fix the cells for 20 min at room temperature. The cells were washed with dPBS and 50 µl 0.1 % crystal violet (dissolved in 20 % EtOH) were added for a 30 min incubation step at room temperature on a shaker. The crystal violet buffer was discarded and the cells were washed 10-15 times with ddH_20 until no violet color was recognized any more in the water. After three more wash steps, dPBS was removed and the plate was dried overnight. The day after the assay, 100 µl of 10 % acetic acid were added and the cells were mixed by pipetting up and down and incubated for 15 min at room temperature. Next, 50 µl per well were transferred into a new 96-well plate with 50 µl ddH_2O (dilution 1:1). The plate was measured with the Tecan Reader Spark™ 10M 1 point per well at 595 nm. The absorbance values were used for normalization after subtraction of blank values and added into the Wave Software V.2.6. for automated normalization. The OD values below 0.04 were excluded due to too low viabilities and manually excluded in the Wave Software V.2.6..

	Stocksolution	Fibroblasts	iPSCs	iPSC-CMs
Seahorse XF RPMI medium, pH 7,4				
Glucose	1 M	25 mM	25 mM	10 mM
Pyruvate	100mM	1 mM	1 mM	1 mM
Glutamax	200 mM	4 mM	x	2 mM
pH exactly!		7.4	7.4	7.4
Oligomycin	1 mM	1 µM	1 µM	1 µM
FCCP	1 mM	1 µM	1 µM	1 µM
Rotenone/Antimycin A	500 µM	0.5 µM	0.5 µM	0.5 µM

2.2.29 Electrophysiology with the IonOptix system

The IonOptix system usage was taught and controlled by the supervisor of the Core Facility for Cellular Electrophysiology Dr. Michael Kohlhaas. The IonOptix system with the appropriate filter and mirror sets was installed according to the following figures. For the functional assessment of Ca^{2+} uptake and release 40,000 iPSC-CMs were cultured on matrigel-mattresses on a glass coverslip prepared in a 48-well plate for at least 120 days to enable IonOptix experiments of mature stages (Feaster et al., 2015). iPSC-CMs were selected visually by typical hallmarks like elongated cell shape, single cell confluency and the capacity to contract. A maximum of two metabolic enrichments was sufficient to enable purified conditions. One day before the measurements, iPSC-CMs received fresh CBM (250 µl per one well of 48-well plate) and were controlled for maintenance of contraction. On the day of the measurements, iPSC-CMs were stained in x µM Indo-1-AM (0.5 µl Indo-1-AM in 500 µl CBM, 1:1000 dilution) for 12 min at 37°C in the incubator. Afterwards, cells were washed with prewarmed CBM and replaced into the incubator for at least 30 min to allow resting after the stressful staining procedure. iPSC-CMs containing glass coverslips were placed on a second 24 x 50 mm larger glass coverslip and mounted in the measuring chamber which has been immediately filled with prewarmed CBM. Themeasurement chamber was placed into a dark box, transferred to the IonOptix system and immediately installed into the holding of the microscope by using the 20x objective to connect the iPSC-CMs with the system. iPSC-CMs were maintained at 37°C during the measurements and flow was activated allowing inflow of

prewarmed Normal Tyrode solution into the chamber while the liquid surrounding the iPSC-CMs was aspirated continuously to avoid overflow of the chamber by retaining the same volume in the chamber. iPSC-CMs were electrically stimulated by 100mA with a duration of 0.5 s and a frequency of 0.5 Hz. A maximum of 30 min waiting was allowed to enable longer resting phases for the cells until contractions were visually recognized. Next, one contracting iPSC-CM was visually placed into the imaging center by usage of the cell framing adapter and controlled visually for survival by observing Ca^{2+} transients. To asses contractility the grey value scale of the image was used by placing individual selected points manually on the side borders of the cell to allow edge detection. During the measurements a stress protocol was performed including 2 mM Ca^{2+} in N-Tyrode and increasing Iso concentrations 10 nM, 30 nM, 100 nM followed by 2 mM Ca^{2+} in N-Tyrode again. Each step was aquired for 4 minutes, of which the first two were not included into the analyses due to 2 min wash-in phases. At the end of the measurement, the background signal was determined to be able to subtract this signal value in the analysis by adaptation of the image section into an area without cells, where the signal was recorded for a few seconds. Only iPSC-CMs were included that were still alive after the whole measurement, that was determined by visible transients on the last 2 mM Ca^{2+} in N-Tyrode phase. As most of the cells did not react to electric stimulation, all measurements were analyzed manually using the program IonWizard 6.6.1.108. After opening the data file, the screen template and the analysis template had to be adjusted considering following parameters: 'Indo 1, AM-Numeric subtracted | Ratio', 'Edge 20x-Length | Length' and 'Indo 1, AM-Numeric subtracted | Calcium', the template 'Monotonic Transient Analysis Options' was loaded and modified: t0 had been defined as the time of the departure. Baseline, departure velocity, peak, return velocity, time to % peak, time to % baseline and exponential fit were chosen as important parameters. The analysis criteria for the departure were modified, velocity was selected to only 'include time' and times were set to 'relative to t0'. The peak parameter covered the 'height [peak h]', the 'height%baseline [bl%peakh]' and 'include time'. The parameter return velocity 'include time' was selected together with 'times relative to t peak'. Moreover, for the duration until a given percentage from baseline to peak was reached 'time to peak 50 %', 'times relative to t0', 'time to baseline 50 %' and 'time to baseline 90 %' were defined. For times to return a given percentage from peak to baseline, 'times relative to t peak', 'exponential fit' was chosen with 'fit from peak' and `tau`was selected. First, Ca^{2+} concentrations were examined after subtraction of the background signal by manual evaluation of the numerator and denominator values. Each transient was set manually by determining ten transients in a row per treatment to allow the program to analyze each individual transient. As some transients could not be analyzed given the low signal-to-noise ratio, the automated filtering was used for all measurements, to allow the comparison regarding Ca^{2+} kinetics of all measurements. All values were based on the ratiometric principle of Indo-1-AM, consisting of the excitation of $\boldsymbol{\lambda_{exc}}$ 340 nm that emits light of two different wavelengths after entering the cell, depending on the bound status to Ca^{2+} $\boldsymbol{\lambda_{em}}$ 405 nm for bound to Ca^{2+} and $\boldsymbol{\lambda_{em}}$ 485 nm for unbound molecules. Consequently, detecting the emitted fluorescence intensity of the two wavelengths and the ratio of bound to unbound allowed the detection of changes in the cellular Ca^{2+} concentration. The analysis of the cell shortening was performed on the same transients respectively by using the tab 'Edge 20x-Length | Length'. Then the values of the curve in µm were automatically calculated by pushing the button 'M Tran'. Contractility and Ca^{2+} homeostasis were assessed simultaneously in living CMs and the generated values were exported into an Excel sheet. For each measurement and each condition, a list of all values for each of the ten transients were automatically generated with all named parameters. As time parameter values depend on the frequency, all kinetic values were corrected using the adaptation from Bazett's formula by dividing the time parameter values by the square root of the time Δt, which corresponds to the average time period of one contraction phase (Bazett, 1920). The frequency correction was approved by Dr. M. Kohlhaas, Core Facility of Cellular Electrophysiolgy, November, 2020. The mean and standard error of the mean (SEM) of ten transients per treatment were calculated and used for graphical representation and statistical tests with the help of the software GraphPad Prism 6 by performing a two-way ANOVA together with Bonferroni posttests. iPSC-CMs were partially assessed for Ca^{2+} handling properties with the help of the Bachelor student Miriam Leskien.

Table 2.29 Stress protocol used for Indo-1-AM measurements to assess Ca^{2+} homeostasis in iPSC-CMs

Application of	Minimal wash-in time [sec]	Minimal residence time [sec]
2 mM Ca^{2+} in N-Tyrode	120	120
10 nM isoproterenol + 2 mM Ca^{2+} in N-Tyrode	120	120
30 nM isoproterenol + 2 mM Ca^{2+} in N-Tyrode	120	120
100 nM isoproterenol + 2 mM Ca^{2+} in N-Tyrode	120	120
2 mM Ca^{2+} in N-Tyrode	120	120
Background signal	A few seconds	

2.2.30 Softwares

Software	Application	Manufacturer/Reference
Adobe Illustrator CS5 & Adobe Illustrator 2020 30-day-trial	Figure design (alphabetical numbering, descriptive text, arrow labeling)	Adobe Inc., USA
BD FACSDiva v6.1.3	Flow cytometry data acquisition	BD Biosciences, USA
BioRender	Figure creation and scheme design	BioRender, Canada (BioRender, 2017)
Fiji (ImageJ)	Image stitching, Z-focus stacking, scalebar positioning, image analysis, macro quantifications (supplementary section 5.4)	(Schindelin et al., 2012)
FlowJo7.6.1	Flow cytometry data acquisition	FlowJo, LLC, USA
GraphPad Prism 5.01, 6	Graphing and statistical analysis	GraphPad Software Inc., USA
IonWizard software v.6.6.1.108	Ca^{2+} handling analysis	IonOptix, USA
Office 365	Word processing and documentation	Microsoft Corporation, USA
Quantity One v.4.6.2	Western blot analysis	Bio-Rad Laboratories GmbH, USA
SnapGene® 3.3.3	CRISPR/Cas9 design illustration and gene alignment	GSL Biotech LLC, USA
TraceFinder software V. 3.3	Mass spectrometric analysis	Thermo Fisher Scientific Inc., USA

3. Results

3.1 Generation of human iPSCs using the non-integrating Sendai virus (SeV)

The generation of human iPSC-based *in vitro* model systems to study inherited cardiomyopathies requires human somatic (non-germ) cells. In this thesis terminally differentiated dermal fibroblasts were used for reprogramming into iPSCs. The single-RNA SeV was elected as delivery method for reprogramming to generate transgene-free iPSC lines and to investigate the reprogramming efficiency on dermal fibroblasts of different genders and ages, different origins and subsequently different genetic backgrounds (Ban et al., 2011).

3.1.1 Cell line overview: patient-derived and healthy control dermal fibroblasts

Patient-derived dermal fibroblasts originate from the Hutterite population in Calgary, Canada (DCMAP1, DCMAP2, LEMD2 p.L13R fibroblasts, Tab. 3.1). The male patient with an identified *LEMD2* (NM_181336.4):c.38T>G, p.L13R mutation presented a severe manifestation of DCMJC at the age of 38. The siblings DCMAP1 (male) and DCMAP2 (female) were diagnosed with early onset DCMA and carry a homozygous splice acceptor site mutation in *DNAJC19* (NM_145261.4):c.130-1G>C (Tab. 3.1). All patient-derived dermal fibroblasts were obtained by Prof. Dr. Brenda Gerull and Prof. Dr. Henry Duff at the Libin Cardiovascular Institute of Alberta, University of Calgary (Tab. 3.1; ethical approval ID-E20729). Other control cell lines were commercially available and were chosen according to their age and gender to match the patients' conditions (NC6M, NC47F fibroblasts, Tab. 3.1). All five dermal fibroblast cell lines were proven mycoplasma-negative and mutant cell lines were validated by Sanger sequencing. Primarily, NC6M iPSCs were selected as positive control to determine the success of reprogramming and to characterize pluripotent properties. The positive control was generated by Dr. K. Günther using lentiviral transduction of NC6M fibroblasts at the Institute of Anatomy, Würzburg ((Günther, 2016, Kwok et al., 2018); Stem cell research ID: JMUi001-A; Tab. 3.1).

Table 3.1: Overview of all dermal fibroblast cell lines for the generation of iPSCs.
§ homozygous mutation; *p.* passage number at day of viral transduction; *$* received from Dr. K. Günther (Günther, 2016, Kwok et al., 2018)

iPS cell line name	Original cell line	Healthy/ disease	Genotype of locus	Reprogramming method	P.	Ethnicity	Gender	Donor age
NC6M	NC6M fibroblasts	healthy	-	lentiV$	x	Caucasian	male	6
NC6M-SeV	NC6M fibroblasts	healthy	-	SeV	10	Caucasian	male	6
NC47F	NC47F fibroblasts	healthy	-	SeV	8	Caucasian	female	47
LEMD2 p.L13R	LEMD2 p.L13R fibroblasts	DCMJC	NM_181336.4 (*LEMD2*):c.38T>G, p.L13R (§)	SeV	5	Caucasian Hutterite	male	38
DCMAP1	DCMAP1 fibroblasts	DCMA	NM_145261.4 (*DNAJC19*):c.130-1G>C (§)	SeV	10	Caucasian Hutterite	male	8
DCMAP2	DCMAP2 fibroblasts	DCMA	NM_145261.4 (*DNAJC19*):c.130-1G>C (§)	SeV	8	Caucasian Hutterite	female	12

3.1.2 The formation of stem cell-like colonies

DCMAP2 fibroblasts were depicted for illustration of the reprogramming procedure (Fig. 3.1). Dermal fibroblasts of five donors were transduced at low passages (≤10) with the integration-free SeV according to the lot-specific MOI titer (Fig. 3.1 a). Substantial changes in cellular morphology were observed turning from a thin elongated fibroblast cell shape into a round stem cell-like appearance within the first week (Fig. 3.1 b). The reseeding of transduced fibroblasts on MEFs, the switch to iPSC medium and the supplementation of bFGF were crucial to ensure survival and growth of iPSC colonies according to the manufacturers' instructions (Fig. 3.1 c). Between 12 to 20 days after viral transduction the activation of pluripotency-associated genes resulted in the formation of stem cell-like shaped colonies in all cell lines (Fig. 3.1 d). Colony growth to the appropriate size of 0.5-1 mm diameter was observed in all cell lines (Fig. 3.1 d, Tab. 3.2).

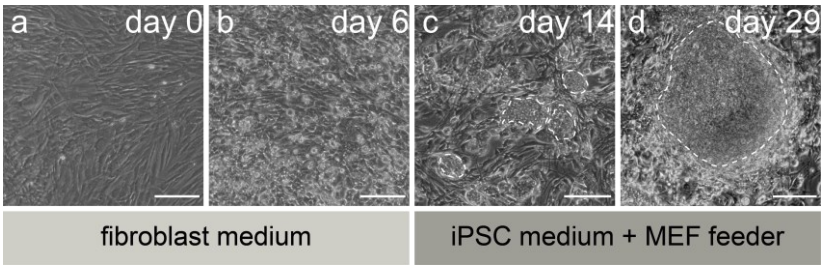

Figure 3.1: SeV priming of dermal fibroblasts led to morphological changes and the formation of stem cell- like colonies.
Bright field images of DCMAP2 dermal fibroblasts at four different time points are depicted to illustrate morphological changes during reprogramming. **(a)** Prior to viral induction DCMAP2 fibroblasts exhibited typical elongated morphological features of dermal fibroblasts (day 0). **(b)** Round cells appeared six days post SeV priming. **(c)** Reseeding on MEFs and switch to iPSC cultivation medium supported the formation of stem-cell like colonies on day 14 post transduction. **(d)** After 29 days, colony enlargement to the appropriate size (~500 micrometer (µm)) allowed manual picking of colonies. scale bar = 200 µm

3.1.3 Evaluation of reprogramming efficiency, expansion time and colony survival

Stem cell-like colonies appeared in all conditions but differed in the amount ranging from <50 colonies/well in NC47F and LEMD2 p.L13R to 86 colonies/well in NC6M up to >100 colonies/well in DCMAP1 and DCMAP2 by visual determination (Fig. 3.1 d, Tab. 3.2). With regard to the number of seeded fibroblasts prior to transduction (150000 cells) the appearance of colonies after reseeding on MEFs was used to calculate the reprogramming efficiency on the basis of the publication of Ban et al., 2011. The efficiency varied between 0.02 % (LEMD2 p.L13R) to 0.09 % (DCMAP2). The timeframe until most of the colonies fulfilled the size requirements for manual picking varied between 29 (NC47F) to 44 days (LEMD2 p.L13R) (Tab. 3.2). Approximately 13 to 48 colonies per cell line were manually picked and individually transferred into hESC-Matrigel^{TM}-coated wells under feeder-free conditions (Tab. 3.2). The survival of the picked stem cell-like shaped colonies varied between 31.6 % (LEMD2 p.L13R) to 69.2 % (NC6M) (Tab. 3.2). All colonies were grown separately to ensure high population purities. After three passages of expansion all promising colonies were cryopreserved. Three colonies per cell line were chosen for further expansion according to the best morphology compared to the positive control NC6M iPSCs. Typical stem-cell like morphology was hallmarked by sharp colony edges, closely adjacent cells and homogenous cell shape as best quality criteria (Fig. 3.8). One representative colony per cell line was used for further experiments including iPSC characterization (Tab. 3.2).

Table 3.2: Comparison of generated iPSC lines regarding reprogramming efficiency, expenditure of time and colony survival.
The appearance of colonies was evaluated concerning the following criteria: +++ very efficient (>100 colonies/well of a 12-well plate); ++ efficient (51-100 colonies/well of a 12-well plate); + low efficiency (0-50 colonies/well of a 12-well plate). The efficiency was calculated by dividing the number of counted colonies after reseeding on MEFs by the number of seeded fibroblasts at the day of transduction (150000 cells in all conditions) (Ban et al., 2011). # colony number

iPS cell line name	Colony formation	Efficiency [%]	Picked colonies [n]	Vital colonies [n]	Survival colonies [%]	Picked on day x after transduction	Representative colony
NC6M	positive control (Günther, 2016, Kwok et al., 2018)						#2
NC6M-SeV	++ (n=86)	0.06 %	13	9	69.23 %	34	#1
NC47F	+ (n=49)	0.03 %	48	23	47.92 %	29	#25
LEMD2 p.L13R	+ (n=36)	0.02 %	19	6	31.58 %	44	#7
DCMAP1	+++ (n=120)	0.08 %	15	7	46.67 %	34	#1
DCMAP2	+++ (n=135)	0.09 %	19	12	63.16 %	34	#1

3.1.4 Sequence validation of reprogrammed patient-derived and control iPSCs

The genetic identity of patient-derived dermal fibroblasts and their corresponding iPSC lines was investigated via Sanger sequencing after clonal expansion. Isolated DNA was amplified specifically for the disease-associated genes *LEMD2* or *DNAJC19*. Sanger sequencing was performed to confirm the presence of mutations in patient-derived cell lines (DCMAP1, DCMAP2, LEMD2 p.L13R) and the absence in control iPSC lines (NC6M, NC47F). The DCMJC-associated mutation *LEMD2* (NM_181336.4):c.38T>G, p.L13R was still present in LEMD2 p.L13R iPSCs and absent in both control iPSC lines NC6M and NC47F (Fig. 3.2 A). DCMAP1 and DCMAP2 iPSCs both presented the homozygous splice acceptor site mutation in *DNAJC19* (NM_145261.4):c.130-1G>C whereas no *DNAJC19* mutation was detected in NC6M and NC47F iPSCs (Fig. 3.2 B). All five reprogrammed iPSC lines demonstrated the same genetic identity within the genes *LEMD2* and *DNAJC19* compared to their original donor dermal fibroblast cell lines (Fig. 3.2). Taken together, two control and three patient-derived iPSC lines were generated underlining the high reprogramming efficiency of the non-integrating SeV.

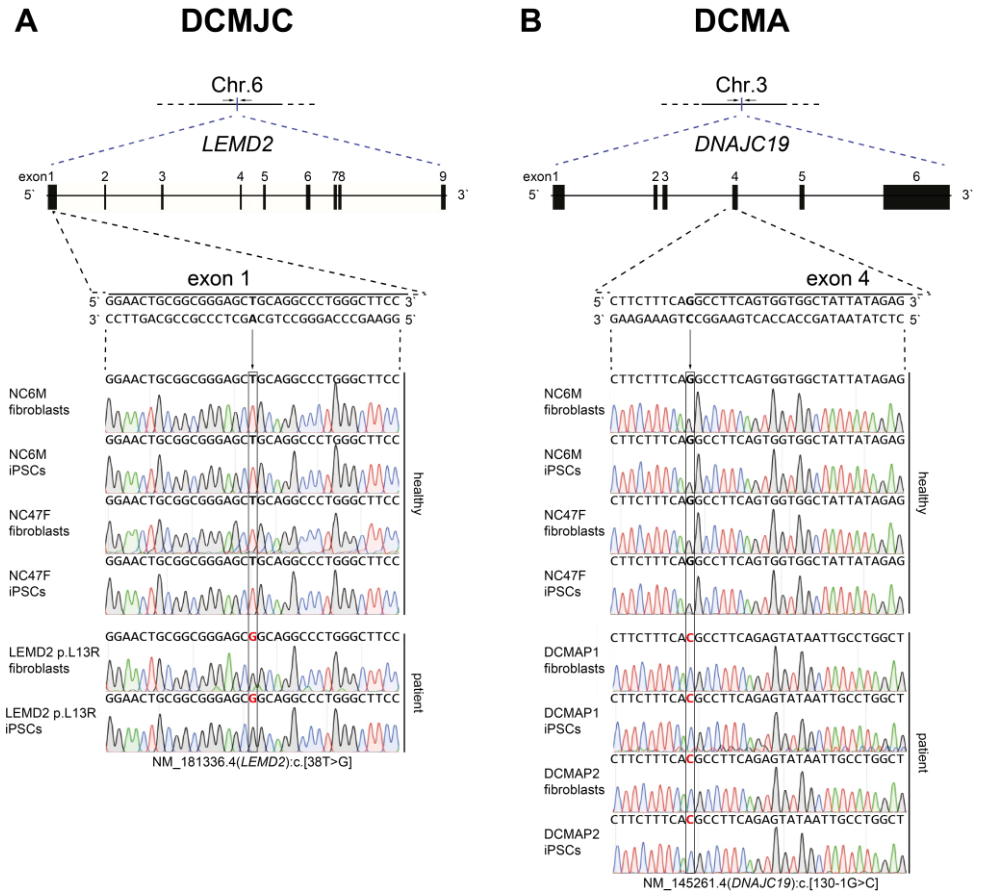

Figure 3.2: Sequence validation of generated iPSC lines.
(A) Sanger sequencing alignment of LEMD2 exon 1 of NC6M, NC47F and LEMD2 p.L13R fibroblasts and their corresponding iPSC lines showed no sequence alterations after reprogramming. The DCMJC-associated homozygous mutation NM_181336.4 (*LEMD2*):c.[38T>G] was present in LEMD2 p.L13R fibroblasts and their corresponding iPSCs and absent in both healthy control NC6M and NC47F fibroblast lines as well as in the respective iPSC lines. **(B)** The chromatogram alignment of the intron3_exon4 spacing region within *DNAJC19* on chr. 3 of NC6M, NC47F, DCMAP1 and DCMAP2 showed no changes when comparing the original fibroblast cell lines to the iPSCs. The homozygous mutation NM_145261.4(*DNAJC19*):c.[130-G>C] was identified in both DCMA patient-derived dermal fibroblast cell lines DCMAP1 and DCMAP2 as well as in both corresponding iPSC lines. Healthy control NC6M and NC47F fibroblasts and iPSCs showed no mutations within *DNAJC19*.

3.2 Generation of isogenic mutant controls with CRISPR/Cas9

The main benefit of the generated patient-derived iPSCs is the identical genetic footprint of the individual cardiomyopathy patient. To exclude the postulated impact of the genetic background on the strength of the phenotype, disease-associated mutations were introduced into the `healthy` genotype of NC6M iPSCs. The generation of isogenic mutant controls allows the direct correlation of the phenotype to the mutation itself. Therefore, we used the gene editing system CRISPR/Cas9 to establish iPSC based *in vitro* model systems of two inherited cardiomyopathies: ACM and DCMA. To gain experience with the CRISPR/Cas9 system two knock-out iPSC lines were aimed to be generated by depletion of the desmosomal genes *PKP2* and *DSG2* to recapitulate an ACM-associated phenotype. Next, the CRISPR/Cas9 system was used to mimic the splice acceptor site mutation of intron 3 in *DNAJC19*, which is present in both generated DCMA patient-derived iPSC lines (DCMAP1, DCMAP2). To achieve the patient-related C-terminal truncation of DNAJC19, specific positioning of the cleavage site in order to target the last bp of intron 3 or the first bp of exon 4 on the genomic level was required to mimic skipping of exon 4 on the transcriptional level.

3.2.1 Optimized nucleofection protocol based on healthy control iPSCs

Prior to *in silico* design and cloning, an iPSC-based nucleofection protocol was required. The protocol was established by nucleofection of healthy control NC6M iPSCs with the pSpCas9(BB)-2A-GFP plasmid via the NEON^{TM} Transfection System. The nucleofection parameters were adapted after the Mouse Embryonic Stem Cells NEON^{TM} Transfection protocol, herein referred to as nucleofection strategy #1 (Thermo Fisher Scientific, 2018). The mESC protocol was optimized for iPSC nucleofection in six steps with focus on viability and transfection efficiency. The detailed experimental summary is depicted in Tab. 5.5. Step #1, #3, #5 and #7 are depicted to represent essential optimization levels (Fig. 3.3 A, C). Bright field images were used to calculate the number of viable cells after nucleofection compared to non-electroporated iPSCs. The transfection efficiency was calculated by counting the number of surviving eGFP^{+} cells within the iPSC population, exemplarily shown by step #1 and #7 (Fig. 3.3 B). Data are represented as mean ± SEM together with each technical replicate, experimental details can be found in supplementary Tab. 5.5. The usage of the standard mESC protocol resulted in low survival rates of 7.2 % together with a transfection efficiency of 32.9 % eGFP^{+} iPSCs (Fig. 3.3). Nucleofection protocol #3 enhanced the survival of iPSCs significantly from 7.2 % in to 71 % by reduction of three pulses to two pulses combined with a reduced voltage of 1400 V to 1200 V (unpaired t-test #1 vs. #3 **, p=0.0069, Fig. 3.3 A, C). Despite of the high survival rate the transfection efficiency was not enhanced and only 10.1 % eGFP^{+} cells were observed compared to the 4.4 % eGFP^{+} cells when using the mESC standard protocol (Fig. 3.3 C). In step #5, the amount of plasmid was increased to 40 µg, which significantly enhanced the transfection efficiency to 65.2 % eGFP^{+} iPSCs (unpaired t-test #1 vs. #5 *, p=0.0272) but was accompanied by low survival of 3.8 % (Fig. 3.3 A, C). Instead, we kept 35 µg plasmid and increased the amount of cells from 150000 into 250000 cells together with an increase in the pulse length from 25 ms to 35 ms (step#7) (Fig. 3.3). The new parameters resulted in a stable survival of about 44.2 % together with a transfection efficiency of 46.4 % eGFP^{+} cells (Fig. 3.3). We were able to significantly enhance the survival from 7.2 % to 44.2 % (unpaired t-test #1 vs. #7 **, p=0.0016) accompanied by a significant increase in the transfection efficiency from 32.9 % to 46.45 % eGFP^{+} cells (unpaired t-test #1 vs. #7 **, p=0.0022) (Fig. 3.3). Thus, we succeeded in generating a stable nucleofection protocol for the transfection of NC6M iPSCs which was used as basis for the establishment of all CRISPR/Cas9 gene-edited iPSC lines within this thesis.

A

Nucleofection strategies / Parameters	#1	#3	#5	#7
Voltage [V]	1400	**1200**	1200	1200
Pulse length [ms]	25	25	25	**35**
Number of pulses [n]	3	**2**	2	2
Cells [n]	150 000	150 000	150 000	**250 000**
Plasmid [µg]	35	35	**40**	35
Survival [%]	7.2	71	3.8	44.2
eGFP$^+$ [%]	32.9	10.1	65.2	46.4

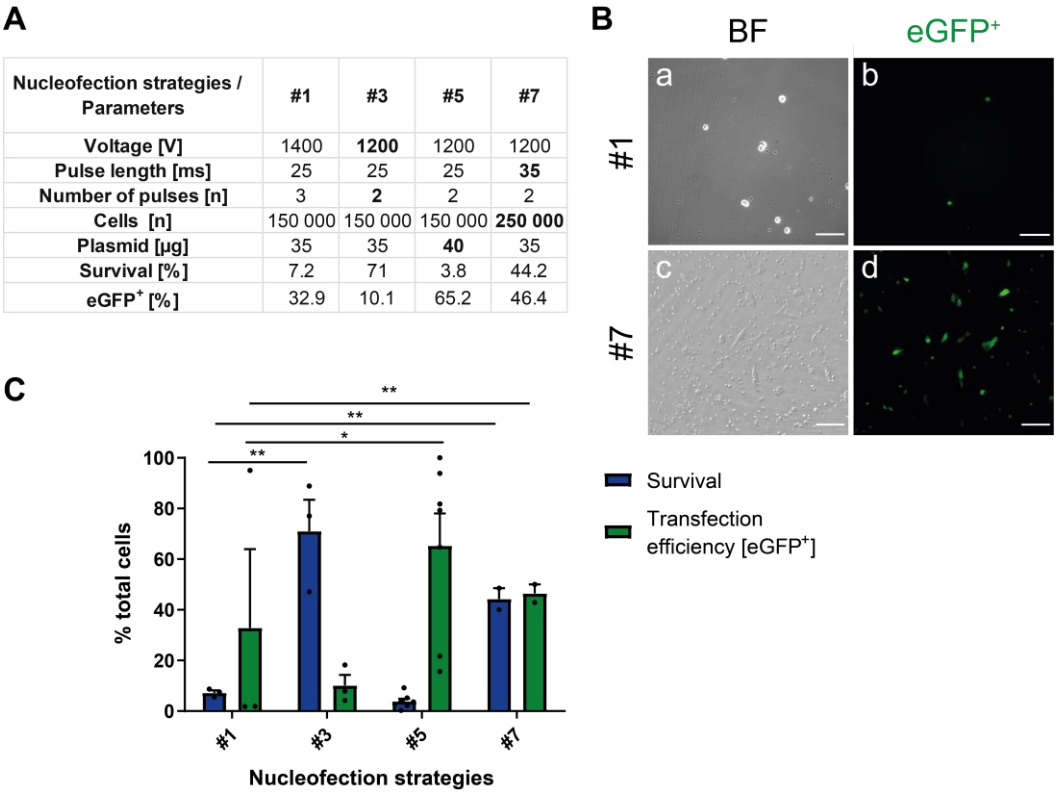

Figure 3.3: Optimized nucleofection parameters enhanced survival of iPSCs and increased transfection efficiencies.
(A) Table of electroporation strategies numbered #1, #3, #5, #7, the appropriate parameters voltage [V], pulse length [ms], number of pulses [n], cells [n], plasmid [µg] and the individual resulting survival [%] and transfection efficiency [%]. The optimized parameters after each step are marked in bold. **(B)** Representative images of nucleofected iPSCs with the standard mESC protocol #1 **(a, b)** and the optimized conditions in nucleofection strategy #7 **(c, d)**. Brightfield images **(a, c)** and fluorescence images **(b, d)** were depicted to illustrate higher survival and increased amount of eGFP$^+$ cells after using strategy #7 **(c, d)** compared to strategy #1 **(a, b)**. **(C)** Quantitative analysis of the percentage of surviving iPSCs compared to non-transfected controls (blue bars) and the percentage of eGFP$^+$ cells (green bars) of all surviving iPSCs for each individually performed nucleofection strategy. Nine fields were imaged per well using the 20x magnification and were calculated as one technical replicate with ImageJ. Each nucleofection protocol was tested in at least two to three technical replicates (2-3 wells/condition) from one to three independent cultures. Data is represented as mean ± SEM together with the mean of the corresponding technical replicates (boxes). ** $p<0.01$, * $p<0.05$ using unpaired-t test calculated versus nucleofection strategy #1. *BF* bright field; scale bar = 100 µm

3.2.2 *In silico* CRISPR/Cas9 experimental designs

Prior to *in silico* design the Genome Reference Consortium Human Build 38 patch release 13 (GRCh38.p13) database of the NCBI was used to get access to biomedical and genomic information of the disease related reference genes *PKP2* (NG_009000.1), *DSG2* (NG_007072.3) and *DNAJC19* (NG_022933.1). All human transcript variants and isoforms of the named genes were aligned to the individual genomic locus to clearly identify coding genomic regions using SnapGene® 3.3.3 software. To target all annotated proteins of PKP2 and DSG2 the first shared exon was used for knock-out design. In both cases the used sequence was exon 1, in detail for PKP2-KO design NM_001005242 (*PKP2*):c.1-223 and for DSG2-KO design NM_001943.5 (*DSG2*):c.1-45 were used. For DCMA, the gRNA template to design a DSB at the splice acceptor site of intron 3 comprised 100 bp intron 3 followed by 80 bp exon 4 in the *DNAJC19* gene, in detail NG_022933.1 (*DNAJC19*):g.2615_2794. Next, Sanger sequencing was performed to detect the presence of single nucleotide polymorphisms (SNPs) within the individual genomic loci of NC6M iPSCs Fig. 3.4). The healthy genetic background of NC6M iPSCs demonstrated no nucleotide changes within the three genomic regions of interest *PKP2* (A), *DSG2* (B) and *DNAJC19* (C) when compared to their NCBI reference sequences (Fig. 3.4).

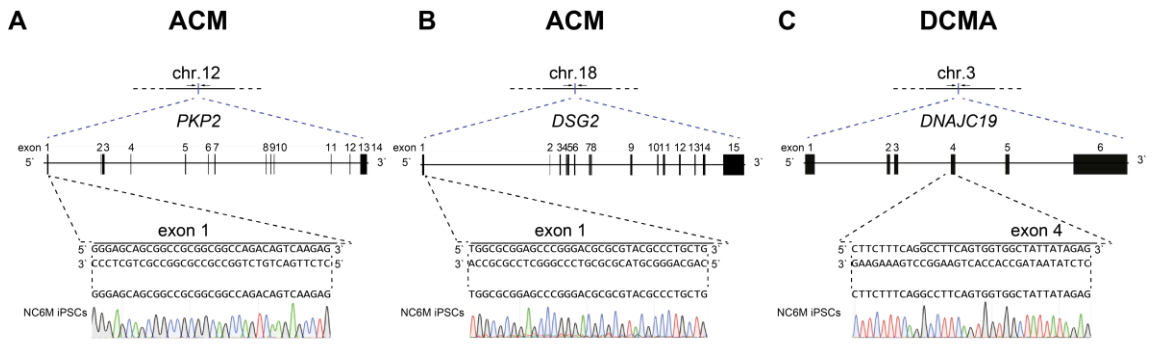

Figure 3.4: Sanger sequencing alignment demonstrated the absence of single nucleotide polymorphisms (SNPs) within the individual genomic loci of NC6M iPSCs.
DNA sequence chromatograms of **(A)** *PKP2*, **(B)** *DSG2* and **(C)** *DNAJC19* genomic regions did not reveal any nucleotide alterations when compared to the NCBI database, representing suitable sequences for CRISPR/Cas9 *in silico* design of ACM **(A, B)** and DCMA **(C)**.

Next, the computational design of the CRISPR/Cas9 gRNA to target the individual specific genomic regions was performed by using the Zhang laboratory CRISPR online design tool (Ran et al., 2013b, Zhang Laboratory at the broadinstitute, 2018). The computational prediction was used to estimate the position of DSBs in the sequences of interest. The program automatically scored the gRNAs by an inverse likelihood of off-target binding. The PKP2-exon1-sgRNA had the highest score 625 with seven off-targets in genes. The DSG2-exon1-sgRNA was scored as 94 with twelve off-targets in genes. The DNAJC19-intron3_exon4-sgRNA was scored as 56 with 21 off-targets in genes and showed a predicted cleavage site 8 bp downstream of the splice acceptor site of intron 3. Due to its closest proximity to the splice acceptor site of intron 3 the higher number of predicted off-targets in genes was tolerated. All four gRNAs were termed as high-quality guides according to their computationally postulated efficiency. The gRNAs with the highest on-target cleavage efficiency and lowest off-target specificity in genes were cloned into the pSpCas9(BB)-2A-Puro (PX459) backbone (PKP2e1-PX459, DSG2e1-PX459, DNAJC19i3_e4-PX459). The sequence-validated all-in-one plasmids contained the individual gRNAs directly linked to the gRNA scaffold, the sequence encoding the Cas9 protein and a puromycin selection cassette. All cloned plasmids were amplified together with control plasmids pSpCas9(BB)-2A-GFP (PX458) which had the Cas9 protein linked to eGFP instead of puromycin and did not contain any cloned gRNA.

3.2.3 Establishment of CRISPR/Cas9-edited iPSC lines

Nucleofection of healthy control NC6M iPSCs (JMUi001-A, (Kwok et al., 2018, Günther, 2016)) was performed with the adjusted parameters of nucleofection strategy #7 [voltage: 1200 V, pulse length: 35 ms, number of pulses: 2, plasmid: 35 µg] (Section 3.2.1, Fig. 3.3) together with the individually purified PKP2e1-PX459, DSG2e1-PX459 or DNAJC19i3_e4-PX459 plasmids. Nucleofected iPSCs were selected by medium supplementation with 1 µg/µl puromycin for 24-48 h, thus eliminating iPSCs with inefficiently expressed CRISPR/Cas9 plasmid. After two to three weeks, the surviving clonal colonies reached a size of 0.5-1 mm in diameter and were manually picked. To identify a potential PKP2 knock-out, 96 colonies were picked of which 78 colonies survived, representing a survival of 81.2 % (Tab. 3.3). In the context of DSG2, 47 potential colonies were picked of which 22 colonies survived (46.8 %) (Tab. 3.3). NC6M iPSCs that were nucleofected with DNAJC19i3_e4-PX459 yielded 60 potential colonies of which 45 colonies survived, demonstrating a survival of 75.0 % (Tab. 3.3). All manually picked colonies were cultivated and expanded individually. We observed extreme variations in growth rate between and within all conditions that ranged from 7 (PKP2) to 23 (DSG2) days of cultivation prior to the first passaging. Cell pellets for DNA extraction or protein analysis were collected over a timeframe of four to six weeks in all conditions. The central aim was to identify potential gene-edited iPSC lines that carried mutations in PKP2, DSG2 or DNAJC19 respectively. Of secondary importance was the comparison of the CRISPR/Cas9 efficiency on targeting different genetic loci in one healthy control iPSCs line. The following CRISPR/Cas9 efficiency represents an estimation that was calculated by using a fraction of

analyzed colonies only, as not every surviving colony has been checked for genetic changes. In the context of PKP2 and DNAJC19 prescreening of expression changes on protein level was performed by dot blot analysis based on positive translation of the housekeeping gene glyceraldehyde 3-phosphate dehydrogenase (*GAPDH*), which was used to calculate the respective gene editing efficiencies (Tab. 3.3). First, prescreening of the PKP2-KO iPSC line showed 12 of 78 colonies with $PKP2^{-}$ /$GAPDH^{+}$ expression that refer to an efficiency of 15.3 % DSBs (image not shown, Tab. 3.3). Second, dot blot analysis for prescreening of candidate colonies of a possible DSG2-KO was not feasible due to insufficient detection or too low expression levels of DSG2 protein in healthy control NC6M iPSCs. Therefore, Sanger sequencing was performed and enabled the identification of genomic modifications within the *DSG2* gene in one out of ten randomized colonies which can be extrapolated to a minimum DSB efficiency of 4.5 % when taking into account all 22 surviving iPSC colonies (Tab. 3.3). Third, dot blot analysis revealed 6 out of 45 colonies with reduced DNAJC19 expression but high GAPDH content indicating a minimum of 13.3 % DSBs (images not shown, Tab. 3.3). On average 11.1 % DSBs were observed using the optimized nucleofection strategy (#7) in NC6M iPSCs.

Table 3.3: Summary of CRISPR/Cas9-edited iPSC lines generated in the healthy control NC6M iPSCs.
The robustness of CRISPR/Cas9 in creating DSBs to high efficiencies allowed the generation of mutant isogenic controls by editing the disease-associated genes *PKP2*, *DSG2* or *DNAJC19*. *§* only performed if stem cell expression of the protein of interest was previously tested as positive via western blot; *C* colony; *sc* subcolony

Original cell line	Disease to mimic	Modified gene	Picked colonies n	Surviving colonies n	Preselected colonies via dot blot[§] n	Sequenced colonies n	Gene-edited colonies n	Further cultivated colonies #	Efficiency of DSBs [%]
NC6M iPSCs	ACM	*PKP2*	96	78 (81.2 %)	12	4	2	C27sc1 C78sc1	15.4 (12/78)
NC6M iPSCs	ACM	*DSG2*	47	22 (46.8 %)	x	10	1	CD20sc1	4.5 (1/22)
NC6M iPSCs	DCMA	*DNAJC19*	60	45 (75.0 %)	6	6	1	C7sc3	13.3 (6/45)

3.2.4 Validation of engineered iPSC colonies by Sanger sequencing

Following DNA extraction and PCR amplification of the genes of interest, Sanger sequencing was performed to identify nucleotide changes that were able to result in genetic knock-out in the context of PKP2 and DSG2 or a protein truncation with regard to DNAJC19. *PKP2* sequence alignment of clone C27 unraveled a homozygous 4 bp deletion in exon 1 together with a nucleotide substitution in close proximity to the depleted region c.148C>A (Fig. 3.5 A). The cleavage site was identified to be 4-7 bp upstream of the 5`-NGG PAM (Fig. 3.5 A). The genetic alterations in the generated PKP2-KO cell line C27 are systematically termed as NM_001005242 (*PKP2*):c.[142_145delGGCC;148C>A]; [142_145delGGCC;148C>A] (Fig. 3.5 A). In the second set up, Sanger sequencing of ten randomized colonies revealed the presence of a potential DSG2 knock-out colony CD20 with a 16 bp deletion in exon 1. The CRISPR/Cas9-mediated mutation of the DSG2-KO colony is denominated NM_001943.5 (*DSG2*):c.[9_24del16];[9_24del16]. The cleavage site could not be identified clearly due to the large size of the deletion (Fig. 3.5 B). In both CRISPR/Cas9-edited iPSC lines a frameshift resulting in a premature stop codon was predicted which was proved by a loss of PKP2 and DSG2 expression in PKP2-KO and DSG2-KO respectively (supplementary Fig. 5.2).

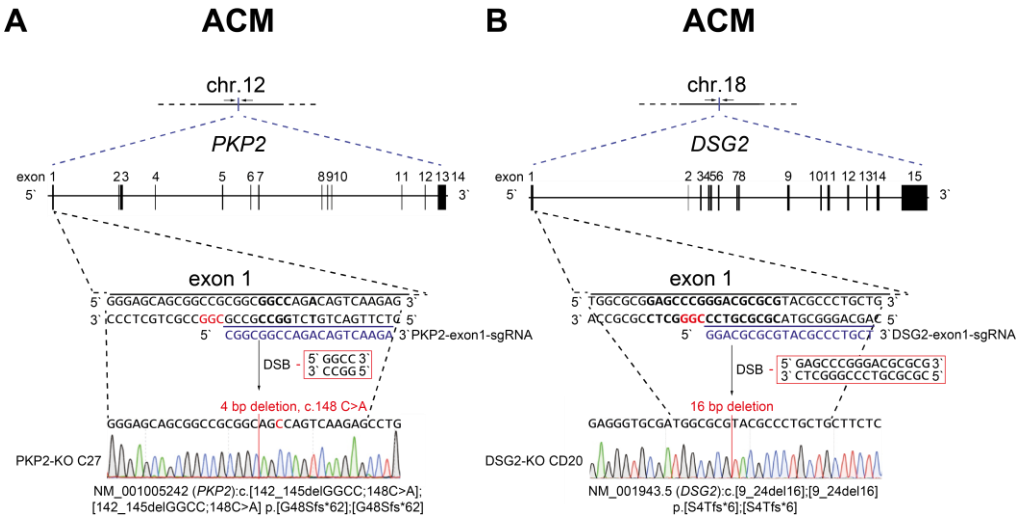

Figure 3.5 Sanger sequencing revealed genomic changes in PKP2-KO C27 and DSG2-KO colony CD20 after CRISPR/Cas9 nucleofection.
Sanger sequencing of the CRISPR/Cas9-edited iPSC lines revealed the presence of the mutation **(A)** NM_001005242 (*PKP2*):c.[142_145delGGCC;148C>A];[142_145delGGCC;148C>A] in the PKP2-KO colony C27 and a **(B)** NM_001943.5 (*DSG2*):c.[9_24del16];[9_24del16] mutation in the DSG2-KO colony CD20 in close proximity to the predicted cleavage sites.

Sequencing of the intron3-exon4 spacing region in *DNAJC19* revealed genomic modifications in all six preselected colonies. Interestingly, all six colonies presented biallelic modifications that were not clearly identifiable. The detailed allele identification was performed by PCR product cloning of the DNAJC19tv colony C7sc3 and demonstrated one allele that carried a 12 bp insertion 8 bp downstream the intron 3 splice acceptor site and the other allele showed a 10 bp deletion 1 bp downstream the intron 3 splice acceptor site (Fig. 3.6). Therefore, the mutation of the new generated gene-edited cell line DNAJC19tv is systematically termed *DNAJC19* (NM_145261.4):c.[131_140del];[137_138insAGTATAATTGCC] (Fig. 3.6). Subcloning was performed with all gene-edited colonies to eliminate the possibility of mixed iPSC populations which was counterchecked by sequencing. Finally, one representative colony per gene-edited iPSC line was used for further experiments.

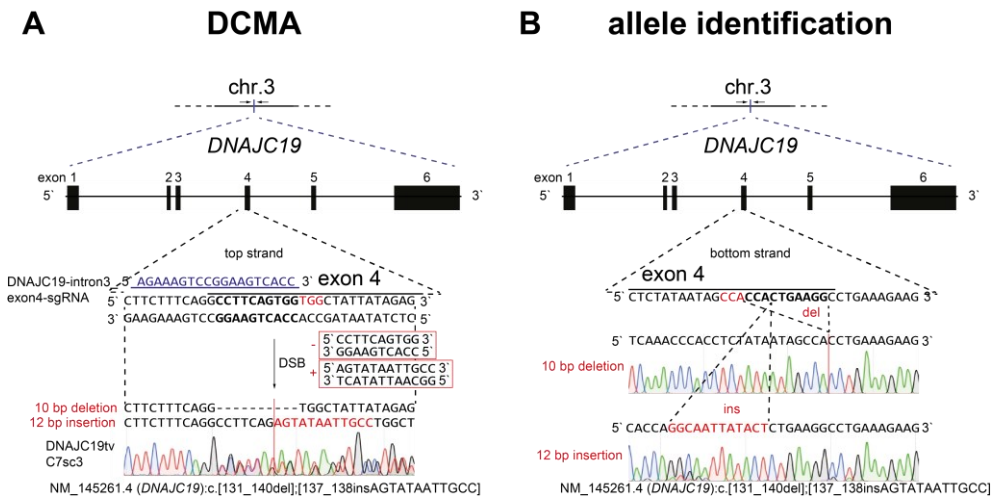

Figure 3.6: *DNAJC19* sequencing electropherograms showed the presence of biallelic changes in the DNAJC19tv colony C7sc3.
(A) Sanger sequencing of DNAJC19tv pC7sc3 revealed double sequences close to the predicted cleavage site of DNAJC19intron3_exon4-sgRNA. **(B)** Allele identification unraveled a biallelic modification including one allele with a 10 bp deletion and the other one with a 12 bp insertion that is systematically termed *DNAJC19* (NM_145261.4):c.[131_140del];[137_138insAGTATAATTGCC].

3.2.5 Off-target analysis confirmed CRISPR/Cas9 specificity

After the generation of targeted DSBs in the three genes of interest *PKP2*, *DSG2* and *DNAJC19* the probability of undesired DSBs was analyzed through computational identification of predicted off-target sites in genes (Fig. 3.7). The three most likely off-target sites in genes were used for assessment of off-target modifications. First, iPSC lines referring to ACM were checked for cleavage of potential off-target sites (Fig. 3.7 A, B). PKP2-exon1-sgRNA potential off-targets in genes were centrin 1 (*CETN1*, NM_004066), netrin 3 (*NTN3*, NM_006181) and 1-acylglycerol-3-phosphate O-acyltransferase 2 (*AGPAT2*, NM_001012727) with four mismatches (Fig. 3.7 A). DSG2-exon1-sgRNA had three mismatches in the gene janus kinase and microtubule interacting protein 1 (*JAKMIP1*, NM_144720) and four mismatches in the genes solute carrier family 35 member B4 (*SLC35B4*, NM_032826) and capping actin protein of muscle Z-line subunit beta (*CAPZB*, NM_004930) and therefore a slightly lower probability of an unwanted DSB (Fig. 3.7 B). Sanger sequencing of *CETN1*, *NTN3* and *AGPAT2* within PKP2-KO iPSCs (C27) and *JAKMIP1*, *SLC35B* and *CAPZB* within DSG2-KO iPSCs (CD20) revealed no genetic changes in each of the three off-target genes when compared to the original sequence of NC6M iPSCs respectively (Fig. 3.7 A, B). Second, the off-target DNA sites GLI pathogenesis related 2 (*GLIPR2*, NM_022343), ankyrin 1 (*ANK1*, NM_020476), coiled-coil domain containing 178 (*CCDC178*, NM_198995) with three mismatching bases each compared to the sequence of the DNAJC19-intron3_exon4-sgRNA were investigated in DNAJC19tv iPSCs (C7sc3) (Fig. 3.7 C). In comparison to the original NC6M iPSC line no genetic alterations were detected within all predicted off-target sites *GLIPR2*, *ANK1* and *CCDC178* (Fig. 3.7 C). Taken together, three different genes *PKP2*, *DSG2* and *DNAJC19* were successfully modified in the genetic background of NC6M iPSCs. PKP2-KO iPSCs (C27), DSG2-KO iPSCs (CD20) and DNAJC19tv iPSCs (C7sc3) were generated to potentially mimic their associated diseases ACM and DCMA underlining the preciseness and the robustness of the CRISPR/Cas9 system within NC6M iPSCs.

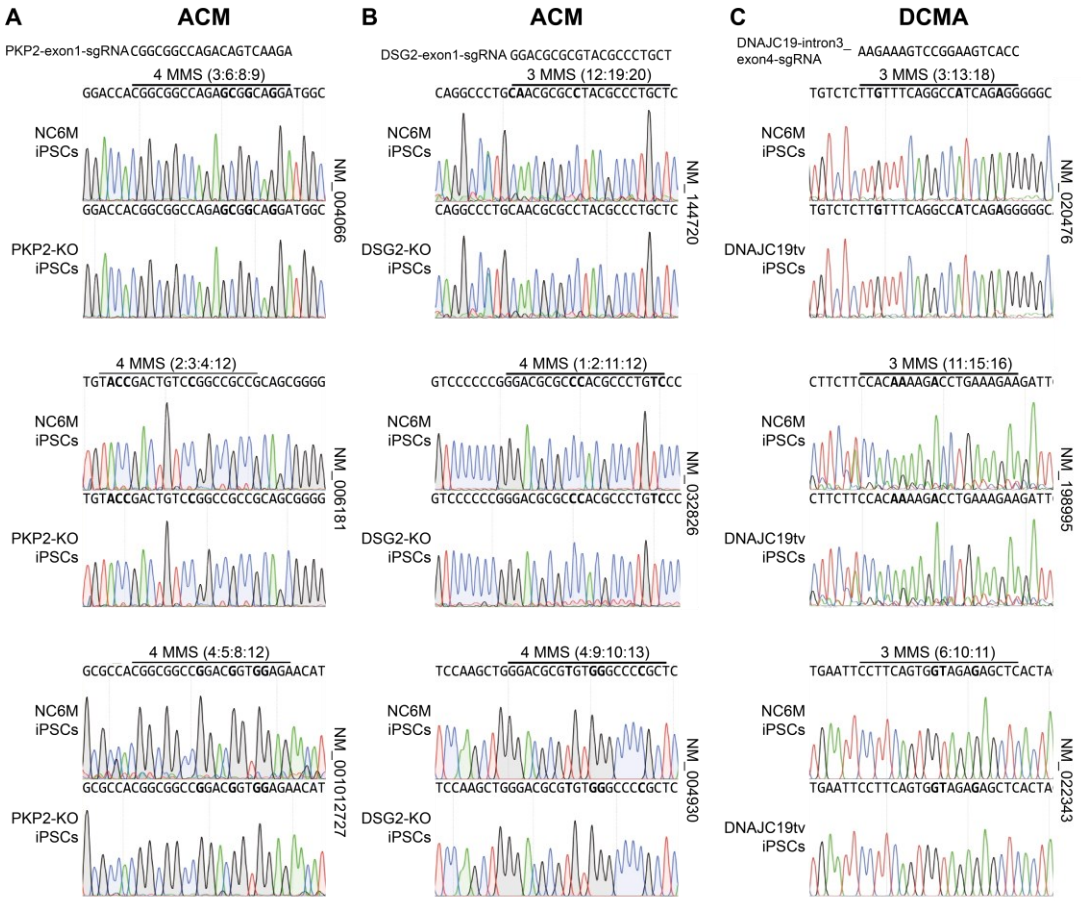

Figure 3.7 The assessment of potential off-target sites in genes of PKP2-KO, DSG2-KO and DNAJC19tv did not reveal any unwanted genetic alterations.
DNA of **(A+B)** ACM-associated and **(C)** DCMA-associated cell lines: **(A)** PKP2-KO C27, **(B)** DSG2-KO CD20 and **(C)** DNAJC19tv C7sc3 were isolated and corresponding potential off-target regions in genes were amplified and sequenced. The three most likely off-target sites in genes were compared to the original sequence of NC6M iPSCs. Examination of **(A)** *CETN1* (NM_004066), *NTN3* (NM_006181), *AGPAT2* (NM_001012727) in PKP2-KO; **(B)** *JAKMIP1*, *SLC35B*, *CAPZB* in DSG2-KO and **(C)** *GLIPR2* (NM_022343), *ANK1* (NM_020476), *CCDC178* (NM_198995) in DNAJC19tv showed no genetic changes. *MMS* mismatches

3.3 Characterization of the generated iPSC lines

To fulfill all requirements of the *in vitro* model systems of ACM, DCMJC and DCMA the reprogrammed and genome-edited iPSC lines were characterized regarding their pluripotent state according to the guidelines of stem cell research (Elsevier B.V. Copyright © 2021, 2017). The usability of iPSCs in disease modeling is highly dependent on the iPSC quality. Therefore, the eight listed self-generated iPSC lines were analyzed with respect to iPSC morphology, expression of pluripotency-associated markers, capacity of three lineage differentiation, karyotype, short tandem repeat (STR) profile, mycoplasma contamination and SeV inactivation.

Table 3.4: Summary of patient-derived and gene-edited iPSC lines generated in the present thesis.
§ homozygous mutation; * disease associated with; *$* stem cell ID Janz et al., 2020 & Janz et al., 2021

iPS cell line name	Original cell line	Healthy/ disease	Disease-associated gene	Genotype of locus	Method of generation	Gender	Donor age
NC6M	NC6M fibroblasts	healthy	-	-	LeV (Kwok et al., 2018, Günther, 2016)	male	6
NC6M-SeV	NC6M fibroblasts	healthy	-	-	SeV reprogramming	male	6
NC47F	NC47F fibroblasts	healthy	-	-	SeV reprogramming	female	47
LEMD2 p.L13R	LEMD2 p.L13R fibroblasts	DCMJC	*LEMD2*	NM_181336.4 (*LEMD2*):c.38T>G, p.L13R (§)	SeV reprogramming	male	38
DCMAP1 (LIBUCi001-A)$	DCMAP1 fibroblasts	DCMA	*DNAJC19*	NM_145261.4 (*DNAJC19*):c.130-1G>C (§)	SeV reprogramming	male	8
DCMAP2 (LIBUCi002-A)$	DCMAP2 fibroblasts	DCMA	*DNAJC19*	NM_145261.4 (*DNAJC19*):c.130-1G>C (§)	SeV reprogramming	female	12
DNAJC19tv (JMUi001-A-1)$	NC6M	DCMA*	*DNAJC19*	NM_145261.4 *(DNAJC19)*:c.[131_140del]; [137_138insAGTATAATTGCC]	CRISPR/Cas9 gene-edited	male	6
PKP2-KO (JMUi001-A-2)$	NC6M	ACM*	*PKP2*	NM_001005242 (*PKP2*):c.[142_145delGGCC;148C>A]; [142_145delGGCC;148C>A] (§)	CRISPR/Cas9 gene-edited	male	6
DSG2-KO (JMUi001-A-3)$	NC6M	ACM*	*DSG2*	NM_001943.5 *(DSG2)*: c.[9_24del16];[9_24del16] (§)	CRISPR/Cas9 gene-edited	male	6

3.3.1 All generated iPSC lines presented stem-cell like morphological features

Brightfield images of the five human donor dermal fibroblasts demonstrated typical spindle-shaped elongated cellular morphology in healthy as well as patient-derived dermal fibroblasts (Fig. 3.8 A, a-e). After SeV-reprogramming and clonal expansion all representative individual colonies experienced a change in cellular morphology hallmarked by prominent nuclei, less intercellular space and sharp-edged stem-cell like clusters (Fig. 3.8 A, f-j). Reprogramming of NC6M fibroblast (a) into NC6M-SeV (f) presented the same stem cell-like appearance as the LeV-reprogrammed positive control NC6M (k) (Fig. 3.8 A, B). Genome editing of NC6M iPSCs did not change its typical stem cell-like morphology. PKP2-KO (l), DSG2-KO (m) and DNAJC19tv (n) presented all with the same small, round cells showing a high nucleus to cytoplasm ratio as well as compact colonies with well-defined edges (Fig. 3.8 B). Taken together, all eight generated iPSC lines displayed morphological features of undifferentiated cells.

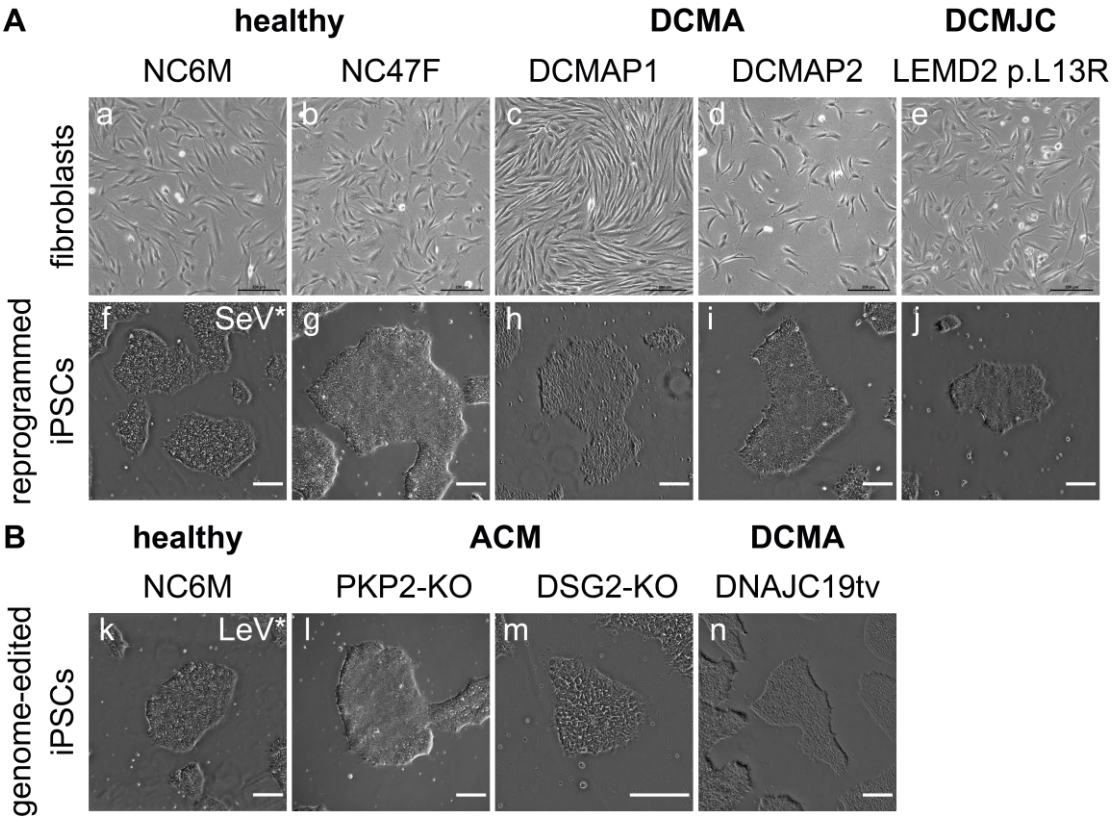

Figure 3.8: Bright field images of patient-derived and genome-edited iPSC lines demonstrated typical stem-cell like morphologies.
(A+B) Bright field images of all eight self-generated iPSC lines were acquired and compared to typical stem cell morphology of the positive control NC6M iPSCs (k). All eight iPSC lines demonstrated small, round cells in compact colonies with well-defined edges.

3.3.2 Immunofluorescence staining confirmed expression of typical pluripotency markers

Next, pluripotent properties were analyzed by immunofluorescent staining of OCT3/4 (left column), SOX2 (middle column) and TRA-1-81 (right column) (Fig. 3.9). The positive control NC6M iPSCs displayed nuclear OCT3/4 (a) and SOX2 (b) staining as well as dispersed expression of TRA-1-81 (c) (Fig. 3.9, 1st row). All eight reprogrammed (2nd to 5th row) and genome-edited (6th to 9th row) iPSC lines presented the same positive signal of OCT3/4 and SOX2 in the nucleus as well as the same cell surface expression of TRA-1-81 when compared to NC6M iPSCs (1st row) (Fig. 3.9).

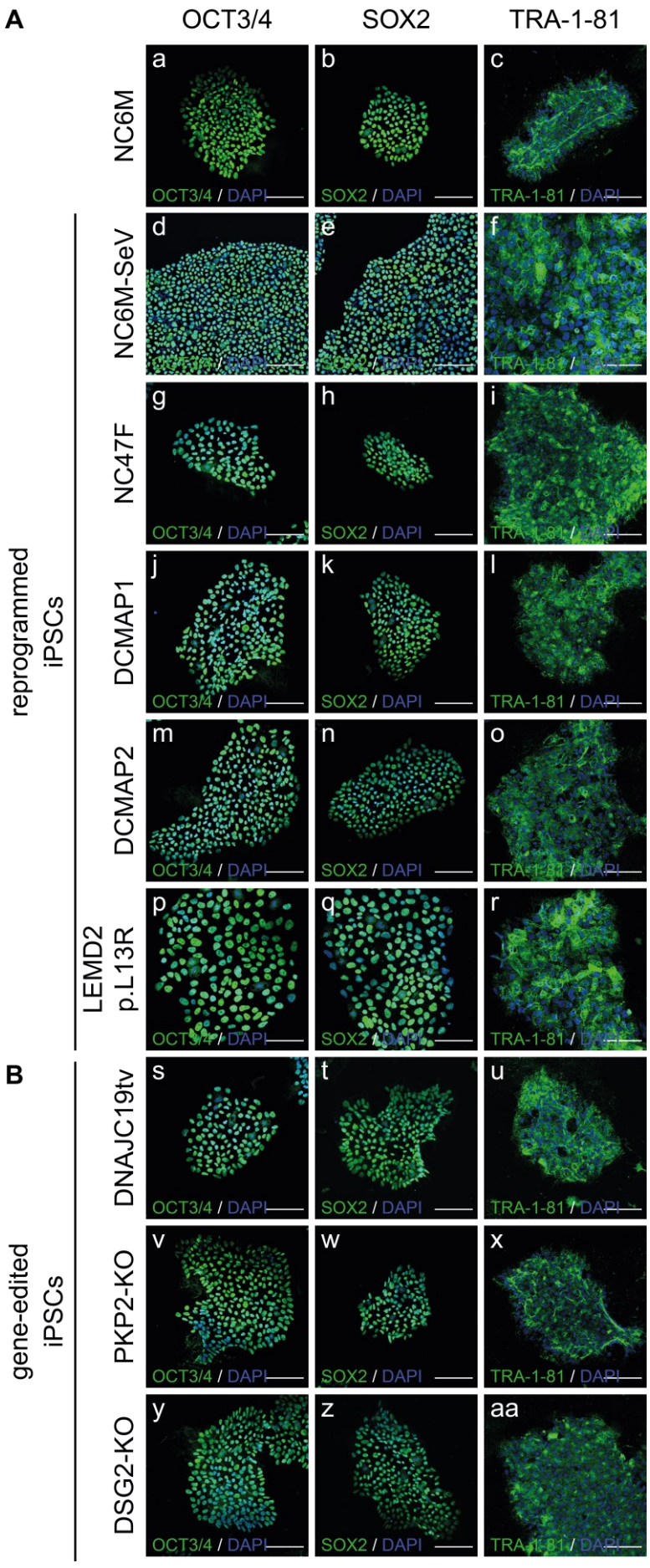
A
OCT3/4
SOX2
TRA-1-81
NC6M
NC6M-SeV
NC47F
DCMAP1
DCMAP2
LEMD2 p.L13R
reprogrammed iPSCs
B
DNAJC19tv
PKP2-KO
DSG2-KO
gene-edited iPSCs
OCT3/4 / DAPI
SOX2 / DAPI
TRA-1-81 / DAPI

Figure 3.9: Immunofluorescence staining of OCT3/4, SOX2 and TRA-1-81 revealed pluripotency-associated expression patterns in all eight generated iPSC lines.
(A+B) Eight self-made iPSC lines (second to ninth column) were stained for typical pluripotency-associated proteins and compared to the positive control NC6M iPSCs (first column). The first row displays nuclear localization of OCT3/4 in all nine iPSC lines. The second row illustrates positive expression of SOX2 in the nucleus in all iPSC lines. All colonies demonstrated the presence of TRA-1-81 proteins on the cell surface. DAPI was used to counterstain nuclei in all images. Scale bar = 100 µm

3.3.3 Flow cytometric analysis proved stem cell-rich populations

The maintenance of the expression of pluripotency markers throughout a given stem cell population is critical to ensure high iPSC purities prior to usage for further applications. The analysis of the stage-specific embryonic antigen 4 (SSEA-4) and the cell-surface antigen TRA-1-60 enabled the flow cytometric detection of pluripotent cells within a given cell population. The positive control NC6M iPSCs presented 99.5 % SSEA-4$^+$ and 99.2 % TRA-1-60$^+$ cells (Fig. 3.10 A). The two other controls displayed extremely high fractions of pluripotent cells as well with 99.3 % SSEA-4$^+$, 99.0 % TRA-1-60$^+$ in NC6M-SeV and 97.4 % SSEA-4$^+$, 97.9 % TRA-1-60$^+$ in NC47F iPSCs (Fig. 3.10 A). All three patient-derived iPSC lines demonstrated high expression of both pluripotency surface markers with 98.7 % SSEA-4$^+$, 98.5 % TRA-1-60$^+$ in DCMAP1, 95.1 % SSEA-4$^+$,99.4 % TRA-1-60$^+$ in DCMAP2 and 97.4 % SSEA-4$^+$,97.3 % TRA-1-60$^+$ in LEMD2 p.L13R iPSCs (Fig. 3.10 A). The genome-edited DNAJC19tv iPSCs were 94.1 % SSEA-4$^+$ and 92.3 % TRA-1-60$^+$ (Fig. 3.10 B). The CRISPR/Cas9-edited cell line PKP2-KO was 92.1 % positive for SSEA-4 and 98.2 % positive for TRA-1-60 (Fig. 3.10 B). With 97.6 % SSEA-4$^+$ and 92.3 % TRA-1-60$^+$ DSG2-KO iPSCs showed a high percentage of pluripotent cells. All measurements included unstained negative controls that showed no shifts in all measurements (Fig. 3.10 B). Experiments and analyses were conducted together with Dr. Ruping Chen. The correlation to the results of the immunofluorescence staining confirmed the high proportions of pluripotent cells within all iPSC lines.

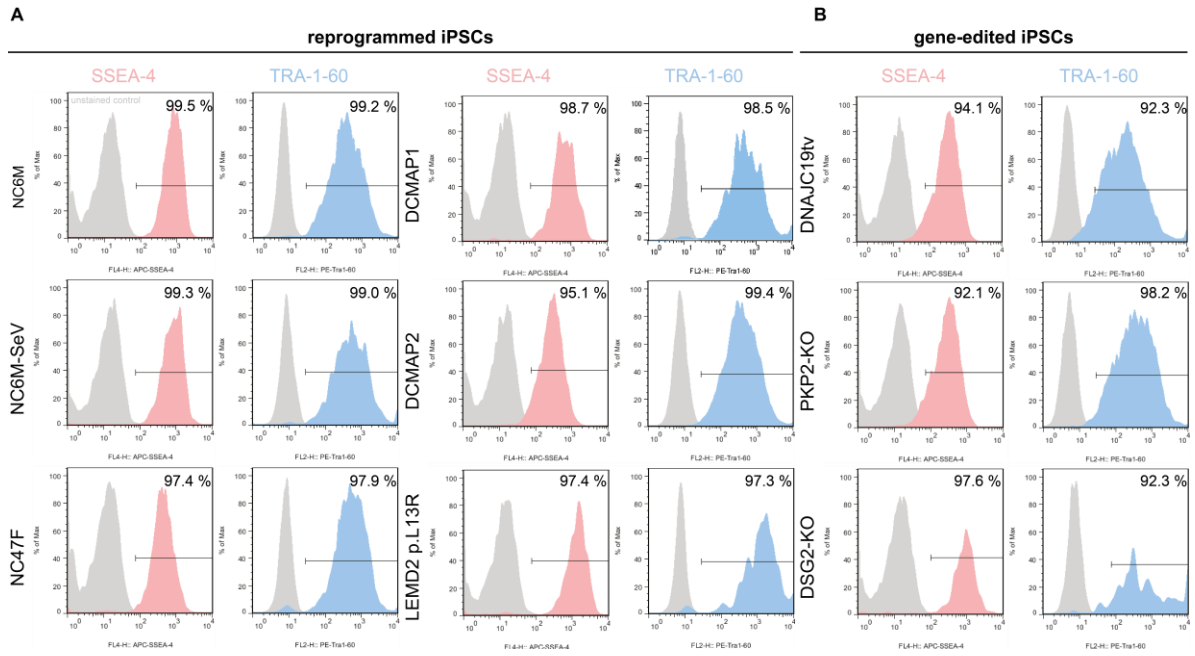

Figure 3.10: Flow cytometric analysis of pluripotent surface markers TRA-1-60 and SSEA-4 confirmed high purities for all generated iPSC lines.
(A+B) iPSCs were stained for pluripotency surface markers SSEA-4 (red) and TRA-1-60 (blue). Unstained samples were included as negative controls (grey). All eight generated iPSC lines showed at least purities of ~92.1 % SSEA-4$^+$ and ~92.3 % TRA-1-60$^+$ cells similar to purities of ~99.5 % SSEA-4$^+$ and ~99.2 % TRA-1-60$^+$ cells in the NC6M positive iPSC control. Experiments and quantifications of population purities were conducted together with Dr. R. Chen.

3.3.4 Approved differentiation potential into all three germ layers

Another characteristic hallmark of iPSCs resides in their capability to differentiate into endodermal, ectodermal and mesodermal cell types. The examination of the cellular ability to subsequently

differentiate into cell types of the three germ layers was simulated in a long-term *in vitro* experiment, termed germ layer differentiation. The presence of associated proteins was identified by immunofluorescence. First, α-smooth muscle actin (α-SMA)-positive cells were detected in all healthy (NC6M (a), NC6M-SeV (d), NC47F(g)), in all patient-derived (DCMAP1 (j), DCMAP2 (m), LEMD2 p.L13R (p)) and all gene-edited (DNAJC19tv (s), PKP2-KO (v), DSG2-KO (y)) iPSCs (Fig. 3.11, 1st column). The cells showed typical α-SMA expression in the region of the cytoplasmic actin cytoskeleton and represented mesodermal fate (Fig. 3.11, 1st column). The endodermal fate was analyzed by α-1-fetoprotein (AFP) expression. Similar to the positive control NC6M (b) iPSCs, all additional eight cell lines (middle column, except b) were able to differentiate into the endodermal lineage, shown by the presence of a cell-wide dispersed AFP expression (Fig. 3.11, 2nd column). Cells of the ectodermal lineage were identified by tubulin-β-III (TUBB3)-positive expression. As a structural protein of neuronal cell bodies TUBB3 is typically recognizable through its radial alignment and bipolar morphology. All generated iPSC lines were able to produce cells of the ectoderm by displaying TUBB3 expression in axon-like cell shapes (Fig. 3.11, 3rd column).

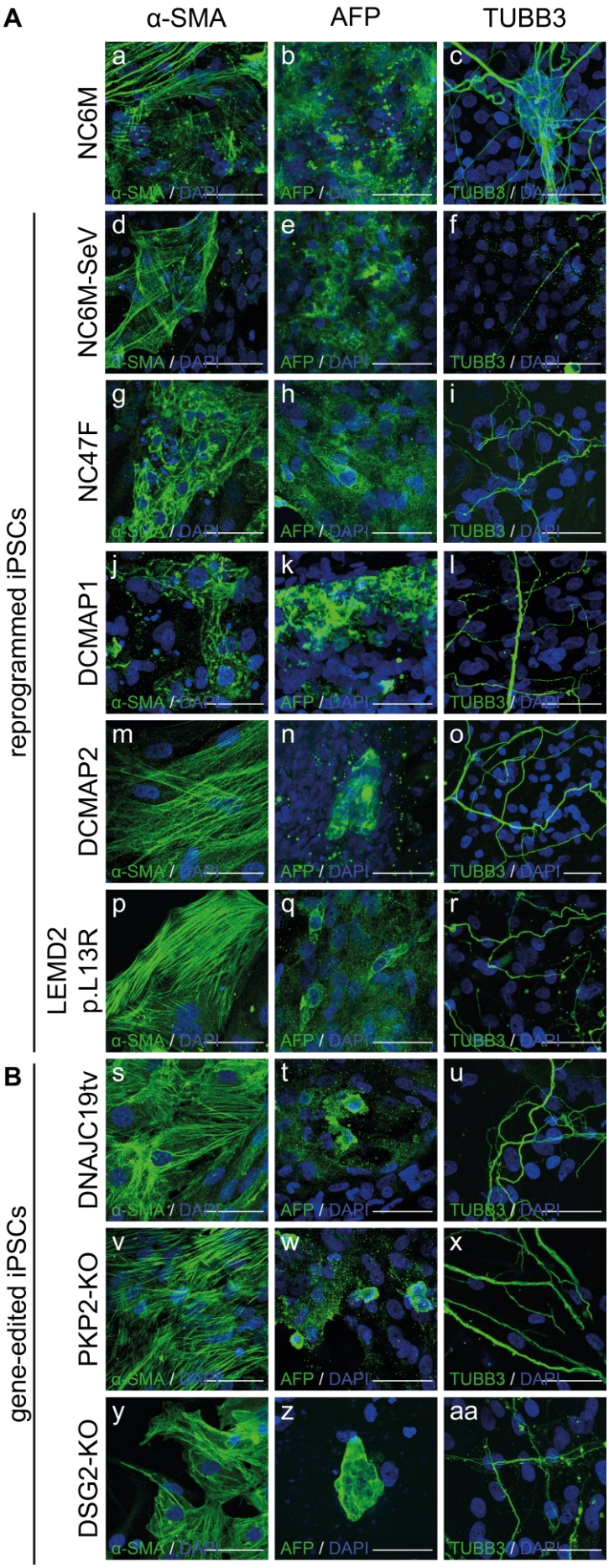
A
α-SMA
AFP
TUBB3
NC6M
NC6M-SeV
NC47F
DCMAP1
DCMAP2
LEMD2 p.L13R
reprogrammed iPSCs
B
DNAJC19tv
PKP2-KO
DSG2-KO
gene-edited iPSCs
α-SMA / DAPI
AFP / DAPI
TUBB3 / DAPI

Figure 3.11: Germ layer fate determination resulted in expression of mesodermal (α-SMA), endodermal (AFP) and ectodermal markers (TUBB3) in all iPSC lines.
(A+B) After default differentiation, iPSCs were stained for various cell types representing the three germ layers via immunofluorescence. The first column displays α-SMA-positive expression indicating mesodermal fate. The second column demonstrates AFP-positive cells in all iPSC lines which illustrates the presence of endodermal germ layer cells. The third column represents TUBB3 expression which resemble cell types of neural origin (ectoderm). Taken together, all eight generated iPSC lines demonstrated various cell types of distinct germ layer origin similar to the NC6M positive control (first row). Scale bar = 50 µm

3.3.5 Karyotyping revealed no chromosomal changes

Given the persistent activation of pluripotency key genes iPSCs possess an endless proliferative capacity. Prolonged cultivation time as well as the reprogramming process itself can have a negative impact on the genetic content of iPSCs and can cause chromosomal aberrations as a discriminatory consequence (Schlaeger et al., 2015). Therefore, karyotype assessment is another criterion to ensure iPSCs cultures of high quality. The positive control NC6M as well as the eight other iPSC lines underwent karyotyping by G-banding (Fig. 3.12). For each cell line ten metaphases were analyzed for numerical or structural changes of the chromosomal structures. NC6M, NC6M-SeV, DCMAP1, LEMD2 p.L13R, DNAJC19tv, PKP2-KO and DSG2-KO iPSCs consisted of 22 chromosome pairs together with one X and one Y chromosome (Fig. 3.12). NC47F and DCMAP2 were the two only iPSC lines of female origin and displayed 22 chromosomes with XX gonosomes (Fig. 3.12). No numeric or chromosomal aberrations were detected among all iPSC lines underlining the presence of genomically stable iPSC lines for further studies (Fig. 3.12).

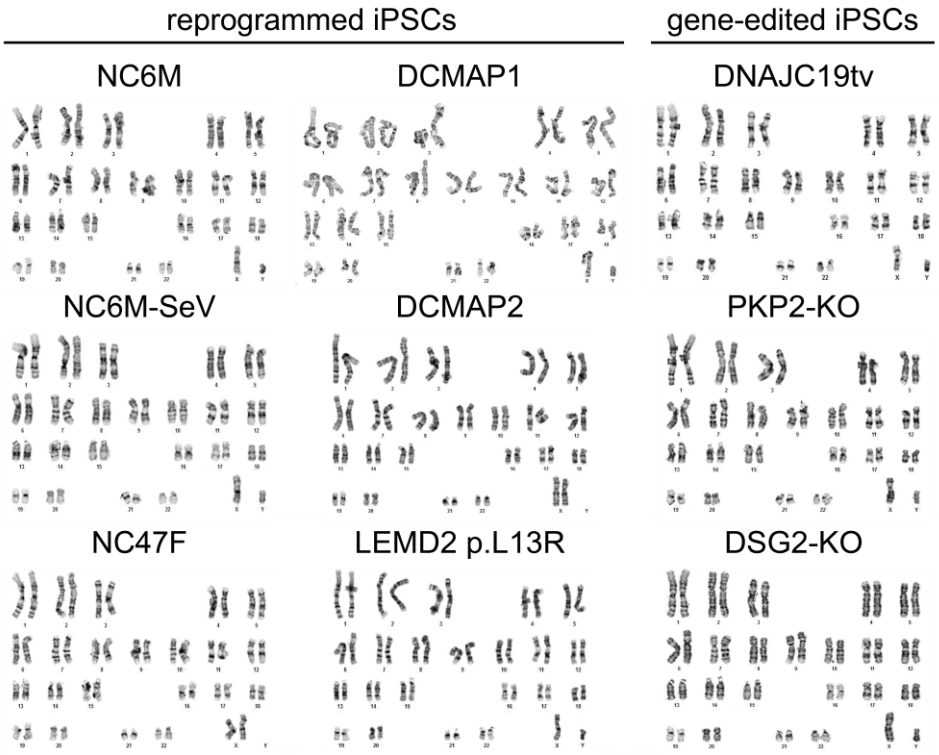

Figure 3.12: G-band karyotyping revealed normal karyotypes in all reprogrammed and gene-edited iPSC lines.
Analysis of ten metaphases for each self-generated iPSC line revealed normal human male and female karyotypes without numeric or chromosomal aberrations.

3.3.6 STR analysis confirmed cell-to-cell identities

The comparison of allele repeats at specific genomic loci enabled the detection of genetic identities between individuals as every individual has its own STR-profile. The power of STR is the simultaneous analysis of multiple STR loci. The discrimination between the DNA profile of the original fibroblast and the iPSC line allowed the verification of their genetic identities. Within the present thesis the following nine loci were investigated: AMEL, D3S1358, SE33, THO1, D18S51, FGA, vWA, D21S11 and D8S1179. First, the positive control NC6M iPSCs as well as their reprogrammed equivalent NC6M-SeV displayed the same STR profile as the original NC6M fibroblast line (supplementary Tab. 5.1). The DNA fingerprint of the female NC47F iPSC line proved to have the same STR profile as the NC47F fibroblast line (supplementary Tab. 5.1). STR profiling of nine genetic loci revealed the male origin in DCMAP1 and LEMD2 p.L13R as well as the female origin in DCMAP2 as in their previous dermal fibroblast cell lines without other changes regarding the other genetic loci (supplementary Tab. 5.2). DNA fingerprint analysis after gene editing of NC6M iPSCs confirmed the male origin of all genetic modified iPSC lines by the same heterozygous STR profile in eight genetic regions and homozygous localization for D21S11 in PKP2-KO, DSG2-KO and DNAJC19tv (supplementary Tab. 5.3).

3.3.7 Confirmation of mycoplasma-negative cell culture

Somatic cell isolation of dermal fibroblasts as well as long cultivation times during iPSC generation are increasing the risk of bacterial infection. The testing of an adventitious mycoplasma contamination was critical to ensure high quality iPSC lines. Every three months a possible contamination of mycoplasmas was investigated in all iPSC lines that were in culture at that time. During the time span of four years no mycoplasma contamination was detected as depicted in the report (supplementary Fig. 5.1).

3.3.8 The absence of residual SeV RNA sequences

The confirmation of the absence of SeV-derived viral vectors is an important aspect regarding safety concerns. Remaining viral RNA-sequences were detected by using SeV-vector specific primers according to the manufacturers', experimental details can be found in supplementary Tab. 5.4. Successful RNA isolation and reverse transcription were verified by *GAPDH*-specific primers, demonstrating the presence of detectable RNA as basis for the identification of viral RNA-sequences in all conditions (Fig. 3.13, 5th row). NC6M fibroblasts without SeV priming served as negative control (Fig. 3.13, 2nd lane). NC6M fibroblasts transduced with all `KMOS`-expressing vectors were collected one day (Fig. 3.13, 1st lane) and two days (Fig. 3.13, 3rd lane) after viral transduction and functioned as positive controls of different activities. The freshly infected NC6M positive controls demonstrated the robust expression of *SEV*, weak expression of *KOS* and already no detectable expression of *KLF4* and *c-MYC* (Fig. 3.13, 1st lane). The positive control collected two days after SeV priming displayed residual expression of SEV only (Fig. 3.13, 3rd lane). NC6M iPSCs served as an additional negative control due to the LeV-based reprogramming method (Fig. 3.13, 4th lane). All eight self-generated iPSC lines demonstrated the absence of all SeV RNA-sequences due to negative bands after using *SEV*, *KOS*, *KLF4*, *c-MYC*-specific primers already at early time points with the lowest analyzed passage twelve (LEMD2 p.L13R) (Fig. 3.13, 5th to 13th lane), corresponding passages can be found in supplementary Tab. 5.4). To exclude the possibility of a detection insensitivity of *KLF4* and *c-MYC*-specific primers a proper positive control would be required that was not accessible from other working groups or the manufacturer.

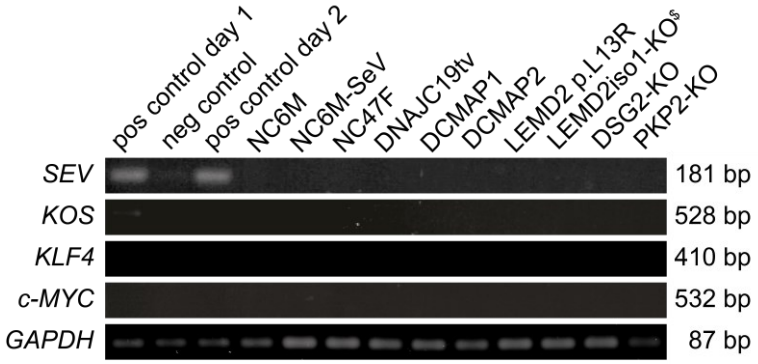

Figure 3.13: RT-PCR did not unravel any residual `*KMOS*` expression.
RT-PCR on iPSC-derived isolated RNA with SeV RNA-specific primers of *SEV* (first column), *KOS* (second column), *KLF4* (third column), *c-MYC* (fourth column) and an internal control *GAPDH* (fifth column) demonstrated the absence of SeV-specific RNA in all iPSC lines (lane 5 to lane 12) when compared to both positive controls (lane 1 and 3) and both negative controls (lane 2 = NC6M fibroblasts and lane 4 = LeV reprogramming). *KOS* combined vector with KLF4, OCT3/4, SOX2; *pos* positive; *neg* negative

3.3.9 Summary of iPSC characterization

In the present thesis, iPSC characterization of eight self-generated iPSC lines displayed a characteristic embryonic stem cell-like morphology (Fig. 3.8), together with robust expression of key pluripotency markers to high purities (Fig. 3.9, 3.10). As a proof of pluripotent capacity after non-directed germ layer differentiation, progenies of all iPSC lines showed robust expression of mesodermal proteins like αSMA, ectodermal fate by TUBB3 and endoderm formation via AFP (Fig. 3.11). All iPSC lines were mycoplasma-negative and showed inactivation of the SeV vectors (supplementary Fig. 5.1, Fig. 3.13). Conventional karyotyping revealed no numerical or structural chromosome abnormalities (Fig. 3.12). Sanger Sequencing, STR and off-target analysis uncovered the same genetic identity in the generated iPSC lines compared to the original patient fibroblasts or healthy NC6M iPSC line without additional genomic changes (supplementary Tab. 5.1, 5.2, 5.3; Fig. 3.2, 3.5, 3.6, 3.7). Taken together, we have successfully generated eight iPSC lines of high quality showing robust expression of key pluripotency markers, a normal karyotype and the capacity to differentiate into cells of all three germ layers. Therefore, we provided iPSC lines of three model systems to allow the study on the inherited cardiomyopathies DCMJC, ACM and DCMA, not only in patient-derived but also in genetically modified iPSCs.

Table 3.5: Summary of patient-derived and gene-edited iPSC lines after validation of quality criteria

Classification	Experiment	Result	Data
Morphology	Photography	Typical embryonic stem cell-like morphology in all generated iPSC lines.	Fig. 3.8
Phenotype	Qualitative	All generated iPSC lines showed positive expression of pluripotency markers OCT3/4, SOX2 and TRA-1-81 via immunofluorescence.	Fig. 3.9
	Quantitative analysis (Flow cytometry)	Expression of SSEA-4 and TRA-1-60 in high purities in all generated cell lines. NC6M: 99.2 % TRA-1-60$^+$, 99.5 % SSEA-4$^+$ NC6M-SeV: 99.0 % TRA-1-60$^+$, 99.3 % SSEA-4$^+$ NC47F: 97.9 % TRA-1-60$^+$, 97.4 % SSEA-4$^+$ DCMAP1: 98.5 % TRA-1-60$^+$, 98.7 % SSEA-4$^+$ DCMAP2: 99.4 % TRA-1-60$^+$, 95.1 % SSEA-4$^+$ LEMD2 p.L13R: 97.3 % TRA-1-60$^+$, 97.4 % SSEA-4$^+$ DNAJC19tv: 92.3 % TRA-1-60$^+$, 94.1 % SSEA-4$^+$ PKP2-KO: 98.2 % TRA-1-60$^+$, 92.1 % SSEA-4$^+$ DSG2-KO: 97.6 % TRA-1-60$^+$, 92.3 % SSEA-4$^+$	Fig. 3.10
Genotype	Karyotype (GTG-banding) and resolution	NC6M:46,XY NC6M-SeV:46,XY NC47F:46,XX DCMAP1: 46,XY DCMAP2: 46,XX LEMD2 p.L13R: 46,XY DNAJC19tv: 46,XY PKP2-KO: 46,XY DSG2-KO: 46,XY Resolution: 400-450	Fig. 3.12
Identity	STR analysis	STR analysis of: AMEL, D3S1358, SE33, TH01, D18S51, FGA, vWA, D21S11, D8S1179. All eight generated iPSC lines match to the individual host profile.	supplementary Tab. 5.1, 5.2, 5.3
Mutation analysis	Sequencing	NC6M, NC6M-SeV, NC47F have no identified disease-associated mutations. DCMAP1: *DNAJC19* (NM_145261.4):c.130-1G>C DCMAP2: *DNAJC19* (NM_145261.4):c.130-1G>C LEMD2 p.L13R: *LEMD2* (NM_181336.4):c.38T>G, p.L13R DNAJC19tv: *DNAJC19* (NM_145261.4):c.[131_140del];[137_138insAGTATAATTGCC] PKP2-KO: *PKP2* (NM_001005242):c.[142_145delGGCC;148C>A];[142_145delGGCC;148C>A] DSG2-KO: *DSG2* (NM_001943.5):c.[9_24del16];[9_24del16]	Fig. 3.2, 3.5, 3.6
Off-target analysis	Sequencing	DNAJC19tv: NM_020476, NM_198995, NM_022343 PKP2-KO: NM_004066, NM_00618, NM_001012727 DSG2-KO: NM_144720, NM_032826, NM_004930 All analyzed off-targets were not changed after CRISPR/Cas9 gene editing.	Fig. 3.7
Microbiology and virology	Mycoplasma	Mycoplasma testing was performed by Eurofins Genomics. All iPSC lines were mycoplasma-negative.	supplementary Fig. 5.1
Differentiation potential	Embryoid body formation	Eight self-generated iPSC lines were able to differentiate into cells of mesodermal, endodermal and ectodermal fate by expression of α-SMA, AFP, TUBB3.	Fig. 3.11

3.4 Generation of iPSC-derived CMs to investigate DCMA in a monolayer approach

iPSCs have an enormous potential in disease modeling given the possibility of directed differentiation into any somatic cell type of interest. In the field of cardiovascular diseases, the differentiation of iPSCs towards the mesodermal lineage to generate *in vitro*-derived CMs is promising for the identification of novel pathomechanisms accompanied by the discovery of potential therapeutics. The main aim of this thesis was to recapitulate DCMA in an *in vitro* setting. Therefore, the differentiation capacities of both control iPSC lines (NC6M, NC47F), the gene-edited DNAJC19tv iPSC line and the patient-derived iPSC lines (DCMAP1, DCMAP2) were included in the present thesis only. DCMAP1, DCMAP2 and DNAJC19tv were summarized as DCMA lines to simplify the description of disease-associated phenotypic changes. We are aware of the fact that DNAJC19tv was not obtained from a DCMA patient directly and represents a gene-edited mutation carrier iPSC line only having the potential to mimic DCMA-associated phenotypes on the cellular level.

3.4.1 Adaptation of differentiation strategies to obtain CMs

The generation of CMs was adapted after the protocol of Kadari et al., 2015. The precise timing of Wnt activation and inhibition together with TGFβ modulation was optimized for each iPSC line separately by using a subset of prominent growth factors and small molecules: CHIR, BMP4 and IWR1. The original protocol is divided into four phases: cardiac induction, cardiac specification, cardiac proliferation and cardiac enrichment. The cardiomyocyte differentiation protocol already included optimized conditions that are known to promote CM efficiencies such as basal medium supplementation with ascorbic acid, removal of insulin during cardiac specification and glucose removal together with lactate increase during cardiac enrichment (Kadari et al., 2015) (Fig. 3.14 A). NC6M iPSCs were chosen as representative cell line that displayed the described heterogeneous morphological changes during cardiac differentiation (Fig. 3.14 B).

The first phase, cardiac induction differed between all five iPSC lines (Fig. 3.14 A, B, a). The seeding day was set two days before cardiac induction, shorter or longer timespans did not result in CM generation at all. The seeding densities two days prior to differentiation varied between 0.5 to 1 million cells per one well of a 12-well plate in all five iPSC lines that needed constant adjustments. After achieving 70-90 % confluency at the starting day (day 0) all five iPSC lines were induced to the mesodermal fate by BMP4 (25 ng/ml) and CHIR medium supplementation (5 µM) within the first 24 h (Fig. 3.14 A). The day after, NC6M, NC47F, DNAJC19tv and DCMAP2 iPSCs were further supplemented with CHIR (5 µM) to achieve proper Wnt activation (Fig. 3.14 A). Instead, DCMAP1 iPSCs were successfully differentiated into CMs only after skipping the second day of Wnt activation (Fig. 3.14 A). Activation of Wnt signaling was recognized by morphological changes of cell clusters that moved together closely, distanced nuclei and elongated cell shapes, thus indicating mesodermal induction within the first one to two days (Fig. 3.14 B, b). Afterwards the differentiation protocol was proceeded uniformly by one day of break in which no small molecule was added to the cardiac specification medium (Fig. 3.14 A). Next, cardiac specification phase was initiated by removal of insulin and supplementation with IWR1 (10 µM) to inhibit Wnt signaling that resulted in spindle shaped clusters of densely populated cells (Fig. 3.14 A, B, c). The onset of contraction was visually observed between seven to twelve days after cardiac induction (Fig. 3.14 A, B, d). Wherein, longer time spans correlated with decreased CMs yields. All five iPSC lines were successfully differentiated into CMs with typical spontaneously beating cells or whole clusters of CMs accompanied by non-beating regions that were visually referred to as non-CMs. Newly differentiated iPSC-derived CMs were additionally stained for the expression of cTnT together with nuclear counterstaining by DAPI to validate the generation of CMs *in vitro* (Fig. 3.14 B, e). Moreover, immunofluorescence staining revealed triangular shaped iPSC-CMs characterized by non-aligned sarcomeres and the presence of mononuclear cells, thus indicating immature CM states directly after cardiac differentiation (Fig. 3.14 B, e). After a short proliferative phase of three to five days, the cardiac enrichment phase was initiated by switch to glucose-depleted cardiac basal medium containing abundant lactate, referred to as cardiac enrichment medium (CEM) (Fig. 3.14 A). The metabolic

enrichment phase ranged from five (Kadari et al., 2015) to seven days (Tohyama et al., 2013) and was expected to result in purified CMs populations. Unfortunately, enrichment of a minimum of five days was not feasible for DCMAP1, DCMAP2 and DNAJC19tv CMs due to tremendous CMs death between day four (DCMAP1) to five (DCMAP2, DNAJC19tv). Shortening the time span of enrichment to three days (DCMAP1) and four days (DCMAP2, DNAJC19tv) resulted in higher CM yields together with increased fractions of surviving non-CMs (Fig. 3.14 A). These observations indicated first mutation-associated metabolic differences in lactate metabolism among all DCMA lines that were identifiable in young CMs already. Additional adjustments to increase CM yields were tested by decreased (24 h, 36 h) or increased (60 h) Wnt activation phases and/or concentration adjustments of CHIR (3 µM, 7.5 µM, 10 µM), BMP4 (3 µM, 7.5 µM, 10 µM) and IWR1 (12.5 µM,15 µM) that had no beneficial effects regardless of whether the conditions were taken individually or together. Furthermore, we observed tremendous differences regarding reproducibility in the generation of CMs and the resulting CM yields between and within all five iPSC lines for which the underlying cause could not be clearly be identified. Taken together, the optimal seeding densities two days prior to cardiac induction and the individual modulation of Wnt activation were the two critical factors in the generation of iPSC-derived CMs for all five cell lines.

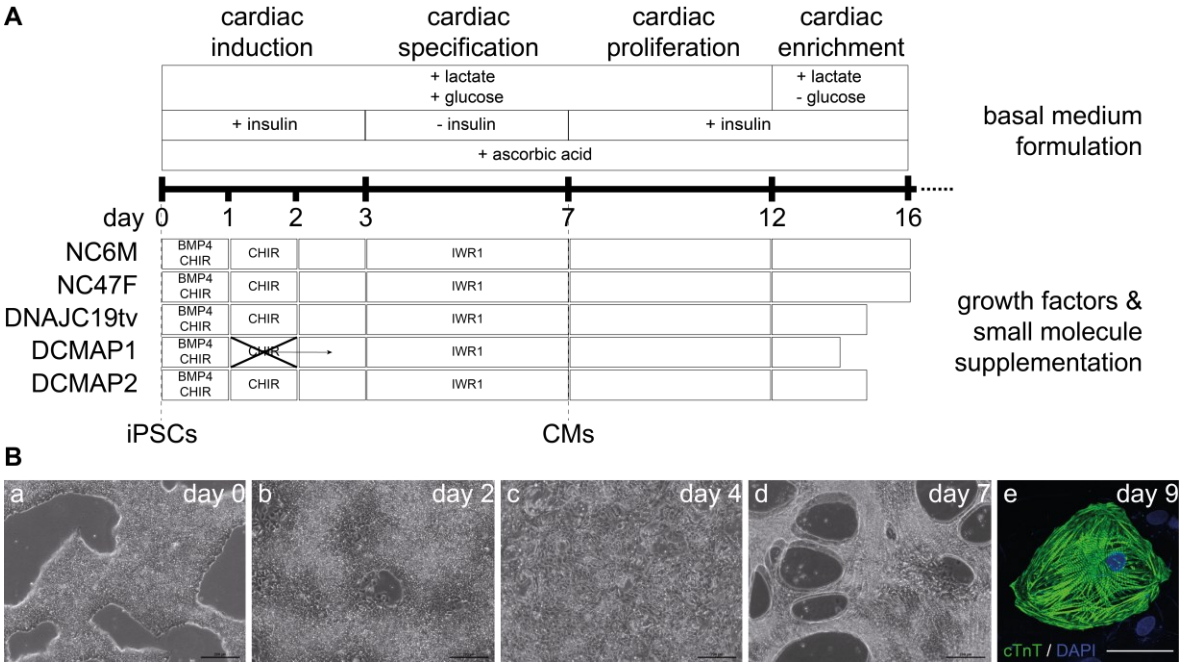

Figure 3.14: The adaption of the cardiac differentiation protocol to generate iPSC-CMs of all five iPSC lines.
(A) Applied CM differentiation protocol (Kadari et al., 2015) to produce contracting CMs within seven days that is divided into three different phases: cardiac induction, cardiac specification, cardiac proliferation and cardiac enrichment. **(B)** NC6M iPSCs are depicted as representative cell line to illustrate morphological changes during cardiac differentiation. **(a)** Prior to cardiac induction seeded iPSCs covered the dish area to ~70 % confluency. Morphological changes were provoked by **(b)** activation and **(c)** inhibition of Wnt signaling. **(d)** After 7 days, differentiation success was visually recognized by the onset of contracting cells or cardiomyocyte networks. **(e)** Immunofluorescence stains of iPSC-derived CMs on day 9 with cTnT (green) and DAPI (blue) counterstaining were performed to validate a typical cardiomyocyte-associated protein expression. Triangular cell shapes, mononuclearity and the absence of aligned sarcomeres displayed typical immature characteristic states. Scale bar bright field images = 200 µm; scale bar immunofluorescence image = 50 µm

3.4.2 Identification of ventricular CMs as predominant cell type

The efficiency in the generation of iPSC-derived CMs depends on the cellular fitness and the used differentiation protocol (Zhang et al., 2009, Burridge et al., 2012, Lian et al., 2013, Laco et al., 2018). In general, all cardiomyocyte subtypes nodal, atrial as well as ventricular CMs can be generated within one single differentiation procedure or directed towards a specific subtype by chemically defined factors (Josowitz et al., 2014, Cyganek et al., 2018, Devalla et al., 2015, Protze et al., 2017). The established protocol after Kadari et al., 2015 did not asses CM subtype specificity. Therefore, the generation of CMs was confirmed and the subtype identity was examined via immunofluorescence. CMs were identified by the expression of structural proteins of the troponin-tropomyosin complex, composed of cTnI, cTnC and

cTnT, that activates actin-myosin interaction in response to increased intracellular Ca^{2+} $[Ca^{2+}]_i$ levels (Yang et al., 2009), cardiac α-actin (Schwartz et al., 1992) or subtype specific isoforms of the cardiac myosin light chain MLC2v for the ventricular and MLC2a for the atrial isoform respectively that displayed the typical striation pattern of sarcomeres in CMs that served as basis for all further immunofluorescence stains in the present thesis (Chuva de Sousa Lopes et al., 2006) (Fig. 3.15 A). NC6M iPSC-CMs were depicted to illustrate the co-localization of MLC2v with cTnT in cells of ventricular subtype identity (Fig. 3.15 A). The disease phenotype sets the need of the corresponding CM subtype and in the context of DCMA the identity of interest were ventricular CMs. Therefore, the fraction of ventricular CMs ($MLC2v^+$) within the CMs population ($cTnT^+$) was examined (Fig. 3.15 A). Data are represented as mean ± SEM together with each biological replicate (BR, boxes), experimental details can be found in supplementary Tab. 5.6. NC6M presented on average 97.73 % $MLC2v^+/cTnT^+$ cells (Fig. 3.15 B). A comparable percentage was observed in NC47F CMs with a mean of 97.50 % $MLC2v^+/cTnT^+$ cells (Fig. 3.15 B). DNAJC19tv displayed 97.22 % double-positive cells, as well as DCMAP1 that demonstrated a predominant ventricular subtype of 96.67 % similar to DCMAP2 with 97.08 % $MLC2v^+/cTnT^+$ cells (Fig. 3.15 B). Statistical analysis of NC47F, DNAJC19tv, DCMAP1, DCMAP2 with NC6M CMs did not reveal significant changes (unpaired t-test NC6M vs. NC47F ns, p=0.9486; NC6M vs. DNAJC19tv ns, p=0.8926; NC6M vs. DCMAP1 ns, p=0.7952; NC6M vs. DCMAP2 ns, p=0.8317) (Fig. 3.15 B). Taken together, the usage of adapted conditions after Kadari et al., 2015 resulted in robust generation of $cTnT^+$ cells representative for CMs. The assessment of the ventricular subtype demonstrated $MLC2v^+/cTnT^+$ cells in equal high fractions of above 96.0 % indicating ventricular CMs as predominant subtype in all five cell lines (Fig. 3.15).

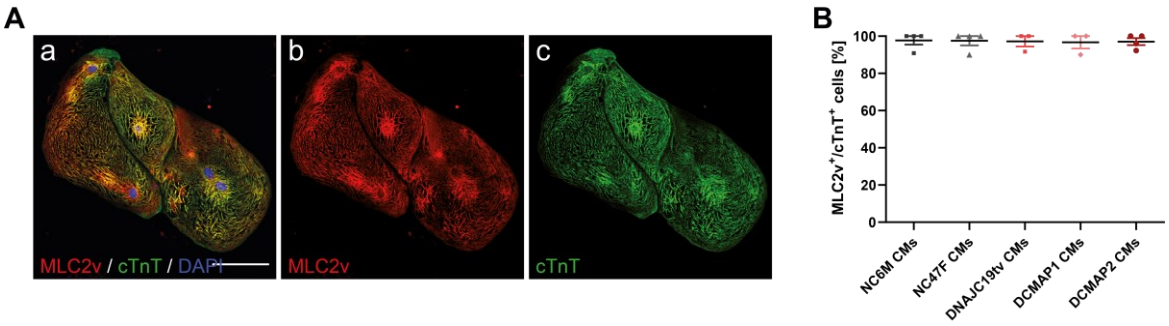

Figure 3.15: Co-staining after cardiac differentiation unraveled ventricular CMs as the predominant subtype. Immunofluorescence staining of at least 60-day-old iPSC-CMs were performed to analyze the *in vitro* generated cardiomyocyte subtypes after adaptation of the Kadari et al., 2015 cardiac differentiation protocol. Antibodies against MLC2v (red) and cTnT (green) together with DAPI (blue) were used to investigate the number of cells expressing the ventricular isoform of MLC2 in a cardiomyocyte population. **(A)** NC6M iPSC-CMs were depicted to illustrate the co-localization of MLC2v with cTnT in cells of ventricular subtype identity. **(B)** Quantitative analysis of the percentage of $MLC2v^+/cTnT^+$ cells of all five DCMA-related cell lines displayed similar ventricular CM fractions. The calculation was based on all iPSC-CMs present in ten images (technical replicates) per coverslip using the 40x magnification in one biological replicate. Each staining was performed in at least three to four biological replicates (from independent cardiac differentiations). Data are represented as mean ± SEM together with each biological replicate (boxes). ns p>0.05 using unpaired t-test calculated versus NC6M control. *MLC2v* myosin light chain-2 ventricular isoform; scale bar = 100 µm

3.4.3 Purification of iPSC-derived CMs via combination of cardiac enrichment and MACS

Even though we were able to generate CMs of all five cell lines the cardiac enrichment phase was not the optimal method for enriching CMs in mixed cell populations due to the mentioned premature death of DCMA CMs and the proportionally higher survival rate of non-CMs (section 3.4.1). Therefore, population purities were assessed using immunofluorescence staining with antibodies detecting cTnT together with DAPI counterstaining. The percentage of $cTnT^+/DAPI^+$ per total number of cells (non-CMs = $cTnT^-/DAPI^+$) was examined to identify population purities after cardiac enrichment. Data are represented as mean ± SEM together with each biological replicate (boxes), experimental details can be found in supplementary Tab. 5.7. Glucose depletion and increased lactate concentrations in the cultivation medium resulted in 77.46 % $cTnT^+$ and 68.89 % $cTnT^+$ cells for the healthy control conditions of NC6M and NC47F, respectively (Fig. 3.16). After shortening the enrichment phase to three days

(DCMAP1) and four days (DCMAP2, DNAJC19tv), we examined 72.38 % cTnT$^+$ cells in DNAJC19, 49.07 % cTnT$^+$ cells in DCMAP1 and 81.69 % cTnT$^+$ cells in DCMAP2-derived cells (Fig. 3.16). We observed on average similar fractions of ~ 70 % (NC6M, NC47F, DNAJC19tv, DCMAP2) that were not statistically significant except for DCMAP1 iPSC-CMs which showed reduced purities using standard metabolic enrichment strategies (unpaired t-test NC6M vs. NC47F ns, p=0.5811; NC6M vs. DNAJC19tv ns, p=0.7055; NC6M vs. DCMAP1 *, p=0.0390; NC6M vs. DCMAP2 ns, p=0.6808) (Fig. 3.16). Regarding data distribution, we observed high variations in all five cell lines (Fig. 3.16). The CM yields represented by cTnT$^+$/DAPI$^+$ fractions differed among all cell lines as well as within each cell line with respect to the individual cardiomyocyte differentiation experiments. We observed that the success of enrichment was highly depending on the amount of CMs, which initially resulted directly after cardiomyocyte differentiation. For precise investigations in an approach-dependent manner, like expression changes as well as metabolic assessments, the enrichment needed further optimizations.

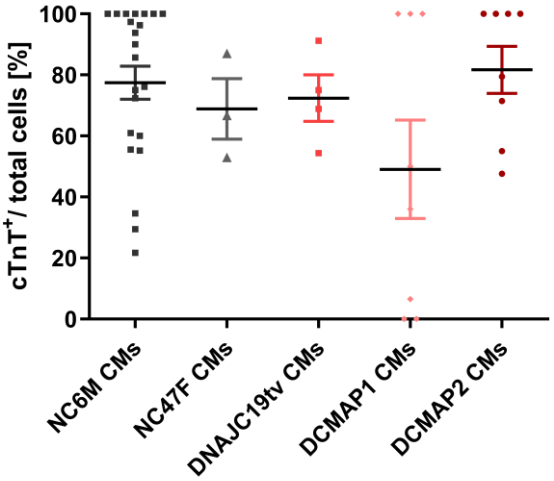

Figure 3.16: Shortened metabolic enrichment phase is sufficient to enrich CM yields.
Immunofluorescence staining using cTnT and DAPI was performed on iPSC-CMs after at least 25 days in culture to analyze cardiomyocyte yields in a cell population after metabolic enrichment. cTnT$^+$/DAPI$^+$ cells resembled CMs whereas nuclei stained by DAPI only represented non-CM cell fractions. Summarizing both values allowed the assessment of overall cell numbers for the individual calculations. The quantifications were based on ten images (technical replicates) per coverslip using the 40x magnification in one biological replicate. Each staining was performed in at least 3-22 biological replicates, derived from independent cardiac differentiations. Data are represented as mean ± SEM together with each biological replicate (boxes). ns p>0.05 using unpaired t-test calculated versus NC6M control.

Therefore, vital CMs were isolated using non-genetic magnetic separation to enrich CM yields in a two-way procedure. The MACS experiment included a mixture of antibodies recognizing the non-CMs fraction that need to be depleted followed by the second step of positively labelling CMs. Immunofluorescence staining of cTnT and vimentin together with DAPI was performed to identify the percentage of population purities as previously described. The additional application of the antibody anti-vimentin was used to identify non-CMs due to its ubiquitous expression in stromal cells (Huebsch et al., 2016). In detail, vimentin is expressed in cardiac fibroblasts (Camelliti et al., 2004), endothelial cells (Franke et al., 1979) and smooth muscle cells (Gabbiani et al., 1981) that evolve as a byproduct during cardiac differentiation (Huebsch et al., 2016, Humeres and Frangogiannis, 2019). The percentage of population purities was assessed before and after the two-step MACS procedure in the NC6M condition only, after cardiac enrichment has been already performed (Fig. 3.17). Quantified population fractions are represented as mean ± SEM together with each biological replicate (BR, boxes), details can be found in supplementary Fig. 5.7.

The examination of mixed cell populations after cardiac enrichment but before MACS revealed the presence of both 48.88 % cTnT$^+$ and 51.15 % vimentin$^+$ cells on average as illustrated in the NC6M line representatively nine days after the initiation of contraction (Fig. 3.17 A, B, a). This was an example of high survival of vimentin-positive cells after the lactate enrichment phase (Fig. 3.17 B, a). After MACS, the purified non-CMs fraction demonstrated 97.48 % vimentin$^+$ and 2.51 % cTnT$^+$ cells which sum up to nearly no CMs in this fraction (Fig. 3.17 A, B, b). With 94.85 % cTnT$^+$ and 5.15 % vimentin$^+$ cells the purified CM-rich fraction contained the highest achieved CM population purity consistent in six individually performed experiments (Fig. 3.17 A, B, c). Statistical analysis unraveled significantly increased cTnT$^+$ fractions in the CM-positive population (unpaired t-test of cTnT$^+$/total cells [%]: before MACS vs. CM fraction after MACS ***, p=0.0006) as well as significantly decreased cTnT$^+$ yields in the non-CMs fraction (unpaired t-test of cTnT$^+$/total cells [%]: before MACS vs. non-CM fraction after MACS ***, p=0.0005) after MACS when compared to the previously reported mixed cell population before MACS (Fig. 3.17 A). Even though highly enriched cell populations were achieved a notable mortality of CMs was recognized. The time-consuming procedure included single cell suspensions as well as enormous mechanical stress for proper CM selection, thus providing suitable reasons for the increased loss of viable CMs. Therefore, the combination of CEM and MACS was performed in an approach-dependent manner only. If not indicated, CEM enrichment was performed as the only method of purification. Taken together, we were able to combine the CEM strategy together with MACS to achieve CM-rich populations in our *in vitro* setting with on average 94.8 % cTnT$^+$ pure populations (Fig. 3.17 A, B, c).

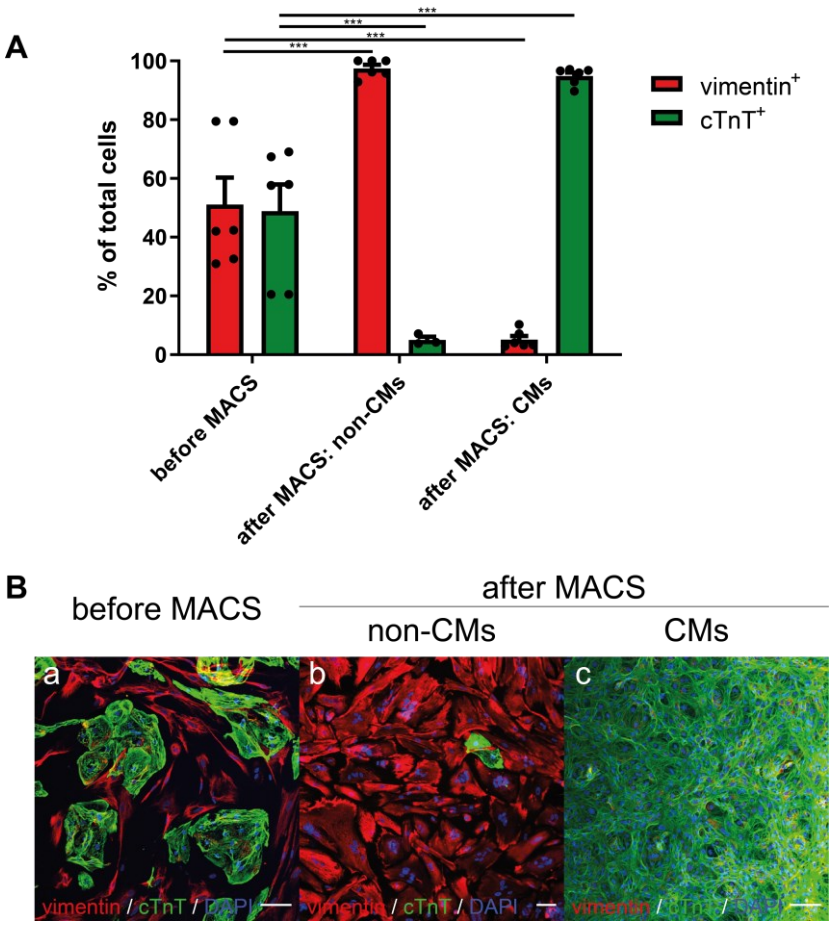

Figure 3.17: MACS-sorting enabled high population purities.
Co-staining of cTnT (green), vimentin (red) and DAPI (blue) was performed on healthy NC6M iPSCs after cardiac differentiation to quantify CM proportion of a cell population before and after MACS. **(a)** Only CEM enrichment without MACS was not sufficient to purify the mixed cell population. **(b)** The positively selected cell fraction presented a highly purified CM population after magnetic enrichment **(c)** The non-cardiomyocyte fraction revealed a non-CM-rich cell population, by showing a high percentage of vimentin-positive cells. The quantifications were based on five images (technical replicates) per coverslip using the 20x magnification in one biological replicate. Each staining was performed for NC6M as representative cell line only in 6 biological replicates, derived from independent cardiac differentiations. Data are represented as mean ± SEM together with each biological replicate (boxes). *** $p<0.001$, ns, $p>0.05$ using unpaired t-test calculated versus the individual cell fraction before MACS. Scale bar = 100 µm

3.4.4 Maturation of iPSC-derived CMs

After confirmation of high purities and ventricular identity the next aim was to assess the maturation state of the generated iPSC-CMs. To investigate DCMA, more mature CMs are required to investigate mitochondrial morphology, function and potential abnormities that can be linked to the patients` cardiac phenotype. Important criteria to investigate the cardiac phenotype of DCMA in an *in vitro* setting are essential key features of maturity like CM size, mitochondrial and sarcomere content, sarcomere size and alignment, increased nucleation and tightly connected cell-cell-contacts. Quantifications of the mentioned criteria were performed for all five iPSC-derived CM lines to evaluate disease-associated differences simultaneously. First, prolonged cultivation time was used to address maturation states in iPSC-derived CMs, which was evaluated for NC6M iPSC-CMs only that served as representative cell line.

3.4.4.1 Increased maturation upon prolonged cultivation times

NC6M iPSC-CMs were generated, enriched and reseeded on hESC-Matrigel™-coated coverslips to equal densities (40000 cells/ ~10 mm coverslip). Immunofluorescence staining using cTnT was performed to identify CMs and to assess their morphological changes over prolonged cultivation time at four different time points: day 30 (a), day 60 (b), day 90 (c), day 120 (d) (Fig. 3.19 a-e). iPSC-CM sizes are represented as mean ± SEM together with each technical replicate (dots), experimental details can be found in supplementary Tab. 5.9. Quantifications of CM areas using ImageJ software revealed small CMs on day 30 with an average size of 2950.43 ± 193.88 μm^2 which was remarkably increased on day 60 to an average size of 4606.07 ± 243.57 μm^2 and even more enlarged on day 90 with an average size of 11359.22 ± 844.56 μm^2 until the maximum sizes were reached on day 120 with 15822.96 ± 793.80 μm^2 on average (Fig. 3.18 e). Statistical analysis using one-way ANOVA proved a highly significant change in CM sizes over prolonged cultivation time (one-way ANOVA ####, $p<0.0001$). After performing prolonged cultivation of NC6M iPSC-CMs, we recognized a high variation in CM sizes on each time point which was even increased upon prolonged cultivation times (Fig. 3.18 e). Moreover, 120-day-cultured iPSC-CMs presented loss of bi-directionality, hypertrophy and reduced fiber densities to higher fractions, indicating a lack of cell-cell proximities over prolonged cultivation times (Fig. 3.18 d). Additionally, we visually observed an enhanced alignment of sarcomeres as well as a higher abundance of binucleated cells on day 60 already (Fig. 3.18 b). Next, TEM images of NC6M iPSC-CMs after 136 days of cultivation were acquired to assess maturation hallmarks on the ultrastructural level (Fig. 3.18 f, g). We observed the presence of contractile filaments with a typical bi-directional sarcomere-like organization, including Z-lines, A- and I-bands and partly M-bands as well as intermyofibrillar mitochondria and fascia adherens-like structures (Fig 3.18 f, g). Moreover, co-localization studies using the adult-isoform cTnI and the maturation state indicator connexin 43 (Cx43) revealed a typical expression on cell-cell contact sites via immunofluorescence, representatively shown in NC6M iPSC-CMs (Fig. 3.18 h, i).

We conclude, that in our model system prolonged cultivation to 120 days is indeed feasible to achieve the highest degree of mature-like CMs including morphological features such as size increase, binucleation, sarcomere alignment on the ultrastructural level and typical age-associated expression of cell-cell contact proteins such as Cx43. However, we observed critical maturation hallmarks already at earlier stages as 60-day-old iPSC-CMs showed size increase, sarcomere-like alignment and rod-shaped morphologies.

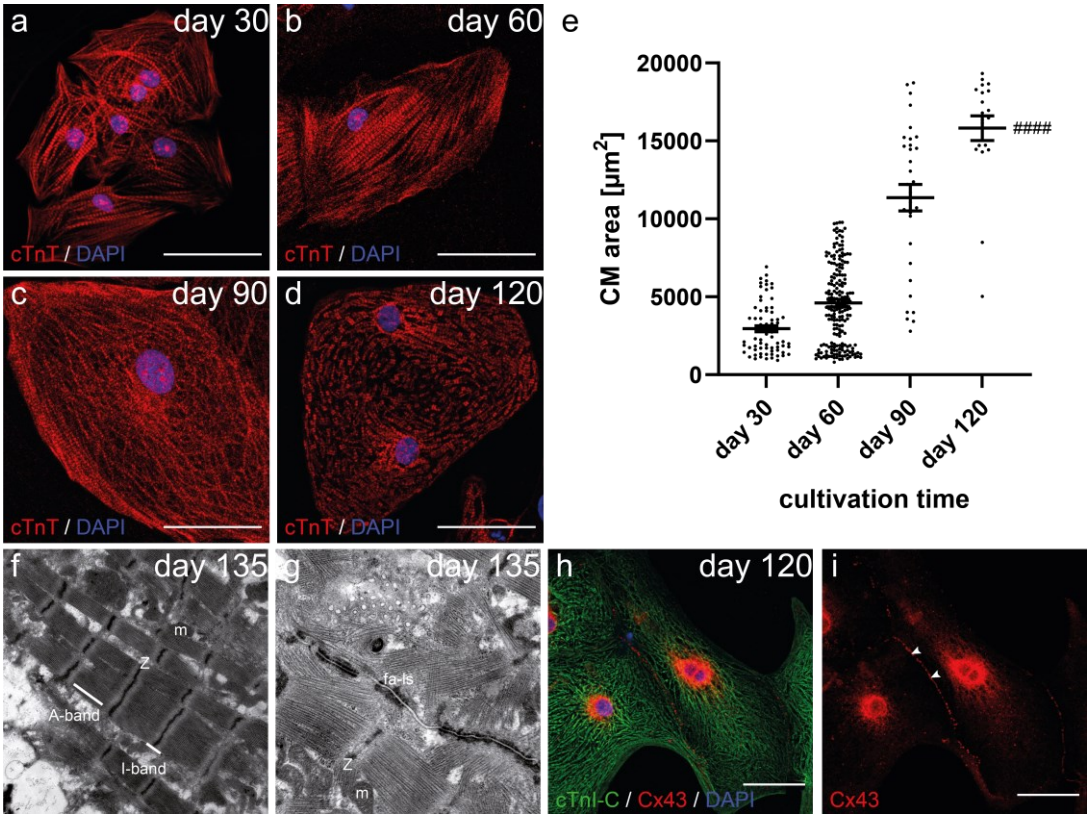

Figure 3.18: Typical hallmarks of adult-like CMs after prolonged cultivation time.
(a-d) NC6M iPSC-derived CMs were stained for DAPI and cTnT to visualize CM size increase at different timepoints **(a)** day 30, **(b)** day 60, **(c)** day 90 and **(d)** day 120. **(e)** Quantification of cardiomyocyte sizes of *in vitro*-aged CMs at different time points presented significant increase in CM area over prolonged cultivation time (cTnT [µm^2], one-way ANOVA ####, p<0.0001). **(f, g)** TEM analysis of healthy NC6M iPSC-derived CMs after 135 days of standard cultivation display **(f)** sarcomere-like organization of contractile filaments including Z-lines (Z), A- and I-bands, intermyofibrillar mitochondria (m) and **(g)** fascia adherens-like structures (fa-ls) of cellular contacts. **(h, i)** Co-staining of cTnI-C (green), DAPI (blue) and Cx43 (red) of healthy CMs after 120 days of standard cultivation revealed typical Cx43 expression at cell-cell contact sites. Scale bar immunofluorescence = 50 µm

3.4.4.2 Acceleration of maturation by physical stiffness

Even though all maturation hallmarks were achieved after 120 days of cultivation, we recognized characteristic features of adult states already after 60 days, including size increase of CMs and sarcomere alignment (Fig. 3.18). To reach higher maturation states on earlier cultivation times we aimed to accelerate maturation in iPSC-CMs via adaptation of the cultivation strategy after Feaster et al., 2015 for NC6M as representative cell line for all DCMA conditions (Fig. 3.19). Normally, iPSCs were seeded on 1:100 diluted hESC-Matrigel™ coating as standard cultivation procedure (Fig. 3.19). On the contrary, the matrigel-mattress-based method uses an undiluted comparable Matrigel® Growth Factor Reduced matrix to draw a line on the coverslip or the cell culture dish directly (Fig. 3.19). After bi-directional polymerization of the matrigel-mattress, iPSC-CMs were seeded on the visually identifiable line in the size of approximately 2 x 10 mm to force the iPSC-CMs to align bi-directional (Fig. 3.19 a, b). The assessment of higher maturation states was performed by immunofluorescence staining of cTnT and junctophilin-2 (JP2), a typical maturation state indicator that is undeniable in T-tubule formation and their anchoring to the SR.

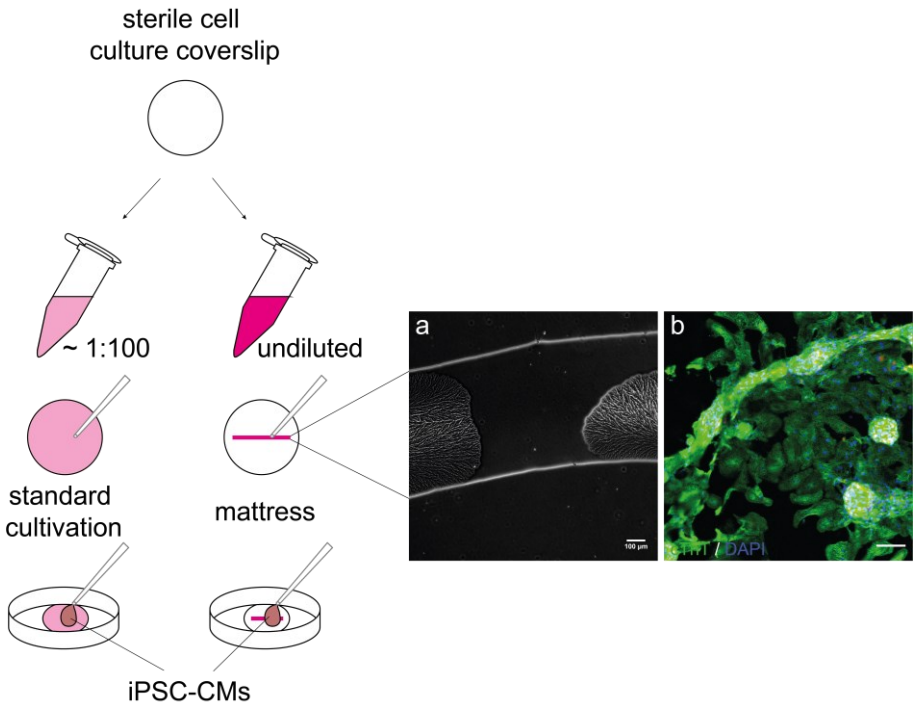

Figure 3.19 Schematic overview of standard coating versus mattress-based cultivation of iPSC-CMs.
On the left-hand side, standard cultivation is illustrated by using hESC-Matrigel™ in a 1:100 dilution for coating of coverslips or cell culture dishes prior to seeding of CMs. On the right-hand-side, the matrigel-mattress method is displayed by drawing a line (2 x 10 mm) with undiluted Matrigel® Growth Factor Reduced directly on the coverslips or cell culture dishes. The higher magnification shows the edge of the mattress and its bi-directional polymerization **(a)** as well as seeded iPSC-CMs that align bi-directional to form muscle fiber like structures, validated by immunofluorescence via cTnT staining **(b)**. The plating of iPSC-CMs was performed in parallel, on control (left) and mattress (right) conditions. Scale bar = 100 µm

Co-staining of cTnT and JP2 was performed on NC6M iPSC-CMs using standard cultivation versus matrigel-mattress cultivation strategy on three different periods: 20-30, 40-50 and 60-70 cultivation days (Fig. 3.20). The examination of different maturation states was evaluated according to the cellular distribution of JP2 visually (A) and quantitively (B, C) according to the cellular distribution of JP2 using ImageJ software. Data are represented as mean ± SEM together with each technical replicate (dots), experimental details can be found in supplementary Tab. 5.10. On day 23 of standard cultivation JP2 expression was restricted to the perinuclear region (Fig. 3.20 A, a, b). Similar observations were made with mattress-cultured cells of the same age, that showed bi-directional alignment of iPSC-CMs and a tendency towards diffuse expression of JP2 over the whole cell body (Fig. 3.20 A, g, h). On day 40 we observed a size increase with both cultivation strategies that was accompanied by a higher expression of JP2 particularly when using matrigel-mattress, whereas JP2 localization was more restricted to the perinuclear region after standard cultivation (Fig. 3.20 A, c, d, I, j). After 64 days of cultivation, standard-cultured iPSC-CMs showed typical maturation hallmarks like size increase, binuclearity and enhanced JP2 expression (Fig. 3.20 A, e, f). After the comparison with mattress-cultured iPSC-CMs, we recognized even higher maturation states by showing a homogenous distribution of JP2 over the whole cell body, enhanced sizes and increased sarcomere-alignment (Fig. 3.20 k, l).

For quantification, maximum intensity projections of the acquired immunofluorescence stains were used to calculate the CMs sizes based on $cTnT^+$ areas as well as $JP2^+$ areas per cell area to quantify the expression of JP2 given its role as a typical maturation state marker that is required for T-tubule biogenesis (Fig. 3.21 B, C). As previously observed, standard-cultured iPSC-CMs demonstrated a similar increase in cell size with an average of 1054.37 ± 72.84 µm^2 between day 20-30 that gave rise to 3189.14 ± 313.50 µm^2 large cells when cultured 40-50 days or even 5516.84 ± 363.76 µm^2 after cultivation for 60-70 days (Fig. 3.21 B). Compared to matrigel-mattress-cultivated iPSC-CMs we

observed an average size of 2695.40 ± 264.33 µm^2 between 20-30 days, that was significantly accelerated to 5604.21 ± 312.94 µm^2 between day 40-50 and even more enhanced to 7262.78 ± 705.40 µm^2 between day 60-70 and therefore displayed a significantly expedited gain in iPSC-CMs size (two-way ANOVA standard cultivation vs. mattress cultivation ####, p<0.0001) (Fig. 3.20 B).

Next, we analyzed the expression and localization of JP2, which is expressed in the nucleus at early states and is gradually translocated into the cytoplasm as differentiation progresses, where it is homogenously expressed at adult-stages (Fig. 3.20 A, C). Quantification of JP2 areas per CMs area (calculated based on cTnT staining) revealed the same content of JP2 per CM for both cultivation strategies on day 20-30 (Fig. 3.20 C). iPSC-CMs under standard cultivation had a JP2 density of 18.46 ± 1.09 %, whereas mattress-cultured iPSC-CMs showed 17.81 ± 1.68 % JP2 expression (Fig. 3.20 C). Between day 40-50 JP2 expression was comparable as standard-cultured iPSC CMs displayed a JP2 content of 31.24 ± 1.46 % which was similar to mattress-cultured iPSC-CMs with 30.10 ± 1.88 % (Fig. 3.20 C). With 53.33 ± 3.04 % mattress-cultured iPSC-CMs showed a considerable shift towards higher JP2 expression between day 60-70 than standard-cultured iPSC-CMs with 34.48 ± 1.54 % (Fig. 3.20 C). The statistical comparison of both cultivation strategies revealed highly significant differences between both approaches (two-way ANOVA standard cultivation vs. mattress cultivation ###, p=0.004) (Fig. 3.20 C).

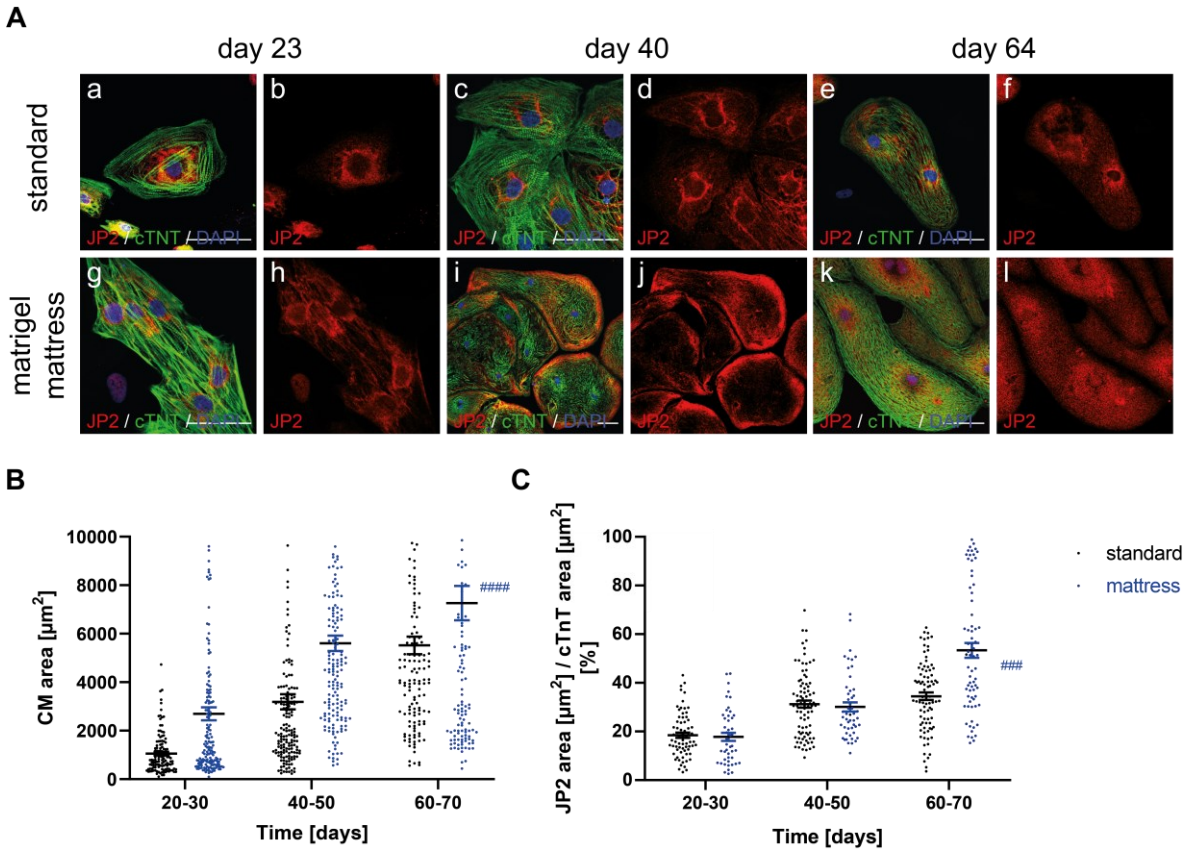

Figure 3.20 iPSC CMs seeded on matrigel-mattress versus standard cultivation exhibited increased subcellular distribution of T-tubule related protein JP2 and accelerated hypertrophy
(A) Representative cell images after co-labeling for cTnT (green), the T-tubule related protein junctophilin-2 (JP2, red) and DAPI (blue) of healthy NC6M *in vitro* aged CMs on day 23, day 40 and day 64 under standard cultivation conditions (upper panel) versus CMs seeded on a matrigel-mattress (lower panel). Images were depicted to illustrate quantified averages. CMs seeded on mattress are aligned bi-directionally and show accelerated alignment of sarcomeres as well as enhanced uniform translocation of the maturation status indicator JP2 from the nucleus to the cytoplasm with intensified patterns over prolonged cultivation times (mattress protocol after Feaster et al., 2015). **(B)** Quantification of iPSC-CMs sizes using extrapolated cTnT labelling by ImageJ. **(C)** Maturation states were assessed by quantification of the percentage of the JP2-stained area compared to the total CM area. Data are reported as mean ± SEM for each individual measurement. Statistical analysis was performed using regular two-way ANOVA #### p<0.0001, ### p<0.001. a: 3949.2 µm^2 with 13.9 % JP2, c: 2666.9 ± 624.7 µm^2 with 47.9 ± 5.5 % JP2, e: 12222.7 µm^2 with 38.7 % JP2, g: 1451.2 ± 149.7 µm^2 with 13.1 ± 3.5% JP2, i: 19283.9 ± 4986.7 µm^2 with 42.7 ± 5.6 % JP2, k: 15471.1 µm^2 with 61.2 % JP2. Scale bars = 50 µm

3.5 Molecular characterization of DNAJC19 expression profiles and subcellular localization

As the patients` mutation *DNAJC19* (NM_145261.4):c.130-1G>C are predicted to prevent splicing of the exon 4 coding sequence as well as the CRISPR/Cas9-mediated mutation *DNAJC19* (NM_145261.4):c.[131_140del];[137_138insAGTATAATTGCC] in DNAJC19tv is predicted to cause loss of full-length *DNAJC19* as well, the presence of both *DNAJC19* transcript variants was analyzed on mRNA level by RT-PCR. The predicted loss of ∆ex4 in mutant cells will result in a C-teminal truncated DNAJC19 isoform lacking the DnaJ domain and the loss of full-length DNAJC19 protein on the translational level was analyzed on the translational level using western blot (WB). Whether the predicted translational differences were accompanied by a change in DNAJC19 subcellular localization was analyzed using immunofluorescence stains.

3.5.1 Analysis of splicing defects and tissue-specific expression of transcript variants of *DNAJC19*

DNAJC19 specific RT-PCR was performed on cDNA isolated from fibroblasts (supplementary Fig. 5.3), iPSCs (supplementary Fig. 5.4) and iPSC-CMs (Fig. 3.22) to simultaneously allow the assessment of a cell type specific expression. The full-length transcript corresponds to the 525 bp band, whereas the ∆ex4 transcript corresponds to the 445 bp band (Fig. 3.21). The quantification of the individual bands was performed using the QIAxcell system to investigate the expression of the individual PCR products of *DNAJC19* (ng/µl) versus *GAPDH* (ng/µl), thus allowing to determine the splicing defect as well as the quantification of endogenous ∆ex4 transcript levels. To assure the detection of unspecific PCR products a negative control containing water (ddH_2O) only without cDNA was included in all steps. For statistical analysis unpaired t-test was used for the analysis of DNAJC19 transcript variants in all three cell types: dermal fibroblasts (supplementary Fig. 5.3), iPSCs (supplementary Fig. 5.4) and iPSC-CMs (Fig. 3.22).

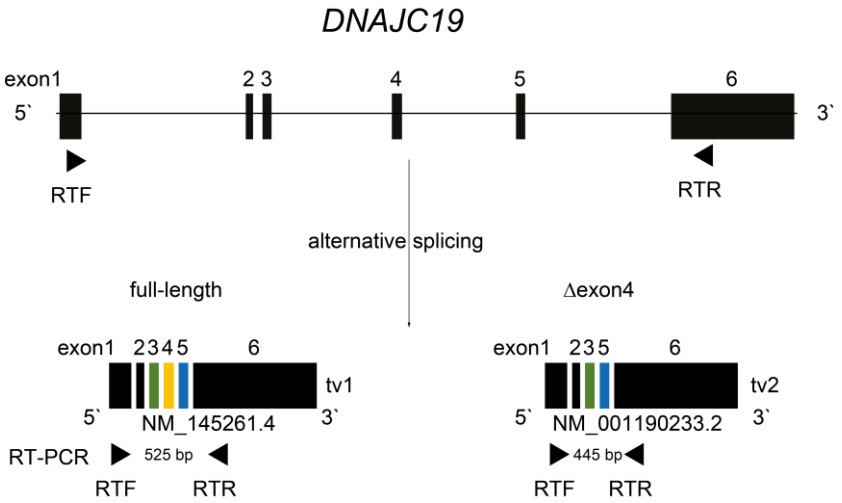

Figure 3.21: Both existing transcript variants of *DNAJC19* and corresponding sizes of PCR products.
Primers RTF and RTR were designed to target *DNAJC19* (Davey et al., 2006). RT-PCR using cDNA of healthy cells is predicted to identify two transcript variants: the 525 bp band corresponds to the full-length transcript, the 445 bp band corresponds to the ∆exon4 transcript.

3.5.2 Splicing defect in patient-derived iPSC-CMs and shared loss of full-length *DNAJC19* transcript in all DCMA mutants

The RT-PCR analysis of iPSC-CM-derived cDNA was depicted to illustrate cardiac-specific transcriptional differences between DCMA-associated mutants and healthy controls (details supplementary Tab. 5.11). The analysis of NC6M and NC47F iPSC-CMs revealed the expression of the 525 bp band predominantly and only a weak expression of the 445 bp band (Fig. 3.22 A). On the contrary, DCMAP1 and DCMAP2 showed a loss of full-length *DNAJC19* and the 445 bp was strongly expressed (Fig. 3.22 A). Interestingly DNAJC19tv neither displayed the 525 bp band visually, nor the 445 bp band as only two differently sized bands of ~537 bp and ~515 bp were observed (size analysis was performed using the QIAxcell system (Fig. 3.22 A). The quantification of the transcript variant expression levels using the QIAxcell system demonstrated high and similar expression levels in both healthy controls with a strong expression of the 525 bp PCR-product and extremely low levels of the 445 bp PCR-product that were statistically not significant (525 bp unpaired t-test NC6M vs. NC47F ns, p=0.8636; 445 bp unpaired t-test NC6M vs. NC47F ns, p=0.4738) (Fig. 3.22 B). In contrast, the investigation of the *DNAJC19* transcript variant expression levels revealed the opposite trend in both mutants, as QIAxcell analysis confirmed a loss of the 525 bp band, representing the loss of the full-length transcript of *DNAJC19* to non-significant degrees (unpaired t-test NC6M vs. DCMAP1 ns, p=0.1689; NC6M vs. DCMAP2 ns, p=0.1707) (Fig. 3.22 B). These observations were accompanied by an increase of the 445 bp band intensity representing increased ∆ex4 transcription levels in both patients, with a significant difference for DCMAP2 only (unpaired t-test NC6M vs. DCMAP1 ns, p=0.0839; NC6M vs. DCMAP2 **, p=0.0086) (Fig. 3.22 B). DNAJC19 cDNA quantification of CRISPR/Cas9 gene-edited DNAJC19tv iPSC-CMs showed a non-significant loss of *DNAJC19* full-length (unpaired t-test NC6M vs. DNAJC19tv ns, p=0.1755) and comparable low endogenous ∆ex4 transcript levels as observed in NC6M and NC47F iPSC-CMs (unpaired t-test NC6M vs. DNAJC19tv ns, p=0.4802) (Fig. 3.22 B).

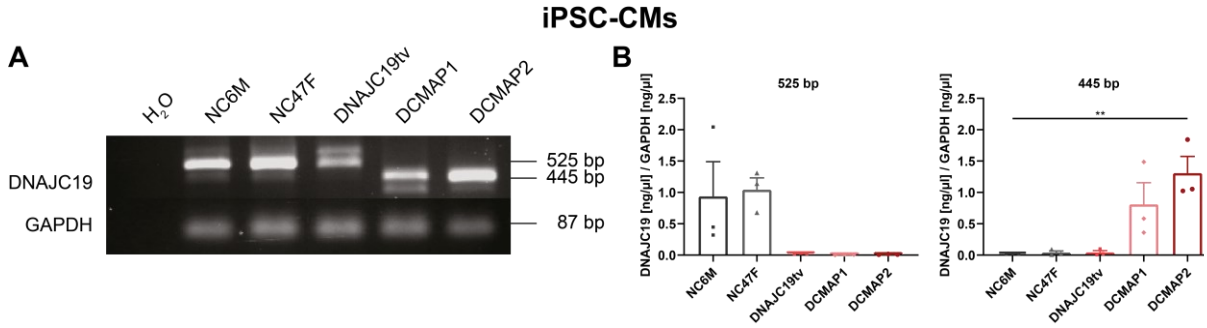

Figure 3.22 Expression analysis of *DNAJC19* revealed a shared loss of full-length *DNAJC19* in all mutant iPSC-CMs and abnormal splicing in both patients.
(A) RT-PCR analysis of *DNAJC19* using gene specific primers and isolated RNA of *in vitro* derived iPSC-CMs from two patients (DCMAP1, DCMAP2), one CRISPR/Cas9 mutant cell line (DNAJC19tv) together with two controls (NC6M, NC47F). In both controls two bands were amplified: one strong band of 525 bp which corresponds to the full-length cDNA of *DNAJC19* and the less abundant 445 bp band which corresponds to the ∆ex4 transcript. Expression analysis of DNAJC19tv was carried out and demonstrated two different bands close to the 525 bp band, that illustrate the biallelic modification via the CRISPR/Cas9 system. The same strategy on DCMAP1 and DCMAP2 iPSC-CMs revealed a loss of the 525 bp band together with a strong 445 bp band that showed a higher expression of the ∆ex4 transcript in both patient cells. **(B)** QIAxcell analysis by quantification of RT-PCR amplified transcript variants was calculated versus the internal control GAPDH. The 525 bp was not quantifiable in all mutant conditions, whereas an increase of the ∆ex4 transcript was observed in both patient-derived cell lines only. Data are shown as mean ± SEM together with each individual biological replicate. ** $p<0.01$, ns $p>0.05$ using unpaired t-test calculated versus NC6M iPSC-CMs.

Taken together, we observed a shared loss of the full-length transcript in both patient-derived cell lines as well as in the gene-edited cell line DNAJC19tv in fibroblasts (not available for DNAJC19tv) (supplementary Fig. 5.3), in iPSCs (supplementary Fig. 5.4) and in iPSC-CMs (Fig. 3.22). We demonstrated low levels of endogenous ∆ex4 transcript in both controls as well as the CRISPR/Cas9-edited DNAJC19tv cell line but a strong expression in both patient-derived cell lines, indicating abnormal splicing on the splice acceptor site of intron 3. We recognized overall shared levels of the *DNAJC19* 525

bp and 445 bp products between both controls as well as both patients within one respective cell type (supplementary Fig. 5.3, 5.4; Fig. 3.22). Moreover, the comparison of the full-length and the ∆ex4 transcripts of *DNAJC19* revealed a positive expression in all analyzed cell types (supplementary Fig. 5.3, 5.4; Fig. 3.22). We did not observe significant differences between both control lines after *DNAJC19* cDNA expression analysis in fibroblasts (supplementary Fig. 5.3), iPSCs (supplementary Fig. 5.4) and iPSC-CMs (Fig. 3.22), but a trend of reduced *DNAJC19* expression in CEM-enriched iPSC-CMs (at age day 32-37) only. Furthermore, the comparison of both genders revealed no significant differences on the transcriptional level.

3.5.3 Analysis of DNAJC19 on the translational level

Next, protein quantifications were performed to analyze the tissue-specific expression of DNAJC19 and the presence of the translated proteins of the full-length or ∆ex4 transcript when comparing mutants to healthy controls. The full length (525 bp) transcript encodes a protein of predicted 116 aa with the molecular weight of 12.5 kDa, whereas the translation of the ∆ex4 transcript (445 bp) is expected to result in a C-terminal truncated DNAJC19 isoform in the size of 47 aa and a corresponding molecular weight of approximately 5 kDa as visualized in Fig. 3.23. Therefore, western blot analysis was performed on fibroblasts (supplementary Fig. 5.5), iPSCs (supplementary Fig. 5.5) and iPSC-CMs (Fig. 3.24) to quantify DNAJC19 protein content versus the internal control GAPDH. Quantifications on expression level intensities were normalized based on the expression of the positive control NC6M and statistically analysed using an unpaired t-test calculated versus NC6M in all three cell types.

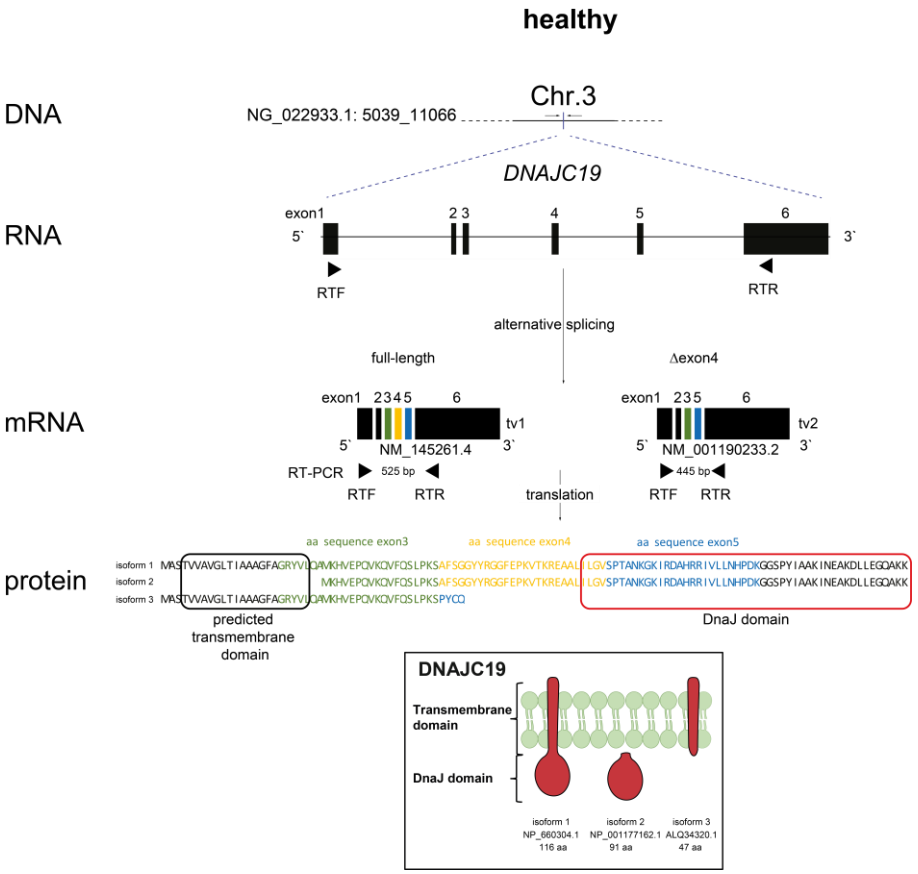

Figure 3.23 Schematic representation of the different expression levels of DNAJC19 and corresponding protein isoforms in healthy cells.
The transcription of the *DNAJC19* gene produces two different transcript variants after alternative splicing, one full-length and one lacking exon 4 (∆exon4). Both transcript variants result in the expression of in total three DNAJC19 isoforms that comprise a transmembrane domain and/or a DnaJ domain. In detail, translation of the full-length transcript results in two different isoforms, 1 and 2, due to an alternative start codon. The ∆exon4 transcript results in isoform 3, consisting of the transmembrane domain only. DNAJC19 isoforms are illustrated according to the information of the NCBI database and previous reports (Davey et al., 2006, Richter-Dennerlein et al., 2014)

3.5.4 Loss of the full-length isoform in patient-derived and CRISPR/Cas9-edited iPSC-CMs

iPSC-CMs lysates of both healthy controls (NC6M and NC47F), the gene-edited mutant control (DNAJC19tv) and both patients (DCMAP1 and DCMAP2) were subjected to western blotting to analyze DNAJC19 expression. Data are represented as mean ± SEM together with each biological replicate (boxes), experimental details can be found in supplementary Tab. 5.12. NC6M and NC47F iPSC-CMs demonstrated a strong expression of DNAJC19 with the molecular weight of 12.5 kDa, but with a non-significant trend towards stronger expression in the NC47F iPSC-CMs (unpaired t-test NC6M vs. NC47F ns, p=0.6936) (Fig. 3.24). The gene-edited DNAJC19tv iPSC-CMs showed a loss of the 12.5 kDa band, the expression of which was also not observable in DCMAP1 and DCMAP2 (Fig. 3.24). Chemiluminescence quantification of DNAJC19 confirmed a significant loss of the 12.5 kDa DNAJC19 isoform in DNAJC19tv (NC6M vs. DNAJC19tv ****, p<0.0001), DCMAP1 (NC6M vs. DCMAP1 ****, p<0.0001) and DCMAP2 (NC6M vs. DCMAP2 ****, p<0.0001) (Fig. 3.24).

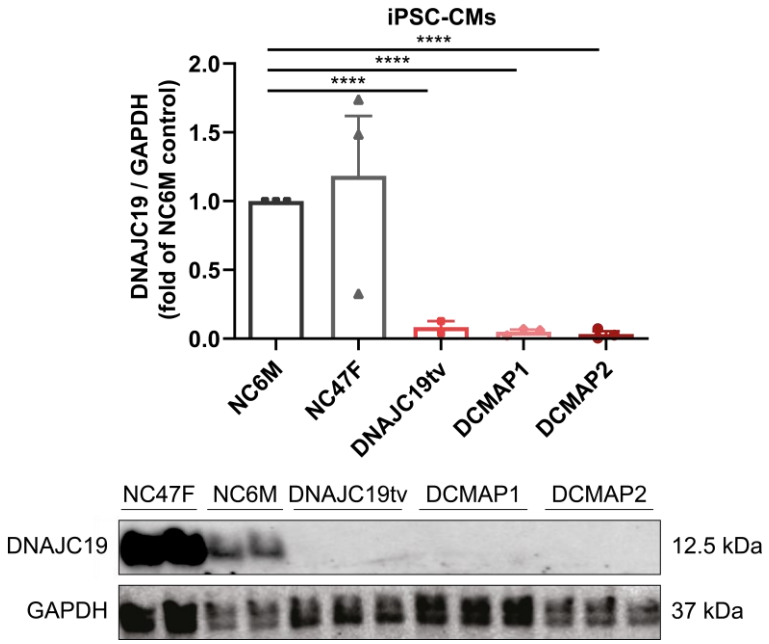

Figure 3.24: Shared DNAJC19 full-length loss in all DCMA-associated cell lines in iPSC-derived CMs.
Two healthy controls, NC6M and NC47F, together with three mutants, DNAJC19tv, DCMAP1, DCMAP2 were assessed for DNAJC19 expression via immunoblotting. Both controls displayed a strong expression of the 12.5 kDa DNAJC19 isoform, whereas all mutant conditions shared the loss of the full-length isoform as no band was observed in all three mutant conditions after assessment of iPSC-CMs. Data are shown as mean ± SEM together with each individual biological replicate. **** p<0.0001, ns p>0.05 using unpaired t-test, calculated versus NC6M after normalization to NC6M signal.

Taken together, western blot analysis was feasible to detect the full-length isoform (12.5 kDa) in all three cell types: fibroblasts (supplementary Fig. 5.5), iPSCs (supplementary Fig. 5.5) and iPSC-CMs (Fig. 3.24). The predicted expression of the C-terminal truncated DNAJC19 isoform with the corresponding molecular weight of approximately 5 kDa could not be detected using conventional western blotting. We observed a trend towards higher expression levels in the female control NC47F, that was significantly increased in fibroblasts only (supplementary Fig. 5.5). On the contrary, DNAJC19tv, DCMAP1 and DCMAP2 shared loss of full-length DNAJC19 in fibroblasts (supplementary Fig. 5.5), iPSCs (supplementary Fig. 5.5) and iPSC-derived CMs (Fig. 3.24).

3.5.5 Investigation of DNAJC19 subcellular localization

Regarding the positive expression of the protein of interest DNAJC19 in dermal fibroblasts, iPSCs and iPSC-CMs the next question to address was the localization of DNAJC19 in healthy cells versus DNAJC19 mutant cell lines. We aimed to assess DNAJC19 localization in cell types of low mitochondrial-content such as iPSCs and high mitochondrial-content as iPSC-CMs. The immunofluorescence staining was performed to additionally visualize the loss of full-length DNAJC19 in all mutant conditions and to assess in a second examination the presence of the predicted C-terminal truncated DNAJC19 isoform. Signal intensities were adjusted towards a negative control that underwent the same staining procedure without the usage of the DNAJC19-specific primary antibody. Maximum intensity projections were chosen for illustration of DNAJC19 in all following figures as well as for each individual immunofluorescence-based quantification after semi-automated extrapolation using ImageJ software.

3.5.5.1 Nuclear-restricted DNAJC19 expression in DCMA iPSC lines

The immunofluorescence analyses were carried out on healthy NC6M, NC47F (not shown) and mutant DNAJC19tv, DCMAP1 and DCMAP2 iPSC lines. Co-staining for OCT3/4 and DAPI was used for internal validation of the iPS cell type as well as for cell compartment determination of the nucleus. DNAJC19 is a protein of the IMM and is assumed to localize in the perinuclear region of iPSCs. The examination of DNAJC19 revealed a diffuse signal in nuclei and enhanced intensities in the perinuclear region in NC6M iPSCs as well as in NC47F iPSCs (not shown) (Fig. 3.25 a-d). Unexpectedly, the investigation of DNAJC19 in DNAJC19tv iPSCs (e-h) resulted in a nuclear restricted expression with a loss of cytoplasmic signal that was observable in DCMAP2 iPSCs (m-p) as well, but with lower intensities (Fig. 3.25). To a less extent DCMAP1 iPSCs yielded a relatively distributed and decreased signal (Fig. 3.25 i-l). Common observations in all mutant conditions were the loss of DNAJC19 in the cytoplasm that was accompanied by a nuclear restricted DNAJC19 signal to different intensities (Fig. 3.25 e-p).

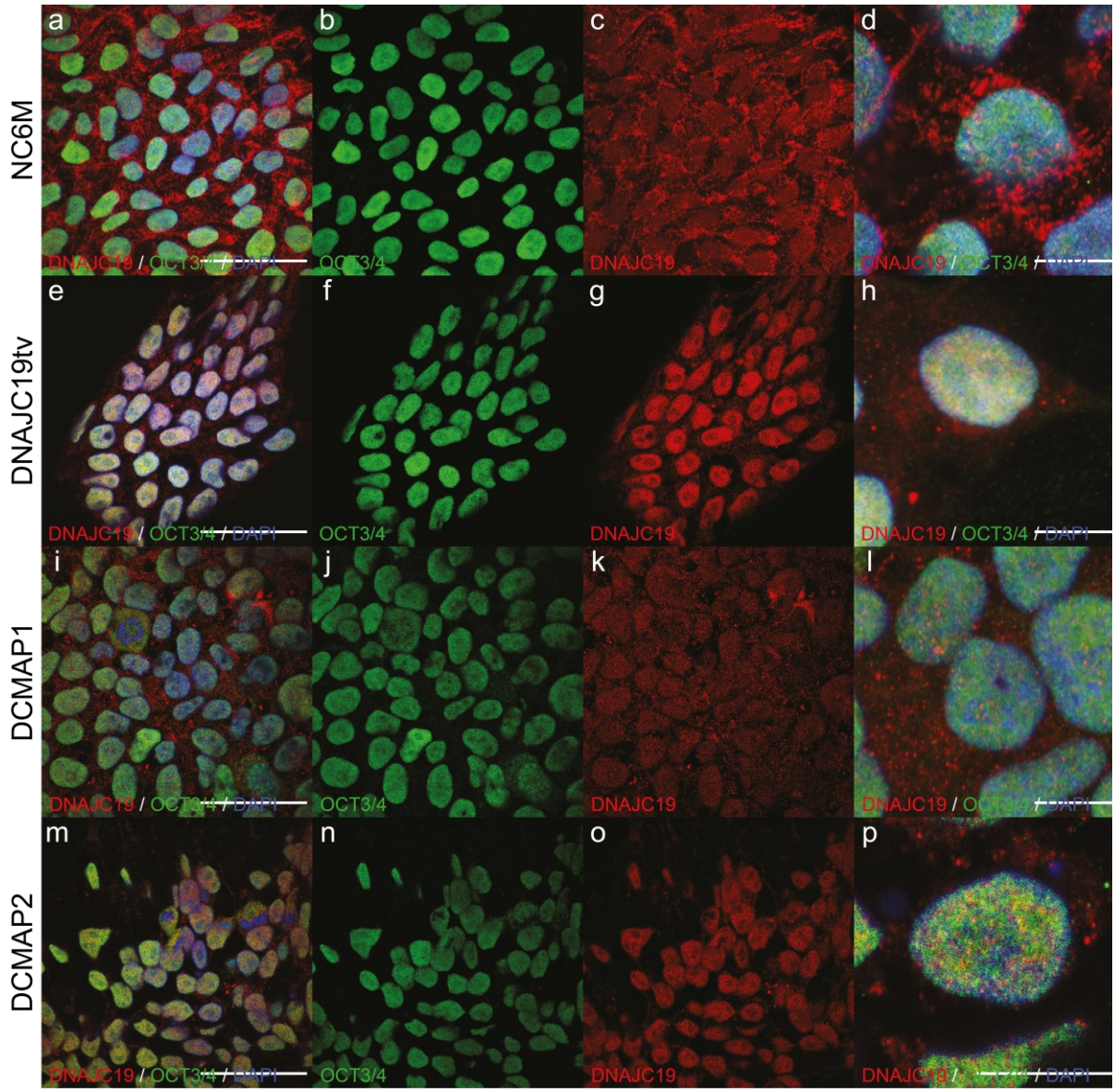

Figure 3.25 Immunofluorescence-based analysis of DNAJC19 localization in iPSCs revealed a nuclear restricted expression pattern in mutant iPSCs.
Immunofluorescence based imaging of DNAJC19 counterstained with OCT3/4 as iPSC-specific protein and DAPI for nuclear regions was performed to investigate DNAJC19 subcellular localization. **(a-d)** DNAJC19 accumulated significantly in the perinuclear region of NC6M iPSCs **(a-d)**, but not in those of DNAJC19tv **(e-h)**, DCMAP1 **(i-l)** and DCMAP2 iPSCs **(m-p)**. In all cell lines a nuclear localization of DNAJC19 was observed to different intensities. **(a-c, e-g, i-k, m-o)** Scale bars = 50 µm, **(d, h, l, p)** scale bars = 10 µm

3.5.5.2 Loss of mitochondrial co-localization of DNAJC19 accompanied by a nuclear translocation in iPSC-CMs

Given the proposed role of the IMM-located protein DNAJC19 in biogenesis and CL remodeling of the mitochondrion, we wanted to examine whether DNAJC19 co-localizes with mitochondrial structures to determine mitochondrial-linked dysfunctions in DCMA-associated mutation carrier cell lines. Therefore, at least 60-day-old iPSC-CMs were used that were predicted to have an enhanced mitochondrial content to identify DNAJC19 in different subcellular compartments like mitochondrial structures (MitoTracker, violet), nuclear regions (DAPI, blue) and for cytoplasmic localization (cTnT, red) by immunofluorescence (Fig. 3.26). The usage of the cardiomyocyte-specific cTnT signal further allowed the validation of CM-specific analyses.

The assessment of cTnT and DAPI signals revealed enlarged CMs as well as the presence of binucleation and highly aligned sarcomeres, thus indicating similar maturation states between all conditions prior to mitochondrial examination (Fig. 3.26 a, e, i, m, q). The analysis of MitoTracker to examine mitochondrial structures within CMs unraveled main differences between healthy versus mutant iPSC-CMs. In healthy iPSC-CMs (NC6M 1st row, NC47F 2nd row) we observed thinner and elongated mitochondrial structures with dense regions in particular in the perinuclear region and in some cases mitochondrial aggregations close to the cell-cell-contact sites (Fig. 3.26 b-c, f-g). However, all mutant iPSC-CMs showed an enhanced aggregation and fragmentation of mitochondrial structures distributed over the whole cell body (Fig. 3.26 j-k, n-o, r-s). Moreover, DNAJC19 expression in healthy NC6M and NC47F iPSC-CMs again displayed a nuclear expression, higher intensities in the perinuclear region and enhanced expression levels in the cardiomyocyte periphery (Fig. 3.26 b, d, f, h). We observed a clear co-localization of DNAJC19 with MitoTracker labelled mitochondrial structures (Fig. 3.26 b, f). On the contrary, DNAJC19tv (3rd row), DCMAP1 (4th row) and DCMAP2 (5th row) predominantly showed the expression of DNAJC19 in the nucleus (Fig. 3.26 j, l, n, p, r, t). Mainly with regard to DCMAP1, we rarely observed a cytoplasmic expression of DNAJC19 that, when present, co-localized at the cardiomyocyte edges which was not seen in DNAJC19tv and DCMAP2 (Fig. 3.26 n, p). The investigation of DNAJC19 together with the MitoTracker pattern resulted in a loss of DNAJC19-specific signal that was not found to co-localize with mitochondrial structures. Taken together, DNAJC19tv, DCMAP1 and DCMAP2 iPSC-CMs showed loss of the major part of the DNAJC19 expression that was excluded from cytoplasmic compartments which was accompanied by enhanced fragmentation of mitochondrial structures and a remaining nuclear localization of DNAJC19 (Fig. 3.26 j-l, n-p, r-t).

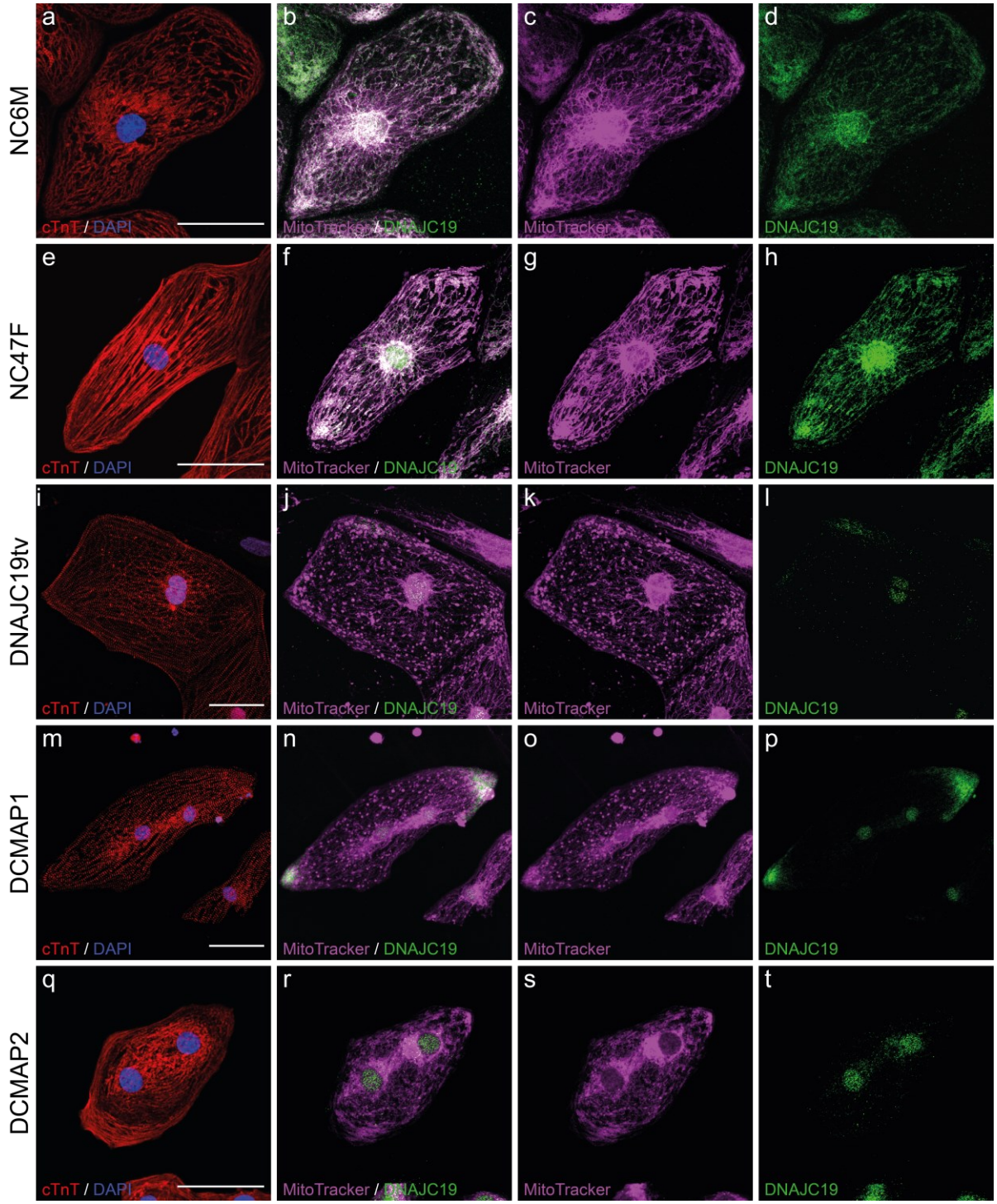

Figure 3.26 Immunofluorescence analyses of DNAJC19 expression and localization in 60-day-old CMs revealed a remaining nuclear expression in DNAJC19 mutant iPSC-CMs.
Immunofluorescence staining was performed using cTnT (red) in combination with DAPI counterstaining (blue**, a, e, l, m, q**), together with MitoTracker-based mitochondrial membrane labelling (violet, **c, g, k, o, s**) and DNAJC19 labeling (green, **d, h, l, p, t**). cTnT staining was used as internal validation of the generated iPSC-CMs. Maximum intensity projections of z-stacks were acquired using a laser scanning microscope (LSM). **(b, f, j, n, r)** DNAJC19 co-localized with mitochondrial structures (white) in healthy CMs (NC6M: upper row and NC47F second row). **(j, n, r)** Co-localization of DNAJC19 with mitochondrial structures could not be observed in mutant cells, except in some rare events in the cell edges of DCMAP1 only (n). DNAJC19 is expressed over the whole cell body in healthy controls (**d**: NC6M, **h**: NC47F) whereas a predominantly nucleus restricted expression of DNAJC19 was recognized in mutants **(l, p, t)**. Scale bars = 50 µm

3.5.5.3 Confirmation of DNAJC19 subcellular compartmentalization

The visually observed localization changes of DNAJC19 were further examined and quantified using ImageJ software. cTnT-positive regions were used to specify CM areas within maximum intensity projections after extrapolation, whereas DAPI staining was used to identify nuclei regions. DNAJC19 localization was assessed by the identification of pixels that show a minimum signal of intensity of DNAJC19 based on an automated threshold. Next, the sum of DNAJC19-positive pixels was calculated in μm^2 for the cytoplasm (CM area-nuclei area) and the nuclei. Each measured iPSC-CM is displayed individually (box) with at least 3-4 biological replicates per cell line, details can be found in the supplementary Tab. 5.13 and supplementary Tab. 5.14.

The assessment of DNAJC19 in healthy iPSC-CMs revealed a shared cytoplasmatic expression of DNAJC19 to ~ 6.17 ± 0.21 % in NC6M as well as ~ 6.86 ± 0.37 % in NC47F (unpaired t-test NC6M vs. NC47F ns, p=0.0924) (Fig. 3.27 A). In contrast, all DCMA mutant iPSC-CM lines showed significantly reduced cytoplasmatic expression of DNAJC19 (Fig. 3.27 A). In detail, DNAJC19tv represented ~ 2.45 ± 0.15 %, DCMAP1 displayed ~ 2.87 ± 0.28 % and DCMAP2 demonstrated ~ 2.85 ± 0.15 % DNAJC19 areas per cytoplasm (NC6M vs. DNAJC19tv ****, p<0.0001; NC6M vs. DCMAP1 ****, p<0.0001; NC6M vs. DCMAP2 ****, p<0.0001) (Fig. 3.27 A).

The amount of DNAJC19 in the nucleus was also addressed and with 34.79 ± 1.46 % and 33.80 ± 2.21 % the controls NC6M and NC47F showed nuclear DNAJC19 expression to a similar extent, respectively (unpaired t-test NC6M vs. NC47F ns, p=0.7173) (Fig. 3.27 B). The nuclear restricted expression of DNAJC19 was reduced to 24.38 ± 1.18 % in DNAJC19tv and to 30.52 ± 2.24 % in DCMAP1, but slightly more decreased in DCMAP2 by showing 24.63 ± 1.05 % nuclear restricted DNAJC19-specific expression, with significant differences in DNAJC19tv and DCMAP2 only (unpaired t-test NC6M vs. DNAJC19tv ***, p=0.0003; NC6M vs. DCMAP1 ns, p=0.2742; NC6M vs. DCMAP2 ****, p<0.0001) (Fig. 3.27 B).

Taken together, DNAJC19 expression indeed was identified in DCMA mutant iPSC-CMs but with a nuclear restricted expression only, to slightly reduced yields as in control cells. The cytoplasmatic expression of DNAJC19 was significantly reduced in all three mutant conditions.

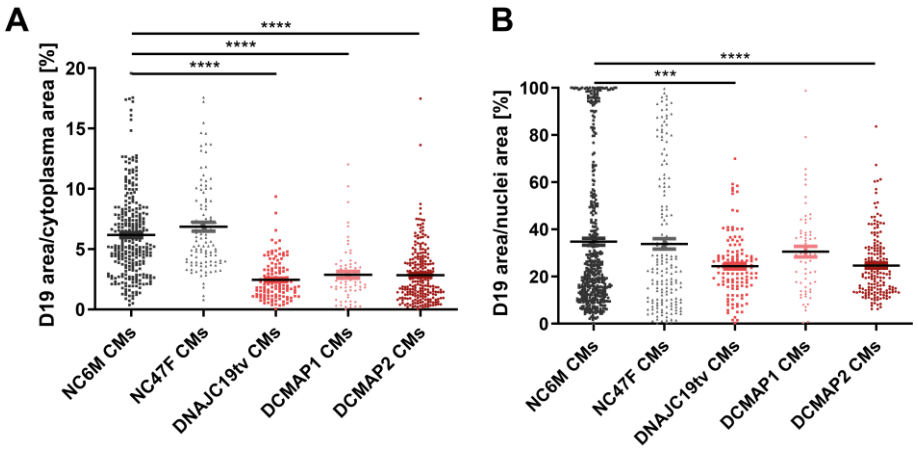

Figure 3.27 Immunofluorescence quantifications of DNAJC19 in subcellular compartments.
Maximum intensity projections were quantitatively assessed to elucidate DNAJC19 expression areas in [μm^2] calculated versus the cytoplasm area (cell area-nuclei regions, [μm^2], **A**) or versus the nuclei areas ([μm^2], **B**) using a semi-automated calculation of the ImageJ software. Each individually analyzed iPSC-CM of 3-5 independent experiments (biological replicates) is displayed for both healthy controls (NC6M, NC47F) and three DNAJC19 mutation carrier cell lines (DNAJC19tv, DCMAP1, DCMAP2). Data are shown as mean ± SEM together with each individual technical replicate. **** p<0.0001, *** p<0.001, ns p>0.05 using unpaired t-test calculated versus NC6M CMs together with each individual technical replicate.

Taken together, we observed remaining DNAJC19 signals that were mainly restricted to nuclei areas in iPSCs and iPSC-CMs. The significant reduction of DNAJC19 signal in the cytoplasm was quantified and additionally verified the impression of a loss of DNAJC19 co-localization with mitochondrial membranes that was previously visually recognized.

3.6 Investigation of iPSC-CMs morphologies in DCMA

To examine DCMA-specific cellular changes, immunofluorescence stains were used to assess central morphological aspects of CMs comprised by mitochondrial- and sarcomere-related contents (fiber densities) (section 3.6.1), CM sizes and shapes (section 3.6.2.1), cTnT diameter-regularity (section 3.6.2.2) as well as nuclei sizes and multinucleation states (section 3.6.2.3). Mean ± SEM of all single measurements of iPSC-CMs or nuclei are displayed which derived out of at least three biological replicates.

3.6.1 Quantification of mitochondrial and sarcomere-related protein contents in iPSC-CMs revealed a disbalanced ratio in mutant DCMA iPSC-CMs

Next, mitochondrial content and sarcomere-related protein contents were quantified using maximum intensity projections of the previously immunofluorescence-stained iPSC-CMs on day 60. Therefore, automated quantifications of MitoTracker areas per cell area as well as cTnT areas per cell area were individually examined (Fig. 3.28) (details supplementary Tab. 5.15, 5.16). NC6M showed a percentage of 59.59 ± 0.76 % and NC47F demonstrated a percentage of 56.78 ± 1.62 % mitochondria contents underlining a high number of mitochondria in healthy iPSC-CMs at day ~60 (unpaired t-test NC6M vs. NC47F ns, p=0.0841) (Fig. 3.28 A). All DNAJC19 mutant iPSC-CMs unraveled highly significantly reduced mitochondrial contents, as DNAJC19tv showed 44.58 ± 0.78 %, DCMAP1 displayed 47.44 ± 1.26 % and DCMAP2 revealed 50.04 ± 1.15 % MitoTracker areas per iPSC-CM area (unpaired t-test NC6M vs. DNAJC19tv ****, p<0.0001; NC6M vs. DCMAP1 ****, p<0.0001; NC6M vs. DCMAP2 ****, p<0.0001) (Fig. 3.28 A).

Moreover, we investigated the content of sarcomere-related proteins using $cTnT^+$ areas per iPSC-CM area (Fig. 3.28 B). We observed shared cTnT yields per iPSC-CM among all five cell lines (Fig. 3.28 B). NC6M demonstrated on average 31.23 ± 0.81 % and NC47F showed on average 30.64 ± 0.95 % $cTnT^+$ areas per cell (Fig. 3.28 B). Regarding the mutant conditions we observed 31.99 ± 1.17 % $cTnT^+$ content in DNAJC19tv, 33.72 ± 0.90 % in DCMAP1 and 33.17 ± 0.66 % in DCMAP2 (Fig. 3.28 B). These data illustrated non-significant differences between all five cell lines with focus on sarcomere-related protein contents represented by cTnT staining, further also referred to as fiber densities (unpaired t-test NC6M vs. NC47F ns, p=0.6466; NC6M vs. DNAJC19tv ns, p=0.5931; NC6M vs. DCMAP1 ns, p=0.0571; NC6M vs. DCMAP2 ns, p=0.0633) (Fig. 3.28 B).

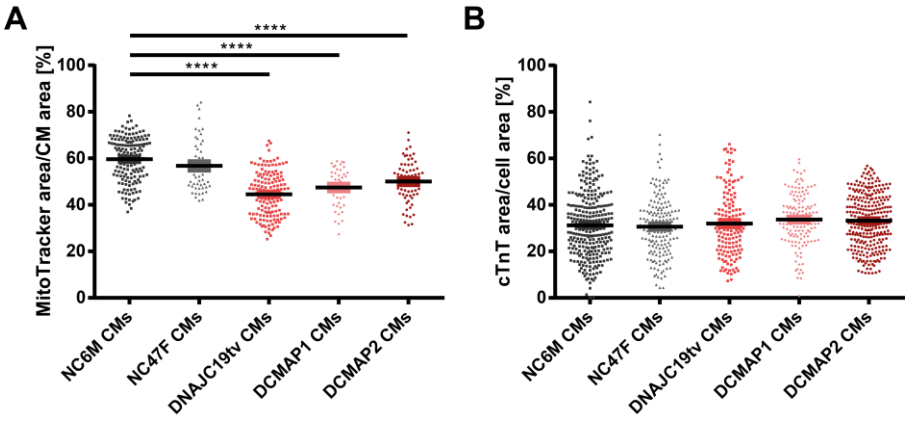

Figure 3.28 Reduced mitochondrial content but shared fiber-densities unraveled a disbalanced ratio in DCMA mutant iPSC-CMs.
Maximum intensity projections were further quantified to elucidate mitochondrial content via MitoTracker areas in [µm^2] and sarcomere-related protein contents using cTnT areas in [µm^2]. Those were calculated versus the individual cell areas [µm^2] using a semi-automated macro by defining the MitoTracker content and cardiac fiber density through an intensity threshold for MitoTracker and cTnT staining respectively, inside the individual CM areas using ImageJ software. The diagrams show the distinct contents for each individually examined iPSC-CM of 3-5 independent experiments (biological replicates) for both healthy controls (NC6M, NC47F) and three DNAJC19 mutants (DNAJC19tv, DCMAP1, DCMAP2). Data are shown as mean ± SEM together with each individual technical replicate. **** p<0.0001, ns p>0.05 using unpaired t-test calculated versus NC6M iPSC-CMs together with each individual technical replicate.

Taken together, we observed reduced mitochondrial content in each DNAJC19 mutant iPSC-CM line that was accompanied by equal sarcomere-related contents, thus indicating a disbalanced ratio between mitochondria and fiber densities at the maturation stage on day ~60.

3.6.2 Computational analysis of cardiomyocyte characteristics

The usage of the maximum intensity projections of the previously explained immunofluorescence staining allowed further insights regarding morphological features, that were not primarily expected but may elucidate additive aspects of DCMA using ImageJ software. Therefore, CMs sizes and shapes were evaluated to gain insights into hypertrophic cell growth during maturation. Moreover, cTnT staining was used to determine structural changes according to the regularly seen striation pattern of the sarcomeres, that were quantified as thin filament diameters (cTnT diameter [µm]). In addition, maturation states were assessed by determining nuclearities as well as nuclei sizes (DAPI diameter [µm^2]) staining.

3.6.2.1 Smaller cardiomyocyte areas and unchanged shapes

In the next step, iPSC-CMs sizes and morphological features were assessed by extrapolation of cTnT staining. In total, CMs areas [µm^2], CM perimeter [µm], CM feret´s diameter [µm] as well as shapes such as circularity [0-1], roundness [0-1] and solidity [0-1] were examined simultaneously (details supplementary Tab. 5.17). iPSC-CMs sizes and the shape descriptor circularity were depicted only to representatively show changed morphological features in supplementary Fig. 5.7. NC6M iPSC-CMs and NC47F iPSC-CMs yielded the largest CMs with an average size of 4260.59 ± 223.13 µm^2 and 4461.26 ± 324.00 µm^2, respectively (unpaired t-test NC6M vs. NC47F ns, p=0.6005) (Fig. 3.29 A). On the contrary, DCMA iPSC-CMs displayed significantly reduced cell sizes when compared to healthy iPSC-CMs (unpaired t-test NC6M vs. DNAJC19tv **, p=0.0094; NC6M vs. DCMAP1 ****, p<0.0001; NC6M vs. DCMAP2 ****, p<0.0001) (Fig. 3.29 A). DNAJC19tv showed an average size of 3398.12 ± 142.782 µm^2, DCMAP1 demonstrated the size of 2645.17 ± 179.47 µm^2 and DCMAP2 had the size of 2341.62 ± 98.72 µm^2 (Fig. 3.29 A). Further size-related descriptors such as iPSC-CM perimeters as well as Feret´s diameter showed an equal trend towards reduced sizes in mutant iPSC-CMs (supplementary Fig. 5.7).

Next, cell shape was investigated by quantification of iPSC-CMs circularity (Fig. 3.29 B). NC6M demonstrated 0.55 ± 0.01 circularity similar to NC47F with 0.59 ± 0.001 circularity, that was significantly

enhanced even though the difference comprised 0.04 only (unpaired t-test NC6M vs. NC47F **, p=0.0061) (Fig. 3.29 B). Equal ranges were observed in all three mutants, wherein DNAJC19tv displayed circularities of 0.54 ± 0.01, DCMAP1 0.54 ± 0.01 and DCMAP2 0.57 ± 0.01 (unpaired t-test NC6M vs. DNAJC19tv ns, p=0.4370; NC6M vs. DCMAP1 ns, p=0.6888; NC6M vs. DCMAP2 ns, p=0.1392) (Fig. 3.29 B).

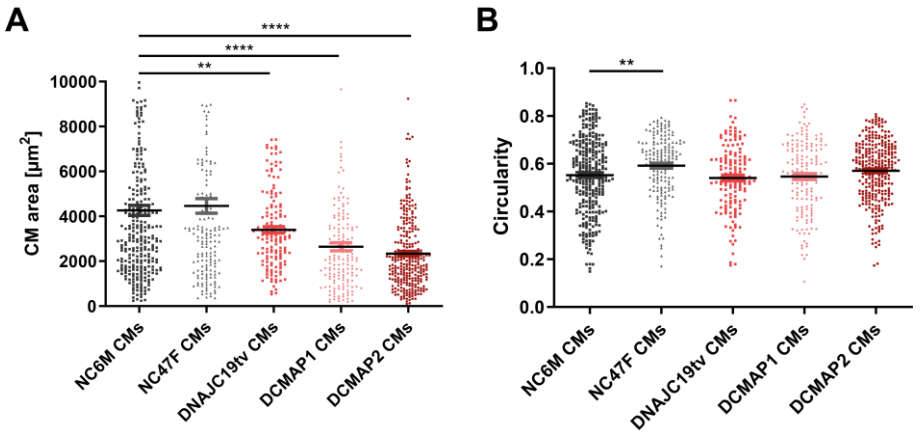

Figure 3.29 Smaller CMs but equal cell shapes in DCMA-associated iPSC-CMs.
The cTnT-based cell size areas of the used maximum intensity projections served as basis to quantify CM areas in [µm²] **(A)** and cell shapes by circularity **(B)** using a semi-automated macro of the ImageJ software. The diagrams display the individual CM sizes **(A)** and the shape descriptor circularity **(B)** for each individually examined iPSC-CM of 3-5 independent experiments (biological replicates) for both healthy controls (NC6M, NC47F) and three DNAJC19 mutants (DNAJC19tv, DCMAP1, DCMAP2). Data are shown as mean ± SEM together with each individual technical replicate. **** p<0.0001, ** p<0.01, ns p>0.05 using unpaired t-test calculated versus NC6M iPSC-CMs together with each individual technical replicate.

3.6.2.2 Equal sarcomere-related protein diameters

As we did not identify changes regarding sarcomere content, we wanted to examine cTnT diameter to examine structural changes in the striation pattern of sarcomeres. cTnT staining was used to calculate sarcomere-related protein diameters in µm after adaptation of the automated crosswise quantification to assess thin filament diameters (Giovanni Cardone and Maria Spletter, 2017). Data are represented as mean ± SEM together with each technical replicate (boxes), experimental details can be found in supplementary Tab. 5.18. In NC6M and NC47F iPSC-CMs the cTnT signal yielded an average sarcomere diameter of ~1.87 µm and ~1.82 µm, respectively, that was not statistically relevant (unpaired t-test NC6M vs. NC47F ns, p= 0.2438) (Fig. 3.30). The same calculation revealed ~1.92 µm in DNAJC19tv iPSC-CMs, ~1.93 µm in DCMAP1 and ~1.83 µm in DCMAP2 (unpaired t-test Fig. 3.30). Compared to the healthy control NC6M the cTnT based calculation was equal in all three mutant cell lines (unpaired t-test NC6M vs. DNAJC19tv ns, p=0.3121; NC6M vs. DCMAP1 ns, p=0.2338; NC6M vs. DCMAP2 ns, p=0.3886) (Fig. 3.30).

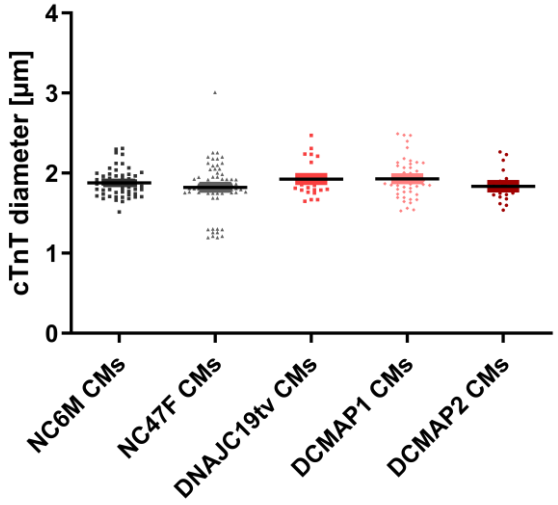

Figure 3.30 Shared structural features of sarcomeres represented by equal cTnT diameters.
The cTnT specific signal was used to evaluate the sarcomere-typical striation pattern based on a calculation of maximum intensity projections with an automated macro of the ImageJ software that could be used with high-resolution images only (Giovanni Cardone and Maria Spletter, 2017). The diagrams showed the individual cTnT diameters that corresponded to sarcomere diameters for each individually examined iPSC-CM of 3-5 independent experiments (biological replicates) for both healthy controls (NC6M, NC47F) and three DNAJC19 mutants (DNAJC19tv, DCMAP1, DCMAP2). Data are shown as mean ± SEM together with each individual technical replicate. ns p>0.05 using unpaired t-test calculated versus NC6M iPSC-CMs together with each individual technical replicate.

3.6.2.3 Similar nucleation levels and nuclei sizes

During cell morphology evaluations using immunofluorescence staining, parameters such as size of the nuclei and the percentage of mono-, bi-, trinuclear and higher nuclearities were considered as well (details supplementary Tab 5.20). The area of nuclei on average was determined for each cell line using DAPI counterstaining (details supplementary Tab 5.19). Data are represented as mean ± SEM together with each technical replicate (boxes, Fig 3.31 A) or with each biological replicate (boxes, Fig. 3.31 B).

The NC6M control iPSC-CMs possessed nuclei with an average of 117.10 ± 1.80 µm^2 in size (Fig 3.31 A). The second control NC47F iPSC-CMs were slightly but not significantly larger with 123.00 ± 2.02 µm^2 (unpaired t-test NC6M vs. NC47F ns, p=0.0582) (Fig 3.31 A). The CRISPR/Cas9-edited DNAJC19tv condition yielded nuclei in the size of 120.6 ± 2.23 µm^2 (Fig 3.31 A). The DCMAP1 condition showed nuclei in the size of 120.7 ± 2.77 µm^2, whereas DCMAP2 nuclei demonstrated an area of 114.1 ± 1.08 µm^2 (Fig 3.31 A). As all five cell lines displayed nearly the same average area ranging from 110-125 µm^2, the statistical comparison did not show significant differences (unpaired t-test NC6M vs. DNAJC19tv ns, p=0.2651; NC6M vs. DCMAP1 ns, p=0.2709; NC6M vs. DCMAP2 ns, p=0.1484) (Fig 3.31 A).

The accumulation of more than one nucleus per cardiomyocyte is a hallmark of maturation, the number of nuclei per CM was determined based on immunofluorescence counterstaining of DAPI and cTnT. As we did not observe higher nuclearities than three nuclei per cell and even this condition was rarely seen, binuclear cells were considered only (Fig. 3.31 B). Mononuclear and trinuclear categories are depicted in the supplementary Fig. 5.8. NC6M had 35.12 ± 6.11 % binuclear iPSC-CMs on average (Fig. 3.31 B). With 44.37 ± 4.76 % binuclear cells NC47F displayed higher mean values that however were not significantly different (unpaired t-test NC6M vs. NC47F ns, p=0.2766) (Fig. 3.31 B). With 26.68 ± 6.76 % in DNAJC19tv, 32.66 ± 6.96 % in DCMAP1 and 27.29 ± 3.39 % in DCMAP2 all mutant cell lines

yielded similar percentages of binuclear cells respectively (unpaired t-test NC6M vs. DNAJC19tv ns, p= 0.4072; NC6M vs. DCMAP1 ns, p= 0.8099; NC6M vs. DCMAP2 ns, p=0.3253) (Fig. 3.31 B).

In general, we monitored shared nuclear sizes and similar percentages of binuclear iPSC-CMs in all five cell lines, thus indicating equal maturation states.

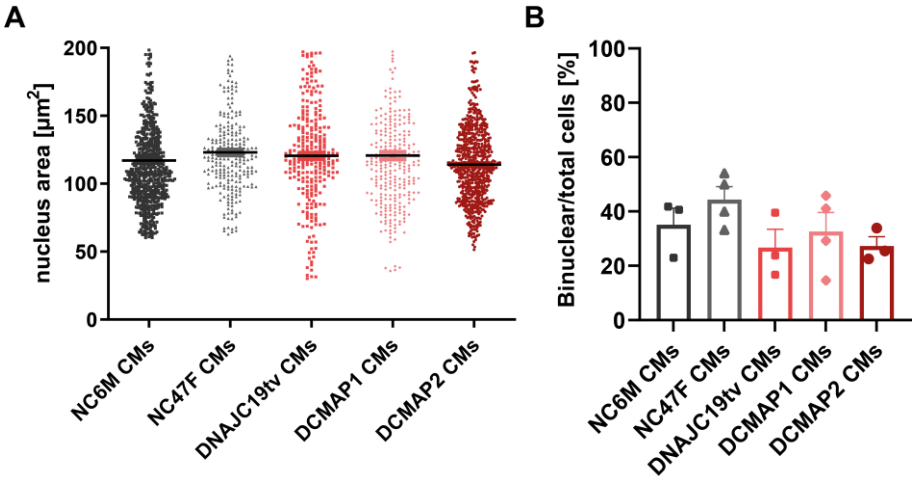

Figure 3.31 DAPI-signal based quantification of immunofluorescence stains revealed shared nuclei areas and equal fractions of binuclear cells in all five cell lines.
(A) The area of each nucleus in [µm²] was quantified using a semi-automated quantification with the ImageJ software and revealed shared nuclei sizes. **(B)** The fraction of binuclear cells was quantified for each cardiac differentiation that was used for immunofluorescence stains which allowed the validation of shared maturation states in all five cell lines. Data are shown as mean ± SEM together with each technical replicate (left) and biological replicate (right). ns p>0.05 using unpaired t-test calculated versus NC6M iPSC-CMs.

Taken together, with focus on morphological features we did not observe any differences regarding sarcomere-related protein diameters, nuclei areas, nucleation or cell shapes. The only difference was observed with regard to the CM sizes that proved to be reduced in all mutant conditions.

3.7 Investigation of mitochondrial structures in CMs

Initial findings regarding mitochondrial contents pointed out abnormities in DCMA-associated mutant iPSC-CMs that yield reduced mitochondrial masses on MitoTracker-based immunofluorescence staining. As at this point changes in mitochondrial structures were recognized already, higher magnifications were processed to visualize mitochondrial network morphology. Moreover, ultrastructural analyses were performed to assess mitochondrial abnormities in more detail by transmission electron microscopy (TEM).

3.7.1 Fragmentation of the mitochondrial network in DCMA mutants

NC6M and NC47F iPSC-CMs showed a recognizable lumenal mitochondrial network with dense mitochondrial clusters in the perinuclear region. Both healthy controls displayed long tubular mitochondrial structures with bi-directional alignment and a clear colocalization of DNAJC19 with mitochondrial networks (Fig. 3.32 a, b, e, f). In fact, contrary to the healthy control conditions all three mutant lines displayed abnormities regarding mitochondrial network morphology (Fig. 3.32 i-k, m-o, q-s). Representative images of DNAJC19tv iPSC-CMs demonstrated aggregated and fragmented mitochondrial structures that were accompanied by a loss of tubular connected mitochondrial networks as well as the absence of mitochondria-related DNAJC19 signals (Fig. 3.32 i-l). Similar observations were made with regard to DCMAP1 iPSC-CMs with the exception of DNAJC19-positive labelling on the cell-cell-contact-associated edges (Fig. 3.32 m-p). Moreover, DCMAP2 iPSC-CMs showed the same changes in mitochondrial morphology and to higher degrees a diffuse signal that referred to thinner not clearly distinguishable mitochondrial structures (Fig. 3.32 q-t). In all five cell lines mitochondria were

densely packed in the perinuclear areas, thus hindering clear morphological visualizations by confocal microscopy at that subcellular compartment (Fig. 3.32 a, e, l, m, q).

Taken together, DCMA iPSC-CMs demonstrated increased fragmentation of mitochondrial structures that was accompanied by a shared loss of the colocalization of DNAJC19 signal with mitochondrial membranes.

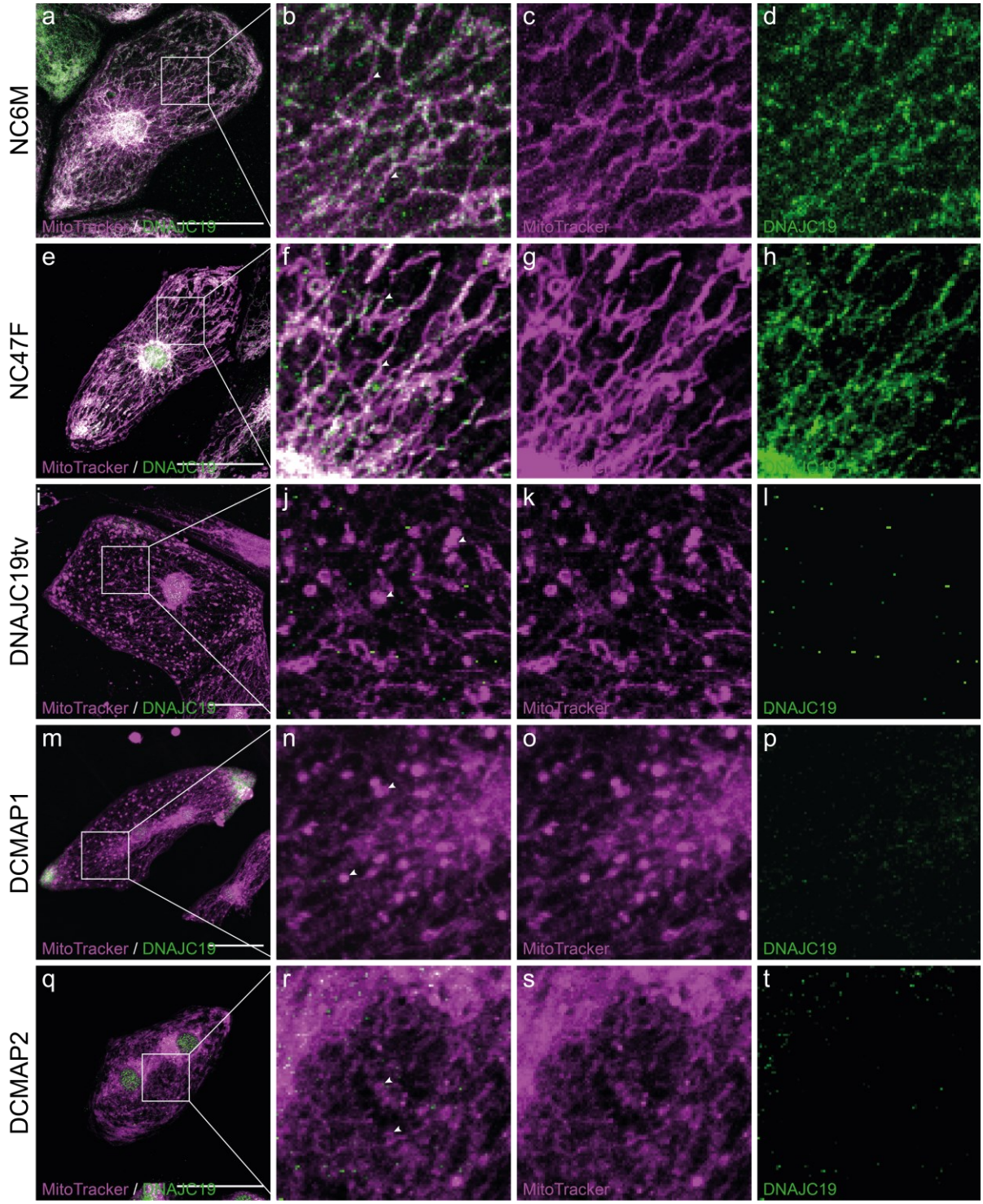

Figure 3.32 Localization analysis of DNAJC19 in DCMA cell lines.
Immunofluorescence co-staining of MitoTracker (magenta) and DNAJC19 (green) showed a co-localization of DNAJC19 with mitochondrial structures as well as a nuclear expression in healthy iPSC-CMs (NC6M, NC47F). All three mutant iPSC-CM lines showed a remaining nuclear DNAJC19 signal. DNAJC19tv, DCMAP1 and DCMAP2 displayed a loss of colocalization of DNAJC19 with mitochondria and fragmentation and aggregation of mitochondrial structures. Scale bar = 50 µm, *Arrows* indicate mitochondrial structures

3.7.2 Ultrastructural analyses revealed smaller mitochondria with equal shapes

As the overall mitochondrial network morphology is dynamically controlled by a balance of mitochondrial fusion and fission, we assumed that this process may be disrupted in DCMA-associated CMs due to the presence of aggregated mitochondrial structures. To analyze this potential pathomechanism, TEM images were acquired to investigate mitochondrial sizes and shapes on the ultrastructural level. Images were selected according to the presence of sarcomeres which was used as internal control to validate cardiomyocyte-associated phenotypes. NC47F mitochondria are depicted in a representative image to display mitochondrial morphology and distribution of healthy control iPSC-CMs (Fig. 3.33 A, a). NC47F iPSC-CMs demonstrated intermyofibrillar mitochondria with a clearly visible cristae lumen and densely packed mitochondrial matrix that complemented to a regular cristae pattern (Fig. 3.33 A, a). On the contrary, all mutant iPSC-CMs displayed smaller mitochondria with the absence of clearly identifiable cristae as depicted in DNAJC19tv and DCMAP2 iPSC-CMs (Fig. 3.33 A, b-d). In some cases, some tubular mitochondria were still present as illustrated in DCMAP1 that was accompanied by decreased cristae content and brighter matrix areas (Fig. 3.33 A, c). With regard to mitochondrial shapes, we did not observe remarkable changes. Moreover, the visual determination of sarcomeres revealed similar sarcomere structures owing to the alignment and the presence of Z-lines, A-, I-bands and M-bands in all five cell lines (Fig. 3.33 A).

Next, TEM images were used to manually determine mitochondrial sizes and morphologies using ImageJ software with the following parameters: mitochondria areas [μm^2], mitochondria perimeter [µm], mitochondria feret´s diameter [µm], circularity [0-1], roundness [0-1] and solidity [0-1]. Mitochondrial areas (μm^2) and the circularity are depicted and the remaining parameters can be found in the supplementary Fig. 5.9 (details supplementary Tab. 5.21). Notably, healthy control iPSC-CM mitochondria showed equal sizes as NC6M mitochondria had the size of 0.355 ± 0.01 μm^2 and NC47F had the size of 0.371 ± 0.03 μm^2 (unpaired t-test NC6M vs. NC47F ns, p=0.7140) (Fig. 3.33 B). On the contrary, the quantification of DNAJC19tv-derived iPSC-CMs revealed mitochondria of 0.24 ± 0.01 μm^2 in size, that were significantly reduced after statistical analysis compared to the control (NC6M vs. DNAJC19tv ****, p<0.0001) (Fig. 3.33 B). The same abnormity was observed in both patient-derived iPSC-CMs by displaying an average mitochondrial size of 0.140 ± 0.004 μm^2 in DCMAP1 and 0.174 ± 0.003 μm^2 in DCMAP2 (NC6M vs. DCMAP1 ****, p<0.0001; NC6M vs. DCMAP2 ****, p<0.0001) (Fig. 3.33 B). Regarding the mitochondrial morphology, circularity levels were compared between all five conditions. NC6M displayed mitochondria of 0.57 ± 0.004 circularity that was similar to NC47F with 0.58 ± 0.0015 circularity (unpaired t-test NC6M vs. NC47F ns, p=0.4723) (Fig. 3.33 C). Equal shapes were also observed in DNAJC19tv with 0.56 ± 0.0094 and 0.57 ± 0.006 in DCMAP1 (unpaired t-test NC6M vs. DNAJC19tv ns, p=0.5975; NC6M vs. DCMAP1 ns, p=0.6538) (Fig. 3.33 C). Notably, DCMAP2 was the only condition that revealed significantly higher circularities with 0.628 ± 0.02 (unpaired t-test NC6M vs. DCMAP2 ****, p<0.0001) (Fig. 3.33 C).

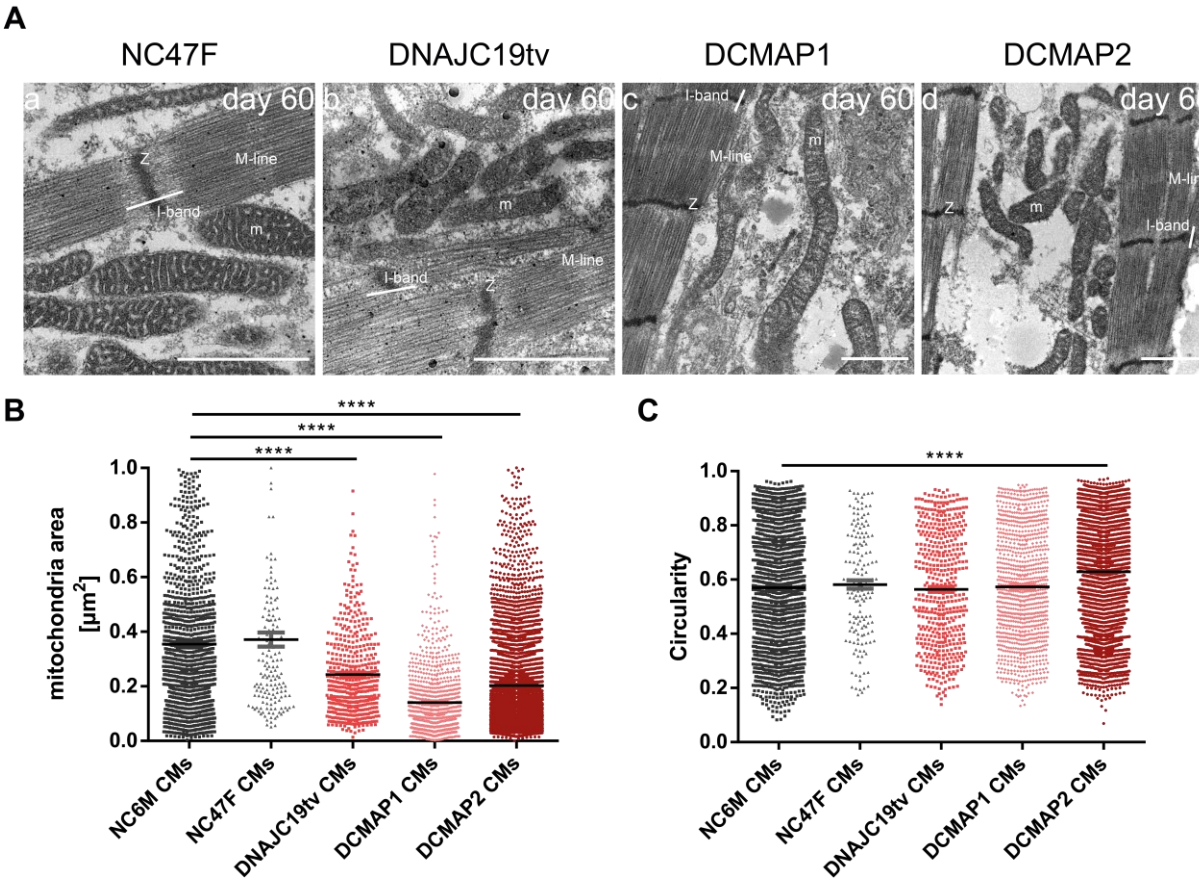

Figure 3.33 TEM images displayed smaller mitochondria but shared morphology parameters in DCMA-associated mutant iPSC-CMs
(A) Representative TEM images are depicted for the healthy control NC47F **(a)** and three DNAJC19 mutant iPSC-CMs lines **(b)** DNAJC19tv, **(c)** DCMAP1 and **(d)** DCMAP2. The presence of sarcomere-associated M- and Z-lines (Z), A- and I-bands together with intermyofibrillar mitochondria (m) enabled the internal validation of CMs during TEM analysis without the presence of obvious structural abnormities in all depicted four conditions. Smaller mitochondria were visually observed in some cases. TEM images were quantified using ImageJ software to assess mitochondrial areas in [µm^2] **(B)** and mitochondria shapes by circularity assessment [0-1] **(C)**. The TEM quantifications revealed equal shapes but smaller mitochondria in all mutant iPSC-CMs wherein DCMAP1 displayed the smallest areas. Data are shown as mean ± SEM together with each technical replicate. **** $p<0.0001$, ns $p>0.05$ using unpaired t-test calculated versus NC6M iPSC-CMs. Scale bars = 1 µm

3.7.3 Abnormal cristae structures and densities in DCMA cell lines

TEM pictures of higher magnification were further examined to investigate cristae shapes in more detail. Two pictures are depicted for each cell line to illustrate different observations. NC47F mitochondria were representative for the healthy condition by displaying a regular pattern of parallel organized cristae with equal cristae lumen and a densly packed mitochondrial matrix (Fig. 3.34 a, e). On the contrary, DNAJC19tv mitochondria displayed abnormally shaped cristae that were either collapsed or bulked (Fig. 3.34 b, f). The regular cristae pattern was absent and overall less cristae were observed that was accompanied by a less densely packed matrix (Fig. 3.34 b, f). DCMAP1 and DCMAP2 presented abnormal mitochondrial cristae to a similar extent, less cristae per mitochondrion and the invaginations of the IMM were not clearly distinguishable (Fig. 3.34 c, d, g, h). All mutant iPSC-CMs displayed the presence of disarrayed mitochondrial cristae, local mitochondrial swelling and dissolved mitochondrial structures (Fig. 3.34 b-d, f-h). Moreover, in particular DCMAP1 showed a tendency to higher fractions of non-identifiable cristae structures (Fig. 3.34 c, g). All mutant conditions displayed higher numbers of mitochondria with dissolved membrane structures (Fig. 3.34 b-d, f-h).

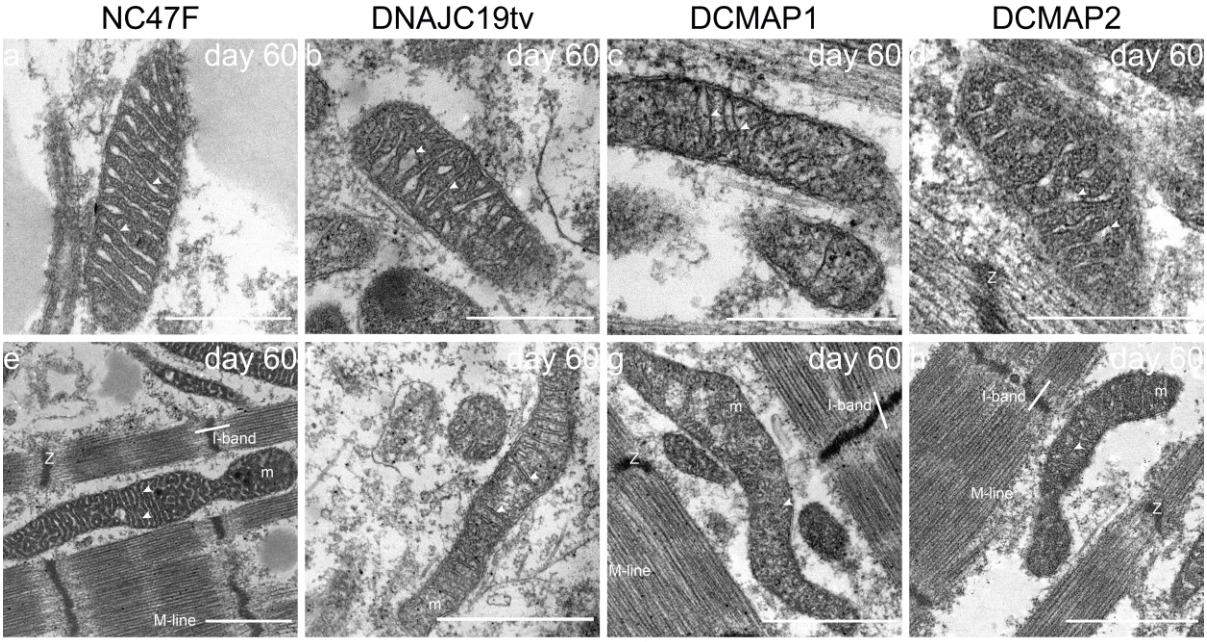

Figure 3.34 Higher magnifications of TEM images displayed abnormal invaginations of the IMM and a smaller number of cristae per mitochondrion in mutant cells.
Two representative TEM images are depicted for each condition, comprising the healthy control NC47F **(a, e)** and three DNAJC19 mutant iPSC-CMs lines DNAJC19tv **(b, f)**, DCMAP1 **(c, g)** and DCMAP2 **(d, h)**. A regular cristae pattern was observed in healthy mitochondria **(a, e)** accompanied by a dense matrix and shared cristae morphologies across the whole mitochondrion. On the contrary, DNAJC19tv **(b, f)**, DCMAP1 **(c, g)** and DCMAP2 **(d, h)** displayed abnormally shaped cristae with irregular cristae pattern and higher degrees of dissolved cristae membranes in all mutant conditions. *Z* Z-lines; *m* intermyofibrillar mitochondria; *Arrows* indicate cristae invaginations of the IMM; (a-d) 1st row scale bars = 0.5 µm; (e-h) 2nd row scale bars = 1 µm

In summary, we observed fundamental structural differences regarding cristae morphologies, distribution, densities as well as reduced mitochondrial sizes in DCMA mutant iPSC-CMs when compared to healthy conditions.

3.8 Mitochondrial phospholipid analysis unraveled an abnormal CL acyl chain composition

The observed abnormities regarding the cristae provide a direct link towards the phospholipid composition of the mitochondrion. Therefore, mass spectrometric analyses of *in vitro* derived iPSC-CMs on day 60 were performed to investigate phospholipid changes of the IMM especially with regard to the phospholipid CL (Fig. 3.35, details supplementary Tab. 5.22). CL profiles were assessed by calculating two parameters, the acyl chain length (A) and the amount of double bonds (B) (Fig. 3.35). Solely preliminary data of one control condition NC6M and one mutant condition DCMAP2 was acquired (Fig. 3.35). The highest peak regarding the acyl chain length was 74 carbon atoms in healthy iPSC-CMs and higher chain lengths were accompanied by decreased intensities (Fig. 3.35 A). On the contrary, DCMAP2 mutant iPSC-CMs displayed two main peaks at 76 and 80 carbon atoms underlining a tendency towards longer acyl chains in DCMA-cells (Fig. 3.35 A). Regarding the presence of double bonds, healthy cells did mainly display three double bonds, whereas double bonds above nine were rarely seen (Fig. 3.35 B). When investigating DCMAP2 CLs, the amount of double bonds was overall higher than in control cells with the highest abundance of eight double bonds (Fig. 3.35 B). In brief, our preliminary data showed a tendency towards altered CL composition and structures in DNAJC19 mutant iPSC-CMs.

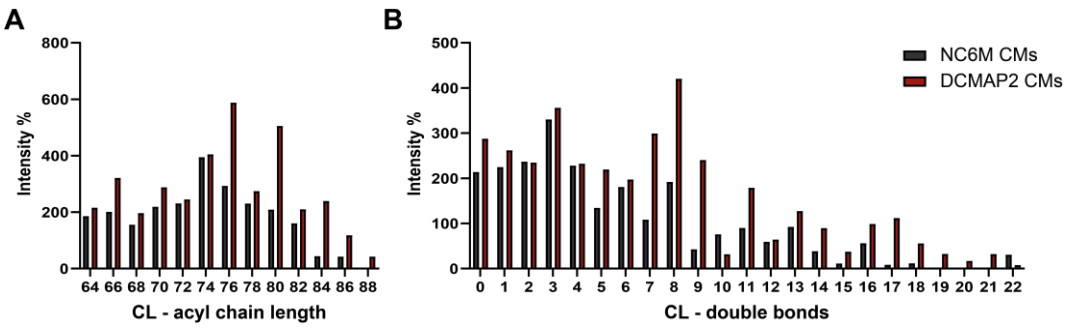

Figure 3.35 Indications of impaired CL remodeling in DCMAP2 iPSC-CMs.
Mass spectrometric analysis of CL profiles in DCMAP2 iPSC-CMs showed an increase in acyl chain length **(A)** and higher abundance of double bonds **(B)**, demonstrating a shift towards polyunsaturated FA upon preliminary analysis.

3.9 ETC complexes in mitochondrial function

To assess mitochondrial dysfunctions, we performed metabolic flux analysis using the Seahorse XF96 extracellular flux analyzer. Proton excretion (glycolysis) and cellular oxygen consumption (OXPHOS) cause rapid recognizable changes in the surrounding medium and change the concentrations of oxygen ions and free protons in the transient microchamber (Fig. 3.36). These alterations can be measured within seconds by a solid-state sensor that resides 200 µm above the cell monolayer. The seahorse system measures the concentration of the OCR and ECAR for each well individually in a time frame of 3-5 min allowing the simultaneous investigation of the two major energy pathways to quantitatively assess the bioenergetic states of viable cells. ECAR represents the rate of glycolysis through medium acidification due to lactate production and OCR corresponds to OXPHOS activities. Both parameters were acquired simultaneously on viable dermal fibroblasts, iPSCs and iPSC-CMs on day 60 after additional MACS. The standard Mito Stress Test Assay was performed using three different treatments following the quantification of the metabolic parameters under basal conditions including step-wise injections of 1 µM oligomycin, 1 µM FCCP and 0.5 µM rotenone/antimycin A (all cell types) (Fig. 3.36). Oligomycin was able to block the proton channel (F_o subunit) of the ATP synthase hindering the re-phosphorylation of ADP into ATP (Fig. 3.36). Therefore, the reduction of the oxygen consumption could be directly linked to the ATP synthase activity. As a consequence, the cell was forced to activate glycolysis to generate ATP that was recognized by elevated ECAR rates (Fig. 3.36). In the next step the ionophore FCCP was added that acts as an uncoupling agent that disrupts the mitochondrial membrane potential by allowing the diffusion of protons (hydrogen ions) into the mitochondrial matrix (Fig. 3.36). The increased concentrations of hydrogen ions in the matrix enhanced the ETC activity to work on maximum, that could be trailed by elevated OCRs (Fig. 3.36). Afterwards a combination of rotenone together with antimycin A was added to inhibit complex I and III simultaneously that hindered the electron donation between the complexes and abolished the ETC function completely (Fig. 3.36). The residual oxygen consumption corresponded to non-mitochondrial oxygen consumption (Fig. 3.36). Moreover, additional parameters like proton leakage and spare respiratory capacity were calculated as depicted in the Mito Stress Assay scheme Fig. 3.36. Mitochondrial function was assessed in human skin fibroblasts (Fig. 3.37, 3.38), iPSCs (Fig. 3.39, 3.40) and iPSC-CMs (Fig. 3.41, 3.42) using comparable protocols. The diagrams of all cell lines individually are shown as individual mean ± SEM (NC6M, NC47F, DNAJC19tv, DCMAP1, DCMAP2) and as collection (healthy vs. DCMA). Cells were seeded to equal viability numbers and were normalized after the measurement using crystal violet staining (OD_{595nm}).

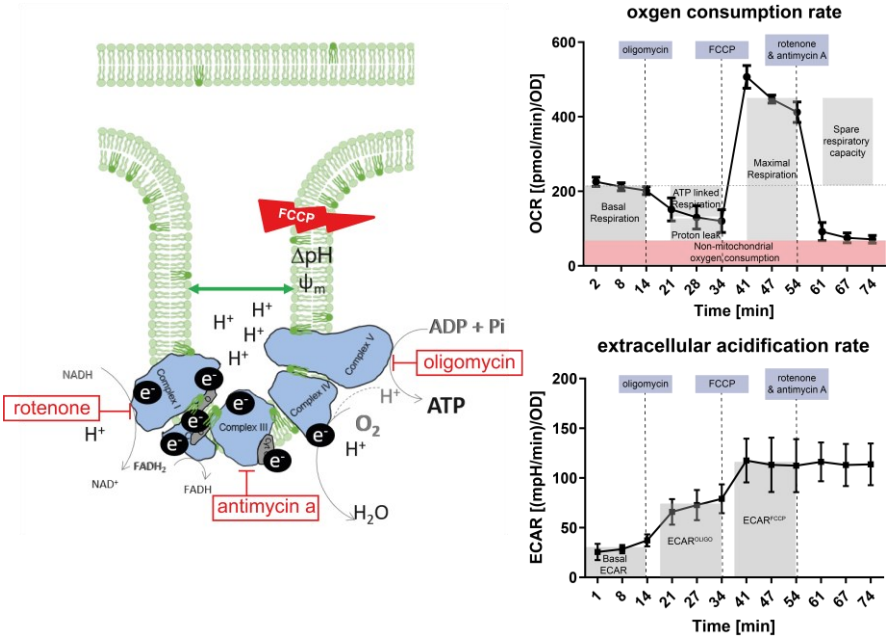

Figure 3.36: Quantification of the OCR and the ECAR on viable iPSC-CMs with the Seahorse XF96 extracellular flux analyzer.
The assessment of mitochondrial function was determined based on the OCR of viable iPSC-CMs followed by the specific inhibition of the ATP synthase (complex V) via oligomycin. In the next step FCCP was used as uncoupling agent of the mitochondrial membrane and lastly the respiratory chain complex inhibitors rotenone & antimycin A were added. The diagram was adapted after the publication of Ferrick et al., 2008. The ECAR was assessed simultaneously to gain additional information about the utilization of glucose via glycolysis under stress conditions.

3.9.1 Increased oxygen consumption in dermal fibroblasts of DCMA patients

First, OCR and ECAR were analyzed in adherent dermal fibroblasts, 24 hours after seeding in the Seahorse XF96 Cell Culture Microplate according to the appropriate protocol. Two healthy conditions (NC6M, NC47F) and both patient-derived dermal fibroblasts (DCMAP1, DCMAP2) were used (Fig. 3.37). We observed a tendency towards higher OCRs in both mutants, that was significantly increased in DCMAP1 (two-way ANOVA NC6M vs. NC47F ns, p=0.4343; NC6M vs. DCMAP1 *, p=0.0254; NC6M vs. DCMAP2 ns, p=0.1890) (Fig. 3.37 a). The comparison of healthy versus DCMA conditions as well revealed overall higher OCRs to a more significant extent (two-way ANOVA healthy vs. DCMA **, p=0.0067) (Fig. 3.37 e). Next, all parameters: basal respiration, maximal respiration, respiratory capacity, ATP synthase-linked respiration, H^+ (proton) leakage and non-mitochondrial oxygen consumption were assessed (Fig. 3.37 b-d, f-h). In particular basal respiration was increased by ~1.43-fold which was statistically relevant (unpaired t-test healthy vs. DCMA **, p=0.0054) (Fig. 3.37 b). The remaining parameters did not show significant differences and unraveled a tendency to higher OCRs only (unpaired t-test healthy vs. DCMA: (c) maximal respiration: ns, p=0.0755, (d) spare respiratory capacity: ns, p=0.2510, (f) ATP production: ns, p=0.1527, (g) non-mitochondrial oxygen consumption: ns, p=0.1953, (h) proton leak: ns, p=0.0541) (Fig. 3.37 c, d, f-h).

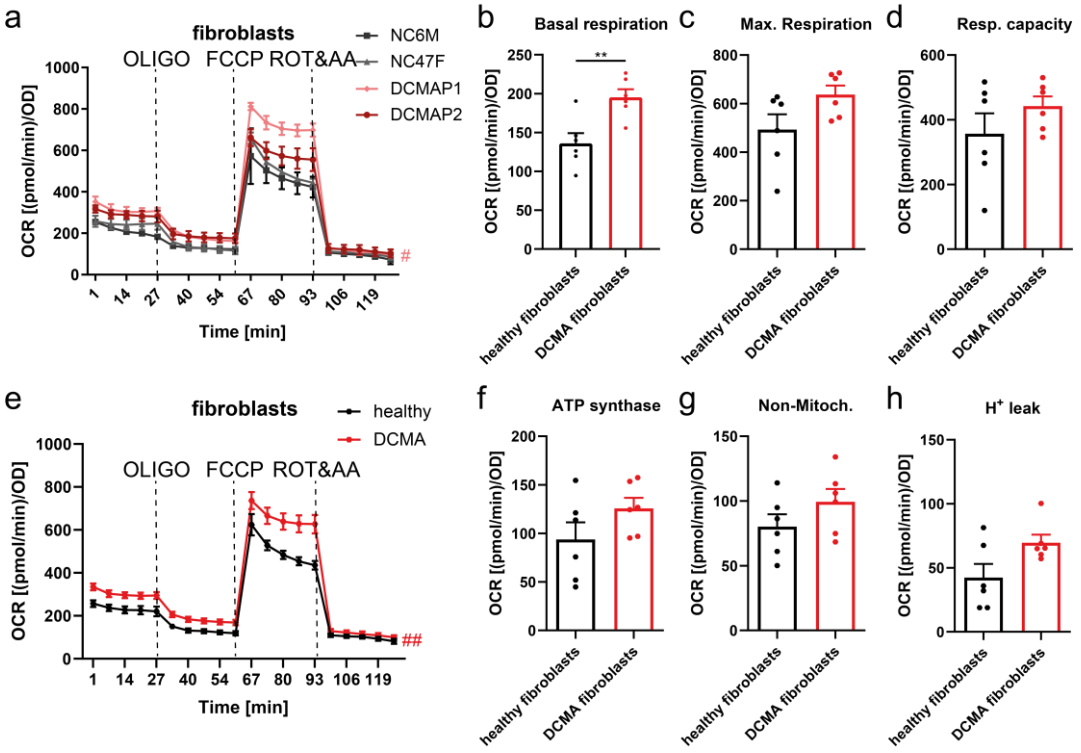

Figure 3.37 OCRs of mitochondria were increased in patient-derived fibroblasts.
(a, e) The OCR of dermal fibroblasts were measured in the presence of 1 µM FCCP, 1 µM oligomycin and 0.5 µM rotenone/antimycin A with the Seahorse XF96 extracellular flux analyzer. Two healthy controls (NC6M, NC47F) and two DCMA-patient (DCMAP1, DCMAP2) conditions are displayed individually **(a)** or in groups **(e)**. **(b, c, d, f, g, h)** Six different parameters were calculated to assess ETC function on five measured timepoints per condition from three independent cultures in 18-23 technical replicates (18-23 wells/condition). Data are represented as mean ± SEM together with each biological replicate for each group (according to (a) genotype or (b-h) grouping of healthy or DCMA-associated genotypes, boxes). ## p<0.01, # p<0.05, ns p>0.05 using regular two-way ANOVA calculated versus NC6M **(a)** or healthy control CMs **(b)**, ** p<0.01, ns p>0.05 using unpaired t-test calculated versus healthy control iPSC-CMs.

The attempt to monitor the glycolytic rate is based on the determination of the extracellular space acidity which in turn is based on the assumption that the enzymatic processing of the uncharged glucose or glycogen into lactate$^-$ + H^+ is the main source of acidification. The ECAR rates of healthy control fibroblasts were equal to the rate of DCMA-associated fibroblasts (two-way ANOVA healthy vs. DCMA ns, p=0.8871) (Fig. 3.38 a). Moreover, we did not observe any differences regarding basal ECAR rates (unpaired t-test healthy vs. DCMA ns, p=0.3992), oligomycin-induced ECARs (unpaired t-test healthy vs. DCMA ns, p=0.6538) and FCCP-mediated ECARs (unpaired t-test healthy vs. DCMA ns, p=0.3500) (Fig. 3.38 b-d).

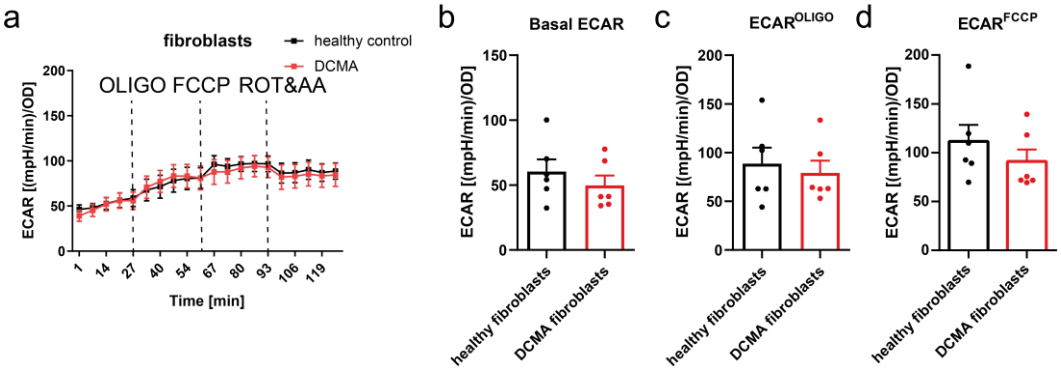

Figure 3.38 The ECAR was equal between healthy and DCMA fibroblasts.
The seahorse system allowed the quantification of changed levels of extracellular hydrogen ions (H^+) that was calculated in a certain time frame to evaluate the ECAR. Three different parameters were calculated to assess ETC function on five measured timepoints per condition from three independent cultures in 18-23 technical replicates (18-23 wells/condition). **(a)** The overall ECAR trend was similar. **(b)** Basal ECAR without any treatment, **(c)** ECAR upon oligomycin treatment and **(d)** FCCP-mediated ECAR. Data are represented as mean ± SEM together with each biological replicate for each group (according to healthy or DCMA-associated genotypes, boxes). ns>0.05 using regular two-way ANOVA calculated versus healthy fibroblasts, ns>0.05 using unpaired t-test calculated versus healthy fibroblasts.

3.9.2 Enhanced oxygen turnover without alterations in extracellular acidification in mutant iPSCs

The same procedure was performed using all five iPSC lines and their grouping according to healthy or DCMA-associated genotypes (Fig. 3.39). Regarding oxygen consumption we observed a similar trend as in dermal fibroblasts, wherein DCMAP1 was the only cell line to show a significantly elevated OCR (two-way ANOVA NC6M vs. NC47F ns p=0.0751; NC6M vs. DNAJC19tv ns, p=0.1402; NC6M vs. DCMAP1 **, p=0.0042; NC6M vs. DCMAP2 ns, p=0.2040) (Fig. 3.39 a, e). The comparison of all healthy versus all mutant conditions displayed increased OCR with a decreased significance (two-way ANOVA healthy vs. DCMA *, p=0.0485) (Fig. 3.39 e). The analysis of the individual parameters showed significantly elevated OCRs under basal conditions only, whereas the remaining parameters were not significantly changed (unpaired t-test healthy vs. DCMA: (b) basal respiration: **, p=0.0063, (c) maximal respiration: ns, p=0.1966, (d) spare respiratory capacity: ns, p=0.2623, (f) ATP production: ns, p=0.4955, (g) non-mitochondrial oxygen consumption: ns, p=0.7843, (h) proton leak: ns, p=0.6736) (Fig. 3.39 b-d, f-h).

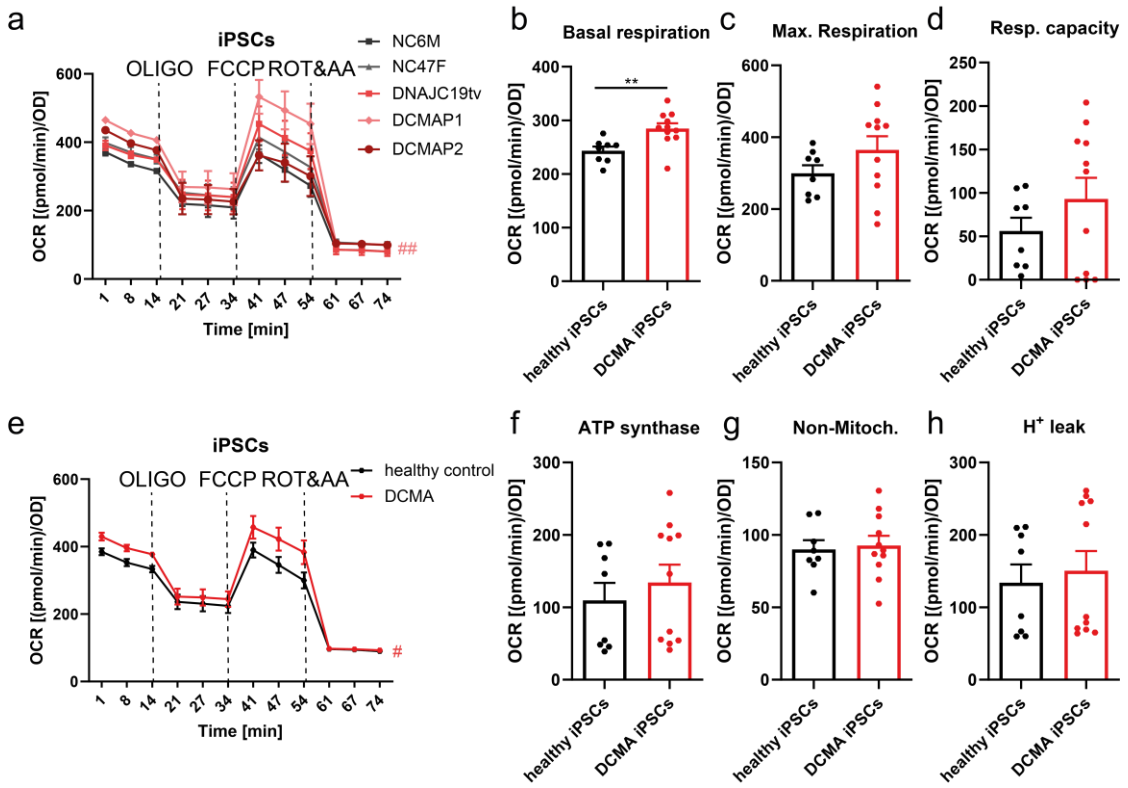

Figure 3.39 Increased OCRs in iPSCs with strongest phenotype in DCMAP1 iPSCs.
(a, e) OCRs of iPSCs during standard measurement of the Mito Stress Test Assay with different substrates (1 µM FCCP, 1 µM oligomycin and 0.5 µM Rotenone/Antimycin A) using the Seahorse XF96 extracellular flux analyzer. Two healthy control (NC6M, NC47F) and three DCMA-associated mutant (DCMAP1, DCMAP2) iPSC lines are shown individually **(a)** or collected in groups **(e)**. **(b, c, d, f, g, h)** Six different parameters were calculated to assess ETC function on three measured timepoints per condition from four to five independent cultures in 16-19 technical replicates (16-19 wells/condition). Data are represented as mean ± SEM together with each biological replicate for each group (according to (a) genotype or (b-h) grouping of healthy or DCMA-associated genotypes, boxes). ## $p<0.01$, # $p<0.05$, ns $p>0.05$ using regular two-way ANOVA calculated versus NC6M **(a)** or healthy control CMs **(b)**, ** $p<0.01$, ns $p>0.05$ using unpaired t-test calculated versus healthy control iPSC-CMs.

The ECAR rates of healthy control iPSCs were equal to the rate of DCMA-associated iPSCs (two-way ANOVA healthy vs. DCMA ns, p=0.0850) (Fig. 3.40). In particular after oligomycin treatment, we observed increased ECARs, however this shift is similar in DCMA and healthy control iPSCs, indicating no differences regarding glucose utilization after assessment of basal ECAR rates (unpaired t-test healthy vs. DCMA ns, p=0.7981) and oligomycin-induced ECAR rates (unpaired t-test healthy vs. DCMA ns, p=0.8505) (Fig. 3.40 a-c). Furthermore, FCCP-treated iPSCs did not display significantly elevated extracellular acidification levels when comparing mutant and control iPSCs (unpaired t-test healthy vs. DCMA ns, p=0.3221) (Fig. 3.40 d).

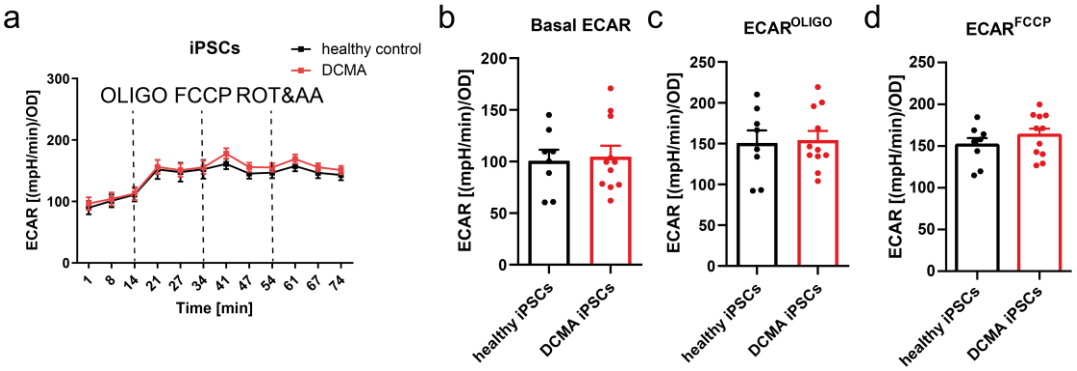

Figure 3.40 The ECAR of iPSCs did not reveal any differences regarding the utilization of glucose.
The quantification of changed levels of extracellular hydrogen ions (H^+) via the quantification of the ECAR using the Seahorse XFe96 system revealed overall equal ECAR trends, without changes regarding basal ECARs and ECARs upon oligomycin or FCCP treatment. Three different parameters were calculated to assess ETC function on three measured timepoints per condition from four to five independent cultures in 16-19 technical replicates (16-19 wells/condition). Data are represented as mean ± SEM together with each biological replicate for biological replicate for each group (according to healthy or DCMA-associated genotypes, boxes). ns>0.05 using regular two-way ANOVA calculated versus healthy control iPSCs, ns>0.05 using unpaired t-test calculated versus healthy control iPSCs.

3.9.3 Elevated oxygen consumption and extracellular acidification rates in DCMA iPSC-CMs

As iPSC-CMs possess the highest biomass of mitochondria, the Mito Stress Test Assay was performed as well (details supplementary Tab. 5.23). Compared to healthy iPSC-CMs (NC6M, NC47F) all three mutant cell lines (DNAJC19tv, DCMAP1, DCMAP2) showed overall highly significantly elevated OCRs (two-way ANOVA NC6M vs. NC47F ns, p=0.6746; NCM vs. DNAJC19tv ***, p=0.0003; NC6M vs. DCMAP1 **, p=0.0023; NC6M vs. DCMAP2 **, p=0.0036) (Fig. 3.41 a). The comparison of all mutant versus all healthy conditions revealed highly elevated OCRs after statistical analysis (two-way ANOVA healthy vs. DCMA ****, p<0.0001) (Fig. 3.41 e). With regard to basal respiration, a ~1.69-fold increase was observed when comparing mutant with healthy cells (unpaired t-test healthy vs. DCMA basal respiration: ****, p<0.0001) (Fig. 3.41 b). The maximum respiratory capacity likewise was significantly enhanced in DCMA-associated iPSC-CMs (unpaired t-test healthy vs. DCMA maximal respiration: **, p=0.0023) (Fig. 3.41 c). We did not observe remarkable changes regarding H^+ leakage and respiratory capacities as only a tendency to higher rates was observed (unpaired t-test healthy vs. DCMA proton leak: ns, p=0.0594, spare respiratory capacity: ns, p=0.0669) (Fig. 3.41 d, h). Notably, increased amount of oxygen is consumed with regards to ATP-linked respiration in mutant iPSC-CMs (unpaired t-test healthy vs. DCMA ATP production: **, p=0.0020) (Fig. 3.41 f). Unexpectedly, concerning non-mitochondrial oxygen consumption, also significant OCRs were observed in DCMA iPSC-CMs (unpaired t-test healthy vs. DCMA non-mitochondrial oxygen consumption: ***, p=0.0006) (Fig. 3.41 g).

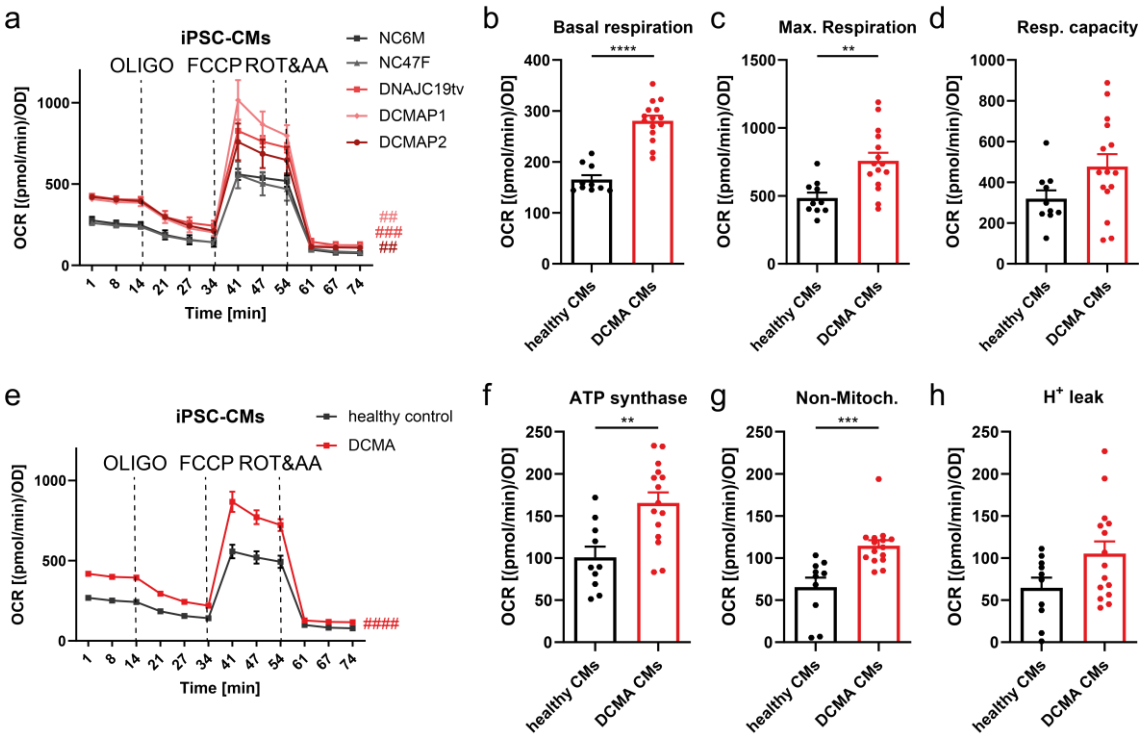

Figure 3.41 Elevated OCRs in iPSC-CMs with significant increases in ETC-linked processes in DCMA mutants. **(a, e)** The OCR of iPSC-CMs on day 60 was analyzed ~10 days after MACS sorting. The standard Mito Stress Test Assay was performed with different substrates (1 µM FCCP, 1 µM oligomycin and 0.5 µM Rotenone/Antimycin A) using the Seahorse XF96 system. Two healthy control (NC6M, NC47F) and three DCMA-associated mutant (DCMAP1, DCMAP2) iPSC-CMs lines were analyzed and are depicted individually **(a)** or collected in groups **(e)**. **(b, c, d, f, g, h)** Six different parameters were calculated to assess ETC function on three measured timepoints per condition from four to five independent cultures in 16-23 technical replicates (16-23 wells/condition). Data are represented as mean ± SEM together with each biological replicate for each cell line (according to (a) genotype or (b-h) grouping of healthy or DCMA-associated genotypes, boxes). #### p<0.0001, ### p<0.001, ## p<0.01 using regular two-way ANOVA calculated versus NC6M **(a)** or healthy control CMs **(b)**, **** p<0.0001, *** p<0.001, ** p<0.01, * p<0.05, ns p>0.05 using unpaired t-test calculated versus healthy control iPSC-CMs.

The energy generation of iPSC-CMs mainly relies on mitochondrial OXPHOS, whereas glucose is utilized primarily under stress conditions. The capacity to use glucose as a substrate was determined by the quantification of the ECAR (details supplementary Fig. 5.10). We observed significantly increased ECARs in DCMA iPSC-CMs during the whole measurement (two-way ANOVA healthy vs. DCMA ####, p<0.0001) (Fig. 3.42 a). The examination of the ECARs of healthy control versus DCMA-associated iPSC-CMs displayed a significant increase in extracellular acidification by ~50 % (unpaired t-test healthy vs. DCMA *, p=0.0146) (Fig. 3.42 b). Upon oligomycin treatment, OXPHOS-based ATP synthesis was completely interrupted, forcing the iPSC-CMs to maximize their ability to utilize glucose. Regarding the oligomycin-induced ECARs, highly significantly increased extracellular hydrogen ion concentrations were observed in DCMA iPSC-CMs (unpaired t-test healthy vs. DCMA ***, p=0.0004) (Fig. 3.42 c). Furthermore, FCCP-mediated collapse of the proton gradient across the IMM significantly maximized ECARs of mutants when compared to healthy control iPSC-CMs (unpaired t-test healthy vs. DCMA ***, p=0.0006) (Fig. 3.42 d).

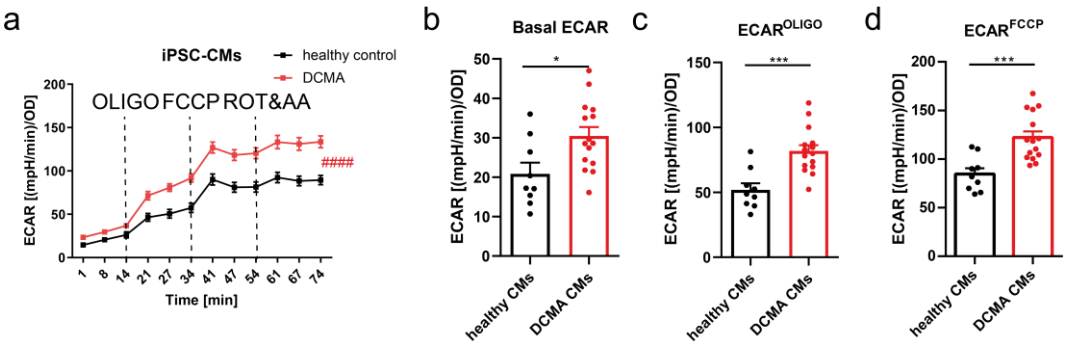

Figure 3.42: DCMA iPSC-CMs demonstrated increased ECARs, basal, upon oligomycin and FCCP treatment.
The changes of the extracellular flux traces of H^+ of *in vitro*-derived 60 days aged and MACS-sorted iPSC-CMs were quantified during the Mito Stress Test Assay using the Seahorse XFe96 system. Two different parameters were calculated to assess glycolysis switch on three measured timepoints per condition from four to five independent cultures in 16-23 technical replicates (16-23 wells/condition). **(a)** ECARs over time allowed insights into overall increased extracellular acidification in DCMA iPSC-CMs. **(b)** Basal ECARs, **(c)** oligomycin-induced and **(d)** FCCP-mediated ECARs indicated higher flux traces of H^+ in DCMA iPSC-CMs. Data are represented as mean ± SEM together with each biological biological replicate for each group (according to healthy or DCMA-associated genotypes, boxes). #### p<0.0001 using regular two-way ANOVA calculated versus healthy control CMs and *** p<0.001, * p<0.05 using unpaired t-test, calculated versus healthy control CMs.

Taken together, excess oxygen consumption was observed in less mitochondrial content cell types (dermal fibroblasts, iPSCs) as well as in high mitochondrial content cell types (iPSC-CMs) to more enhanced levels in all mutant conditions but with aggreviated features in particular in DCMAP1. Elevated ECARs were observed in DNAJC19 mutant iPSC-CMs only, thus providing a link towards altered metabolic features in DCMA iPSC-CMs.

3.10 Impact of mitochondrial dysfunction on cellular injury

3.10.1 The assessment of substrate utilization revealed a metabolic shift towards reduced fatty acid uptake in DCMA

To assess metabolic features of *in vitro*-derived 60-day-old iPSC-CMs, double radioactive tracer uptakes were performed to simultaneously measure glucose and FA metabolism by quantification of the cellular uptake of ^{18}F-FDG (^{18}F-2-fluoro-2-deoxy-d-glucose) and ^{125}I-BMIPP (^{125}I-β-methyl-iodo-phenyl-pentadecanoic acid) respectively (Fig. 3.43, details supplementary Tab. 3.48). In total five to six biological replicates were examined using the counts per minute (CPM) values of the γ counter measured on MACS-sorted iPSC-CMs lysates that were normalized to the protein content using the BCA Protein Assay. The cellular uptake of each radioactively labelled tracer was normalized towards the cellular uptakes of the NC6M control. The calculation of the individual radioactive tracer uptake index was displayed as mean ± SEM. NC47F demonstrated equal uptake ranges regarding both 1.08 ± 0.09-fold of ^{18}F-FDG and 0.96 ± 0.07-fold of ^{125}I-BMIPP the NC6M control (^{18}F-FDG paired t-test NC6M vs. NC47F ns, p=0.4296; ^{125}I-BMIPP paired t-test NC6M vs. NC47F ns, p=0.6343) (Fig. 3.43 A, B). The comparison of the three DNAJC19 mutants with healthy control iPSC-CMs revealed a shared reduction in the cellular uptake of ^{125}I-BMIPP that corresponds to FAs (Fig. 3.43 A). In detail, DNAJC19tv presented radioactive tracer ^{125}I-BMIPP uptake reduced to 0.65 ± 0.05-fold, DCMAP1 to 0.78 ± 0.07-fold and DCMAP2 to 0.40 ± 0.05-fold of the NC6M control (^{125}I-BMIPP paired t-test NC6M vs. DNAJC19tv ***, p=0.0010; NC6M vs. DCMAP1 *, p=0.0299; NC6M vs. DCMAP2 ****, p<0.0001) (Fig. 3.43 A). The cellular uptake of ^{18}F-FDG, representing glucose, revealed levels of 0.65 ± 0.07-fold in DNAJC19tv, 1.73 ± 0.19-fold in DCMAP1 and 0.85 ± 0.09-fold in DCMAP2 compared to NC6M iPSC-CMs (^{18}F-FDG paired t-test NC6M vs. DNAJC19tv **, p=0.0046; NC6M vs. DCMAP1 *, p=0.0197; NC6M vs. DCMAP2 ns, p=0.1959) (Fig. 3.43 B).

DCMA iPSC-CMs overall displayed decreased FA uptake that was accompanied by enhanced glucose uptake in one patient cell line only, whereas both other mutant conditions showed even reduced glucose uptake underlining a shift towards the utilization of other substrates.

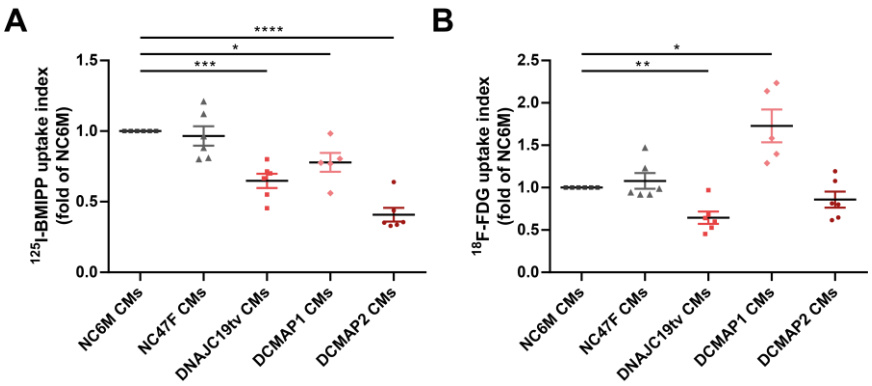

Figure 3.43: Double radioactive tracer uptakes revealed decreased FA uptake (^{125}I-BMIPP) but discordant utilization of glucose (^{18}F-FDG).
MACS-sorted and at least 60 days *in vitro* aged iPSC-CMs were incubated with ^{18}F-FDG and ^{125}I-BMIPP to examine the cellular uptake of both tracers to evaluate glucose and FA utilization simultaneously by a γ counter. Data for each biological replicate (each box) were examined via calculation of the uptake index that was normalized to the protein content using BCA Protein Assay and additionally normalized to the uptake of the NC6M control. Data are represented as mean ± SEM together with each biological replicate (boxes). Each biological replicate consisted of two to four technical replicates that were examined based on five to six independent cultures. **(a)** DCMA iPSC-CMs displayed reduced uptake of ^{125}I-BMIPP to different degrees. **(b)** ^{18}F-FDG uptake was decreased in DNAJC19tv and DCMAP2, whereas it was increased in DCMAP1 only. **** p<0.0001, *** p<0.001, ** p<0.01, * p<0.05, ns p>0.05 using paired t-test calculated versus the normalized uptake index of NC6M iPSC-CM controls.

3.10.2 Arrhythmias, abnormal Ca^{2+} homeostasis and reduced contractility after assessment of single-cell DCMA iPSC-CMs

To establish the link between metabolic changes and mechano-energetic coupling processes, Ca^{2+} kinetics, contractility and arrhythmic potential were addressed in NC6M, DNAJC19tv, DCMAP1 and DCMAP2 iPSC-CMs using the IonOptix system. NC47F iPSC-CMs were not included as the minimum of three biological replicates was not fulfilled. The investigation of Ca^{2+} handling was performed on >120 days mattress-matured iPSC-CMs by ratiometric dye staining with Indo-1-AM (details supplementary Tab. 5.25). Indo-1-AM diffuses into viable CMs and in an unbound state it emits light of a wavelength of 405 nm, whereas the emissions spectrum shifts towards 485 nm upon Ca^{2+} binding. Therefore, the ratio between both wavelengths allowed to quantitatively assess intracellular Ca^{2+} concentration $[Ca^{2+}]_i$ (Fig. 3.44). As a simplification, the values of the emission spectra ratios of 405 nm over 485 nm are further referred to as Ca^{2+} concentrations $[Ca^{2+}]_c$. For example, stimulus-initiated Ca^{2+} influx to a maximum intracellular Ca^{2+} level is referred to as systolic Ca^{2+} whereas sufficient export to baseline is termed diastolic Ca^{2+} concentration (Fig. 3.44). Therefore, Ca^{2+} influx and efflux of single-cell iPSC-CMs could be visualized as transients (Fig. 3.44). Detailed investigation of efflux rates to monitor the relaxation times at 50 % ($RT_{50\%}$) and 90 % ($RT_{90\%}$) included detailed shape analysis by using formulas like single exponential tau (sin exp tau) that allowed further insights into Ca^{2+} kinetics. The additive edge-detection function enabled the simultaneous analysis of cell shortenings [µm] (Fig. 3.44). Moreover, Ca^{2+} kinetics and contractility were assessed under basal conditions in normal Tyrode (NT) as well as under stress conditions, that were induced by increased Iso concentrations (10 nM, 30 nM, 100nM) (Fig. 3.44). The analyzed values were included only if the survival of the respective iPSC-CM was ensured over the whole protocol, which was controlled by the ability stimulate CMs by 0.5 Hz or by the observation of an endogenous beating rhythm. If possible, all different cell lines were measured on the same day (minimum one healthy and one mutant iPSC-CMs line) to achieve an equal age as well as the same experimental conditions for each cell line to exclude unspecific environmental influences on the measurements. Each diagram depicts the mean of all experiments combined with the standard error of the mean (SEM). For statistical analysis regular two-way ANOVA was performed together with the Bonferroni post-test (details supplementary Tab. 5.25).

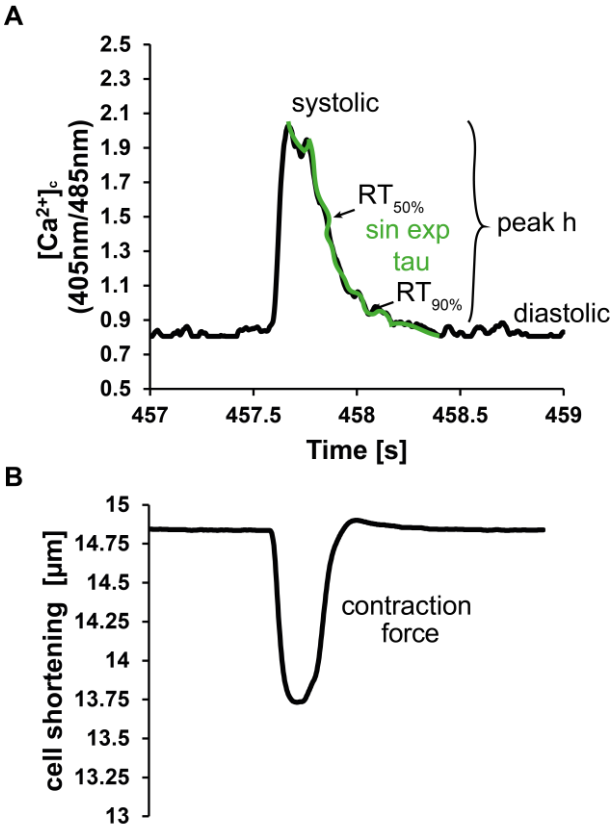

Figure 3.44: Illustration of Ca^{2+} homeostasis and contraction force in healthy NC6M iPSC-CMs to investigate physiological functions of iPSC-CMs with the IonOptix system.
(A) Ca^{2+} handling was quantified in healthy iPSC-CMs using the ratiometric dye Indo-1 AM. Ca^{2+} influx and efflux are shown in one representative Ca^{2+} transient to illustrate systolic and diastolic Ca^{2+} levels that were used to calculate the overall influx by analysis of the peak height h. Ca^{2+} efflux was analyzed at two different relaxation times: 50 % and 90 % as well as via sin exp tau evaluation. **(B)** Ca^{2+} influx resulted in the contraction of iPSC-CMs, that can be quantified simultaneously represented by cell shortening in µm using edge detection. *sin exp tau* single exponential tau

3.10.2.1 Enhanced beating frequencies in DNAJC19 mutants

The quantification of the contraction speed was performed by counting the occurrence of transients over a specific time span as frequency (1/sec) under NT, 10 nM, 30 nM and 100 nM Iso. In order to achieve a more defined set up and to allow a more detailed quantification of the frequency-dependent kinetics, iPSC-CMs were electrically stimulated with 100 mA over 0.5 s and a frequency of 0.5 Hz. Unexpectedly, most iPSC-CMs were not excitable and did not contract at all in the determined frequency of the electrical stimulation, thus allowing the assessment of endogenous contraction rhythms only.

On the first view, all DCMA conditions displayed overall enhanced frequencies (Fig. 3.45). Whereas NC6M iPSC-CMs were contracting at an average frequency of 0.41 ± 0.04 Hz, DNAJC19tv together with DCMAP2 showed an increased contraction speed with 1.02 ± 0.14 Hz and 0.79 ± 0.08 Hz respectively (Fig. 3.45). DCMAP1 revealed a similar behavior but with a slight increase by 0.51 ± 0.08 Hz at NT only (Fig. 3.45). Upon increased Iso concentrations we observed a tremendous gain in contraction speed especially in DNAJC19tv and DCMAP2 iPSC-CMs. Revisiting the frequency data, DNAJC19tv iPSC-CMs were highly significant at NT (***), at 10 nM (****), at 30 nM (****) and at 100 nM (****) Iso, thus resulting in an overall significantly changed behavior when compared to NC6M iPSC-CMs (two-way ANOVA NC6M vs. DNAJC19tv ####, $p<0.0001$) (Fig. 3.45). In detail, the frequency in

DNAJC19tv was raised to 1.33 ± 0.18 Hz at 10 nM Iso, to 1.40 ± 0.19 Hz at 30 nM Iso and 1.42 ± 0.20 Hz at 100 nM Iso (Fig. 3.45). Similar observations were made in DCMAP2, by showing significant differences at NT (***), at 10 nM (****), at 30 nM (****) and 100 nM (****) Iso, thus resulting in an overall highly significant difference when compared to NC6M (two-way ANOVA NC6M vs. DCMAP2 ####, p<0.0001) (Fig. 3.45). DCMAP2 showed 1.13 ± 0.12 Hz at 10 nM Iso, Iso 1.08 ± 0.11 Hz at 30 nM and 1.18 ± 0.10 Hz at 100 nM Iso (Fig. 3.45). Even though DCMAP1 did not display the same strongly enhanced frequencies, the difference between the overall data versus NC6M were highly significant as well (two-way ANOVA NC6M vs. DCMAP1 ###, p=0.0004) (Fig. 3.45). DCMAP1 presented only slightly increased frequencies with 0.61 ± 0.12 Hz at 10 nM Iso, 0.61 ± 0.12 Hz at 30 nM Iso and 0.66 ± 0.13 Hz at 100 nM Iso (Fig. 3.45).

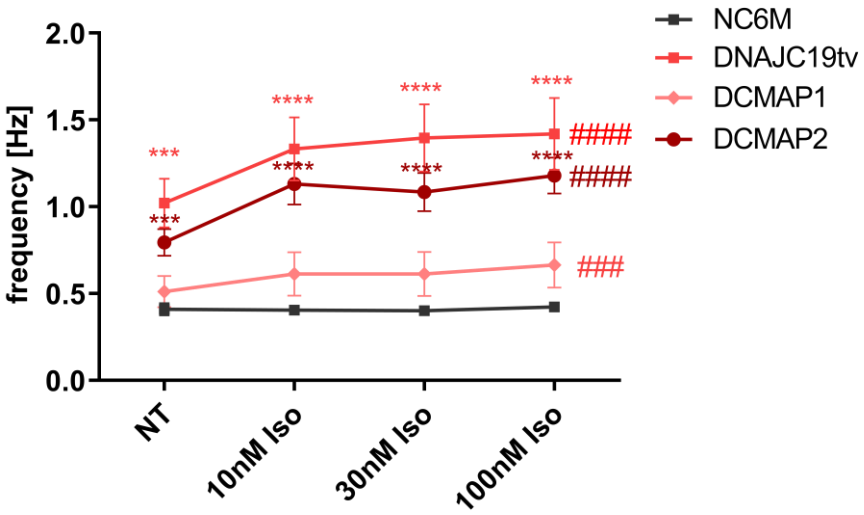

Figure 3.45 All mutants presented higher frequencies basally and with raising Iso concentrations.
Frequency assessment was performed on at least 120 days mattress-aged iPSC-CMs using the IonOptix system. The frequencies of iPSC-CMs were quantified by comparison of three mutants (DNAJC19tv, DCMAP1, DCMAP2) with the healthy control (NC6M) and are displayed as grouped data represented as mean ± SEM. Frequencies were increased basally and upon raised Iso concentrations with discordant levels. DCMAP1 showed moderate increase, whereas DCMAP2 and DNAJC19 were considerably increased with enhanced Iso concentrations. #### p<0.0001, ### p<0.001, ## p<0.01, # p<0.05, ns p>0.05 using regular two-way ANOVA with **** p<0.0001, *** p<0.001, ** p<0.01, * p<0.05, ns p>0.05 Bonferroni post-tests calculated versus NC6M iPSC-CMs.

3.10.2.2 Transient evaluation of arrhythmic events unraveled DAD/EADs and fibrillation-like features

In order to examine arrhythmic events and their relation to a disease-specific phenotype, iPSC-CMs were assigned to defined groups with individual characteristics (Fig. 3.46). Two different categories were determined: rhythmic (A) and arrhythmic (B, C, D), wherein arrhythmic features included the presence of breaks (B), DAD/EADs (C) or a fibrillation-like phenotype (D, threshold >1Hz) (Fig. 3.46). Subjective evaluation was partly additionally performed with the help of the Bachelor student Miriam Leskien, which led to the same results. Each category was determined using a time frame of 120 sec for each treatment (after the 120 sec wash-in phase) and only if the phenotype was present in at least four cases to exclude false-evaluation independent of the reaction towards electric stimulation. If two different phenotypes were observed, the predominant phenotype was assigned. For the overall evaluation the characteristic phenotype was defined when it was present in at least three of the five treatments. Regularly contracting iPSC-CMs were `rhythmic`, whereas the presence of `breaks` was interpreted as long non-periodic irregular or regular breaks. The term EAD and rarely also DAD was used to describe abnormal depolarizations of different phases. A fibrillation-like phenotype was set if visually observed and corrected if the individual frequency was above the threshold of 1 Hz.

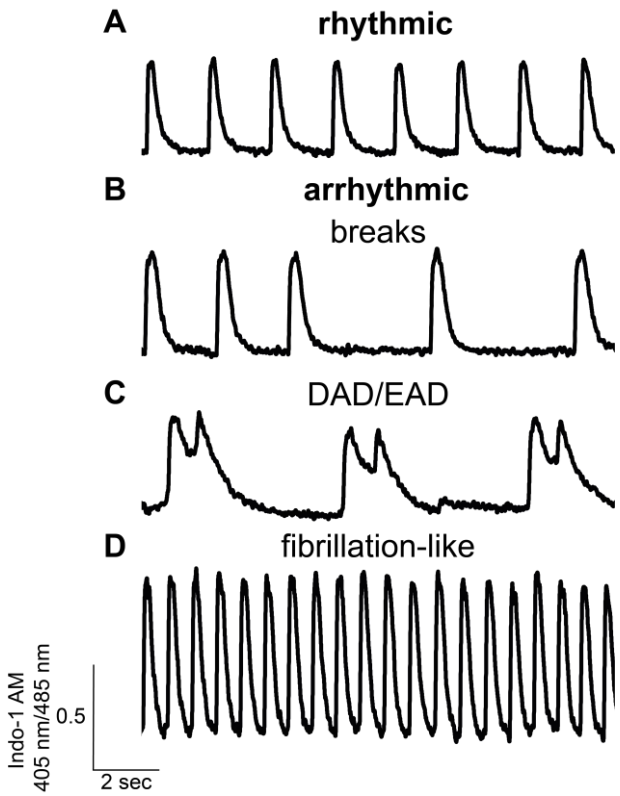

Figure 3.46 Categorization of different characteristic events of rhythmic and arrhythmic features.
Schematic overview of transient categories to evaluate arrhythmic and rhythmic events. Rhythmic included both: periodic transients caused by self-rhythm and upon external stimulation. Arrhythmic events were divided in subcategories breaks (longer irregular breaks, periodic regular breaks), DAD/EADs and fibrillation-like events.

The individual arrhythmic events were assessed for all cell lines regarding the presence of arrhythmias and the more detailed evaluation with the presence of breaks, DAD/EADs and a fibrillation-like phenotype. Data are displayed as mean ± SEM grouped for iPSC-CMs and grouped for each biological replicate that was set for the individual cardiac differentiations (boxes). Comparing the overall arrhythmic differences, the NC6M control presented with 28.3 ± 6.6 % arrhythmic events, DNAJC19tv with 68.8 ± 11.9 %, DCMAP1 with 65.3 ± 19.2 % and DCMAP2 with 34.0 ± 5.9 % (Fig. 3.47 A). All mutants displayed a tendency towards increased abnormal rhythm behaviors, wherein DNAJC19tv was the only cell line to demonstrate a significant difference (unpaired t-test NC6M vs. DNAJC19tv *, p=0.0126; NC6M vs. DCMAP1 ns, p=0.0540; NC6M vs. DCMAP2 ns, p=0.6041) (Fig. 3.47 A). In detail, the presence of breaks was only observed in the healthy condition with 13.9 ± 9.0 % that seemed to be more unspecific (unpaired t-test NC6M vs. DNAJC19tv ns, p=0.1556; NC6M vs. DCMAP1 ns, p=0.3290; NC6M vs. DCMAP2 ns, p=0.3290) (Fig. 3.47 B). The presence of DAD/EADs was only observed in mutant iPSC-CMs with the highest percentage in DCMAP1 with 65.2 ± 19.3 % and lower proportions in DNAJC19tv with 20.8 ± 12.5 % and DCMAP2 with 10.4 ± 5.8 %, that were significantly increased in DCMAP1 only (unpaired t-test NC6M vs. DNAJC19tv ns, p=0.1116; NC6M vs. DCMAP1 **, p=0.0020; NC6M vs. DCMAP2 ns, p=0.1645) (Fig. 3.47 B). In some cases, fibrillation-like phenotypes were observed in NC6M with 13.9 ± 9.0 %, in DNAJC19tv with 27.0 ± 10.4 % and DCMAP2 with 23.7 ± 8.5 %, whereas this phenotype was not observed in DCMAP1 (unpaired t-test NC6M vs. DNAJC19tv ns, p=0.3731; NC6M vs. DCMAP1 ns, p=0.3290; NC6M vs. DCMAP2 ns, p=0.5166) (Fig. 3.47 B).

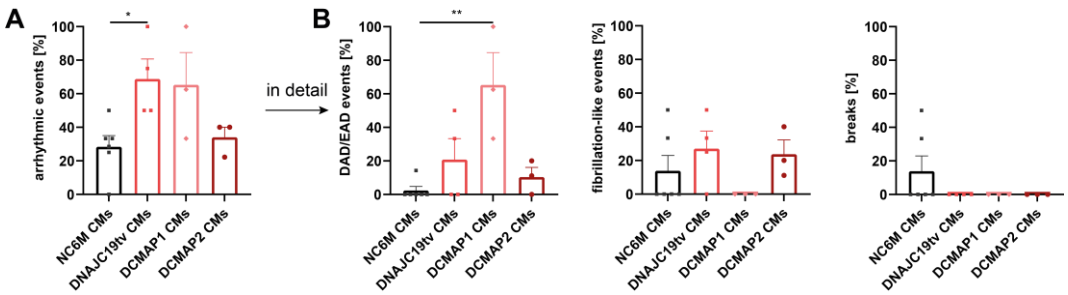

Figure 3.47 Increased arrhythmic events in mutant iPSC-CMs by subjective evaluation and discordant preference of breaks, DAD/EADs and fibrillation-like events.
(A) Measured iPSC-CMs of each biological replicate (each box corresponds to one cardiac differentiation) were grouped based on the occurrence of arrhythmic events in percent and are displayed as mean ± SEM. **(B)** Detailed examination of arrhythmic events displayed breaks **(B, right)**, DAD/EADs **(B, left)** and the presence of fibrillation-like events **(B, center)**. Unpaired t-test with ** p<0.01, * p<0.05, ns p>0.05 calculated versus NC6M iPSC-CMs.

Detailed examinations of Ca^{2+} transient shapes revealed - overall - marked arrhythmic features in mutant cells, comprised by both the occurrence of DADs/EADs and fibrillation-like events with discordant preferences. In our *in vitro* model, the male patient DCMAP1 showed a preference for the formation of DADs or EADs whereas the female patient DCMAP2 tended to have a fibrillation-like phenotype. Interestingly, the isogenic mutant control DNAJC19tv displayed the presence of DAD/EADs and fibrillation-like events to more equal fractions. Breaks were recognized in healthy iPSC-CMs only and seemed to be more unspecific, as a cause of the stressful procedure during the IonOptix measurements.

3.10.2.3 Increased diastolic Ca^{2+} concentrations but equal systolic Ca^{2+} levels in mutant DNAJC19 iPSC-CMs

First, systolic and diastolic Ca^{2+} concentrations were assessed (Fig. 3.48). The diastolic Ca^{2+} concentration of NC6M control iPSC-CMs was 1.08 ± 0.04 $[Ca^{2+}]_c$ and was slightly influenced by increasing Iso concentrations (10 nM Iso: 1.08 ± 0.04 $[Ca^{2+}]_c$; 30 nM Iso: 1.09 ± 0.03 $[Ca^{2+}]_c$; 100 nM Iso: 1.11 ± 0.03 $[Ca^{2+}]_c$) (Fig. 3.48). The diastolic Ca^{2+} levels of DNAJC19tv were 1.16 ± 0.07 $[Ca^{2+}]_c$, DCMAP1 had 1.18 ±0.04 $[Ca^{2+}]_c$ and DCMAP2 presented 1.19 ± 0.04 $[Ca^{2+}]_c$ measured before Iso stimulation at NT (Fig. 3.48). DNAJC19tv iPSC-CMs showed significantly higher diastolic Ca^{2+} concentrations in comparison to the NC6M control, considering the values of all conditions (NC6M vs. DNAJC19tv ##, p = 0.0095; DNAJC19tv:10 nM Iso: 1.16 ± 0.06 $[Ca^{2+}]_c$; 30 nM Iso: 1.20 ± 0.07 $[Ca^{2+}]_c$; 100 nM Iso: 1.20 ± 0.07 $[Ca^{2+}]_c$) (Fig. 3.48). Furthermore, DCMAP1 as well as DCMAP2 demonstrated significantly higher diastolic Ca^{2+} concentrations when compared to NC6M controls as well (two-way ANOVA NC6M vs. DCMAP1 ####, p<0.0001; NC6M vs. DCMAP2 ####, p<0.0001) (DCMAP1 10 nM Iso: 1.20 ± 0.03 $[Ca^{2+}]_c$; 30 nM Iso: 1.22 ± 0.04 $[Ca^{2+}]_c$; 100 nM Iso: 1.25 ± 0.04 $[Ca^{2+}]_c$) (Fig. 3.48). In particular diastolic Ca^{2+} concentrations of DCMAP2 increased stronger with rising Iso concentrations that were significantly different from NC6M control at 10 nM (*), 30 nM (*) and 100 nM (**) (DCMAP2 10 nM Iso: 1.23 ± 0.05 $[Ca^{2+}]_c$; 30 nM Iso: 1.27 ± 0.05 $[Ca^{2+}]_c$; 100 nM Iso: 1.30 ± 0.05 $[Ca^{2+}]_c$) (Fig. 3.48). The quantification of diastolic Ca^{2+} concentrations at 100 nM Iso unraveled larger differences, DNAJC19tv showed diastolic Ca^{2+} levels of 1.20 ± 0.07 $[Ca^{2+}]_c$, DCMAP1 of 1.25 ± 0.04 $[Ca^{2+}]_c$ and DCMAP2 of 1.30 ± 0.05 $[Ca^{2+}]_c$, whereas NC6M control presented only 1.11 ± 0.03 $[Ca^{2+}]_c$ (Fig. 3.48).

The initial systolic Ca^{2+} concentrations of NC6M equaled roughly to 1.76 ± 0.08 $[Ca^{2+}]_c$, similar to DNAJC19tv with 1.65 ± 0.09 $[Ca^{2+}]_c$, DCMAP1 with 1.85 ± 0.08 $[Ca^{2+}]_c$ and DCMAP2 with 1.76 ± 0.08 $[Ca^{2+}]_c$ (Fig. 3.48). Only mutant cells presented a trend towards slightly increased systolic Ca^{2+} concentrations upon increased Iso concentrations (Fig. 3.48). The systolic Ca^{2+} concentrations of DNAJC19tv iPSC-CMs were lower by trend, whereas DCMAP1 together with DCMAP2 were higher by trend than the ones of the NC6M control without significant differences (two-way ANOVA NC6M vs. DNAJC19tv ns, p=0.2031; NC6M vs. DCMAP1 ns, p=0.0486; NC6M vs. DCMAP2 ns, p=0.4563) (Fig. 3.48). We observed a systolic Ca^{2+} concentration that was very similar to the NC6M control cell line especially in DCMAP2 (Fig. 3.48).

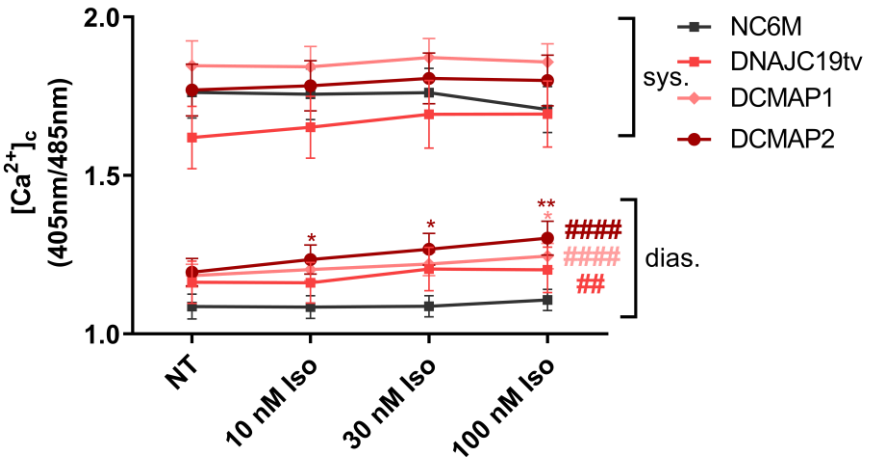

Figure 3.48: Shared systolic but increased diastolic Ca^{2+} concentrations in DCMA mutant iPSC-CMs.
Diastolic and systolic Ca^{2+} concentration assessment in $[Ca^{2+}]_c$ was performed on at least 120 days mattress-aged iPSC-CMs using the IonOptix system. iPSC-CMs, that survived the measurement procedure, enabled the comparison of Ca^{2+} levels of three mutants (DNAJC19tv, DCMAP1, DCMAP2) and the healthy control (NC6M) that are displayed as grouped data and are represented as mean ± SEM. Diastolic Ca^{2+} concentrations were increased to different rates basally and upon raised Iso concentrations (10nM, 30nM, 100nM). DNAJC19tv showed a moderate increase, whereas DCMAP1 and DCMAP2 displayed stronger increase with enhanced Iso concentrations. #### p<0.0001, ### p<0.001, ## p<0.01, # p<0.05, ns p>0.05 using regular two-way ANOVA with **** p<0.0001, *** p<0.001, ** p<0.01, * p<0.05, ns p>0.05 Bonferroni post-tests calculated versus NC6M iPSC-CMs.

3.10.2.4 Decreased Ca^{2+} influx and efflux in DNAJC19tv and DCMAP2 iPSC-CMs only

Next, overall Ca^{2+} influx and efflux were analyzed by calculating the difference between systolic and diastolic Ca^{2+} concentration referring to peak height (peak h) of the Ca^{2+} transients (Fig. 3.49). The Ca^{2+} influx of NC6M initially contained 0.68 ± 0.06 $[Ca^{2+}]_c$, similar to DCMAP1 with 0.65 ± 0.06 $[Ca^{2+}]_c$, whereas DNAJC19tv with 0.46 ± 0.09 $[Ca^{2+}]_c$ and DCMAP2 with 0.57 ± 0.05 $[Ca^{2+}]_c$ showed decreased influx of Ca^{2+} ions when compared to the NC6M control (Fig. 3.49). Comparing DNAJC19tv with the isogenic control NC6M the mean peak high at NT was approximately ~70 % of the mean peak height of the control transients (Fig. 3.49). The remarkable decrease in Ca^{2+} influx was further present upon Iso stimulation, underlining significant differences when compared to NC6M controls (two-way ANOVA NC6M vs. DNAJC19tv ##, p=0.0022) (Fig. 3.49). Regarding the trendline of DCMAP1 it almost equaled to the Ca^{2+} influx of NC6M control iPSC-CMs (two-way ANOVA NC6M vs. DCMAP1 ns, p=0.7893) (Fig. 3.49). Additionally, DCMAP2 iPSC-CMs presented the same behavior as decreased Ca^{2+} influx was recognized during the whole measurements that was significant as well when compared to NC6M iPSC-CMs (two-way ANOVA NC6M vs. DCMAP2: ##, p=0.0040) (Fig. 3.49). Upon 100 nM Iso stimulation, Ca^{2+} influx ratios were not changed as NC6M with 0.61 ± 0.06 $[Ca^{2+}]_c$ showed similar influx levels like DCMAP1 with 0.63 ± 0.05 $[Ca^{2+}]_c$, whereas DNAJC19tv with 0.49 ± 0.11 $[Ca^{2+}]_c$ equaled to DCMAP2 with 0.50 ± 0.04 $[Ca^{2+}]_c$ and demonstrated maintained decreased influx of Ca^{2+} ions when compared to the NC6M control (Fig. 3.49). No clear statement could be made regarding the relationship of Iso stimulation and Ca^{2+} influx due to high variations and discordant trends as DCMAP1 showed slightly increased influx whereas DCMAP2 displayed slightly decreased influx rates (Fig. 3.49).

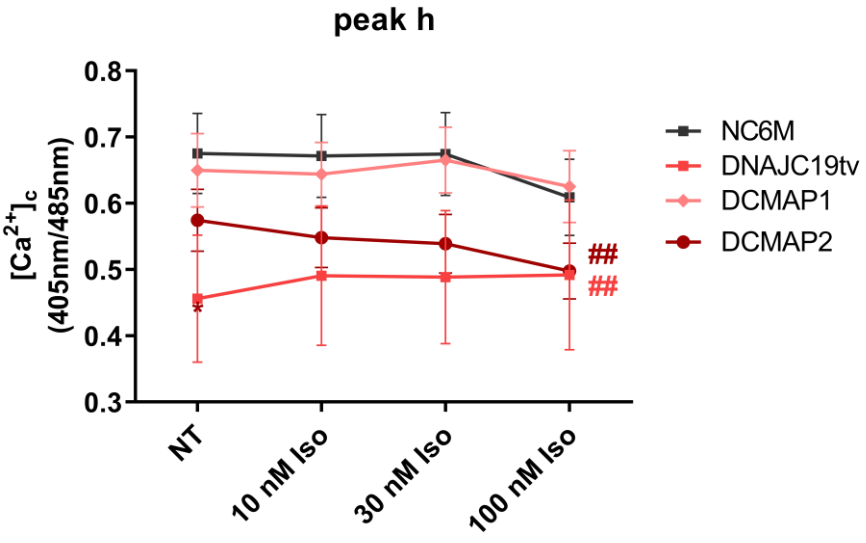

Figure 3.49 The calculation of the Ca^{2+} peak height revealed reduced Ca^{2+} influx and efflux in DNAJC19tv and DCMAP1.
The Ca^{2+} peak height was calculated by the difference of systolic and diastolic Ca^{2+} concentrations for each individual measurement and is displayed as mean of the individual groups including all measurements with SEM in $[Ca^{2+}]_c$. The Ca^{2+} influx and efflux in DNAJC19tv and DCMAP2 was significantly reduced in comparison to control NC6M iPSC-CMs and slightly decreased with increasing stress. ## $p<0.01$, ns $p>0.05$ using regular two-way ANOVA with Bonferroni post-tests calculated versus NC6M iPSC-CMs.

Taken together, all mutant cell lines displayed significantly higher diastolic Ca^{2+} concentrations, whereupon this effect was stronger in DCMAP1 and DCMAP2 than in DNAJC19tv iPSC-CMs. The systolic Ca^{2+} concentrations showed no significant difference between DNAJC19 mutation carrier iPSC-CMs and the NC6M control. The amount of Ca^{2+} influx and efflux was not changed in DCMAP1 but significantly reduced in DNAJC19tv and DCMAP2 iPSC-CMs.

3.10.2.5 Reduced relaxation capacities in DCMA mutants

The extracellular transport of Ca^{2+} that is needed to return to basal diastolic Ca^{2+} levels is referred to as relaxation time. This is mediated by Ca^{2+}-buffering at the myofilaments and reuptake by the SR and the sodium-calcium exchanger (NCX antiporter). 50 % of the relaxation time ($RT_{50\%}$) can represent both the activity of the myofilament Ca^{2+} decay and fast SERCA uptake (SR Ca-ATPase), while 90 % of the relaxation time ($RT_{90\%}$) values display the activity of the slower NCX antiporter. Since the relaxation time is dependent on the frequency, a correlation known as frequency-dependent acceleration of relaxation (FDAR) (Endoh, 2004), and iPSC-CMs were often not reacting to field stimulation of 0.5 Hz, Bazett's formula, that is frequently used for the correction of the QT intervals in the electrocardiogram, was adapted (Bazett, 1920) (Fig. 3.50). On the first view, the diagram unraveled that both 50 % and 90 % relaxation times were influenced by increasing Iso concentrations in all cell lines by accelerating the Ca^{2+} transport out of the cell (Fig. 3.50). The initial $RT_{50\%}$ of NC6M was around 0.19 ± 0.02 $RT_{50\%}[s]/\sqrt{\Delta t[s]}$ which was similar to DNAJC19tv with 0.19 ± 0.03 $RT_{50\%}[s]/\sqrt{\Delta t[s]}$ and DCMAP2 with 0.22 ± 0.01 $RT_{50\%}[s]/\sqrt{\Delta t[s]}$ (Fig. 3.50). DCMAP1 showed remarkably prolonged relaxation times with 0.35 ± 0.06 $RT_{50\%}[s]/\sqrt{\Delta t[s]}$ at NT (**) as well as with 0.38 ± 0.09 $RT_{50\%}[s]/\sqrt{\Delta t[s]}$ upon 10 nM (**) Iso stimulation and an overall significant increase in $RT_{50\%}$ when compared to the NC6M control (two-way ANOVA NC6M vs. DCMAP1: ###, p=0.0003) (Fig. 3.50). Interestingly, $RT_{50\%}$ relaxation times of DCMAP1 were almost similar to NC6M iPSC-CMs at 30 nM and 100 nM (NC6M 0.15 ± 0.01 $RT_{50\%}[s]/\sqrt{\Delta t[s]}$ at 30 nM Iso; DCMAP1 0.14±0.03 $RT_{50\%}[s]/\sqrt{\Delta t[s]}$ at 30 nM Iso; NC6M 0.16 ± 0.01 $RT_{50\%}[s]/\sqrt{\Delta t[s]}$ at 100 nM Iso; DCMAP1 0.18 ± 0.01 $RT_{50\%}[s]/\sqrt{\Delta t[s]}$ at 100 nM Iso) (Fig. 3.50). Although not obvious DCMAP2 as well demonstrated an overall significant increase in $RT_{50\%}[s]/\sqrt{\Delta t[s]}$ when compared to healthy control iPSC-CMs (two-way ANOVA NC6M vs. DCMAP2 ###, p=0.0004), which was not observed in DNAJC19tv iPSC CMs (two-way ANOVA NC6M vs. DNAJC19tv ns, p=0.8177) (Fig. 3.50).

Next, the $RT_{90\%}$ values were assessed and NC6M presented 0.46 ± 0.02 $RT_{90\%}$[s]/√Δt[s] roughly equal to DNAJC19tv with 0.40 ± 0.06 $RT_{90\%}$[s]/√Δt[s] and DCMAP2 with 0.49 ±0.02 $RT_{90\%}$[s]/√Δt[s] at NT (Fig. 3.50). Again, only DCMAP1 showed remarkable changes with increased $RT_{90\%}$ times at NT and 10 nM Iso (**) and an overall significantly slowed extracellular transport of Ca^{2+} ions when compared to NC6M (two-way ANOVA NC6M vs. DCMAP1 ##, p=0.0037) (Fig. 3.50). The examination of $RT_{90\%}$ of DNAJC19tv iPSC-CMs and DCMAP2 iPSC-CMs did not unravel significant differences (two-way ANOVA NC6M vs. DNAJC19tv ns, p=0.2980, NC6M vs. DCMAP2 ns, p=0.0812) (Fig. 3.50). The investigation of $RT_{90\%}$ at 100 nM Iso showed equal values in all cell lines, in detail: NC6M 0.36 ± 0.02 $RT_{90\%}$[s]/√Δt[s], DNAJC19tv 0.35 ±0.08 $RT_{90\%}$[s]/√Δt[s], DCMAP1 0.38 ± 0.03 $RT_{90\%}$[s]/√Δt[s] and DCMAP2 0.39 ± 0.01 $RT_{90\%}$[s]/√Δt[s] (Fig. 3.50).

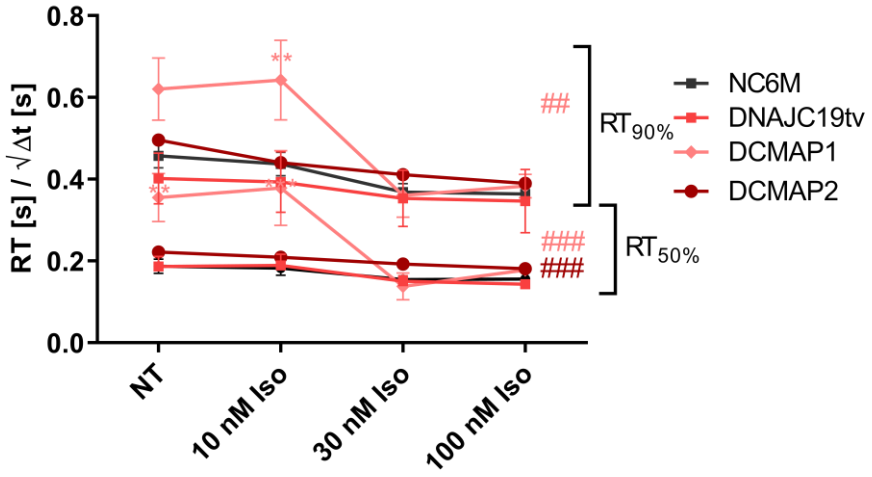

Figure 3.50: Frequency-corrected relaxation times at 50 % and 90 % displayed slowed Ca^{2+} efflux predominantly in DCMAP1, slightly in DCMAP2 but not in DNAJC19tv.
NC6M control, DNAJC19tv, DCMAP1 and DCMAP2 iPSC-CMs are presented at $RT_{50\%}$ and $RT_{90\%}$. The 50 % relaxation times of DCMAP1 and DCMAP2 were significantly higher compared to the NC6M control. DNAJC19tv did not display significant changes. The 90 % relaxation times were significantly higher in DCMAP1 only compared to the NC6M control. Each stress protocol was tested in at least three to five biological replicates (cardiac differentiations) from at least 13-21 independent technical replicates (iPSC-CMs). iPSC-CMs were analyzed at least 122 ± 4 to 129 ± 2 days after initiation of contraction. Data are represented as mean ± SEM. Statistical analysis was performed using regular two-way ANOVA: #### p<0.0001, ### p<0.001, ## p<0.01, # p<0.05, ns p>0.05 and Bonferroni post-tests: **** p<0.0001, *** p<0.001, ** p<0.01, * p<0.05, ns p>0.05, calculated versus NC6M controls. *RT* relaxation time

Moreover, the single exponential tau (sin exp tau) values were determined to investigate the ability of overall Ca^{2+} efflux and cellular recovery in more detail. The sin exp tau parameter was calculated automatically using the IonWizard software v.6.6.1.108. More specific, the slope of the downward course of the Ca^{2+} transient was calculated and afterwards set in relation to the frequency to represent a normalized measure for the velocity of recovery. As a simplification, a high sin exp tau value corresponded to a long time of recovery (IonOptix LLC, 2020).

The initial speed of recovery was increased in all mutant lines compared to NC6M with 0.23 ± 0.03 sin exp tau [s]/√Δt[s] (Fig. 3.51). DNAJC19tv presented 0.33 ± 0.05 sin exp tau [s]/√Δt[s], DCMAP1 displayed 0.56 ± 0.08 sin exp tau [s]/√Δt[s] and DCMAP2 demonstrated 0.35 ±0.02 sin exp tau [s]/√Δt[s], wherein DCMAP1 presented the strongest prolongation (Fig. 3.51). All mutant as well as healthy iPSC-CMs presented a shared increased speed of recovery upon raising Iso concentrations (Fig. 3.51). DNAJC19tv iPSC-CMs demonstrated an overall significant prolongation of the speed of recovery when compared to NC6M iPSC-CMs (two-way ANOVA NC6M vs. DNAJC19tv: ###, p=0.0008) (Fig. 3.51). A similar trend was observed in DCMAP2 iPSC-CMs with strikingly significant differences to NC6M iPSC-CMs (two-way ANOVA NC6M vs. DCMAP2 ####, p<0.0001), wherein all conditions were significantly increased (NT **, 10 nM Iso ***, 30 nM Iso ****, 100 nM Iso **) (Fig. 3.51). The examination of the DCMAP1 speed of recovery showed the strongest effect of prolongation that was overall highly

significant when compared to controls (NC6M vs. DCMAP1 ####, p<0.0001) (Fig. 3.51). In the conditions NT (**), 10 nM Iso (****) and 30 nM Iso (**) particularly showed remarkable changes when compared to healthy cells (Fig. 3.51). The comparison of the speed of recovery at 100 nM Iso revealed values that approached to each other in all iPSC-CM lines as NC6M showed 0.16 ± 0.01 sin exp tau [s]/√Δt[s], DNAJC19tv 0.22 ± 0.02 sin exp tau [s]/√Δt[s], DCMAP1 0.27 ±0.03 sin exp tau [s]/√Δt[s] and DCMAP2 0.29 ± 0.01 sin exp tau [s]/√Δt[s] (Fig. 3.51).

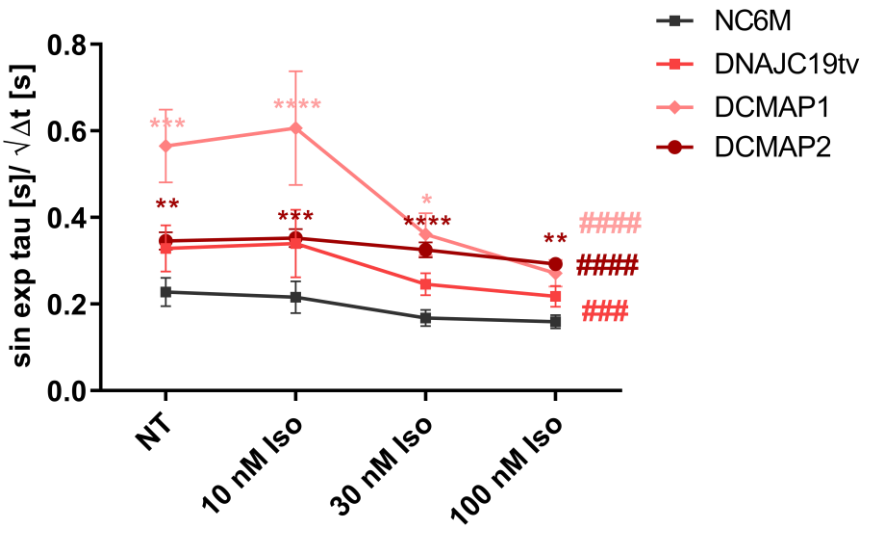

Figure 3.51 Prolonged time of recovery in all mutant iPSC-CMs.
The quantification of the sin exp tau parameter and the correction using Bazetts formula revealed a lower speed of recovery in DNAJC19tv, DCMAP1 and DCMAP2 iPSC-CMs compared to the NC6M control (high sin exp tau values correspond to prolonged times of recovery). p<0.0001, ### p<0.001, ## p<0.01, # p<0.05, ns p>0.05 using regular two-way ANOVA with **** p<0.0001, *** p<0.001, ** p<0.01, * p<0.05, ns p>0.05 Bonferroni post-tests calculated versus NC6M iPSC-CMs.

In conclusion, DCMAP1 demonstrated the most significantly prolonged relaxation times at $RT_{50\%}$ as well as $RT_{90\%}$, whereas DCMAP2 demonstrated increased $RT_{50\%}$ times only. DNAJC19tv did not display significant changes with regard to $RT_{50\%}$ and $RT_{90\%}$. Considering the speed of recovery after sin exp tau DNAJC19tv, DCMAP2 and most strikingly DCMAP1 iPSC-CMs needed longer for the return to the baseline that was highly significant in all mutant conditions. Thus, the Ca^{2+} export seemed to be slower in DNAJC19 mutation carrier iPSC-CMs compared to the NC6M control.

3.10.2.6 Decreased cell shortenings led to reduced contractility in DCMA mutants

The IonOptix measurements were performed in combination with the edge detection system to simultaneously assess cell shortenings [µm] (Fig. 3.52). NC6M iPSC-CMs displayed a cell shortening of 1.55 ± 0.30 µm at NT, whereas mutant cells demonstrated reduced contractile capacities as DNAJC19tv showed 1.03 ± 0.31 µm, DCMAP1 0.72 ± 0.20 and DCMAP2 1.20 ± 0.23 µm at NT (Fig. 3.52). With increasing Iso concentrations DNAJC19 mutant iPSC-CMs developed enhanced cell shortenings with a maximum following the 100 nM Iso condition (Fig. 3.52). DNAJC19tv had 1.17 ± 0.33 µm, DCMAP1 displayed 0.97 ± 0.28 µm and DCMAP2 showed 1.20 ± 0.29 µm at 100 nM Iso (Fig. 3.52). The comparison of the overall cell shortening capacities resulted the conclusion that DNAJC19tv`s and DCMAP1`s capacities were significantly reduced (two-way ANOVA NC6M vs. DNAJC19tv #, p=0.0327; NC6M vs. DCMAP1 ##, p=0.0016; NC6M vs. DCMAP2 ns, p=0.1104) (Fig. 3.52).

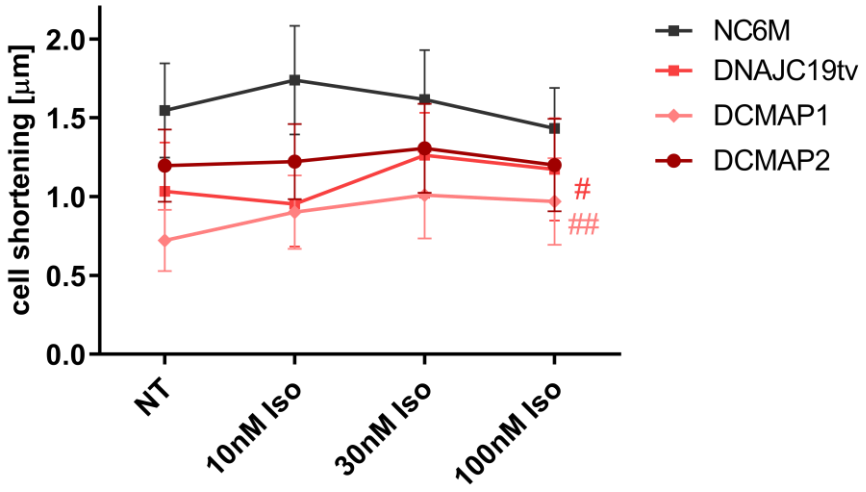

Figure 3.52 Edge-detection using the IonOptix system unraveled decreased cell shortenings in all mutant iPSC-CMs.
The quantification of the cell shortening parameter was calculated in µm to allow the comparison regarding contractile capacities of DNAJC19tv, DCMAP1 and DCMAP2 iPSC-CMs compared to the NC6M control. All mutants displayed lowered capacities of cell shortening. p<0.0001, ### p<0.001, ## p<0.01, # p<0.05, ns p>0.05 using regular two-way ANOVA with **** p<0.0001, *** p<0.001, ** p<0.01, * p<0.05, ns p>0.05 Bonferroni post-tests calculated versus NC6M iPSC-CMs.

In summary, molecular changes were directly connected to altered physiological processes with respect to calcium kinetics, contractility and arrhythmic potential. We observed significantly increased beating frequencies, elevated diastolic calcium concentrations and a shared trend towards reduced cell shortenings in all mutant cell lines basally and upon isoproterenol stimulation. Extended speed of recovery was seen in all mutant iPSC-CMs but most strikingly in DCMAP1, that additionally showed significantly prolonged relaxation times. The investigation of calcium transient shapes pointed towards enhanced arrhythmic features in all mutant iPSC-CMs comprised by both the occurrence of DADs/EADs and fibrillation-like events with discordant manifestations.

3.11 Summarized morphological and functional changes of DCMA-associated phenotypes using iPSC-CMs

Table 3.6: Summarized findings of DCMA-associated phenotypes using iPSC-CMs.
N/A not available, § preliminary data, ↑ increased, ↓ decreased, ↔ equal, **** p<0.0001, *** p<0.001, ** p<0.01, * p<0.05, *ns* p>0.05 calculated versus NC6M controls (or healthy controls) using paired or unpaired t-tests, #### p<0.0001, ### p<0.001, ## p<0.01, # p<0.05, *ns* p>0.05 calculated versus NC6M controls (or healthy controls) unsing regular two-way ANOVA

Cell lines	NC6M	NC47F	DNAJC19tv	DCMAP1	DCMAP2
Cell morphology					
DNAJC19 localization	nuclei, perinuclear, co-localized with mitochondrial structures	nuclei, perinuclear, co-localized with mitochondrial structures	nuclei	nuclei, CM-edges (rarely seen)	nuclei
CM shape	rod and elongated, circularity 0.55 ± 0.01	rod and elongated, circularity 0.59 ± 0.01 (**)	rod and elongated, circularity 0.54 ± 0.01	rod and elongated, circularity 0.54 ± 0.01	rod and elongated, circularity 0.57 ± 0.01
CM size	4260.59 ± 223.13 μm^2	4461.26 ± 324.00 μm^2	3398.12 ± 142.78 μm^2 (**)	2645.17 ± 179.47 μm^2 (****)	2341.62 ± 98.72 μm^2 (****)
Nuclei per cell	35.12 ± 6.11 % multinucleated	~44.37 ± 4.76 % multinucleated	~26.68 ± 6.75 % multinucleated	~32.66 ± 6.96 % multinucleated	~27.29 ± 3.39 % multinucleated
Multicellular organization	organized	organized	organized	organized	organized
Nuclei size	117.10 ± 1.80 μm^2	123.00 ± 2.02 μm^2	120.6 ± 2.23 μm^2	120.7 ± 2.77 μm^2	114.1 ± 1.18 μm^2
Sarcomeres					
Appearance	organized	organized	organized	organized	organized
Diameter	~1.87 µm (cTnT)	~1.82 µm (cTnT)	~1.92 µm (cTnT)	~1.93 µm (cTnT)	~1.83 µm (cTnT)
Protein-MLC2v/a	97.73 % $MLC2v^+/cTnT^+$	97.50 % $MLC2v^+/cTnT^+$	97.22 % $MLC2v^+/cTnT^+$	96.67 % $MLC2v^+/cTnT^+$	97.08 % $MLC2v^+/cTnT^+$
Protein-troponin I	cTnI ↑	cTnI ↑	cTnI ↑	cTnI ↑	cTnI ↑
Units- Z-lines and A & I-bands	Z-lines, A- & I-bands	Z-lines, A- & I-bands	Z-lines, A- & I-bands	Z-lines, A- & I-bands	Z-lines, A- & I-bands
Units- M-bands	M-bands	M-bands	M-bands	M-bands	M-bands
sarcomere-related protein contents (cTnT)/ fiber density	high, 31.23 ± 0.81 % cTnT	high, 30.64 ± 0.95 % cTnT	high, 31.99 ± 1.17 % cTnT	high, 33.72 ± 0.90 % cTnT	high, 33.17 ± 0.66 % cTnT
Calcium handling					
Ca^{2+} transient	efficient	efficient	efficient	efficient	efficient
E-C coupling	fast	fast	fast	fast	fast
Force-frequency relationship	positive	positive	positive	positive	positive
Frequency [Hz] w/o Iso	0.41 ± 0.04 Hz	N/A	1.02 ± 0.14 Hz (####)	0.51 ± 0.08 Hz (###)	0.79 ± 0.08 Hz (####)
diastolic Ca^{2+} concentration	1.08 ± 0.04 $[Ca^{2+}]_c$	N/A	1.16 ± 0.07 $[Ca^{2+}]_c$ (##)	1.18 ± 0.04 $[Ca^{2+}]_c$ (####)	1.19 ± 0.04 $[Ca^{2+}]_c$ (####)
systolic Ca^{2+} concentration	1.76 ± 0.08 $[Ca^{2+}]_c$	N/A	1.65 ± 0.09 $[Ca^{2+}]_c$	1.85 ± 0.08 $[Ca^{2+}]_c$	1.76 ± 0.08 $[Ca^{2+}]_c$
Ca^{2+} peak h	0.68 ± 0.06 $[Ca^{2+}]_c$	N/A	0.46 ± 0.09 $[Ca^{2+}]_c$ (##)	0.65 ± 0.06 $[Ca^{2+}]_c$	0.57 ± 0.05 $[Ca^{2+}]_c$ (##)
$RT_{50\%}$[s]/$\sqrt{\Delta t}$[s]	0.19 ± 0.02	N/A	0.19 ± 0.03	0.35 ± 0.06 (###)	0.22 ± 0.01 (###)
$RT_{90\%}$[s]/$\sqrt{\Delta t}$[s]	0.46 ± 0.02	N/A	0.40 ± 0.06	0.62 ± 0.07 (##)	0.49 ± 0.02
sin exp tau [s]/$\sqrt{\Delta t}$[s]	0.23 ±0.03	N/A	0.33 ± 0.05 (###)	0.56 ± 0.08 (####)	0.35 ± 0.02 (####)

Arrhythmic events					
IonOptix Indo-1-AM transient shapes	28.3 ± 6.6 %	N/A	68.8 ± 11.9 % (*), DAD/EADs ↔ fibrillation-like	65.3 ± 19.2 %, DAD/EADs↑	34.0 ± 5.9 %, fibrillation-like↑
Contractility					
Edge detection IonOptix	1.55 ± 0.30 µm	N/A	1.03 ± 0.31 µm (#)	0.72 ± 0.20 µm (##)	1.20 ± 0.23 µm
Mitochondrial homeostasis & bioenergetics					
Number mitochondria	high	high	low	low	low
Mitochondrial area	high, 59.59 ± 0.76 % MitoTracker	high, 56.78 ± 1.73 % MitoTracker	low, 44.58 ± 0.78 % MitoTracker (****)	low, 47.44 ± 1.26 % MitoTracker (****)	low, 50.04 ± 1.15 % MitoTracker (****)
Structure mitochondrial network	regular distribution, aligned, close to sarcomeres	regular distribution, aligned, close to sarcomeres	irregular distribution, fragmented, close to sarcomeres↓	irregular distribution, fragmented, close to sarcomeres↓	irregular distribution, fragmented, close to sarcomeres↓
Mitochondrial size (TEM)	0.355 ± 0.01 μm^2	0.371 ± 0.03 μm^2	0.242 ± 0.01 μm^2 (****)	0.140 ± 0.004 μm^2 (****)	0.174 ± 0.003 μm^2 (****)
Mitochondrial shape (TEM)	round and elongated, circularity 0.57 ± 0.004	round and elongated, circularity 0.58 ± 0.0015	rounder and less elongated, circularity 0.56 ± 0.0094	rounder and less elongated, circularity 0.57 ± 0.006	rounder and less elongated, circularity 0.628 ± 0.02
Cristae	prominent cristae, dense matrix, regular cristae pattern	prominent cristae, dense matrix, regular cristae pattern	abnormal cristae, dissolved matrix, irregular cristae pattern	abnormal cristae, dissolved matrix, irregular cristae pattern	abnormal cristae, dissolved matrix, irregular cristae pattern
OCR	normal	normal	increased (###)	increased (##)	Increased (##)
Metabolic features					
Substrate utilization	dominant FA uptake (^{125}I-BMIPP), mild glucose uptake (^{18}F-FDG)	dominant FA uptake (^{125}I-BMIPP), mild glucose uptake (^{18}F-FDG)	FA uptake ↓ (^{125}I-BMIPP), mild glucose uptake (18F-FDG) ↓	FA uptake ↓ (^{125}I-BMIPP), increased glucose uptake (18F-FDG) ↑↑	FA uptake ↓ (^{125}I-BMIPP), mild glucose uptake (18F-FDG) ↓
ECAR	normal	normal	increased	increased	increased
Adrenergic signaling					
Responses to β-adrenergic stimulation	inotropic reaction	inotropic reaction	inotropic reaction	inotropic reaction	inotropic reaction
Phospholipid composition					
Cardiolipin profiles	regular[§]	N/A	N/A	N/A	increased acyl chain length, polyunsaturated[§]

4. Discussion

4.1 Robust generation of five iPSC lines using the non-integrating SeV

The generation of iPSCs has great potential for disease modeling especially in the field of inherited cardiomyopathies. The accessibility to human heart cells in particular concerning rare genetic disorders is almost impossible. Therefore, main insights into pathological mechanisms rely on model organisms such as mice (*mus musculus*) or zebrafish (*danio rerio*). As an alternative cell source, patient-derived somatic cells can be reprogrammed into iPSCs which can be transformed into CMs using directed differentiation methods in order to mimic the disease *in vitro*. The reprogramming success to generate iPSCs heavily relies on the somatic cell source. For example, reprogramming of keratinocytes derived from skin biopsies or plucked hair is more efficient than reprogramming of dermal fibroblasts (Aasen et al., 2008). Furthermore, reprogramming of mesenchymal stem cells from amniotic membranes, umbilical cord and cord blood into iPSCs can be performed by even less transcription factors than `KMOS` (OCT3/4, SOX2 for cord blood)(Cai et al., 2010, Giorgetti et al., 2010, Haase et al., 2009). To date, a high variety of cell sources like adipose-tissue derived cells (Sugii et al., 2010), hepatocytes (Liu et al., 2010) and even urine-derived cells (Zhou et al., 2012) can be successfully reprogrammed. Up to now, there is no gold standard regarding the optimal reprogramming method that corresponds to the individual cell source. The major differences can be observed in efficiency, time-consumption, aneuploidy rates depending on the starting cell type, the chosen reprogramming method and quality control requirements according to Gonzalez et al., 2011. In the present thesis the original somatic cell line was a fixed condition: dermal fibroblasts. Therefore, the optimal reprogramming method needed to be adjusted towards the accessible somatic cell type. For the generation of *in vitro* model systems of genetic disorders like inherited cardiomyopathies, integration-free reprogramming methods can be used only, because the presence of integrated sequences would hinder downstream phenotypic investigations. The advantage of non-integrating systems relies in avoiding uncontrolled gene disruption that can result in tumor development after translational use *in vivo* (Stadtfeld and Hochedlinger, 2010, Goh et al., 2013, Okita et al., 2007, Fusaki et al., 2009). Therefore, an optimized non-integrating reprogramming method was required for the use in dermal fibroblasts.

The most frequent integration-free reprogramming systems for dermal fibroblasts are based on mRNA (Warren et al., 2010), episomal plasmids (Okita et al., 2011, Chou et al., 2011, Goh et al., 2013, Awe et al., 2013), AAV (Zhou and Freed, 2009) or SeV systems (Malik and Rao, 2013, Ban et al., 2011, Fusaki et al., 2009). The fastest (~20 days) and at the same time most efficient (1.4 %) reprogramming method is the transfection of mRNA which fully replaces the need of plasmids or viruses. This method requires 5 % O_2 cultivation conditions as well as extensive workload due to daily transfections and was therefore not chosen as the most feasible reprogramming method (Warren et al., 2010). AAV-based reprogramming results in only 0.0002 % successful generation of iPSCs when using human cells (Zhou and Freed, 2009). Episomal delivery contributes to 0.01 % efficiency when using dermal fibroblasts (Goh et al., 2013, Awe et al., 2013). Therefore, the non-integrating SeV was chosen as best reprogramming method given efficiencies of 0.1-1 % for fibroblasts and the appearance of colonies within ~25 days (Ban et al., 2011, Fusaki et al., 2009). Reprogramming using the non-integrating SeV works efficiently not only for fibroblasts but also for cord blood and peripheral blood cells (Ban et al., 2011, Fusaki et al., 2009, Merling et al., 2013).

The reprogramming efficiency of the SeV system can be improved by using small molecules like GSK3β inhibitor and Wnt activator CHIR which can additionally be combined with ascorbic acid (Lian et al., 2012, Cao et al., 2012). In the thesis of K. Günther the SeV reprogramming conditions were optimized through ascorbic acid medium supplementation that conferred antioxidant potential to enhance the efficiency of iPSC generation (Esteban et al., 2010, Bar-Nur et al., 2014, Esfandiari et al., 2012, Lin et al., 2009, Shi et al., 2008, Günther, 2016).

After using of the optimized protocol conditions all five dermal fibroblast cell lines were successfully reprogrammed into iPSCs using the non-integrating SeV. The reprogramming efficiencies ranged from 0.02 %-0.09 %, which is about tenfold smaller than the highest reported efficiency of 1 % (Ban et al., 2011). The published work used a reporter line to quantify the reprogramming efficiency which may explain the discordant efficiencies. Due to the inaccessibility of a reporter line, the reprogramming efficiency was calculated based on the visual appearance of colonies. This method is highly subjective and probably leads to exclusion of too small colonies. Therefore, the reprogramming efficiency was additionally visually scored. Colony formation and growth were present in all cell lines, even though NC6M, DCMAP1 and DCMAP2 demonstrated a higher number of evident colonies than NC47F and LEMD2 p.L13R. NC6M, DCMAP1 and DCMAP2 were derived from young donors ≤12 years of age whereas NC47F and LEMD2 p.L13R donors were ≥38 years old which indicates an age-related correlation regarding the reprogramming success. These findings are consistent to previous studies where the reprogramming efficiency declined with increasing donor-age (Trokovic et al., 2015). The survival rates in NC6M, NC47F, DCMAP1 and DCMAP2 were higher than the ones in LEMD2 p.L13R (31.58 %). Comparing the time spans, all colonies arose early between 29-34 days except for LEMD2 p.L13R iPSCs that required 44 days until reaching the appropriate size. In comparison to the previously published average of 25 days until colonies could be manually picked, only LEMD2 p.L13R showed a slowed colony formation (Ban et al., 2011, Fusaki et al., 2009). The differences between all five dermal fibroblast cell lines are the method of fibroblast obtainment, the genders, the donor-ages and the individual genetic backgrounds. LEMD2 p.L13R was the only cell line that demonstrated the lowest colony number, the lowest survival rates and the longest time spans of colony formation. We did not observe tremendous differences when comparing male to female, commercially available versus self-obtained or DNAJC19 mutant versus healthy cell lines.

Taken together, our findings support a donor-age related reprogramming efficiency with deviating observations in LEMD2 p.L13R only. Phenotypic investigations of LEMD2 p.L13R dermal fibroblasts of the same patient revealed reduced proliferative capacities together with abnormally shaped nuclei when compared to controls (Abdelfatah et al., 2019b). Interestingly, the investigation of the proliferative capacities of dermal fibroblasts that originate from different anatomical sites (neck, breast, arm) demonstrated the contrary, reduced proliferative capacity is even enhancing reprogramming success (Xu et al., 2013, Sacco et al., 2019). Therefore, the function of LEMD2 in tethering special DNA regions to the nuclear envelope is more likely to negatively impact reprogramming. A study on LMNA, a corresponding nuclear envelope protein, revealed prolonged time spans and decreased reprogramming efficiency due to upregulation of LMNA. This finding is demonstrating the importance of nuclear envelope proteins in maintaining nuclear integrity during reprogramming (Zuo et al., 2012). Based on those results, the function of LEMD2 as nuclear envelope protein in maintaining nuclear structural integrity, genomic stability and DNA-repair and the impact on reprogramming needs further investigations. Moreover, several studies have shown, that donor-to-donor variability as well as different anatomical sites are highly influencing reprogramming success of dermal fibroblasts (Mack et al., 2011, Trokovic et al., 2015, Sacco et al., 2019). Despite of the mutation-linked conspicuousness of LEMD2 p.L13R, the reprogramming efficiency depends on the cell quality, donor-age and passage number of the starting dermal fibroblast cell line (Hausburg et al., 2015). According to these criteria starting conditions within this study were optimal as the cells were mycoplasma-negative and were derived from young to mid-aged donors (6-47 years) with fibroblast passage numbers ≤ 10 at the day of transduction.

Altogether, it is of great importance to accurately evaluate the reprogramming method for the somatic cell line of choice that also fits to the local laboratory conditions. The fulfillment of all SeV-based essential criteria such as quality, donor-age and passage number resulted in robust generation of iPSCs with typical stem-cell like morphology. The generation of five individual iPSC lines within short time spans demonstrated the efficiency of the commercially available SeV system in a highly reproducible manner. Sanger sequencing revealed the same genetic identity within the genomic loci of LEMD2 and DNAJC19 when comparing dermal fibroblasts to their corresponding iPSC lines. Concerning the disease-associated genes of interest, the presence of the mutations in the patient-derived iPSC lines and the absence in the healthy controls was confirmed. Therefore, we were able to generate stem-cell like

shaped iPSC lines to establish *in vitro* models of DCMJC and DCMA by using patient- and healthy donor-derived fibroblast lines. Admittedly, the SeV system has two disadvantages such as higher safety requirements and higher aneuploidy rates. Therefore, quality control experiments were required to confirm important iPSC-related criteria such as self-renewal, differentiation potential and genomic integrity that were discussed together with CRISPR/Cas9-edited iPSC lines in section 4.3.

4.2 Preciseness of CRISPR/Cas9 in iPSCs to mimic ACM and DCMA

The combination of CRISPR/Cas9 and iPSC technology provides a powerful system to generate isogenic disease or isogenic healthy control cell lines. The comparison of introduced genetic aberrations in isogenic *in vitro* systems unravel the direct contribution of the mutation to the outcome of the phenotype regardless of the patient genetic background. Therefore, we aimed to mimic two inherited cardiomyopathies, ACM and DCMA, by the generation of mutant isogenic iPSC lines within the original healthy genetic background of NC6M iPSCs by using CRISPR/Cas9 technology. NC6M was used as shared healthy control iPSC line for both diseases due to the young age of the donor (6 years) that can be linked to the early onset of DCMA (Davey et al., 2006) as well as of ACM (Gerull et al., 2004, Awad et al., 2008, Pilichou et al., 2006). ACM as disease of dysfunctional desmosomes offers a great gene editing platform to establish CRISPR/Cas9 technology by mutating known desmosomal genes like PKP2 and DSG2. The generation of both homozygous knock-out iPSC lines within the same healthy genetic background has the power to uncover the importance of PKP2 and DSG2 in maintaining tissue integrity and how desmosomal disturbances evoke the cardiac phenotype of ACM. After gaining experience with the CRISPR/Cas9 system, the more advanced usage by the generation of a specifically positioned DSB at the splice acceptor site of intron 3 in the DNAJC19 gene was aimed. The introduction of the patient-associated mutation in the healthy genetic background of NC6M will help to examine DNAJC19 dysfunctions in forcing the development of DCMA in the absence of other patient-specific genetic factors. Furthermore, gene editing within one cell line enables insights into cleavage efficiencies and the preciseness of CRISPR/Cas9 on editing multiple genetic loci.

4.2.1 CRISPR/Cas9 gene editing relies on stable nucleofection

To establish CRISPR/Cas9 technology as gene editing tool, the combination of the delivery method of nucleofection together with the DNA-based Cas9 system was chosen and further optimized towards its use in NC6M iPSCs. Based on the equality of iPSCs with ESCs, the NEON^{TM} Nucleofection protocol of mESCs was optimized (Thermo Fisher Scientific). iPSCs are like ESCs highly suggestible by environmental cues, thus impeding their handling in multiple applications. We observed a tremendous heterogeneity from batch to batch making it very challenging to produce consistent and reproducible protocols especially regarding nucleofection as reported in previous studies (Chen et al., 2014). The optimization of each individual parameter as well as high plasmid purities were required to achieve enhanced survival rates and increased transfection efficiencies. The optimal environmental conditions in each handling step prior to, during and post nucleofection were crucial to ensure viability of transfected iPSCs. Nevertheless, we observed massive cell death of nucleofected iPSCs that could be reduced after adaptation of RI supplementation over a prolonged time span of 24-72h. We recognized, that the RI-mediated prevention of dissociation-induced apoptosis considerably improved iPSC survival as reported in previous examinations (Watanabe et al., 2007, Ohgushi et al., 2010). Consequently, it is assumed that prolonged RI-supplementation may increase the likelihood of enhanced genome editing efficiencies (Li et al., 2018). The new established protocol enables high survival rates of 44.2 % together with efficient transfection to an average of 46.4 % eGFP^{+} cells when using NC6M iPSCs. Other reports using a comparable setup demonstrated even lower survival rates (5-20 %) and a lower amount of positively transfected iPSCs (25 %) (Li et al., 2018). Taken toether, we showed that the established protocol is suitable for nucleofection of NC6M iPSCs and potentially either allows successful CRISPR/Cas9 delivery to other iPSC lines. However, due to the observed heterogeneity we assume that its applicability towards its general usage needs iPSC line-specific minor adaptations.

4.2.2 Nucleofection of CRISPR/Cas9 all-in-one plasmids allows efficient generation of three individually gene-edited iPSC lines

The new identified nucleofection parameters formed the basis for gene editing in the generation of all three aimed iPSC lines (PKP2-KO, DSG2-KO, DNAJC19tv). The nucleofection of the individual CRISPR/Cas9 gene editing plasmids led to different amounts of colonies ranging from 47 (DSG2) to 96 (PKP2) together with differences in the survival rates from 46.8 % (DSG2) to 81.2 % (PKP2) and variations in the estimated DSB efficiencies from 4.5 % (DSG2) to 15.4 % (PKP2). A correlation of the individual genomic locus on the amount of achieved colonies, their survival and a corresponding DSB efficiency was observed. Gene editing of *PKP2* showed the highest amount of colonies, the highest survival rates and the highest estimated DSB efficiencies. Targeting the *DNAJC19* locus consistently resulted in the midfield regarding all criteria, whereas *DSG2* overall showed the lowest values. Our findings support the computationally determined prediction score of efficiency as PKP2exon1-gRNA had the highest score with 625, whereas DSG2-exon1-gRNA (score 94) and DNAJC19intron3_exon4-gRNA (score 56) were much lower. These observations fit to other findings, wherein the gene editing outcomes highly depend on the individual gene locus (Miyaoka et al., 2016). Additionally, CRISPR/Cas9-mediated DSB efficiencies depend on the individual cell type, as editing efficiencies are remarkably lower in iPSCs than in HEK293T cells (Miyaoka et al., 2016). The cleavage efficiency is also dependent on the spatial accessibility to different genetic locations as it is higher in euchromatic (opened) than in heterochromatic (closed) regions (Jensen et al., 2017). Therefore, the individual chosen genetic loci and their three-dimensional accessibility determine the efficiency of CRISPR/Cas9 and might explain the observed variations from 4.5 % (DSG2-KO) to 13.3 % (DNAJC19tv) and 15.4 % DSBs (PKP2-KO). After calculating the average of all three editing efficiencies, we observed an overall high percentage of 11.1 % estimated DSBs. The comparison to other reports revealed high variations either, some reports demonstrated NHEJ events in the range of 2 % to 6 % (Miyaoka et al., 2016), whereas other showed efficiencies of 30 % (Geng et al., 2020) using a similar Cas9 approach. Up to now, Ding et al., 2013 demonstrated the highest gene editing efficiency of 79 % DSBs using human PSCs with an optimized Cas9 plasmid due to the addition of a nuclear localization signal (Ding et al., 2013). These findings underline the tremendous suitability of CRISPR/Cas9 all-in-one plasmids that can efficiently be delivered using electrical stimulation to generate genetically modified iPSC lines in an enhanced setting. In particular the presence of the 5`NGG-PAM every 8-12 bp highlights the broad applicability of the classical CRISPR/Cas9 system in editing multiple genetic loci (Cong et al., 2013, Hsu et al., 2013).

The screening of the 5`NGG-PAM revealed a high abundance of possible target sites in *PKP2* as well as in *DSG2*. The comparison of the *in silico* design to mimic ACM via targeting exon 1 of either *PKP2* or *DSG2* indeed unraveled the presence of deletions in both iPSC lines after additional subcloning and Sanger sequencing. The PKP2-KO iPSC line carries the mutation NM_001005242 (*PKP2*):c.[142_145delGGCC;148C>A];[142_145delGGCC;148C>A] whereas the DSG2-KO carries the mutation NM_001943.5 *(DSG2*):c.[9_24del16];[9_24del16]. More precise analysis and computational prediction suggests that mRNA translation is proposed to result in a frameshift in PKP2 (p.[G48Sfs*62];[G48Sfs*62]) as well as in DSG2 (p.[S4Tfs*6];[S4Tfs*6]), that is in both cases accompanied by a premature stop codon. As mRNA transcripts that contain premature stop codons have a high probability to be eliminated via the nonsense-mediated mRNA decay mechanism, we confirmed, that both iPSC lines represent knock-out models of PKP2 and DSG2 on the translational level with the potential to mimic ACM-associated phenotypes *in vitro* (supplementary Fig. 5.2 (Janz et al., 2021)).

Screening for a useful 5`NGG-PAM at the intron3_exon4 boundary sites in *DNAJC19* unraveled only few usable gRNAs. On the one hand, gRNAs that target genomic regions upstream were lying within intron 3 and will therefore have no effect on the translational level when not ranging into exon 4. On the other hand, too big distances downstream of the splice acceptor site of intron 3 are more likely to result in frameshifts and not in exon 4 skipping, thus may lead to changed transcriptional expressions of DNAJC19∆ex4. Therefore, the close proximity of ± 7 bp to the splice acceptor site of intron 3 was crucial to mimic DCMA-specific conditions. Unexpectedly, only one gRNA was predicted to create a DSB + 8

bp downstream of the splice acceptor site of intron 3, illustrating that gene editing of *DNAJC19* at one specifically positioned site in a less GC-rich region was more difficult. After additional subcloning Sanger sequencing revealed mainly colonies with biallelic modifications as in the representative colony DNAJC19tv, termed NM_145261.4 *(DNAJC19)*:c.[131_140del];[137_138insAGTATAATTGCC]. Theoretically, transcription of both alleles will result in a frameshift and a premature stop codon with a high probability to be degraded by nonsense-mediated mRNA decay. Computational prediction unraveled a theoretical loss of full-length *DNAJC19*, thus we were able to mimic the DCMA patient's conditions on the genomic level first. The classical Cas9 system was suitable for the generation of all three gene-edited cell lines within the same NC6M iPSC line, underlining the cellular preference in iPSCs to repair DNA damage via the activation of the error-prone NHEJ pathway due to indel formation in multiple subclones. As DNAJC19tv presents an insertion either, the identification of the inserted fragment via NCBI blasting did not uncover whether the inserted sequence originates as a result of unwanted off-target cleavage. Interestingly, the preference of NHEJ to evoke insertions rather than deletions depends on the activation of an alternative NHEJ mechanism including the DNA polymerase theta (Polθ) that synthesizes novel nt independently during the re-annealing step (summarized (Rodgers and McVey, 2016)). Considering this, the inserted nucleotides in DNAJC19tv most likely originate from the alternative NHEJ system.

Taken together, the classical CRISPR/Cas9 system is suitable for the generation of genetic knock-outs like PKP2-KO and DSG2-KO and to generate protein truncation variants like in DNAJC19tv in iPSCs. The classical CRISPR/Cas9 system has its limitations regarding the identification of potential target sites in GC-poor genetic regions which in turn restricts its efficiency, as its efficiency increases proportionally to the GC content (Ren et al., 2019, Liu et al., 2016). Moreover, 20nt as gRNA-DNA recognition site is relatively small when compared to other editing systems as TALENs (Christian et al., 2010) or ZNFs (Kim et al., 1996) and limits the identification of unique genetic target sites to some extent. This issue can be solved after making use of other Cas proteins with different PAMs or more precise editing approaches by using the Cas9 nickase system in combination with HDR-mediated repair mechanism (Ran et al., 2013a, Garneau et al., 2010, Cong et al., 2013, Hou et al., 2013).

4.2.3 Reality converges prediction: High specificity of the classical CRISPR/Cas9 system in iPSCs

Besides the high efficiencies, the used classical CRISPR/Cas9 DNA-based approach has a tremendous advantage during the screening process. The usage of selection cassettes enables easier identification of genetically modified iPSC lines, wherein the puromycin resistance is more sensitive than fluorescence reporter genes such as eGFP (Ran et al., 2013b). Moreover, eGFP-dependent fluorescence-activated cell sorting (FACS) of cells is accompanied by increased shear stress leading to a higher cell mortality rate (Fernandes et al., 2014). In fact, we observed increased cell death after puromycin selection. Since a high percentage of the surviving colonies contained genetic changes, we demonstrated that the selection procedure using the DNA-based method was very efficient. Although DNA transfection is stressful for cells, the plasmid persists for few days resulting in prolonged expression of antibiotic resistance genes or other reporters as well as prolonged expression of the CRISPR/Cas9 components (Sun et al., 2013). This ensures on the one hand the efficiency to generate genetic changes but on the other hand increases the probability of off-target DSBs (Liang et al., 2015). It is well known that off-target cleavages can occur but only to very low frequencies (Jiang et al., 2013, Fu et al., 2013, Hsu et al., 2013, Cradick et al., 2013). The development of novel screening and *in silico* design tools allowed the identification for possible off-target effects prior to transfection to enhance the specificity of the gene editing system (Zhang et al., 2015). To identify off-target cleavages all potential off-target sites in genes that have one to three mismatches were analyzed as Cas9 nucleases do not tolerate more than three bp of mismatches of the gRNA complementary DNA sequence (Hsu et al., 2013, Ran et al., 2013b). We observed a high specificity of the CRISPR/Cas9 system in all three generated iPSC lines due to no identified alterations in off-target genes after Sanger sequencing when compared to the original NC6M iPSC DNA. Important factors that may contribute to unspecific targeting are the amount of transfected DNA as well as the position and the amount of sgRNA-target DNA mismatches. It was demonstrated

that especially within the seed sequence, 8-12 bp upstream of the PAM, no mismatches were tolerated at all. These criteria were fulfilled when comparing the used gRNAs towards in total nine off-target sites in genes highlighting a tremendous specificity of the gene editing system. To further examine the specificity, we compared the computationally determined cleavage position that was reported to be 3 to 4 bp upstream of the 5`NGG-PAM by Sanger sequencing as accurate as possible (Ran et al., 2013b, Jinek et al., 2013). DSG2-KO showed a big deletion of 16 nucleotides that impaired a more detailed investigation of the cleavage site. The biallelic genetic modification within DNAJC19tv as well presented a bigger deletion of 10 bp on one allele hindering the examination of the detailed cleavage site. On the second allele a 12 bp insertion was directly introduced into DNAJC19 3 bp upstream of the 5`NGG-PAM, demonstrating the high correlation of computational prediction to the preciseness of CRISPR/Cas9. The identified cleavage site in PKP2-KO was very specific as well, given the cleavage site in the range of 4 to 8 bp upstream of the PAM, highlighting a tremendous agreement between prediction and reality thus enabling precise gene editing applications in iPSCs.

4.2.4 CRISPR/Cas9 as useful gene editing tool with future perspectives

Taken together, the classical CRISPR/Cas9 system is highly efficient in the generation of mutant isogenic control cell lines with a gene-locus specific dependency. We observed a tremendous compliance comparing computational prediction and actual DSBs. Furthermore, a high specificity was observed, since no off-target sites were cleaved. The demonstrated high efficiency allows us to reduce the amount of picked colonies in further experiments thus minimizing workload, time- and cost-extensive cultivation. The efficiency can be further improved by using the Cas9 nickase system (Ran et al., 2013a) or protein-RNA based approaches, but these optimization steps need much more workload, disable reliable selection mechanisms and are of higher risk to cause impurities prior to CRISPR/Cas9 delivery. The three generated iPSC lines are predicted to be a suitable model system for either ACM or DCMA thus enabling to get more insights into the causative effect of mutations when comparing the effect within a healthy genetic background versus a patient-derived genetic background. In particular, the generated *in vitro* model system of DCMA allows insights in the necessity of a patient-specific permissive background and the sufficiency of the mutation in a protective genetic background in parallel. Additionally, the gene-edited iPSC lines enable detailed investigations on the cellular level to potentially identify novel therapeutics particularly for genetic disorders like ACM or DCMA. Furthermore, the optimization of CRISPR/Cas9 technology towards its usage *in vivo* requires the necessity of its translation to tissue and organ level to pave the way for potential gene therapeutic applications in humans.

4.3 Quality validation of all eight self-generated iPSC lines

Given the huge variability of iPSC lines that arose due to different reprogramming techniques, different somatic origins or genetic modifications, novel quality criteria were defined to decrease unspecific variations in iPSC lines to further allow their usage on the translational level for disease-associated phenotypic characterizations (Elsevier B.V. Copyright © 2021, 2017). Disease-modeling using iPSCs requires defined and carefully evaluated iPSC clones to avoid data misinterpretation when drawing conclusion to the individual diseases. Especially, the investigation of genetic disorders presupposes the validation of genetic background retention including healthy or mutated sequences respectively in the individual disease systems without other genetic alterations to ensure genome stability. In addition to genomic examinations, karyotypic analysis, STR analysis and typical hallmarks of iPSCs such as morphological features, *in vitro* differentiation capacities (three germ layers, and the expression of pluripotency markers (OCT3/4, SOX2, SSEA-4, TRA-1-60, TRA-1-81) need to be confirmed. Moreover, before iPSC line banking, contamination of mycoplasma and reprogramming viruses should ideally be tested to ensure high quality criteria.

4.3.1 Genetically stable zero-footprint iPSC lines

Sanger sequencing of the three patient-derived, the two healthy donor-derived as well as the three CRISPR/Cas9 gene-edited iPSC lines revealed the same genetic identity as their origin cell source. Additionally, short tandem repeat analysis confirmed the same genetic DNA-fingerprints compared to the original cell source, in detail dermal fibroblasts for reprogrammed iPSC lines and NC6M iPSCs for gene-edited iPSC lines. However, some studies reported that the acquisition of novel mutations during prolonged cultivation is unavoidable and leads to the requirement of cultivating early passaged iPSC clones directly after the entire characterization of all quality criteria. The passaging of iPSCs provokes even more restrictions that manifest in karyotypic alterations which can be acquired over prolonged cultivation time (Rebuzzini et al., 2016, Yoshihara et al., 2017) or by increased culture densities (Jacobs et al., 2016). The exact factors that promote karyotype abnormalities are not known so far. Some studies have not excluded that to some extent karyotypic abnormalities could occur due to pre-existing genetic and epigenetic differences within the individual original somatic cell source (Cheng et al., 2012). However, some studies revealed that karyotypic alterations can be acquired during reprogramming per se (Rebuzzini et al., 2016, Yoshihara et al., 2017, Cheng et al., 2012). Interestingly, when using SeV-based reprogramming higher aneuploidy rates were reported when compared to other reprogramming techniques such as mRNA-based reprogramming (Schlaeger et al., 2015). Therefore, karyotypes were investigated for all generated iPSC lines as well as for the positive control NC6M. For each cell line, ten metaphases were analyzed at early passages without showing karyotypic alterations. In the present work, we were able to confirm, that genetically stable iPSC lines with normal karyotypes were used only. When compared to ESC studies, extensive cultivation can give rise to 35 % karyotype abnormalities (Lim et al., 2011, Dekel-Naftali et al., 2012, Jacobs et al., 2014). To overcome this issue some studies reported higher ROS states that were driving karyotype anomalies, so it was recommended to create a hypoxic environment through cultivation of iPSCs below 5 % oxygen to stabilize the karyotype (Lim et al., 2011). Once karyotypic changes occur, higher proliferation rates are expected accompanied by decreased apoptosis, which may result in overgrown iPSC populations (Spits et al., 2008, Amps et al., 2011, Lund et al., 2012, Avery et al., 2013, Nguyen et al., 2014, Nguyen et al., 2013). These quality limitations are reported to decrease the differentiation potential and alter gene expression profiles, thus hindering downstream phenotypic investigations (Werbowetski-Ogilvie et al., 2009, Gopalakrishna-Pillai and Iverson, 2010, Fazeli et al., 2011). In conclusion, we confirmed the generation of genetically stable zero-footprint iPSC lines within the present thesis, that allow detailed phenotypic investigations of the individual diseases.

4.3.2 Absence of viral RNA and mycoplasma contamination

The second disadvantage of the SeV-based reprogramming method is the prolonged presence of `KMOS` within iPSCs. Especially the prolonged presence of the tumorigenic transcription factor (TF) c-MYC, that persists up to 25 passages in the cells, raises safety concerns. c-MYC has the ability to act in signaling pathways that are involved in self-renewal and cell immortalization (Ban et al., 2011, Wang et al., 1998, Okita et al., 2007). Therefore, alternative protocols arose wherein the removal of c-MYC was reported to result in lower reprogramming efficiencies (Nakagawa et al., 2008, Wernig et al., 2008). Avoiding the usage of c-MYC in our setting was not feasible, therefore all generated iPSC lines were analyzed towards the persisting presence of residual viral RNA between passages 15 to 22. The comparison to the positive control revealed the absence of the residual viral RNA of the *KOS* (*KLF4*, *OCT3/4*, *SOX2*), *c-MYC* and *KLF4* vectors two days after viral induction already. As different available positive controls were tested and standard approaches by the manufacturer were used, we assumed that there was no residual viral `*KMOS*` RNA in all generated iPSC lines. The unexpected absence of *c-MYC* and *KLF4* RNA in the positive control after one day already, could be explained by a second thawing cycle prior to reprogramming that may have altered viral activity to a lower level but with sufficient activity for iPSC generation. Additionally, the absence of mycoplasma contamination was validated in all iPSCs to allow their usage in other experimental approaches such as characterization of pluripotent capacities. The continuous monitoring for mycoplasma infection was essential given their

effect in altering cellular properties in ways that might confound phenotypic analyses (Musunuru et al., 2018).

4.3.3 Stem-cell like characteristics in all generated iPSC lines

First, the investigation of iPSC morphology provides enormous information about the undifferentiated state and population purities. When pure, stem cell-like cell clusters are highly dense, whereas spacing of the cells can be observed during differentiation. The visual observation of cellular spacing allowed a qualitative estimation of the iPSC states in the working routine (Wakui et al., 2017). In contrast to fibroblasts, bright field images revealed closely neighbored cells in all eight generated iPSC lines, which were in accordance with the positive control NC6M. All cell lines displayed typical stem cell-like cluster formation without enhanced distance between individual iPSCs. Additionally, typical stem-cell like prominent nucleoli were observed with less intercellular spacing, thus confirming pluripotent properties on a regular base during continuous cultivation of iPSC lines over prolonged time spans.

Second, the expression of typical stem cell markers OCT3/4, SOX2 and TRA-1-81 was assessed via immunofluorescence. We observed the nuclear expression of the TFs OCT3/4 and SOX2 in all generated iPSC lines when compared to the positive control. The nuclear localization in all cell lines verified the presence of essential TFs for undifferentiated cells, thus confirming their involvement in self-renewal and maintenance of pluripotency within all iPSC lines. The expression of TRA-1-81 as type I transmembrane glycoprotein was confirmed in all iPSC lines as well to validate an additional exogenous pluripotency-associated protein. Flow cytometric analysis of stem cell-characteristic cell surface antigens displayed at least 92.1 % SSEA-4^{+} (PKP2-KO) and 92.3 % TRA-1-60^{+} cells (DSG2-KO, DNAJC19tv) providing a proof of high population purities in all generated iPSC lines.

Third, the capacity of iPSCs to subsequently differentiate into cells of all three germ layers was analyzed by immunofluorescence staining after embryoid body formation in a long-term *in vitro* experiment. The expression of α-SMA, AFP and TUBB3 in all iPSC lines illustrated mesodermal, endodermal and ectodermal fate respectively. The presence of cell types belonging to all three germ layers confirmed their differentiation capacity.

Taken together, the main hallmarks of iPSCs defined by self-renewal and the potential to differentiate were verified for all eight cell lines. Extended quality criteria like typical stem-cell like morphological features, the absence of viral or mycoplasma contaminations, the genetic stability of the healthy lines as well as the individual mutation carrier cell lines were confirmed which allowed the further usage of all iPSC lines for cardiac differentiation to generate *in vitro* systems of ACM, DCMJC and DCMA.

4.4 Robust CMs differentiation and arising challenges

The detailed investigation of inherited cardiomyopathies in an *in vitro* setting requires the robust generation of iPSC-derived CMs. Therefore, efficient and consistent cardiac differentiation protocols are needed that are free of cost-intensive media supplementation. To date, various cardiac differentiation protocols emerged, however a gold standard protocol that is applicable to multiple iPSC lines is still needed. Interestingly, major differences arose upon usage of different protocols for the recapitulation of individual cardiac diseases including applicability, CM subtype identity, population purities and maturation states. Kadari et al., 2015 developed an optimized monolayer protocol to differentiate iPSCs into CMs that was already approved in the NC6M control iPSC line (Kadari et al., 2015). Based on this applicability, the cardiac differentiation protocol was adapted for the differentiation of all DCMA-associated iPSC lines. In total, five different iPSC lines, three mutated (DNAJC19tv, DCMAP1, DCMAP2) and two control lines (NC6M, NC47F) were successfully driven to the cardiogenic path within seven to twelve days. Comparing the line-dependent protocol adaptations we observed that defined seeding densities needed to be assessed individually prior to cardiac induction. Cardiac differentiation is initiated by the application of the GSK3β inhibitor CHIR, an indirect activator of Wnt signaling (Wu and Pan, 2010) and BMP4 (Kattman et al., 2011) to activate BMP signaling. As the standard concentrations proved to be optimal for the generation of CMs, we report that 5 µM CHIR together with 25 ng/ml BMP4 were sufficient to induce the mesodermal fate in all five cell lines. This concentration-dependent

induction of cardiac specification depends on the proportion of iPSCs in the S/G_2/M stage of the cell cycle (Laco et al., 2018) that in turn primarily relies on cell densities and cultivation time (Rosowski et al., 2015, Zhao et al., 2019, Burridge et al., 2012). These invariable factors constantly change which leads to the requirement of permanent adaptations. These insights serve as an example for the observed heterogeneity in *in vitro* differentiation settings and the limited usage of iPSC-derived CMs. We also observed high variabilities between the different CM differentiation procedures even if the set up was standardized, thus hindering efficient generation of CMs. The activation and inhibition of Wnt signaling at certain timepoints is a key player in the generation of cardiac cells. In our monolayer approach standard time frames were applied to NC6M, NC47F, DNAJC19tv and DCMAP2. In contrast, DCMAP1 iPSCs required the skipping of day 1 of the standard protocol to be successfully differentiated. Therefore, DCMAP1 needed a reduced time frame of Wnt activation which could in turn mean that extended activation of Wnt has a negative effect on the generation of DCMAP1 iPSC-CMs.

The precise modulation of Wnt signaling from mesendoderm to cardiac mesoderm is the most important step in the generation of CMs. It was reported that this specification step determines the overall efficiency of the CMs yields and purities (Zhao et al., 2019). Imprecise modulation resulted in definitive endoderm due to low Wnt signaling or presomitic mesoderm due to enhanced Wnt signals (Zhao et al., 2019). Many studies emerged for the robust generation of CMs and unraveled the impact of human genetic variations in driving the heterogeneity and their influence on differentiation (DeBoever et al., 2017, Kyttala et al., 2016, Kilpinen et al., 2017) due to changes in methylation profiles (Kyttala et al., 2016), copy number variations (Kilpinen et al., 2017) and alterations in gene expression profiles (DeBoever et al., 2017) that provide an additional proof for the requirement of isogenic systems. Moreover, the efficiency not only depends on the donor tissue but also on the cell source used for reprogramming which confers different epigenetic memories in iPSCs (Zhao et al., 2019, Burridge et al., 2012). Other general limitations are set by the lack of proliferation after CM differentiation hindering the large-scale production and the unknown influence of complex multicellular ecosystems, including intercellular communications between cells and tissues or other organ systems as well as pathogens. Therefore, multicellular organoid systems and scalable production via the usage of 3D systems were developed to optimize iPSC-CMs in *in vitro* settings. This feasibility is very limited due to the high costs and labor-intense work in contrast to 2D approaches. However, there are difficulties in using monolayer-derived CMs as well, as this condition requires more specific medium compositions than 3D approaches and the detachment of CMs is frequently observed after prolonged cultivation time which results in increased cell loss (Eschenhagen et al., 2015). After being able to generate iPSC-derived CMs, disease-specific and approach-dependent *in vitro* settings need to be established regarding the scientific aim. To investigate DCMA, three main challenges arose to be able to fully recapitulate disease-associated phenotypes: CM subtype identity, population purities and approach-dependent maturation states.

4.4.1 Verification of the ventricular identity

Depending on the individual CM differentiation protocol one or even more CM subtypes can evolve, including atrial-like, nodal-like and ventricular-like CMs with variable yields (He et al., 2003, Zhang et al., 2009). DCMA manifests in ventricular enlargement and thinning that compromises ejection fraction of the patient, therefore iPSC-CMs of ventricular identity were required to fully recapitulate disease-associated phenotypes. Differentiated CMs typically represent a mixture of all three subtypes that contain mainly ventricular cells (He et al., 2003) like in the report of Burridge et al.,2012 with ~57 % of cells that express a ventricular-like phenotype (Burridge et al., 2012). As Kadari et al., 2015 did not specify on the resulting predominant subtype, immunofluorescence staining was performed to exclude subtype-specific heterogeneity in our DCMA *in vitro* setting. Co-staining of the cardiomyocyte-specific cTnT together with MLC2v allowed the identification of double-positive cells revealing ventricular CM fractions in a given cell population (Kane and Terracciano, 2017). Quantifications resulted in ventricular-like CMs as predominant subtype to over 95.0 % $MLC2v^+/cTnT^+$ cells to equal yields in all five cell lines. Other studies unraveled the usage of IWR-1, a canonical Wnt/β-catenin pathway antagonist (Chen et al., 2009), as a key player in cardiomyocyte subtype specification to gain ventricular identity (Karakikes et al., 2014). As this molecule is used in the standard protocol of Kadari et al., 2015 we considered the

ventricular identity to equal yields in all five iPSC lines as basis prior to all phenotypic investigations. As obtaining pure populations of only one subtype is a challenge in general, major advances were made to achieve atrial-like and nodal-like subtypes, either by stage-specific protocol modulation of retinoic acid alone (Josowitz et al., 2014, Cyganek et al., 2018, Devalla et al., 2015) or together with BMP-signaling pathway activation (Protze et al., 2017) respectively.

4.4.2 Achievement of high purity cardiomyocyte populations

The existing protocols of iPSC differentiation towards the cardiovascular lineage often result in mixed cell populations including CMs and non-CMs comprising endothelial cells, smooth muscle cells (Yang et al., 2008) and cardiac fibroblasts (Huebsch et al., 2016, Humeres and Frangogiannis, 2019). The usage of the non-CMs marker vimentin, that is ubiquitously expressed in stromal cells (Huebsch et al., 2016) allows the identification of cardiac fibroblasts (Camelliti et al., 2004), endothelial cells (Franke et al., 1979) and smooth muscle cells (Gabbiani et al., 1981) that evolve as a byproduct during cardiac differentiation via immunofluorescence (Huebsch et al., 2016, Humeres and Frangogiannis, 2019). It was reported that fine tuning of Wnt signaling is the key to achieve high CMs yields (Zhao et al., 2019). Inconsistent activation and inactivation of Wnt signaling cascades results in high variations in CM yields and was even observed under standardized conditions in a cell line specific manner (Zhao et al., 2019). A high CM yield and consistent generation of high-quality CMs would not only allow more precise insights into disease remodeling but furthermore open the way towards treatment after infarct events or myocardial disease via autologous transplantation. In comparison to other differentiation strategies large differences can be observed for the cultivation reagents of iPSCs, the subset of small molecules and the maintenance medium of iPSC-CMs that directly contributes to different iPSC-CMs subtypes, purities and maturation levels. For some approaches a mixed cell population of CMs and non-CMs might be tolerable as long as it is possible to visually check for spontaneously beating cells or identify CMs by co-staining of CM-specific markers in order to focus the analysis only on those cells regarding protein localization studies via immunofluorescence or electrophysiological approaches.

Scientists try to overcome impurities of CM yields by developing purification methods that can be performed after CM generation by focusing on the difference between CMs and non-CMs. The higher mitochondrial content allows CMs to metabolically use lactate as energy source. Therefore, it was reported that iPSC-CM cultivation in glucose-depleted, lactate-rich medium increases the yield of iPSC-CMs to as high as 99 % (Tohyama et al., 2013). The same system was used in the standard protocol of Kadari et al., 2015 that was able to enrich CMs yields to 95 % $cTnT^+$ cells (Kadari et al., 2015), whereas the same enrichment strategy demonstrated lower purities of 82 % $cTnT^+$ cells in other *in vitro* systems (Rupert et al., 2020). The adaptation to our *in vitro* system resulted in visually observed increased mortality after five days of enrichment in the DNAJC19 mutant cell lines, which forced us to shorten the time span of enrichment to three days (DCMAP1) and four days (DCMAP2, DNAJC19tv) which was sufficient to acquire higher CM yields but increased fractions of surviving non-CMs as well. These insights provided a first hint towards metabolic alteration in DCMA iPSC-CMs to link defects in lactate uptake or further metabolic processing to metabolic changes that will be discussed in section 4.5.9. The shortened enrichment time span resulted in an average of 71.9 % $cTnT^+$ cells in all five iPSC lines. We recognized a high variation that clearly depends on the initial CM yields.

To overcome this problem, other prominent purification methods arose that comprise antibody labelled cell sorting such as FACS or MACS. We adapted the nongenetic strategy MACS that includes a two-step procedure to purify iPSC-CMs: antibody-based elimination of non-CMs and the positive selection of CMs via signal-regulatory protein-α (SIRPA) (Dubois et al., 2011) or vascular cell adhesion molecule 1 (VCAM1) (Uosaki et al., 2011) that was reported to give rise to >95 % pure populations of functional CMs (Uosaki et al., 2011). Prior to MACS, the mixed population of NC6M iPSC-CMs revealed the presence of both 48.8 % $cTnT^+$ and 51.1 % $vimentin^+$ cells that were divided into a CM fraction and a non-CM fraction. After performing the PSC-derived cardiomyocyte isolation 94.8 % $cTnT^+$ cells were identified in the CM fraction whereas the non-CM fraction consisted of 97.4 % $vimentin^+$ cells, confirmed in NC6M iPSC-CMs representatively. Even though high CM purities were achieved, increased mortality of iPSC-CMs was observed that might be accounted to the detachment, the time-consuming procedure

as well as increased mechanical stress. Therefore, MACS was performed prior to more precise investigations only such as metabolic and expression profile analyses, that require purified CMs populations to over 95 %. To date, no nongenetic cardiac differentiation protocol exists that can consistently produce iPSC-derived CMs to above 90 % $cTnT^+$ yields (Zhao et al., 2019). In general, high purity hiPSC-cardiomyocyte populations of higher than 80 % were set as minimum standard for clinical translation (Eschenhagen et al., 2017).

4.4.3 Characteristic hallmarks of adult-like maturation stages

During cardiac differentiation the kinetics of gene expression profiles range from pluripotency markers, mesoderm specification, primitive streak-like, cardiac mesoderm, cardiovascular progenitors and terminally differentiated CMs in a time course of eight days after cardiac induction (Karakikes et al., 2014). The generation of CMs can be recognized by a spontaneous beating behavior in which fetal gene expression profiles were identified (Cao et al., 2008) that refer to immature CMs during the first-trimester gestational stage (van den Berg et al., 2015, Xu et al., 2009, Synnergren et al., 2012). General morphological features were assessed directly after the onset of contraction and revealed triangular shape, mononuclearity, no bi-directed alignment of sarcomeres as well as small CM sizes underlining the presence of immature CMs. These findings are in line with previous studies that reported a fetal-like morphology (Snir et al., 2003), immature ion channel composition (Beqqali et al., 2006) and premature electrophysiology (Davis et al., 2011). The biggest differences when comparing iPSC-CMs to adult heart tissue becoming obvious with regard to cardiac ion channel and Ca^{2+} handling genes that were reported to be still immature on day 22 even though on the molecular level high similarities to human heart tissue were validated (Synnergren et al., 2008, Synnergren et al., 2010). To date a big debate is still active concerning the degree of immaturity of iPSC-derived CMs to certain time points and whether this system can be used as a model for early-onset cardiac diseases (Eschenhagen et al., 2015). Currently research is focused intensly on the maturation state of iPSC-derived CMs and the identification of approaches to accelerate maturation *in vitro*. CM maturation approaches can be divided into hormone-based, mechanical or electrical stimuli (Nunes et al., 2013), co-cultivation (Tulloch et al., 2011), physical stiffness and prolonged cultivation times (>80 days) (Lundy et al., 2013). Each study showed that maturation can be promoted towards a more mature state, especially the generation of 3D tissues that combines mechanical load with a 3D network can promote maturation to higher degrees (Ronaldson-Bouchard et al., 2019, Ronaldson-Bouchard et al., 2018). Common to all methods are a less-fetal but still not fully adult CM criteria (Schaaf et al., 2011, Mannhardt et al., 2016, Uzun et al., 2016, Lemoine et al., 2017). All approaches lead to induction of maturation to different degrees, but none of them is sufficient to meet all requirements of adult human CMs completely (Robertson et al., 2013, Yang et al., 2014, Karakikes et al., 2015a, Sayed et al., 2016). Depending on the individual scientific question or the scientific approach different maturity levels are required. Nonetheless, a disease-specific recapitulation in “rejuvenated” cellular properties allows additional insights into developmental process and can give insights into disease-progression. In particular remodeling of inherited cardiomyopathies requires an iPSC-CM model system that is able to fully recapitulate disease relevant cellular subtypes, maturation stages and approach-dependent purities during the investigation of disease-specific phenotypes. The patients of our *in vitro* model system to mimic DCMA are comprised of a 8-year-old boy (DCMAP1) and his 10-year-old sister (DCMAP2) that presented manifestations of DCMA very early thus allowing to investigate disease-associated phenotypes using adult-like iPSC-CMs. To study DCMA adult-like cellular properties the main features were set towards high mitochondrial content, large CM sizes, sarcomere-like alignment, OXPHOS metabolic states and formed T-tubules.

4.4.3.1 Promoting maturation via prolonged cultivation times

Higher maturation levels can be promoted by extension of the cultivation time but this needs to be confirmed individually due to high variabilities among the different iPSC-CM lines (Kanda et al., 2016, Yang et al., 2014). CM sizes were assessed at defined time points (day 30, day 60, day 90 and day 120) to quantify typical hallmarks of mature-like CMs by semi-automated ImageJ quantifications of immunofluorescence stains and by visual observations. The assessment of typical adult-like features on day 30 revealed no remarkable maturation states represented by round or polygonal CMs,

mononucleated cells, disorganized sarcomeres and small cell sizes of (~ 2950.43 µm^2). Nevertheless, a significant increase in CM sizes was observed especially on day 60 with an average size ~ 4606.7 µm^2. On that stage, rod and elongated CM shapes, higher yields of binucleated cells as well as organized sarcomeres were recognized. Prolonged cultivation times to 90 or 120 days resulted in even bigger CM sizes but with higher variabilities that were accompanied by reduced rod-shaped morphologies and reduced fiber-densities. Compared to other publications extended cultivation times to ~360 days revealed a CM size of ~4067.9 µm^2 (Kamakura et al., 2013). These enhanced sizes were reached on day 60 in our setting. The investigation of the cardiac muscle gene expression was monitored at day 60 and unraveled a stable plateau of cardiogenesis in embryonic bodies (Zhang et al., 2009). Moreover, the human heart CMs lose their capacity to proliferate with the progression of age and similar observations were made *in vitro* wherein CMs experienced a tremendous reduction of proliferation during 60 days in culture (Zhang et al., 2009). Additionally, the striated MLC2v labeling at the A-band of the sarcomere is also a well-known indicator of higher maturation levels and was observed in CMs from all cell lines (Zhang et al., 2009, Cyganek et al., 2018, Guo and Pu, 2020). On day 120, the expression of typical maturation-associated proteins such as cTnI-C and Cx43 at cell-cell contact sites was further confirmed, that are hallmarks that are in particular associated with E-C coupling. Importantly, higher maturation states can be recognized by a switch of the fetal slow skeletal TnI (ssTnI) to the postnatal cardiac cTnI-C (Chun et al., 2015, Guo and Pu, 2020). TEM analysis of healthy CMs after 135 days of standard cultivation additionally displayed the presence of other key features like fascia adherens-like structures as well as sarcomere-like organization of contractile filaments with already identifiable A- and I-band and Z-line structures as well as M-bands and the presence of intermyofibrillar mitochondria. The observed difficulties regarding prolonged culture were characterized in particular by lowered CM viabilities as previously reported (Rajamohan et al., 2013, Denning et al., 2016). Moreover, the analysis of at least 60-day-old iPSC-CMs during phenotypic investigations of DCMA unraveled adult-like characteristics already at earlier time points, that were approved to fulfill mature characteristics that are individually discussed in the corresponding sections.

4.4.3.2 Physical stiffness accelerated maturation

To improve the maturation process, we adapted a mattress-based cultivation method that comprises a specified matrix, which is able to polymerize bi-directionally. Therefore, CMs are forced to align in a bi-directional manner and the physical stiffer environment is predicted to promote maturation of the seeded CMs (Feaster et al., 2015). The individual maturation stages using standard cultivation versus mattress-based cultivation were analyzed in NC6M as representative cell line on three different time frames and the examination of two main hallmarks, CM sizes and the translocation of JP2 from the nucleus to the cytoplasm were assessed using ImageJ semi-quantitative examination. The usage of the mattress-cultivation strategy revealed a faster alignment of rod and elongated CMs, a bi-directional alignment of sarcomeres, an accelerated translocation of JP2, higher multinucleation and increased cell sizes together with a homogenous distribution of JP2 that shifted from 13.1 % on day 20-30 to 61.2 % on day 60-70. A homogenous distribution of JP2 is particularly required to anchor the SR to the T-tubules to allow proper T-tubule biogenesis, a main compartment that contains proteins such as LTCC that enable proper Ca^{2+} handling (Feaster et al., 2015, Beavers et al., 2014). Other reports on fetal CMs confirmed the necessity of JP2 in Ca^{2+} handling (Itzhaki et al., 2011, Lieu et al., 2009). Thus, we could confirm the successful adaptation of the mattress-based cultivation strategy by enhancing maturation processes that in turn allows the investigation of E-C coupling processes theoretically earliest on day 60 when using matrigel-mattress cultivation. To date it is well known that during heart development the extracellular matrix is crucial and therefore important to enhance maturation processes (Chun et al., 2015). Other techniques like microcontact printing or even engineered heart tissues are currently performed by using a comparable strategy to improve maturation states such as sarcomere alignment and Ca^{2+} handling properties by the modification of extracellular matrix components such as fibrinogen combined with hESC-Matrigel^{TM} (Wang et al., 2014, Stoehr et al., 2014). The advantage of mattress-cultivation is little lot-to-lot variability, the usage of standard equipment and the less-cost intense applicability that was enabled by simultaneous examination of contractility and Ca^{2+} homeostasis (Feaster et al., 2015). Studies on stiffness-mediated maturation revealed that the activation via

mechano-sensing at focal adhesions affects the phosphorylation of a variety of protein kinases that are essential during cardiomyogenesis (Young et al., 2014). Moreover, the cultivation of neonatal rat ventricular CMs on different substrates unraveled enhanced maturations states that involved RhoA/ROCK signaling pathways (Jacot et al., 2008).

4.4.4 Approach-dependent cultivation strategies for accurate phenotypic investigation of DCMA

Taken together, MACS after cardiac enrichment resulted in extremely highly enriched CM yields for each population, whereas mattress-based cultivation in combination with a prolonged cultivation time of ~120 days ensured enhanced maturation states. Even though the combination of both strategies would be the optimal system to assess all morphological and physiological aspects, their implementation as standard cultivation is not beneficial due to high costs and time-consuming procedures that would require more manpower. However, regarding the individual approach, distinct purities as well as maturation states were selected to accurately allow the examination of a cardiomyopathy-associated phenotype. The present and future assessment of morphological or structural questions (IF, TEM), expression profiles (protein, RNA) as well as OMICS approaches (Proteomics, Lipidomic, Metabolomics) was directed after performing the standard cultivation of at least 60 days with the optional incorporation of a second enrichment strategy to achieve higher CM yields to a minimum of estimated 70 % $cTnT^+$ purified cell populations (Fig. 4.1 A). This adaptation already represented mature-like cell states and enabled an approach-dependent calculation compared to endogenous CM levels by using cTnT or α-sarcomeric actinin expression as an internal control as well as equal purity states prior to phenotypic investigation. With regard to metabolic features, measurements using the seahorse system or radioactive tracer uptakes on viable cells hindered downstream normalization of CM contents and thus required MACS to ensure high population purities. Moreover, 60-day-old CMs were needed to ensure high OXPHOS states already prior to examination of metabolic changes in DCMA derived cells (Fig. 4.1 B). The investigation of electrophysiological aspects by using the IonOptix system allowed the analysis of Ca^{2+} handling, contractility as well as arrhythmic potential on single cell level by visual identification of contracting cells prior to analysis. This examination required the highest identifiable maturation states that were assumed to be achieved after combining the mattress-based cultivation method together with a prolonged cultivation time of at least 120 days (Fig. 4.1 C). Summarizing, in total three adapted cardiac differentiation strategies were applied to address the individual scientific questions with the appropriate required purities and maturation states, allowing a detailed examination of the molecular mechanisms that are directly linked to DCMA. Despite the close association of molecular and physiological properties of *in vitro*-derived CMs a critical evaluation is needed in particular for the translational usage of potential treatments (Brandao et al., 2017).

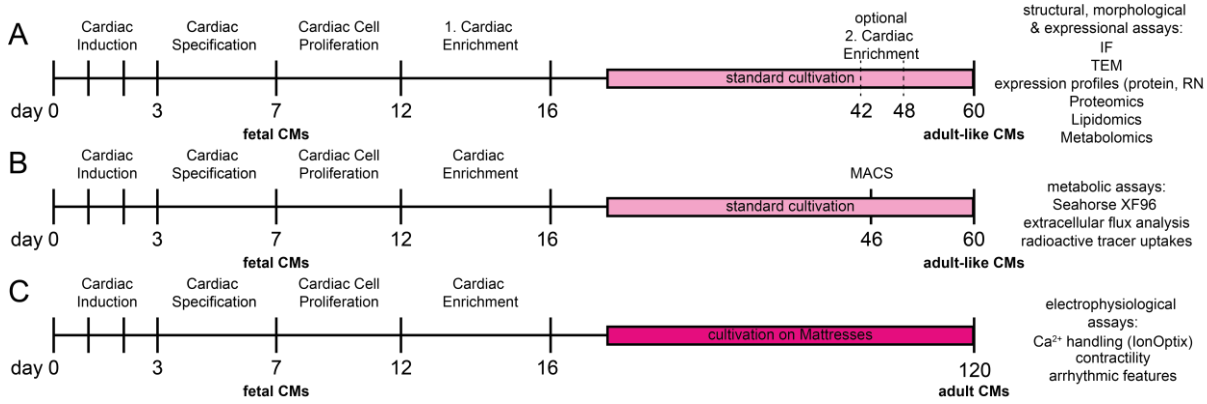

Figure 4.1 Summary of three adapted cardiac differentiation strategies for the individual approaches with required purities and maturation states.
(A) Standard cultivation using the cardiac differentiation protocol after Kadari et al., 2005 with the optional incorporation of a second enrichment phase when undesirable growth of non-CMs is observed. Highly purified CM yields and mature states were used to assess the protein localization (IF), expression studies (WB, RT-PCR, qPCR), ultrastructure (TEM), proteomics, lipidomics and metabolomics. **(B)** Adapted CM differentiation protocol of (A) by including an additional MACS step on average two weeks before the individual assays such as Seahorse XF96 extracellular flux analyzer experiments and radioactive tracer uptakes. **(C)** Combination of the cardiac differentiation protocol after Kadari et al., 2005 with the matrigel-mattress method after Feaster et al., 2015 and the prolonged cultivation to at least 120 days to ensure proper T-tubule formation and higher maturation levels prior to electrophysiological assays like Ca^{2+} handling studies, arrhythmic behavior and contractility quantifications.

4.5 Unraveling pathomechanisms with a self-generated model system of DCMA

Cardiomyopathies like DCMA are mainly influenced by genetic factors predisposing to the development of heart failure, one of the most common causes of death in industrialized countries (Yusuf et al., 2001b, Yusuf et al., 2001a, Mathers and Loncar, 2006). Metabolic aspects, energetic deficits and oxidative stress play a causal role in the pathophysiology of heart failure in general and are key aspects in mitochondrial cardiomyopathies as well (Sabbah, 2020). The latter includes DCMA an autosomal recessive disorder arising from homozygous mutations in the *DNAJC19* gene. The main clinical features are characterized by cerebellar ataxia, DCM, 3-MGA, a metabolic syndrome as well as a high variability of other phenotypes like prolonged QT interval. The original study on a cohort of 18 DCMA patients from a consanguineous Canadian Hutterite population identified the association of a shared splice acceptor site mutation in the *DNAJC19* gene, (NM_145261.4):c.130-1G>C with DCMA causing a lack of the full-length transcript (Davey et al., 2006). The association of *DNAJC19* with DCMA was previously reported by the shared loss of full-length transcripts (Wortmann et al., 2012, Ojala et al., 2012, Ucar et al., 2017). The usage of rare genetic model disease systems often recapitulates common phenotypes and offers the unique opportunity to study disease mechanisms, pathological developmental processes and to discover novel diagnostic and treatment strategies (Maron et al., 2006). In the present thesis, a DCMA-based *in vitro* system was generated with patient-derived and genetically modified iPSC lines to focus on mechanistic insights and the role of DNAJC19 in forcing disease-linked phenotypes. DCMA association to a metabolic syndrome leads to the assumption of impaired mitochondrial homeostasis. To maintain mitochondrial function, essential processes are required including mitochondrial biogenesis consisting of mitochondrial protein import and dynamics (fission and fusion), lipid processing and quality control. One hypothesis suggests a defect in mitochondrial pre-sequence protein import due to the lack of interaction of DNAJC19 with the TIM23 translocase subunit mtHsp70 and subsequently **mitochondrial biogenesis** (Davey et al., 2006). Another more recent hypothesis suggests, that DNAJC19 is a direct interaction partner of PHB2 and therefore involved in the regulation of **CL remodeling** (Richter-Dennerlein et al., 2014). The chronology of pathological molecular and metabolic events will help to understand how proposed alterations in mitochondrial function can lead to DCM and heart rhythm disturbances. In more general, advances may also enhance our understanding of how energetic deficits and oxidative stress play a role in the pathophysiology of heart failure. The personalized model system to study DCMA by using human iPSCs-derived CMs offers a revolutionary *in vitro* platform and a novel potential in the development of new therapies (Ross et al., 2016).

4.5.1 Loss of full-length *DNAJC19* on transcriptional and translational level in DCMA cell lines

Sanger sequencing analysis of the DNA of both affected siblings of the Canadian Hutterite population displayed the same homozygous *DNAJC19*(NM_145261.4):c.130-1G>C mutation, similar to the report of Davey et al., 2006, in fibroblasts as well as in the generated iPSC lines. Whole exome sequencing of DCMAP1 and DCMAP2 fibroblasts presented the same splice acceptor site mutation of intron 3 without other rare cardiac disease-associated genetic variants (validated by PD Simone Rost, Institute of Human Genetics, University of Würzburg). As previously described, the homozygous mutation is predicted to cause aberrant splicing by exon 4 skipping and therefore results in the loss of the full-length *DNAJC19* transcript. RT-PCR analysis by using the same primer sets as in the report of Davey et al., 2006 allowed the detection of both annotated transcript variants in the generated healthy control lines (NC6M, NC47F). As in the report of Davey et al., 2006 the detection of a 525 bp band corresponds to the full-length coding sequence, whereas the 445 bp band resembles the transcript variant lacking exon 4 (∆ex4). We observed a very strong 525 bp and a weak 445 bp band in fibroblasts, iPSCs and iPSC-CMs when using cDNA of both healthy controls that indicate that alternative splicing is common at this site (Davey et al., 2006). RT-PCR analysis of DCMAP1 and DCMAP2 revealed the loss of the full-length transcript (525 bp) in the generated iPSC lines and their differentiated derivates. Additionally, the higher expression of the 445 bp transcript strongly underlined the splicing defect that resulted in exon 4 loss that was identified in all three analyzed cell types. This leads to the assumption, that both patient-derived cell lines accumulate the 445 bp transcript to higher levels due to aberrant splicing to achieve the same transcription levels as healthy cells. The examination of the CRISPR/Cas9-edited DNAJC19tv iPSC line demonstrated a biallelic mutation *DNAJC19* (NM_145261.4):c.[131_140del];[137_138insAGTATAATTGCC]. RT-PCR using DNAJC19tv cDNA as template resulted in the presence of two bands close to the 525 bp band illustrating that instead of the aimed single bp substitution a biallelic modification was generated in DNAJC19tv. The two different transcript variants, one allele representing a 10 bp deletion (~515 bp band) and the other allele a 12 bp insertion (~537 bp band), are theoretically out of frame with exon 5 and in both cases lead to a predicted premature termination codon indicating a high probability of mRNA degradation by the nonsense-mediated mRNA decay mechanism. We were not able to identify the full-length 525 bp transcript, but a weak 445 bp ∆ex4 band. Thus, we assumed that the loss of full-length *DNAJC19* and the presence of the 445 bp (∆ex4) as the only transcript resulted in the expression of a C-terminal truncated DNAJC19 protein variant. In contrast to both patient conditions the endogenous level of the ∆ex4 variant is expressed in DNAJC19tv only. According to the guidelines of Santostefano et al., 2015 an optimal system requires an isogenic control apart from patient material that was provided by the CRISPR/Cas9 technology in our DCMA *in vitro* system, thus also eliminates the necessity of multiple clonal cell lines per experiment (Musunuru et al., 2018, Santostefano et al., 2015).

The translation of the full-length transcript results in a DNAJC19 isoform that contains 116 aa and has the molecular weight of 12.5 kDa (NM_145261.4 → NP_660304.1), whereas the ∆ex4 transcript contributes to a C-terminal truncated DNAJC19 protein isoform in the size of 47 aa (ALQ34320.1) and a theoretical molecular weight of 5 kDa. The DCMA-associated predicted translation of *DNAJC19* ∆ex4 yields a 43 aa sequence that is caused by a frame shift in the exon 5 coding region due to exon 4 skipping which additionally provokes the coding of four aa (PYCQ) followed by a premature termination codon (Davey et al., 2006). Protein expression analysis unraveled the loss of the 12.5 kDa full-length isoform in both patient-derived and in the gene-edited DNAJC19tv cell lines in fibroblasts (apart from DNAJC19tv), iPSCs as well as iPSC-CMs. Unexpectedly, we were not able to identify the 5 kDa DNAJC19 protein in all five cell lines in all analyzed cell types. These findings were in line with the DNAJC19 protein expression study that reported the same loss of full-length DNAJC19 due to the frameshift mutation *DNAJC19* (NM_145261.3):c.300delA (p.Ala100fsX11)to be causative for DCMA (Ojala et al., 2012). We therefore assumed that conventional WB is not suitable to identify proteins of that small molecular weights and aim to investigate the presence of DNAJC19 lacking the C-terminal proportion via blue native polyacrylamide gel electrophoresis (BN-PAGE). Since in all three cell lines the predicted C-terminal truncated DNAJC19 protein isoform did not have a DnaJ domain and the full

length DNAJC19 was absent as well, we assume a shared loss of the DnaJ interaction domain in DCMAP1, DCMAP2 and DNAJC19tv.

Theoretically also a third DNAJC19 variant exists that is expressed in healthy cells (NM_001190233.2 → NP_001177162.1). This protein isoform is based on the full-length (525 bp) transcript but lacks a portion of the 5' coding region by using a downstream in-frame start codon. The third N-terminal truncated DNAJC19 protein variant comprises 91 aa and consists of the DnaJ domain only. Loss of ∆ex4 would theoretically result in a 22 aa protein in this isoform that is not predicted to be expressed due to a high likelihood of nonsense-mediated mRNA decay. Since in the present studies on DNAJC19 protein isoforms only the first two described genetic variants of *DNAJC19* were linked to DCMA, we proposed that in particular the DnaJ domain containing full-length isoform makes the difference with regard to intact mitochondrial function. Unexpectedly, we observed slightly higher DNAJC19 expression on mRNA and protein level in NC47F fibroblasts, iPSCs and iPSC-CMs than in NC6M, indicating differences on the transcriptional level that can be related to gender, donor-age or other microenvironmental factors. In conclusion, all mutated fibroblasts, iPSC lines and their differentiated CMs presented the same loss of full-length DNAJC19 on mRNA and protein level that underlines that the lack of the DnaJ domain may be causative for the progression of DCMA.

4.5.2 Loss of mitochondrial localization and nucleus-restricted DNAJC19 expression pattern in mutant cells

Immunofluorescence stains in both healthy iPSCs (NC6M, NC47F) revealed DNAJC19 expression in the nucleus as well as in the perinuclear region. Unexpectedly, weak but specific DNAJC19 signal was observed in all three mutant iPSC lines that was limited to the nucleus only. The same expression pattern was observed after investigation of 60-day-old mutant iPSC-CMs by demonstrating a subcellular compartmentalization of DNAJC19 in the nucleus only. All DCMA conditions presented a loss of the co-localization of DNAJC19 with mitochondria accompanied by an overall nearly non-detectable cytoplasmic DNAJC19 expression when compared to both controls. Contrary to the WB results we conclude that the C-terminal truncated protein variant is still present in DNAJC19 mutation carrier cell lines and this protein variant is predominantly limited to the nucleus. As in both cases the same polyclonal DNAJC19 antibody was used, that is able to detect all isoforms, we predict that the obtained nuclear signal in the immunofluorescence of all DCMA lines can be accounted to the C-terminal truncated DNAJC19 variant lacking the DnaJ domain. To date, the function of DNAJC19 in the nucleus remains elusive and requires further studies. Interestingly, PHB1 as well as PHB2 are also localized in both: mitochondria and nuclei (Tatsuta et al., 2005). Increased nuclear expression of PHB was directly associated to the reduction of complex IV expression levels and thereby was linked to transition from higher energy demands into lower ones, highlighting mechanistic insights into a regulatory function of PHB that might be fundamental for DNAJC19 as well (Taanman et al., 1996, Saraste, 1999, Thompson et al., 2001, Tatsuta et al., 2005). Further transcriptomics and proteomics approaches will help to identify temporal changes at different expressional levels to examine the involved molecular and signaling pathways in DCMA and subsequently heart failure. The nuclear localization of the supposed C-terminal truncated DNAJC19 variant contradicts the assumption that the predicted mitochondrial targeting signal at the N-terminus is crucial for its mitochondrial import. We therefore conclude that an additional C-terminal MTS is required for accurate transport into the mitochondrion which is given in the full-length DNAJC19 protein only. Cristal structures of the full-length DNAJC19 would help to three-dimensionally illustrate a detailed structure of DNAJC19. Further functional investigations are required to identify whether DNAJC19 localization in CMs is the same as in other reports with HEK293T cells wherein DNAJC19 is anchored via the predicted transmembrane domain in the IMM facing its DnaJ domain to the matrix (Davey et al., 2006, Richter-Dennerlein et al., 2014). In summary, all mutated iPSC and iPSC-CMs demonstrated the same loss of full-length DNAJC19 in mitochondrial structures confirming a high suitability of both patient-derived and the gene-edited cell lines to remodel DCMA.

4.5.3 Mitochondrial fragmentation as a primary link to altered DCMA-associated homeostasis

The first mitochondria-associated phenotype was observed during the DNAJC19 co-localization studies where the mitochondrial networks in all three mutant conditions appeared more fragmented and aggregated when compared to control iPSC-CMs. Highly interconnected mitochondrial networks are present in active metabolic cells like CMs (Skulachev, 2001) and have a more fragmented pattern in quiescent cells (Collins et al., 2002). Additionally, mitochondria are highly dynamic organelles that differ in their shape depending on their subcellular localization (Frederic and Chevremont, 1952). In cardiac muscle three distinct populations of mitochondria are proposed to exist: perinuclear mitochondria (PN) and subsarcolemmal mitochondria (SM) that are small and round as well as intermyofibrillar mitochondria (IM) that are in close contact with the contractile sarcomeres and fuse together to form long tubular structures (Piquereau et al., 2013, Frederic and Chevremont, 1952). The maintenance of proper mitochondrial homeostasis requires strict control of the balance between mitophagy and biogenesis and is the key for CMs to adapt to the individual energy demands. The process of mitochondrial biogenesis involves mitochondrial dynamics, such as fusion and fission, and in particular mitochondrial import that serves as a direct link to the proposed function of DNAJC19. Moreover, mitochondria with structural abnormities are closely associated to heart failure (Ide et al., 2001).

4.5.3.1 DNAJC19 predicted function in mitochondrial presequence import

Five different pathways are known that contribute to mitochondrial protein import, which include the classical predominant presequence pathway that uses the translocases of the OMM TOM20 or TOM22 and translocases of the IMM TIM23 by importing newly synthesized proteins from the cytoplasm into the mitochondrial matrix based on a MTS (Yamamoto et al., 2002, Becker et al., 2012). The potential of a direct interaction between DNAJC19 with TIM23 was already proven (Richter-Dennerlein et al., 2014). Even more, the yeast DNAJC19 orthologue Pam18/TIM14 was confirmed to be a constituent of the TIM23 import machinery, thus providing a direct link to function in mitochondrial presequence import (Mokranjac et al., 2003, Truscott et al., 2003, D'Silva et al., 2003). To date, the yeast orthologue of DNAJC19 TIM14 is proposed to be part of the core TIM23 translocon subcomplex in which it is hypothesized to act as a molecular co-chaperone for mtHsp70 by aiding the import and folding of newly synthesized proteins with the help of the DnaJ domain in an ATP- and membrane potential dependent manner (Ohtsuka and Hata, 2000, Mayer and Bukau, 2005, van der Laan et al., 2007). We and others assume that a loss of the DnaJ domain will result in insufficient binding of newly imported proteins which might promote backsliding of mitochondrial presequence proteins and consequently will effect impaired import efficiencies (Davey et al., 2006, Rehling et al., 2003). Additionally, as mitochondrial import and folding of nascent protein chains go hand in hand, DNAJC19 might not only strictly influence the import mechanism but also folding and assembly processes (Mayer and Bukau, 2005). Therefore, it is likely, that loss of DnaJ interaction results in abnormal folding and the aggregation of proteins especially under increased workload or stress for which CMs are prone (Mayer and Bukau, 2005). Interestingly, DNAJC19-deficient HEK293T cells did not display import deficiencies indicating that the DnaJ interaction seemed to not be critical for the functionality of the presequence import pathway (Mokranjac et al., 2003, Davey et al., 2006, Richter-Dennerlein et al., 2014). This hypothesis was further confirmed by a study on the motor-free form of TIM23 that was still able to mediate integration of preproteins into the membrane by a voltage driven preprotein translocation (van der Laan et al., 2007). Up to now it is not entirely clear whether the yeast TIM14 in fact is the human DNAJC19 orthologue despite of the highly conserved sequence similarities especially regarding the DnaJ domain (Davey et al., 2006). But the preservation of the DnaJ chaperone family (heat shock protein 40kD (Hsp40)) in protein translation, folding and translocation throughout evolution underline its hypothesized indispensability in mitochondrial homeostasis. However, these insights point towards another main function of DNAJC19 in mitochondria (Qiu et al., 2006).

4.5.3.2 Insights into abnormal CL remodeling in DCMA

The report of Richter-Dennerlein et al., 2014 hypothesized a novel function of DNAJC19 in mitochondrial homeostasis due to an observed direct interaction with PHB2. It was shown that DNAJC19 is not crucial for the assembly of PHB complexes rather than essential to form a functional complex with PHB rings that are able to serve as scaffolds for diverse phospholipids and proteins (Richter-Dennerlein et al., 2014). Due to the fact that this interaction is mediated by the DnaJ domain, we hypothesized abnormities in the lipid composition of the IMM, as DNAJC19 loss led to alterations in the CL profile (Richter-Dennerlein et al., 2014). Preliminary mass spectrometry data in our study on iPSC-derived CMs revealed a change in CL composition underlining the indispensability of the DnaJ domain in CL remodeling. We observed aberrant CL remodeling due to a shift of CLs to longer and more unsaturated acyl chains in one DCMA-derived condition. The same change in CL profiles was observed in DNAJC19-deficient HEK293T cells that demonstrated longer acyl chains with an increased number of double bonds (Richter-Dennerlein et al., 2014). In addition, changes concerning the acylation of other lipid classes PE, PS, PI were also reported (Richter-Dennerlein et al., 2014). Therefore, we assumed that apart from alterations in phospholipid classes in general, main differences concern the CL structure, without any effect on the overall CL contents as in the report of Richter-Dennerlein et al., 2014. In contrast to our study, the recent report of Rohani et al., 2020 did not identify any changes in saturation and acyl chain composition in DCMA patient-derived iPSC-CMs. Notably they used 20/21-day-old CMs that represented immature states only (Rohani et al., 2020). We assume that proper CL composition is accomplished during the process of cardiomyocyte maturation, given an increase in mitochondrial biogenesis that was observed over prolonged cultivation time (Dai et al., 2017). iPSC-CMs with immature states (<25 days) have low levels of mitochondrial content and may therefore interfere with the characterization of a cardiomyopathy phenotype that itself is increased in prolonged culture systems which in turn allows investigation of mitochondria with enhanced maturation states as well (Dai et al., 2017). Taken together, our investigations on DNAJC19 mutated mature iPSC-CMs demonstrated first abnormal CL profiles and allow the suggestion of a direct interaction of the DnaJ domain with PHB complexes in CMs as the underlying cause of DCMA.

Interestingly, CL and phospholipid profiles were also changed in the DCMA-associated disease BTHS. Shared abnormities were observed with regard to a tendency towards longer and less saturated acyl chains but a decrease in overall CL content upon TAZ-deficiency (Richter-Dennerlein et al., 2014). However, TAZ-deficient cells exhibited an overall decrease in global CL content, that was accompanied by the presence of higher amounts of the immature MLCL in BTHS conditions (Richter-Dennerlein et al., 2014, Dudek and Maack, 2017, Lu and Claypool, 2015). With regard to MLCL contents we did not observe remarkable differences on first side, concluding to the possibility of an at least partly shared pathomechanism in both diseases that remains to be elusive. Our findings highlight that the DnaJ domain might be essential in the formation of functional DNAJC19-PHB-complexes that probably create specific membrane domains within the IMM. It was already demonstrated, that PHB rings are able to form membrane domains that scaffold proteins and lipids and have a proposed function in biosynthetic pathways like for example PE (Osman et al., 2009b, Birner et al., 2003). We suggest, that DNAJC19 interaction is crucial to create and to stabilize these membrane domains within the IMM. In addition, we assume that these microdomains serve as a scaffold for TAZ to efficiently accomplish reacylation of MLCL by making use of LA to result in the heart-specific mature $CL(18:2)_4$ species. In a TAZ-deficient condition reacylation is impaired and therefore leads to accumulation of the immature MLCLs as previously reported (Wang et al., 2014, Dudek et al., 2016, Dudek et al., 2013). In a DNAJC19 mutant condition, TAZ remains functional and is still able to remodel CL, which can be observed by the same overall CL levels as in healthy cells in our *in vitro* system, serving as an explanation for the unchanged MLCL content. It is well known that TAZ has no intrinsic acyl chain specificity and the certain acyl chain composition of CL is dependent on the cellular environment or especially on the physical composition of the IMM (Schlame et al., 2003, Malhotra et al., 2009). These insights provide a link that accumulation of specific acyl groups in microdomains, which are formed by DNAJC19-PHB-complexes, might be essential in conferring FA specificity to TAZ. The DNAJC19 dependent microdomain formation is further confirmed by a yeast study that identified that the membrane insertion of PHB complexes into the IMM

is mediated by TIM23 in a mitochondrial membrane potential dependent manner (Tatsuta et al., 2005). Interestingly, loss of PHB2 or DNAJC19 demonstrated similar alterations in the acyl chain composition of CL species towards longer and less saturated acyl chains (Richter-Dennerlein et al., 2014). Moreover, depletion of TAZ in a DNAJC19 or PHB deficient condition did not lead to further alterations in acylation of all IMM phospholipid classes when compared to TAZ deficiency alone, thus provides a direct link of DNAJC19-PHB-complexes in regulating the acyl chain usage of TAZ to obtain mature CL from MLCL (Richter-Dennerlein et al., 2014).

Furthermore, the impairment of other known acyl transferases like MLCLAT-1 (TFPα) (Taylor and Hatch, 2009, Taylor et al., 2012) and ALCAT1 (Li et al., 2012, Li et al., 2010) upon DNAJC19-PHB-complex depletion had no effect on CL remodeling and was therefore considered unlikely. The function of PHB is linked to important cellular processes like transcriptional control, apoptosis and in particular mitochondrial biogenesis (Tatsuta et al., 2005, Berger and Yaffe, 1998). It therefore stands to reason that the basis of the DCMA-associated abnormities relies in the loss of the DnaJ domain that in turn impairs DNAJC19 interaction capacities and results in abnormal CL compositions, thus negatively influences mitochondrial homeostasis in a high variety of biological functions (Lu and Claypool, 2015). Abnormal CL species are affecting the assembly and function of the IMM and OMM translocases as well that draw parallels to DNAJC19 function in presequence import. Moreover, interaction capacities as well as the integrity of the TIM23 complex within the IMM require CL (Malhotra et al., 2009, Tamura et al., 2006, van der Laan et al., 2007). Additionally, CL influences other essential mitochondrial processes like mitochondrial dynamics (fusion and fission), mitochondrial morphology (cristae formation), mitophagy and the positioning of the OXPHOS complexes as well as mitochondrial solute carriers in the IMM, that are individually discussed in the following sections. We conclude that abnormal CL species are the most upstream mitochondrial defect in DCMA.

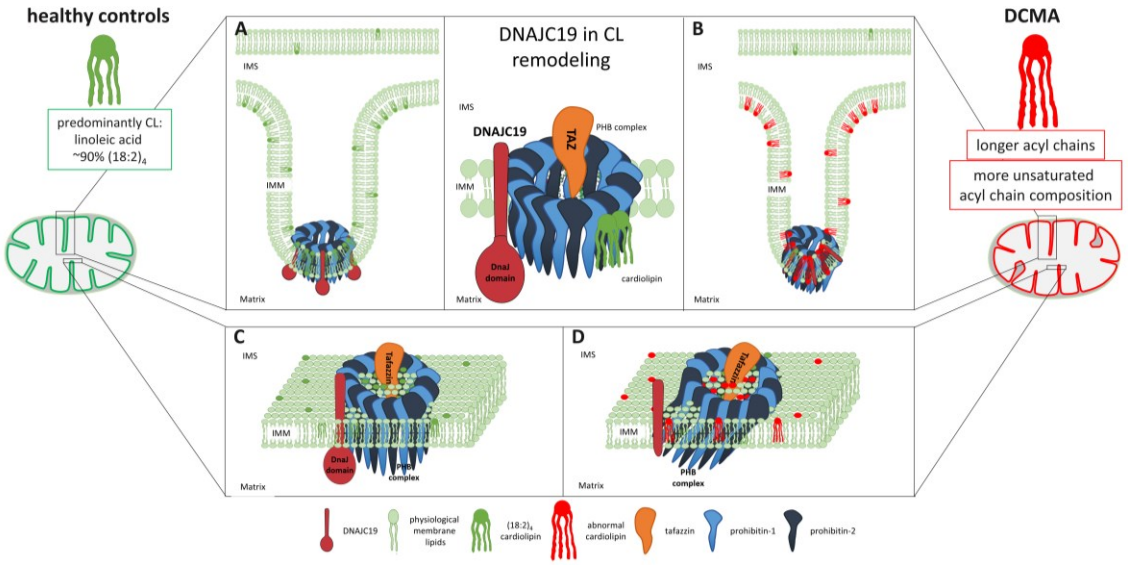

Figure 4.2 A potential molecular mechanism underlying DCMA
The displayed mechanism was modified after (Merkwirth and Langer, 2009, Hernando-Rodriguez and Artal-Sanz, 2018, Osman et al., 2009b, Lu and Claypool, 2015) and combined with the main findings of the present thesis. (**A+B**) Cross sections of cristae of healthy **(A)** and DCMA mutant **(B)** mitochondria. **(C+D)** Top view on the cristae tip as section between the inter-mitochondrial space and the matrix between healthy **(C)** and DCMA **(D)**. DNAJC19 is a heat shock protein that is anchored in the IMM by a transmembrane domain facing its C-terminal domain to the matrix. It is able to interact with PHB complexes (membrane-spanning hetero-oligomeric ring complexes formed by the subunits PHB1 and PHB2) that are undeniable in the formation of membrane domains. The IMM domains confer acyl chain specificity to TAZ, the main acyl transferase in CL maturation. In healthy cells the induced specificity allows abundant formation of the physiologically relevant CL$(18:2)_4$ species. On the contrary, *DNAJC19* mutation carriers lack the C-terminal DnaJ domain that is crucial for PHB interaction. The formation of special physical membrane domains is impaired, which provokes unspecific TAZ remodeling resulting in untypical acyl chain patterns in CL that impede proper cristae formation.

4.5.4 Defects in mitochondrial dynamics

The fact that CLs are able to stimulate fusion and fission by activation of dynamin-related GTPases provide an additional link to the observed fragmentation in DNAJC19-mutant CMs (Ban et al., 2010). In general, mitochondria are highly dynamic organelles that are able to rapidly adapt to the cellular demands referred to as mitochondrial dynamics that is maintained by two essential highly intertwined mechanisms: fusion and fission (Benard et al., 2007, Bereiter-Hahn, 1990, Hackenbrock, 1966, Karbowski and Youle, 2003, Mannella, 2006, Rossignol et al., 2004, Soubannier and McBride, 2009). Fusion is regulated by mitofusin-2 (MFN2) in the OMM and optic atrophy protein-1 (OPA1) in the IMM to hold the membranes of two neighbored cells together until they fuse to form elongated mitochondrial structures. In healthy cells this is in balance with mitochondrial fission that is mediated by dynamin-related protein 1 (Drp1) on the OMM of elongated mitochondrial structures which form ring-like structures that narrow progressively to generate two mitochondria out of one. Fission occurs mainly at mitochondria-ER contact sites (Friedman et al., 2011) in a Ca^{2+}-dependent manner (Chakrabarti et al., 2018). To assess the fragmentation of mitochondrial structures in our study in more detail mitochondria sizes and perimeters were analyzed. Ultrastructural quantifications of perinuclear mitochondria unraveled that the loss of the DnaJ domain was accompanied by mitochondria of significantly smaller sizes and significantly decreased perimeters when comparing DCMA mutants to healthy controls without tremendous changes in mitochondrial shapes. In detail, NC6M and NC47F iPSC-CMs displayed 0.355 ± 1.20 μm^2 and 0.371 ± 2.60 μm^2 respectively. A study using 100-day-old iPSC-CMs showed even decreased mitochondrial sizes with on average ~0.24 μm^2 (Dai et al., 2017), thus validating high maturation states prior to mitochondrial examinations in our *in vitro* system. DCMA mutants displayed significantly smaller mitochondrial size as DNAJC19tv demonstrated 0.24 ± 0.74 μm^2 and DCMAP2 showed 0.17 ± 0.33 μm^2 that were even more decreased in DCMAP1 with 0.140 ± 0.45 μm^2.

Assessment of the same subcellular area in controls and DCMA CMs indicated that mitochondria were not only smaller in all three conditions but also eventually appeared accumulated in clusters to higher extent. Therefore, we analyzed whether intermyofibrillar mitochondria sizes and shapes were altered at ultrastructural level. We stated a loss of highly tubular mitochondria that were partly still associated with sarcomeres in DCMA iPSC-CMs. The assessment of the total amount of mitochondria per CMs revealed significantly decreased mitochondrial content in all DCMA conditions. In general, healthy cardiac tissue varies in mitochondrial content from 25.33 % in human (Barth et al., 1992) up to 37.88 % in mice (Barth et al., 1992). Interestingly, reduced mitochondrial and myofibrillar areas as well as significantly smaller mitochondria in ventricular DCM patient tissue underline a pathogenic relevance (Tashiro et al., 1990). The balance of mitochondrial area to myofibrillar area is essential to ensure proper cardiac function and needs to be maintained throughout the whole development of the human heart. Comparing fetal ESC-derived CMs' mitochondrial content (Cao et al., 2008) with adult CMs` content (Xu et al., 2009) the mitochondrial mass increases over prolonged cultivation times. The assessment of 60-day-old DCMA iPSC-CM contents unraveled decreased mitochondrial contents with shared fiber densities, underlining a pathogenic relevance of DNAJC19 in mitochondrial biosynthesis especially during early developmental stages. Early CMs present higher mitochondrial synthesis rates (Piquereau et al., 2013) as well as faster dynamics (Chen et al., 2011, Dorn, 2013) than CMs after postnatal development (Piquereau et al., 2013). These developmental changes may provide a possible explanation to discordant disease progression states observed in DCMA patients that present with a more severe manifestation at early stages than at older stages (Chen et al., 2011, Dorn, 2013).

The higher fragmentation and the decreased mitochondrial perimeters in DCMA iPSC-CMs are similar to a recently published paper of Rohani et al., 2020. This study used a comparable iPSC-derived CM model system of two unrelated patients carrying the same homozygous *DNAJC19* (NM_145261.4):c.130-1G>C mutation that was identified in the Canadian Hutterite cohort as well. As already mentioned, this study examined mitochondrial abnormities at an immature state only (day 20+21) that can be recognized after comparing the average perimeter of healthy controls 2.75 ± 0.05 µm NC6M and 2.9 ± 0.15 µm NC47F (supplementary Fig. 5.8 A) of our study to their healthy mitochondria with 2.2 µm (Rohani et al., 2020). Nevertheless, this study offers additional insights into

earlier disease processes (Rohani et al., 2020) considering mitochondrial fragmentation to be a central aspect during disease progression. Due to higher fragmentation, smaller mitochondria and overall reduced mitochondrial sizes we assume that either fission is upregulated or fusion is impaired to serve as a possible explanation for the fragmented punctuated structures observed in DCMA CMs. As fragmentation is induced by OPA1 decrease, fusion defects are more likely as L-OPA1 is downregulated in DNAJC19 deficient cells (Richter-Dennerlein et al., 2014). To date there is no link, that DNAJC19 is a direct interaction partner of OPA1, but Rohani et al., 2020 reported an imbalanced isoform ratio of the mitochondrial protein OPA1 in DCMA-patient derived iPSC-CMs (Rohani et al., 2020). In addition, depletion of PHB2 leads to the degradation of the protein L-OPA1 as well (Richter-Dennerlein et al., 2014). On this basis, we assume that a downregulation of OPA1 in DNAJC19 mutants might lead to a higher number of smaller mitochondria that are not able to properly fuse into stretched tubular mitochondrial structures. Further studies are required to investigate the expression levels of OPA1 in 60-day-old DNAJC19 iPSC-CMs as mitochondrial fragmentation is a critical hallmark of disturbed fusion & fission and is known to cause cardiomyopathy (Bergmann et al., 2004).

4.5.5 Mitochondrial morphology changes in DCMA

Furthermore, L-OPA1 is not only essential in mitochondrial fusion but also involved in the maintenance of mitochondrial cristae structures (Anand et al., 2014, Ishihara et al., 2006). We observed that loss of full-length DNAJC19 caused abnormities in mitochondrial cristae formation. The IMM invaginations seemed to be shorter, did not reach deep into the matrix and either had a hardly visible or a bulky cristae lumen when analyzed on the ultrastructural level. In addition, DCMA iPSC-CMs derived mitochondria displayed an irregular cristae pattern that was less dense than in healthy mitochondria. The same observations of abnormal cristae morphologies were also made in the study of Richter-Dennerlein et al., 2014 upon siRNA-mediated knock-down of DNAJC19 in HEK293T cells. In this report, a rescue experiment was performed to stabilize OPA1 by downregulation of the metalloendopeptidase OMA1 that was indeed able to restore OPA1 levels but not cristae formation, thus indicating an indirect mechanism of DNAJC19 in affecting OPA1 expression (Richter-Dennerlein et al., 2014). This indirect link might be provided by the altered CL composition in DCMA, as it is well known that CLs are essential in cristae formation given their conical structure (Khalifat et al., 2008). Another connection is supplied as BTHS conditions also displayed abnormal cristae and reduced cristae surfaces (Acehan et al., 2007). Additionally, small interfering RNA (siRNA)-mediated PHB2 depletion led to disturbed mitochondrial ultrastructures (Richter-Dennerlein et al., 2014). Interestingly, PHB complexes have a similar diameter as cristae tubules whereby the assembly of PHB subunits perpendicular to the cristae tubules axis is conceivable (Osman et al., 2009b, Tatsuta et al., 2005, Merkwirth and Langer, 2009). Moreover, loss of DNAJC19-mediated stabilization may impair PHB positioning and thus prevents PHB rings from being used as a scaffold to establish cristae lumen. Furthermore, cristae are highly dynamic structures that reversibly fuse and divide, depending on energy requirements (Mannella, 2006). Therefore, it is not surprising that CMs have the highest density of cristae (Vafai and Mootha, 2012). The observation of abnormal cristae in DCMA iPSC-CMs and less density of cristae led to the assumption that DCMA mitochondria have an overall smaller IMM surface area that might indicate reduced content of OXPHOS complexes and other IMM proteins. It is well known that the organization of internal mitochondrial membranes is critical for an optimal function of the respiratory complexes and ATP formation (Davies et al., 2011). Furthermore, cristae are prerequisite to establish the mitochondrial proton gradient to achieve ATP synthase functioning (Strauss et al., 2008). In addition, the proper function of the mitochondrial inner membrane organizing system (MINOS) complex is crucial to ensure the formation of cristae and the interaction with the OMM that is also dependent of CL microdomains (Zerbes et al., 2012, Koob et al., 2015, Weber et al., 2013).

4.5.6 The role of mitophagy in DCMA

The global functionality of CLs enables functional purposes regarding apoptosis, function of metabolite carriers and mitophagy (Pickles et al., 2018). The mission of mitophagy includes the reversion of imbalances by disposal of dysfunctional mitochondria and goes hand in hand with mitochondrial fragmentation to ensure quality control (Pickles et al., 2018). We assumed that the interplay between

both processes, degradation and biogenesis, is impaired in DCMA and therefore proper mitochondrial homeostasis cannot be guaranteed which may contribute to the observed phenotype of higher mitochondrial fragmentation and reduced mitochondrial content. In particular under stress, unsaturated acyl chains of membrane lipids are oxidized by molecular oxygen and afterwards externalized to the OMM (Saric et al., 2015, Tyurina et al., 2014). An increased content of oxidized CL provides a signaling platform for microtubule-associated protein 1A/1B-light chain 3 (LC3)-dependent mitochondrial quality control (Ardail et al., 1990, Simbeni et al., 1990, Anton et al., 2016, Chu et al., 2013). The oxidation of CL to 4-HNE is involved in mPTP opening and cytochrome c release. It was shown that isolated mitochondria with increased amounts of oxidized CLs are able to induce mPTP opening upon increased mitochondrial Ca^{2+} concentrations and thereby initiate mitophagy (Petrosillo et al., 2006). This is further supported by the contribution of excessive mitochondrial Ca^{2+} uptake, mitochondrial membrane collapse and ROS to the opening of the mPTP (Bhosale et al., 2015). Regarding the mitochondrial biomass reduction in DCMA conditions, the increase in mitophagy-based mitochondrial degradation might be a fundamental process involved in the pathogenesis of DCMA. Mitochondrial mitophagy of defective mitochondria could be visually recognized to some extent on ultrastructural images that revealed higher numbers of dissolved cristae as well as local mitochondrial swelling in all mutants. This assumption is further supported by the report of Richter-Dennerlein et al., 2014 where a direct interaction of DNAJC19 with the m-AAA protease subunit ATPase family gene 3-like 2 (AFG3L2) was stated. Moreover, PHB complexes interact with the m-AAA protease, suggesting a regulatory role in this process (Steglich et al., 1999).

4.5.7 The impact on cardiomyocyte morphology

With respect to BTHS syndrome-associated phenotypes structural abnormities of sarcomeres were observed. Therefore, sarcomere organization, fiber densities as well as general morphological features of iPSC-CMs were assessed in this study. Moreover, due to a possible mismatch of energy demand and supply, and an assumed increase in oxidative stress, a high probability of structural damage was suggested in CMs particularly affecting the sarcomeres. Sarcomere alignment was addressed by immunofluorescence of iPSC-CMs co-stained with cTnT using confocal microscopy. For each image, the cTnT sizes that correspond to thin-filament lengths were assessed to identify sarcomere disorganizations by increased standard errors among measurements. The thin filament diameter according to cTnT staining and sarcomere densities were measured for each cell and did not reveal any differences regarding the mean or the deviation among the individual CMs. The sarcomere density and the cTnT-labelled thin filament diameters in all iPSC-CM lines ranged from 30.64 % (NC47F) to 33.72 % (DCMAP1) and 1.82 µm (NC47F) to 1.93 µm (DCMAP1) respectively. Visual examination revealed equally organized sarcomeres in immunofluorescence stains as well as at an ultrastructural level in TEM-images. The ultrastructural analysis demonstrated the presence of Z-lines, A-, I- and M-bands emphasizing shared adult-like states in all conditions. We therefore concluded that no structural changes of sarcomeres were observed in DCMA iPSC-CMs. Moreover, nuclei sizes of all cell lines were in the same range from 114.1 μm^2 (DCMAP2) to 123.0 μm^2 (NC47F) and equal multinucleation levels from 26.68 % (DNAJC19tv) to 35.12 % (NC6M) were observed as well except for NC47F that presented an increased ratio with 44.37 %, thus indicating slightly higher maturation states. With regard to CM cell shape and sizes, all five conditions displayed rod and elongated CMs with a circularity range from 0.54 (DCMAP1, DNAJC19tv) to 0.59 (NC47F). Interestingly, all mutants had significantly smaller CM sizes when compared to controls. So far, no evidence exists, that smaller CM sizes are linked to DCMA. We therefore assume, that loosened cell densities during the immunofluorescence analyses allowed more space for hypertrophy of *in vitro*-derived CMs. The production of a higher biomass during cell growth by an increase of both translation rates as well as mitochondrial dynamics might be higher in our *in vitro* set up than *in vivo*, as iPSC-CMs were not embedded in a highly connected tissue like the human heart. We propose, that healthy iPSC-CMs can increase their biomass more efficiently than DCMA mutants and we assume, that in particular the reduced mitochondrial content is the rate limiting step in this issue due to the proposed higher energy demands that could be represented by smaller cell sizes in DCMA mutant iPSC-CMs.

4.5.8 Dysfunctional mitochondria caused defects in the respiratory chain

The real-time analysis of the OCR and the ECAR on viable cells using the Seahorse XF96 extracellular flux analyzer allow insights into mitochondrial function (Ferrick et al., 2008). The assessment of the proportional contribution of both energetic pathways, glycolysis and OXPHOS, allowed more detailed views into metabolic processes that are discussed in section 4.5.9. Another advantage of this system is the assessment of different treatments by step-wise injection like in the performed Mito Stress Test Assay. The study of key parameters of the mitochondrial function are analyzed starting with the basal OCRs, followed by oligomycin-mediated inhibition of ATP synthase. Then FCCP-uncoupling of the mitochondrial membrane was performed and application of rotenone/antimycin A resulted in the inhibition of complex I and complex III respectively. These modulators allowed insights into the functionalities of the individual ETC complexes as part of OXPHOS.

4.5.8.1 Increased basal respiration in cell types with low mitochondrial content

First, low-mitochondrial-content cell types such as dermal fibroblasts and iPSCs were assessed using the Mito Stress Test Assay. Real-time quantifications revealed an increased oxygen consumption in DCMA mutants in both cell types. The significant difference when comparing DCMA mutants to healthy controls relies mainly in the resting state as significantly excess basal respiration states were observed. These findings indicate a defect in the respiratory complexes and/or higher energy demands of the cells under baseline conditions.

4.5.8.2 Elevated oxygen turnover suggesting increased energy demands and decoupling of the ETC complexes in DCMA iPSC-CMs

The respiration states of cell types with high mitochondrial content, such as MACS-derived iPSC-CMs on day 60, were also quantified. DCMA iPSC-CMs demonstrated higher amounts of consumed oxygen and elevated basal respiration rates to higher levels when compared to low-mitochondrial cell types. In general, enhanced turnover of oxygen is required to generate sufficient ATP in CMs to ensure contractile properties, whereas this energy demand is lower in quiescent cells. The requirement of higher ATP yields in iPSC-CMs force the outcome of DCMA-associated excess oxygen consumption to higher levels. Since basal respiration is calculated by subtracting the non-mitochondrial OCR, this defect can be directly linked to the functionality of the ETC chain. The reinforced phenotype of iPSC-CMs in addition comprised increased non-mitochondrial OCR, enhanced ATP-linked respiration and elevated maximal respiratory capacities, whereas spare respiratory capacities were similar. When compared to fibroblasts and iPSCs, excess non-mitochondrial OCRs were observed in iPSC-CMs only and indicated alterations in metabolic processes to facilitate the supply of NADH and $FADH_2$ (discussed in section 4.5.9). Oligomycin treatment blocked the H^+ flow through the ATP synthase which subsequently provoked inhibition of the re-phosphorylation of ADP to ATP. Elevated ATP-linked respiration indicated that higher ETC activities were needed to export H^+ out of the matrix into the extracellular space, meaning that increased ETC cycles were needed to establish the mitochondrial membrane potential and the corresponding proton motive force. This assumption was further supported upon FCCP-mediated uncoupling of the mitochondrial membrane potential that resulted in a significantly elevated OCR in DCMA iPSC-CMs. FCCP led to the collapse of the proton gradient as it allowed direct diffusion of protons (H^+ ions) through the IMM and no longer through the ATP synthase. The sudden increase of protons in the matrix hyperactivated the ETC to work on maximum to re-establish the mitochondrial membrane potential and the proton motive force that are undeniable for ATP synthesis. In addition, the FCCP-stimulated OCR allowed the calculation of the spare respiratory capacity as an indicator of cellular fitness. Shared spare respiratory capacities were observed, thus the cellular abilities to respond to an increased energy demand under stress was unexpectedly high in DCMA iPSC-CMs highlighting common cellular fitness levels. These findings underlined the cellular ability of DCMA mutants to increase the ETC cycling to higher frequencies proportional to the individual ATP demands. In cardiac muscle, a close correlation of the basal OCR and the mitochondrial volume density exists (Barth et al., 1992). Unexpectedly, mitochondrial content analysis revealed an even decreased number of mitochondria per CM in DCMA iPSC-CMs. The elevated OCRs could be partly explained by increased non-mitochondrial OCRs as an indicator of enhanced metabolic processes that require more oxygen.

Even after considering the account of non-mitochondrial respiration, the OCR levels were still elevated, which could have multiple reasons like proton leakage, higher ATP demand, mispositioning of the ETC complexes, abnormal supercomplex formation and/or loss of the proton trap function.

We assume a loss of mitochondrial membrane integrity due to defective CL composition, which allows higher amounts of protons to leak through the IMM. The resulting increase in protons in the matrix subsequently requires a higher workload to maintain the mitochondrial membrane potential. The elevated OCR levels might also be caused by the generally observed higher beating frequencies that increase ATP utilization to a higher extent than healthy iPSC-CMs, thus leading to hyperactivated ETC states. Whether ATP utilization is indeed changed, needs further examination which however is challenging given the fact that ATP is a molecule that is continuously consumed.

Higher OCRs are often linked to the decoupling of the ETC complexes, as the close proximity of those complexes and the ATP synthase are required to achieve an efficient OXPHOS turnover for energy supply (Szeto, 2014, Guo et al., 2017, Iwata et al., 1998). Some evidence exists that the TIM23 machinery can directly interact with complex III and IV to enable sufficient protein insertion in a membrane potential dependent manner, in which DNAJC19 as well as PHB complexes might also play a pivotal role (van der Laan et al., 2006, Wiedemann et al., 2007, Dienhart and Stuart, 2008, Nijtmans et al., 2000, Merkwirth and Langer, 2009). The proposed function involves PHBs and probably also DNAJC19, that act as holdases during the assembly of the respiratory chain (Tatsuta et al., 2005, Nijtmans et al., 2000). Moreover, the investigation of reduced OPA1 levels, that accounted for mitochondrial fragmentation and abnormally shaped cristae, was directly linked to reduced functionalities of complex I, complex II and complex IV as well as a decrease in cell shortening and elevated ROS, highlighting a direct association of mitochondrial dysfunctions to cardiac phenotypes (Alexander et al., 2000, Delettre et al., 2000, Chen et al., 2012). In addition, the assembly of OXPHOS complexes as well as mitochondrial carrier proteins, like TIM23, within the IMM is highly dependent on the CL composition (Cheneval et al., 1983, Eble et al., 1990, Shinzawa-Itoh et al., 2007, Claypool, 2009). The CL(18:2)$_4$-rich composition is crucial to maintain the enzymatic activity of the complex IV and the mitochondrial respiratory capacity (Heerdt et al., 2002). The ATP synthase interacts with four molecules of tetralinoleoyl CL and two molecules of trilinoleoyl-monolinolenoyl CL that facilitates normal ATP synthase physiology (Schlame et al., 1991, Claypool, 2009). Furthermore, two CLs and eleven other lipids are required for complex IV stabilization (Shinzawa-Itoh et al., 2007). A study reported, that in the absence of CL, the absolute activity of the ETC is reduced due to distancing of complex III and IV (Claypool et al., 2008a, Claypool et al., 2008b, Claypool, 2009). These findings highly support the assumption, that CL changes directly affect OXPHOS function (Claypool, 2009). We therefore conclude that DCMA-associated CL profile changes in acyl chain length and poly-unsaturation may result in an impaired ETC assembly and a disclose positioning of ETC complexes. Closely packed ETC compounds are referred to as supercomplexes (or respirasomes) that are regularly found in oligomeric chains at cristae tips (Szeto, 2014, Guo et al., 2017, Iwata et al., 1998). Even in healthy cells the ETC system works below 100 % efficient, as electron leakage can be observed that interacts with oxygen to form ROS. Electron leakage primarily occurs via complex I (I_F and I_Q sites in complex I), with minor leakage reported from the II_F subunit in complex II and site III_{Qo} in complex III (Szeto, 2014, Brand, 2016). The assumed disconnection of the OXPHOS supercomplexes may result in higher numbers of electrons that leak into the matrix, that subsequently contribute to higher ROS states in DCMA and result in enhanced mitochondrial fragmentation. The direct interplay of ROS with mitochondrial dynamics to cause mitochondrial fragmentation was already reported as fission increases within seconds upon higher ROS states (Plotnikov et al., 2008).

Moreover, CL itself has an additional function as proton trap within the IMM as the pharmacokinetic value (pK(2)) is above 8.0 and therefore the head groups are able to absorb protons. This enables the collection of protons in close proximity to the OXPHOS complexes (Haines and Dencher, 2002). Therefore, a defective CL composition might impair the CLs' function as proton trap within the IMM, which in turn would negatively impact the function of respiratory chain complexes.

Interestingly, previously reported patients with DNAJC19 defects demonstrated alterations in the respiratory chain activity. Ucar et al., 2017 showed a reduced complex IV activity to ~53 % in muscle tissue (Ucar et al., 2017). The analysis of skeletal muscle of another DCMA patient revealed slightly reduced ATP production as well as partially reduced complex I, complex II and complex IV activities that were accompanied by equal expression of respiratory chain enzymes (Ojala et al., 2012). The report of Al Teneiji et al., 2016 monitored reduced ETC activities in all OXPHOS complexes of DCMA-derived dermal fibroblasts. These publications clearly underline a DCMA-specific impairment of the OXPHOS due to dysfunctions of the ETC complexes that are in line with our assumption of DCMA-associated increase of the ETC cycles to compensate for the deficits.

The comparison with BTHS-specific expression analyses of the mitochondrial respiratory chain c1 subunit of complex III, subunit 5 of complex I, and the catalytic core-subunit of the ATP synthase unraveled decreased levels of all components in TAZ-deficient mice (Huang et al., 2015). Findings in iPSC-CMs of patients with BTHS confirmed that abnormal CL remodeling affects respiratory chain function and organization (Dudek et al., 2016, Wang et al., 2014). The OCR of BTHS iPSC-CMs displayed a similar turnover of oxygen as our DCMA iPSC-CMs under basal conditions as well as regarding ATP-linked respiration. The deficits were also linked to abnormal CL species, as smaller mitochondria and enhanced fragmentation were observed as well. On the contrary to our model, BTHS iPSC-CMs displayed reduced maximal respiratory together with reduced spare respiratory capacities, whereas elevated levels of H^+ leakage were also observed which was in line with our findings. Nevertheless, we assume a shared inefficiency especially with regard to the ATP synthase function and the requirement of hyperactivated ETC cycles to provide enough ATP, as ATP flux is found reduced in BTHS iPSC-CMs (Wang et al., 2014). Interestingly, BTHS-derived dermal fibroblasts as well as iPSCs displayed non-significant alterations regarding OCRs which are contrary to our DCMA-associated findings.

4.5.9 DCMA-associated metabolic changes

Changes in the energy metabolism in human CMs often are the key for deciphering cardiac diseases, especially in inherited cardiomyopathies that comprise metabolic syndromes such as DCMA. In healthy adult hearts ATP is regenerated from FA catabolism (Chabowski et al., 2008, Stanley et al., 2005). Depending on disease-specific pathologies, metabolic flexibility allows to switch between different carbon sources (Stanley et al., 2005, Davila-Roman et al., 2002). We hypothesized that the loss of DNAJC19 induces a carbon source shift from FAs to glucose as previously observed in the phenotypic closely related BTHS (Fatica et al., 2019). Moreover, DCM is known to be prone for reduced FA oxidation and increased glucose uptake (Neglia et al., 2007). To assess metabolic features, OCRs together with ECARs as well as radioactive tracer uptakes were performed on different cell types.

First, dermal fibroblasts and iPSCs represented cell types of low mitochondrial content with different main energy pathways that rely on OXPHOS and glycolysis respectively (Folmes et al., 2011). The usage of the Seahorse XF96 extracellular flux analyzer in combination with the Mito Stress Test Assay directly included the cultivation of cells in appropriate medium compositions. In the standard set up to report mitochondrial dysfunctions, dermal fibroblasts were cultured in glucose/glutamine/pyruvate-containing cell culture medium, whereas iPSCs were cultivated in a medium composed of glucose and pyruvate. Therefore, the environmental conditions were not forcing dermal fibroblasts or iPSCs to prefer one specific metabolic pathway for energy generation, thus allowing the assessment of bioenergetic pathways under basal conditions for each individual cell type. Even though, all individual substrates were given as input, increased OCRs were observed in DCMA conditions that were clearly linked to mitochondrial-based oxygen consumption as non-mitochondrial OCRs were not increased in both cell types. As the ECAR was also similar, we did not observe differences towards enhanced utilization of glucose to meet cellular energy demands via glycolysis in cell types of low mitochondrial content. These findings underlined that mitochondrial-related oxygen consumption increased despite of whether OXPHOS was the preferential pathway or not. As the basal respiration in dermal fibroblasts was elevated to higher degrees from 136.1 ± 13.12 (pmol/min (healthy control) to 195.2 ± 10.40 pmol/min (DCMA) (59.08 pmol/min ↑) than in iPSCs from 243.4 ± 7.78 pmol/min (healthy control) to 284.8 ± 9.75

pmol/min (DCMA) (41.8 pmol/min ↑) the preference for OXPHOS over glycolysis and its limited use in DCMA mutants was confirmed in fibroblasts.

To specify these findings, cells of high mitochondrial content such as iPSC-CMs were analyzed. It is well known, that alterations in protein expression exhibit a metabolic shift from glycolysis to OXPHOS during maturation (Hellen et al., 2019). Some reports on early immature states like for example ~20-day-old iPSC-CMs demonstrated that glycolysis was mainly used for energy production which resembled the metabolic behavior of fetal CMs (Hu et al., 2018, Rana et al., 2012, Kim et al., 2013). Human fetal CMs are able to exhibit the shift from glycolysis to OXPHOS within post-natal week one (Yatscoff et al., 2008). Nose et al. reported a metabolic switch to maximal FA utilization after eight weeks in culture (~56 days) by using the same healthy NC6M control cell line in their study (termed FS-hiPSC-CMs (Nose et al., 2018). Therefore, 60-day-old MACS-derived iPSC-CMs were used to mimic metabolic features of adult CMs to investigate DCMA-associated metabolic features *in vitro*. iPSC-CMs exhibited comparable overall enhanced OCRs when compared to fibroblasts and iPSCs but to higher levels as OCRs of basal respiration for example raised from 165.38 ± 8.51 pmol/min (healthy) to 280.7 ± 10.02 pmol/min (DCMA) (115.3 pmol/min ↑) which was highly significant in mutant cells. We therefore concluded that the DCMA-associated phenotype of increased OCRs was more prominent in cell types of higher mitochondrial content and that raised OCRs can be linked to higher ETC activity and therefore contribute to a higher turnover of NADH and $FADH_2$. Whether NADH and $FADH_2$ levels are changed in DCMA requires further examination as well. However, we additionally observed excess non-mitochondrial OCRs that were observed in iPSC-CMs only. Non-mitochondrial oxygen consumption comprises multiple enzymatic reactions to run metabolic processes outside of mitochondria. These observations indicated higher activities of other oxygen-based enzymatic processes of different metabolites to generate energy to form sufficient NADH and $FADH_2$. We assume that a shift to other metabolic substrates than FAs is more likely to enable higher production rates. To gain more insights into metabolic features radioactive tracer uptakes using ^{18}F-FDG and ^{125}I-BMIPP as transport markers of glucose and FAs respectively were performed by using the same strategy as in the report of Nose., et al 2018. We were able to quantitatively confirm a reduction of ^{125}I-BMIPP uptake that corresponded to decreased uptake and utilization of FAs. Decreased FA uptakes in turn contribute to lower NADH levels, therefore other substrates need to be utilized as alternative energy sources. The simultaneous assessment of glucose uptake demonstrated a switch in substrate utilization from FAs to glucose in the male patient DCMAP1 condition only. DCMAP2 displayed a trend towards reduced glucose uptake ranges, whereas DNAJC19tv showed even significantly decreased glucose uptake. These findings indicated genotype independent preferences for the utilization of alternative carbohydrates instead of FAs or even glucose in our *in vitro* model.

To further confirm the glucose-related uptakes in iPSC-CMs glycolytic rates were simoultanously addressed by qualitative ECAR measurements using the Seahorse XF96 extracellular flux analyzer. We observed significantly increased ECARs after grouping of all three mutant conditions under basal conditions. Moreover, oligomycin-mediated inhibition of the ATP synthase and FCCP-mediated collapse of the mitochondrial membrane potential allowed the step-wise increase to higher ECARs, which was significantly elevated in mutant cell lines as well. The main fraction of the shift towards glycolysis was based on enhanced ECAR levels in DCMAP1-derived iPSC-CMs (supplementary Fig. 5.10). The enhanced ECARs in DCMA mutants correspond to increased proton concentrations in the extracellular space, which mainly result of glycolysis. The ECAR increase qualitatively indicated that DCMA iPSC-CMs attempt to maintain their energy balance upon increasing glycolytic events.

The observed discrepancies in the ECARs of DCMAP2 and DNAJC19tv between the seahorse set up and the radioactive tracer uptake with regard to glycolysis can be explained by the main differences in the medium composition during the measurements. iPSC-CMs were measured in medium containing glucose/glutamine/pyruvate in the seahorse setup, whereas the cell culture medium during tracer uptakes consisted of ^{18}F-FDG (glucose) and ^{125}I-BMIPP (FAs) only. As the three biological replicates for both experiments derived from the same cardiac differentiation and MACS procedure, a more detailed connection can be encountered between both experiments. The observed differences can be traced

back to the presence of the substrates glutamine and pyruvate that may serve as an alternative energy source to different degrees in DCMAP2 and DNAJC19tv and may enhance extracellular acidification if present in the cellular environment. For example, the reduction of pyruvate by the lactate dehydrogenase into lactate catalyzes NADH into $NAD^+ + H^+$ allowing the additional protons to contribute to enhanced extracellular acidifications (Nelson and Cox, 2012). Interestingly, a recently published article monitored that cells are able to acidify the extracellular medium not only through converting glucose or glycogen to $lactate^- + H^+$ via glycolysis but also by producing carbon dioxide (CO_2) in the context of substrate oxidation, as CO_2 is hydrated to carbonic acid (H_2CO_3), which then dissociates to $HCO_3^- + H^+$ and enriches in the extracellular environment (Mookerjee et al., 2015). This insight supported that increased ECARs in particular in DNAJC19tv and DCMAP2 iPSC-CMs might raise due to the production of CO_2 derived from the TCA cycle during the oxidation of substrates. For example, the glycolysis-derived CO_2 contributes to 34 % of the cellular extracellular acidification, whereas palmitate or pyruvate contribute to 67-100 % of the cellular extracellular acidification upon glucose depletion (Mookerjee et al., 2015). These insights indicated that DCMAP1 is the only mutant cell line that prefers glucose as primary energy source. Reasons for decreased glucose uptake in DCMAP2 and DNAJC19tv might be expressional changes of the glucose transporters GLUT1 and GLUT4 or FA transporters FABP3, FABP4 to different degrees that were not examined in the present thesis. Notably, a study on BTHS revealed similar metabolic alterations as long chain FA uptake was reduced due to decreased cellular uptake of $^{13}C_{16}$ (palmitate). Thereafter glucose utilization was enhanced in $TAZ^{517delG}$-iPSC-CMs that was accompanied by elevated expressions of FABP4 (Fatica et al., 2019). The same study displayed, that glutamine as well is an important fuel that is able to replenish the Krebs cycle as carbon source for purine and pyrimidine synthesis and can be utilized in BTHS iPSC-CMs (Fatica et al., 2019).

Other metabolic aspects, such as increased cell death during lactate-based metabolic enrichment, especially in DCMAP1 iPSC-CMs provided an additional hint at a more distant point of view already. DCMAP1 utilized glucose as main energy source that might have hindered sufficient lactate metabolism, whereas minor affects were observed in both other mutant conditions. It is reported that depleting glucose in the culture medium reduces hypoxia-inducible factor 1-alpha (HIF1α) expression and its downstream target lactate dehydrogenase A (LDHA) (Hu et al., 2018) and thus indicates that lactate-based cultivation induces metabolic stress to increase the shift towards OXPHOS (Rupert et al., 2020). Moreover, BTHS iPSC-CMs studies uncovered a link between mitochondrial abnormities and CL remodeling that result in altered HIF1α signaling (Chowdhury et al., 2018). A study using TAZ-deficient mice reported that CL deficiency has the consequence of disrupting the activity of FA oxidizing enzymes and electron transfer chain supercomplexes (Huang et al., 2015). Proteomic analyses unraveled the upregulation of enzymes of amino acid metabolic pathways together with a downregulation of enzymes involved in OXPHOS (Huang et al., 2015). The same study provided insights into CL-dependent metabolic hypercomplex stabilization of FA oxidation enzymes and ETC complexes where both pathways converged (Huang et al., 2015). Moreover, lactate uptake of CMs is mediated by monocarboxylic acid transporters (MCTs), of which subtype 1 forms complexes with complex IV of the ETC chain to act as a proton-coupled passive transporter that mediates lactate uptake in CMs by chemical and proton concentration gradients that are established via the highly active TCA cycle (Tohyama et al., 2013, Hashimoto et al., 2006).

Taken together, we observed first insights into DCMA-associated metabolic changes that were modeled in *in vitro*-derived iPSC-CMs. The detailed pathomechanisms require further studies to clearly determine metabolic alterations. Interestingly, DCMA patients displayed cardiomyopathic changes during the postnatal phase, some demonstrated severe heart failure with the requirement of heart transplant, whereas some recovered without a severe progression over years. We propose that postnatal metabolic changes may contribute to the disease development. As we observed discordant preferences among the mutant cell lines, we assume that non-genetic modifiers that are involved in molecular signaling pathways are key components that are to date unidentified. Interestingly, the 3-MGA biochemical marker allows the identification of patients with mitochondrial dysfunction of still unknown origin (Wortmann et al., 2012). As BTHS patients and DCMA patients displayed shared increased 3-MGA levels a common

metabolic pathomechanism is assumed for example for sterol or isoprenoid metabolism (Kelley et al., 1991). Another hypothesis states that OXPHOS dysfunctions may influence NADP-NADPH-dependent enzymes, like the 3-MGA-hydratase by a disbalance of NADP to NADPH (Wortmann et al., 2012). To date, it is not clear how mitochondrial dysfunction can elevate urinary excretion of 3-MGA.

4.5.10 Abnormal Ca^{2+} homeostasis, reduced contractility and increased arrhythmic events

In the present thesis the DNAJC19 mutation-based influences on cellular injury of CMs were analyzed using the ratiometric dye Indo-1-AM to assess Ca^{2+} handling, the arrhythmic phenotype and contraction capacities by the IonOptix system on single-cell basis. New understanding on DCMA-specific cardiac E-C coupling could be gained by studying the second messenger Ca^{2+} that directs the CMs' contraction (Bers, 2002b, Bers, 2002a). As heart failure is prone for Ca^{2+} mishandling, new insights into DCMA-associated pathomechanisms were aimed to be gained (Pogwizd et al., 2001). In healthy CMs the AP-mediated depolarization-activated Ca^{2+} channels trigger Ca^{2+} release from the SR that in turn increases $[Ca^{2+}]_i$ to allow Ca^{2+} ion binding to the contractile protein cTnC that initiates contraction. For relaxation $[Ca^{2+}]_i$ must decline which is mediated by four different ion channel families: SERCA2a, NCX, sarcolemmal Ca^{2+}-ATPases (PMCA) or mitochondrial Ca^{2+} uniporter (MCU). A study using rabbit-derived CMs unraveled that the main fraction (~70 %) is conveyed by SERCA2a followed by NCX(~28 %), whereas PMCA and MCU facilitated removal of the residual Ca^{2+} ions (~2 %) (Bassani and Bers, 1994).

4.5.10.1 Enhanced beating frequencies, increased diastolic Ca^{2+} concentrations and impaired relaxation properties

First DCMA-associated insights into Ca^{2+} handling revealed increased beating frequencies without any treatment to different degrees, with the strongest phenotype observed in the isogenic mutant DNAJC19tv. As our *in vitro* model system comprised isolated CMs that were protected from external influences, we were able to observe so far unknown DCMA-associated intracellular mechanisms that resulted in increased beating frequencies. A study using mouse ventricular CMs showed a $[Ca^{2+}]_i$-frequency response that is dependent of a balance between increased SR content and the loss of trigger $I_{Ca,L}$ (Antoons et al., 2002). Therefore, $[Ca^{2+}]_i$ was analyzed and revealed that all mutants shared the same phenotype as increased diastolic Ca^{2+} concentrations with similar systolic Ca^{2+} levels were observed. Based on our findings, increased $[Ca^{2+}]_i$ levels are prerequisite for enhanced frequencies and/or vice versa. Moreover, β-adrenergic stimulation by the non-selective β-adrenergic agonist (β1 &β2) Iso is known to enhance beating frequencies which is typically accompanied by an increase in the Ca^{2+} amplitude, which is essentially caused by a larger Ca^{2+} release from the SR. The raise of increased $[Ca^{2+}]_i$ levels by Iso is generally accompanied by an increase in myocardial contractility that is termed as inotropic effect (Bers, 2002b, Bers and Weber, 2002, Brandes and Bers, 1997, Bers, 2002a). The ability to respond to β-adrenergic stimulation serves as an additional hallmark of maturation states, as a lack of inotropic reaction was observed in immature iPSC-CMs only (Pillekamp et al., 2012). Our study revealed even more increased diastolic Ca^{2+} levels upon Iso treatment, indicative for compromised Ca^{2+} reuptake under stress that was accompanied by enhanced beating frequencies to higher degrees when compared to healthy control CMs. Therefore, we were able to observe elevated workload and insufficient Ca^{2+} export that was even more severe upon Iso-based stress induction in DCMA iPSC-CMs.

As increased workload corresponds to higher frequencies of E-C coupling, ATP hydrolysis might be enhanced in DCMA (Brandes and Bers, 1997, Bers, 2002b). These insights implicate changed ratios between ATP to ADP or rather pCr to Cr in DCMA, suggesting that energy supply and demand are not in balance to maintain cardiomyocyte function, which requires further examination. In the human heart the ability to accurately respond to frequent changes in workload requires a precise matching of ATP supply and demand to maintain cardiac function. On the other hand, high ATP utilization may impair Ca^{2+} homeostasis as well. Interestingly, the amount of Ca^{2+} ions during influx and efflux ($sysCa^{2+}$ - $diasCa^{2+}$) is significantly decreased in DCMAP2 and DNAJC19tv, whereas DCMAP1 showed the same trend as control iPSC-CMs. As diastolic and systolic Ca^{2+} levels were both slightly increased in

DCMAP1, the overall amount of entering and leaving Ca^{2+} ions was not significantly influenced. Decreased Ca^{2+} ion influx and efflux indicated a higher dependency on SERCA2a-mediated Ca^{2+} recruitment into the SR rather than the extracellular environment via NCX given the same extracellular Ca^{2+} concentrations in the experimental set up (2 mM Ca^{2+}). The suggested impaired relaxation capacities in DCMA iPSC-CMs were further confirmed based on the transient shape analysis via single exponential tau (sin exp tau) quantification to evaluate the cellular speed of recovery in dependency of the individual beating frequencies. Significantly higher sin exp tau values referred to slowed speed of recovery that was observed in all three mutants with the strongest phenotype in DCMAP1. The longer relaxation times in DCMAP1 could be explained by the overall higher amount of Ca^{2+} ions that require more time to be exported into the extracellular space. Upon increased Iso concentrations an enhanced speed to recover was observed in all four cell lines underlining the ionotropic response capacity of mature iPSC-CMs. The strongest effect on accelerated relaxation speed was observed in DCMAP1 that seemed to reach the same velocities when compared to both other mutants, pointing towards an enhanced Ca^{2+} ion export channel sensitivity following β-adrenergic stimulation.

As the main fraction of the cytoplasmatic Ca^{2+} pool is recruited by the fast SERCA2a and the remaining Ca^{2+} ions are exported into the extracellular space by the Na^{+}/Ca^{2+} exchanger (NCX) both direct and indirect (Shattock et al., 2015) ATP-dependent functionalities were assessed by determining the relaxation time at 50 % ($RT_{50\%}$) and 90 % ($RT_{90\%}$) respectively. Similar to our previous findings especially DCMAP1 displayed prolonged relaxation times at $RT_{50\%}$ and $RT_{90\%}$, DCMAP2 presented slightly but significantly increased $RT_{50\%}$, whereas DNAJC19tv displayed no changes when compared to healthy cells. The stepwise decreased functionalities confirmed that the obtained results are independent of the genetic background and might be a result of discordant ATP levels and demands that may differ among the three mutant cell lines and highlight the intracellular dynamics in bioenergetic pathways. Upon Iso stimulation increased activities of SERCA2a and NCX were achieved in DCMAP1 that were able to accomplish a similar Ca^{2+}efflux as controls, and thus revealed a tendency towards impaired functions that can be restored upon β-adrenergic stimulation. Other publications implied that SERCA2a expression is reduced in heart failure whereas NCX expression is increased (Brandes and Bers, 1997). Whether SERCA2a and NCX expression changes or activity states are indeed affected in DCMA CMs needs further examination. Overall, we could observe the Iso-based lusitropy effect (Bers, 2002b, Bers, 2002a) by accelerating relaxation times with regard to overall speed of recovery (sin exp tau) and SERCA2a and NCX activities ($RT_{50\%}$, $RT_{90\%}$). As Iso treatment in general accelerates relaxation capacities, enhancement of Ca^{2+} re-uptake into the SR or export into the extracellular space would be expected that would in turn result in reduced $[Ca^{2+}]_i$. However, the opposite effect was seen as even increased diastolic Ca^{2+} concentrations were quantified upon Iso, thus indicating reduced recruitment to the SR that was even more impaired under stress. The direct link to phenotype-associated changes in Ca^{2+} handling was previously confirmed as the report of Itzhaki et al., 2011 demonstrated both the expression of RYR2, SERCA2a and LTCC and their functionality to restore $[Ca^{2+}]_i$ into the SR or into the extracellular environment using ~50-day-old iPSC-CMs. This was further validated by the expression of cardiac specific RNA and proteins, like for example RYR2 (Synnergren et al., 2012). Taken together, increased diastolic Ca^{2+} concentrations, higher beating frequencies and prolonged relaxation times implied abnormal Ca^{2+} handling that can be directly linked to the DNAJC19 mutation.

4.5.10.2 Reduced cell shortening capacity in DCMA

The effect of impaired Ca^{2+} handling on contractility was assessed simultaneously. In healthy CMs the contraction force highly depends on $[Ca^{2+}]_i$ (Bers, 2002a, Solaro, 1999, Moss and Magleby, 2001). In comparison, we were able to observe a contrary effect as DCMA iPSC-CMs presented even decreased capacities to contract due to reduced cell shortenings even though we could confirm similar systolic Ca^{2+} concentrations basally and upon increased Iso treatment and similar number of sarcomere-related proteins (cTnT) in all iPSC-CMs. As we observed incomplete export of Ca^{2+}, more Ca^{2+} ions might remain bound to cTnC and therefore promote a semi-contractile position, whereby new entering Ca^{2+} ions result in a contraction that might be observed as decreased cell shortening capacities. Interestingly, the hallmark of adult-like conditions is a positive force-frequency relationship that was observed by an increase in cell shortening accompanied by elevated frequencies upon Iso treatment only (Germanguz

et al., 2011). These findings indicate that two more factors may change contractile capacities: the alteration of Ca^{2+} transient (amplitude or duration) and the sensitivity of the myofilaments to Ca^{2+} itself (Bers, 2002b, Bers, 2002a). Other publications have shown that the Ca^{2+} sensitivity of the myofilaments reduces upon β-adrenergic stimulation (Bers, 2002b, Bers, 2002a). The high diastolic Ca^{2+} observed can additionally be accounted to incomplete response to pharmacological addition of Iso, since past studies in humans showed a disrupted adrenergic activation (Hamdani et al., 2008). A potential influence of Iso on Ca^{2+} sensitivity of the myofilaments might cause hypercontractile myofilaments with still closely bound Ca^{2+} and is potentially causative for the observed increased cell shortenings upon β-adrenergic stimulation. Whether Ca^{2+} sensitivity is affected in DCMA requires further examinations. Normally, healthy cells have a positive force to frequency relationship (Antoons et al., 2002). Nonetheless, we observed a negative force-frequency relation in DCMA iPSC-CMs that is pronounced in heart failure. We assume that DCMA iPSC-CMs are unable to increase SR Ca^{2+} content despite higher frequencies and thus are not able to overcome the refractoriness of the SR Ca^{2+} release (Pieske et al., 1999).

4.5.10.3 Increased diastolic Ca^{2+} levels as proarrhythmic trigger in DCMA

Another explanation for the decreased cell shortening in DCMA cell lines can result from the elevation of cellular ADP - due to inefficient ATP flux - that causes a rigor-like contracture activation. The increase in beating frequencies indicated DCMA-associated elevated workload that might require higher cellular energy demands which may result in a rigor-like contraction with insufficient Ca^{2+} recruitment (extracellular and SR) (Sequeira et al., 2015). Whether the SR Ca^{2+} storage capacities are changed in DCMA needs further examination by using the ratiometric dye Rhod-2-AM that specifically accumulates in mitochondria together with the pharmacological activation effect of caffeine on RYR receptors (Eisner, 2014). The recording of Ca^{2+} transients unraveled a higher tendency towards arrhythmic events in mutant conditions that showed discordant preferences as well. DCMAP1 displayed a highly increased accumulation of predominantly EADs but also DADs, DNAJC19tv demonstrated similar fractions of EAD/DADs as well as fibrillation-like events, whereas DCMAP2 presented a fibrillation-like phenotype only. In particular, in DCMAP1 some cells displayed less arrhythmic events upon Iso stimulation underlining the positive effect of β-adrenergic stimulation on DCMAP1. Some publications revealed that besides elevated Ca^{2+} concentrations in the SR also increased amounts of Ca^{2+} in the cytoplasm are enhancing the RYR sensitivity that triggers spontaneous Ca^{2+} release which in turn provokes DADs or EADs (Bers, 2002a). Moreover, it was reported, that higher diastolic Ca^{2+} levels increase the susceptibility to Ca^{2+} overload that is a well-known proarryhtmic trigger (Landstrom et al., 2017). In addition, during the relaxation, Ca^{2+} ions are removed and exchanged by the NCX resulting in an increased transient inward current of sodium ions (Eisner, 2014). Increased sodium influx can lead to DADs as well and may cause lower SR Ca^{2+} stores (Landstrom et al., 2017).

4.5.10.4 Linking abnormal Ca^{2+} handling to mitochondrial defects

A low amount of Ca^{2+} ions is able to enter mitochondria that has no influence on ECC directly but changes the intra-mitochondrial $[Ca^{2+}]_m$ level, that is known to regulate the TCA cycle. Generally speaking, increased $[Ca^{2+}]_m$ induces the production of NADH and consequently ATP to fulfill higher energy demands (Brandes and Bers, 1997, Kohlhaas et al., 2010). Higher beating frequencies support the implication of accelerated turnover rates of NADH in DNAJC19 mutants. We therefore assume that due to increased diastolic Ca^{2+} concentrations also intra-mitochondrial $[Ca^{2+}]_m$ increases that might enhance the production of NADH to higher levels than controls. The important uniporter in this process is MCU that mediates the transport of Ca^{2+} ions into mitochondria in a mitochondrial membrane potential dependent manner (Eisner et al., 2017b). Interestingly, Ghosh, et al., 2020 have published that CL is required for stability and function of the mitochondrial uniporter (Ghosh et al., 2020). This study validated decreased MCU levels in BTHS patient-derived cardiac tissue that directly links MCU to pathological processes that are potentially based on defective mitochondrial Ca^{2+} signaling (Ghosh et al., 2020). Therefore, MCU expressional or functional changes are likely to occur in DCMA as well, that can also contribute to a decreased mitochondrial Ca^{2+} entry. On the contrary, $[Ca^{2+}]_m$ concentrations over the physiological level activate the mitochondrial permeability transition pore that induces mitophagy which was also hypothesized as potentially dissolved structures could be observed in ultrastructural TEM

images (Weiss et al., 2003). Whether and to which extent $[Ca^{2+}]_m$ levels and the direction of Ca^{2+}-flux are affected in DCMA mutants was not yet investigated and requires further examination.

Another direct link to mitochondrial function is the typically close contact of the SR and mitochondria in healthy CMs. The close proximity is crucial to enable the formation of hot spots with high Ca^{2+} concentrations (Dorn, 2013). As enhanced mitochondrial fragmentation and decreased mitochondrial content were observed, these hot spots might be missing in DCMA mutants. In addition, the loss of the direct neighboring between mitochondria and sarcomeres is very likely to impair the cellular function of directly supplying the contractile apparatus with ATP regeneration. The hypothesized loosened connection and the reduced mitochondrial contents may result in decreased energetic levels that in turn lead to insufficient supply for proper contraction in DCMA. This assumption is further supported as other studies have proved that the direct energy transfer (Piquereau et al., 2013) and the mitochondrial volume subsequently impact the myofibril-mediated force (Kaasik et al., 2004).

4.6 Suitability of *in vitro*-derived iPSC-CMs to mimic DCMA patient phenotypes

Taken together, especially Ca^{2+} homeostasis, contractility as well as metabolic processes are tightly connected, therefore abnormalities interact and influence each other by means of highly dynamic interplays. The present data sustains the clinical picture of DCMA, as these patients experience different kinds of clinical features. The male patient DCMAP1 had a severely reduced cardiac function and required a heart transplant at the age of two years. DCMAP2 iPSC-CMs derived from a female individual, who recovered her cardiac function in early childhood, but suffered from ventricular arrhythmias and a prolonged QT interval of >510 ms that raised the necessity of the implantation of an ICD. She presented arrhythmic features including fibrillation-like events and DADs/EADs. We additionally observed that the CRISPR/Cas9-edited cell line presented similar phenotypes like for example the same fragmentation pattern, reduced mitochondrial mass and increased OCRs as well as similar arrhythmic characteristics as observed in the patient-derived iPSC-CMs. We therefore concluded that loss of full-length DNAJC19 forces the outcome of DCMA-associated mitochondrial fragmentation independently of the Canadian Hutterite genetic background. This suggestion is in line to DCMA cases in Finnish (Ojala et al., 2012) and Turkish (Ucar et al., 2017) patients.

The presence of fragmented mitochondria during early (Rohani et al., 2020) and in our studies late developmental iPSC-CM states seemed to be fundamental during the course of DCMA. With regard to DCMA disease progression, first cardiomyopathic changes occurred during the postnatal phase that either developed to a more severe clinical outcome and thereby raised the requirement of a heart transplant like in DCMAP1, or recovered with standard heart failure therapy like in DCMAP2. We therefore proposed, that in particular postnatal metabolic changes contribute to disease-development in DCMA. However, the different phenotypes especially with regard to Ca^{2+} handling and metabolic processes described in our *in vitro* model are probably consistent with the heterogenous clinical presentation of both patients as well as other described DCMA patients (Nissenkorn et al., 1999). It is well known, that disease-specific backgrounds can have genetic modifiers that either mitigate or even intensify the mutational phenotypes (Chandler et al., 2013). The male individual presented the strongest phenotype that was also observed in our *in vitro* model, in particular with regard to the smallest mitochondrial sizes, higher fractions of non-identifiable cristae structures, the highest OCRs in all cell types, higher ECAR rates in iPSC-CMs, highest glucose uptakes (^{18}F-FDG), main fractions of DAD/EADs, slowest relaxation times ($RT_{50\%}$, $RT_{90\%}$, sin exp tau) as well as lowest cell shortening capacities. These findings led to the assumption of a reinforced genetic background in DCMAP1, whereas DCMAP2 showed more similarities to the isogenic mutant control DNAJC19tv. Some reports unraveled 95 % disease-associated SNPs found in non-coding regions that can give rise to phenotypic variations (Maurano et al., 2012). The comparison of in total 25 different iPSC lines of healthy iPSC lines allowed the investigation of the influence of the genetic background and identified that the majority of the variations can be linked to the genetic background and not to epigenetic contribution, which needs to be considered when modeling a disease by an *in vitro* approach (Sullivan et al., 2010, Hu et al., 2010,

Bhutani et al., 2010, Rouhani et al., 2014, Bassett, 2017). Indeed, *in vitro*-derived iPSC-CMs have proved their potential in recapitulating disease-associated pathomechanisms linked to LQT syndromes (Itzhaki et al., 2011) to gain more insights into the development of bradyrhythmias or tachyarrhythmias (Zecchin et al., 2019) ranging up to different forms of long QT syndrome (Elliott et al., 2008, Lakdawala et al., 2013, Wilde and Behr, 2013). In addition, a study using phospholamban (PLN) p.Arg14del iPSC-CMs to remodel DCM was able to support an inhibitory function on SERCA2a activity that reduced Ca^{2+} reuptake into the SR, leading to similar phenotypes of reduced contraction force, Ca^{2+} overload induced arrhythmias (DADs) as well as higher diastolic Ca^{2+} concentrations (Haghighi et al., 2006, Ceholski et al., 2012). Taken together, the established *in vitro* system using iPSC-CMs proved to have the power to accurately recapitulate the DCMA-associated phenotypes and allows the identification of the underlying pathomechanism to pave the way for effective therapeutical treatments in the future.

5. Supplement

5.1 Additive Figures

Identification		Results			
Barcode	Cell line name	Testing date	PCR inhib. *	Mycoplasma	Summary
88678160	NC6M iPSCs	29/11/2018	absent	absent	clean
88678191	NC6M-SeV iPSCs	29/11/2018	absent	absent	clean
88678252	LEMD2 p.L13R iPSCs	29/11/2018	absent	absent	clean
88678269	DCMAP2 iPSCs	29/11/2018	absent	absent	clean
88678276	DCMAP1 iPSCs	29/11/2018	absent	absent	clean
88678283	DNAJC19tv iPSCs	29/11/2018	absent	absent	clean
88678306	NC47F iPSCs	29/11/2018	absent	absent	clean
88678313	DSG2-KO iPSCs	29/11/2018	absent	absent	clean
88678320	PKP2-KO iPSCs	29/11/2018	absent	absent	clean
88678337	LEMD2iso1-KO iPSCs	29/11/2018	absent	absent	clean

Figure 5.1 Mycoplasma testing did not reveal any contamination in all generated iPSC lines.
The medium supernatants of all generated iPSC lines were collected and tested for residual mycoplasma DNA to identify the presence of a contamination. * PCR inhibition: present, will result in an invalid mycoplasma test

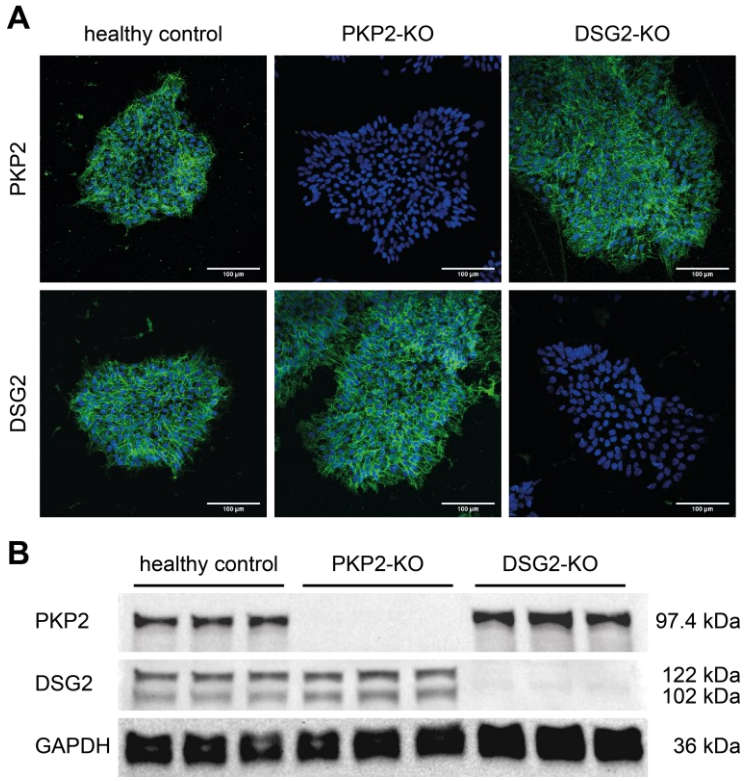

Figure 5.2 Validation of PKP2 and DSG2 depletion in the corresponding knock-out iPSC-lines after CRISPR/Cas9 genome editing.
(A) Immunofluorescence stains using PKP2 (1st row) and DSG2 (2nd row)-specific antibodys confirmed the loss of PKP2 expression in PKP2-KO and the absence of DSG2 in DSG2-KO iPSC lines when compared to healthy control NC6M iPSCs. **(B)** Western blot analysis using the same antibodies as well as GAPDH-specific antibodies as internal control confirmed the loss of PKP2 and DSG2 in the corresponding knock-out iPSC lines. Scale bars = 100 µm

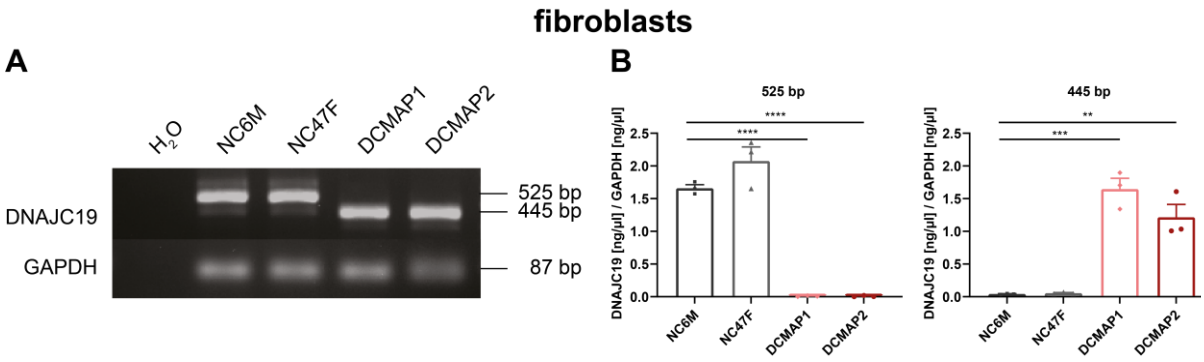

Figure 5.3 Examining *DNAJC19* transcript variants in somatic cells of two patients and two healthy individuals prior to reprogramming.
(A) *DNAJC19* amplification was performed based on cDNA generated from dermal fibroblasts of two patients (DCMAP1, DCMAP2) suffering from DCMA and two healthy control individuals (NC6M, NC47F) via RT-PCR. Both healthy conditions showed the presence of two bands, one strong band in the size of 525 bp, that represented the full-length cDNA of *DNAJC19*, and a weak 445 bp band, corresponding to the ∆ex4 transcript. On the contrary, DCMAP1 and DCMAP2 dermal fibroblasts showed no 525 bp band but a strong expression of the 445 bp band (∆ex4 transcript). **(B)** QIAxcell analysis by quantification of RT-PCR amplified transcript variants of *DNAJC19* was calculated versus the internal control *GAPDH*. The 525 bp was significantly reduced to not quantifiable levels in all mutant conditions, whereas the ∆ex4 transcript was clearly expressed in both patient-derived iPSC lines only. Data are shown as mean ± SEM together with each individual biological replicate. **** p<0.0001, *** p<0.001, ** p<0.01, ns p>0.05 using unpaired t-test calculated versus NC6M fibroblasts.

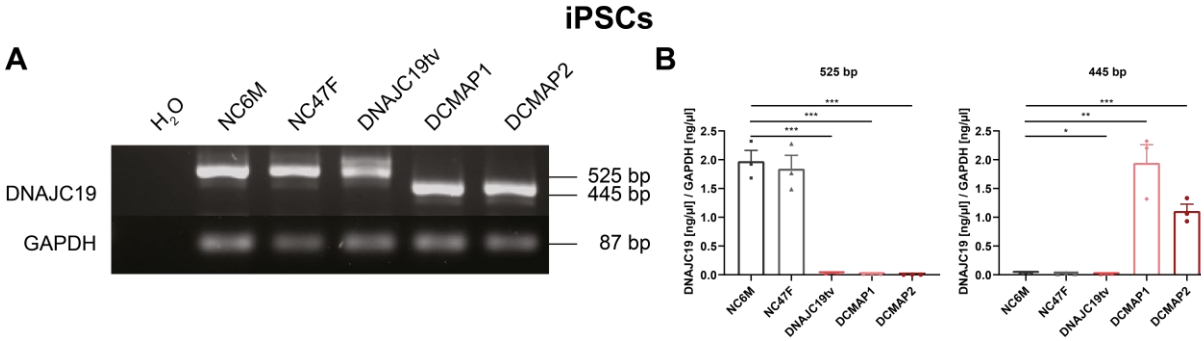

Figure 5.4 Investigation of *DNAJC19* transcript variants of healthy and mutant iPSCs.
(A) RT-PCR was performed on cDNA generated from five iPSC lines, two patients (DCMAP1, DCMAP2), one CRISPR/Cas9-edited mutant cell line (DNAJC19tv) and two controls (NC6M, NC47F) by using *DNAJC19* specific primers. Both controls displayed two bands, one enhanced band in the size of 525 bp, corresponding to the full-length cDNA of *DNAJC19*, and the less expressed 445 bp band, corresponding to the ∆ex4 transcript. Examination of DNAJC19tv iPSCs displayed two different bands close to the 525 bp band that showed the biallelic modification via the CRISPR/Cas9 system. The investigation of DCMAP1 and DCMAP2 iPSC revealed the absence of the 525 bp band together with a high expression of the 445 bp band that represent a higher expression of the ∆ex4 transcript in both patient-derived iPSC lines. **(B)** QIAxcell analysis was used for quantification of RT-PCR amplified transcript variants of *DNAJC19* that was calculated versus the internal control *GAPDH*. The 525 bp was not detectable in all mutant conditions, whereas an enhanced presence of the ∆ex4 transcript was observed in both patient-derived iPSC lines only. Data are shown as mean ± SEM together with each individual biological replicate. *** p<0.001, ** p<0.01, * p<0.05, ns p>0.05 using unpaired t-test calculated versus NC6M iPSCs

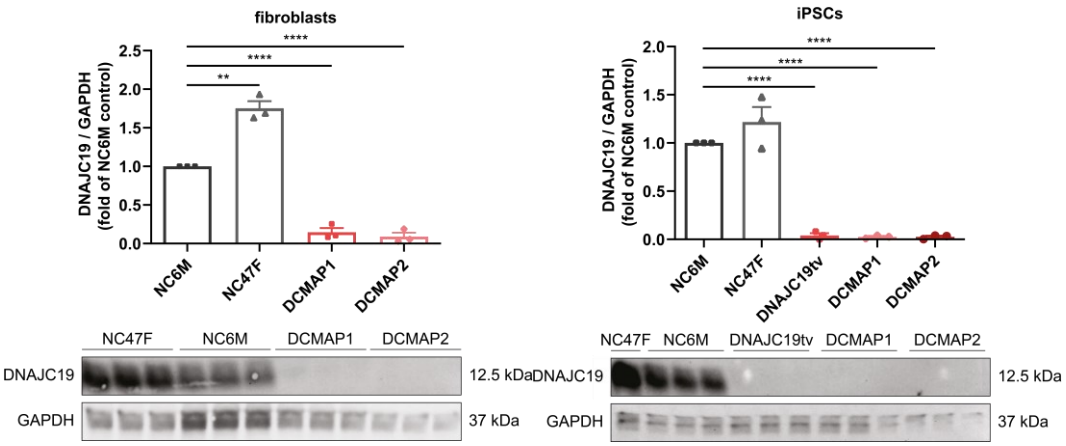

Figure 5.5: Western blot analysis of dermal fibroblasts and iPSCs revealed the loss of full-length DNAJC19 in both patient-derived firboblast lines.
Western blot of DNAJC19 in dermal fibroblasts **(left)** and iPSCs **(right)** of two controls (NC6M, NC47F), the CRISPR/Cas9-edited cell line (DNAJC19tv) and two DCMA patients (DCMAP1, DCMAP2) revealed a loss of full-length DNAJC19 in the size of 12.5 kDa in the isogenic mutant control **(right)** and in both patient-derived cell lines. Densitometric western blot quantification of DNAJC19 in the controls, the isogenic mutant control and patient-derived cell types presented a loss of DNAJC19 in DNAJC19 mutant conditions. Data are shown as mean ± SEM together with each individual biological replicate. **** p<0.0001, ** p<0.01, ns p>0.05 using unpaired t-test, calculated versus NC6M after normalization to NC6M signal

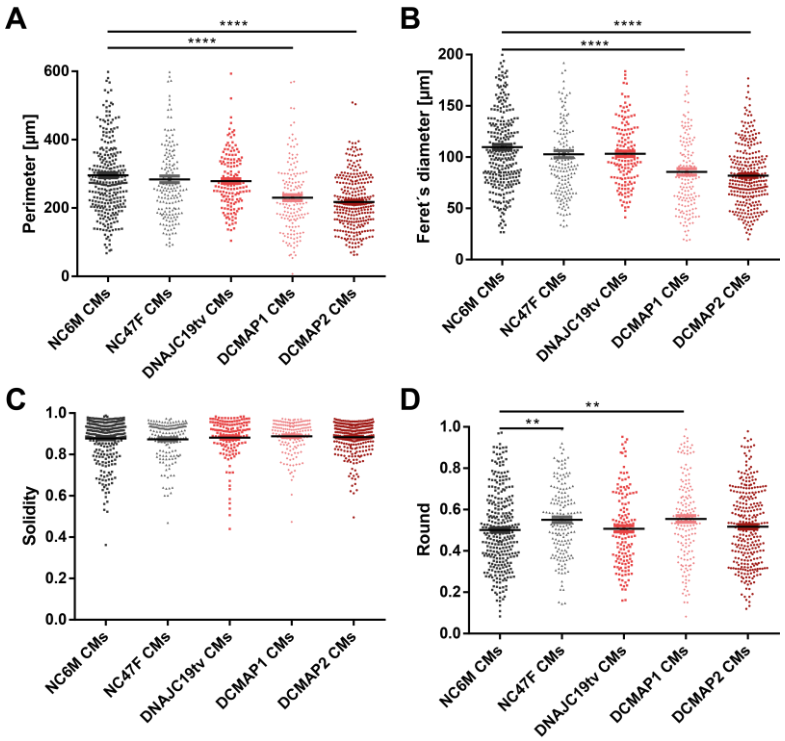

Figure 5.6 Quantifications of CM perimeters, Feret´s diameter and cell shape parameters of DCMA mutants and healthy control iPSC-CMs.
Maximum intensity projections were quantitatively assessed to elucidate CM size [µm^2] features **(A+B)** and shape parameters **(C+D)** calculated for each individual iPSC-CM using semi-automated evaluation of the ImageJ software. Each individually analyzed iPSC-CM of 3-5 independent experiments (biological replicates) is displayed for both healthy controls (NC6M, NC47F) and three DNAJC19 mutation carrier cell lines (DNAJC19tv, DCMAP1, DCMAP2). Data are shown as mean ± SEM together with each individual technical replicate. **** p<0.0001, ** p<0.01, ns p>0.05 using unpaired t-test

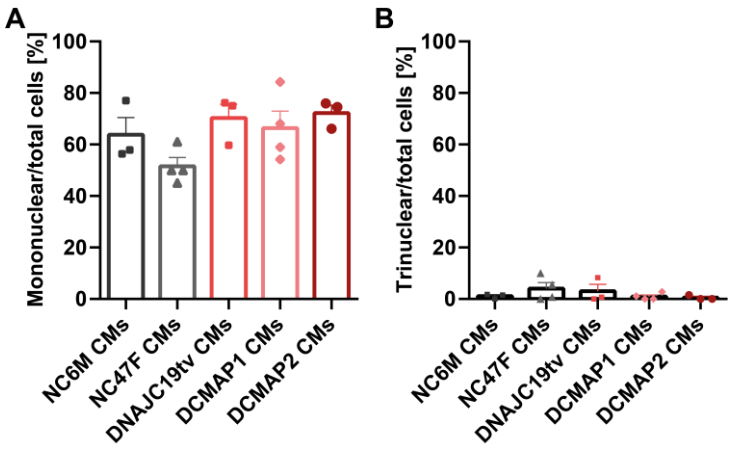

Figure 5.7 Nuclearity states were not altered between DCMA mutant and healthy control iPSC-CMs.
The fraction of **(A)** mononuclear and **(B)** trinuclear iPSC-CMs was quantified for each cardiac differentiation that was used for immunofluorescence stains which allowed the validation of shared maturation states in all five cell lines. Data are shown as mean ± SEM together with each biological replicate. ns $p>0.05$ using unpaired t-test calculated versus NC6M iPSC-CMs

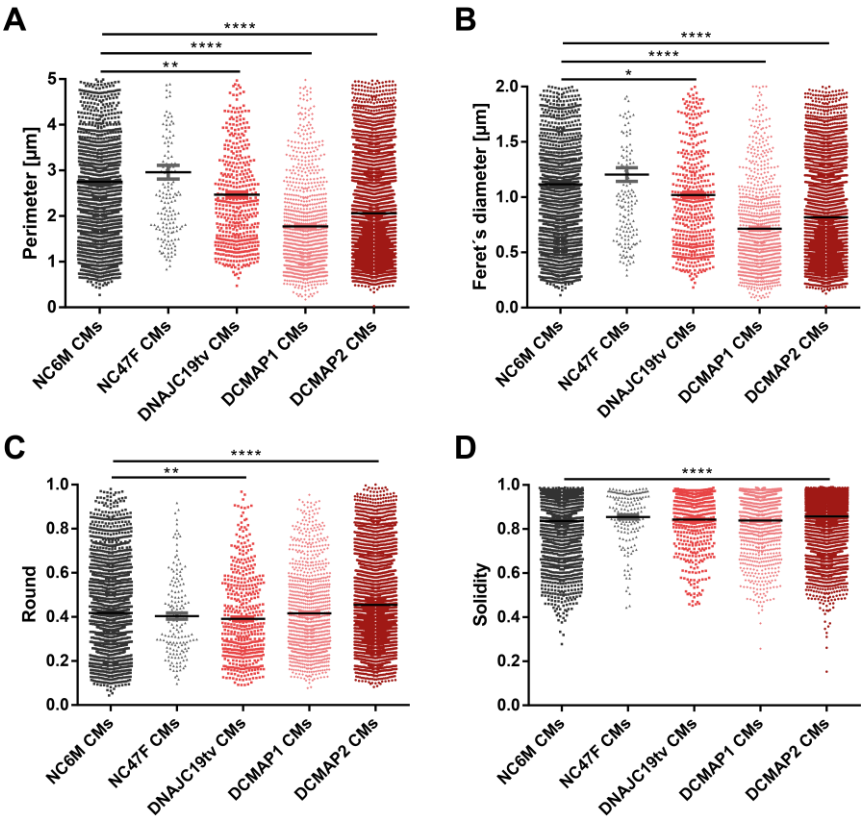

Figure 5.8 Quantification of iPSC-derived mitochondria morphologies using TEM images.
(A+B) Mitochondrial size and **(C+D)** shape parameters were quantified using TEM images in combination with the ImageJ software. Data are shown as mean ± SEM together with each technical replicate, represented by each measured mitochondrion for in total three biological replicates. **** $p<0.0001$, ** $p<0.01$, * $p<0.05$, ns $p>0.05$ using unpaired t-test calculated versus NC6M iPSC-CMs

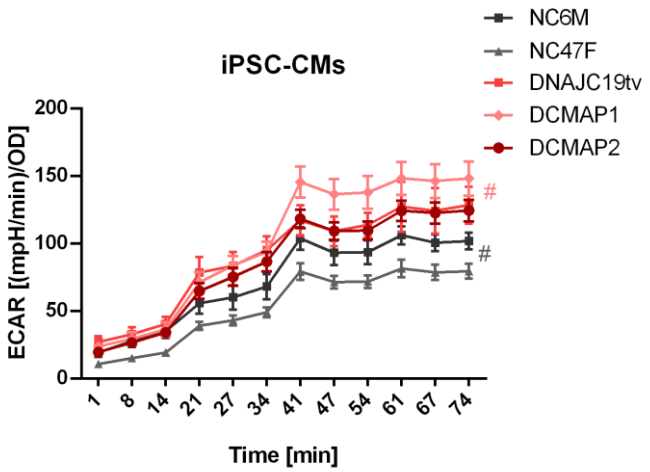

Figure 5.9 DCMAP1 showed the highest degree of extracellular acidification.
The changes of the extracellular flux traces of H^+ of *in vitro*-derived 60 day-old and MACS-derived iPSC-CMs were quantified during the Mito Stress Test Assay using the Seahorse XFe96 extracellular flux analyzer. ECARs were calculated to assess glycolytic switch on three measured timepoints per condition from four to five independent cultures in 16-23 technical replicates (16-23 wells/condition). ECARs over time allowed insights into overall increased extracellular acidification in DCMA iPSC-CMs for each cell line individually. Data are represented as mean ± SEM. # p<0.0001 using regular two-way ANOVA calculated versus healthy control NC6M iPSC-CMs.

5.2 Additive tables

Table 5.1 STR profile analysis of healthy gender- and age-matched control cell lines.

	NC6M fibroblasts				NC6M-SeV iPSCs				NC6M iPSCs			
AMEL	X	84	Y	87	X	84	Y	87	X	84	Y	87
D3S1358	14	121	15	125	14	121	15	125	14	121	15	125
SE33	17	245	18	249	17	245	18	249	17	245	18	249
TH01	7	160	9.3	172	7	160	9.3	172	7	160	9.3	172
D18S51	13	260	15	268	13	260	15	268	13	260	15	268
FGA	23	201	24	205	23	201	24	205	23	201	24	205
vWA	16	119	17	123	16	119	17	123	16	119	17	123
D21S11	31.2	232	31.2	232	31.2	232	31.2	232	31.2	232	31.2	232
D8S1179	10	136	14	154	10	136	14	154	10	136	14	154
	NC47F fibroblasts				NC47F iPSCs							
AMEL	X	84	X	84	X	84	X	84				
D3S1358	14	121	15	125	14	121	15	125				
SE33	20.2	258	25.2	277	20.2	258	25.2	277				
TH01	6	156	9	168	6	156	9	168				
D18S51	12	256	14	264	12	256	14	264				
FGA	22	197	22	197	22	197	22	197				
vWA	17	123	18	127	17	123	18	127				
D21S11	29	222	32.2	236	29	222	32.2	236				
D8S1179	13	150	13	150	13	150	13	150				

Table 5.2 Reprogramming did not alter DNA fingerprints of patient-derived cells.

	DCMAP1 fibroblasts				DCMAP1 iPSCs			
AMEL	X	84	Y	87	X	84	Y	87
D3S1358	14	121	14	121	14	121	14	121
SE33	19	253	27.2	286	19	253	27.2	286
TH01								
D18S51	12	256	17	277	12	256	17	277
FGA	22	197	24	205	22	197	24	205
vWA	16	119	17	123	16	119	17	123
D21S11	28	218	30	226	28	218	30	226
D8S1179	12	145	13	150	12	145	13	150
	DCMAP2 fibroblasts				DCMAP2 iPSCs			
AMEL	X	84	X	84	X	84	X	84
D3S1358	14	121	18	137	14	121	18	137
SE33	18	249	27.2	285	18	249	27.2	285
TH01	6	156	7	160	6	156	7	160
D18S51	13	260	17	277	13	260	17	277
FGA	22	197	24	205	22	197	24	205
vWA	16	119	17	123	16	119	17	123
D21S11	28	218	33.2	240	28	218	33.2	240
D8S1179	12	145	13	150	12	145	13	150
	LEMD2 p.L13R fibroblasts				LEMD2 p.L13R iPSCs			
AMEL	X	84	Y	87	X	84	Y	87
D3S1358	16	129	17	133	16	129	17	133
SE33	17	245	20	256	17	245	20	256
TH01	6	156	6	156	6	156	6	156
D18S51	12	256	17	276	12	256	17	276
FGA	22	197	23	201	22	197	23	201
vWA	14	111	17	123	14	111	17	123
D21S11	28	218	30	226	28	218	30	226
D8S1179	10	136	13	150	10	136	13	150

Table 5.3 The STR profiles of CRISPR/Cas9 gene-edited iPSC lines as validation of the same genetic identity with NC6M iPSCs.

	NC6M iPSCs				DNAJC19tv iPSCs			
AMEL	X	84	Y	87	X	84	Y	87
D3S1358	14	121	15	125	14	121	15	125
SE33	17	245	18	249	17	245	18	249
TH01	7	160	9.3	172	7	160	9.3	172
D18S51	13	260	15	268	13	260	15	268
FGA	23	201	24	205	23	201	24	205
vWA	16	119	17	123	16	119	17	123
D21S11	31.2	232	31.2	232	31.2	232	31.2	232
D8S1179	10	136	14	154	10	136	14	154
	PKP2-KO iPSCs				DSG2-KO iPSCs			
AMEL	X	84	Y	87	X	84	Y	87
D3S1358	14	121	15	125	14	121	15	125
SE33	17	245	18	249	17	245	18	249
TH01	7	160	9.3	172	7	160	9.3	172
D18S51	13	260	15	268	13	260	15	268
FGA	23	201	24	205	23	201	24	205
vWA	16	119	17	123	16	119	17	123
D21S11	31.2	232	31.2	232	31.2	232	31.2	232
D8S1179	10	136	14	154	10	136	14	154

Table 5.4 cDNA isolated of depicted cell lines used for RT-PCR to identify residual `KMOS` expression after SeV-priming.
pos positive; *neg* negative; $ not included in the present thesis

Name	lane	passage
pos control day 1	1	13
neg control (NC6M fibroblasts)	2	20
pos control day 2	3	13
neg control NC6M iPSCs^{LeV}	4	38
NC6M-SeV	5	13
NC47F	6	15
DNAJC19tv	7	4(42)
DCMAP1	8	16
DCMAP2	9	22
LEMD2 p.L13R	10	12
LEMD2iso1-KO$^{\$}$	11	4(43)
DSG2-KO	12	5(43)
PKP2-KO	13	7(45)

5.3 Experimental details

The individual tables are depicted to give an overview of detailed experimental set ups and the individual age states in mean ± SEM, which were defined after the visually observed intitiation of contraction that is further termed as average age mean ± SEM in days (onset of contraction= age day 0 and cardiac differentiation day 7-12). The summarized number of biological replicates refers to the *in vitro* generated iPSC-CMs derived out of one cardiac differentiation culture that is termed n_{BR}. The number of technical replicates represented either the total number of wells per experiment (n_{TR_wells}) or the total amount of cells used for quantifications (n_{TR_CMs}/n_{TR_iPSCs}) for all experiments.

Table 5.5 Experiment overview of the optimized nucleofection protocol using in NC6M iPSCs as depicted in Fig. 3.3.
The number of eGFP$^+$ cells was used to calculate transfection efficiencies in the surviving cell fraction. The percentage of surviving cells per total used cells/number of cells negative control (not electroporated) are displayed as sum of all biological replicates.

Nucleofection strategy	n_{BR}	n_{TR_wells}	n_{TR_iPSCs} eGFP$^+$/survived cells/ total cells
#1	3	2	4/131/1753
#3	3	2	322/2868/4602
#5	6	2	146/406/13292
#7	2	2	930/2290/4170

Table 5.6 Experiment overview to determine ventricular subtype identity in Fig. 3.15.
The sum of iPSC-CMs of all biological replicates is displayed as n_{TR_CMs}, comprised by the MLC2v$^+$ fraction of all cTnT$^+$ cells.

Cell line name	n_{BR}	n_{TR_CMs} (MLC2v$^+$/ cTnT$^+$)	Average age (mean ± SEM)
NC6M	4	95/96	63 ± 5.6
NC47F	4	86/88	63 ± 5.6
DNAJC19tv	3	100/103	61 ± 2.2
DCMAP1	3	60/62	64 ± 1.7
DCMAP2	4	72/74	67 ± 7.2

Table 5.7 Experiment overview to assess CM yields after metabolic enrichment in Fig. 3.16.
The sum of iPSC-CMs of all biological replicates is displayed as n_{TR_CMs}, comprised by the cTnT$^+$ fraction of all DAPI$^+$ cells (manually corrected for binucleated cells).

Cell line name	n_{BR}	n_{TR_CMs} (cTnT$^+$/ DAPI$^+$)	Average age (mean ± SEM)
NC6M	22	1158/1751	44 ± 7.8
NC47F	3	148/184	36 ± 2.3
DNAJC19tv	4	356/521	32 ± 2.6
DCMAP1	8	141/278	40 ± 1.8
DCMAP2	8	447/666	26 ± 6.9

Table 5.8: Experiment overview of MACS representatively shown in NC6M iPSC-CMs in Fig. 3.17.
The sum of iPSC-CMs of all biological replicates is displayed as n_{TR_CMs}, comprised by the cTnT$^+$ fraction of all DAPI$^+$ cells (manually corrected for binucleated cells).

Experimental procedure	n_{BR}	n_{TR_CMs} (cTnT$^+$/ DAPI$^+$)	Average age (mean ± SEM)
Before MACS	6	3202/16285	36 ± 9.5
After MACS- non-CMs	6	2321/49598	36 ± 9.5
After MACS- CMs	6	9234/9583	36 ± 9.5

Table 5.9 Experiment overview of the impact of prolonged cultivation times on maturation representatively shown in NC6M iPSC-CMs in Fig. 3.18.
The sum of iPSC-CMs of all biological replicates is displayed as n_{TR_CMs}, comprised by all cTnT$^+$ cells used for the calculation of iPSC-CMs sizes.

Group names	n_{BR}	n_{TR_CMs}	Average age (mean ± SEM)
Day 30	3	71	32±1.2
Day 60	3	205	60±1.0
Day 90	3	32	91±4.4
Day 120	3	20	124±6.7

Table 5.10: Experiment overview of mattress-based maturation representatively shown in NC6M iPSC-CMs in Fig. 3.20.
The sum of iPSC-CMs of all biological replicates is displayed as n_{TR_CMs}, comprised by all cTnT$^+$ cells used for the calculation of mattress-cultured iPSC-CM sizes and JP2 content.

Experimental procedure: CM sizes	n_{BR}	n_{TR_CMs}	Average age (mean ± SEM)
Standard cultivation	3	127	22 ± 1.9
	3	168	44 ± 0.3
	3	140	63 ± 2.2
Mattress-cultivation	3	170	20 ± 2.7
	3	170	45 ± 6.3
	3	127	66 ± 2.6
Experimental procedure: JP2 content	n_{BR}	n_{TR_CMs}	Average age (mean ± SEM)
Standard cultivation	3	70	19 ± 1.8
	3	85	40 ± 5.6
	3	85	63 ± 2.2
Mattress-cultivation	3	46	20 ± 2.7
	3	50	40 ± 2.3
	3	71	63 ± 1.7

Table 5.11 Experiment overview to assess *DNAJC19* transcript variants in iPSC-CMs via RT-PCR on cDNA level Fig. 3.22.
The total number of wells of collected iPSC-CMs of all biological replicates is displayed as n_{TR_CMs}.

Cell line name	n_{BR}	n_{TR_wells}	Average age (mean ± SEM)
NC6M	3	3	32 ± 1.3
NC47F	3	3	33 ± 2.6
DNAJC19tv	3	3	33 ± 2.6
DCMAP1	3	3	36 ± 1.8
DCMAP2	3	3	37 ± 2.1

Table 5.12 Experiment overview to assess DNAJC19 protein expression in iPSC-CMs via western blot analysis Fig. 3.24.
The total number of wells of collected iPSC-CMs of all biological replicates is displayed as n_{TR_CMs}.

Cell line name	n_{BR}	n_{TR_wells}	Average age (mean ± SEM)
NC6M	3	3	61 ± 0.3
NC47F	3	3	63 ± 1.6
DNAJC19tv	3	3	61 ± 0.6
DCMAP1	3	3	65 ± 1.3
DCMAP2	3	3	61 ± 0.3

Table 5.13 Experiment overview to assess DNAJC19 expression in iPSC-CMs in the cytoplasm using immunofluorescence images Fig. 3.27.
The sum of iPSC-CMs of all biological replicates is displayed as n_{TR_CMs}, comprised by all $cTnT^+$ cells used for calculation of DNAJC19 subcellular localization.

Cell line name	n_{BR}	n_{TR_CMs}	Average age (mean ± SEM)
NC6M	3	281	63.13 ± 0.15
NC47F	4	109	63.59 ± 0.31
DNAJC19tv	3	125	62.36 ± 0.13
DCMAP1	3	67	63.73 ± 0.30
DCMAP2	3	234	65.62 ± 0.17

Table 5.14 Experiment overview to assess DNAJC19 expression in iPSC-CMs in the nucleus using immunofluorescence images Fig. 3.27.
The sum of iPSC-CMs of all biological replicates is displayed as n_{TR_CMs}, comprised by all $DAPI^+/cTnT^+$ cells used for calculation of DNAJC19 subcellular localization.

Cell line name	n_{BR}	n_{TR_CMs}	Average age (mean ± SEM)
NC6M	3	457	63.55 ± 0.16
NC47F	4	175	63.88 ± 0.25
DNAJC19tv	3	125	62.36 ± 0.13
DCMAP1	3	67	63.73 ± 0.30
DCMAP2	3	168	65.97 ± 0.22

Table 5.15 Experiment overview to assess MitoTracker expression in iPSC-CMs using immunofluorescence images Fig. 3.28.
The sum of iPSC-CMs of all biological replicates is displayed as n_{TR_CMs}, comprised by all $cTnT^+$ cells used for calculation of the MitoTracker content.

Cell line name	n_{BR}	n_{TR_CMs}	Average age (mean ± SEM)
NC6M	3	155	64.42 ± 0.27
NC47F	3	51	63.29 ± 0.36
DNAJC19tv	3	147	62.85 ± 0.16
DCMAP1	3	44	62.81 ± 0.27
DCMAP2	3	64	65.62 ± 0.34

Table 5.16 Experiment overview to assess cTnT expression in iPSC-CMs using immunofluorescence images Fig. 3.28.
The sum of iPSC-CMs of all biological replicates is displayed as n_{TR_CMs}, comprised by all $cTnT^+$ cells used for calculation of the cTnT content.

Cell line name	n_{BR}	n_{TR_CMs}	Average age (mean ± SEM)
NC6M	3	292	63.30 ± 0.16
NC47F	4	170	63.41 ± 0.23
DNAJC19tv	3	147	62.88 ± 0.16
DCMAP1	3	147	63.71 ± 0.23
DCMAP2	3	289	64.94 ± 0.16

Table 5.17 Experiment overview to assess iPSC-CM areas in [µm²] by extrapolation of cTnT staining using immunofluorescence images Fig. 3.29.
The sum of iPSC-CMs of all biological replicates is displayed as n_{TR_CMs}, comprised by all $cTnT^+$ cells used for the calculation of iPSC-CMs sizes.

Cell line name	n_{BR}	n_{TR_CMs}	Average age (mean ± SEM)
NC6M	3	292	63.30 ± 0.16
NC47F	4	170	63.41 ± 0.23
DNAJC19tv	3	147	62.88 ± 0.16
DCMAP1	3	160	64.22 ± 0.25
DCMAP2	3	289	64.94 ± 0.16

Table 5.18 Experiment overview to assess thin filament lengths in [µm] via cTnT staining using immunofluorescence images Fig. 3.30.
The sum of iPSC-CMs of all biological replicates is displayed as n_{TR_CMs}, comprised by all $cTnT^+$ cells used for the calculation of thin filament lengths.

Cell line name	n_{BR}	n_{TR_CMs}	Average age (mean ± SEM)
NC6M	3	54	64.59 ± 0.16
NC47F	4	66	65.52 ± 0.23
DNAJC19tv	3	24	64.75 ± 0.16
DCMAP1	3	45	64.22 ± 0.25
DCMAP2	3	19	64.42 ± 0.16

Table 5.19 Experiment overview to assess nuclei areas [µm²] in iPSC-CMs by DAPI staining using immunofluorescence images Fig. 3.31.
The sum of iPSC-CMs derived nuclei of all biological replicates is displayed as n_{TR_CMs}, comprised by all $DAPI^+/cTnT^+$ cells used for the calculation of nuclear sizes.

Cell line name	n_{BR}	n_{TR_CMs}	Average age (mean ± SEM)
NC6M	3	614	63.23 ± 0.17
NC47F	4	247	63.35 ± 0.15
DNAJC19tv	3	266	62.94 ± 0.13
DCMAP1	4	281	65.02 ± 0.19
DCMAP2	3	632	66.04 ± 0.14

Table 5.20 Experiment overview to assess nuclearities in iPSC-CMs by DAPI staining per cell [%] using immunofluorescence images Fig. 3.31.
The sum of iPSC-CMs derived nuclei of all biological replicates is displayed as n_{TR_CMs}, comprised by all $DAPI^+/cTnT^+$ cells. The calculation was based on the percentage of nuclearity states for each biological replicate.

Cell line name	n_{BR}	n_{TR_CMs}	Average age (mean ± SEM)
NC6M	3	614	63.23 ± 0.17
NC47F	4	247	63.35 ± 0.15
DNAJC19tv	3	266	62.94 ± 0.13
DCMAP1	4	281	65.02 ± 0.19
DCMAP2	3	632	66.04 ± 0.14

Table 5.21 Experiment overview to assess mitochondrial areas [µm²] and shapes in iPSC-CMs using TEM images in Fig. 3.33.
The sum of iPSC-CMs of all biological replicates is displayed as n_{TR_CMs}, comprised by all visually determined intermyofibrillar mitochondria used for the calculation of mitochondrial sizes.

Cell line name	n_{BR}	n_{TR_CMs}	Average age (mean ± SEM)
NC6M	3	2207	63.78 ± 0.56
NC47F	3	161	64.20 ± 0.08
DNAJC19tv	3	494	68.33 ± 2.23
DCMAP1	3	1022	69.34 ± 1.63
DCMAP2	3	5341	75.06 ± 6.86

Table 5.22: Summary of biological replicates for CL profiles corresponding to mass spectrometric analysis in Fig. 3.35.
3 x 10^6 iPSC-CMs out of one well of a 12-well plate were used for the measurement.

Cell line	n_{BR}	n_{TR_wells}	Average age (mean ± SEM)
NC6M	1	1	62
DCMAP2	1	1	62

Table 5.23: Summary experiment overview Mito Stress Test Assay of iPSC-CMs in Fig. 3.46.
The sum of iPSC-CMs of all biological replicates is represented by n_{BR}. n_{TR_wells} describes the number of measured wells averaged for each experiment and refers to technical replicates.

Cell line name	n_{BR}	n_{TR_wells}	Average age (mean ± SEM)
NC6M	4	16-23	62 ± 0.22
NC47F	5	16-23	61 ± 0.33
DNAJC19tv	5	16-23	61 ± 0.33
DCMAP1	5	16-23	61 ± 0.33
DCMAP2	5	16-23	61 ± 0.33

Table 5.24: Summary of biological replicates for radioactive tracer uptakes corresponding to Fig. 3.48.
The sum of iPSC-CMs of all biological replicates is represented by n_{BR}. n_{TR_wells} describes the number of measured wells averaged for each experiment and refers to technical replicates.

Cell line	n_{BR}	n_{TR_wells}	Average age (mean ± SEM)
NC6M	6	2-4	63 ± 1.69
NC47F	6	2-4	63 ± 1.69
DNAJC19tv	6	2-4	63 ± 1.69
DCMAP1	5	2-4	62 ± 1.43
DCMAP2	6	2-4	63 ± 1.69

Table 5.25: Summary of iPSC-CMs analyzed using the IonOptix system in Fig. 3.45, 3.47, 3.48, 3.49, 3.50, 3.51, 3.52.
The sum of iPSC-CMs of all biological replicates (n_{BR}), which comprised the total sum of measured single cell iPSC-CMs that are counted as technical replicates n_{TR_CMs}.

Cell line	n_{BR}	n_{TR_CMs}	Average age (mean ± SEM)
NC6M	5	22	122.43 ± 6.08
DNAJC19tv	4	13	126.15 ± 2.81
DCMAP1	3	15	129.25 ± 1.93
DCMAP2	3	17	126.59 ± 1.67

5.4 Macros

The software Fiji was used for immunofluorescence-based quantifications (Schindelin et al., 2012). General accessible Macros were used such as MyofibrilJ-0.1.0 for identification of thin filament diameters based on cTnT staining (Giovanni Cardone and Maria Spletter, 2017). Other quantifications were performed on self-designed macros for nuclei quantifications, cell and shape descriptor quantifications and signal intensities within a given region of interest (ROI). All quantifications shared following preadjustments: run("8-bit"); inputDirectory= getDirectory("image"); outputDirectoryName= inputDirectory + "Analysis"; outputDirectoryPath= outputDirectoryName+File.separator; File.makeDirectory(outputDirectoryName). The channel acquisition set up of the Laser scanning confocal microscope LSM 780 channels needed to be assigned individually: originalImageName=getTitle(); red="C1-"+originalImageName; green="C2-"+originalImageName; blue="C3-"+originalImageName; run("Split Channels"). For nuclei quantifications following parameters were used to identify DAPI positive pixels on pictures acquired with the 63x or 40 x objective: selectWindow(blue); run("Duplicate...", "title=[copy_"+blue+"]"); copyOfBlue=getTitle(); run("Median...", "radius=5"); run("Auto Threshold", "method=RenyiEntropy white"); run("Options...", "iterations=1 count=1 black do=Nothing"); run("Watershed"); run("Set Measurements...", "area redirect=None decimal=3"); run("Analyze Particles...", "size=60-Infinity display clear add"); close(copyOfBlue); roiManager("save", outputDirectoryPath+"C3-"+originalImageName+".zip") waitForUser("Please copy area of Nuclei to excel sheet and press OK"); close("Roi Manager"); saveAs("Results", outputDirectoryPath+"C3-"+originalImageName+".tsv"); close("Results"). For iPSC-CMs quantifications following parameters were used to identify cTnT positive pixels on pictures acquired with the 63x or 40x objective: selectWindow(green); run("Duplicate...", "title=[copy_"+green+"]"); copyOfGreen=getTitle(); run("Enhance Contrast...", "saturated=0.3 normalize"); run("Auto Threshold", "method=Li white"); run("Options...", "iterations=3 count=1 black do=Nothing"); run("Close-"); run("Fill Holes"). If nuclei or CMs could not be filled or separated automatically, manual adjustments were made on binary pictures using: run("Colors...", "foreground=black background=white selection=red"); waitForUser("Please seperate CMs and press OK"); run("Colors...", "foreground=white background=black selection=red"); waitForUser("Please fill up CM Area if neccessary and press OK"). Analysis was performed using: run("Set Measurements...", "area perimeter shape feret's redirect=None decimal=3"); run("Analyze Particles...", "size=100-Infinity display exclude add"); waitForUser("Please copy Results of CMs to excel sheet, close table and press OK"); close(copyOfGreen); selectWindow(green); run("Enhance Contrast...", "saturated=0.3 normalize"); run("Auto Threshold", "method=Moments white"); run("Set Measurements...", "area"); roiManager("save", outputDirectoryPath+"C2-"+originalImageName+".zip") saveAs("Results", outputDirectoryPath+"C2-"+originalImageName+".tsv"); close("Results"). To quantifiy positively labelled pixels in a specified region (ROI of nuclei or ROI of iPSC-CMs) ROIs needed to be activated manually with following adjustments: roiManager("Select", 0); run("Analyze Particles...", " show=Overlay display clear"); waitForUser("Please copy Results to excel sheet and press OK"). Given the individual immunofluorescence stains and antibody-dependent intensities common autothresholds were used such as Li, RenyiEntropy, Moments, MaxEntropy to allow equal intensity thresholds during image calculation.

6. Bibliography

AASEN, T., RAYA, A., BARRERO, M. J., GARRETA, E., CONSIGLIO, A., GONZALEZ, F., VASSENA, R., BILIC, J., PEKARIK, V., TISCORNIA, G., EDEL, M., BOUE, S. & IZPISUA BELMONTE, J. C. 2008. Efficient and rapid generation of induced pluripotent stem cells from human keratinocytes. *Nat Biotechnol,* 26**,** 1276-84.

ABDELFATAH, N., CHEN, R., DUFF, H. J., SEIFER, C. M., BUFFO, I., HUCULAK, C., CLARKE, S., CLEGG, R., JASSAL, D. S., GORDON, P. M. K., OBER, C., CARE4RARE CANADA, C., FROSK, P. & GERULL, B. 2019a. Characterization of a Unique Form of Arrhythmic Cardiomyopathy Caused by Recessive Mutation in LEMD2. *JACC Basic Transl Sci,* 4**,** 204-221.

ABDELFATAH, N., CHEN, R., DUFF, H. J., SEIFER, C. M., BUFFO, I., HUCULAK, C., CLARKE, S., CLEGG, R., JASSAL, D. S., GORDON, P. M. K., OBER, C., FROSK, P. & GERULL, B. 2019b. Characterization of a Unique Form of Arrhythmic Cardiomyopathy Caused by Recessive Mutation in LEMD2. *JACC Basic Transl Sci,* 4**,** 204-221.

ABEYTA, M. J., CLARK, A. T., RODRIGUEZ, R. T., BODNAR, M. S., PERA, R. A. & FIRPO, M. T. 2004. Unique gene expression signatures of independently-derived human embryonic stem cell lines. *Hum Mol Genet,* 13**,** 601-8.

ACEHAN, D., XU, Y., STOKES, D. L. & SCHLAME, M. 2007. Comparison of lymphoblast mitochondria from normal subjects and patients with Barth syndrome using electron microscopic tomography. *Lab Invest,* 87**,** 40-8.

AGILENT TECHNOLOGIES. 2018. *Measuring mitochondrial defects in human skin fibroblasts* [Online]. Available: https://www.agilent.com/cs/pubimages/misc/TB_Fibroblasts.pdf [Accessed].

AGILENT TECHNOLOGIES. 2019. *Seahorse XF Cell Mito Stress Test Kit User Guide* [Online]. Available: https://www.agilent.com/en/product/cell-analysis/real-time-cell-metabolic-analysis/xf-assay-kits-reagents-cell-assay-media/seahorse-xf-cell-mito-stress-test-kit-740885#support [Accessed 15th August 2019].

AGUILAR-GALLARDO, C., POO, M., GOMEZ, E., GALAN, A., SANCHEZ, E., MARQUES-MARI, A., RUIZ, V., MEDRANO, J., RIBOLDI, M., VALBUENA, D. & SIMON, C. 2010. Derivation, characterization, differentiation, and registration of seven human embryonic stem cell lines (VAL-3, -4, -5, -6M, -7, -8, and -9) on human feeder. *In Vitro Cell Dev Biol Anim,* 46**,** 317-26.

AKHYARI, P., FEDAK, P. W., WEISEL, R. D., LEE, T. Y., VERMA, S., MICKLE, D. A. & LI, R. K. 2002. Mechanical stretch regimen enhances the formation of bioengineered autologous cardiac muscle grafts. *Circulation,* 106**,** I137-42.

AL TENEIJI, A., SIRIWARDENA, K., GEORGE, K., MITAL, S. & MERCIMEK-MAHMUTOGLU, S. 2016. Progressive Cerebellar Atrophy and a Novel Homozygous Pathogenic DNAJC19 Variant as a Cause of Dilated Cardiomyopathy Ataxia Syndrome. *Pediatr Neurol,* 62**,** 58-61.

ALEXANDER, C., VOTRUBA, M., PESCH, U. E., THISELTON, D. L., MAYER, S., MOORE, A., RODRIGUEZ, M., KELLNER, U., LEO-KOTTLER, B., AUBURGER, G., BHATTACHARYA, S. S. & WISSINGER, B. 2000. OPA1, encoding a dynamin-related GTPase, is mutated in autosomal dominant optic atrophy linked to chromosome 3q28. *Nat Genet,* 26**,** 211-5.

AMPS, K., ANDREWS, P. W., ANYFANTIS, G., ARMSTRONG, L., AVERY, S., BAHARVAND, H., BAKER, J., BAKER, D., MUNOZ, M. B., BEIL, S., BENVENISTY, N., BEN-YOSEF, D., BIANCOTTI, J. C., BOSMAN, A., BRENA, R. M., BRISON, D., CAISANDER, G., CAMARASA, M. V., CHEN, J., CHIAO, E., CHOI, Y. M., CHOO, A. B., COLLINS, D., COLMAN, A., CROOK, J. M., DALEY, G. Q., DALTON, A., DE SOUSA, P. A., DENNING, C., DOWNIE, J., DVORAK, P., MONTGOMERY, K. D., FEKI, A., FORD, A., FOX, V., FRAGA, A. M., FRUMKIN, T., GE, L., GOKHALE, P. J., GOLAN-LEV, T., GOURABI, H., GROPP, M., LU, G., HAMPL, A., HARRON, K., HEALY, L., HERATH, W., HOLM, F., HOVATTA, O., HYLLNER, J., INAMDAR, M. S., IRWANTO, A. K., ISHII, T., JACONI, M., JIN, Y., KIMBER, S., KISELEV, S., KNOWLES, B. B., KOPPER, O., KUKHARENKO, V., KULIEV, A., LAGARKOVA, M. A., LAIRD, P. W., LAKO, M., LASLETT, A. L., LAVON, N., LEE, D. R., LEE, J. E., LI, C., LIM, L. S., LUDWIG, T. E., MA, Y., MALTBY, E., MATEIZEL, I., MAYSHAR, Y., MILEIKOVSKY, M., MINGER, S. L., MIYAZAKI, T., MOON, S. Y., MOORE, H., MUMMERY, C., NAGY, A., NAKATSUJI, N., NARWANI, K., OH, S. K., OLSON, C., OTONKOSKI, T., PAN, F., PARK, I. H., PELLS, S., PERA, M. F., PEREIRA, L. V., QI, O., RAJ, G. S., REUBINOFF, B., ROBINS, A., ROBSON, P., ROSSANT, J., SALEKDEH, G. H., SCHULZ, T. C., et al. 2011. Screening ethnically diverse human embryonic stem cells identifies a chromosome 20 minimal amplicon conferring growth advantage. *Nat Biotechnol,* 29**,** 1132-44.

ANAND, R., WAI, T., BAKER, M. J., KLADT, N., SCHAUSS, A. C., RUGARLI, E. & LANGER, T. 2014. The i-AAA protease YME1L and OMA1 cleave OPA1 to balance mitochondrial fusion and fission. *The Journal of cell biology,* 204**,** 919-29.

ANTON, Z., LANDAJUELA, A., HERVAS, J. H., MONTES, L. R., HERNANDEZ-TIEDRA, S., VELASCO, G., GONI, F. M. & ALONSO, A. 2016. Human Atg8-cardiolipin interactions in mitophagy: Specific properties of LC3B, GABARAPL2 and GABARAP. *Autophagy,* 12**,** 2386-2403.

ANTOONS, G., MUBAGWA, K., NEVELSTEEN, I. & SIPIDO, K. R. 2002. Mechanisms underlying the frequency dependence of contraction and [Ca(2+)](i) transients in mouse ventricular myocytes. *J Physiol,* 543**,** 889-98.

ARDAIL, D., PRIVAT, J. P., EGRET-CHARLIER, M., LEVRAT, C., LERME, F. & LOUISOT, P. 1990. Mitochondrial contact sites. Lipid composition and dynamics. *J Biol Chem,* 265**,** 18797-802.

ARTAL-SANZ, M. & TAVERNARAKIS, N. 2009. Prohibitin and mitochondrial biology. *Trends Endocrinol Metab,* 20**,** 394-401.

ARTAL-SANZ, M., TSANG, W. Y., WILLEMS, E. M., GRIVELL, L. A., LEMIRE, B. D., VAN DER SPEK, H. & NIJTMANS, L. G. 2003. The mitochondrial prohibitin complex is essential for embryonic viability and germline function in Caenorhabditis elegans. *J Biol Chem,* 278**,** 32091-9.

AUSTIN, K. M., TREMBLEY, M. A., CHANDLER, S. F., SANDERS, S. P., SAFFITZ, J. E., ABRAMS, D. J. & PU, W. T. 2019. Molecular mechanisms of arrhythmogenic cardiomyopathy. *Nat Rev Cardiol,* 16**,** 519-537.

AVERY, S., HIRST, A. J., BAKER, D., LIM, C. Y., ALAGARATNAM, S., SKOTHEIM, R. I., LOTHE, R. A., PERA, M. F., COLMAN, A., ROBSON, P., ANDREWS, P. W. & KNOWLES, B. B. 2013. BCL-XL mediates the strong selective advantage of a 20q11.21 amplification commonly found in human embryonic stem cell cultures. *Stem Cell Reports,* 1**,** 379-86.

AWAD, M. M., CALKINS, H. & JUDGE, D. P. 2008. Mechanisms of disease: molecular genetics of arrhythmogenic right ventricular dysplasia/cardiomyopathy. *Nat Clin Pract Cardiovasc Med,* 5**,** 258-67.

AWE, J. P., LEE, P. C., RAMATHAL, C., VEGA-CRESPO, A., DURRUTHY-DURRUTHY, J., COOPER, A., KARUMBAYARAM, S., LOWRY, W. E., CLARK, A. T., ZACK, J. A., SEBASTIANO, V., KOHN, D. B., PYLE, A. D., MARTIN, M. G., LIPSHUTZ, G. S., PHELPS, P. E., PERA, R. A. & BYRNE, J. A. 2013. Generation and characterization of transgene-free human induced pluripotent stem cells and conversion to putative clinical-grade status. *Stem Cell Res Ther,* 4**,** 87.

BAGHBADERANI, B. A., SYAMA, A., SIVAPATHAM, R., PEI, Y., MUKHERJEE, O., FELLNER, T., ZENG, X. & RAO, M. S. 2016. Detailed Characterization of Human Induced Pluripotent Stem Cells Manufactured for Therapeutic Applications. *Stem Cell Rev Rep,* 12**,** 394-420.

BAGHBADERANI, B. A., TIAN, X., NEO, B. H., BURKALL, A., DIMEZZO, T., SIERRA, G., ZENG, X., WARREN, K., KOVARCIK, D. P., FELLNER, T. & RAO, M. S. 2015. cGMP-Manufactured Human Induced Pluripotent Stem Cells Are Available for Pre-clinical and Clinical Applications. *Stem Cell Reports,* 5**,** 647-59.

BAHARVAND, H., JAFARY, H., MASSUMI, M. & ASHTIANI, S. K. 2006. Generation of insulin-secreting cells from human embryonic stem cells. *Dev Growth Differ,* 48**,** 323-32.

BALABAN, R. S. 2002. Cardiac energy metabolism homeostasis: role of cytosolic calcium. *J Mol Cell Cardiol,* 34**,** 1259-71.

BAN, H., NISHISHITA, N., FUSAKI, N., TABATA, T., SAEKI, K., SHIKAMURA, M., TAKADA, N., INOUE, M., HASEGAWA, M., KAWAMATA, S. & NISHIKAWA, S. 2011. Efficient generation of transgene-free human induced pluripotent stem cells (iPSCs) by temperature-sensitive Sendai virus vectors. *Proceedings of the National Academy of Sciences of the United States of America,* 108**,** 14234-9.

BAN, T., HEYMANN, J. A., SONG, Z., HINSHAW, J. E. & CHAN, D. C. 2010. OPA1 disease alleles causing dominant optic atrophy have defects in cardiolipin-stimulated GTP hydrolysis and membrane tubulation. *Hum Mol Genet,* 19**,** 2113-22.

BAR-NUR, O., BRUMBAUGH, J., VERHEUL, C., APOSTOLOU, E., PRUTEANU-MALINICI, I., WALSH, R. M., RAMASWAMY, S. & HOCHEDLINGER, K. 2014. Small molecules facilitate rapid and synchronous iPSC generation. *Nat Methods,* 11**,** 1170-6.

BARTH, E., STAMMLER, G., SPEISER, B. & SCHAPER, J. 1992. Ultrastructural quantitation of mitochondria and myofilaments in cardiac muscle from 10 different animal species including man. *J Mol Cell Cardiol,* 24**,** 669-81.

BARTH, P. G., SCHOLTE, H. R., BERDEN, J. A., VAN DER KLEI-VAN MOORSEL, J. M., LUYT-HOUWEN, I. E., VAN 'T VEER-KORTHOF, E. T., VAN DER HARTEN, J. J. & SOBOTKA-PLOJHAR, M. A. 1983. An X-linked mitochondrial disease affecting cardiac muscle, skeletal muscle and neutrophil leucocytes. *J Neurol Sci,* 62**,** 327-55.

BASSANI, R. A. & BERS, D. M. 1994. Na-Ca exchange is required for rest-decay but not for rest-potentiation of twitches in rabbit and rat ventricular myocytes. *J Mol Cell Cardiol,* 26**,** 1335-47.

BASSETT, A. R. 2017. Editing the genome of hiPSC with CRISPR/Cas9: disease models. *Mamm Genome,* 28**,** 348-364.

BAZETT, H. C. 1920. The time relations of the blood-pressure changes after excision of the adrenal glands, with some observations on blood volume changes. *J Physiol,* 53**,** 320-39.

BEAVERS, D. L., LANDSTROM, A. P., CHIANG, D. Y. & WEHRENS, X. H. 2014. Emerging roles of junctophilin-2 in the heart and implications for cardiac diseases. *Cardiovasc Res,* 103**,** 198-205.

BECKER, A. J., MC, C. E. & TILL, J. E. 1963. Cytological demonstration of the clonal nature of spleen colonies derived from transplanted mouse marrow cells. *Nature,* 197**,** 452-4.

BECKER, T., BOTTINGER, L. & PFANNER, N. 2012. Mitochondrial protein import: from transport pathways to an integrated network. *Trends Biochem Sci,* 37**,** 85-91.

BENARD, G., BELLANCE, N., JAMES, D., PARRONE, P., FERNANDEZ, H., LETELLIER, T. & ROSSIGNOL, R. 2007. Mitochondrial bioenergetics and structural network organization. *J Cell Sci,* 120**,** 838-48.

BEQQALI, A., KLOOTS, J., WARD-VAN OOSTWAARD, D., MUMMERY, C. & PASSIER, R. 2006. Genome-wide transcriptional profiling of human embryonic stem cells differentiating to cardiomyocytes. *Stem Cells,* 24**,** 1956-67.

BEREITER-HAHN, J. 1990. Behavior of mitochondria in the living cell. *Int Rev Cytol,* 122**,** 1-63.

BERGER, K. H. & YAFFE, M. P. 1998. Prohibitin family members interact genetically with mitochondrial inheritance components in Saccharomyces cerevisiae. *Mol Cell Biol,* 18**,** 4043-52.

BERGMANN, C., SENDEREK, J., KUPPER, F., SCHNEIDER, F., DORNIA, C., WINDELEN, E., EGGERMANN, T., RUDNIK-SCHONEBORN, S., KIRFEL, J., FURU, L., ONUCHIC, L. F., ROSSETTI, S., HARRIS, P. C., SOMLO, S., GUAY-WOODFORD, L., GERMINO, G. G., MOSER, M., BUTTNER, R. & ZERRES, K. 2004. PKHD1 mutations in autosomal recessive polycystic kidney disease (ARPKD). *Hum Mutat,* 23**,** 453-63.

BERS, D. M. 2002a. Cardiac excitation-contraction coupling. *Nature,* 415**,** 198-205.

BERS, D. M. 2002b. Sarcoplasmic reticulum Ca release in intact ventricular myocytes. *Front Biosci,* 7**,** d1697-711.

BERS, D. M. 2006. Altered cardiac myocyte Ca regulation in heart failure. *Physiology (Bethesda),* 21**,** 380-7.

BERS, D. M. & PEREZ-REYES, E. 1999. Ca channels in cardiac myocytes: structure and function in Ca influx and intracellular Ca release. *Cardiovasc Res,* 42**,** 339-60.

BERS, D. M. & WEBER, C. R. 2002. Na/Ca exchange function in intact ventricular myocytes. *Ann N Y Acad Sci,* 976**,** 500-12.

BERTERO, E. & MAACK, C. 2018. Metabolic remodelling in heart failure. *Nat Rev Cardiol,* 15**,** 457-470.

BESSMAN, S. P. & GEIGER, P. J. 1981. Transport of energy in muscle: the phosphorylcreatine shuttle. *Science,* 211**,** 448-52.

BHATTACHARYA, B., MIURA, T., BRANDENBERGER, R., MEJIDO, J., LUO, Y., YANG, A. X., JOSHI, B. H., GINIS, I., THIES, R. S., AMIT, M., LYONS, I., CONDIE, B. G., ITSKOVITZ-ELDOR, J., RAO, M. S. & PURI, R. K. 2004. Gene expression in human embryonic stem cell lines: unique molecular signature. *Blood,* 103**,** 2956-64.

BHAYA, D., DAVISON, M. & BARRANGOU, R. 2011. CRISPR-Cas systems in bacteria and archaea: versatile small RNAs for adaptive defense and regulation. *Annu Rev Genet,* 45**,** 273-97.

BHOSALE, G., SHARPE, J. A., SUNDIER, S. Y. & DUCHEN, M. R. 2015. Calcium signaling as a mediator of cell energy demand and a trigger to cell death. *Mitochondrial Research in Translational Medicine,* 1350**,** 107-116.

BHUTANI, N., BRADY, J. J., DAMIAN, M., SACCO, A., CORBEL, S. Y. & BLAU, H. M. 2010. Reprogramming towards pluripotency requires AID-dependent DNA demethylation. *Nature,* 463**,** 1042-7.

BIANCONI, E., PIOVESAN, A., FACCHIN, F., BERAUDI, A., CASADEI, R., FRABETTI, F., VITALE, L., PELLERI, M. C., TASSANI, S., PIVA, F., PEREZ-AMODIO, S., STRIPPOLI, P. & CANAIDER, S. 2013. An estimation of the number of cells in the human body. *Ann Hum Biol,* 40**,** 463-71.

BIONE, S., D'ADAMO, P., MAESTRINI, E., GEDEON, A. K., BOLHUIS, P. A. & TONIOLO, D. 1996. A novel X-linked gene, G4.5. is responsible for Barth syndrome. *Nat Genet,* 12**,** 385-9.

BIORENDER. 2017. Available: https://biorender.com/privacy/ [Accessed 4th February 2021].

BIRKET, M. J., RIBEIRO, M. C., KOSMIDIS, G., WARD, D., LEITOGUINHO, A. R., VAN DE POL, V., DAMBROT, C., DEVALLA, H. D., DAVIS, R. P., MASTROBERARDINO, P. G., ATSMA, D. E., PASSIER, R. & MUMMERY, C. L. 2015. Contractile Defect Caused by Mutation in MYBPC3 Revealed under Conditions Optimized for Human PSC-Cardiomyocyte Function. *Cell Rep,* 13**,** 733-745.

BIRNER, R., NEBAUER, R., SCHNEITER, R. & DAUM, G. 2003. Synthetic lethal interaction of the mitochondrial phosphatidylethanolamine biosynthetic machinery with the prohibitin complex of Saccharomyces cerevisiae. *Mol Biol Cell,* 14**,** 370-83.

BISSLER, J. J., TSORAS, M., GORING, H. H., HUG, P., CHUCK, G., TOMBRAGEL, E., MCGRAW, C., SCHLOTMAN, J., RALSTON, M. A. & HUG, G. 2002. Infantile dilated X-linked cardiomyopathy, G4.5 mutations, altered lipids, and ultrastructural malformations of mitochondria in heart, liver, and skeletal muscle. *Lab Invest,* 82**,** 335-44.

BLIGH, E. G. & DYER, W. J. 1959. A rapid method of total lipid extraction and purification. *Can J Biochem Physiol,* 37**,** 911-7.

BODI, I., MIKALA, G., KOCH, S. E., AKHTER, S. A. & SCHWARTZ, A. 2005. The L-type calcium channel in the heart: the beat goes on. *J Clin Invest,* 115**,** 3306-17.

BOGDANOV, M., MILEYKOVSKAYA, E. & DOWHAN, W. 2008. Lipids in the assembly of membrane proteins and organization of protein supercomplexes: implications for lipid-linked disorders. *Subcell Biochem,* 49**,** 197-239.

BOONE, P. M., YUAN, B., GU, S., MA, Z., GAMBIN, T., GONZAGA-JAUREGUI, C., JAIN, M., MURDOCK, T. J., WHITE, J. J., JHANGIANI, S. N., WALKER, K., WANG, Q., MUZNY, D. M., GIBBS, R. A., HEJTMANCIK, J. F., LUPSKI, J. R., POSEY, J. E. & LEWIS, R. A. 2016. Hutterite-type cataract maps to chromosome 6p21.32-p21.31, cosegregates with a homozygous mutation in LEMD2, and is associated with sudden cardiac death. *Mol Genet Genomic Med,* 4**,** 77-94.

BOUDOU, T., LEGANT, W. R., MU, A., BOROCHIN, M. A., THAVANDIRAN, N., RADISIC, M., ZANDSTRA, P. W., EPSTEIN, J. A., MARGULIES, K. B. & CHEN, C. S. 2012. A microfabricated platform to measure and manipulate the mechanics of engineered cardiac microtissues. *Tissue Eng Part A,* 18**,** 910-9.

BOVERI, T. 1887. Ueber die Befruchtung der Eier von Ascaris megalocephala. *Sitz.-Ber. Ges. Morph. Phys. Mçnchen,* 3**,** 71-80.

BOVERI, T. 1892. *Befruchtung*, JF Bergmann.

BRADLEY, A., EVANS, M., KAUFMAN, M. H. & ROBERTSON, E. 1984. Formation of germ-line chimaeras from embryo-derived teratocarcinoma cell lines. *Nature,* 309**,** 255-6.

BRAND, M. D. 2016. Mitochondrial generation of superoxide and hydrogen peroxide as the source of mitochondrial redox signaling. *Free Radic Biol Med,* 100**,** 14-31.

BRANDAO, K. O., TABEL, V. A., ATSMA, D. E., MUMMERY, C. L. & DAVIS, R. P. 2017. Human pluripotent stem cell models of cardiac disease: from mechanisms to therapies. *Dis Model Mech,* 10**,** 1039-1059.

BRANDES, R. & BERS, D. M. 1997. Intracellular Ca2+ increases the mitochondrial NADH concentration during elevated work in intact cardiac muscle. *Circ Res,* 80**,** 82-7.

BRANDNER, K., MICK, D. U., FRAZIER, A. E., TAYLOR, R. D., MEISINGER, C. & REHLING, P. 2005. Taz1, an outer mitochondrial membrane protein, affects stability and assembly of inner membrane protein complexes: implications for Barth Syndrome. *Mol Biol Cell,* 16**,** 5202-14.

BRIMBLE, S. N., ZENG, X., WEILER, D. A., LUO, Y., LIU, Y., LYONS, I. G., FREED, W. J., ROBINS, A. J., RAO, M. S. & SCHULZ, T. C. 2004. Karyotypic stability, genotyping, differentiation, feeder-free maintenance, and gene expression sampling in three human embryonic stem cell lines derived prior to August 9, 2001. *Stem Cells Dev,* 13**,** 585-97.

BROWN, D. A., PERRY, J. B., ALLEN, M. E., SABBAH, H. N., STAUFFER, B. L., SHAIKH, S. R., CLELAND, J. G., COLUCCI, W. S., BUTLER, J., VOORS, A. A., ANKER, S. D., PITT, B., PIESKE, B., FILIPPATOS, G., GREENE, S. J. & GHEORGHIADE, M. 2017. Expert consensus document: Mitochondrial function as a therapeutic target in heart failure. *Nat Rev Cardiol,* 14**,** 238-250.

BUGANIM, Y., FADDAH, D. A., CHENG, A. W., ITSKOVICH, E., MARKOULAKI, S., GANZ, K., KLEMM, S. L., VAN OUDENAARDEN, A. & JAENISCH, R. 2012. Single-cell expression analyses during cellular reprogramming reveal an early stochastic and a late hierarchic phase. *Cell,* 150**,** 1209-22.

BUGANIM, Y., FADDAH, D. A. & JAENISCH, R. 2013. Mechanisms and models of somatic cell reprogramming. *Nat Rev Genet,* 14**,** 427-39.

BUKAU, B. & HORWICH, A. L. 1998. The Hsp70 and Hsp60 chaperone machines. *Cell,* 92**,** 351-66.

BURRIDGE, P. W., KELLER, G., GOLD, J. D. & WU, J. C. 2012. Production of de novo cardiomyocytes: human pluripotent stem cell differentiation and direct reprogramming. *Cell Stem Cell,* 10**,** 16-28.

CAI, J., LI, W., SU, H., QIN, D., YANG, J., ZHU, F., XU, J., HE, W., GUO, X., LABUDA, K., PETERBAUER, A., WOLBANK, S., ZHONG, M., LI, Z., WU, W., SO, K. F., REDL, H., ZENG, L., ESTEBAN, M. A. & PEI, D. 2010. Generation of human induced pluripotent stem cells from umbilical cord matrix and amniotic membrane mesenchymal cells. *J Biol Chem,* 285**,** 11227-34.

CALKINS, H. & MARCUS, F. 2008. Arrhythmogenic right ventricular cardiomyopathy/dysplasia: an update. *Curr Cardiol Rep,* 10**,** 367-75.

CAMELLITI, P., GREEN, C. R., LEGRICE, I. & KOHL, P. 2004. Fibroblast network in rabbit sinoatrial node: structural and functional identification of homogeneous and heterogeneous cell coupling. *Circ Res,* 94**,** 828-35.

CAO, F., WAGNER, R. A., WILSON, K. D., XIE, X., FU, J. D., DRUKKER, M., LEE, A., LI, R. A., GAMBHIR, S. S., WEISSMAN, I. L., ROBBINS, R. C. & WU, J. C. 2008. Transcriptional and functional profiling of human embryonic stem cell-derived cardiomyocytes. *PLoS One,* 3**,** e3474.

CAO, N., LIU, Z., CHEN, Z., WANG, J., CHEN, T., ZHAO, X., MA, Y., QIN, L., KANG, J., WEI, B., WANG, L., JIN, Y. & YANG, H. T. 2012. Ascorbic acid enhances the cardiac differentiation of induced pluripotent stem cells through promoting the proliferation of cardiac progenitor cells. *Cell Res,* 22**,** 219-36.

CARTWRIGHT, P., MCLEAN, C., SHEPPARD, A., RIVETT, D., JONES, K. & DALTON, S. 2005. LIF/STAT3 controls ES cell self-renewal and pluripotency by a Myc-dependent mechanism. *Development,* 132**,** 885-96.

CARVAJAL-VERGARA, X., SEVILLA, A., D'SOUZA, S. L., ANG, Y. S., SCHANIEL, C., LEE, D. F., YANG, L., KAPLAN, A. D., ADLER, E. D., ROZOV, R., GE, Y., COHEN, N., EDELMANN, L. J., CHANG, B., WAGHRAY, A., SU, J., PARDO, S., LICHTENBELT, K. D., TARTAGLIA, M., GELB, B. D. & LEMISCHKA, I. R. 2010. Patient-specific induced pluripotent stem-cell-derived models of LEOPARD syndrome. *Nature,* 465**,** 808-12.

CASPI, O., HUBER, I., GEPSTEIN, A., ARBEL, G., MAIZELS, L., BOULOS, M. & GEPSTEIN, L. 2013. Modeling of arrhythmogenic right ventricular cardiomyopathy with human induced pluripotent stem cells. *Circ Cardiovasc Genet,* 6**,** 557-68.

CEHOLSKI, D. K., TRIEBER, C. A., HOLMES, C. F. & YOUNG, H. S. 2012. Lethal, hereditary mutants of phospholamban elude phosphorylation by protein kinase A. *J Biol Chem,* 287**,** 26596-605.

CERRONE, M. & DELMAR, M. 2014. Desmosomes and the sodium channel complex: implications for arrhythmogenic cardiomyopathy and Brugada syndrome. *Trends Cardiovasc Med,* 24**,** 184-90.

CERRONE, M., MONTNACH, J., LIN, X., ZHAO, Y. T., ZHANG, M., AGULLO-PASCUAL, E., LEO-MACIAS, A., ALVARADO, F. J., DOLGALEV, I., KARATHANOS, T. V., MALKANI, K., VAN OPBERGEN, C. J. M., VAN BAVEL, J. J. A., YANG, H. Q., VASQUEZ, C., TESTER, D., FOWLER, S., LIANG, F., ROTHENBERG, E., HEGUY, A., MORLEY, G. E., COETZEE, W. A., TRAYANOVA, N. A., ACKERMAN, M. J., VAN VEEN, T. A. B., VALDIVIA, H. H. & DELMAR, M. 2017. Plakophilin-2 is required for transcription of genes that control calcium cycling and cardiac rhythm. *Nat Commun,* 8**,** 106.

CHABOWSKI, A., GORSKI, J., GLATZ, J. F., JJ, P. L. & BONEN, A. 2008. Protein-mediated Fatty Acid Uptake in the Heart. *Curr Cardiol Rev,* 4**,** 12-21.

CHAKRABARTI, R., JI, W. K., STAN, R. V., DE JUAN SANZ, J., RYAN, T. A. & HIGGS, H. N. 2018. INF2-mediated actin polymerization at the ER stimulates mitochondrial calcium uptake, inner membrane constriction, and division. *J Cell Biol,* 217**,** 251-268.

CHAMBERS, I. 2004. The molecular basis of pluripotency in mouse embryonic stem cells. *Cloning Stem Cells,* 6**,** 386-91.

CHANDLER, C. H., CHARI, S. & DWORKIN, I. 2013. Does your gene need a background check? How genetic background impacts the analysis of mutations, genes, and evolution. *Trends Genet,* 29**,** 358-66.
CHANG, S. C., HEACOCK, P. N., MILEYKOVSKAYA, E., VOELKER, D. R. & DOWHAN, W. 1998. Isolation and characterization of the gene (CLS1) encoding cardiolipin synthase in Saccharomyces cerevisiae. *J Biol Chem,* 273**,** 14933-41.
CHAPMAN, J. R., TAYLOR, M. R. & BOULTON, S. J. 2012. Playing the end game: DNA double-strand break repair pathway choice. *Mol Cell,* 47**,** 497-510.
CHEN, B., DODGE, M. E., TANG, W., LU, J., MA, Z., FAN, C. W., WEI, S., HAO, W., KILGORE, J., WILLIAMS, N. S., ROTH, M. G., AMATRUDA, J. F., CHEN, C. & LUM, L. 2009. Small molecule-mediated disruption of Wnt-dependent signaling in tissue regeneration and cancer. *Nat Chem Biol,* 5**,** 100-7.
CHEN, D., ZHANG, X. Y. & SHI, Y. 2006. Identification and functional characterization of hCLS1, a human cardiolipin synthase localized in mitochondria. *Biochem J,* 398**,** 169-76.
CHEN, K. G., MALLON, B. S., MCKAY, R. D. & ROBEY, P. G. 2014. Human pluripotent stem cell culture: considerations for maintenance, expansion, and therapeutics. *Cell Stem Cell,* 14**,** 13-26.
CHEN, L., LIU, T., TRAN, A., LU, X., TOMILOV, A. A., DAVIES, V., CORTOPASSI, G., CHIAMVIMONVAT, N., BERS, D. M., VOTRUBA, M. & KNOWLTON, A. A. 2012. OPA1 mutation and late-onset cardiomyopathy: mitochondrial dysfunction and mtDNA instability. *J Am Heart Assoc,* 1**,** e003012.
CHEN, Y., LIU, Y. & DORN, G. W., 2ND 2011. Mitochondrial fusion is essential for organelle function and cardiac homeostasis. *Circ Res,* 109**,** 1327-31.
CHENEVAL, D., MULLER, M. & CARAFOLI, E. 1983. The mitochondrial phosphate carrier reconstituted in liposomes is inhibited by doxorubicin. *FEBS Lett,* 159**,** 123-6.
CHENG, L., HANSEN, N. F., ZHAO, L., DU, Y., ZOU, C., DONOVAN, F. X., CHOU, B. K., ZHOU, G., LI, S., DOWEY, S. N., YE, Z., CHANDRASEKHARAPPA, S. C., YANG, H., MULLIKIN, J. C. & LIU, P. P. 2012. Low incidence of DNA sequence variation in human induced pluripotent stem cells generated by nonintegrating plasmid expression. *Cell Stem Cell,* 10**,** 337-44.
CHERNY, R. A., STOKES, T. M., MEREI, J., LOM, L., BRANDON, M. R. & WILLIAMS, R. L. 1994. Strategies for the isolation and characterization of bovine embryonic stem cells. *Reprod Fertil Dev,* 6**,** 569-75.
CHO, S. W., KIM, S., KIM, J. M. & KIM, J. S. 2013. Targeted genome engineering in human cells with the Cas9 RNA-guided endonuclease. *Nat Biotechnol,* 31**,** 230-2.
CHOU, B. K., MALI, P., HUANG, X., YE, Z., DOWEY, S. N., RESAR, L. M., ZOU, C., ZHANG, Y. A., TONG, J. & CHENG, L. 2011. Efficient human iPS cell derivation by a non-integrating plasmid from blood cells with unique epigenetic and gene expression signatures. *Cell Res,* 21**,** 518-29.
CHOWDHURY, A., AICH, A., JAIN, G., WOZNY, K., LUCHTENBORG, C., HARTMANN, M., BERNHARD, O., BALLEINIGER, M., ALFAR, E. A., ZIESENISS, A., TOISCHER, K., GUAN, K., RIZZOLI, S. O., BRUGGER, B., FISCHER, A., KATSCHINSKI, D. M., REHLING, P. & DUDEK, J. 2018. Defective Mitochondrial Cardiolipin Remodeling Dampens HIF-1alpha Expression in Hypoxia. *Cell Rep,* 25**,** 561-570 e6.
CHRISTIAN, M., CERMAK, T., DOYLE, E. L., SCHMIDT, C., ZHANG, F., HUMMEL, A., BOGDANOVE, A. J. & VOYTAS, D. F. 2010. Targeting DNA double-strand breaks with TAL effector nucleases. *Genetics,* 186**,** 757-61.
CHRISTIE, D. A., LEMKE, C. D., ELIAS, I. M., CHAU, L. A., KIRCHHOF, M. G., LI, B., BALL, E. H., DUNN, S. D., HATCH, G. M. & MADRENAS, J. 2011. Stomatin-like protein 2 binds cardiolipin and regulates mitochondrial biogenesis and function. *Mol Cell Biol,* 31**,** 3845-56.
CHU, C. T., JI, J., DAGDA, R. K., JIANG, J. F., TYURINA, Y. Y., KAPRALOV, A. A., TYURIN, V. A., YANAMALA, N., SHRIVASTAVA, I. H., MOHAMMADYANI, D., WANG, K. Z. Q., ZHU, J., KLEIN-SEETHARAMAN, J., BALASUBRAMANIAN, K., AMOSCATO, A. A., BORISENKO, G., HUANG, Z., GUSDON, A. M., CHEIKHI, A., STEER, E. K., WANG, R., BATY, C., WATKINS, S., BAHAR, I., BAYIR, H. & KAGAN, V. E. 2013. Cardiolipin externalization to the outer mitochondrial membrane acts as an elimination signal for mitophagy in neuronal cells. *Nat Cell Biol,* 15**,** 1197-1205.
CHUN, Y. W., BALIKOV, D. A., FEASTER, T. K., WILLIAMS, C. H., SHENG, C. C., LEE, J. B., BOIRE, T. C., NEELY, M. D., BELLAN, L. M., ESS, K. C., BOWMAN, A. B., SUNG, H. J. & HONG, C. C. 2015. Combinatorial polymer matrices enhance in vitro maturation of human induced pluripotent stem cell-derived cardiomyocytes. *Biomaterials,* 67**,** 52-64.
CHUVA DE SOUSA LOPES, S. M., HASSINK, R. J., FEIJEN, A., VAN ROOIJEN, M. A., DOEVENDANS, P. A., TERTOOLEN, L., BRUTEL DE LA RIVIERE, A. & MUMMERY, C. L. 2006. Patterning the heart, a template for human cardiomyocyte development. *Dev Dyn,* 235**,** 1994-2002.
CIRNU, A., KOLOKOTRONIS, K., WALZ, K., KILINC, A., JANZ, A., WILLIAMS, T., BUSCH, A., ROST, S. & GERULL, B. 2021. Novel Mutation in LOX Associates With a Complex Aneurysmal Vascular and Cardiac Phenotype. *Circ Genom Precis Med***,** CIRCGEN120003217.
CLAYPOOL, S. M. 2009. Cardiolipin, a critical determinant of mitochondrial carrier protein assembly and function. *Biochim Biophys Acta,* 1788**,** 2059-68.
CLAYPOOL, S. M., BOONTHEUNG, P., MCCAFFERY, J. M., LOO, J. A. & KOEHLER, C. M. 2008a. The cardiolipin transacylase, tafazzin, associates with two distinct respiratory components providing insight into Barth syndrome. *Mol Biol Cell,* 19**,** 5143-55.
CLAYPOOL, S. M. & KOEHLER, C. M. 2012. The complexity of cardiolipin in health and disease. *Trends Biochem Sci,* 37**,** 32-41.
CLAYPOOL, S. M., MCCAFFERY, J. M. & KOEHLER, C. M. 2006. Mitochondrial mislocalization and altered assembly of a cluster of Barth syndrome mutant tafazzins. *J Cell Biol,* 174**,** 379-90.
CLAYPOOL, S. M., OKTAY, Y., BOONTHEUNG, P., LOO, J. A. & KOEHLER, C. M. 2008b. Cardiolipin defines the interactome of the major ADP/ATP carrier protein of the mitochondrial inner membrane. *J Cell Biol,* 182**,** 937-50.
COATES, P. J., NENUTIL, R., MCGREGOR, A., PICKSLEY, S. M., CROUCH, D. H., HALL, P. A. & WRIGHT, E. G. 2001. Mammalian prohibitin proteins respond to mitochondrial stress and decrease during cellular senescence. *Exp Cell Res,* 265**,** 262-73.
COELHO, R., HANNA, R., FLAGG, A., STEMPAK, L. M., ONDREJKA, S., PROCOP, G. W., HARRINGTON, S., ZEMBILLAS, A., KUSICK, K. & GONZALEZ, B. E. 2017. Mycobacterium genavense-induced spindle cell pseudotumor in a pediatric hematopoietic stem cell transplant recipient: Case report and review of the literature. *Transpl Infect Dis,* 19.
COLE, L. K., MEJIA, E. M., VANDEL, M., SPARAGNA, G. C., CLAYPOOL, S. M., DYCK-CHAN, L., KLEIN, J. & HATCH, G. M. 2016. Impaired Cardiolipin Biosynthesis Prevents Hepatic Steatosis and Diet-Induced Obesity. *Diabetes,* 65**,** 3289-3300.
COLLINS, T. J., BERRIDGE, M. J., LIPP, P. & BOOTMAN, M. D. 2002. Mitochondria are morphologically and functionally heterogeneous within cells. *EMBO J,* 21**,** 1616-27.
CONG, L., RAN, F. A., COX, D., LIN, S., BARRETTO, R., HABIB, N., HSU, P. D., WU, X., JIANG, W., MARRAFFINI, L. A. & ZHANG, F. 2013. Multiplex genome engineering using CRISPR/Cas systems. *Science,* 339**,** 819-23.

COWAN, C. A., ATIENZA, J., MELTON, D. A. & EGGAN, K. 2005. Nuclear reprogramming of somatic cells after fusion with human embryonic stem cells. *Science,* 309**,** 1369-73.

CRADICK, T. J., FINE, E. J., ANTICO, C. J. & BAO, G. 2013. CRISPR/Cas9 systems targeting beta-globin and CCR5 genes have substantial off-target activity. *Nucleic Acids Res,* 41**,** 9584-92.

CYGANEK, L., TIBURCY, M., SEKERES, K., GERSTENBERG, K., BOHNENBERGER, H., LENZ, C., HENZE, S., STAUSKE, M., SALINAS, G., ZIMMERMANN, W. H., HASENFUSS, G. & GUAN, K. 2018. Deep phenotyping of human induced pluripotent stem cell-derived atrial and ventricular cardiomyocytes. *JCI Insight,* 3.

D'SILVA, P. D., SCHILKE, B., WALTER, W., ANDREW, A. & CRAIG, E. A. 2003. J protein cochaperone of the mitochondrial inner membrane required for protein import into the mitochondrial matrix. *Proc Natl Acad Sci U S A,* 100**,** 13839-44.

DAI, D. F., DANOVIZ, M. E., WICZER, B., LAFLAMME, M. A. & TIAN, R. 2017. Mitochondrial Maturation in Human Pluripotent Stem Cell Derived Cardiomyocytes. *Stem Cells Int,* 2017**,** 5153625.

DAVEY, K. M., PARBOOSINGH, J. S., MCLEOD, D. R., CHAN, A., CASEY, R., FERREIRA, P., SNYDER, F. F., BRIDGE, P. J. & BERNIER, F. P. 2006. Mutation of DNAJC19, a human homologue of yeast inner mitochondrial membrane co-chaperones, causes DCMA syndrome, a novel autosomal recessive Barth syndrome-like condition. *J Med Genet,* 43**,** 385-93.

DAVIES, K. M., STRAUSS, M., DAUM, B., KIEF, J. H., OSIEWACZ, H. D., RYCOVSKA, A., ZICKERMANN, V. & KUHLBRANDT, W. 2011. Macromolecular organization of ATP synthase and complex I in whole mitochondria. *Proc Natl Acad Sci U S A,* 108**,** 14121-6.

DAVILA-ROMAN, V. G., VEDALA, G., HERRERO, P., DE LAS FUENTES, L., ROGERS, J. G., KELLY, D. P. & GROPLER, R. J. 2002. Altered myocardial fatty acid and glucose metabolism in idiopathic dilated cardiomyopathy. *J Am Coll Cardiol,* 40**,** 271-7.

DAVIS, R. P., VAN DEN BERG, C. W., CASINI, S., BRAAM, S. R. & MUMMERY, C. L. 2011. Pluripotent stem cell models of cardiac disease and their implication for drug discovery and development. *Trends Mol Med,* 17**,** 475-84.

DAYER, M. & COWIE, M. R. 2004. Heart failure: diagnosis and healthcare burden. *Clin Med (Lond),* 4**,** 13-8.

DEBOEVER, C., LI, H., JAKUBOSKY, D., BENAGLIO, P., REYNA, J., OLSON, K. M., HUANG, H., BIGGS, W., SANDOVAL, E., D'ANTONIO, M., JEPSEN, K., MATSUI, H., ARIAS, A., REN, B., NARIAI, N., SMITH, E. N., D'ANTONIO-CHRONOWSKA, A., FARLEY, E. K. & FRAZER, K. A. 2017. Large-Scale Profiling Reveals the Influence of Genetic Variation on Gene Expression in Human Induced Pluripotent Stem Cells. *Cell Stem Cell,* 20**,** 533-546 e7.

DEBOWSKI, K., DRUMMER, C., LENTES, J., CORS, M., DRESSEL, R., LINGNER, T., SALINAS-RIESTER, G., FUCHS, S., SASAKI, E. & BEHR, R. 2016. The transcriptomes of novel marmoset monkey embryonic stem cell lines reflect distinct genomic features. *Sci Rep,* 6**,** 29122.

DEKEL-NAFTALI, M., AVIRAM-GOLDRING, A., LITMANOVITCH, T., SHAMASH, J., REZNIK-WOLF, H., LAEVSKY, I., AMIT, M., ITSKOVITZ-ELDOR, J., YUNG, Y., HOURVITZ, A., SCHIFF, E. & RIENSTEIN, S. 2012. Screening of human pluripotent stem cells using CGH and FISH reveals low-grade mosaic aneuploidy and a recurrent amplification of chromosome 1q. *Eur J Hum Genet,* 20**,** 1248-55.

DEKELVER, R. C., CHOI, V. M., MOEHLE, E. A., PASCHON, D. E., HOCKEMEYER, D., MEIJSING, S. H., SANCAK, Y., CUI, X., STEINE, E. J., MILLER, J. C., TAM, P., BARTSEVICH, V. V., MENG, X., RUPNIEWSKI, I., GOPALAN, S. M., SUN, H. C., PITZ, K. J., ROCK, J. M., ZHANG, L., DAVIS, G. D., REBAR, E. J., CHEESEMAN, I. M., YAMAMOTO, K. R., SABATINI, D. M., JAENISCH, R., GREGORY, P. D. & URNOV, F. D. 2010. Functional genomics, proteomics, and regulatory DNA analysis in isogenic settings using zinc finger nuclease-driven transgenesis into a safe harbor locus in the human genome. *Genome Res,* 20**,** 1133-42.

DELETTRE, C., LENAERS, G., GRIFFOIN, J. M., GIGAREL, N., LORENZO, C., BELENGUER, P., PELLOQUIN, L., GROSGEORGE, J., TURC-CAREL, C., PERRET, E., ASTARIE-DEQUEKER, C., LASQUELLEC, L., ARNAUD, B., DUCOMMUN, B., KAPLAN, J. & HAMEL, C. P. 2000. Nuclear gene OPA1, encoding a mitochondrial dynamin-related protein, is mutated in dominant optic atrophy. *Nat Genet,* 26**,** 207-10.

DELLEFAVE, L. & MCNALLY, E. M. 2010. The genetics of dilated cardiomyopathy. *Curr Opin Cardiol,* 25**,** 198-204.

DELTCHEVA, E., CHYLINSKI, K., SHARMA, C. M., GONZALES, K., CHAO, Y., PIRZADA, Z. A., ECKERT, M. R., VOGEL, J. & CHARPENTIER, E. 2011. CRISPR RNA maturation by trans-encoded small RNA and host factor RNase III. *Nature,* 471**,** 602-7.

DENNING, C., BORGDORFF, V., CRUTCHLEY, J., FIRTH, K. S., GEORGE, V., KALRA, S., KONDRASHOV, A., HOANG, M. D., MOSQUEIRA, D., PATEL, A., PRODANOV, L., RAJAMOHAN, D., SKARNES, W. C., SMITH, J. G. & YOUNG, L. E. 2016. Cardiomyocytes from human pluripotent stem cells: From laboratory curiosity to industrial biomedical platform. *Biochim Biophys Acta,* 1863**,** 1728-48.

DESBAILLETS, I., ZIEGLER, U., GROSCURTH, P. & GASSMANN, M. 2000. Embryoid bodies: an in vitro model of mouse embryogenesis. *Exp Physiol,* 85**,** 645-51.

DEVALLA, H. D., SCHWACH, V., FORD, J. W., MILNES, J. T., EL-HAOU, S., JACKSON, C., GKATZIS, K., ELLIOTT, D. A., CHUVA DE SOUSA LOPES, S. M., MUMMERY, C. L., VERKERK, A. O. & PASSIER, R. 2015. Atrial-like cardiomyocytes from human pluripotent stem cells are a robust preclinical model for assessing atrial-selective pharmacology. *EMBO Mol Med,* 7**,** 394-410.

DIENHART, M. K. & STUART, R. A. 2008. The yeast Aac2 protein exists in physical association with the cytochrome bc1-COX supercomplex and the TIM23 machinery. *Mol Biol Cell,* 19**,** 3934-43.

DING, Q., REGAN, S. N., XIA, Y., OOSTROM, L. A., COWAN, C. A. & MUSUNURU, K. 2013. Enhanced efficiency of human pluripotent stem cell genome editing through replacing TALENs with CRISPRs. *Cell Stem Cell,* 12**,** 393-4.

DORN, G. W., 2ND 2013. Mitochondrial dynamics in heart disease. *Biochim Biophys Acta,* 1833**,** 233-41.

DOYLE, M. J., LOHR, J. L., CHAPMAN, C. S., KOYANO-NAKAGAWA, N., GARRY, M. G. & GARRY, D. J. 2015. Human Induced Pluripotent Stem Cell-Derived Cardiomyocytes as a Model for Heart Development and Congenital Heart Disease. *Stem Cell Rev Rep,* 11**,** 710-27.

DUBOIS, N. C., CRAFT, A. M., SHARMA, P., ELLIOTT, D. A., STANLEY, E. G., ELEFANTY, A. G., GRAMOLINI, A. & KELLER, G. 2011. SIRPA is a specific cell-surface marker for isolating cardiomyocytes derived from human pluripotent stem cells. *Nat Biotechnol,* 29**,** 1011-8.

DUDEK, J., CHENG, I. F., BALLEININGER, M., VAZ, F. M., STRECKFUSS-BOMEKE, K., HUBSCHER, D., VUKOTIC, M., WANDERS, R. J., REHLING, P. & GUAN, K. 2013. Cardiolipin deficiency affects respiratory chain function and organization in an induced pluripotent stem cell model of Barth syndrome. *Stem Cell Res,* 11**,** 806-19.

DUDEK, J., CHENG, I. F., CHOWDHURY, A., WOZNY, K., BALLEININGER, M., REINHOLD, R., GRUNAU, S., CALLEGARI, S., TOISCHER, K., WANDERS, R. J., HASENFUSS, G., BRUGGER, B., GUAN, K. & REHLING, P. 2016. Cardiac-specific succinate dehydrogenase deficiency in Barth syndrome. *EMBO Mol Med,* 8**,** 139-54.

DUDEK, J. & MAACK, C. 2017. Barth syndrome cardiomyopathy. *Cardiovasc Res,* 113**,** 399-410.

EBLE, K. S., COLEMAN, W. B., HANTGAN, R. R. & CUNNINGHAM, C. C. 1990. Tightly associated cardiolipin in the bovine heart mitochondrial ATP synthase as analyzed by 31P nuclear magnetic resonance spectroscopy. *J Biol Chem,* 265**,** 19434-40.

ECKFELDT, C. E., MENDENHALL, E. M. & VERFAILLIE, C. M. 2005. The molecular repertoire of the 'almighty' stem cell. *Nat Rev Mol Cell Biol,* 6**,** 726-37.

EISNER, D. 2014. Calcium in the heart: from physiology to disease. *Exp Physiol,* 99**,** 1273-82.

EISNER, D. A., CALDWELL, J. L., KISTAMAS, K. & TRAFFORD, A. W. 2017a. Calcium and Excitation-Contraction Coupling in the Heart. *Circ Res,* 121**,** 181-195.

EISNER, V., CUPO, R. R., GAO, E., CSORDAS, G., SLOVINSKY, W. S., PAILLARD, M., CHENG, L., IBETTI, J., CHEN, S. R., CHUPRUN, J. K., HOEK, J. B., KOCH, W. J. & HAJNOCZKY, G. 2017b. Mitochondrial fusion dynamics is robust in the heart and depends on calcium oscillations and contractile activity. *Proc Natl Acad Sci U S A,* 114**,** E859-E868.

ELLIOTT, P., ANDERSSON, B., ARBUSTINI, E., BILINSKA, Z., CECCHI, F., CHARRON, P., DUBOURG, O., KUHL, U., MAISCH, B., MCKENNA, W. J., MONSERRAT, L., PANKUWEIT, S., RAPEZZI, C., SEFEROVIC, P., TAVAZZI, L. & KEREN, A. 2008. Classification of the cardiomyopathies: a position statement from the European Society Of Cardiology Working Group on Myocardial and Pericardial Diseases. *Eur Heart J,* 29**,** 270-6.

ELSEVIER B.V. COPYRIGHT © 2021. 2017. *Scientific guidelines for Lab Resources* [Online]. Available: https://www.journals.elsevier.com/stem-cell-research/lab-resources/scientific-guidelines-for-lab-resources [Accessed 10th May 2017].

ENDOH, M. 2004. Force-frequency relationship in intact mammalian ventricular myocardium: physiological and pathophysiological relevance. *Eur J Pharmacol,* 500**,** 73-86.

ESCHENHAGEN, T., BOLLI, R., BRAUN, T., FIELD, L. J., FLEISCHMANN, B. K., FRISEN, J., GIACCA, M., HARE, J. M., HOUSER, S., LEE, R. T., MARBAN, E., MARTIN, J. F., MOLKENTIN, J. D., MURRY, C. E., RILEY, P. R., RUIZ-LOZANO, P., SADEK, H. A., SUSSMAN, M. A. & HILL, J. A. 2017. Cardiomyocyte Regeneration: A Consensus Statement. *Circulation,* 136**,** 680-686.

ESCHENHAGEN, T., MUMMERY, C. & KNOLLMANN, B. C. 2015. Modelling sarcomeric cardiomyopathies in the dish: from human heart samples to iPSC cardiomyocytes. *Cardiovasc Res,* 105**,** 424-38.

ESFANDIARI, F., FATHI, A., GOURABI, H., KIANI, S., NEMATI, S. & BAHARVAND, H. 2012. Glycogen synthase kinase-3 inhibition promotes proliferation and neuronal differentiation of human-induced pluripotent stem cell-derived neural progenitors. *Stem Cells Dev,* 21**,** 3233-43.

ESHKIND, L., TIAN, Q., SCHMIDT, A., FRANKE, W. W., WINDOFFER, R. & LEUBE, R. E. 2002. Loss of desmoglein 2 suggests essential functions for early embryonic development and proliferation of embryonal stem cells. *Eur J Cell Biol,* 81**,** 592-8.

ESTEBAN, M. A., WANG, T., QIN, B., YANG, J., QIN, D., CAI, J., LI, W., WENG, Z., CHEN, J., NI, S., CHEN, K., LI, Y., LIU, X., XU, J., ZHANG, S., LI, F., HE, W., LABUDA, K., SONG, Y., PETERBAUER, A., WOLBANK, S., REDL, H., ZHONG, M., CAI, D., ZENG, L. & PEI, D. 2010. Vitamin C enhances the generation of mouse and human induced pluripotent stem cells. *Cell Stem Cell,* 6**,** 71-9.

EVANS, M. J. & KAUFMAN, M. H. 1981. Establishment in culture of pluripotential cells from mouse embryos. *Nature,* 292**,** 154-6.

FATICA, E. M., DELEONIBUS, G. A., HOUSE, A., KODGER, J. V., PEARCE, R. W., SHAH, R. R., LEVI, L. & SANDLERS, Y. 2019. Barth Syndrome: Exploring Cardiac Metabolism with Induced Pluripotent Stem Cell-Derived Cardiomyocytes. *Metabolites,* 9.

FAZELI, A., LIEW, C. G., MATIN, M. M., ELLIOTT, S., JEANMEURE, L. F., WRIGHT, P. C., MOORE, H. & ANDREWS, P. W. 2011. Altered patterns of differentiation in karyotypically abnormal human embryonic stem cells. *Int J Dev Biol,* 55**,** 175-80.

FEASTER, T. K., CADAR, A. G., WANG, L., WILLIAMS, C. H., CHUN, Y. W., HEMPEL, J. E., BLOODWORTH, N., MERRYMAN, W. D., LIM, C. C., WU, J. C., KNOLLMANN, B. C. & HONG, C. C. 2015. Matrigel Mattress: A Method for the Generation of Single Contracting Human-Induced Pluripotent Stem Cell-Derived Cardiomyocytes. *Circ Res,* 117**,** 995-1000.

FERIC, N. T. & RADISIC, M. 2016. Maturing human pluripotent stem cell-derived cardiomyocytes in human engineered cardiac tissues. *Adv Drug Deliv Rev,* 96**,** 110-34.

FERNANDES, T. G., RODRIGUES, C. A. V., DIOGO, M. M. & CABRAL, J. M. S. 2014. Stem cell bioprocessing for regenerative medicine. *Journal of Chemical Technology & Biotechnology,* 89**,** 34-47.

FERRICK, D. A., NEILSON, A. & BEESON, C. 2008. Advances in measuring cellular bioenergetics using extracellular flux. *Drug Discov Today,* 13**,** 268-74.

FOLMES, C. D., NELSON, T. J., MARTINEZ-FERNANDEZ, A., ARRELL, D. K., LINDOR, J. Z., DZEJA, P. P., IKEDA, Y., PEREZ-TERZIC, C. & TERZIC, A. 2011. Somatic oxidative bioenergetics transitions into pluripotency-dependent glycolysis to facilitate nuclear reprogramming. *Cell Metab,* 14**,** 264-71.

FORTUNEL, N. O., OTU, H. H., NG, H. H., CHEN, J., MU, X., CHEVASSUT, T., LI, X., JOSEPH, M., BAILEY, C., HATZFELD, J. A., HATZFELD, A., USTA, F., VEGA, V. B., LONG, P. M., LIBERMANN, T. A. & LIM, B. 2003. Comment on " 'Stemness': transcriptional profiling of embryonic and adult stem cells" and "a stem cell molecular signature". *Science,* 302**,** 393; author reply 393.

FRANK, R., FONTAINE, G., VEDEL, J., MIALET, G., SOL, C., GUIRAUDON, G. & GROSGOGEAT, Y. 1978. [Electrocardiology of 4 cases of right ventricular dysplasia inducing arrhythmia]. *Arch Mal Coeur Vaiss,* 71**,** 963-72.

FRANKE, W. W., SCHMID, E., OSBORN, M. & WEBER, K. 1979. Intermediate-sized filaments of human endothelial cells. *The Journal of cell biology,* 81**,** 570-80.

FREDERIC, J. & CHEVREMONT, M. 1952. [Investigations on the chondriosomes of living cells by phase contrast microscopy and microcinematography]. *Arch Biol (Liege),* 63**,** 109-31.

FRIEDMAN, J. R., LACKNER, L. L., WEST, M., DIBENEDETTO, J. R., NUNNARI, J. & VOELTZ, G. K. 2011. ER tubules mark sites of mitochondrial division. *Science,* 334**,** 358-62.

FU, Y., FODEN, J. A., KHAYTER, C., MAEDER, M. L., REYON, D., JOUNG, J. K. & SANDER, J. D. 2013. High-frequency off-target mutagenesis induced by CRISPR-Cas nucleases in human cells. *Nat Biotechnol,* 31**,** 822-6.

FUSAKI, N., BAN, H., NISHIYAMA, A., SAEKI, K. & HASEGAWA, M. 2009. Efficient induction of transgene-free human pluripotent stem cells using a vector based on Sendai virus, an RNA virus that does not integrate into the host genome. *Proc Jpn Acad Ser B Phys Biol Sci,* 85**,** 348-62.

FUSARO, G., DASGUPTA, P., RASTOGI, S., JOSHI, B. & CHELLAPPAN, S. 2003. Prohibitin induces the transcriptional activity of p53 and is exported from the nucleus upon apoptotic signaling. *J Biol Chem,* 278**,** 47853-61.

GABALDON, T. & KOONIN, E. V. 2013. Functional and evolutionary implications of gene orthology. *Nat Rev Genet,* 14**,** 360-6.

GABBIANI, G., SCHMID, E., WINTER, S., CHAPONNIER, C., DE CKHASTONAY, C., VANDEKERCKHOVE, J., WEBER, K. & FRANKE, W. W. 1981. Vascular smooth muscle cells differ from other smooth muscle cells: predominance of vimentin

filaments and a specific alpha-type actin. *Proceedings of the National Academy of Sciences of the United States of America,* 78**,** 298-302.
GARCIA-GRAS, E., LOMBARDI, R., GIOCONDO, M. J., WILLERSON, J. T., SCHNEIDER, M. D., KHOURY, D. S. & MARIAN, A. J. 2006. Suppression of canonical Wnt/beta-catenin signaling by nuclear plakoglobin recapitulates phenotype of arrhythmogenic right ventricular cardiomyopathy. *The Journal of clinical investigation,* 116**,** 2012-21.
GARNEAU, J. E., DUPUIS, M. E., VILLION, M., ROMERO, D. A., BARRANGOU, R., BOYAVAL, P., FREMAUX, C., HORVATH, P., MAGADAN, A. H. & MOINEAU, S. 2010. The CRISPR/Cas bacterial immune system cleaves bacteriophage and plasmid DNA. *Nature,* 468**,** 67-71.
GASIUNAS, G., BARRANGOU, R., HORVATH, P. & SIKSNYS, V. 2012. Cas9-crRNA ribonucleoprotein complex mediates specific DNA cleavage for adaptive immunity in bacteria. *Proceedings of the National Academy of Sciences of the United States of America,* 109**,** E2579-86.
GENG, B. C., CHOI, K. H., WANG, S. Z., CHEN, P., PAN, X. D., DONG, N. G., KO, J. K. & ZHU, H. 2020. A simple, quick, and efficient CRISPR/Cas9 genome editing method for human induced pluripotent stem cells. *Acta Pharmacol Sin,* 41**,** 1427-1432.
GERMANGUZ, I., SEDAN, O., ZEEVI-LEVIN, N., SHTRICHMAN, R., BARAK, E., ZISKIND, A., ELIYAHU, S., MEIRY, G., AMIT, M., ITSKOVITZ-ELDOR, J. & BINAH, O. 2011. Molecular characterization and functional properties of cardiomyocytes derived from human inducible pluripotent stem cells. *J Cell Mol Med,* 15**,** 38-51.
GERULL, B., HEUSER, A., WICHTER, T., PAUL, M., BASSON, C. T., MCDERMOTT, D. A., LERMAN, B. B., MARKOWITZ, S. M., ELLINOR, P. T., MACRAE, C. A., PETERS, S., GROSSMANN, K. S., DRENCKHAHN, J., MICHELY, B., SASSE-KLAASSEN, S., BIRCHMEIER, W., DIETZ, R., BREITHARDT, G., SCHULZE-BAHR, E. & THIERFELDER, L. 2004. Mutations in the desmosomal protein plakophilin-2 are common in arrhythmogenic right ventricular cardiomyopathy. *Nat Genet,* 36**,** 1162-4.
GHOSH, S., BASU BALL, W., MADARIS, T. R., SRIKANTAN, S., MADESH, M., MOOTHA, V. K. & GOHIL, V. M. 2020. An essential role for cardiolipin in the stability and function of the mitochondrial calcium uniporter. *Proc Natl Acad Sci U S A,* 117**,** 16383-16390.
GILES, J. R., YANG, X., MARK, W. & FOOTE, R. H. 1993. Pluripotency of cultured rabbit inner cell mass cells detected by isozyme analysis and eye pigmentation of fetuses following injection into blastocysts or morulae. *Mol Reprod Dev,* 36**,** 130-8.
GIORGETTI, A., MONTSERRAT, N., RODRIGUEZ-PIZA, I., AZQUETA, C., VEIGA, A. & IZPISUA BELMONTE, J. C. 2010. Generation of induced pluripotent stem cells from human cord blood cells with only two factors: Oct4 and Sox2. *Nat Protoc,* 5**,** 811-20.
GIOVANNI CARDONE AND MARIA SPLETTER. 2017. *MyofribilJ plugin* [Online]. Available: https://imagej.net/MyofibrilJ.html#Introduction [Accessed].
GIUDICESSI, J. R. & ACKERMAN, M. J. 2012. Potassium-channel mutations and cardiac arrhythmias--diagnosis and therapy. *Nat Rev Cardiol,* 9**,** 319-32.
GLATZ, J. F., LUIKEN, J. J., VAN NIEUWENHOVEN, F. A. & VAN DER VUSSE, G. J. 1997. Molecular mechanism of cellular uptake and intracellular translocation of fatty acids. *Prostaglandins Leukot Essent Fatty Acids,* 57**,** 3-9.
GOH, P. A., CAXARIA, S., CASPER, C., ROSALES, C., WARNER, T. T., COFFEY, P. J. & NATHWANI, A. C. 2013. A systematic evaluation of integration free reprogramming methods for deriving clinically relevant patient specific induced pluripotent stem (iPS) cells. *PLoS One,* 8**,** e81622.
GONZALEZ, F., BOUE, S. & IZPISUA BELMONTE, J. C. 2011. Methods for making induced pluripotent stem cells: reprogramming a la carte. *Nat Rev Genet,* 12**,** 231-42.
GOPALAKRISHNA-PILLAI, S. & IVERSON, L. E. 2010. Astrocytes derived from trisomic human embryonic stem cells express markers of astrocytic cancer cells and premalignant stem-like progenitors. *BMC Med Genomics,* 3**,** 12.
GREENHAFF, P. L. 2001. The creatine-phosphocreatine system: there's more than one song in its repertoire. *J Physiol,* 537**,** 657.
GROSSMANN, K. S., GRUND, C., HUELSKEN, J., BEHREND, M., ERDMANN, B., FRANKE, W. W. & BIRCHMEIER, W. 2004. Requirement of plakophilin 2 for heart morphogenesis and cardiac junction formation. *The Journal of cell biology,* 167**,** 149-60.
GU, Z., VALIANPOUR, F., CHEN, S., VAZ, F. M., HAKKAART, G. A., WANDERS, R. J. & GREENBERG, M. L. 2004. Aberrant cardiolipin metabolism in the yeast taz1 mutant: a model for Barth syndrome. *Mol Microbiol,* 51**,** 149-58.
GÜNTHER, K. 2016. *Generation of early human neuroepithelial progenitors from primary cells for biomedical applications.*
GUO, R., ZONG, S., WU, M., GU, J. & YANG, M. 2017. Architecture of Human Mitochondrial Respiratory Megacomplex I2III2IV2. *Cell,* 170**,** 1247-1257 e12.
GUO, Y. & PU, W. T. 2020. Cardiomyocyte Maturation: New Phase in Development. *Circ Res,* 126**,** 1086-1106.
GURDON, J. B., ELSDALE, T. R. & FISCHBERG, M. 1958. Sexually mature individuals of Xenopus laevis from the transplantation of single somatic nuclei. *Nature,* 182**,** 64-5.
HAASE, A., OLMER, R., SCHWANKE, K., WUNDERLICH, S., MERKERT, S., HESS, C., ZWEIGERDT, R., GRUH, I., MEYER, J., WAGNER, S., MAIER, L. S., HAN, D. W., GLAGE, S., MILLER, K., FISCHER, P., SCHOLER, H. R. & MARTIN, U. 2009. Generation of induced pluripotent stem cells from human cord blood. *Cell Stem Cell,* 5**,** 434-41.
HACKENBROCK, C. R. 1966. Ultrastructural bases for metabolically linked mechanical activity in mitochondria. I. Reversible ultrastructural changes with change in metabolic steady state in isolated liver mitochondria. *J Cell Biol,* 30**,** 269-97.
HACKNEY, J. A., CHARBORD, P., BRUNK, B. P., STOECKERT, C. J., LEMISCHKA, I. R. & MOORE, K. A. 2002. A molecular profile of a hematopoietic stem cell niche. *Proceedings of the National Academy of Sciences of the United States of America,* 99**,** 13061-6.
HAECKEL, E. 1868. *Natürliche Schöpfungsgeschichte. Gemeinverständliche wissenschaftliche Vorträge über die Entwickelungslehre im Allgemeinen und diejenige von Darwin, Goethe und Lamarck im Besonderen... Mit Tafeln, Holzschnitten, etc*.
HAGHIGHI, K., KOLOKATHIS, F., GRAMOLINI, A. O., WAGGONER, J. R., PATER, L., LYNCH, R. A., FAN, G. C., TSIAPRAS, D., PAREKH, R. R., DORN, G. W., 2ND, MACLENNAN, D. H., KREMASTINOS, D. T. & KRANIAS, E. G. 2006. A mutation in the human phospholamban gene, deleting arginine 14, results in lethal, hereditary cardiomyopathy. *Proc Natl Acad Sci U S A,* 103**,** 1388-93.
HAINES, T. H. & DENCHER, N. A. 2002. Cardiolipin: a proton trap for oxidative phosphorylation. *FEBS Lett,* 528**,** 35-9.
HAKALA, H., RAJALA, K., OJALA, M., PANULA, S., AREVA, S., KELLOMAKI, M., SUURONEN, R. & SKOTTMAN, H. 2009. Comparison of biomaterials and extracellular matrices as a culture platform for multiple, independently derived human embryonic stem cell lines. *Tissue Eng Part A,* 15**,** 1775-85.
HAMDANI, N., KOOIJ, V., VAN DIJK, S., MERKUS, D., PAULUS, W. J., REMEDIOS, C. D., DUNCKER, D. J., STIENEN, G. J. & VAN DER VELDEN, J. 2008. Sarcomeric dysfunction in heart failure. *Cardiovasc Res,* 77**,** 649-58.

HAMILTON, B., FENG, Q., YE, M. & WELSTEAD, G. G. 2009. Generation of induced pluripotent stem cells by reprogramming mouse embryonic fibroblasts with a four transcription factor, doxycycline inducible lentiviral transduction system. *J Vis Exp*.

HANDYSIDE, A., HOOPER, M. L., KAUFMAN, M. H. & WILMUT, I. 1987. Towards the isolation of embryonal stem cell lines from the sheep. *Rouxs Arch Dev Biol,* 196**,** 185-190.

HARRISON, N. J., BAKER, D. & ANDREWS, P. W. 2007. Culture adaptation of embryonic stem cells echoes germ cell malignancy. *Int J Androl,* 30**,** 275-81; discussion 281.

HASHIMOTO, T., HUSSIEN, R. & BROOKS, G. A. 2006. Colocalization of MCT1, CD147, and LDH in mitochondrial inner membrane of L6 muscle cells: evidence of a mitochondrial lactate oxidation complex. *Am J Physiol Endocrinol Metab,* 290**,** E1237-44.

HAUSBURG, F., NA, S., VORONINA, N., SKORSKA, A., MULLER, P., STEINHOFF, G. & DAVID, R. 2015. Defining optimized properties of modified mRNA to enhance virus- and DNA- independent protein expression in adult stem cells and fibroblasts. *Cell Physiol Biochem,* 35**,** 1360-71.

HE, J. Q., MA, Y., LEE, Y., THOMSON, J. A. & KAMP, T. J. 2003. Human embryonic stem cells develop into multiple types of cardiac myocytes: action potential characterization. *Circ Res,* 93**,** 32-9.

HEERDT, P. M., SCHLAME, M., JEHLE, R., BARBONE, A., BURKHOFF, D. & BLANCK, T. J. 2002. Disease-specific remodeling of cardiac mitochondria after a left ventricular assist device. *Ann Thorac Surg,* 73**,** 1216-21.

HEFFERIN, M. L. & TOMKINSON, A. E. 2005. Mechanism of DNA double-strand break repair by non-homologous end joining. *DNA Repair (Amst),* 4**,** 639-48.

HEINEMANN, T. & HONNEFELDER, L. 2002. Principles of ethical decision making regarding embryonic stem cell research in Germany. *Bioethics,* 16**,** 530-43.

HELLEN, N., PINTO RICARDO, C., VAUCHEZ, K., WHITING, G., WHEELER, J. X. & HARDING, S. E. 2019. Proteomic Analysis Reveals Temporal Changes in Protein Expression in Human Induced Pluripotent Stem Cell-Derived Cardiomyocytes In Vitro. *Stem Cells Dev,* 28**,** 565-578.

HERNANDO-RODRIGUEZ, B. & ARTAL-SANZ, M. 2018. Mitochondrial Quality Control Mechanisms and the PHB (Prohibitin) Complex. *Cells,* 7.

HERRMANN, D. 1939. THE CHEMICAL NATURE OF HEART FAILURE. *Annals of Internal Medicine,* 12**,** 1233-1244.

HERRON, T. J., ROCHA, A. M., CAMPBELL, K. F., PONCE-BALBUENA, D., WILLIS, B. C., GUERRERO-SERNA, G., LIU, Q., KLOS, M., MUSA, H., ZARZOSO, M., BIZY, A., FURNESS, J., ANUMONWO, J., MIRONOV, S. & JALIFE, J. 2016. Extracellular Matrix-Mediated Maturation of Human Pluripotent Stem Cell-Derived Cardiac Monolayer Structure and Electrophysiological Function. *Circ Arrhythm Electrophysiol,* 9**,** e003638.

HO, J. C., ZHOU, T., LAI, W. H., HUANG, Y., CHAN, Y. C., LI, X., WONG, N. L., LI, Y., AU, K. W., GUO, D., XU, J., SIU, C. W., PEI, D., TSE, H. F. & ESTEBAN, M. A. 2011. Generation of induced pluripotent stem cell lines from 3 distinct laminopathies bearing heterogeneous mutations in lamin A/C. *Aging (Albany NY),* 3**,** 380-90.

HOCH, F. L. 1992. Cardiolipins and biomembrane function. *Biochim Biophys Acta,* 1113**,** 71-133.

HOCKEMEYER, D. & JAENISCH, R. 2010. Gene targeting in human pluripotent cells. *Cold Spring Harb Symp Quant Biol,* 75**,** 201-9.

HOCKEMEYER, D., SOLDNER, F., BEARD, C., GAO, Q., MITALIPOVA, M., DEKELVER, R. C., KATIBAH, G. E., AMORA, R., BOYDSTON, E. A., ZEITLER, B., MENG, X., MILLER, J. C., ZHANG, L., REBAR, E. J., GREGORY, P. D., URNOV, F. D. & JAENISCH, R. 2009. Efficient targeting of expressed and silent genes in human ESCs and iPSCs using zinc-finger nucleases. *Nat Biotechnol,* 27**,** 851-7.

HOCKEMEYER, D., SOLDNER, F., COOK, E. G., GAO, Q., MITALIPOVA, M. & JAENISCH, R. 2008. A drug-inducible system for direct reprogramming of human somatic cells to pluripotency. *Cell Stem Cell,* 3**,** 346-353.

HOCKEMEYER, D., WANG, H., KIANI, S., LAI, C. S., GAO, Q., CASSADY, J. P., COST, G. J., ZHANG, L., SANTIAGO, Y., MILLER, J. C., ZEITLER, B., CHERONE, J. M., MENG, X., HINKLEY, S. J., REBAR, E. J., GREGORY, P. D., URNOV, F. D. & JAENISCH, R. 2011. Genetic engineering of human pluripotent cells using TALE nucleases. *Nat Biotechnol,* 29**,** 731-4.

HORVATH, S. E. & DAUM, G. 2013. Lipids of mitochondria. *Prog Lipid Res,* 52**,** 590-614.

HOSTETLER, K. Y., VAN DEN BOSCH, H. & VAN DEENEN, L. L. 1971. Biosynthesis of cardiolipin in liver mitochondria. *Biochim Biophys Acta,* 239**,** 113-9.

HOU, Z., ZHANG, Y., PROPSON, N. E., HOWDEN, S. E., CHU, L. F., SONTHEIMER, E. J. & THOMSON, J. A. 2013. Efficient genome engineering in human pluripotent stem cells using Cas9 from Neisseria meningitidis. *Proc Natl Acad Sci U S A,* 110**,** 15644-9.

HOUTKOOPER, R. H., TURKENBURG, M., POLL-THE, B. T., KARALL, D., PEREZ-CERDA, C., MORRONE, A., MALVAGIA, S., WANDERS, R. J., KULIK, W. & VAZ, F. M. 2009. The enigmatic role of tafazzin in cardiolipin metabolism. *Biochim Biophys Acta,* 1788**,** 2003-14.

HSU, P. D., LANDER, E. S. & ZHANG, F. 2014. Development and applications of CRISPR-Cas9 for genome engineering. *Cell,* 157**,** 1262-1278.

HSU, P. D., SCOTT, D. A., WEINSTEIN, J. A., RAN, F. A., KONERMANN, S., AGARWALA, V., LI, Y., FINE, E. J., WU, X., SHALEM, O., CRADICK, T. J., MARRAFFINI, L. A., BAO, G. & ZHANG, F. 2013. DNA targeting specificity of RNA-guided Cas9 nucleases. *Nat Biotechnol,* 31**,** 827-32.

HU, B. Y., WEICK, J. P., YU, J., MA, L. X., ZHANG, X. Q., THOMSON, J. A. & ZHANG, S. C. 2010. Neural differentiation of human induced pluripotent stem cells follows developmental principles but with variable potency. *Proceedings of the National Academy of Sciences of the United States of America,* 107**,** 4335-40.

HU, D., LINDERS, A., YAMAK, A., CORREIA, C., KIJLSTRA, J. D., GARAKANI, A., XIAO, L., MILAN, D. J., VAN DER MEER, P., SERRA, M., ALVES, P. M. & DOMIAN, I. J. 2018. Metabolic Maturation of Human Pluripotent Stem Cell-Derived Cardiomyocytes by Inhibition of HIF1alpha and LDHA. *Circ Res,* 123**,** 1066-1079.

HUANG, Y., POWERS, C., MADALA, S. K., GREIS, K. D., HAFFEY, W. D., TOWBIN, J. A., PUREVJAV, E., JAVADOV, S., STRAUSS, A. W. & KHUCHUA, Z. 2015. Cardiac metabolic pathways affected in the mouse model of barth syndrome. *PLoS One,* 10**,** e0128561.

HUEBSCH, N., LOSKILL, P., DEVESHWAR, N., SPENCER, C. I., JUDGE, L. M., MANDEGAR, M. A., FOX, C. B., MOHAMED, T. M., MA, Z., MATHUR, A., SHEEHAN, A. M., TRUONG, A., SAXTON, M., YOO, J., SRIVASTAVA, D., DESAI, T. A., SO, P. L., HEALY, K. E. & CONKLIN, B. R. 2016. Miniaturized iPS-Cell-Derived Cardiac Muscles for Physiologically Relevant Drug Response Analyses. *Sci Rep,* 6**,** 24726.

HUMERES, C. & FRANGOGIANNIS, N. G. 2019. Fibroblasts in the Infarcted, Remodeling, and Failing Heart. *JACC Basic Transl Sci,* 4**,** 449-467.

IDE, T., TSUTSUI, H., HAYASHIDANI, S., KANG, D., SUEMATSU, N., NAKAMURA, K., UTSUMI, H., HAMASAKI, N. & TAKESHITA, A. 2001. Mitochondrial DNA damage and dysfunction associated with oxidative stress in failing hearts after myocardial infarction. *Circ Res,* 88**,** 529-35.

IKON, N. & RYAN, R. O. 2017. Cardiolipin and mitochondrial cristae organization. *Biochim Biophys Acta Biomembr,* 1859**,** 1156-1163.

INGWALL, J. 2002. ATP and the Heart. 11.

INVITROGEN. 2020. *CytoTune™-iPS 2.0 Sendai Reprogramming Kit - User Guide* [Online]. Available: https://assets.thermofisher.com/TFS-Assets/LSG/manuals/cytotune_ips_2_0_sendai_reprog_kit_man.pdf [Accessed 17th February 2021].

IONOPTIX LLC. 2020. *Monotonic Transient Analysis Parameters* [Online]. Available: http://www.ionoptix.com/wp-content/uploads/2014/07/Monotonic-Transient-Analysis-Defined.pdf [Accessed 1st November 2020].

ISHIHARA, N., FUJITA, Y., OKA, T. & MIHARA, K. 2006. Regulation of mitochondrial morphology through proteolytic cleavage of OPA1. *EMBO J,* 25**,** 2966-77.

ITSKOVITZ-ELDOR, J., SCHULDINER, M., KARSENTI, D., EDEN, A., YANUKA, O., AMIT, M., SOREQ, H. & BENVENISTY, N. 2000. Differentiation of human embryonic stem cells into embryoid bodies compromising the three embryonic germ layers. *Mol Med,* 6**,** 88-95.

ITZHAKI, I., RAPOPORT, S., HUBER, I., MIZRAHI, I., ZWI-DANTSIS, L., ARBEL, G., SCHILLER, J. & GEPSTEIN, L. 2011. Calcium handling in human induced pluripotent stem cell derived cardiomyocytes. *PLoS One,* 6**,** e18037.

IVANOVA, N. B., DIMOS, J. T., SCHANIEL, C., HACKNEY, J. A., MOORE, K. A. & LEMISCHKA, I. R. 2002. A stem cell molecular signature. *Science,* 298**,** 601-4.

IWATA, S., LEE, J. W., OKADA, K., LEE, J. K., IWATA, M., RASMUSSEN, B., LINK, T. A., RAMASWAMY, S. & JAP, B. K. 1998. Complete structure of the 11-subunit bovine mitochondrial cytochrome bc1 complex. *Science,* 281**,** 64-71.

JACOBS, K., MERTZANIDOU, A., GEENS, M., NGUYEN, H. T., STAESSEN, C. & SPITS, C. 2014. Low-grade chromosomal mosaicism in human somatic and embryonic stem cell populations. *Nat Commun,* 5**,** 4227.

JACOBS, K., ZAMBELLI, F., MERTZANIDOU, A., SMOLDERS, I., GEENS, M., NGUYEN, H. T., BARBE, L., SERMON, K. & SPITS, C. 2016. Higher-Density Culture in Human Embryonic Stem Cells Results in DNA Damage and Genome Instability. *Stem Cell Reports,* 6**,** 330-41.

JACOT, J. G., MCCULLOCH, A. D. & OMENS, J. H. 2008. Substrate stiffness affects the functional maturation of neonatal rat ventricular myocytes. *Biophys J,* 95**,** 3479-87.

JANG, H. K., SONG, B., HWANG, G. H. & BAE, S. 2020. Current trends in gene recovery mediated by the CRISPR-Cas system. *Exp Mol Med,* 52**,** 1016-1027.

JANZ, A., ZINK, M., CIRNU, A., HARTLEB, A., ALBRECHT, C., ROST, S., KLOPOCKI, E., GÜNTHER, K., EDENHOFER, F., ERGÜN, S. & GERULL, B. 2021. CRISPR/Cas9-edited PKP2 knock-out (JMUi001-A-2) and DSG2 knock-out (JMUi001-A-3) iPSC lines as an isogenic human model system for arrhythmogenic cardiomyopathy (ACM). *Stem Cell Research***,** 102256.

JASTROCH, M., DIVAKARUNI, A. S., MOOKERJEE, S., TREBERG, J. R. & BRAND, M. D. 2010. Mitochondrial proton and electron leaks. *Essays Biochem,* 47**,** 53-67.

JENSEN, K. T., FLOE, L., PETERSEN, T. S., HUANG, J., XU, F., BOLUND, L., LUO, Y. & LIN, L. 2017. Chromatin accessibility and guide sequence secondary structure affect CRISPR-Cas9 gene editing efficiency. *FEBS Lett,* 591**,** 1892-1901.

JIANG, F. & DOUDNA, J. A. 2017. CRISPR-Cas9 Structures and Mechanisms. *Annu Rev Biophys,* 46**,** 505-529.

JIANG, W., BIKARD, D., COX, D., ZHANG, F. & MARRAFFINI, L. A. 2013. RNA-guided editing of bacterial genomes using CRISPR-Cas systems. *Nat Biotechnol,* 31**,** 233-9.

JINEK, M., CHYLINSKI, K., FONFARA, I., HAUER, M., DOUDNA, J. A. & CHARPENTIER, E. 2012. A programmable dual-RNA-guided DNA endonuclease in adaptive bacterial immunity. *Science,* 337**,** 816-21.

JINEK, M., EAST, A., CHENG, A., LIN, S., MA, E. & DOUDNA, J. 2013. RNA-programmed genome editing in human cells. *Elife,* 2**,** e00471.

JOSOWITZ, R., LU, J., FALCE, C., D'SOUZA, S. L., WU, M., COHEN, N., DUBOIS, N. C., ZHAO, Y., SOBIE, E. A., FISHMAN, G. I. & GELB, B. D. 2014. Identification and purification of human induced pluripotent stem cell-derived atrial-like cardiomyocytes based on sarcolipin expression. *PLoS One,* 9**,** e101316.

KAASIK, A., JOUBERT, F., VENTURA-CLAPIER, R. & VEKSLER, V. 2004. A novel mechanism of regulation of cardiac contractility by mitochondrial functional state. *FASEB J,* 18**,** 1219-27.

KADARI, A., MEKALA, S., WAGNER, N., MALAN, D., KOTH, J., DOLL, K., STAPPERT, L., ECKERT, D., PEITZ, M., MATTHES, J., SASSE, P., HERZIG, S., BRUSTLE, O., ERGUN, S. & EDENHOFER, F. 2015. Robust Generation of Cardiomyocytes from Human iPS Cells Requires Precise Modulation of BMP and WNT Signaling. *Stem Cell Rev Rep,* 11**,** 560-9.

KAMAKURA, T., MAKIYAMA, T., SASAKI, K., YOSHIDA, Y., WURIYANGHAI, Y., CHEN, J., HATTORI, T., OHNO, S., KITA, T., HORIE, M., YAMANAKA, S. & KIMURA, T. 2013. Ultrastructural maturation of human-induced pluripotent stem cell-derived cardiomyocytes in a long-term culture. *Circ J,* 77**,** 1307-14.

KANDA, Y., YAMAZAKI, D., KUROKAWA, J., INUTSUKA, T. & SEKINO, Y. 2016. Points to consider for a validation study of iPS cell-derived cardiomyocytes using a multi-electrode array system. *J Pharmacol Toxicol Methods,* 81**,** 196-200.

KANE, C. & TERRACCIANO, C. M. N. 2017. Concise Review: Criteria for Chamber-Specific Categorization of Human Cardiac Myocytes Derived from Pluripotent Stem Cells. *Stem Cells,* 35**,** 1881-1897.

KANT, S., HOLTHOFER, B., MAGIN, T. M., KRUSCHE, C. A. & LEUBE, R. E. 2015. Desmoglein 2-Dependent Arrhythmogenic Cardiomyopathy Is Caused by a Loss of Adhesive Function. *Circ Cardiovasc Genet,* 8**,** 553-63.

KARAKIKES, I., AMEEN, M., TERMGLINCHAN, V. & WU, J. C. 2015a. Human induced pluripotent stem cell-derived cardiomyocytes: insights into molecular, cellular, and functional phenotypes. *Circ Res,* 117**,** 80-8.

KARAKIKES, I., SENYEI, G. D., HANSEN, J., KONG, C. W., AZELOGLU, E. U., STILLITANO, F., LIEU, D. K., WANG, J., REN, L., HULOT, J. S., IYENGAR, R., LI, R. A. & HAJJAR, R. J. 2014. Small molecule-mediated directed differentiation of human embryonic stem cells toward ventricular cardiomyocytes. *Stem Cells Transl Med,* 3**,** 18-31.

KARAKIKES, I., STILLITANO, F., NONNENMACHER, M., TZIMAS, C., SANOUDOU, D., TERMGLINCHAN, V., KONG, C. W., RUSHING, S., HANSEN, J., CEHOLSKI, D., KOLOKATHIS, F., KREMASTINOS, D., KATOULIS, A., REN, L., COHEN, N., GHO, J., TSIAPRAS, D., VINK, A., WU, J. C., ASSELBERGS, F. W., LI, R. A., HULOT, J. S., KRANIAS, E. G. & HAJJAR, R. J. 2015b. Correction of human phospholamban R14del mutation associated with cardiomyopathy using targeted nucleases and combination therapy. *Nat Commun,* 6**,** 6955.

KARBOWSKI, M. & YOULE, R. J. 2003. Dynamics of mitochondrial morphology in healthy cells and during apoptosis. *Cell Death Differ,* 10**,** 870-80.

KATTMAN, S. J., WITTY, A. D., GAGLIARDI, M., DUBOIS, N. C., NIAPOUR, M., HOTTA, A., ELLIS, J. & KELLER, G. 2011. Stage-specific optimization of activin/nodal and BMP signaling promotes cardiac differentiation of mouse and human pluripotent stem cell lines. *Cell Stem Cell,* 8**,** 228-40.

KAZANTZIS, M. & STAHL, A. 2012. Fatty acid transport proteins, implications in physiology and disease. *Biochim Biophys Acta,* 1821**,** 852-7.

KELLEY, R. I., CHEATHAM, J. P., CLARK, B. J., NIGRO, M. A., POWELL, B. R., SHERWOOD, G. W., SLADKY, J. T. & SWISHER, W. P. 1991. X-linked dilated cardiomyopathy with neutropenia, growth retardation, and 3-methylglutaconic aciduria. *J Pediatr,* 119**,** 738-47.

KHALIFAT, N., PUFF, N., BONNEAU, S., FOURNIER, J. B. & ANGELOVA, M. I. 2008. Membrane deformation under local pH gradient: mimicking mitochondrial cristae dynamics. *Biophys J,* 95**,** 4924-33.

KILPINEN, H., GONCALVES, A., LEHA, A., AFZAL, V., ALASOO, K., ASHFORD, S., BALA, S., BENSADDEK, D., CASALE, F. P., CULLEY, O. J., DANECEK, P., FAULCONBRIDGE, A., HARRISON, P. W., KATHURIA, A., MCCARTHY, D., MCCARTHY, S. A., MELECKYTE, R., MEMARI, Y., MOENS, N., SOARES, F., MANN, A., STREETER, I., AGU, C. A., ALDERTON, A., NELSON, R., HARPER, S., PATEL, M., WHITE, A., PATEL, S. R., CLARKE, L., HALAI, R., KIRTON, C. M., KOLB-KOKOCINSKI, A., BEALES, P., BIRNEY, E., DANOVI, D., LAMOND, A. I., OUWEHAND, W. H., VALLIER, L., WATT, F. M., DURBIN, R., STEGLE, O. & GAFFNEY, D. J. 2017. Corrigendum: Common genetic variation drives molecular heterogeneity in human iPSCs. *Nature,* 546**,** 686.

KIM, C., WONG, J., WEN, J., WANG, S., WANG, C., SPIERING, S., KAN, N. G., FORCALES, S., PURI, P. L., LEONE, T. C., MARINE, J. E., CALKINS, H., KELLY, D. P., JUDGE, D. P. & CHEN, H. S. 2013. Studying arrhythmogenic right ventricular dysplasia with patient-specific iPSCs. *Nature,* 494**,** 105-10.

KIM, E. J., KANG, K. H. & JU, J. H. 2017. CRISPR-Cas9: a promising tool for gene editing on induced pluripotent stem cells. *Korean J Intern Med,* 32**,** 42-61.

KIM, S., KIM, D., CHO, S. W., KIM, J. & KIM, J. S. 2014. Highly efficient RNA-guided genome editing in human cells via delivery of purified Cas9 ribonucleoproteins. *Genome Res,* 24**,** 1012-9.

KIM, Y. G., CHA, J. & CHANDRASEGARAN, S. 1996. Hybrid restriction enzymes: zinc finger fusions to Fok I cleavage domain. *Proceedings of the National Academy of Sciences of the United States of America,* 93**,** 1156-60.

KLEINMAN, H. K. 2001. Preparation of basement membrane components from EHS tumors. *Curr Protoc Cell Biol,* Chapter 10**,** Unit 10 2.

KOHLHAAS, M., LIU, T., KNOPP, A., ZELLER, T., ONG, M. F., BOHM, M., O'ROURKE, B. & MAACK, C. 2010. Elevated cytosolic Na+ increases mitochondrial formation of reactive oxygen species in failing cardiac myocytes. *Circulation,* 121**,** 1606-13.

KOOB, S., BARRERA, M., ANAND, R. & REICHERT, A. S. 2015. Data supporting the role of the non-glycosylated isoform of MIC26 in determining cristae morphology. *Data Brief,* 4**,** 135-9.

KREBS, J. J., HAUSER, H. & CARAFOLI, E. 1979. Asymmetric distribution of phospholipids in the inner membrane of beef heart mitochondria. *J Biol Chem,* 254**,** 5308-16.

KRUSCHE, C. A., HOLTHOFER, B., HOFE, V., VAN DE SANDT, A. M., ESHKIND, L., BOCKAMP, E., MERX, M. W., KANT, S., WINDOFFER, R. & LEUBE, R. E. 2011. Desmoglein 2 mutant mice develop cardiac fibrosis and dilation. *Basic Res Cardiol,* 106**,** 617-33.

KURIYAN, A. E., ALBINI, T. A., TOWNSEND, J. H., RODRIGUEZ, M., PANDYA, H. K., LEONARD, R. E., 2ND, PARROTT, M. B., ROSENFELD, P. J., FLYNN, H. W., JR. & GOLDBERG, J. L. 2017. Vision Loss after Intravitreal Injection of Autologous "Stem Cells" for AMD. *N Engl J Med,* 376**,** 1047-1053.

KWOK, C. K., UEDA, Y., KADARI, A., GUNTHER, K., ERGUN, S., HERON, A., SCHNITZLER, A. C., ROOK, M. & EDENHOFER, F. 2018. Scalable stirred suspension culture for the generation of billions of human induced pluripotent stem cells using single-use bioreactors. *J Tissue Eng Regen Med,* 12**,** e1076-e1087.

KYTTALA, A., MORAGHEBI, R., VALENSISI, C., KETTUNEN, J., ANDRUS, C., PASUMARTHY, K. K., NAKANISHI, M., NISHIMURA, K., OHTAKA, M., WELTNER, J., VAN HANDEL, B., PARKKONEN, O., SINISALO, J., JALANKO, A., HAWKINS, R. D., WOODS, N. B., OTONKOSKI, T. & TROKOVIC, R. 2016. Genetic Variability Overrides the Impact of Parental Cell Type and Determines iPSC Differentiation Potential. *Stem Cell Reports,* 6**,** 200-12.

LACO, F., WOO, T. L., ZHONG, Q., SZMYD, R., TING, S., KHAN, F. J., CHAI, C. L. L., REUVENY, S., CHEN, A. & OH, S. 2018. Unraveling the Inconsistencies of Cardiac Differentiation Efficiency Induced by the GSK3beta Inhibitor CHIR99021 in Human Pluripotent Stem Cells. *Stem Cell Reports,* 10**,** 1851-1866.

LAFLAMME, M. A., CHEN, K. Y., NAUMOVA, A. V., MUSKHELI, V., FUGATE, J. A., DUPRAS, S. K., REINECKE, H., XU, C., HASSANIPOUR, M., POLICE, S., O'SULLIVAN, C., COLLINS, L., CHEN, Y., MINAMI, E., GILL, E. A., UENO, S., YUAN, C., GOLD, J. & MURRY, C. E. 2007. Cardiomyocytes derived from human embryonic stem cells in pro-survival factors enhance function of infarcted rat hearts. *Nat Biotechnol,* 25**,** 1015-24.

LAKDAWALA, N. K., WINTERFIELD, J. R. & FUNKE, B. H. 2013. Dilated cardiomyopathy. *Circ Arrhythm Electrophysiol,* 6**,** 228-37.

LAKSHMIPATHY, U., PELACHO, B., SUDO, K., LINEHAN, J. L., COUCOUVANIS, E., KAUFMAN, D. S. & VERFAILLIE, C. M. 2004. Efficient transfection of embryonic and adult stem cells. *Stem Cells,* 22**,** 531-43.

LAN, F., LEE, A. S., LIANG, P., SANCHEZ-FREIRE, V., NGUYEN, P. K., WANG, L., HAN, L., YEN, M., WANG, Y., SUN, N., ABILEZ, O. J., HU, S., EBERT, A. D., NAVARRETE, E. G., SIMMONS, C. S., WHEELER, M., PRUITT, B., LEWIS, R., YAMAGUCHI, Y., ASHLEY, E. A., BERS, D. M., ROBBINS, R. C., LONGAKER, M. T. & WU, J. C. 2013. Abnormal calcium handling properties underlie familial hypertrophic cardiomyopathy pathology in patient-specific induced pluripotent stem cells. *Cell Stem Cell,* 12**,** 101-13.

LANDSTROM, A. P., DOBREV, D. & WEHRENS, X. H. T. 2017. Calcium Signaling and Cardiac Arrhythmias. *Circ Res,* 120**,** 1969-1993.

LEE, Y. K., LAU, Y. M., CAI, Z. J., LAI, W. H., WONG, L. Y., TSE, H. F., NG, K. M. & SIU, C. W. 2017. Modeling Treatment Response for Lamin A/C Related Dilated Cardiomyopathy in Human Induced Pluripotent Stem Cells. *J Am Heart Assoc,* 6.

LEMOINE, M. D., MANNHARDT, I., BRECKWOLDT, K., PRONDZYNSKI, M., FLENNER, F., ULMER, B., HIRT, M. N., NEUBER, C., HORVATH, A., KLOTH, B., REICHENSPURNER, H., WILLEMS, S., HANSEN, A., ESCHENHAGEN, T. & CHRIST, T. 2017. Human iPSC-derived cardiomyocytes cultured in 3D engineered heart tissue show physiological upstroke velocity and sodium current density. *Sci Rep,* 7**,** 5464.

LI, F., HU, J. & HE, T. C. 2017. iPSC-based treatment of age-related macular degeneration (AMD): The path to success requires more than blind faith. *Genes Dis,* 4**,** 41-42.

LI, H. L., FUJIMOTO, N., SASAKAWA, N., SHIRAI, S., OHKAME, T., SAKUMA, T., TANAKA, M., AMANO, N., WATANABE, A., SAKURAI, H., YAMAMOTO, T., YAMANAKA, S. & HOTTA, A. 2015. Precise correction of the dystrophin gene in

duchenne muscular dystrophy patient induced pluripotent stem cells by TALEN and CRISPR-Cas9. *Stem Cell Reports,* 4**,** 143-154.
LI, J., LIU, X., WANG, H., ZHANG, W., CHAN, D. C. & SHI, Y. 2012. Lysocardiolipin acyltransferase 1 (ALCAT1) controls mitochondrial DNA fidelity and biogenesis through modulation of MFN2 expression. *Proceedings of the National Academy of Sciences of the United States of America,* 109**,** 6975-80.
LI, J., ROMESTAING, C., HAN, X., LI, Y., HAO, X., WU, Y., SUN, C., LIU, X., JEFFERSON, L. S., XIONG, J., LANOUE, K. F., CHANG, Z., LYNCH, C. J., WANG, H. & SHI, Y. 2010. Cardiolipin remodeling by ALCAT1 links oxidative stress and mitochondrial dysfunction to obesity. *Cell Metab,* 12**,** 154-65.
LI, X. L., LI, G. H., FU, J., FU, Y. W., ZHANG, L., CHEN, W., ARAKAKI, C., ZHANG, J. P., WEN, W., ZHAO, M., CHEN, W. V., BOTIMER, G. D., BAYLINK, D., ARANDA, L., CHOI, H., BECHAR, R., TALBOT, P., SUN, C. K., CHENG, T. & ZHANG, X. B. 2018. Highly efficient genome editing via CRISPR-Cas9 in human pluripotent stem cells is achieved by transient BCL-XL overexpression. *Nucleic Acids Res,* 46**,** 10195-10215.
LI, Y., MCCLINTICK, J., ZHONG, L., EDENBERG, H. J., YODER, M. C. & CHAN, R. J. 2005. Murine embryonic stem cell differentiation is promoted by SOCS-3 and inhibited by the zinc finger transcription factor Klf4. *Blood,* 105**,** 635-7.
LIAN, X., HSIAO, C., WILSON, G., ZHU, K., HAZELTINE, L. B., AZARIN, S. M., RAVAL, K. K., ZHANG, J., KAMP, T. J. & PALECEK, S. P. 2012. Robust cardiomyocyte differentiation from human pluripotent stem cells via temporal modulation of canonical Wnt signaling. *Proceedings of the National Academy of Sciences of the United States of America,* 109**,** E1848-57.
LIAN, X., ZHANG, J., AZARIN, S. M., ZHU, K., HAZELTINE, L. B., BAO, X., HSIAO, C., KAMP, T. J. & PALECEK, S. P. 2013. Directed cardiomyocyte differentiation from human pluripotent stem cells by modulating Wnt/beta-catenin signaling under fully defined conditions. *Nat Protoc,* 8**,** 162-75.
LIANG, X., POTTER, J., KUMAR, S., ZOU, Y., QUINTANILLA, R., SRIDHARAN, M., CARTE, J., CHEN, W., ROARK, N., RANGANATHAN, S., RAVINDER, N. & CHESNUT, J. D. 2015. Rapid and highly efficient mammalian cell engineering via Cas9 protein transfection. *J Biotechnol,* 208**,** 44-53.
LIEU, D. K., LIU, J., SIU, C. W., MCNERNEY, G. P., TSE, H. F., ABU-KHALIL, A., HUSER, T. & LI, R. A. 2009. Absence of transverse tubules contributes to non-uniform Ca(2+) wavefronts in mouse and human embryonic stem cell-derived cardiomyocytes. *Stem Cells Dev,* 18**,** 1493-500.
LIM, H. J., HAN, J., WOO, D. H., KIM, S. E., KIM, S. K., KANG, H. G. & KIM, J. H. 2011. Biochemical and morphological effects of hypoxic environment on human embryonic stem cells in long-term culture and differentiating embryoid bodies. *Mol Cells,* 31**,** 123-32.
LIN, T., AMBASUDHAN, R., YUAN, X., LI, W., HILCOVE, S., ABUJAROUR, R., LIN, X., HAHM, H. S., HAO, E., HAYEK, A. & DING, S. 2009. A chemical platform for improved induction of human iPSCs. *Nat Methods,* 6**,** 805-8.
LINO, C. A., HARPER, J. C., CARNEY, J. P. & TIMLIN, J. A. 2018. Delivering CRISPR: a review of the challenges and approaches. *Drug Deliv,* 25**,** 1234-1257.
LIU, G., DAVID, B. T., TRAWCZYNSKI, M. & FESSLER, R. G. 2020. Advances in Pluripotent Stem Cells: History, Mechanisms, Technologies, and Applications. *Stem Cell Rev Rep,* 16**,** 3-32.
LIU, H., YE, Z., KIM, Y., SHARKIS, S. & JANG, Y. Y. 2010. Generation of endoderm-derived human induced pluripotent stem cells from primary hepatocytes. *Hepatology,* 51**,** 1810-9.
LIU, W., PORTER, N. A., SCHNEIDER, C., BRASH, A. R. & YIN, H. 2011. Formation of 4-hydroxynonenal from cardiolipin oxidation: Intramolecular peroxyl radical addition and decomposition. *Free Radic Biol Med,* 50**,** 166-78.
LIU, X., HOMMA, A., SAYADI, J., YANG, S., OHASHI, J. & TAKUMI, T. 2016. Sequence features associated with the cleavage efficiency of CRISPR/Cas9 system. *Sci Rep,* 6**,** 19675.
LOFGREN, L., STAHLMAN, M., FORSBERG, G. B., SAARINEN, S., NILSSON, R. & HANSSON, G. I. 2012. The BUME method: a novel automated chloroform-free 96-well total lipid extraction method for blood plasma. *J Lipid Res,* 53**,** 1690-700.
LOMBARDO, A., GENOVESE, P., BEAUSEJOUR, C. M., COLLEONI, S., LEE, Y. L., KIM, K. A., ANDO, D., URNOV, F. D., GALLI, C., GREGORY, P. D., HOLMES, M. C. & NALDINI, L. 2007. Gene editing in human stem cells using zinc finger nucleases and integrase-defective lentiviral vector delivery. *Nat Biotechnol,* 25**,** 1298-306.
LOPASCHUK, G. D., USSHER, J. R., FOLMES, C. D., JASWAL, J. S. & STANLEY, W. C. 2010. Myocardial fatty acid metabolism in health and disease. *Physiol Rev,* 90**,** 207-58.
LOSER, P., SCHIRM, J., GUHR, A., WOBUS, A. M. & KURTZ, A. 2010. Human embryonic stem cell lines and their use in international research. *Stem Cells,* 28**,** 240-6.
LOVELL-BADGE, R. 2001. The future for stem cell research. *Nature,* 414**,** 88-91.
LU, B., XU, F. Y., JIANG, Y. J., CHOY, P. C., HATCH, G. M., GRUNFELD, C. & FEINGOLD, K. R. 2006. Cloning and characterization of a cDNA encoding human cardiolipin synthase (hCLS1). *J Lipid Res,* 47**,** 1140-5.
LU, Y. W. & CLAYPOOL, S. M. 2015. Disorders of phospholipid metabolism: an emerging class of mitochondrial disease due to defects in nuclear genes. *Front Genet,* 6**,** 3.
LUDWIG, T. & J, A. T. 2007. Defined, feeder-independent medium for human embryonic stem cell culture. *Curr Protoc Stem Cell Biol,* Chapter 1**,** Unit 1C 2.
LUDWIG, T. E., LEVENSTEIN, M. E., JONES, J. M., BERGGREN, W. T., MITCHEN, E. R., FRANE, J. L., CRANDALL, L. J., DAIGH, C. A., CONARD, K. R., PIEKARCZYK, M. S., LLANAS, R. A. & THOMSON, J. A. 2006. Derivation of human embryonic stem cells in defined conditions. *Nat Biotechnol,* 24**,** 185-7.
LUND, R. J., NARVA, E. & LAHESMAA, R. 2012. Genetic and epigenetic stability of human pluripotent stem cells. *Nat Rev Genet,* 13**,** 732-44.
LUNDY, S. D., ZHU, W. Z., REGNIER, M. & LAFLAMME, M. A. 2013. Structural and functional maturation of cardiomyocytes derived from human pluripotent stem cells. *Stem Cells Dev,* 22**,** 1991-2002.
LUO, M. & ANDERSON, M. E. 2013. Mechanisms of altered Ca(2)(+) handling in heart failure. *Circ Res,* 113**,** 690-708.
MACK, A. A., KROBOTH, S., RAJESH, D. & WANG, W. B. 2011. Generation of induced pluripotent stem cells from CD34+ cells across blood drawn from multiple donors with non-integrating episomal vectors. *PLoS One,* 6**,** e27956.
MALHOTRA, A., XU, Y., REN, M. & SCHLAME, M. 2009. Formation of molecular species of mitochondrial cardiolipin. 1. A novel transacylation mechanism to shuttle fatty acids between sn-1 and sn-2 positions of multiple phospholipid species. *Biochim Biophys Acta,* 1791**,** 314-20.
MALI, P., YANG, L., ESVELT, K. M., AACH, J., GUELL, M., DICARLO, J. E., NORVILLE, J. E. & CHURCH, G. M. 2013. RNA-guided human genome engineering via Cas9. *Science,* 339**,** 823-6.
MALIK, N. & RAO, M. S. 2013. A review of the methods for human iPSC derivation. *Methods Mol Biol,* 997**,** 23-33.
MANCUSO, D. J., SIMS, H. F., HAN, X., JENKINS, C. M., GUAN, S. P., YANG, K., MOON, S. H., PIETKA, T., ABUMRAD, N. A., SCHLESINGER, P. H. & GROSS, R. W. 2007. Genetic ablation of calcium-independent phospholipase A2gamma leads

to alterations in mitochondrial lipid metabolism and function resulting in a deficient mitochondrial bioenergetic phenotype. *J Biol Chem,* 282**,** 34611-22.
MANDAI, M., KURIMOTO, Y. & TAKAHASHI, M. 2017. Autologous Induced Stem-Cell-Derived Retinal Cells for Macular Degeneration. *N Engl J Med,* 377**,** 792-793.
MANITI, O., LECOMPTE, M. F., MARCILLAT, O., DESBAT, B., BUCHET, R., VIAL, C. & GRANJON, T. 2009. Mitochondrial creatine kinase binding to phospholipid monolayers induces cardiolipin segregation. *Biophys J,* 96**,** 2428-38.
MANNELLA, C. A. 2006. Structure and dynamics of the mitochondrial inner membrane cristae. *Biochim Biophys Acta,* 1763**,** 542-8.
MANNHARDT, I., BRECKWOLDT, K., LETUFFE-BRENIERE, D., SCHAAF, S., SCHULZ, H., NEUBER, C., BENZIN, A., WERNER, T., EDER, A., SCHULZE, T., KLAMPE, B., CHRIST, T., HIRT, M. N., HUEBNER, N., MORETTI, A., ESCHENHAGEN, T. & HANSEN, A. 2016. Human Engineered Heart Tissue: Analysis of Contractile Force. *Stem Cell Reports,* 7**,** 29-42.
MARIN-GARCIA, J. & GOLDENTHAL, M. J. 2002. [The mitochondrial organelle and the heart]. *Rev Esp Cardiol,* 55**,** 1293-310.
MARKS, A. R. 2013. Calcium cycling proteins and heart failure: mechanisms and therapeutics. *The Journal of clinical investigation,* 123**,** 46-52.
MARON, B. J., TOWBIN, J. A., THIENE, G., ANTZELEVITCH, C., CORRADO, D., ARNETT, D., MOSS, A. J., SEIDMAN, C. E., YOUNG, J. B., AMERICAN HEART, A., COUNCIL ON CLINICAL CARDIOLOGY, H. F., TRANSPLANTATION, C., QUALITY OF, C., OUTCOMES, R., FUNCTIONAL, G., TRANSLATIONAL BIOLOGY INTERDISCIPLINARY WORKING, G., COUNCIL ON, E. & PREVENTION 2006. Contemporary definitions and classification of the cardiomyopathies: an American Heart Association Scientific Statement from the Council on Clinical Cardiology, Heart Failure and Transplantation Committee; Quality of Care and Outcomes Research and Functional Genomics and Translational Biology Interdisciplinary Working Groups; and Council on Epidemiology and Prevention. *Circulation,* 113**,** 1807-16.
MARSANO, A., CONFICCONI, C., LEMME, M., OCCHETTA, P., GAUDIELLO, E., VOTTA, E., CERINO, G., REDAELLI, A. & RASPONI, M. 2016. Beating heart on a chip: a novel microfluidic platform to generate functional 3D cardiac microtissues. *Lab Chip,* 16**,** 599-610.
MARTIN, G. R. 1981. Isolation of a pluripotent cell line from early mouse embryos cultured in medium conditioned by teratocarcinoma stem cells. *Proceedings of the National Academy of Sciences of the United States of America,* 78**,** 7634-8.
MARTIN, M. J., MUOTRI, A., GAGE, F. & VARKI, A. 2005. Human embryonic stem cells express an immunogenic nonhuman sialic acid. *Nat Med,* 11**,** 228-32.
MARUYAMA, T., DOUGAN, S. K., TRUTTMANN, M. C., BILATE, A. M., INGRAM, J. R. & PLOEGH, H. L. 2015. Increasing the efficiency of precise genome editing with CRISPR-Cas9 by inhibition of nonhomologous end joining. *Nat Biotechnol,* 33**,** 538-42.
MASUR, S. K., DEWAL, H. S., DINH, T. T., ERENBURG, I. & PETRIDOU, S. 1996. Myofibroblasts differentiate from fibroblasts when plated at low density. *Proceedings of the National Academy of Sciences of the United States of America,* 93**,** 4219-4223.
MATHERS, C. D. & LONCAR, D. 2006. Projections of global mortality and burden of disease from 2002 to 2030. *PLoS Med,* 3**,** e442.
MATOUSCHEK, A., PFANNER, N. & VOOS, W. 2000. Protein unfolding by mitochondria. The Hsp70 import motor. *EMBO Rep,* 1**,** 404-10.
MAURANO, M. T., HUMBERT, R., RYNES, E., THURMAN, R. E., HAUGEN, E., WANG, H., REYNOLDS, A. P., SANDSTROM, R., QU, H., BRODY, J., SHAFER, A., NERI, F., LEE, K., KUTYAVIN, T., STEHLING-SUN, S., JOHNSON, A. K., CANFIELD, T. K., GISTE, E., DIEGEL, M., BATES, D., HANSEN, R. S., NEPH, S., SABO, P. J., HEIMFELD, S., RAUBITSCHEK, A., ZIEGLER, S., COTSAPAS, C., SOTOODEHNIA, N., GLASS, I., SUNYAEV, S. R., KAUL, R. & STAMATOYANNOPOULOS, J. A. 2012. Systematic localization of common disease-associated variation in regulatory DNA. *Science,* 337**,** 1190-5.
MAYER, M. P. & BUKAU, B. 2005. Hsp70 chaperones: cellular functions and molecular mechanism. *Cell Mol Life Sci,* 62**,** 670-84.
MEI, Y., WANG, Y., CHEN, H., SUN, Z. S. & JU, X. D. 2016. Recent Progress in CRISPR/Cas9 Technology. *J Genet Genomics,* 43**,** 63-75.
MENDELSON, A. & FRENETTE, P. S. 2014. Hematopoietic stem cell niche maintenance during homeostasis and regeneration. *Nat Med,* 20**,** 833-46.
MERKWIRTH, C. & LANGER, T. 2009. Prohibitin function within mitochondria: essential roles for cell proliferation and cristae morphogenesis. *Biochim Biophys Acta,* 1793**,** 27-32.
MERLING, R. K., SWEENEY, C. L., CHOI, U., DE RAVIN, S. S., MYERS, T. G., OTAIZO-CARRASQUERO, F., PAN, J., LINTON, G., CHEN, L., KOONTZ, S., THEOBALD, N. L. & MALECH, H. L. 2013. Transgene-free iPSCs generated from small volume peripheral blood nonmobilized CD34+ cells. *Blood,* 121**,** e98-107.
MERTENS, C., KUHN, C. & FRANKE, W. W. 1996. Plakophilins 2a and 2b: constitutive proteins of dual location in the karyoplasm and the desmosomal plaque. *The Journal of cell biology,* 135**,** 1009-1025.
METCALF, D. 1971. *Haemopoietic cells. [By] D. Metcalf and M. A. S. Moore,* Amsterdam, North-Holland Pub. Co.
MILLER, J. C., HOLMES, M. C., WANG, J., GUSCHIN, D. Y., LEE, Y. L., RUPNIEWSKI, I., BEAUSEJOUR, C. M., WAITE, A. J., WANG, N. S., KIM, K. A., GREGORY, P. D., PABO, C. O. & REBAR, E. J. 2007. An improved zinc-finger nuclease architecture for highly specific genome editing. *Nat Biotechnol,* 25**,** 778-85.
MIT TECHNOLOGY REVIEW. 2019. *China's CRISPR babies: Read exclusive excerpts from the unseen original research* [Online]. Available: https://www.technologyreview.com/2019/12/03/131752/chinas-crispr-babies-read-exclusive-excerpts-he-jiankui-paper/ [Accessed].
MIYAOKA, Y., BERMAN, J. R., COOPER, S. B., MAYERL, S. J., CHAN, A. H., ZHANG, B., KARLIN-NEUMANN, G. A. & CONKLIN, B. R. 2016. Systematic quantification of HDR and NHEJ reveals effects of locus, nuclease, and cell type on genome-editing. *Sci Rep,* 6**,** 23549.
MOKRANJAC, D., SICHTING, M., NEUPERT, W. & HELL, K. 2003. Tim14, a novel key component of the import motor of the TIM23 protein translocase of mitochondria. *EMBO J,* 22**,** 4945-56.
MOOKERJEE, S. A., GONCALVES, R. L. S., GERENCSER, A. A., NICHOLLS, D. G. & BRAND, M. D. 2015. The contributions of respiration and glycolysis to extracellular acid production. *Biochim Biophys Acta,* 1847**,** 171-181.
MORETTI, A., BELLIN, M., WELLING, A., JUNG, C. B., LAM, J. T., BOTT-FLUGEL, L., DORN, T., GOEDEL, A., HOHNKE, C., HOFMANN, F., SEYFARTH, M., SINNECKER, D., SCHOMIG, A. & LAUGWITZ, K. L. 2010. Patient-specific induced pluripotent stem-cell models for long-QT syndrome. *N Engl J Med,* 363**,** 1397-409.
MORRISON, S. J. & SCADDEN, D. T. 2014. The bone marrow niche for haematopoietic stem cells. *Nature,* 505**,** 327-34.

MOSS, B. L. & MAGLEBY, K. L. 2001. Gating and conductance properties of BK channels are modulated by the S9-S10 tail domain of the alpha subunit. A study of mSlo1 and mSlo3 wild-type and chimeric channels. *J Gen Physiol,* 118**,** 711-34.

MOUSE GENOME SEQUENCING, C., WATERSTON, R. H., LINDBLAD-TOH, K., BIRNEY, E., ROGERS, J., ABRIL, J. F., AGARWAL, P., AGARWALA, R., AINSCOUGH, R., ALEXANDERSSON, M., AN, P., ANTONARAKIS, S. E., ATTWOOD, J., BAERTSCH, R., BAILEY, J., BARLOW, K., BECK, S., BERRY, E., BIRREN, B., BLOOM, T., BORK, P., BOTCHERBY, M., BRAY, N., BRENT, M. R., BROWN, D. G., BROWN, S. D., BULT, C., BURTON, J., BUTLER, J., CAMPBELL, R. D., CARNINCI, P., CAWLEY, S., CHIAROMONTE, F., CHINWALLA, A. T., CHURCH, D. M., CLAMP, M., CLEE, C., COLLINS, F. S., COOK, L. L., COPLEY, R. R., COULSON, A., COURONNE, O., CUFF, J., CURWEN, V., CUTTS, T., DALY, M., DAVID, R., DAVIES, J., DELEHAUNTY, K. D., DERI, J., DERMITZAKIS, E. T., DEWEY, C., DICKENS, N. J., DIEKHANS, M., DODGE, S., DUBCHAK, I., DUNN, D. M., EDDY, S. R., ELNITSKI, L., EMES, R. D., ESWARA, P., EYRAS, E., FELSENFELD, A., FEWELL, G. A., FLICEK, P., FOLEY, K., FRANKEL, W. N., FULTON, L. A., FULTON, R. S., FUREY, T. S., GAGE, D., GIBBS, R. A., GLUSMAN, G., GNERRE, S., GOLDMAN, N., GOODSTADT, L., GRAFHAM, D., GRAVES, T. A., GREEN, E. D., GREGORY, S., GUIGO, R., GUYER, M., HARDISON, R. C., HAUSSLER, D., HAYASHIZAKI, Y., HILLIER, L. W., HINRICHS, A., HLAVINA, W., HOLZER, T., HSU, F., HUA, A., HUBBARD, T., HUNT, A., JACKSON, I., JAFFE, D. B., JOHNSON, L. S., JONES, M., JONES, T. A., JOY, A., KAMAL, M., et al. 2002. Initial sequencing and comparative analysis of the mouse genome. *Nature,* 420**,** 520-62.

MUECKLER, M. & THORENS, B. 2013. The SLC2 (GLUT) family of membrane transporters. *Mol Aspects Med,* 34**,** 121-38.

MUMMERY, C. L., ZHANG, J., NG, E. S., ELLIOTT, D. A., ELEFANTY, A. G. & KAMP, T. J. 2012. Differentiation of human embryonic stem cells and induced pluripotent stem cells to cardiomyocytes: a methods overview. *Circ Res,* 111**,** 344-58.

MUSUNURU, K., SHEIKH, F., GUPTA, R. M., HOUSER, S. R., MAHER, K. O., MILAN, D. J., TERZIC, A., WU, J. C., AMERICAN HEART ASSOCIATION COUNCIL ON FUNCTIONAL, G., TRANSLATIONAL, B., COUNCIL ON CARDIOVASCULAR DISEASE IN THE, Y., COUNCIL ON, C. & STROKE, N. 2018. Induced Pluripotent Stem Cells for Cardiovascular Disease Modeling and Precision Medicine: A Scientific Statement From the American Heart Association. *Circ Genom Precis Med,* 11**,** e000043.

NAKAGAWA, M., KOYANAGI, M., TANABE, K., TAKAHASHI, K., ICHISAKA, T., AOI, T., OKITA, K., MOCHIDUKI, Y., TAKIZAWA, N. & YAMANAKA, S. 2008. Generation of induced pluripotent stem cells without Myc from mouse and human fibroblasts. *Nat Biotechnol,* 26**,** 101-6.

NEGLIA, D., DE CATERINA, A., MARRACCINI, P., NATALI, A., CIARDETTI, M., VECOLI, C., GASTALDELLI, A., CIOCIARO, D., PELLEGRINI, P., TESTA, R., MENICHETTI, L., L'ABBATE, A., STANLEY, W. C. & RECCHIA, F. A. 2007. Impaired myocardial metabolic reserve and substrate selection flexibility during stress in patients with idiopathic dilated cardiomyopathy. *Am J Physiol Heart Circ Physiol,* 293**,** H3270-8.

NELSON, D. L. & COX, M. M. 2012. *Lehninger Principles of Biochemistry: 6th Edition*, Macmillan Learning.

NEUBAUER, S. 2007. The failing heart--an engine out of fuel. *N Engl J Med,* 356**,** 1140-51.

NEUPERT, W. & BRUNNER, M. 2002. The protein import motor of mitochondria. *Nat Rev Mol Cell Biol,* 3**,** 555-65.

NEW ENGLAND BIOLABS, I. 2020. *NEB® PCR Cloning Kit* [Online]. Available: https://international.neb.com/-/media/nebus/files/manuals/manuale1202.pdf?rev=1f29986ac3734c8881476abdd77c0842&hash=0C2F782E6F26D0E1BB3BB0988756F8A8 [Accessed 12th February 2021].

NGUYEN, H. T., GEENS, M., MERTZANIDOU, A., JACOBS, K., HEIRMAN, C., BRECKPOT, K. & SPITS, C. 2014. Gain of 20q11.21 in human embryonic stem cells improves cell survival by increased expression of Bcl-xL. *Mol Hum Reprod,* 20**,** 168-77.

NGUYEN, H. T., GEENS, M. & SPITS, C. 2013. Genetic and epigenetic instability in human pluripotent stem cells. *Hum Reprod Update,* 19**,** 187-205.

NIJTMANS, L. G., DE JONG, L., ARTAL SANZ, M., COATES, P. J., BERDEN, J. A., BACK, J. W., MUIJSERS, A. O., VAN DER SPEK, H. & GRIVELL, L. A. 2000. Prohibitins act as a membrane-bound chaperone for the stabilization of mitochondrial proteins. *EMBO J,* 19**,** 2444-51.

NISHIMASU, H., RAN, F. A., HSU, P. D., KONERMANN, S., SHEHATA, S. I., DOHMAE, N., ISHITANI, R., ZHANG, F. & NUREKI, O. 2014. Crystal structure of Cas9 in complex with guide RNA and target DNA. *Cell,* 156**,** 935-49.

NISSENKORN, A., ZEHARIA, A., LEV, D., FATAL-VALEVSKI, A., BARASH, V., GUTMAN, A., HAREL, S. & LERMAN-SAGIE, T. 1999. Multiple presentation of mitochondrial disorders. *Arch Dis Child,* 81**,** 209-14.

NIWA, H. 2001. Molecular mechanism to maintain stem cell renewal of ES cells. *Cell Struct Funct,* 26**,** 137-48.

NIWA, H., MIYAZAKI, J. & SMITH, A. G. 2000. Quantitative expression of Oct-3/4 defines differentiation, dedifferentiation or self-renewal of ES cells. *Nat Genet,* 24**,** 372-6.

NOSE, N., WERNER, R. A., UEDA, Y., GUNTHER, K., LAPA, C., JAVADI, M. S., FUKUSHIMA, K., EDENHOFER, F. & HIGUCHI, T. 2018. Metabolic substrate shift in human induced pluripotent stem cells during cardiac differentiation: Functional assessment using in vitro radionuclide uptake assay. *Int J Cardiol,* 269**,** 229-234.

NUNES, S. S., MIKLAS, J. W., LIU, J., ASCHAR-SOBBI, R., XIAO, Y., ZHANG, B., JIANG, J., MASSE, S., GAGLIARDI, M., HSIEH, A., THAVANDIRAN, N., LAFLAMME, M. A., NANTHAKUMAR, K., GROSS, G. J., BACKX, P. H., KELLER, G. & RADISIC, M. 2013. Biowire: a platform for maturation of human pluripotent stem cell-derived cardiomyocytes. *Nat Methods,* 10**,** 781-7.

OGAWA, M. 1993. Differentiation and proliferation of hematopoietic stem cells. *Blood,* 81**,** 2844-53.

OHGUSHI, M., MATSUMURA, M., EIRAKU, M., MURAKAMI, K., ARAMAKI, T., NISHIYAMA, A., MUGURUMA, K., NAKANO, T., SUGA, H., UENO, M., ISHIZAKI, T., SUEMORI, H., NARUMIYA, S., NIWA, H. & SASAI, Y. 2010. Molecular pathway and cell state responsible for dissociation-induced apoptosis in human pluripotent stem cells. *Cell Stem Cell,* 7**,** 225-39.

OHTSUKA, K. & HATA, M. 2000. Mammalian HSP40/DNAJ homologs: cloning of novel cDNAs and a proposal for their classification and nomenclature. *Cell Stress Chaperones,* 5**,** 98-112.

OJALA, T., POLINATI, P., MANNINEN, T., HIIPPALA, A., RAJANTIE, J., KARIKOSKI, R., SUOMALAINEN, A. & TYNI, T. 2012. New mutation of mitochondrial DNAJC19 causing dilated and noncompaction cardiomyopathy, anemia, ataxia, and male genital anomalies. *Pediatr Res,* 72**,** 432-7.

OKAMOTO, K., OKAZAWA, H., OKUDA, A., SAKAI, M., MURAMATSU, M. & HAMADA, H. 1990. A novel octamer binding transcription factor is differentially expressed in mouse embryonic cells. *Cell,* 60**,** 461-72.

OKITA, K., ICHISAKA, T. & YAMANAKA, S. 2007. Generation of germline-competent induced pluripotent stem cells. *Nature,* 448**,** 313-7.

OKITA, K., MATSUMURA, Y., SATO, Y., OKADA, A., MORIZANE, A., OKAMOTO, S., HONG, H., NAKAGAWA, M., TANABE, K., TEZUKA, K., SHIBATA, T., KUNISADA, T., TAKAHASHI, M., TAKAHASHI, J., SAJI, H. & YAMANAKA, S. 2011. A more efficient method to generate integration-free human iPS cells. *Nat Methods,* 8**,** 409-12.

OSMAN, C., HAAG, M., POTTING, C., RODENFELS, J., DIP, P. V., WIELAND, F. T., BRUGGER, B., WESTERMANN, B. & LANGER, T. 2009a. The genetic interactome of prohibitins: coordinated control of cardiolipin and phosphatidylethanolamine by conserved regulators in mitochondria. *J Cell Biol,* 184**,** 583-96.

OSMAN, C., MERKWIRTH, C. & LANGER, T. 2009b. Prohibitins and the functional compartmentalization of mitochondrial membranes. *J Cell Sci,* 122**,** 3823-30.

OSMAN, C., VOELKER, D. R. & LANGER, T. 2011. Making heads or tails of phospholipids in mitochondria. *J Cell Biol,* 192**,** 7-16.

PAL, R., MAMIDI, M. K., DAS, A. K. & BHONDE, R. 2013. Comparative analysis of cardiomyocyte differentiation from human embryonic stem cells under 3-D and 2-D culture conditions. *J Biosci Bioeng,* 115**,** 200-6.

PANGBORN, M. C. 1946. A study of the composition of cardiolipin. *Fed Proc,* 5**,** 149.

PARK, I. H., ZHAO, R., WEST, J. A., YABUUCHI, A., HUO, H., INCE, T. A., LEROU, P. H., LENSCH, M. W. & DALEY, G. Q. 2008. Reprogramming of human somatic cells to pluripotency with defined factors. *Nature,* 451**,** 141-6.

PETROSILLO, G., CASANOVA, G., MATERA, M., RUGGIERO, F. M. & PARADIES, G. 2006. Interaction of peroxidized cardiolipin with rat-heart mitochondrial membranes: induction of permeability transition and cytochrome c release. *FEBS Lett,* 580**,** 6311-6.

PEYTA, L., JARNOUEN, K., PINAULT, M., GUIMARAES, C., PAIS DE BARROS, J. P., CHEVALIER, S., DUMAS, J. F., MAILLOT, F., HATCH, G. M., LOYER, P. & SERVAIS, S. 2016. Reduced cardiolipin content decreases respiratory chain capacities and increases ATP synthesis yield in the human HepaRG cells. *Biochim Biophys Acta,* 1857**,** 443-53.

PICKLES, S., VIGIE, P. & YOULE, R. J. 2018. Mitophagy and Quality Control Mechanisms in Mitochondrial Maintenance. *Curr Biol,* 28**,** R170-R185.

PIESKE, B., MAIER, L. S., BERS, D. M. & HASENFUSS, G. 1999. Ca2+ handling and sarcoplasmic reticulum Ca2+ content in isolated failing and nonfailing human myocardium. *Circ Res,* 85**,** 38-46.

PILICHOU, K., NAVA, A., BASSO, C., BEFFAGNA, G., BAUCE, B., LORENZON, A., FRIGO, G., VETTORI, A., VALENTE, M., TOWBIN, J., THIENE, G., DANIELI, G. A. & RAMPAZZO, A. 2006. Mutations in desmoglein-2 gene are associated with arrhythmogenic right ventricular cardiomyopathy. *Circulation,* 113**,** 1171-9.

PILICHOU, K., THIENE, G., BAUCE, B., RIGATO, I., LAZZARINI, E., MIGLIORE, F., PERAZZOLO MARRA, M., RIZZO, S., ZORZI, A., DALIENTO, L., CORRADO, D. & BASSO, C. 2016. Arrhythmogenic cardiomyopathy. *Orphanet J Rare Dis,* 11**,** 33.

PILLEKAMP, F., HAUSTEIN, M., KHALIL, M., EMMELHEINZ, M., NAZZAL, R., ADELMANN, R., NGUEMO, F., RUBENCHYK, O., PFANNKUCHE, K., MATZKIES, M., REPPEL, M., BLOCH, W., BROCKMEIER, K. & HESCHELER, J. 2012. Contractile properties of early human embryonic stem cell-derived cardiomyocytes: beta-adrenergic stimulation induces positive chronotropy and lusitropy but not inotropy. *Stem Cells Dev,* 21**,** 2111-21.

PIQUEREAU, J., CAFFIN, F., NOVOTOVA, M., LEMAIRE, C., VEKSLER, V., GARNIER, A., VENTURA-CLAPIER, R. & JOUBERT, F. 2013. Mitochondrial dynamics in the adult cardiomyocytes: which roles for a highly specialized cell? *Front Physiol,* 4**,** 102.

PLOTNIKOV, E. Y., VASILEVA, A. K., ARKHANGELSKAYA, A. A., PEVZNER, I. B., SKULACHEV, V. P. & ZOROV, D. B. 2008. Interrelations of mitochondrial fragmentation and cell death under ischemia/reoxygenation and UV-irradiation: protective effects of SkQ1, lithium ions and insulin. *FEBS Lett,* 582**,** 3117-24.

POGWIZD, S. M., SCHLOTTHAUER, K., LI, L., YUAN, W. & BERS, D. M. 2001. Arrhythmogenesis and contractile dysfunction in heart failure: Roles of sodium-calcium exchange, inward rectifier potassium current, and residual beta-adrenergic responsiveness. *Circ Res,* 88**,** 1159-67.

POLO, J. M., ANDERSSEN, E., WALSH, R. M., SCHWARZ, B. A., NEFZGER, C. M., LIM, S. M., BORKENT, M., APOSTOLOU, E., ALAEI, S., CLOUTIER, J., BAR-NUR, O., CHELOUFI, S., STADTFELD, M., FIGUEROA, M. E., ROBINTON, D., NATESAN, S., MELNICK, A., ZHU, J., RAMASWAMY, S. & HOCHEDLINGER, K. 2012. A molecular roadmap of reprogramming somatic cells into iPS cells. *Cell,* 151**,** 1617-32.

PORTEUS, M. H. & BALTIMORE, D. 2003. Chimeric nucleases stimulate gene targeting in human cells. *Science,* 300**,** 763.

PROTZE, S. I., LIU, J., NUSSINOVITCH, U., OHANA, L., BACKX, P. H., GEPSTEIN, L. & KELLER, G. M. 2017. Sinoatrial node cardiomyocytes derived from human pluripotent cells function as a biological pacemaker. *Nat Biotechnol,* 35**,** 56-68.

QIAGEN. 2017. *QIAxcel Advanced User Manual - (EN)* [Online]. Available: https://www.qiagen.com/de/resources/resourcedetail?id=e3edf734-1e5a-4ebf-957e-a35e120d6290&lang=en [Accessed 12th February 2021].

QIU, X. B., SHAO, Y. M., MIAO, S. & WANG, L. 2006. The diversity of the DnaJ/Hsp40 family, the crucial partners for Hsp70 chaperones. *Cell Mol Life Sci,* 63**,** 2560-70.

RADISIC, M., PARK, H., SHING, H., CONSI, T., SCHOEN, F. J., LANGER, R., FREED, L. E. & VUNJAK-NOVAKOVIC, G. 2004. Functional assembly of engineered myocardium by electrical stimulation of cardiac myocytes cultured on scaffolds. *Proceedings of the National Academy of Sciences of the United States of America,* 101**,** 18129-34.

RAJALA, K., LINDROOS, B., HUSSEIN, S. M., LAPPALAINEN, R. S., PEKKANEN-MATTILA, M., INZUNZA, J., ROZELL, B., MIETTINEN, S., NARKILAHTI, S., KERKELA, E., AALTO-SETALA, K., OTONKOSKI, T., SUURONEN, R., HOVATTA, O. & SKOTTMAN, H. 2010. A defined and xeno-free culture method enabling the establishment of clinical-grade human embryonic, induced pluripotent and adipose stem cells. *PLoS One,* 5**,** e10246.

RAJAMOHAN, D., MATSA, E., KALRA, S., CRUTCHLEY, J., PATEL, A., GEORGE, V. & DENNING, C. 2013. Current status of drug screening and disease modelling in human pluripotent stem cells. *Bioessays,* 35**,** 281-98.

RAMALHO-SANTOS, M., YOON, S., MATSUZAKI, Y., MULLIGAN, R. C. & MELTON, D. A. 2002. "Stemness": transcriptional profiling of embryonic and adult stem cells. *Science,* 298**,** 597-600.

RAN, F. A., HSU, P. D., LIN, C. Y., GOOTENBERG, J. S., KONERMANN, S., TREVINO, A. E., SCOTT, D. A., INOUE, A., MATOBA, S., ZHANG, Y. & ZHANG, F. 2013a. Double nicking by RNA-guided CRISPR Cas9 for enhanced genome editing specificity. *Cell,* 154**,** 1380-9.

RAN, F. A., HSU, P. D., WRIGHT, J., AGARWALA, V., SCOTT, D. A. & ZHANG, F. 2013b. Genome engineering using the CRISPR-Cas9 system. *Nat Protoc,* 8**,** 2281-2308.

RANA, P., ANSON, B., ENGLE, S. & WILL, Y. 2012. Characterization of human-induced pluripotent stem cell-derived cardiomyocytes: bioenergetics and utilization in safety screening. *Toxicol Sci,* 130**,** 117-31.

REBUZZINI, P., ZUCCOTTI, M., REDI, C. A. & GARAGNA, S. 2016. Achilles' heel of pluripotent stem cells: genetic, genomic and epigenetic variations during prolonged culture. *Cell Mol Life Sci,* 73**,** 2453-66.

REHLING, P., PFANNER, N. & MEISINGER, C. 2003. Insertion of hydrophobic membrane proteins into the inner mitochondrial membrane--a guided tour. *J Mol Biol,* 326**,** 639-57.

REN, F., REN, C., ZHANG, Z., DUAN, W., LECOURIEUX, D., LI, S. & LIANG, Z. 2019. Efficiency Optimization of CRISPR/Cas9-Mediated Targeted Mutagenesis in Grape. *Front Plant Sci,* 10**,** 612.

REUBINOFF, B. E., PERA, M. F., FONG, C. Y., TROUNSON, A. & BONGSO, A. 2000. Embryonic stem cell lines from human blastocysts: somatic differentiation in vitro. *Nat Biotechnol,* 18**,** 399-404.
RICHARDS, M., TAN, S. P., TAN, J. H., CHAN, W. K. & BONGSO, A. 2004. The transcriptome profile of human embryonic stem cells as defined by SAGE. *Stem Cells,* 22**,** 51-64.
RICHTER-DENNERLEIN, R., KORWITZ, A., HAAG, M., TATSUTA, T., DARGAZANLI, S., BAKER, M., DECKER, T., LAMKEMEYER, T., RUGARLI, E. I. & LANGER, T. 2014. DNAJC19, a mitochondrial cochaperone associated with cardiomyopathy, forms a complex with prohibitins to regulate cardiolipin remodeling. *Cell Metab,* 20**,** 158-71.
ROBERTSON, C., TRAN, D. D. & GEORGE, S. C. 2013. Concise review: maturation phases of human pluripotent stem cell-derived cardiomyocytes. *Stem Cells,* 31**,** 829-37.
ROBINTON, D. A. & DALEY, G. Q. 2012. The promise of induced pluripotent stem cells in research and therapy. *Nature,* 481**,** 295-305.
RODGERS, K. & MCVEY, M. 2016. Error-Prone Repair of DNA Double-Strand Breaks. *J Cell Physiol,* 231**,** 15-24.
ROHANI, L., MACHIRAJU, P., SABOUNY, R., MENG, G., LIU, S., ZHAO, T., IQBAL, F., WANG, X., RAVANDI, A., WU, J. C., KHAN, A., SHUTT, T., RANCOURT, D. & GREENWAY, S. C. 2020. Reversible Mitochondrial Fragmentation in iPSC-Derived Cardiomyocytes From Children With DCMA, a Mitochondrial Cardiomyopathy. *Can J Cardiol,* 36**,** 554-563.
RONALDSON-BOUCHARD, K., MA, S. P., YEAGER, K., CHEN, T., SONG, L., SIRABELLA, D., MORIKAWA, K., TELES, D., YAZAWA, M. & VUNJAK-NOVAKOVIC, G. 2018. Advanced maturation of human cardiac tissue grown from pluripotent stem cells. *Nature,* 556**,** 239-243.
RONALDSON-BOUCHARD, K., MA, S. P., YEAGER, K., CHEN, T., SONG, L., SIRABELLA, D., MORIKAWA, K., TELES, D., YAZAWA, M. & VUNJAK-NOVAKOVIC, G. 2019. Author Correction: Advanced maturation of human cardiac tissue grown from pluripotent stem cells. *Nature,* 572**,** E16-E17.
ROSNER, M. H., VIGANO, M. A., OZATO, K., TIMMONS, P. M., POIRIER, F., RIGBY, P. W. & STAUDT, L. M. 1990. A POU-domain transcription factor in early stem cells and germ cells of the mammalian embryo. *Nature,* 345**,** 686-92.
ROSOWSKI, K. A., MERTZ, A. F., NORCROSS, S., DUFRESNE, E. R. & HORSLEY, V. 2015. Edges of human embryonic stem cell colonies display distinct mechanical properties and differentiation potential. *Sci Rep,* 5**,** 14218.
ROSS, S. B., FRASER, S. T. & SEMSARIAN, C. 2016. Induced pluripotent stem cells in the inherited cardiomyopathies: From disease mechanisms to novel therapies. *Trends Cardiovasc Med,* 26**,** 663-672.
ROSSIGNOL, R., GILKERSON, R., AGGELER, R., YAMAGATA, K., REMINGTON, S. J. & CAPALDI, R. A. 2004. Energy substrate modulates mitochondrial structure and oxidative capacity in cancer cells. *Cancer Res,* 64**,** 985-93.
ROUHANI, F., KUMASAKA, N., DE BRITO, M. C., BRADLEY, A., VALLIER, L. & GAFFNEY, D. 2014. Genetic background drives transcriptional variation in human induced pluripotent stem cells. *PLoS Genet,* 10**,** e1004432.
RUPERT, C. E., IROFUALA, C. & COULOMBE, K. L. K. 2020. Practical adoption of state-of-the-art hiPSC-cardiomyocyte differentiation techniques. *PLoS One,* 15**,** e0230001.
SABBAH, H. N. 2020. Targeting the Mitochondria in Heart Failure: A Translational Perspective. *JACC Basic Transl Sci,* 5**,** 88-106.
SACCO, A. M., BELVISO, I., ROMANO, V., CARFORA, A., SCHONAUER, F., NURZYNSKA, D., MONTAGNANI, S., DI MEGLIO, F. & CASTALDO, C. 2019. Diversity of dermal fibroblasts as major determinant of variability in cell reprogramming. *J Cell Mol Med,* 23**,** 4256-4268.
SACHINIDIS, A. 2020. Cardiotoxicity and Heart Failure: Lessons from Human-Induced Pluripotent Stem Cell-Derived Cardiomyocytes and Anticancer Drugs. *Cells,* 9.
SANDER, J. D., DAHLBORG, E. J., GOODWIN, M. J., CADE, L., ZHANG, F., CIFUENTES, D., CURTIN, S. J., BLACKBURN, J. S., THIBODEAU-BEGANNY, S., QI, Y., PIERICK, C. J., HOFFMAN, E., MAEDER, M. L., KHAYTER, C., REYON, D., DOBBS, D., LANGENAU, D. M., STUPAR, R. M., GIRALDEZ, A. J., VOYTAS, D. F., PETERSON, R. T., YEH, J. R. & JOUNG, J. K. 2011. Selection-free zinc-finger-nuclease engineering by context-dependent assembly (CoDA). *Nat Methods,* 8**,** 67-9.
SANJANA, N. E., CONG, L., ZHOU, Y., CUNNIFF, M. M., FENG, G. & ZHANG, F. 2012. A transcription activator-like effector toolbox for genome engineering. *Nat Protoc,* 7**,** 171-92.
SANTOSTEFANO, K. E., HAMAZAKI, T., BIEL, N. M., JIN, S., UMEZAWA, A. & TERADA, N. 2015. A practical guide to induced pluripotent stem cell research using patient samples. *Lab Invest,* 95**,** 4-13.
SARASTE, M. 1999. Oxidative phosphorylation at the fin de siecle. *Science,* 283**,** 1488-93.
SARIC, A., ANDREAU, K., ARMAND, A. S., MOLLER, I. M. & PETIT, P. X. 2015. Barth Syndrome: From Mitochondrial Dysfunctions Associated with Aberrant Production of Reactive Oxygen Species to Pluripotent Stem Cell Studies. *Front Genet,* 6**,** 359.
SATO, N., SANJUAN, I. M., HEKE, M., UCHIDA, M., NAEF, F. & BRIVANLOU, A. H. 2003. Molecular signature of human embryonic stem cells and its comparison with the mouse. *Dev Biol,* 260**,** 404-13.
SAYED, N., LIU, C. & WU, J. C. 2016. Translation of Human-Induced Pluripotent Stem Cells: From Clinical Trial in a Dish to Precision Medicine. *J Am Coll Cardiol,* 67**,** 2161-2176.
SCHAAF, S., SHIBAMIYA, A., MEWE, M., EDER, A., STOHR, A., HIRT, M. N., RAU, T., ZIMMERMANN, W. H., CONRADI, L., ESCHENHAGEN, T. & HANSEN, A. 2011. Human engineered heart tissue as a versatile tool in basic research and preclinical toxicology. *PLoS One,* 6**,** e26397.
SCHINDELIN, J., ARGANDA-CARRERAS, I., FRISE, E., KAYNIG, V., LONGAIR, M., PIETZSCH, T., PREIBISCH, S., RUEDEN, C., SAALFELD, S., SCHMID, B., TINEVEZ, J. Y., WHITE, D. J., HARTENSTEIN, V., ELICEIRI, K., TOMANCAK, P. & CARDONA, A. 2012. Fiji: an open-source platform for biological-image analysis. *Nat Methods,* 9**,** 676-82.
SCHLAEGER, T. M., DAHERON, L., BRICKLER, T. R., ENTWISLE, S., CHAN, K., CIANCI, A., DEVINE, A., ETTENGER, A., FITZGERALD, K., GODFREY, M., GUPTA, D., MCPHERSON, J., MALWADKAR, P., GUPTA, M., BELL, B., DOI, A., JUNG, N., LI, X., LYNES, M. S., BROOKES, E., CHERRY, A. B., DEMIRBAS, D., TSANKOV, A. M., ZON, L. I., RUBIN, L. L., FEINBERG, A. P., MEISSNER, A., COWAN, C. A. & DALEY, G. Q. 2015. A comparison of non-integrating reprogramming methods. *Nat Biotechnol,* 33**,** 58-63.
SCHLAME, M., BEYER, K., HAYER-HARTL, M. & KLINGENBERG, M. 1991. Molecular species of cardiolipin in relation to other mitochondrial phospholipids. Is there an acyl specificity of the interaction between cardiolipin and the ADP/ATP carrier? *Eur J Biochem,* 199**,** 459-66.
SCHLAME, M., KELLEY, R. I., FEIGENBAUM, A., TOWBIN, J. A., HEERDT, P. M., SCHIEBLE, T., WANDERS, R. J., DIMAURO, S. & BLANCK, T. J. 2003. Phospholipid abnormalities in children with Barth syndrome. *J Am Coll Cardiol,* 42**,** 1994-9.
SCHLAME, M. & OTTEN, D. 1991. Analysis of cardiolipin molecular species by high-performance liquid chromatography of its derivative 1,3-bisphosphatidyl-2-benzoyl-sn-glycerol dimethyl ester. *Anal Biochem,* 195**,** 290-5.
SCHLAME, M., REN, M., XU, Y., GREENBERG, M. L. & HALLER, I. 2005. Molecular symmetry in mitochondrial cardiolipins. *Chem Phys Lipids,* 138**,** 38-49.

SCHOLER, H. R., RUPPERT, S., SUZUKI, N., CHOWDHURY, K. & GRUSS, P. 1990. New type of POU domain in germ line-specific protein Oct-4. *Nature,* 344**,** 435-9.
SCHWARTZ, K., BOHELER, K. R., DE LA BASTIE, D., LOMPRE, A. M. & MERCADIER, J. J. 1992. Switches in cardiac muscle gene expression as a result of pressure and volume overload. *Am J Physiol,* 262**,** R364-9.
SCHWARTZ, S. D., HUBSCHMAN, J. P., HEILWELL, G., FRANCO-CARDENAS, V., PAN, C. K., OSTRICK, R. M., MICKUNAS, E., GAY, R., KLIMANSKAYA, I. & LANZA, R. 2012. Embryonic stem cell trials for macular degeneration: a preliminary report. *Lancet,* 379**,** 713-20.
SEQUEIRA, V., NAJAFI, A., MCCONNELL, M., FOWLER, E. D., BOLLEN, I. A., WUST, R. C., DOS REMEDIOS, C., HELMES, M., WHITE, E., STIENEN, G. J., TARDIFF, J., KUSTER, D. W. & VAN DER VELDEN, J. 2015. Synergistic role of ADP and Ca(2+) in diastolic myocardial stiffness. *J Physiol,* 593**,** 3899-916.
SEXTON, A. N., REGALADO, S. G., LAI, C. S., COST, G. J., O'NEIL, C. M., URNOV, F. D., GREGORY, P. D., JAENISCH, R., COLLINS, K. & HOCKEMEYER, D. 2014. Genetic and molecular identification of three human TPP1 functions in telomerase action: recruitment, activation, and homeostasis set point regulation. *Genes Dev,* 28**,** 1885-99.
SHAROV, A. A., PIAO, Y., MATOBA, R., DUDEKULA, D. B., QIAN, Y., VANBUREN, V., FALCO, G., MARTIN, P. R., STAGG, C. A., BASSEY, U. C., WANG, Y., CARTER, M. G., HAMATANI, T., AIBA, K., AKUTSU, H., SHAROVA, L., TANAKA, T. S., KIMBER, W. L., YOSHIKAWA, T., JARADAT, S. A., PANTANO, S., NAGARAJA, R., BOHELER, K. R., TAUB, D., HODES, R. J., LONGO, D. L., SCHLESSINGER, D., KELLER, J., KLOTZ, E., KELSOE, G., UMEZAWA, A., VESCOVI, A. L., ROSSANT, J., KUNATH, T., HOGAN, B. L., CURCI, A., D'URSO, M., KELSO, J., HIDE, W. & KO, M. S. 2003. Transcriptome analysis of mouse stem cells and early embryos. *PLoS Biol,* 1**,** E74.
SHATTOCK, M. J., OTTOLIA, M., BERS, D. M., BLAUSTEIN, M. P., BOGUSLAVSKYI, A., BOSSUYT, J., BRIDGE, J. H., CHEN-IZU, Y., CLANCY, C. E., EDWARDS, A., GOLDHABER, J., KAPLAN, J., LINGREL, J. B., PAVLOVIC, D., PHILIPSON, K., SIPIDO, K. R. & XIE, Z. J. 2015. Na+/Ca2+ exchange and Na+/K+-ATPase in the heart. *J Physiol,* 593**,** 1361-82.
SHI, Y., DO, J. T., DESPONTS, C., HAHM, H. S., SCHOLER, H. R. & DING, S. 2008. A combined chemical and genetic approach for the generation of induced pluripotent stem cells. *Cell Stem Cell,* 2**,** 525-8.
SHIBA, Y., GOMIBUCHI, T., SETO, T., WADA, Y., ICHIMURA, H., TANAKA, Y., OGASAWARA, T., OKADA, K., SHIBA, N., SAKAMOTO, K., IDO, D., SHIINA, T., OHKURA, M., NAKAI, J., UNO, N., KAZUKI, Y., OSHIMURA, M., MINAMI, I. & IKEDA, U. 2016. Allogeneic transplantation of iPS cell-derived cardiomyocytes regenerates primate hearts. *Nature,* 538**,** 388-391.
SHINZAWA-ITOH, K., AOYAMA, H., MURAMOTO, K., TERADA, H., KURAUCHI, T., TADEHARA, Y., YAMASAKI, A., SUGIMURA, T., KURONO, S., TSUJIMOTO, K., MIZUSHIMA, T., YAMASHITA, E., TSUKIHARA, T. & YOSHIKAWA, S. 2007. Structures and physiological roles of 13 integral lipids of bovine heart cytochrome c oxidase. *EMBO J,* 26**,** 1713-25.
SIEMEN, H., NIX, M., ENDL, E., KOCH, P., ITSKOVITZ-ELDOR, J. & BRUSTLE, O. 2005. Nucleofection of human embryonic stem cells. *Stem Cells Dev,* 14**,** 378-83.
SIGNORILE, A., SGARAMELLA, G., BELLOMO, F. & DE RASMO, D. 2019. Prohibitins: A Critical Role in Mitochondrial Functions and Implication in Diseases. *Cells,* 8.
SIMBENI, R., PALTAUF, F. & DAUM, G. 1990. Intramitochondrial transfer of phospholipids in the yeast, Saccharomyces cerevisiae. *J Biol Chem,* 265**,** 281-5.
SIMINOVITCH, L., MCCULLOCH, E. A. & TILL, J. E. 1963. The Distribution of Colony-Forming Cells among Spleen Colonies. *J Cell Comp Physiol,* 62**,** 327-36.
SIMS, R. J., 3RD, NISHIOKA, K. & REINBERG, D. 2003. Histone lysine methylation: a signature for chromatin function. *Trends Genet,* 19**,** 629-39.
SINNECKER, D., GOEDEL, A., DORN, T., DIRSCHINGER, R. J., MORETTI, A. & LAUGWITZ, K. L. 2013a. Modeling long-QT syndromes with iPS cells. *J Cardiovasc Transl Res,* 6**,** 31-6.
SINNECKER, D., GOEDEL, A., LAUGWITZ, K. L. & MORETTI, A. 2013b. Induced pluripotent stem cell-derived cardiomyocytes: a versatile tool for arrhythmia research. *Circ Res,* 112**,** 961-8.
SKULACHEV, V. P. 2001. Mitochondrial filaments and clusters as intracellular power-transmitting cables. *Trends Biochem Sci,* 26**,** 23-9.
SMITH, T. K., NYLANDER, K. D. & SCHOR, N. F. 1998. The roles of mitotic arrest and protein synthesis in induction of apoptosis and differentiation in neuroblastoma cells in culture. *Brain Res Dev Brain Res,* 105**,** 175-80.
SNIR, M., KEHAT, I., GEPSTEIN, A., COLEMAN, R., ITSKOVITZ-ELDOR, J., LIVNE, E. & GEPSTEIN, L. 2003. Assessment of the ultrastructural and proliferative properties of human embryonic stem cell-derived cardiomyocytes. *Am J Physiol Heart Circ Physiol,* 285**,** H2355-63.
SOLARO, R. J. 1999. Is calcium the 'cure' for dilated cardiomyopathy? *Nature Medicine,* 5**,** 1353-1354.
SOLDNER, F. & JAENISCH, R. 2012. Medicine. iPSC disease modeling. *Science,* 338**,** 1155-6.
SOLDNER, F., LAGANIERE, J., CHENG, A. W., HOCKEMEYER, D., GAO, Q., ALAGAPPAN, R., KHURANA, V., GOLBE, L. I., MYERS, R. H., LINDQUIST, S., ZHANG, L., GUSCHIN, D., FONG, L. K., VU, B. J., MENG, X., URNOV, F. D., REBAR, E. J., GREGORY, P. D., ZHANG, H. S. & JAENISCH, R. 2011. Generation of isogenic pluripotent stem cells differing exclusively at two early onset Parkinson point mutations. *Cell,* 146**,** 318-31.
SOMERS, A., JEAN, J. C., SOMMER, C. A., OMARI, A., FORD, C. C., MILLS, J. A., YING, L., SOMMER, A. G., JEAN, J. M., SMITH, B. W., LAFYATIS, R., DEMIERRE, M. F., WEISS, D. J., FRENCH, D. L., GADUE, P., MURPHY, G. J., MOSTOSLAVSKY, G. & KOTTON, D. N. 2010. Generation of transgene-free lung disease-specific human induced pluripotent stem cells using a single excisable lentiviral stem cell cassette. *Stem Cells,* 28**,** 1728-40.
SOMMER, C. A., STADTFELD, M., MURPHY, G. J., HOCHEDLINGER, K., KOTTON, D. N. & MOSTOSLAVSKY, G. 2009. Induced pluripotent stem cell generation using a single lentiviral stem cell cassette. *Stem Cells,* 27**,** 543-9.
SONG, M. 2017. The CRISPR/Cas9 system: Their delivery, in vivo and ex vivo applications and clinical development by startups. *Biotechnol Prog,* 33**,** 1035-1045.
SOUBANNIER, V. & MCBRIDE, H. M. 2009. Positioning mitochondrial plasticity within cellular signaling cascades. *Biochim Biophys Acta,* 1793**,** 154-70.
SPARKES, R., PATTON, D. & BERNIER, F. 2007. Cardiac features of a novel autosomal recessive dilated cardiomyopathic syndrome due to defective importation of mitochondrial protein. *Cardiol Young,* 17**,** 215-7.
SPERGER, J. M., CHEN, X., DRAPER, J. S., ANTOSIEWICZ, J. E., CHON, C. H., JONES, S. B., BROOKS, J. D., ANDREWS, P. W., BROWN, P. O. & THOMSON, J. A. 2003. Gene expression patterns in human embryonic stem cells and human pluripotent germ cell tumors. *Proceedings of the National Academy of Sciences of the United States of America,* 100**,** 13350-5.
SPITALIERI, P., TALARICO, R. V., CAIOLI, S., MURDOCCA, M., SERAFINO, A., GIRASOLE, M., DINARELLI, S., LONGO, G., PUCCI, S., BOTTA, A., NOVELLI, G., ZONA, C., MANGO, R. & SANGIUOLO, F. 2018. Modelling the pathogenesis of

Myotonic Dystrophy type 1 cardiac phenotype through human iPSC-derived cardiomyocytes. *J Mol Cell Cardiol,* 118**,** 95-109.
SPITS, C., MATEIZEL, I., GEENS, M., MERTZANIDOU, A., STAESSEN, C., VANDESKELDE, Y., VAN DER ELST, J., LIEBAERS, I. & SERMON, K. 2008. Recurrent chromosomal abnormalities in human embryonic stem cells. *Nat Biotechnol,* 26**,** 1361-3.
STADTFELD, M. & HOCHEDLINGER, K. 2010. Induced pluripotency: history, mechanisms, and applications. *Genes Dev,* 24**,** 2239-63.
STADTFELD, M., MAHERALI, N., BREAULT, D. T. & HOCHEDLINGER, K. 2008. Defining molecular cornerstones during fibroblast to iPS cell reprogramming in mouse. *Cell Stem Cell,* 2**,** 230-40.
STANLEY, W. C., RECCHIA, F. A. & LOPASCHUK, G. D. 2005. Myocardial substrate metabolism in the normal and failing heart. *Physiol Rev,* 85**,** 1093-129.
STEGLICH, G., NEUPERT, W. & LANGER, T. 1999. Prohibitins regulate membrane protein degradation by the m-AAA protease in mitochondria. *Mol Cell Biol,* 19**,** 3435-42.
STERNECKERT, J. L., REINHARDT, P. & SCHOLER, H. R. 2014. Investigating human disease using stem cell models. *Nat Rev Genet,* 15**,** 625-39.
STILLITANO, F., TURNBULL, I. C., KARAKIKES, I., NONNENMACHER, M., BACKERIS, P., HULOT, J. S., KRANIAS, E. G., HAJJAR, R. J. & COSTA, K. D. 2016. Genomic correction of familial cardiomyopathy in human engineered cardiac tissues. *Eur Heart J,* 37**,** 3282-3284.
STOEHR, A., NEUBER, C., BALDAUF, C., VOLLERT, I., FRIEDRICH, F. W., FLENNER, F., CARRIER, L., EDER, A., SCHAAF, S., HIRT, M. N., AKSEHIRLIOGLU, B., TONG, C. W., MORETTI, A., ESCHENHAGEN, T. & HANSEN, A. 2014. Automated analysis of contractile force and Ca2+ transients in engineered heart tissue. *Am J Physiol Heart Circ Physiol,* 306**,** H1353-63.
STOLL, L. A. Q. 2017. Mitochondria and Heart Disease,. *IntechOpen*.
STRAUSS, M., HOFHAUS, G., SCHRODER, R. R. & KUHLBRANDT, W. 2008. Dimer ribbons of ATP synthase shape the inner mitochondrial membrane. *EMBO J,* 27**,** 1154-60.
SUGII, S., KIDA, Y., KAWAMURA, T., SUZUKI, J., VASSENA, R., YIN, Y. Q., LUTZ, M. K., BERGGREN, W. T., IZPISUA BELMONTE, J. C. & EVANS, R. M. 2010. Human and mouse adipose-derived cells support feeder-independent induction of pluripotent stem cells. *Proceedings of the National Academy of Sciences of the United States of America,* 107**,** 3558-63.
SULLIVAN, G. J., BAI, Y., FLETCHER, J. & WILMUT, I. 2010. Induced pluripotent stem cells: epigenetic memories and practical implications. *Mol Hum Reprod,* 16**,** 880-5.
SUN, N., YAZAWA, M., LIU, J., HAN, L., SANCHEZ-FREIRE, V., ABILEZ, O. J., NAVARRETE, E. G., HU, S., WANG, L., LEE, A., PAVLOVIC, A., LIN, S., CHEN, R., HAJJAR, R. J., SNYDER, M. P., DOLMETSCH, R. E., BUTTE, M. J., ASHLEY, E. A., LONGAKER, M. T., ROBBINS, R. C. & WU, J. C. 2012. Patient-specific induced pluripotent stem cells as a model for familial dilated cardiomyopathy. *Sci Transl Med,* 4**,** 130ra47.
SUN, V. Z., CHOE, U. J., RODRIGUEZ, A. R., DAI, H., DEMING, T. J. & KAMEI, D. T. 2013. Transfection of mammalian cells using block copolypeptide vesicles. *Macromol Biosci,* 13**,** 539-50.
SUNDBERG, M., ANDERSSON, P. H., AKESSON, E., ODEBERG, J., HOLMBERG, L., INZUNZA, J., FALCI, S., OHMAN, J., SUURONEN, R., SKOTTMAN, H., LEHTIMAKI, K., HOVATTA, O., NARKILAHTI, S. & SUNDSTROM, E. 2011. Markers of pluripotency and differentiation in human neural precursor cells derived from embryonic stem cells and CNS tissue. *Cell Transplant,* 20**,** 177-91.
SYNNERGREN, J., AKESSON, K., DAHLENBORG, K., VIDARSSON, H., AMEEN, C., STEEL, D., LINDAHL, A., OLSSON, B. & SARTIPY, P. 2008. Molecular signature of cardiomyocyte clusters derived from human embryonic stem cells. *Stem Cells,* 26**,** 1831-40.
SYNNERGREN, J., AMEEN, C., JANSSON, A. & SARTIPY, P. 2012. Global transcriptional profiling reveals similarities and differences between human stem cell-derived cardiomyocyte clusters and heart tissue. *Physiol Genomics,* 44**,** 245-58.
SYNNERGREN, J., HEINS, N., BROLEN, G., ERIKSSON, G., LINDAHL, A., HYLLNER, J., OLSSON, B., SARTIPY, P. & BJORQUIST, P. 2010. Transcriptional profiling of human embryonic stem cells differentiating to definitive and primitive endoderm and further toward the hepatic lineage. *Stem Cells Dev,* 19**,** 961-78.
SZETO, H. H. 2014. First-in-class cardiolipin-protective compound as a therapeutic agent to restore mitochondrial bioenergetics. *Br J Pharmacol,* 171**,** 2029-50.
TAANMAN, J. W., BURTON, M. D., MARUSICH, M. F., KENNAWAY, N. G. & CAPALDI, R. A. 1996. Subunit specific monoclonal antibodies show different steady-state levels of various cytochrome-c oxidase subunits in chronic progressive external ophthalmoplegia. *Biochim Biophys Acta,* 1315**,** 199-207.
TADA, M., TAKAHAMA, Y., ABE, K., NAKATSUJI, N. & TADA, T. 2001. Nuclear reprogramming of somatic cells by in vitro hybridization with ES cells. *Curr Biol,* 11**,** 1553-8.
TAKAHASHI, K., TANABE, K., OHNUKI, M., NARITA, M., ICHISAKA, T., TOMODA, K. & YAMANAKA, S. 2007. Induction of pluripotent stem cells from adult human fibroblasts by defined factors. *Cell,* 131**,** 861-72.
TAKAHASHI, K. & YAMANAKA, S. 2006. Induction of pluripotent stem cells from mouse embryonic and adult fibroblast cultures by defined factors. *Cell,* 126**,** 663-76.
TAMURA, Y., HARADA, Y., YAMANO, K., WATANABE, K., ISHIKAWA, D., OHSHIMA, C., NISHIKAWA, S., YAMAMOTO, H. & ENDO, T. 2006. Identification of Tam41 maintaining integrity of the TIM23 protein translocator complex in mitochondria. *J Cell Biol,* 174**,** 631-7.
TAPIA, O., FONG, L. G., HUBER, M. D., YOUNG, S. G. & GERACE, L. 2015. Nuclear envelope protein Lem2 is required for mouse development and regulates MAP and AKT kinases. *PLoS One,* 10**,** e0116196.
TASHIRO, A., MASUDA, T. & SEGAWA, I. 1990. Morphometric comparison of mitochondria and myofibrils of cardiomyocytes between hypertrophic and dilated cardiomyopathies. *Virchows Arch A Pathol Anat Histopathol,* 416**,** 473-8.
TATSUTA, T., MODEL, K. & LANGER, T. 2005. Formation of membrane-bound ring complexes by prohibitins in mitochondria. *Mol Biol Cell,* 16**,** 248-59.
TAYLOR, W. A. & HATCH, G. M. 2009. Identification of the human mitochondrial linoleoyl-coenzyme A monolysocardiolipin acyltransferase (MLCL AT-1). *J Biol Chem,* 284**,** 30360-71.
TAYLOR, W. A., MEJIA, E. M., MITCHELL, R. W., CHOY, P. C., SPARAGNA, G. C. & HATCH, G. M. 2012. Human trifunctional protein alpha links cardiolipin remodeling to beta-oxidation. *PLoS One,* 7**,** e48628.
TECHNOLOGIES, A. 2016. *Determining Metabolic Switch in Induced Pluripotent Stem Cells (iPSCs)* [Online]. Available: https://www.agilent.com/cs/library/applications/5991-7130EN.pdf [Accessed].
TERNS, M. P. & TERNS, R. M. 2011. CRISPR-based adaptive immune systems. *Curr Opin Microbiol,* 14**,** 321-7.

THE NOBEL PRIZE. 2012. *The Nobel Prize in Physiology or Medicine* [Online]. Available: https://www.nobelprize.org/prizes/medicine/2012/summary/ [Accessed].

THE NOBEL PRIZE. 2020. *The Nobel Prize in Chemistry* [Online]. Available: https://www.nobelprize.org/prizes/chemistry/2020/summary/ [Accessed].

THERMO FISHER SCIENTIFIC. 2018. *NEON™ Transfection system for Mouse Embryonic Stem Cells* [Online]. Available: https://www.thermofisher.com/content/dam/LifeTech/migration/en/filelibrary/cell-culture/neon-protocols.par.27415.file.dat/mouse%20embryonic%20stem%20cells-blastocyst.pdf [Accessed 31st July 2018].

THOMPSON, W. E., BRANCH, A., WHITTAKER, J. A., LYN, D., ZILBERSTEIN, M., MAYO, K. E. & THOMAS, K. 2001. Characterization of prohibitin in a newly established rat ovarian granulosa cell line. *Endocrinology,* 142**,** 4076-85.

THOMSON, J. A., ITSKOVITZ-ELDOR, J., SHAPIRO, S. S., WAKNITZ, M. A., SWIERGIEL, J. J., MARSHALL, V. S. & JONES, J. M. 1998. Embryonic stem cell lines derived from human blastocysts. *Science,* 282**,** 1145-7.

TIEMANN, U., SGODDA, M., WARLICH, E., BALLMAIER, M., SCHOLER, H. R., SCHAMBACH, A. & CANTZ, T. 2011. Optimal reprogramming factor stoichiometry increases colony numbers and affects molecular characteristics of murine induced pluripotent stem cells. *Cytometry A,* 79**,** 426-35.

TILL, J. E. & MC, C. E. 1961. A direct measurement of the radiation sensitivity of normal mouse bone marrow cells. *Radiat Res,* 14**,** 213-22.

TILL, J. E. & MCCULLOCH, E. A. 1980. Hemopoietic stem cell differentiation. *Biochim Biophys Acta,* 605**,** 431-59.

TOHYAMA, S., HATTORI, F., SANO, M., HISHIKI, T., NAGAHATA, Y., MATSUURA, T., HASHIMOTO, H., SUZUKI, T., YAMASHITA, H., SATOH, Y., EGASHIRA, T., SEKI, T., MURAOKA, N., YAMAKAWA, H., OHGINO, Y., TANAKA, T., YOICHI, M., YUASA, S., MURATA, M., SUEMATSU, M. & FUKUDA, K. 2013. Distinct metabolic flow enables large-scale purification of mouse and human pluripotent stem cell-derived cardiomyocytes. *Cell Stem Cell,* 12**,** 127-37.

TROKOVIC, R., WELTNER, J., NOISA, P., RAIVIO, T. & OTONKOSKI, T. 2015. Combined negative effect of donor age and time in culture on the reprogramming efficiency into induced pluripotent stem cells. *Stem Cell Res,* 15**,** 254-62.

TRUSCOTT, K. N., VOOS, W., FRAZIER, A. E., LIND, M., LI, Y., GEISSLER, A., DUDEK, J., MULLER, H., SICKMANN, A., MEYER, H. E., MEISINGER, C., GUIARD, B., REHLING, P. & PFANNER, N. 2003. A J-protein is an essential subunit of the presequence translocase-associated protein import motor of mitochondria. *J Cell Biol,* 163**,** 707-13.

TULLOCH, N. L., MUSKHELI, V., RAZUMOVA, M. V., KORTE, F. S., REGNIER, M., HAUCH, K. D., PABON, L., REINECKE, H. & MURRY, C. E. 2011. Growth of engineered human myocardium with mechanical loading and vascular coculture. *Circ Res,* 109**,** 47-59.

TYURINA, Y. Y., DOMINGUES, R. M., TYURIN, V. A., MACIEL, E., DOMINGUES, P., AMOSCATO, A. A., BAYIR, H. & KAGAN, V. E. 2014. Characterization of cardiolipins and their oxidation products by LC-MS analysis. *Chem Phys Lipids,* 179**,** 3-10.

UCAR, S. K., MAYR, J. A., FEICHTINGER, R. G., CANDA, E., COKER, M. & WORTMANN, S. B. 2017. Previously Unreported Biallelic Mutation in DNAJC19: Are Sensorineural Hearing Loss and Basal Ganglia Lesions Additional Features of Dilated Cardiomyopathy and Ataxia (DCMA) Syndrome? *JIMD Rep,* 35**,** 39-45.

UENO, S., WEIDINGER, G., OSUGI, T., KOHN, A. D., GOLOB, J. L., PABON, L., REINECKE, H., MOON, R. T. & MURRY, C. E. 2007. Biphasic role for Wnt/beta-catenin signaling in cardiac specification in zebrafish and embryonic stem cells. *Proceedings of the National Academy of Sciences of the United States of America,* 104**,** 9685-90.

UOSAKI, H., FUKUSHIMA, H., TAKEUCHI, A., MATSUOKA, S., NAKATSUJI, N., YAMANAKA, S. & YAMASHITA, J. K. 2011. Efficient and scalable purification of cardiomyocytes from human embryonic and induced pluripotent stem cells by VCAM1 surface expression. *PLoS One,* 6**,** e23657.

UZUN, A. U., MANNHARDT, I., BRECKWOLDT, K., HORVATH, A., JOHANNSEN, S. S., HANSEN, A., ESCHENHAGEN, T. & CHRIST, T. 2016. Ca(2+)-Currents in Human Induced Pluripotent Stem Cell-Derived Cardiomyocytes Effects of Two Different Culture Conditions. *Front Pharmacol,* 7**,** 300.

VAFAI, S. B. & MOOTHA, V. K. 2012. Mitochondrial disorders as windows into an ancient organelle. *Nature,* 491**,** 374-83.

VAN DEN BERG, C. W., OKAWA, S., CHUVA DE SOUSA LOPES, S. M., VAN IPEREN, L., PASSIER, R., BRAAM, S. R., TERTOOLEN, L. G., DEL SOL, A., DAVIS, R. P. & MUMMERY, C. L. 2015. Transcriptome of human foetal heart compared with cardiomyocytes from pluripotent stem cells. *Development,* 142**,** 3231-8.

VAN DER LAAN, M., MEINECKE, M., DUDEK, J., HUTU, D. P., LIND, M., PERSCHIL, I., GUIARD, B., WAGNER, R., PFANNER, N. & REHLING, P. 2007. Motor-free mitochondrial presequence translocase drives membrane integration of preproteins. *Nat Cell Biol,* 9**,** 1152-9.

VAN DER LAAN, M., WIEDEMANN, N., MICK, D. U., GUIARD, B., REHLING, P. & PFANNER, N. 2006. A role for Tim21 in membrane-potential-dependent preprotein sorting in mitochondria. *Curr Biol,* 16**,** 2271-6.

VANDER HEIDEN, M. G., CHOY, J. S., VANDERWEELE, D. J., BRACE, J. L., HARRIS, M. H., BAUER, D. E., PRANGE, B., KRON, S. J., THOMPSON, C. B. & RUDIN, C. M. 2002. Bcl-x(L) complements Saccharomyces cerevisiae genes that facilitate the switch from glycolytic to oxidative metabolism. *J Biol Chem,* 277**,** 44870-6.

VAZ, F. M., HOUTKOOPER, R. H., VALIANPOUR, F., BARTH, P. G. & WANDERS, R. J. 2003. Only one splice variant of the human TAZ gene encodes a functional protein with a role in cardiolipin metabolism. *J Biol Chem,* 278**,** 43089-94.

VITALE, M. R., ZÖLLER, J., JANSCH, C., JANZ, A., EDENHOFER, F., KLOPOCKI, E., VAN DEN HOVE, D., VANMIERLO, T., RIVERO, O., KASRI, N., ZIEGLER, G. & LESCH, K.-P. 2021. Generation of induced pluripotent stem cell lines deficient for Cadherin 13 (UKWMPi002-A-1/B/C) Bassociated with neurodevelopmental disorders using CRISPR/Cas9. *Stem Cell Research,* 51**,** 102169.

VREKEN, P., VALIANPOUR, F., NIJTMANS, L. G., GRIVELL, L. A., PLECKO, B., WANDERS, R. J. & BARTH, P. G. 2000. Defective remodeling of cardiolipin and phosphatidylglycerol in Barth syndrome. *Biochem Biophys Res Commun,* 279**,** 378-82.

WAKUI, T., MATSUMOTO, T., MATSUBARA, K., KAWASAKI, T., YAMAGUCHI, H. & AKUTSU, H. 2017. Method for evaluation of human induced pluripotent stem cell quality using image analysis based on the biological morphology of cells. *J Med Imaging (Bellingham),* 4**,** 044003.

WALLIMANN, T., WYSS, M., BRDICZKA, D., NICOLAY, K. & EPPENBERGER, H. M. 1992. Intracellular compartmentation, structure and function of creatine kinase isoenzymes in tissues with high and fluctuating energy demands: the 'phosphocreatine circuit' for cellular energy homeostasis. *Biochem J,* 281 (Pt 1)**,** 21-40.

WANG, G., MCCAIN, M. L., YANG, L., HE, A., PASQUALINI, F. S., AGARWAL, A., YUAN, H., JIANG, D., ZHANG, D., ZANGI, L., GEVA, J., ROBERTS, A. E., MA, Q., DING, J., CHEN, J., WANG, D. Z., LI, K., WANG, J., WANDERS, R. J., KULIK, W., VAZ, F. M., LAFLAMME, M. A., MURRY, C. E., CHIEN, K. R., KELLEY, R. I., CHURCH, G. M., PARKER, K. K. & PU, W. T. 2014. Modeling the mitochondrial cardiomyopathy of Barth syndrome with induced pluripotent stem cell and heart-on-chip technologies. *Nat Med,* 20**,** 616-23.

WANG, J., XIE, L. Y., ALLAN, S., BEACH, D. & HANNON, G. J. 1998. Myc activates telomerase. *Genes Dev,* 12**,** 1769-74.

WARREN, L., MANOS, P. D., AHFELDT, T., LOH, Y. H., LI, H., LAU, F., EBINA, W., MANDAL, P. K., SMITH, Z. D., MEISSNER, A., DALEY, G. Q., BRACK, A. S., COLLINS, J. J., COWAN, C., SCHLAEGER, T. M. & ROSSI, D. J. 2010. Highly efficient reprogramming to pluripotency and directed differentiation of human cells with synthetic modified mRNA. *Cell Stem Cell,* 7**,** 618-30.

WATANABE, K., UENO, M., KAMIYA, D., NISHIYAMA, A., MATSUMURA, M., WATAYA, T., TAKAHASHI, J. B., NISHIKAWA, S., MUGURUMA, K. & SASAI, Y. 2007. A ROCK inhibitor permits survival of dissociated human embryonic stem cells. *Nat Biotechnol,* 25**,** 681-6.

WEBER, T. A., KOOB, S., HEIDE, H., WITTIG, I., HEAD, B., VAN DER BLIEK, A., BRANDT, U., MITTELBRONN, M. & REICHERT, A. S. 2013. APOOL is a cardiolipin-binding constituent of the Mitofilin/MINOS protein complex determining cristae morphology in mammalian mitochondria. *PLoS One,* 8**,** e63683.

WEISS, J. N., KORGE, P., HONDA, H. M. & PING, P. 2003. Role of the mitochondrial permeability transition in myocardial disease. *Circ Res,* 93**,** 292-301.

WEISSMAN, I. L. 2000. Stem cells: units of development, units of regeneration, and units in evolution. *Cell,* 100**,** 157-68.

WERBOWETSKI-OGILVIE, T. E., BOSSE, M., STEWART, M., SCHNERCH, A., RAMOS-MEJIA, V., ROULEAU, A., WYNDER, T., SMITH, M. J., DINGWALL, S., CARTER, T., WILLIAMS, C., HARRIS, C., DOLLING, J., WYNDER, C., BOREHAM, D. & BHATIA, M. 2009. Characterization of human embryonic stem cells with features of neoplastic progression. *Nat Biotechnol,* 27**,** 91-7.

WERNIG, M., MEISSNER, A., CASSADY, J. P. & JAENISCH, R. 2008. c-Myc is dispensable for direct reprogramming of mouse fibroblasts. *Cell Stem Cell,* 2**,** 10-2.

WIEDEMANN, N., VAN DER LAAN, M., HUTU, D. P., REHLING, P. & PFANNER, N. 2007. Sorting switch of mitochondrial presequence translocase involves coupling of motor module to respiratory chain. *J Cell Biol,* 179**,** 1115-22.

WIEDENHEFT, B., STERNBERG, S. H. & DOUDNA, J. A. 2012. RNA-guided genetic silencing systems in bacteria and archaea. *Nature,* 482**,** 331-8.

WILDE, A. A. & BEHR, E. R. 2013. Genetic testing for inherited cardiac disease. *Nat Rev Cardiol,* 10**,** 571-83.

WILLEMS, E., SPIERING, S., DAVIDOVICS, H., LANIER, M., XIA, Z., DAWSON, M., CASHMAN, J. & MERCOLA, M. 2011. Small-molecule inhibitors of the Wnt pathway potently promote cardiomyocytes from human embryonic stem cell-derived mesoderm. *Circ Res,* 109**,** 360-4.

WILMUT, I., SCHNIEKE, A. E., MCWHIR, J., KIND, A. J. & CAMPBELL, K. H. 1997. Viable offspring derived from fetal and adult mammalian cells. *Nature,* 385**,** 810-3.

WOBUS, A. M., WALLUKAT, G. & HESCHELER, J. 1991. Pluripotent mouse embryonic stem cells are able to differentiate into cardiomyocytes expressing chronotropic responses to adrenergic and cholinergic agents and Ca2+ channel blockers. *Differentiation,* 48**,** 173-82.

WORTMANN, S. B., KLUIJTMANS, L. A., ENGELKE, U. F., WEVERS, R. A. & MORAVA, E. 2012. The 3-methylglutaconic acidurias: what's new? *J Inherit Metab Dis,* 35**,** 13-22.

WU, D. & PAN, W. 2010. GSK3: a multifaceted kinase in Wnt signaling. *Trends Biochem Sci,* 35**,** 161-8.

WU, X., KRIZ, A. J. & SHARP, P. A. 2014. Target specificity of the CRISPR-Cas9 system. *Quant Biol,* 2**,** 59-70.

XI, J., WANG, Y., ZHANG, P., HE, L., NAN, X., YUE, W. & PEI, X. 2010. Human fetal liver stromal cells that overexpress bFGF support growth and maintenance of human embryonic stem cells. *PLoS One,* 5**,** e14457.

XIAN, B. & HUANG, B. 2015. The immune response of stem cells in subretinal transplantation. *Stem Cell Res Ther,* 6**,** 161.

XU, C., INOKUMA, M. S., DENHAM, J., GOLDS, K., KUNDU, P., GOLD, J. D. & CARPENTER, M. K. 2001. Feeder-free growth of undifferentiated human embryonic stem cells. *Nat Biotechnol,* 19**,** 971-4.

XU, X. Q., SOO, S. Y., SUN, W. & ZWEIGERDT, R. 2009. Global expression profile of highly enriched cardiomyocytes derived from human embryonic stem cells. *Stem Cells,* 27**,** 2163-74.

XU, Y., SUTACHAN, J. J., PLESKEN, H., KELLEY, R. I. & SCHLAME, M. 2005. Characterization of lymphoblast mitochondria from patients with Barth syndrome. *Lab Invest,* 85**,** 823-30.

XU, Y., WEI, X., WANG, M., ZHANG, R., FU, Y., XING, M., HUA, Q. & XIE, X. 2013. Proliferation rate of somatic cells affects reprogramming efficiency. *J Biol Chem,* 288**,** 9767-78.

YAMAMOTO, H., ESAKI, M., KANAMORI, T., TAMURA, Y., NISHIKAWA, S. & ENDO, T. 2002. Tim50 is a subunit of the TIM23 complex that links protein translocation across the outer and inner mitochondrial membranes. *Cell,* 111**,** 519-28.

YAMASHITA, Y. M., FULLER, M. T. & JONES, D. L. 2005. Signaling in stem cell niches: lessons from the Drosophila germline. *J Cell Sci,* 118**,** 665-72.

YANG, L., SOONPAA, M. H., ADLER, E. D., ROEPKE, T. K., KATTMAN, S. J., KENNEDY, M., HENCKAERTS, E., BONHAM, K., ABBOTT, G. W., LINDEN, R. M., FIELD, L. J. & KELLER, G. M. 2008. Human cardiovascular progenitor cells develop from a KDR+ embryonic-stem-cell-derived population. *Nature,* 453**,** 524-8.

YANG, X., PABON, L. & MURRY, C. E. 2014. Engineering adolescence: maturation of human pluripotent stem cell-derived cardiomyocytes. *Circ Res,* 114**,** 511-23.

YANG, Z., YAMAZAKI, M., SHEN, Q. W. & SWARTZ, D. R. 2009. Differences between cardiac and skeletal troponin interaction with the thin filament probed by troponin exchange in skeletal myofibrils. *Biophys J,* 97**,** 183-94.

YATSCOFF, M. A., JASWAL, J. S., GRANT, M. R., GREENWOOD, R., LUKAT, T., BEKER, D. L., REBEYKA, I. M. & LOPASCHUK, G. D. 2008. Myocardial hypertrophy and the maturation of fatty acid oxidation in the newborn human heart. *Pediatr Res,* 64**,** 643-7.

YEH, C. D., RICHARDSON, C. D. & CORN, J. E. 2019. Advances in genome editing through control of DNA repair pathways. *Nat Cell Biol,* 21**,** 1468-1478.

YOSHIHARA, M., HAYASHIZAKI, Y. & MURAKAWA, Y. 2017. Genomic Instability of iPSCs: Challenges Towards Their Clinical Applications. *Stem Cell Rev Rep,* 13**,** 7-16.

YOUNG, J. L., KRETCHMER, K., ONDECK, M. G., ZAMBON, A. C. & ENGLER, A. J. 2014. Mechanosensitive kinases regulate stiffness-induced cardiomyocyte maturation. *Sci Rep,* 4**,** 6425.

YU, J., CHAU, K. F., VODYANIK, M. A., JIANG, J. & JIANG, Y. 2011. Efficient feeder-free episomal reprogramming with small molecules. *PLoS One,* 6**,** e17557.

YU, J., VODYANIK, M. A., SMUGA-OTTO, K., ANTOSIEWICZ-BOURGET, J., FRANE, J. L., TIAN, S., NIE, J., JONSDOTTIR, G. A., RUOTTI, V., STEWART, R., SLUKVIN, II & THOMSON, J. A. 2007. Induced pluripotent stem cell lines derived from human somatic cells. *Science,* 318**,** 1917-20.

YUSUF, S., REDDY, S., OUNPUU, S. & ANAND, S. 2001a. Global burden of cardiovascular diseases: part I: general considerations, the epidemiologic transition, risk factors, and impact of urbanization. *Circulation,* 104**,** 2746-53.

YUSUF, S., REDDY, S., OUNPUU, S. & ANAND, S. 2001b. Global burden of cardiovascular diseases: Part II: variations in cardiovascular disease by specific ethnic groups and geographic regions and prevention strategies. *Circulation,* 104**,** 2855-64.

ZECCHIN, M., MUSER, D., VITALI-SERDOZ, L., BUIATTI, A. & MORGERA, T. 2019. Arrhythmias in Dilated Cardiomyopathy: Diagnosis and Treatment. *In:* SINAGRA, G., MERLO, M. & PINAMONTI, B. (eds.) *Dilated Cardiomyopathy: From Genetics to Clinical Management.* Cham (CH).

ZERBES, R. M., BOHNERT, M., STROUD, D. A., VON DER MALSBURG, K., KRAM, A., OELJEKLAUS, S., WARSCHEID, B., BECKER, T., WIEDEMANN, N., VEENHUIS, M., VAN DER KLEI, I. J., PFANNER, N. & VAN DER LAAN, M. 2012. Role of MINOS in mitochondrial membrane architecture: cristae morphology and outer membrane interactions differentially depend on mitofilin domains. *J Mol Biol,* 422**,** 183-91.

ZHANG, F., CONG, L., LODATO, S., KOSURI, S., CHURCH, G. M. & ARLOTTA, P. 2011. Efficient construction of sequence-specific TAL effectors for modulating mammalian transcription. *Nat Biotechnol,* 29**,** 149-53.

ZHANG, J., WILSON, G. F., SOERENS, A. G., KOONCE, C. H., YU, J., PALECEK, S. P., THOMSON, J. A. & KAMP, T. J. 2009. Functional cardiomyocytes derived from human induced pluripotent stem cells. *Circ Res,* 104**,** e30-41.

ZHANG LABORATORY AT THE BROADINSTITUTE. 2018. *Guide Design Resources* [Online]. Available: https://zlab.bio/guide-design-resources [Accessed 2019].

ZHANG, X. H., TEE, L. Y., WANG, X. G., HUANG, Q. S. & YANG, S. H. 2015. Off-target Effects in CRISPR/Cas9-mediated Genome Engineering. *Mol Ther Nucleic Acids,* 4**,** e264.

ZHAO, M., TANG, Y., ZHOU, Y. & ZHANG, J. 2019. Deciphering Role of Wnt Signalling in Cardiac Mesoderm and Cardiomyocyte Differentiation from Human iPSCs: Four-dimensional control of Wnt pathway for hiPSC-CMs differentiation. *Sci Rep,* 9**,** 19389.

ZHAO, X. Y., LI, W., LV, Z., LIU, L., TONG, M., HAI, T., HAO, J., GUO, C. L., MA, Q. W., WANG, L., ZENG, F. & ZHOU, Q. 2009. iPS cells produce viable mice through tetraploid complementation. *Nature,* 461**,** 86-90.

ZHOU, T., BENDA, C., DUNZINGER, S., HUANG, Y., HO, J. C., YANG, J., WANG, Y., ZHANG, Y., ZHUANG, Q., LI, Y., BAO, X., TSE, H. F., GRILLARI, J., GRILLARI-VOGLAUER, R., PEI, D. & ESTEBAN, M. A. 2012. Generation of human induced pluripotent stem cells from urine samples. *Nat Protoc,* 7**,** 2080-9.

ZHOU, W. & FREED, C. R. 2009. Adenoviral gene delivery can reprogram human fibroblasts to induced pluripotent stem cells. *Stem Cells,* 27**,** 2667-74.

ZIMMER, T., HAUFE, V. & BLECHSCHMIDT, S. 2014. Voltage-gated sodium channels in the mammalian heart. *Glob Cardiol Sci Pract,* 2014**,** 449-63.

ZOU, J., MALI, P., HUANG, X., DOWEY, S. N. & CHENG, L. 2011. Site-specific gene correction of a point mutation in human iPS cells derived from an adult patient with sickle cell disease. *Blood,* 118**,** 4599-608.

ZUO, B., YANG, J., WANG, F., WANG, L., YIN, Y., DAN, J., LIU, N. & LIU, L. 2012. Influences of lamin A levels on induction of pluripotent stem cells. *Biol Open,* 1**,** 1118-27.

List of figures

List of tables

Publications

Peer reviewed journals

The published manuscripts and this thesis contain similar text passages and shared figure materials in adapted form in some sections.

Janz, A., Chen, R., Regensburger, M., Ueda, Y., Rost, S., Klopocki, E., Günther K., Edenhofer, F., Duff, H. J., Ergün, S. & Gerull, B. 2020. Generation of two patient-derived iPSC lines from siblings (LIBUCi001-A and LIBUCi002-A) and a genetically modified iPSC line (JMUi001-A-1) to mimic dilated cardiomyopathy with ataxia (DCMA) caused by a homozygous DNAJC19 mutation. *Stem Cell Res*, 46, 101856.

Cirnu A., Kolokotronis K., Walz K., Kilinc A., **Janz A.**, Williams T., Busch A., Rost S., Gerull B. 2021. Novel Mutation in LOX Associates With a Complex Aneurysmal Vascular and Cardiac Phenotype. *Circ Genom Precis Med*, CIRCGEN120003217. (Cirnu et al., 2021)

Vitale, M. R., Zöller, J., Jansch, C., **Janz, A.**, Edenhofer, F., Klopocki, E., Van den Hove, D., Vanmierlo, T., Rivero, O., Kasri, N., Ziegler, G. & Lesch, K.-P. 2021. Generation of induced pluripotent stem cell lines deficient for Cadherin 13 (UKWMPi002-A-1/B/C) associated with neurodevelopmental disorders using CRISPR/Cas9. *Stem Cell Research,* 51**,** 102169 (Vitale et al., 2021)

Janz A., Zink, M., Cirnu A., Hartleb A., Albrecht C., Regensburger M., Rost S., Klopocki, E., Günther K., Edenhofer, F., Ergün, S. & Gerull, B. 2021. CRISPR/Cas9-edited PKP2 knock-out (JMUi001-A-2) and DSG2 knock-out (JMUi001-A-3) iPSC lines as an isogenic human model system of arrhythmogenic cardiomyopathy (ACM). *Stem Cell Research,* 102256.

Abstracts for oral presentations

Characterization of molecular mechanisms underlying dilated cardiomyopathy with ataxia (DCMA) using pluripotent stem cell (iPSC)-derived cardiomyocytes. (2021) **HFA Winter Meeting on Translational Heart Failure Research 2021 "Digital – together – for our patients", Online Conference, the Heart Failure Association (HFA) of the European Society of Cardiology (ESC)**

Pluripotent stem cells in hereditary Cardiomyopathies. (2020) **Wissenschaftliche Klausurtagung der MedEins 2020, Lichtenfels, Germany**

iPSCs in inherited cardiomyopathies: from organotypic models to personalized therapy. (2019) **Wissenschaftliche Klausurtagung der MedEins 2019, Lichtenfels, Germany**

Abstracts for poster presentations

Janz A., Leskien M., Ueda Y., Regensburger M., Kohlhaas M., Nose N., Wörsdörfer P., Wagner N., Klopocki E., Higuchi T., Duff H., Maack C., Ergün S., Gerull B. (2020) DCMA in the dish: Decoding disease mechanisms with patient and genetically modified human iPSCell-derived cardiomyocytes. **HFA Winter Meeting 2020, the Heart Failure Association (HFA) of the European Society of Cardiology (ESC), Les Diablerets, Switzerland**

Janz A., Ueda Y., Kohlhaas M., Nose N., Wörsdörfer P., Wagner N., Mayer L., Higuchi T., Duff H., Maack C., Klopocki E., Ergün S., Gerull B. (2019) Inherited Cardiomyopathies in the dish: decoding disease mechanisms with human iPSC-derived cardiomyocytes. **Joint Symposium Heart Failure Interfaces, Deutsches Zentrum für Herzinsuffizienz/Deutsche Zentrum für Herz-Kreislauf-Forschung (DZHI/DZHK), Würzburg, Germany**

Janz A., Ueda Y., Kohlhaas M., Wörsdörfer P., Nose N., Wagner N., Maack C., Klopocki E., Ergün S., Gerull B. (2019) From stem cells to disease: human iPS cell-derived cardiomyocytes mimic different forms of inherited cardiomyopathies. **International Society of Stem Cell Research, ISSCR Annual Meeting, Los Angeles, USA**

Janz A., Ueda Y., Kohlhaas M., Wörsdörfer P., Nose N., Wagner N., Klopocki E., Ergün S., Gerull B. (2019) From stem cells to disease: human iPS cell-derived cardiomyocytes mimic different forms of inherited cardiomyopathies. **DGK " Deutsche Gesellschaft für Kardiologie" Herztage 2019, Mannheim, Germany**

Janz A., Ueda Y., Seibert D., Kohlhaas M., Nose N., Wörsdörfer P., Wagner N., Klopocki E., Ergün S., Gerull B. (2018) iPS Cells in Inherited Cardiomyopathies. **DGK " Deutsche Gesellschaft für Kardiologie" Herztage 2018, Berlin, Germany**

Janz A., Ueda Y., Seibert D., Kohlhaas M., Wörsdörfer P., Wagner N., Edenhofer F., Klopocki E., Ergün S., Gerull B. (2018) iPSCs in inherited cardiomyopathies: from organotypic models to personalized therapy (MY.9). ESAB "External Scientific Advisory Board", **Comprehensive Heart Failure Center (CHFC/DZHI), Würzburg, Germany**

Janz A., Ueda Y., Nose N., Kwok C. K., Wörsdörfer P., Knötgen N., Wagner N., Edenhofer F., Klopocki E., Ergün S., Gerull B. (2018) Development and characterization of patient-specific iPSC-derived cardiomyocytes model systems. **Heart Failure 2018 & World Congress on Acute Heart Failure, EACCME "European Accreditation Council for Continuing Medical Education", Vienna, Austria**

Janz A., Ueda Y., Nose N., Kwok C. K., Wörsdörfer P., Knötgen N., Wagner N., Edenhofer F., Klopocki E., Ergün S., Gerull B. (2018) iPS Cells in inherited cardiomyopathies: from organotypic models to personalized therapy. **Wissenschaftliche Klausurtagung der MedEins 2018, Hünfeld, Germany**

Janz A., Ueda Y., Nose N., Kwok C. K., Wörsdörfer P., Knötgen N., Wagner N., Edenhofer F., Klopocki E., Ergün S., Gerull B. (2017) iPS Cells in inherited cardiomyopathies: from organotypic models to personalized therapy. **12th International GSLS Student Symposium "EUREKA" – University of Würzburg, Würzburg, Germany**

Acknowledgements

First of all, I would like to thank **Prof. Dr. Brenda Gerull** cordially for giving me the opportunity to carry out my doctorate thesis under her supervision. I constantly encountered constructive and encouraging advice, guidance and support in countless discussions and meetings. Thank you for sharing your passion for science and innovation and giving me a surrounding to follow my ideas and explore my opportunities. Thank you for allowing me to learn how to grow beyond my limits and learn to achieve things I never thought I could, even if sometimes sweets were needed for our reinforcement.

Next, I express my gratitude towards **Prof. Dr. E. Klopocki**, **Prof. Dr. Süleyman Ergün** and **Prof. Dr. Frank Edenhofer** for willing to be part of my thesis committee and participate in annual meetings, giving useful consultations, creative scientific input, many inspirations for discussion or optimization ideas and finally the assessment of this thesis. I would also like to thank you for your help, especially for the karyotype analysis, the electron microscopical support, the education to cultivate stem cells and everything that goes with it. In particular I would like to thank also my teachers: **N. Nose**, **Dr. Y. Ueda**, **Dr. K. Günther**, **Dr. C. K. Kwok**, **Dr. D. Pühringer** and **Dr. P. Wörsdörfer** for giving me any advice, providing me control samples, the healthy NC6M iPSC-line as well as the helpful assistance to solve experimental problems.

I was fortunate to work in a group surrounded not only by colleagues, but by colleagues who became friends over time more and more. I would like to thank **all AG Gerull group members** for the permanently harmonious cooperation in the laboratory but also for sharing my cake and coffee addiction, you are all awesome! Importantly, I have to mention my `Stem Cell Group` members **Martina Regensburger, Anne Cilinc, Ruping Chen** and in particular **Alexandra Cirnu** for the willingness to work on weekends and above all for keeping the patience that stem cell cultivation entails. For experimental guidance I would like to thank in particular **Dr. Paula Arias**, **Dr. Ruping Chen**, **Alexandra Cirnu** and **Miriam Zink** for giving me constantly advice how an experimental set up can be improved and how problems could be solved with focus on the individual scientific question. Thanks also to **Dr. T. Williams** for your work in official matters, for controlling the laboratories and for teaching me how to handle matters of authority. Thanks to **Susanna Schraut, Anne Kilinç, Anna Karina Lamprecht, Annette Berbner, Daniel Oppelt** and **Michelle Gulentz** for being gracious and lively colleagues but most of all, for keeping the labs going, nothing in the labs would be possible without you.

I would like to make a special mention of my great office neighbor **Miriam Zink**, for the shared suffering, for the tremendous help, for the respectful interaction and friendship that I appreciated so much for the last 4.5 years. Thank you for everything, I cannot find words with which to express my gratitude. I am looking forward to an `after Corona time` to enjoy badminton playing, the recapitulation, or even better, the planning of our vacations, eating Fontana salads and drinking a glass of wine with you. I will always remember our summer lunch breaks in the sun in front of the DZHI building to grab a piece of freedom.

Likewise, I thank **Alexandra Cirnu** for many long hours together in the lab- we were a great team I will miss it a lot! I am thankful for your scientific and mental support and your positive attitude from scratch! With no one than you I could reach so deep into not only the scientific topics but above all in almost every subject area, ranging from sports to culture to food to adventures. You are such a passionate, lovely and tremendously helpful person, without you I would have not been able to do that. Thank you for all the laughing, as you know `it is all a fucking network`. Thank you also for proof-reading and constructive discussions of this thesis despite your workload, I really appreciate your time and hope that one day I can compensate it. In addition, thanks to you, I am able to reach my foot tip again (Yoga). Moreover, I also need to apologize for the `post-it infection`. You are extremely intelligent, hardworking and your understanding of science is incomparable. I am honored to have worked with you and I am sure that one day you will become a famous scientist (or someone else).

Applause for the greatest technician on the planet, **Martina Regensburger**. You know how much you helped me day by day. I am so happy that I was honored to work with you, you are so passionate, so lovely and one of the greatest persons I was ever allowed to meet. Thank you, Martina, for being

constantly helpful, encouraging and positive. Your expertise and your personal attitude were very valuable to me!

A huge thank you also to the current and former AG Gerull members for a nice and creative working atmosphere. Thanks to **Anne Seewald, Miriam Leskien, Alicia Schenzel, Desiree Seibert** and **Annika Hartleb** that working with you during your studies was always fun. You have always done a great job, even though data evaluations were sometimes painful. Big thanks for your reliability, through your independence you have made my life a lot easier.

At this point, I would like to mention my fellow sufferers **Miriam Zink, Antonella Cellini, Ilona Kutschka, Eduardo Bertero** and **Johanna Zöller** as well as my "Stammzell-Selbsthilfegruppe" **Dr. Thomas Klein** and **Dr. Charline Jensch** for sharing my sarrow with your sarrow. Yet I know that without your sympathy and understanding I would not have been able to fight my way through it for the last 4.5 years. What you have gone through all this time amazes me day after day. Thanks to you, I was able to learn that all hurdles, even if they seem so impossible, can somehow be overcome, you are my `superheros`.

In the following I would like to acknowledge our collaborators from our or other institutes, thank you for contributing to my project!

First of all, I would like to thank **Dr. M. Kohlhaas** for explaining the IonOptix measurements, their evaluations and the help with the data interpretation. Without your knowledge, it would not have been possible for me to collect these data sets using iPSC-CMs, thank you for your time-consuming help at all times. At this point I would also like to thank the whole group of **Prof. Dr. C. Maack** and **Dr. J. Dudek** for the patience and the help in understanding mitochondrial complexity. Thanks a lot, to **Dr. V. Siqueira** for proof reading and the constructive criticism to improve this thesis. Thanks also to our neighbors in level -1, especially I would like to thank **Saskia Mühlig** and **Lars Mayer** in the group of **Prof. Dr. T. Higuchi** for being loyal and helpful colleagues and for their help for the tracer uptake studies. Furthermore, **Dr. Nicole Wagner** (Institute of Anatomy and Cell Biology, Würzburg) and **Prof. Dr. C. Stigloher** (Imaging Core Facility Biozentrum Hubland, Würzburg) helped me with the preparation acquisition and interpretation of TEM images. **Dr. Ruping Chen** assisted during the flow cytometry of iPSC characterization. Further, I would like to thank **Dr. Werner Schmitz** (Core Unit Metabolomics, Biozentrum Hubland, Würzburg) together with again **Alexandra Cirnu** for their contribution to this thesis by mass spectrometric analysis. Moreover, I would like to thank **Dr. Simone Rost** (Institute of Human Genetics, Biozentrum Hubland, Würzburg) for STR profile and **Dr. Konstantinos Kolokotronis** for whole exome sequencing analysis. As the objectives of this project required primary tissue of various origin, I am very grateful to all participants who were willing to donate tissue and for **Prof. Dr. Henry Duff** for obtaining the cells.

I am very thankful to **Dr. Gabriele Blum-Oehler** and the **GSLS team** for being supportive, constantly informative and very friendly. Getting enrolled into the GSLS was a nice experience, not only because of the courses, but to a great part because of the interesting and openminded people I could meet within the last years. Thanks for giving my thesis a framework and for the opportunity to get international experiences.

In the following I would like to acknowledge my family and my friends!

I would have never come this far without the love, trust and never-ending support of my mother **Nadeschda Altmann**, my most magnificent brother **Jesse Janz** and my absolute unique sister **Olga Werbitzky**. You are the strongest, most pragmatic and optimistic people I know! Thanks for daily encouragement with super sweet videos of the sweetest child on earth **Fynn** and the funniest Brother-in-law **Sven Werbitzky.** The biggest thanks goes to my sister **Olgi** who accompanied me through every single crisis and helped me never to give up, you are my absolute role model, thanks to you I am the person I am today, which I am very proud of! Without you, I would not be complete.

Thanks to my whole **family `Janz`** for the support but most importantly for the understanding that I often had to cut back because of work. I love you all so much, you are the greatest family anyone could ever imagine!

Next, I have to mention my closest friends **Olesja Garcia Scaglione (Glis), Mona Moll, Marlene Köhler (Mahlö), Sabine Talstov (Erich), Irina Eisele (Inchen), Kim Schell (Scè), Stefanie Appenzeller (Kloi), Nicole Weiß (Collipo)** und **Stefanie Rösel (Schnossa)**. Thanks for being my `**Schneidels**` and my friends even though I was the worst friend one could imagine. We were going and will go through everything together, although half of the time not at the same location. Thank you for being my true friends and believing in me! You are the best and I am proud to say, that I can always count on you no matter what happens, I love you!

Last, but for me the most supportive, patient, funniest, adventurous, honest, trust worthiest and heartwarming person, my love **Fabian Aldinger**. Through you I can experience every day how beautiful life can be, how much there is to experience and what really matters. I think you suffered the most and am infinitely grateful for your strength and patience. I don't know how I can ever give back to you the way you strengthened me the last years, but I will try day by day. Thank you for being exactly who you are, you are my `Swabian` - Manas!

Affidavit

I hereby confirm that my thesis entitled "**Human induced pluripotent stem cells (iPSCs) in inherited cardiomyopathies: Generation and characterization of an iPSC-derived cardiomyocyte model system of dilated cardiomyopathy with ataxia (DCMA)**" is the result of my own work. I did not receive any help or support from commercial consultants. All sources and / or materials applied are listed and specified in the thesis. Furthermore, I confirm that this thesis has not yet been submitted as part of another examination process neither in identical nor in similar form.

Würzburg, Signature

Eidesstattliche Erklärung

Hiermit erkläre ich an Eides statt, die Dissertation „**Humane induzierte pluripotente Stammzellen in vererbbaren Kardiomyopathien: Generierung und Charakterisierung eines auf Stammzellen basierenden Herzmuskelmodellsystems der Dilatativen Kardiomyopathie mit Ataxie (DCMA)**" eigenständig, das heißt insbesondere selbständig und ohne Hilfe eines kommerziellen Promotionsberaters, angefertigt und keine anderen als die von mir angegebenen Quellen und Hilfsmittel verwendet zu haben. Ich erkläre außerdem, dass die Dissertation weder in gleicher noch in ähnlicher Form bereits in einem anderen Prüfungsverfahren vorgelegen hat.

Würzburg, Unterschrift